Titre: Title:	Développement d'un modèle Euler-Lagrange robuste pour la simulation des écoulements solide-liquide dans les opérations de mélange
Auteur: Author:	Bruno Blais
Date:	2016
Type:	Mémoire ou thèse / Dissertation or Thesis
Référence: Citation:	Blais, B. (2016). Développement d'un modèle Euler-Lagrange robuste pour la simulation des écoulements solide-liquide dans les opérations de mélange [Thèse de doctorat, École Polytechnique de Montréal]. PolyPublie. https://publications.polymtl.ca/2219/

UNIVERSITÉ DE MONTRÉAL

DÉVELOPPEMENT D'UN MODÈLE EULER-LAGRANGE ROBUSTE POUR LA SIMULATION DES ÉCOULEMENTS SOLIDE-LIQUIDE DANS LES OPÉRATIONS DE MÉLANGE

BRUNO BLAIS
DÉPARTEMENT DE GÉNIE CHIMIQUE
ÉCOLE POLYTECHNIQUE DE MONTRÉAL

THÈSE PRÉSENTÉE EN VUE DE L'OBTENTION
DU DIPLÔME DE PHILOSOPHIÆ DOCTOR
(GÉNIE CHIMIQUE)
AOÛT 2016

UNIVERSITÉ DE MONTRÉAL

ÉCOLE POLYTECHNIQUE DE MONTRÉAL

Cette thèse intitulée :

DÉVELOPPEMENT D'UN MODÈLE EULER-LAGRANGE ROBUSTE POUR LA SIMULATION DES ÉCOULEMENTS SOLIDE-LIQUIDE DANS LES OPÉRATIONS DE MÉLANGE

présentée par : BLAIS Bruno
en vue de l'obtention du diplôme de : Philosophiæ Doctor
a été dûment acceptée par le jury d'examen constitué de :

M. SRINIVASAN Bala , Ph. D, président
M. BERTRAND François, Ph. D., membre et directeur de recherche
M. PELLETIER Dominique, Ph. D., membre
Mme KRESTA Suzanne Marie, Ph. D., membre externe

DÉDICACE

"Tous les genres sont bons, sauf le genre ennuyeux."
François-Marie Arouet, dit Voltaire

"Not encouraging students to question knowledge, society, and experience tacitly endorses and supports the status quo."
Ira Sher

"Autant tenter un salto avant d'échouer au pied du mur"
Orelsan

REMERCIEMENTS

A priori, je crois qu'il est de mise de remercier mon directeur de recherche, François Bertrand, de m'avoir permis de réaliser ce travail non conventionnel. Son support, sa confiance, sa disponibilité, son optimisme et sa créativité ont grandement contribué à la réussite de ce projet. Surtout, c'est la liberté qu'il m'a conférée qui m'a permis de développer les solutions novatrices amenées dans cette thèse. Sans son apport et les constantes remises en question qui ont émané de ses questions, l'aboutissement de cette thèse serait, j'ose le croire, bien moins intéressant [1].

J'aimerais remercier Louis Fradette, mon co-superviseur non officiel, pour toute l'aide qu'il a pu m'apporter sur l'analyse de mes résultats ainsi que sur tout ce qui se rattachait à l'expérimentation. Sa capacité à trouver solution à tout m'étonne encore à ce jour.

Ce projet fut réalisé en collaboration avec deux étudiants à la maîtrise : Manon Lassaigne et Olivier Bertrand. Manon, je te remercie de m'avoir redonné foi dans le travail en équipe et d'avoir été une coéquipière si formidable. Olivier, j'espère que tu garderas la même attitude positive et allumée jusqu'à la fin de ta maîtrise. C'est ce qui fait de toi non seulement un bon scientifique, mais quelqu'un de si intéressant en général.

J'ai eu la chance, durant ces quatre années de doctorat, de côtoyer des gens formidables [2] : Alexandre (Ahmad) Al-haiek, David Vidal, Warren Sanhye, Guillaume Matte-Deschênes, Vincent Stobiac, Daniel Chauveheid, Hicham Khelladi, Jean-Michel Tucny (mon padawan), Julie Olmicia, Mohammad Ghodratnama, Jean-Christophe Saint-Charles, Yoann Guntzberger, Marine Madinina... et j'en oublie sûrement. Je ne saurais jamais assez vous remercier.

J'aimerais aussi remercier ma gang du baccalauréat en génie chimique : Stephan Letourneau, Laurent Oligny, Cédric Vallée, Alex Castongay, Alexis Brien, Guillaume (Teurf) Lauzon, Massimo Cimmino, Antoine Simoneau, d'avoir toujours cru en ma capacité à faire un doctorat. Si j'avais eu le dixième de la confiance que vous avez pu avoir en moi, mon parcours aurait été parsemé de moins d'angoisses.

Je souhaiterais remercier ma famille, qui a toujours été la pour me supporter dans tout mon cheminement. Mon père Claude, de m'avoir toujours encouragé à poser des questions et d'avoir toujours su alimenter ma curiosité. Ma mère Diane, pour sa douceur, son calme et son empathie. Mon frère Jean-François, d'avoir toujours su me prodiguer de judicieux conseil et d'avoir été le premier scientifique que j'ai pu côtoyer. À mes yeux, il restera toujours le

1. En supposant que la thèse actuelle vous intéresse...
2. Énoncés dans un ordre quelconque

meilleur.

Finalement, j'aimerais remercier ma copine, Christine Beaulieu, pour tous ses encouragements, sa douceur, sa patience sans fin et son optimisme sans borne. Je la remercie d'être là et d'aimer elle aussi les pandas, les loups, les alpagas, les chèvres, les ours polaires, les quetzals, les canards indiens coureurs, les renards polaires, les hordes de bergers allemands, les ratels (ou blaireau à miel) et tous les autres animaux particulièrement mignons, doux ou tout simplement intéressants...

RÉSUMÉ

Les opérations de mélange solide-liquide en cuves agitées jouent un rôle clef dans de nombreux procédés, que ce soit dans la fabrication de produits alimentaires, pharmaceutiques, cosmétiques, ou pour promouvoir l'homogénéité de suspensions, ce qui est particulièrement vital au bon fonctionnement des réacteurs chimiques employant un catalyseur solide. Malgré leur importance indéniable pour l'industrie chimique et les efforts considérables qui ont été déployés afin de mieux les comprendre, la conception et l'optimisation de ces opérations demeurent un grand défi. En effet, la quasi-totalité de la littérature se concentre sur le régime d'opération pleinement turbulent, malgré le fait que de nombreux procédés industriels soient opérés en régimes laminaire ou transitoire. Malheureusement, la littérature sur ces derniers régimes d'opération est quasi-inexistante.

De plus, bien que le régime d'opération turbulent ait fait l'objet d'un grand nombre d'études, celles-ci se sont principalement concentrées sur la prédiction, à l'aide de corrélations empiriques ou semi-empiriques, de la vitesse nécessaire pour la suspension complète des particules (N_{js}), c'est-à dire la vitesse d'agitation nécessaire pour suspendre toutes les particules hors du fond de la cuve. Cependant, de nombreux procédés pourraient être opérés dans des conditions différentes telles que la suspension partielle ou complètement homogène. Le premier cas permettrait d'économiser de l'énergie et d'éviter des contraintes trop fortes sur l'agitateur, tandis que le second assurerait une cinétique de réaction et une qualité de produit nettement mieux contrôlée. Dans ces deux situations, la connaissance de N_{js} n'est que d'une aide limitée. Pour mieux opérer et concevoir ces unités, il est nécessaire de pouvoir prédire la distribution et la dispersion des particules solides ainsi que les patrons d'écoulement au sein de la cuve.

L'étude des systèmes de mélange solide-liquide représente une difficulté importante, car l'opacité des suspensions solide-liquide limite fortement la mesure de variables locales telles que les profils de concentration. Ainsi, la majeure partie des travaux expérimentaux n'ont mesuré que des paramètres globaux, tels que le couple sur l'agitateur, la fraction de particules suspendues ou N_{js}. La mécanique des fluides numérique (CFD), complémentaire à l'expérience, permet quant à elle d'investiguer à la fois les paramètres globaux, mais aussi ce qui se passe localement en tout point de la cuve. Cependant, la modélisation d'écoulements multiphasiques renferme de nombreux défis compte tenu de l'interaction multiéchelle (de temps et d'espace) entre les phases.

Les nombreux modèles capables de modéliser ces types d'écoulements sont décrits dans cette thèse, dans l'objectif de faire ressortir leurs forces ainsi que leurs limites. Parmi ceux-ci, il est

montré que seuls les modèles à deux fluides, où la phase solide est modélisée comme un second fluide, ont été utilisés exhaustivement pour aborder le mélange solide-liquide. Cependant, ces modèles souffrent d'une incapacité à bien décrire les régimes rapides et denses d'écoulement granulaire (comportement de Burnett et de super Burnett) ainsi que de plusieurs difficultés à saturer la concentration de solide lorsque les particules sont à leur fraction maximale d'empilement. La CFD-DEM, une famille de modèles relativement récents qui combinent la CFD pour la phase fluide et la méthode des éléments discrets (DEM) pour les particules solides permet quant à elle de décrire la dynamique de la phase granulaire avec un grand degré de précision et a largement fait ses preuves dans l'étude de milieux solide-gaz. Cependant, cette méthode n'a jamais été employée rigoureusement pour l'étude d'écoulement solide-liquide dans des géométries complexes telles que des mélangeurs. Pour que ceci soit possible, de nombreux développements mathématiques sont nécessaires afin de s'assurer que le schéma soit stable, qu'il converge (en temps et en espace) et qu'il soit capable de simuler des géométries complexes en mouvement tels que les agitateurs. La conception d'un tel modèle et son application à l'étude de la dynamique du mélange solide-liquide et de la mise en suspension de particules solides est l'objectif principal de cette thèse.

En premier lieu, un schéma volume fini de type *Pressure Implicit with Splitting of Operator (PISO)* pour résoudre les équations de Navier-Stokes moyennées volumiquement (VANS), nommé PISO-VANS, est établi. La résolution de ces équations est une partie essentielle d'un modèle CFD-DEM applicable à des écoulements concentrés. Afin de vérifier la cohérence du schéma PISO-VANS pour la résolution des équations VANS, une méthodologie basée sur la méthode des solutions manufacturées est développée afin d'établir des cas tests analytiques permettant d'effectuer des tests de convergence numérique. Ces tests, les premiers de ce genre, démontrent que le schéma proposé converge à la précision désirée, c'est-à-dire qu'il est bien de second ordre en temps et en espace.

Ensuite, cette méthodologie est employée pour vérifier un nouveau schéma permettant de résoudre les équations VANS avec la méthode de Boltzmann sur réseau (LBM). Ce schéma est basé sur un nouvel opérateur de collision. Il est démontré, à l'aide d'une analyse de Chapmann-Enskogg, que la formulation proposée permet de retrouver les équations VANS. Cet opérateur est le premier permettant de résoudre les équations VANS avec la LBM lorsque la fraction volumique n'est pas constante dans l'espace, une capacité essentielle pour l'étude d'écoulements polyphasiques ou dans des milieux poreux.

Dans la troisième partie de ce travail, une nouvelle méthode de condition immergée semi-implicite permettant de modéliser des corps rigides en rotation est développée. Cette méthode est conçue pour bien s'harmoniser avec le schéma PISO et pour être fonctionnelle sur un

maillage non structuré polyédrique tout en demeurant parallèle. Cette méthode est tout d'abord vérifiée sur des cas tests académiques tels que l'allée de von Karman derrière un cylindre, ainsi qu'un écoulement de Taylor-Couette entre deux cylindres. Il est montré que le schéma peut bien reproduire les vortex de von Karman, mais qu'il dégrade l'ordre du schéma volume fini de 2 à 1.33 dans le cas de l'écoulement de Taylor-Couette. Le schéma est finalement validé expérimentalement et comparé à d'autres méthodes numériques permettant de simuler des géométries en rotation. Un accord quasi parfait est obtenu.

La quatrième partie de ce travail résulte directement de la combinaison du schéma volume fini PISO-VANS avec la méthode de conditions immergées afin de simuler le mélange solide-liquide, du démarrage au régime permanent, à l'aide de la CFD-DEM. Différentes stratégies de couplage entre les phases sont testées et il est montré que, contrairement au cas gaz-solide, un couplage explicite est préférable, car il atténue les erreurs de moyenne volumique. Il est aussi démontré qu'un modèle de rhéologie est nécessaire afin de considérer la dissipation à l'échelle inférieure à une taille de maille. Le modèle complet est ensuite validé qualitativement, en comparant des profiles particuliers d'écoulements obtenus au début de la suspension des particules, et quantitativement, à travers la comparaison avec l'expérience de la fraction de particules suspendues mesurée par la technique de pression de jauge (PGT). À nouveau, un excellent accord est obtenu entre les données expérimentales et les résultats du modèle.

Dans la cinquième partie de ce travail, le modèle CFD-DEM est modifié afin de permettre l'étude des écoulements turbulents à l'aide de la simulation aux grandes échelles turbulentes (LES). Suite à une validation avec l'expérience, deux nouvelles techniques de mesure de la fraction de particules suspendues, l'analyse lagrangienne de fraction suspendue (LSFA) et l'analyse de fraction de décorrélation (DFA), sont introduites. Les résultats issus de ces méthodes sont ensuite comparés à ceux obtenus numériquement et expérimentalement par la méthode de pression de jauge. Il est montré que ces deux méthodes sont pratiquement aussi précises que la PGT, mais qu'elles sont aussi plus versatiles, car elles peuvent être appliquées à toutes les géométries et ne nécessitent pas de simulations sur des larges plages de vitesse d'agitation.

Dans la sixième partie de ce travail, le modèle CFD-DEM est utilisé pour étudier en détail le mélange solide-liquide en régime laminaire et transitoire. Notamment, l'impact du dégagement de l'agitateur et de la présence de chicanes sur la fraction de particules suspendues et la dynamique du mélange solide-liquide est établi. Il est montré que de réduire le dégagement au fond de l'agitateur permet de prévenir l'apparition de zone mortes à haute vitesse. De surcroît, une étude de sensibilité sur les paramètres de la DEM est effectuée et montre que seule la friction entre les particules joue un rôle significatif sur la dynamique de la phase

solide.

Finalement, une brève discussion permet de résumer les résultats obtenus et de donner de nombreuses pistes de travaux pouvant faire suite à ce qui fut développé dans le cadre de cette thèse.

ABSTRACT

Despite the fact that solid-liquid mixing plays a key role in the production of a wide variety of consumer goods such as pastes, paints, cosmetics, propellants, pharmaceuticals, and food products as well as in the operation of chemical reactors with solid catalysts, it still faces considerable challenges. Most research on solid-liquid mixing has focused on the fully turbulent regime of operation even though many industrial operations take place in the laminar or transitional regime. In particular, it is unclear how the rheology of a suspension, particle interactions, and a complex rotating geometry impact flow patterns and particles distribution and dispersion in these regimes.

Although more is known about the turbulent regime of operation, most research on this type of regime has been devoted to the prediction of the just-suspended speed (N_{js}), which is the impeller speed at which all particles are suspended in the liquid phase. However, numerous mixing operations require a different state of operation. For these processes, operating at N_{js} can lead to energy overconsumption, product fouling, or inhomogeneous reactions due to the presence of dead zones. Consequently, more information on the velocity patterns and distribution of particles in agitated vessels is required. To shed light on issues related to solid-liquid mixing, numerical and experimental investigations are essential. However, due to the opacity of most viscous suspensions, local measurements of the flow field using optical techniques are highly problematic. Consequently, almost all experimental measurements have been limited to determining the global characteristics of the mixing flow such as the fraction of suspended particles or the torque acting on the impeller. However, CFD simulations of these systems do not suffer from these drawbacks. A variety of models have been developed to simulate solid-liquid flows. These include the classic Eulerian-Eulerian (or two-fluid) model and the combination of the Discrete Element Method (DEM) for the particles and CFD method for the liquid phase (CFD-DEM). Although it possesses enormous potential due to its formulation, notably as regards to its natural capacity to reproduce the maximal packing fraction of solid particles, the ability of the CFD-DEM approach to accurately model solid-liquid flows in complex geometries has not yet been proved. In addition, the method has not been validated experimentally for solid-liquid flows. However, this type of model could theoretically allow for a quantitative assessment of flow patterns, particle distributions, and the fraction of suspended particles.

In this thesis, a CFD-DEM model is developed to model the suspension of particles in a stirred tank, from start-up to steady state and in all regimes of operation. The model is

used to improve our understanding of solid-liquid mixing, notably the issue of predicting the fraction of suspended particles. It is shown to be a quantitative tool that can predict the state and dynamics of a suspension.

A methodology is designed to verify a Pressure Implicit with Splitting of Operator (PISO) scheme for the volume-averaged Navier-Stokes (VANS) equations (Article 1). We recall that these equations are essential for the unresolved CFD-DEM method. The methodology, which is based on the method of manufactured solutions, is used to design analytical solutions for the VANS equations for which order of convergence analyses are carried out. The validity of the semi-implicit scheme is established by demonstrating the second-order convergence of the scheme for various complex 2D cases.

A novel collision operator for the Lattice Boltzmann Method (LBM) is designed to solve the VANS equations (Article 2). It is demonstrated analytically that this operator solves the VANS equations with second-order accuracy. Numerical test cases designed using the process established in Article 1 were used to confirm these results. The model is able to solve cases where there are large void fraction gradients in the domain. To our knowledge, is the first time that this has been achieved.

A semi-implicit immersed boundary method (PISO-IB) is developed to study rotating rigid bodies such as impellers (Article 3). The method is verified using academic test cases, namely the Taylor-Couette flow and the Von Karman vortex street behind a static and a moving cylinder. The scheme accurately reproduces vortex shedding, but degrades the order of convergence of the overall finite volume scheme from 2 to 1.33 in the Taylor-Couette case. The PISO-IB method is validated for single phase mixing, and good agreement is obtained between this method and experimental torque measurements.

The methods developed in the first and third sections are then combined to formulate a CFD-DEM scheme for solid-liquid mixing (Article 4). The formulation of the model is analyzed, and two coupling approaches (implicit and explicit) are investigated. Explicit coupling leads to a more stable scheme for viscous fluids. However, due to unresolved hydrodynamic dissipation at the particle scale, a rheology model be introduced into the model. The complete model is validated qualitatively using photographs of the peculiar particle dynamics observed experimentally as well as quantitatively by comparing the fraction of suspended particles measured numerically with experimental data obtained using the pressure gauge technique.

The validated CFD-DEM model is extended to the turbulent regime using a large-eddy simulation (LES) approach (Article 5). The model accurately reproduces the fraction of suspended particles measured experimentally. Two new techniques to calculate the fraction of

suspended particles, the Lagrangian suspended fraction analysis (LSFA) and the decorrelated fraction analysis (DFA), are developed. These two techniques can be used to calculate the fraction of suspended particles for any vessel bottom, without requiring the simulation of numerous impeller velocities, something that cannot be accomplished using the pressure gauge technique.

The entire set of tools described in the previous article is used to study the suspension of solid particles in the laminar and transitional regimes in detail (Articles 6). A parametric study of the model parameters is performed. It shows that only the coefficient of friction plays a role in the solid dynamics. Alternative geometries are also studied by varying the impeller clearance and by adding or removing baffles. These results show that reducing the clearance results in a better distribution of particles and prevents the creation of a dead zone below the impeller.

This thesis finishes with a short discussion of the overall capabilities of the model and future research that could arise from it.

TABLE DES MATIÈRES

LISTE DES TABLEAUX

LISTE DES FIGURES

LISTE DES SIGLES ET ABRÉVIATIONS

CFD	Computational fluid dynamics
DFA	Decorrelated fraction analysis
DEM	Discrete element method
FEM	Finite element method
FVM	Finite volume method
LBM	Lattice Boltzmann method
LAMMPS	Large-scale atomic/molecular massively parallel Simulator
LES	Large-eddy simulation
LIGGGHTS	LAMMPS improved for general geometry and granular heat transfer simulations
LSFA	Lagrangian suspended fraction analysis
MD	Molecular dynamics
MP-PIC	Multiphase particle-in-cell method
MRF	Multiple reference frame
Open∇FOAM	Open field operation and manipulation
PISO	Pressure implicit with splitting of operator
PGT	Pressure gauge technique
QDM	Quantité de mouvement
QMOM	Quadrature method of moments
RPT	Radioactive particle tracking
SRF	Single Rotating Frame
SM	Sliding mesh
TGI	Tangent-intersection analysis
UVC	Unsuspended volume criterion
VANS	volume-averaged Navier-Stokes

LISTE DES ANNEXES

CHAPITRE 1 INTRODUCTION

Le mélange fait intimement partie de notre quotidien. Que ce soit en brassant un café après y avoir déposé un cube de sucre [1], ou bien lors de la préparation d'une vinaigrette qu'on doit agiter vigoureusement, nous mélangeons des composantes afin d'obtenir quelque chose d'homogène.

Cette action nous semble intuitive, voire primaire. Brasser et agiter sont des gestes qu'il n'est pas nécessaire d'inculquer aux plus jeunes. Cependant, dans des applications demandant davantage de finesse, lorsque le maître pâtissier prépare un gâteau meringué, ou lorsqu'utilisé à l'échelle industrielle, dans des mélangeurs à cuve agitée dont le diamètre est de plusieurs mètres, le mélange ne peut s'effectuer de manière simpliste. Dans le premier cas, un certain degré de technique est nécessaire afin de battre les blancs d'œufs de manière à incorporer l'air à l'œuf tout en fragmentant les bulles d'air introduites par le mouvement azimutal du fluide afin d'obtenir la texture et la consistance désirée [118]. Dans le second cas, il est nécessaire de concevoir des systèmes de mélange de larges tailles permettant un mélange efficace, homogène et dépourvu de zones mortes, tout en respectant les autres contraintes du procédé. À l'instar du maître pâtissier agitant sa meringue en motif de huit, la solution requiert ici aussi un certain degré de finesse. L'augmentation de la vigueur de l'agitation n'est, dans la majeure partie des cas, pas une solution pratique même si elle apparait comme la plus évidente. Elle mène à une surconsommation majeure d'énergie et nécessite un surdimensionnement des équipements sans être garante d'un quelconque succès. Au grand malheur de l'industriel, mais au bonheur du scientifique, la manière de Calliclès [2] ne s'applique pas au mélange : le plus puissant n'est pas nécessairement celui qui mélange le mieux.

Définir l'homogénéité, qui est souvent le but ultime du mélange, se révèle une problématique particulière qui fait fortement appel à une interprétation spatiale de la matière. L'exemple le plus simple est celui d'un simple verre de lait. À l'œil humain, le lait apparaît comme un mélange homogène, doté d'une couleur uniforme et se comportant comme un milieu continu. Cependant, le lait est un mélange d'eau et de multiples composantes : de la graisse, de la caséine et des sels minéraux. À l'échelle microscopique, ces composantes sont présentes sous forme de phases discrètes. Ce sont ces éléments discrets qui diffractent la lumière et qui confèrent sa couleur blanchâtre au lait. Ainsi, l'homogénéité ne peut pas être définie comme un état inhérent de la matière, mais dépend de l'échelle à laquelle un mélange est observé. À

1. Personnellement je le préfère noir, court et bien serré...

2. Personnage clef du Gorgias de Platon. Calliclès s'oppose à la vision socratique du sociétaire comme entité dominante, y opposant plutôt la loi du plus fort.

la Figure 1.1, chaque trait de pinceau dépeignant le crépuscule de San Giorgio Maggiore est d'une seule couleur. Pourtant si on observe la peinture de suffisamment loin, les couleurs du crépuscule semblent varier de manière continue d'un bleu royal au rouge chaleureux du soleil couchant.

Figure 1.1 San Giorgio Maggiore au crépuscule par Claude Monet, tiré de [324]

À chaque procédé industriel correspond une échelle d'homogénéisation qui lui est propre. Ces procédés font intervenir diverses opérations de mélange qui sont généralement classifiées selon la ou les phases (ou états) en leur sein : liquide, solide et gazeuse. Par exemple, il peut être nécessaire d'homogénéiser un mélange de poudres dont un des constituants est un ingrédient actif afin de formuler un comprimé médicamenté. Dans ce cas, nous serons en présence d'un mélange solide (ou granulaire). Dans un second cas, nous pourrions chercher à mélanger deux liquides immiscibles (tels que de l'huile et de l'eau) afin de produire une émulsion (par exemple, une vinaigrette). Ce type d'opération sera qualifié de mélange liquide-liquide, car deux phases liquides distinctes coexistent. Finalement, dans un réacteur chimique en phase liquide dont la réaction nécessite un catalyseur, il peut être nécessaire de suspendre des particules afin de garantir une aire de contact suffisante entre les phases liquide et solide. L'étude de ce type d'opération, baptisé mélange solide-liquide, est l'objet de cette thèse.

Les opérations de mélange solide-liquide jouent un rôle important dans de nombreux procédés

industriels. En effet, elles sont importantes pour les industries minières, pharmaceutiques et agroalimentaires [245]. Ces opérations ont souvent lieu dans des cuves, munis ou non de contre-pales et qui sont agitées par un ou des agitateurs disposés sur un ou plusieurs arbres d'agitation assurant le mélange. De nombreux types d'agitateurs existent et ceux-ci sont classifiés par le patron d'écoulement qu'ils génèrent en proximité de l'agitateur : axial, radial, mixte et de proche paroi.

Dans les opérations de mélange solide-liquide, l'objectif primaire est de mettre en suspension les particules afin de les distribuer dans l'ensemble du volume de liquide, tout en dispersant les agrégats pouvant se former localement. La distinction entre ces deux notions, la distribution et la dispersion, est illustrée à la Figure 1.2.

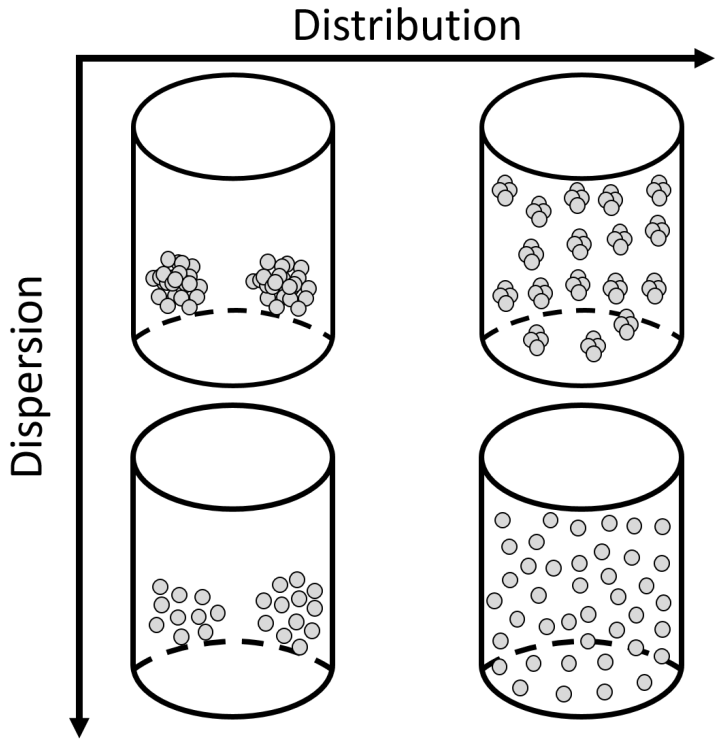

Figure 1.2 Un des objectifs principaux des opérations de mélange solide-liquide est d'obtenir une haute distribution et une haute dispersion. Figure inspirée de [245]

De la même manière que la caractérisation de l'homogénéité dépend de l'échelle d'observation, les procédés de mélange solide-liquide ont des visées bien différentes qui dépendent du besoin industriel. Pour la majeure partie des procédés, il est suffisant de suspendre les particules hors du fond de la cuve afin de maximiser la surface de contact entre les particules et le fluide. Certains réacteurs chimiques, pour les opérations agroalimentaires ainsi que pour

les cristallisoirs, requièrent que la concentration en solide soit homogène partout dans la cuve. Pour les cristallisoirs, les gradients de concentration en solide ont des conséquences dramatiques sur la taille et la qualité des cristaux. Une homogénéité quasi parfaite est alors souhaitée. Pour d'autres opérations, de fortes économies d'énergie peuvent être réalisées en opérant dans des conditions de suspension partielle, sans même affecter la qualité du produit final ou la fiabilité de l'opération. Compte tenu de ces besoins variés, la conception de ces opérations est d'une complexité déroutante. Cette dernière est exacerbée par les interactions entre le fluide et les particules qui a lieu sur un large éventail d'échelles de temps et de longueur. Il est donc nécessaire de se doter d'outils permettant de prédire les écoulements dans ces cuves agitées ainsi que : la distribution et la dispersion des particules, la puissance consommée, la fraction de particules suspendues et le temps de mélange.

La mécanique des fluides numérique (CFD, de l'anglais *Computational Fluid Dynamics*) consiste à résoudre les équations de la mécanique des fluides à l'aide d'ordinateurs [3]. Il s'agit d'un outil performant qui permet de prédire quantitativement l'écoulement au sein de cuves agitées. Bien que largement développée pour des écoulements monophasiques, l'utilisation de la CFD pour étudier des écoulements multiphasiques demeure un défi considérable. La CFD représente la clef de voûte qui permettra de comprendre et de prédire les écoulements dans des géométries complexes telles que les cuves agitées.

Ce projet de doctorat porte sur le développement et sur l'utilisation de la CFD multiphasique. L'objectif final de ce projet est de concevoir un modèle numérique qui pour prédire le degré de suspension ainsi que la répartition de particules solides dans des configurations géométriques réalistes et d'utiliser ce modèle afin de comprendre la dynamique du mélange solide-liquide au sein de cuves agitées. Originalement, la portée de ce travail était restreinte aux régimes laminaire et transitoire, mais les résultats positifs obtenus ont permis d'aborder la problématique particulière du régime turbulent d'opération.

Dans le cadre de cette thèse, une revue de littérature étendue sera d'abord réalisée. L'objectif général de la thèse sera ensuite reformulé en fonction de l'état de l'art et les objectifs spécifiques seront établis. La structure de la thèse sera ensuite détaillée. Une attention particulière sera consacrée au lien unissant les chapitres issus des six contributions (ou articles) réalisées en tant que premier auteur ainsi qu'à la contribution réalisée comme second auteur (en annexe). Une discussion permettra ensuite de conclure de manière plus générale sur les contributions scientifiques issues de cette thèse et abordera des suggestions pour des travaux futurs pouvant en découler.

3. De tailles variables...

CHAPITRE 2 REVUE DE LITTÉRATURE

Compte tenu de la nature pluridisciplinaire de cette thèse, qui combine à la fois les mathématiques appliquées, la modélisation numérique ainsi que les procédés de mélange, la revue de littérature se doit d'aborder un large éventail de sujets. C'est aussi pour cette raison que bien que la conception d'un modèle numérique polyphasique et son application à l'étude du mélange solide-liquide soient le coeur de ce travail, ces thématiques ne sont pas abordées avant les sections 2.5 et 2.6 respectivement.

En premier lieu, des notions fondamentales sur la mécanique des fluides, plus principalement sur les équations de Navier-Stokes et les problématiques de rhéologie et de turbulence s'y rattachant, sont présentées en section 2.1. La section 2.2 aborde des notions générales concernant l'écoulement de fluides autour d'une particule ainsi que sur la dynamique des suspensions. Ensuite, une brève introduction à la théorie cinétique des gaz est effectuée à la section 2.3. Cette introduction, qui peut sembler a priori hors contexte, est un préambule nécessaire à plusieurs modèles pour décrire la dynamique de la phase solide qui sera abordée dans les sections ultérieures. Le lecteur familier avec ces éléments peut volontairement négliger les sections 2.1, 2.2 et 2.3.

Dans la Section 2.4, les schémas numériques généralement utilisés pour résoudre les équations de la mécanique des fluides sont présentés. L'attention est accordée aux méthodes des volumes finis et de Boltzmann sur réseau, qui seront utilisées dans ce travail. De surcroît, la problématique de la modélisation de la turbulence est discutée brièvement, avec une attention particulière portée aux modèles à grandes échelles (LES).

Finalement, une revue exhaustive des approches pour modéliser les écoulements polyphasiques de type solide-liquide est présentée à la Section 2.5. Cette présentation, de nature très mathématique, s'appuie sur les théories développées dans les Sections 2.1 et 2.3. La thématique du mélange solide-liquide est finalement abordée, à la fois d'un point de vue expérimental et numérique, dans le cadre de la Section 2.6. Cet ordre permet de présenter de manière continue les modèles numériques polyphasiques en Section 2.5 avant d'en citer l'utilisation dans la Section 2.6 sans qu'il soit nécessaire, à chaque fois, d'introduire la formulation d'un nouveau modèle. De surcroît, elle permet d'introduire dans un cadre rigoureux des modèles qui, bien que valides pour tout les écoulements solide-liquide, n'ont jamais été utilisés pour étudier les procédés de mélange.

2.1 La mécanique des fluides monophasique

Le concept de mécanique des milieux continus est un degré d'abstraction au-delà de la nature moléculaire de la matière [73]. Dans la mécanique des milieux continus, on peut conceptualiser des éléments continus, fluides ou solides, de taille arbitrairement petite et qui sont constitués de matière continue, même dans la limite où ils se réduisent à un simple point $M(\boldsymbol{x}, t)$ [1]. En suivant l'évolution d'une variable macroscopique (ζ) sur un élément de matière en mouvement, on peut définir un référentiel lagrangien. Le référentiel eulérien, quant à lui, ne considère pas un élément de matière donné, mais une position fixe de l'espace (par exemple $\boldsymbol{x} \in \mathbb{R}^3$).

Les équations décrivant le déplacement continu de milieux continus dans des conditions non relativistes peuvent être établies en utilisant les lois de conservation de la masse, de la quantité de mouvement et de l'énergie. L'hypothèse sous-jacente à la mécanique des milieux continus implique que le libre parcours moyen des molécules ou des atomes constituant le corps est nettement plus petit que l'échelle des déformations ou de l'écoulement observé. Cette description, dite mésoscopique, de la matière est valide dans la limite d'un faible nombre (≤ 0.1) de Knudsen.

$$Kn = \frac{l_m}{L} \tag{2.1}$$

où l_m est le libre parcours moyen des molécules et L une longueur caractéristique de l'écoulement ou de la déformation. Ainsi, un milieu est considéré continu si le nombre de Knudsen est très faible ($Kn < 0.1$).

Les équations présentées dans cette section ne sont pas démontrées exhaustivement. Cependant, elles peuvent être obtenues via différentes approches. Généralement, ces équations sont établies de manière intuitive à l'aide de bilans de masse, de quantité de mouvement et d'énergie sur un volume de contrôle quelconque. À l'aide du théorème de Gauss-Ostrogradski et en prenant la limite mesoscopique d'un volume continu, des équations aux dérivées partielles (dans le temps et l'espace) peuvent être obtenues. Une telle approche est notamment préconisée dans les livres de Bird *et al.* [35] et de Morisson [221]. Une approche plus élégante, quoique plus complexe, se base sur la mécanique des milieux continus et la méthode des puissances virtuelles [222]. Dans cette thèse, nous nous limitons à une simple présentation des équations résultantes dans le contexte général de la mécanique des fluides. La notation

1. Dans cette thèse, les caractères romains gras dénotent des vecteurs (ex : $\boldsymbol{x} \in \mathbb{R}^d$), tandis que les caractères romains de police mathématique ($\boldsymbol{\mathcal{I}}$) ou les caractères grecs gras ($\boldsymbol{\sigma}$) dénotent des tenseurs d'ordre deux ($\boldsymbol{\mathcal{I}}, \boldsymbol{\sigma} \in \mathbb{R}^{d\times d}$). La seule exception à cette règle est la vitesse microscopique $\boldsymbol{\xi}$ dans l'équation de Boltzmann, afin de rester cohérent avec la littérature se rattachant avec cette équation

de Bird *et al.* [35] est utilisée, avec de légères modifications, dans le présent document.

La conservation de la masse et de la quantité de mouvement nous permet d'écrire, sous forme conservative et dans un référentiel eulérien, les équations de continuité et de Cauchy

$$\frac{\partial \rho_f}{\partial t} + \nabla \cdot (\rho_f \boldsymbol{u}) = 0 \tag{2.2}$$

$$\frac{\partial \rho_f \boldsymbol{u}}{\partial t} + \nabla \cdot (\rho_f \boldsymbol{u} \otimes \boldsymbol{u}) + \nabla \cdot \boldsymbol{\sigma} = \rho_f \boldsymbol{g} \tag{2.3}$$

avec ρ_f la masse volumique du fluide, $\boldsymbol{u}$ son vecteur vitesse, $\boldsymbol{\sigma}$ le tenseur des contraintes et $\boldsymbol{g}$ la gravité (ou toute autre force volumique).

Pour un fluide parfait, le tenseur des contraintes s'écrit :

$$\boldsymbol{\sigma} = p\boldsymbol{\mathcal{I}} \tag{2.4}$$

avec p la pression et $\boldsymbol{\mathcal{I}}$ le tenseur identité. Cette définition permet d'obtenir les équations d'Euler. Cependant, cette définition est mésadaptée à la représentation des fluides réels, car elle ne contient pas les forces de cisaillement et est donc limité à des conditions limites de glissement sur les corps solides. En introduisant la loi de comportement de Newton, on obtient :

$$\boldsymbol{\sigma} = p\boldsymbol{\mathcal{I}} - \boldsymbol{\tau} \tag{2.5}$$

$$\boldsymbol{\sigma} = p\boldsymbol{\mathcal{I}} - \mu\dot{\boldsymbol{\gamma}} + \left(\frac{2}{3}\mu - \kappa\right)(\nabla \cdot \boldsymbol{u})\,\boldsymbol{\mathcal{I}} \tag{2.6}$$

$$\boldsymbol{\sigma} = p\boldsymbol{\mathcal{I}} - \mu\left(\nabla\boldsymbol{u} + (\nabla\boldsymbol{u})^T\right) + \left(\frac{2}{3}\mu - \kappa\right)(\nabla \cdot \boldsymbol{u})\,\boldsymbol{\mathcal{I}} \tag{2.7}$$

avec $\boldsymbol{\tau}$ le tenseur des contraintes déviatoriques, μ la viscosité newtonienne, κ le coefficient de Lamé et $\dot{\boldsymbol{\gamma}}$ le tenseur du taux de cisaillement. L'équation constitutive de Newton, ainsi que l'ajout d'une équation de conservation de l'énergie (e), mène aux équations de Navier-Stokes compressibles :

$$\frac{\partial \rho_f}{\partial t} + \nabla \cdot (\rho_f \boldsymbol{u}) = 0 \tag{2.8}$$

$$\frac{\partial \boldsymbol{u}}{\partial t} + \nabla \cdot (\rho_f \boldsymbol{u} \otimes \boldsymbol{u}) = -\nabla p + \nabla\left[\mu \cdot \left(\nabla\boldsymbol{u} + (\nabla\boldsymbol{u})^T\right) + \left(\frac{2}{3}\mu - \kappa\right)(\nabla \cdot \boldsymbol{u})\right] + \rho_f \boldsymbol{g} \tag{2.9}$$

$$\frac{\partial \rho_f e}{\partial t} + \nabla \cdot ((\rho_f e + p)\,\boldsymbol{u}) = \nabla \cdot (\mu\boldsymbol{\gamma} \cdot \boldsymbol{u}) + \rho_f \boldsymbol{g} \cdot \boldsymbol{u} + \nabla \cdot (\lambda \nabla T) \tag{2.10}$$

où e est l'énergie interne, T la température et λ la conductivité thermique. Ainsi, il demeure

6 inconnues $(\rho_f, p, e, \boldsymbol{u})$ pour lesquelles nous avons 5 équations (2.8,2.9 dans les 3 dimensions de $\mathbb{R}^3$, 2.10). Ce système doit être complété par une équation d'état telle que la loi des gaz parfaits :

$$\rho_f = \frac{\gamma_s}{\gamma_s - 1}\frac{p}{e} \tag{2.11}$$

avec $h = H - \frac{1}{2}u^2$ l'enthalpie, H l'enthalpie totale et γ_s la constante isentropique. Ceci permet de définir d'autres relations thermodynamiques, telles que la vitesse du son c :

$$c = \sqrt{\frac{\partial \rho_f}{\partial s}} = \sqrt{\gamma_s \frac{p}{\rho_f}} \tag{2.12}$$

avec s l'entropie. Cependant, pour les liquides tels que l'eau dont la densité est une fonction complexe de la pression et de l'énergie interne il n'existe pas d'équation d'état suffisamment générale. Il est possible de s'affranchir de ce problème en utilisant une équation d'état pour laquelle la masse volumique du fluide est constante en temps et en espace. Cette hypothèse est valable uniquement pour de faibles nombres de Mach ($Ma^2 \leq 0.1$), nombre qui est défini comme le ratio entre la vitesse d'un fluide et la vitesse du son dans ce fluide :

$$Ma = \frac{|\boldsymbol{u}|}{c} \tag{2.13}$$

La compressibilité ne dépend pas seulement de la nature du fluide qui s'écoule, mais aussi de la nature de l'écoulement. Un mal à propos rencontré dans la littérature est de définir un fluide comme compressible (un gaz) ou incompressible (un liquide). Nous aimerions mettre l'accent sur le fait qu'un écoulement de gaz peut être incompressible, alors qu'un écoulement de liquide peut être considéré comme compressible. Conséquemment, la compressibilité est une propriété d'un écoulement et non d'un fluide.

L'équation d'état d'incompressibilité mène aux équations de Navier-Stokes incompressibles, qui, si μ est constant, s'écrit :

$$\nabla \cdot \boldsymbol{u} = 0 \tag{2.14}$$

$$\rho_f \frac{\partial \boldsymbol{u}}{\partial t} + \rho_f \nabla \cdot (\boldsymbol{u} \otimes \boldsymbol{u}) = -\nabla p + \mu \nabla^2 \boldsymbol{u} + \rho_f \boldsymbol{g} \tag{2.15}$$

Ce système d'équations décrit le mouvement d'un fluide newtonien dans la limite de faible nombre de Mach.

Une discussion plus étendue sur ces équations est nécessaire. L'équation d'état incompressible

transforme la pression (p) en un multiplicateur de Lagrange qui impose la conservation de la masse [73,97]. La pression est en fait une pression dynamique, pour laquelle aucune équation d'évolution temporelle ($\frac{\partial p}{\partial t}$) n'existe, mais qui peut être déduite instantanément à partir du champ de vitesse. En effet, en prenant la divergence de (2.15), on obtient une équation de Poisson pour la pression définie à une constante près. Physiquement, ceci correspond à attribuer au fluide une vitesse du son infinie et ceci a fortes conséquences dans les schémas numériques, car le schéma pour la pression doit être implicite.

Les termes du membre gauche de l'équation (2.15) décrit l'évolution temporelle de la quantité de mouvement et son advection par la vitesse. Les termes d'advection confèrent la non-linéarité aux équations de Navier-Stokes. L'opérateur laplacien au membre de droite est un opérateur linéaire auto-adjoint qui diffuse la quantité de mouvement.

2.1.1 Analyse dimensionnelle et nombres adimensionnels

Les nombres adimensionnels tels que les nombres de Knudsen et de Mach sont couramment utilisés en mécanique des fluides et découlent naturellement de l'écriture en forme adimensionnelle des équations de Navier-Stokes [35].

Le nombre de Reynolds est défini comme le ratio entre les forces d'inertie et les forces visqueuses et dicte le régime d'écoulement :

$$Re = \frac{\rho_f \left|\boldsymbol{u}\right| L}{\mu} \tag{2.16}$$

L'expression exacte du nombre de Reynolds dépend de la géométrie étudiée et il est toujours nécessaire de fixer une échelle de vitesse et une longueur pertinente. Pour $Re \to 0$, les forces visqueuses dominent et les équations de Navier-Stokes deviennent les équations de Stokes, où l'opérateur laplacien est l'opérateur dominant. On a alors un écoulement laminaire. En augmentant le nombre de Reynolds, l'écoulement devient d'abord transitoire, puis turbulent. Il est important de noter que les nombres de Reynolds exacts pour lesquels la transition se fait entre un écoulement laminaire, transitoire et turbulent dépendent intrinsèquement de la géométrie ainsi que des conditions expérimentales [253].

Un large éventail de nombres adimensionnels existent permettent de mieux comprendre et caractériser le sujet à l'étude. Ceux-ci seront définis progressivement dans cette thèse.

2.1.2 Rhéologie

On peut se demander si le modèle newtonien pour le tenseur des contraintes est suffisant pour décrire le comportement de tous les fluides. Dans la réalité, plusieurs fluides adoptent des comportements nettement plus complexes qui ne peuvent être reproduits par le modèle newtonien [221]. Quelques exemples, tels que l'effet Weisenberg, qui résulte d'une différence de contraintes normales, et l'effet de rappel (*recoil effect*), dû à la nature viscoélastique de certains liquides ou polymères fondus, sont bien illustrés dans le livre de Carreau *et al.* [59].

Ces fluides sont dits non-newtoniens et l'étude de leur comportement se nomme la rhéologie [35]. La rhéologie est donc l'étude de la déformation et de l'écoulement de la matière. Elle vise à comprendre et à caractériser l'écoulement de fluides complexes tels que les polymères (fondus ou en solution), les suspensions, les boues, etc., qui interviennent dans un large éventail d'industries [221, 238]

Ces fluides peuvent adopter un comportement qui est à la fois visqueux et élastique, et sont donc appelés fluides viscoélastiques. La relation entre le taux de cisaillement appliqué sur le fluide et la contrainte résultante peut être non-linéaire, dépendante du temps, etc. [238]. Deux larges familles de modèles sont utilisées pour décrire les comportements non-newtoniens de certains fluides. La première englobe les fluides newtonien généralisés (GNF) dont la loi de comportement est indépendante du temps [221]. Pour ces fluides, la viscosité non-Newtonienne est une fonction du taux de cisaillement. La seconde famille est constituée des modèles viscoélastiques linéaires et non-linéaires. Ces modèles sont nettement plus complexes, car la réponse du fluide à une déformation et un taux de déformation dépend de son historique de déformations. Ceux-ci ne sont pas discutés dans le contexte du présent travail. Nous référons le lecteur au livre de Morrison pour une présentation de ce sujet [221].

Fluides newtoniens généralisés

Les modèles de fluides newtoniens généralisés (GNF) établissent une relation instantanée entre le taux de cisaillement $\dot{\gamma}$ et la viscosité du fluide. Ceci permet aux modèles GNF de reproduire de manière précise les comportements de fluides rhéoépaississants, rhéofluidifiants et à contrainte seuil. La relation entre la contrainte (*shear stress*) et le taux de cisaillement (*shear rate*) pour ces fluides est illustrée à la figure 2.1.

Le taux de cisaillement est défini comme le second invariant du tenseur du taux de déformation [221] :

$$\dot{\gamma} = \sqrt{\dot{\boldsymbol{\gamma}} : \dot{\boldsymbol{\gamma}}} \tag{2.17}$$

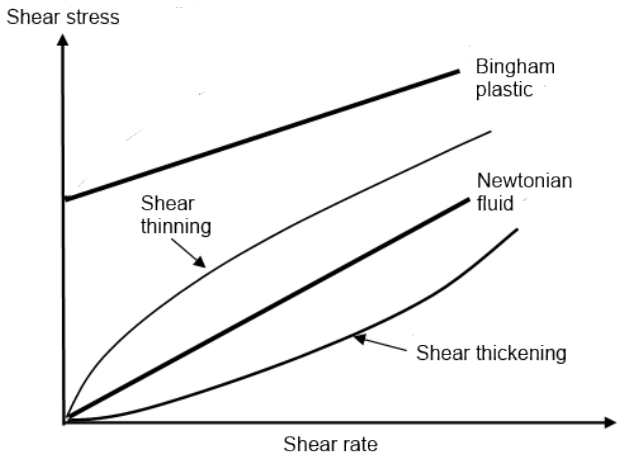

Figure 2.1 Exemples de comportements de fluides newtoniens généralisés - reproduit de [221]

où : est défini comme la double contraction tensorielle d'un tenseur d'ordre deux. Dans les modèles GNF, le tenseur des contraintes prend la forme suivante :

$$\sigma = p\boldsymbol{\mathcal{I}} - \eta\left(\dot{\gamma}\right)\dot{\boldsymbol{\gamma}} \tag{2.18}$$

avec $\eta\left(\dot{\gamma}\right)$ la viscosité non-newtonienne. Le modèle le plus simple de GNF est le modèle de loi de puissance :

$$\eta(\dot{\gamma}) = m\dot{\gamma}^{n-1} \tag{2.19}$$

avec m l'indice de consistance, n le paramètre de loi de pouvoir. Pour $n = 1$ le fluide est newtonien, alors que pour $n < 1$ et $n > 1$ le fluide est rhéofluidifiant et rhéoépaississant, respectivement. Ce modèle est imprécis dans les zones de faibles et de haut taux de cisaillement, car il est incapable de reproduire les plateaux newtoniens que ces fluides atteignent [221]. Un modèle plus avancé est le modèle de Carreau-Yasuda à 5 paramètres :

$$\frac{\eta\left(\dot{\gamma}\right) - \eta_\infty}{\eta_0 - \eta_\infty} = \left(1 + \left(\dot{\gamma}\lambda_t\right)^a\right)^{\frac{n-1}{a}} \tag{2.20}$$

où η_0 est la viscosité pour un taux de cisaillement nul ; η_∞ la viscosité pour un taux de cisaillement infini ; λ_t est un temps de relaxation du fluide et a, un paramètre qui modifie la transition entre le plateau Newtonien et le régime en loi de puissance. Une version à quatre paramètres de ce modèle existe également, où la valeur de a est fixé à 2.

Le modèle de Bingham, quant à lui, décrit un comportement distinct des modèles de Carreau-

Yasuda ou de loi de puissance : les fluides à contrainte seuil. Ce modèle s'exprime tel que :

$$\eta\left(\dot{\gamma}\right) = \begin{cases} \infty & \forall \quad |\boldsymbol{\tau}| < \tau_y \\ \mu_0 + \frac{\tau_y}{\dot{\gamma}} & \forall \quad |\boldsymbol{\tau}| \geq \tau_y \end{cases} \tag{2.21}$$

où τ_y est la contrainte seuil d'écoulement et μ_0 la viscosité du fluide une fois cette contrainte surpassée. Ce type de comportement est fréquemment observé dans les suspensions concentrées ou les pâtes [221].

2.1.3 Turbulence

L'étude de la turbulence demeure le sujet le plus complexe et le plus important en ce qui concerne la mécanique des fluides. En fait, la turbulence joue un rôle déterminant dans la majeure partie des écoulements [74] qu'il est possible d'observer autour de nous. Que ce soit lors de l'agitation du café dans une tasse avec une cuillère ou dans le panache de fumée d'une cheminée industrielle, le caractère turbulent de l'écoulement domine le mélange, la dispersion, la force nécessaire pour mélanger, etc. [253].

Comme nous l'avons mentionné précédemment, la turbulence intervient lorsque les forces inertielles dominent (partiellement ou totalement) sur les forces visqueuses, pour des nombres de Reynolds élevés [2]. Les écoulements turbulents sont caractérisés par leurs irrégularités, la présence de tourbillons et leur caractère rotationnel [57].

C'est ce caractère irrégulier et rotationnel qui fait que la turbulence joue un rôle critique dans les unités de mélange et les réacteurs chimiques grâce à sa capacité intrinsèque à transporter et à mélanger les composantes. Ceci a pour conséquence de favoriser la diffusion qui intervient quant à elle à une échelle spatiale nettement plus petite. C'est pour cette raison que, lorsque possibles, les opérations de mélange sont conçues pour être opérées en régime turbulent.

La turbulence est un problème extrêmement complexe dans lequel un couplage dynamique entre différentes échelles de longueur survient à cause de la non-linéarité des équations de Navier-Stokes [270]. Les mouvements à grande échelle de l'écoulement sont grandement influencés par la géométrie et les conditions limites tandis que le mouvement du fluide à une petite échelle est principalement déterminé par le taux auquel l'énergie est reçue des grandes échelles et auquel elle est dissipée, principalement par l'action des forces visqueuses [253]. Ce transfert d'énergie des grandes échelles aux petites échelles se nomme la cascade de Kolmogorov (ou cascade d'énergie) et la plus petite échelle à laquelle l'énergie est diffusée pour être

2. Le terme élévé demeure vague et la valeur seuil pour laquelle un écoulement devient turbulent dépend fortement de la géométrie et du type d'écoulement

ensuite dissipée est l'échelle de Kolmogorov [57]. Pour une géométrie de longueur caractéristique L, cette échelle est de l'ordre de $\frac{L}{Re^{\frac{3}{4}}}$ pour de la turbulence homogène isotrope [270]. C'est ce vaste spectre d'échelles, ainsi que les interactions entre celles-ci, qui est à la racine même du défi relié à la compréhension (et à la modélisation) de la turbulence. Puisque la majeure partie de l'énergie est transférée des grandes échelles aux petites échelles, là où la dissipation a lieu, il devient nécessaire de simuler l'écoulement à toutes ces échelles. Ceci requiert une résolution spatiale trop élevée, qui croît avec l'augmentation du nombre de Reynolds, ce qui rend la simulation directe d'écoulements à haut nombre de Reynolds impraticable même sur les plus puissants superordinateurs. La modélisation de cette problématique, par le biais d'approches dites moyennées en Reynolds (RANS) ou à grandes échelles (LES) sera abordée dans la Section 2.4.4.

2.2 Les écoulements de suspensions solides-liquides

Dans cette section, la physique des écoulements solides-liquides est étudiée dans une perspective de complexité croissante. En premier lieu, l'écoulement d'une seule particule sphérique dans un écoulement uniforme est abordé. Ensuite, les suspensions de plusieurs particules sont traitées et deux catégories de suspensions sont introduites : homogène et diphasique. Le reste de la section est dédié à l'étude des suspensions diphasiques.

L'écoulement instationnaire et non-uniforme autour d'une particule sphérique est abordé et les forces d'interaction solides-liquides sont détaillées. Les nombres adimensionnels pertinents seront introduits au fur et à mesure du développement. Finalement, l'impact de l'entravement dû à la présence d'autres particules sur les forces d'interaction solide-fluide est abordé. Cette revue, dont la matière est relativement classique, s'inspire des livres de Oesterle [229], de Crowe *et al.* [70], de Ishii et Hibiki [135], de Peker et Helaci [246] et de Brennen [48].

2.2.1 Écoulement en régime permenant autour d'une particule sphérique dans un champ de vitesse uniforme

Dans beaucoup d'écoulements, la force de traînée F_D entre la particule et le fluide est le mécanisme dominant de transfert de quantité de mouvement entre les deux phases [229]. La traînée résulte de l'action des contraintes visqueuses et de la pression sur une particule causée par la vitesse relative entre la particule et le fluide. Sous forme générale, cette force s'exprime :

$$F_D = \frac{1}{2}\rho_f \pi d_p^2 \left|(\boldsymbol{u}-\boldsymbol{v})\right| (\boldsymbol{u}-\boldsymbol{v})\, C_D \tag{2.22}$$

avec d_p le diamètre de la particule, $(\boldsymbol{u} - \boldsymbol{v})$ la vitesse relative entre le fluide (de vitesse $\boldsymbol{u}$) et une particule (de vitesse $\boldsymbol{v}$) et C_D un coefficient de traîné adimensionnel qui dépend du régime d'écoulement. Le régime d'écoulement autour d'une particule peut être défini à partir du nombre de Reynolds particulaire (Re_p) :

$$Re_p = \frac{\rho_f \left|(\boldsymbol{u} - \boldsymbol{v})\right| d_p}{\mu} \tag{2.23}$$

Une courbe classique présentant l'évolution du coefficient de traînée en fonction de Re_p est présentée à la Figure 2.2.

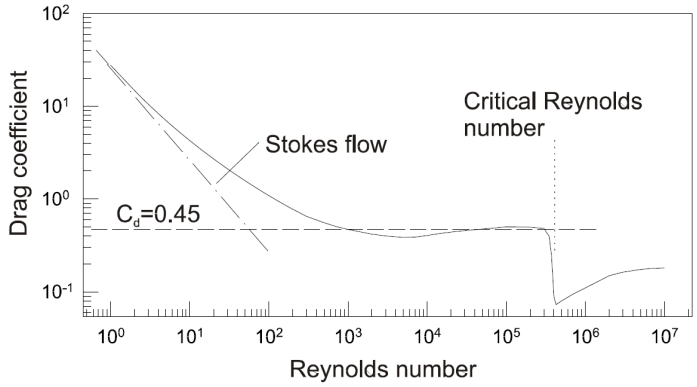

Figure 2.2 Coefficient de traînée pour l'écoulement en régime permanent autour d'une sphère, extrait de [70]

À partir de la solution analytique pour l'écoulement rampant autour d'une sphère, la solution de Stokes pour le coefficient de traînée peut être obtenue :

$$C_{D,\epsilon_f \to 1} = \frac{24}{Re_p} \tag{2.24}$$

où ϵ_f est la fraction volumique de fluide et $C_{D,\epsilon_f \to 1}$ est le coefficient de traînée pour une particule isolée baignant dans un milieu infini ($\epsilon_f \to 1$). Cette solution est valide pour $Re_p < 0.1$, comme on peut le voir à la Figure 2.2. Elle fut étendue par Oseen [48] en utilisant un dévelopement asymptotique, qui malheureusement diverge rapidement pour $Re_p \geq 2$. Des dévelopements à des ordres supérieurs ont été effectuées par d'autres auteurs [229], mais ils divergent rapidement avec l'augmentation du nombre de Reynolds. Nous rappelons que ceci est une des failles inévitables de ce type d'approche [28].

Une solution peut aussi être obtenue dans la limite d'un fluide parfait ($Re_p \to \infty$) pour

un écoulement irrotationel, menant à $C_{D,\epsilon_f \to 1} = 0$. Ce résultat surprenant est connu sous le nom de paradoxe de d'Alembert [48]. Il s'explique par le fait que, même pour de grands nombres de Reynolds, la viscosité joue un rôle dans la traînée autour d'une sphère à travers la turbulence ce qui vient invalider l'hypothèse d'un fluide parfait.

Les étapes principales de l'évolution de l'écoulement autour d'une sphère (et conséquemment de C_D) se résument ainsi. Pour de faibles valeurs de Re_p, l'écoulement autour de la sphère est rampant. Lorsque Re_p augmente, une zone de recirculation apparait dans le sillage de la particule. Cette zone prend de l'expansion et l'angle du point de stagnation en amont recule. Pour $Re_p \approx 500$ les tourbillons derrière la sphère commencent à se détacher et des vortex sont lâchés dans le sillage de la sphère. L'angle du point de stagnation continue à reculer jusqu'à ce qu'un nombre de Reynolds critique ($Re_{p,crit}$) soit atteint au-delà duquel la couche limite se rattache à la sphère. C'est ce recollement de la couche limite qui entraîne une chute brutale du coefficient de traînée tel qu'observé à la Figure 2.2.

Le temps de réponse d'une particule $\tau_p = \frac{\rho_p d_p^2}{18\mu}$ caractérise le temps nécessaire à l'amortissement de la vitesse relative entre le fluide et une particule. Cette définition permet de définir le nombre de Stokes comme le ratio du temps de réponse d'une particule et du fluide [70] :

$$St = \frac{\tau_p}{\tau_f} = \frac{\tau_p U}{L} \tag{2.25}$$

avec U et L des échelles de vitesse et de grandeur de l'écoulement. Dans la limite $St \to 0$, les particules se comportent comme un scalaire passif et suivent le fluide alors que pour $St > 1$ l'inertie des particules est suffisante pour qu'elles se détachent de l'écoulement. Pour $St \to \infty$, le mouvement des particules est indépendant de celui du fluide l'entourant.

Un autre nombre adimensionnel d'importance est le nombre d'Archimède qui est défini comme le ratio entre les forces gravitationnelles et les forces visqueuses agissant sur une particule :

$$Ar = d_p^3 \left(\frac{g\rho_l \left(\rho_p - \rho_l\right)}{\mu^2} \right) \tag{2.26}$$

Finalement, nous définissons la vitesse terminale de chute d'une particule comme étant la vitesse relative maximale qu'elle atteint lorsqu'elle subit l'action de la gravité.

2.2.2 Écoulement en régime instationnaire autour d'une particule sphérique dans un champs de vitesse non-uniforme

Une solution pour l'écoulement transitoire d'une seule particule sphérique dans un écoulement uniforme pour de faibles valeurs de Re_p a été obtenue par Basset, Boussinesq et Oseen, tel que rapporté par Crowe *et al.* [70]. Cette solution a été généralisée au cas d'un écoulement non-uniforme par Maxey [203]. Nous présentons seulement les résultats pour chaque force tels qu'obtenus par Maxey, sans en redémontrer les expressions. L'équation générale permettant de décrire l'accélération d'une particule est [70, 337] :

$$\begin{aligned}\underbrace{m\frac{d\boldsymbol{v}}{dt}}_{Inertie} = & \underbrace{m\boldsymbol{g}}_{\text{Forces volumiques}} + \underbrace{V_p\left(-\nabla p + \nabla\cdot\boldsymbol{\tau}\right)}_{\text{Écoulement non-perturbé}} + \underbrace{\frac{1}{2}\rho_f\pi d_p^2\left|(\boldsymbol{u}-\boldsymbol{v})\right|(\boldsymbol{u}-\boldsymbol{v})\,C_{D,\epsilon_f\to 1}}_{\text{Traînée}} \\ & + \underbrace{\frac{1}{2}\rho_f V_p\frac{d\left(\boldsymbol{u}-\boldsymbol{v}\right)}{dt}}_{\text{Masse virtuelle}} + \underbrace{\frac{3}{2}d_p^2\sqrt{\pi\mu\rho_f}\int_0^t\frac{\frac{d(\boldsymbol{u}-\boldsymbol{v})}{d\theta}}{\sqrt{t-\theta}}d\theta}_{\text{Force de Basset}} \\ & + \underbrace{C_s d_p^2\left(\mu\rho_f\right)^{\frac{1}{2}}\left|\boldsymbol{\omega}\right|^{-\frac{1}{2}}\left((\boldsymbol{u}-\boldsymbol{v})\times\boldsymbol{\omega}\right)}_{\text{Force de Saffman}} \\ & + \underbrace{C_M\frac{\pi}{8}d_p^3\rho_f\left(\left(\frac{1}{2}\boldsymbol{\omega}-\boldsymbol{\omega}_p\right)\times(\boldsymbol{u}-\boldsymbol{v})\right)}_{\text{Force de Magnus}}\end{aligned} \tag{2.27}$$

où V_p est le volume de la particule, C_S le coefficient de Saffman ($C_S = 1.61$ en régime laminaire), $\boldsymbol{\omega}$ la vorticité du fluide ($\omega = \nabla\times\boldsymbol{u}$), $\boldsymbol{\omega}_p$ la vitesse angulaire de la particule et C_M le coefficient de Magnus ($C_M = 1$ en régime laminaire). Les termes de Faxxen prenant en compte la courbure du profil de vitesse (qui sont d'ordre $d_p^2\nabla^2\left|\boldsymbol{u}\right|$) ne sont pas présents dans l'expression précédente, car ils sont presque toujours négligeables, outre dans des situations exceptionnelles [70]. L'explication physique derrière les forces d'inertie, de traînée et les forces volumiques est évidente, mais l'origine des forces supplémentaires n'est pas fondamentalement intuitive et nécessite une certaine discussion.

Forces dues au caractère transitoire de l'écoulement

Masse virtuelle La force de masse virtuelle est due à l'accélération du fluide près de la particule, ce qui augmente l'inertie apparente de la particule. Pour une sphère, l'inertie ajoutée correspond exactement à l'inertie d'un volume de fluide égal à la moitié du volume de la particule. La force de masse virtuelle est toujours négligée dans le cas d'écoulement gaz-solide, mais est importante pour des ratios de densité $\frac{\rho_f}{\rho_p} > 1$.

Force de Basset La force de Basset (ou la force de mémoire) est causée par le développement de la couche limite dans le fluide autour de la particule lorsque la vitesse relative entre la particule et le fluide change dans le temps. Selon Crowe *et al.* [70], la force de Basset peut être vue comme la contrepartie visqueuse de la force de masse virtuelle, qui elle est purement inertielle. La force de Basset peut être négligée lorsque le temps de relaxation de la particule est court ou lorsque l'écoulement ne fluctue pas beaucoup dans le temps.

Forces causées par un champ de vitesse non-uniforme

Écoulement non-pertubé Cette force est due aux gradients de pression et de contraintes visqueuses dans l'écoulement à une échelle plus grande que celles des particules. De manière générale, ces forces ne peuvent être négligées.

Force de portance de Saffman La force de Saffman est une force de portance due à une différence de pression à la surface d'une particule causée par un gradient de vitesse dans l'écoulement moyen.

Force de portance de Magnus La force de Magnus est une force de portance due à la rotation des particules. La vitesse angulaire d'une particule entraîne un différentiel de pression entre les côtés opposés de la particule et il en résulte une force de portance.

2.2.3 Classification des suspensions

On peut distinguer deux types de suspensions. Pour de petites particules de taille colloïdale ($d_p \leq 1\mu$m), la suspension se comporte comme un fluide homogène dont la rhéologie dépend de la concentration (ou fraction volumique) de particuels (ϵ_p). Pour des suspensions diluées ($\epsilon_p < 5\%$), les interactions particule-particule sont négligeables et la viscosité apparente peut être calculée à l'aide de la loi d'Einstein [209]. Pour de plus hautes concentrations ($\epsilon_p > 10\%$), les interactions particule-particule ne sont plus négligeables et des modèles empiriques tels que celui de Krieger-Dougherty [160] doivent être utilisés pour calculer la viscosité de la suspension. De surcroît, ces suspensions peuvent exhiber des comportements rhéofluidifiants ou rhéoépaissisants [209] à cause des interactions complexes entre les particules et des forces colloïdales. D'un point de vue pratique, l'étude de ces suspensions relève davantage de la rhéologie que de la mécanique des fluides polyphasique et elles se comportent souvent comme un seul milieu continu.

Pour les suspensions contenant de plus grandes particules, la suspension est réellement inhomogène et le fluide et les particules doivent être considérés comme deux phases indépendantes.

Ceci est le cas réellement diphasique que nous considérerons dans le reste de cette thèse.

La séparation entre ces deux types de suspensions demeure floue. Certains auteurs proposent une distinction basée uniquement sur la taille des particules [209], alors que d'autres utilisent la vitesse terminale des particules [245] ou le nombre d'Archimède [246]. Les deux dernières approches sont des métriques reliées, car les deux prennent en considération la viscosité du fluide, sa densité et la taille des particules. Selon Peker et Helvaci [246], les suspensions avec $Ar << 1$ se comportent comme des fluides homogènes tandis que les suspensions avec $Ar >> 100$ sont réellement diphasiques. La région intermédiaire, où $Ar \in [1, 100]$, semble être une région où le comportement des suspensions est mal défini.

2.2.4 Influence de l'entravement

Il est important de rappeler que l'Équation (2.27) est valide pour l'écoulement autour d'une seule particule dans un milieu fluide infini. Cependant, outre dans les cas très dilués, les particules sont entourées de particules voisines avec lesquelles elles interagissent hydrodynamiquement, ce qui entrave l'écoulement. L'entravement des particules, qu'il soit dû aux parois ou aux particules, a un impact important sur la traînée (et sur les autres forces hydrodynamiques), ce qui modifie le coefficient de traînée tel que vu par les particules, C_D.

Un écoulement est considéré comme entravé lorsque la distance entre les particules est inférieure à 10 diamètres de particules [229]. Ceci correspond approximativement à une fraction volumique de solide ($\epsilon_p = 1-\epsilon_f$) de 0.1% [229]. Pour les écoulements entravés, il est nécessaire d'utiliser des corrélations empiriques ou mécanistiques pour évaluer la traînée que subit une particule. Une corrélation bien établie est l'équation d'Ergun [94], valide pour $\epsilon_p \in [0.2, 0.8]$. Cette corrélation peut être complétée par la corrélation de Wen-Yu pour de plus faibles fractions de solides [323], ce qui mène à l'équation suivante :

$$F_D = \beta_{fp} \frac{(\boldsymbol{u} - \boldsymbol{v})}{\rho_f} \tag{2.28}$$

$$\beta_{fp} = \begin{cases} 150 \frac{\left(1-\epsilon_f\right)^2}{\epsilon_f} \frac{\mu_f}{(\phi_p d_p)^2} + 1.75 \left(1-\epsilon_f\right) \frac{\rho_f}{\phi_p d_p} |\boldsymbol{u} - \boldsymbol{v}| & \forall\ \epsilon_f \in [0.2, 0.8] \\ \frac{3}{4} C_{D,0} \frac{|\boldsymbol{u}-\boldsymbol{v}_i| \rho_f \left(1-\epsilon_f\right)}{d_p} \epsilon_f^{-2.7} & \forall\ \epsilon_f > 0.8 \end{cases} \tag{2.29}$$

Bien que la corrélation de Wen-Yu et Ergun soit une des plus connues, de nombreuses autres corrélations ont été proposées pour décrire l'impact de l'entravement (à travers la porosité) sur la traînée (ou, de manière similaire, sur la vitesse terminale de chute) telles que celles de Richardson-Zaki [261], Di Felice [84], Ishii-Zuber [135], Schiller-Nauman [183], Ihme [183], Clift [299], Beetstra *et al.* [25–27], Cello *et al.* [60], Rong *et al.* [266] et Kim et Lee [153].

Comme on peut le constater, il existe une multitude de corrélations pour exprimer la dépendance du coefficient de traînée à la porosité. Celles-ci ne sont pas toutes présentées afin de maintenir un certain degré de concision dans le présent document. Cependant, de la forme de ces corrélations, on peut tirer les conclusions suivantes :

- L'effet de l'entravement dépend non seulement de la porosité, mais aussi du nombre de Reynolds particulaire Re_p.
- Les travaux des dernières décennies, tels que [26, 60, 84, 266], suggèrent que l'entravement devrait être pris en compte à travers d'une fonction $f(\epsilon_f, Re_p)$ telle que $C_D = C_{D,\epsilon_f \to 0}(Re_p) f(\epsilon_f, Re_p)$.
- Pour Re_p constant, $C_D(\epsilon_p)$ est une fonction de ϵ_p strictement croissante.

Dans l'ensemble, toutes les corrélations pour le coefficient de traînée C_D ont des limites, car elles ne peuvent pas prendre en considération la distribution spatiale des particules et son impact sur la traînée. De surcroît, ces corrélations ne prennent pas toutes en compte la possible polydispersité de la taille des particules. Des travaux récents [26, 27, 60, 266, 267] s'appuyant sur la simulation directe d'écoulements unidirectionnels à travers des arrangements de sphères monodisperses et polydisperses marquent un progrès vers des corrélations de traînée plus précises et valides pour un plus large éventail de configurations.

2.3 La théorie cinétique des gaz

L'objectif principal de la théorie cinétique des gaz est de décrire les propriétés macroscopiques des gaz, telles que leur pression, température, viscosité, conductivité thermique, etc., à partir des quantités microscopiques associées aux molécules (ou atomes) qui les constituent : la masse, la vitesse, l'énergie cinétique, les forces d'interaction, les degrés de liberté internes, etc. [159].

On peut facilement se demander pourquoi la cinétique des gaz, ainsi que les conclusions qui en dérivent, telles que la distribution maxwellienne et l'équation de Boltzmann, sont importantes pour l'étude des écoulements granulaires ou solides-liquides. Comme nous le verrons dans les sections subséquentes, plusieurs approches de modélisation de la phase solide considèrent que les petites particules solides se comportent comme un gaz de spheres rigides, qui entrent en collision et peuvent relaxer vers un équilibre maxwellien. De sucroît, une méthode numérique utilisée dans la présente thèse, la méthode de Boltzmann sur réseau, est dérivée de la limite hydrodynamique de l'équation de Boltzmann. Conséquement, il apparait raisonnable d'introduire brièvement l'équation de Boltzmann dans un contexte plus générique. La présentation effectuée dans la présente section est principalement dérivée des livres de Kremer [159] et de Saint-Raymond [271] sur l'équation de Boltzmann.

Nous considérons un gaz monoatomique, ou un nuage de particules, fait de N corps compris dans un volume V. La position d'un atome peut être décrite par sa position $\boldsymbol{x} = (x_1, x_2, x_2)^T$ et sa vitesse $\boldsymbol{\xi} = (e_1, e_2, e_3)^T$ dans l'espace des phases (donc dans $\mathbb{R}^6$). L'état d'un gaz peut donc être caractérisé par une fonction de distribution $\boldsymbol{f}(\boldsymbol{x}, \boldsymbol{\xi}, t)$ donnant le nombre de particules dont la position et la vitesse résident dans les intervalles $[\boldsymbol{x}, \boldsymbol{x} + d\boldsymbol{x}]$ et $[\boldsymbol{\xi}, \boldsymbol{\xi} + d\boldsymbol{\xi}]$ à un temps t :

$$f(\boldsymbol{x}, \boldsymbol{\xi}, t)\, d\boldsymbol{x} d\boldsymbol{\xi} = \boldsymbol{f}(\boldsymbol{x}, \boldsymbol{\xi}, t)\, dx_1 dx_2 dx_3 d\xi_1 d\xi_2 d\xi_3 \tag{2.30}$$

L'équation de Boltzmann est une équation intégro-différentielle non-linéaire pour la fonction de distribution. Elle décrit l'évolution de cette dernière dans l'espace des phases :

$$\frac{\partial f}{\partial t} + \underbrace{\boldsymbol{\xi} \cdot \nabla_x f + \boldsymbol{F} \cdot \nabla_e f}_{Transport} = \underbrace{\Omega}_{Collision} \tag{2.31}$$

avec $\boldsymbol{F}$ les forces volumiques externes qui ne dépendent pas de la vitesse des particules. L'opérateur de collision Ω est, dans sa forme la plus générale, une intégrale sur l'espace des vitesses microscopiques, un sous-espace de l'ensemble de l'espace des phases. Cet opérateur peut aussi être relié à la la différence entre le nombre de molécules qui entrent et qui quitte un volume arbitraire dans l'espace des phases (donc un volume dans $\mathbb{R}^6$) qui, conséquemment, vaut 0 lorsque la distribution est à l'équilibre.

On peut démontrer que la distribution maxwellienne f^{eq} satifait tous les critères nécessaires pour une fonction d'équilibre [159] :

$$f^{eq} = n \left(\frac{m}{2\pi k_B T} \right)^{\frac{3}{2}} e^{\left(-\frac{m}{2k_B T} (\boldsymbol{\xi} - \boldsymbol{u})^2 \right)} \tag{2.32}$$

avec k_B la constante de Boltzmann, T la température, n le nombre d'atomes (ou de particules) et m la masse d'une particule. Plusieurs formes simplifiées de l'opérateur de collision existent. Une de celles-ci fut proposée par Bhatnagar, Gross et Krook (BGK) et assume une relaxation de la partie hors équilibre de la distribution autour d'un seul temps de relaxation τ [34] :

$$\Omega = -\frac{(f - f^{eq})}{\tau} \tag{2.33}$$

Cet opérateur de collision, relativement simple, a été utilisé avec grand succès par Bhatnagar *et al.* dans l'étude des gaz ionisés [34] ; il joue un rôle particulièrement important dans la méthode de Boltzmann sur réseau et dans les applications reliées aux écoulements granulaires.

Comme nous l'avons mentionné précédemment, l'état macroscopique d'un gaz peut être décrit à partir des moments de la fonction de distribution :

$$\rho\left(\boldsymbol{x},t\right)=\int f\left(\boldsymbol{x},\boldsymbol{c},t\right)d\boldsymbol{\xi} \tag{2.34}$$

$$\rho\boldsymbol{u}\left(\boldsymbol{x},t\right)=\int \boldsymbol{\xi}f\left(\boldsymbol{x},\boldsymbol{\xi},t\right)d\boldsymbol{\xi} \tag{2.35}$$

$$\rho E\left(\boldsymbol{x},t\right)=\int \boldsymbol{\xi}\cdot\boldsymbol{\xi}f\left(\boldsymbol{x},\boldsymbol{\xi},t\right)d\boldsymbol{\xi} \tag{2.36}$$

où E est l'énergie totale.

Finalement, il est intéressant de noter que les équations de Navier-Stokes, qui sont des équations de natures macroscopiques, peuvent être obtenues à partir de l'équation de Boltzmann par un procédé connu sous le nom d'développement de Chapman-Enskogg. Ce développement est un développement asymptotique à multiple échelles effectuée autour de l'équilibre maxwellien de l'équation de Boltzmann en utilisant le nombre de Knudsen comme paramètre de développement. Brièvement, une développement à multiple échelles consiste à étudier une approximation finie d'une fonction afin d'obtenir une solution approximée dans le voisinage de celle-ci [28]. Ce type de développement ne devrait pas être perçue comme une série traditionnelle (telles que les séries de Taylor), même si elles sont généralement ainsi formalisés, puisque ces approximations divergent dans le temps. Ces développements, dont l'étude relève plutôt des mathématiques, sont souvent utilisés dans l'analyse de la stabilité d'écoulements (voir par example l'excellent livre de Chandrasekhar [63] et les notes de Cossu [69]), et sont décrit avec un fort niveau de rigueur dans le livre de Bender [28]. Le résultat du développement de Chapman-Engskogg sera discuté dans le contexte relativement plus simple de l'opérateur de collision BGK lorsque la méthode de Boltzmann sur réseau pour les écoulements de fluides incompressibles sera introduite. Cependant, ce développement peut également être effectuée de manière analytique dans le cas d'un opérateur de collision générique. Une telle démonstration est effectuée avec grande élégance dans le livre de Kremer [159] et avec beaucoup de rigueur dans le livre de Saint-Raymond [271].

2.4 Résolution numérique des équations de la mécanique des fluides

Dans ce chapitre, nous présentons deux méthodes numériques pour la résolution des équations de Navier-Stokes incompressible : la méthode des volumes finis et la méthode de Boltzmann sur réseau. Ces deux méthodes sont fortement distinctes. La méthode des volumes finis est plus classique et est un outil numérique générique pour la résolution d'équations aux dérivées partielles. La méthode de Boltzmann sur réseau s'appuie quant à elle sur une équation

mésoscopique (l'équation de Boltzmann) afin de reproduire les équations de la mécanique des fluides. Les avantages et les inconvénients de ces deux méthodes seront décrits. De plus, nous abordons la problématique importante de la modélisation de la turbulence ainsi qu'une thématique particulière à l'étude du mélange : les conditions limites en mouvement.

Afin de rester concis, les méthodes qui ne sont pas utilisées dans le présent travail, c'est à dire les méthodes des différences finies et des éléments finis, ne sont pas présentées. Nous notons qu'elles sont déjà expliquées ailleurs.Dans le cas de la méthode des éléments finis, nous référons le lecteur au livre de Lohner [181]. Le lecteur intéressé à la méthode des différences finies dans le contexte de la mécanique des fluides peut quant à lui consulter le livre de Ferziger et Perić [97].

2.4.1 La méthode des volumes finis

La méthode des volumes finis est basée sur une discrétisation du domaine physique en volumes de contrôle au sein desquels les variables physiques (la densité, la vitesse, la pression) sont calculées aux centroïdes des volumes (*cell-centered*), à l'intersection des centroïdes (*cell-centered with staggered mesh*) ou aux noeuds des volumes (*vertex-centered*) [316]. Dans les schémas volumes finis conçus pour opérer sur des maillages non-structurés, les variables physiques sont souvent calculées aux centroïdes des volumes de contrôle. La présentation qui suit demeurera donc dans ce contexte.

La méthode des volumes finis s'appuie principalement sur la notion de flux afin d'abaisser l'ordre des opérateurs différentiels dans les équations aux dérivées partielles (EDP). En effet, en utilisant le théorème de Gauss-Ostrogradsky, les termes en divergence dans les EDP peuvent être calculés comme des flux sur les surfaces des volumes de contrôle [310]. Ceci a plusieurs avantages, notamment d'assurer de manière naturelle la conservation locale des quantités physiques (jusqu'à la précision machine).

Afin de rester concise, la discussion dans la présente section se limitera à deux aspects de la méthode des volumes finis dans le contexte des équations de Navier-Stokes incompressibles : l'imposition de l'incompressibilité et le choix d'un schéma de discrétisation.

2.4.2 L'imposition de l'incompressibilité

Comme nous l'avons mentionné dans la section 2.1, une équation d'état de fluide incompressible implique une vitesse du son infinie. Conséquemment, le calcul de la pression doit être effectué en utilisant un schéma implicite ou partiellement implicite afin d'obtenir un écoulement à divergence nulle [97, 316]. Dans la majorité des plateformes logicielles, telles que

Fluent, CFX, Open∇FOAM ou Code Saturne, ceci est accompli par l'usage d'un schéma de type prédicteur-correcteur. Malgré le fait que plusieurs schémas de ce type existent dans la littérature, ceux-ci partagent de nombreuses similarités. Conséquemment, nous nous limiterons à résumer les étapes essentielles d'un tel schéma en nous basant sur le mieux connu, c'est-à-dire l'algorithme SIMPLE (*Semi-Implicit Method for Pressure-Linkage Equations*) qui fut introduit par Patankar *et al.* [244]. L'objectif de ce type d'algorithme est de permettre le calcul d'un champ de vitesse à divergence nulle, tout en découplant les vecteurs vitesses entre eux et en ne requérant que la solution d'une équation de Poisson pour la pression. Les étapes résultantes sont comme suit :

- calculer un champ de vitesse à partir du champ de pression et des composantes de la vitesse obtenues à l'itération précédente ;
- recalculer les flux aux surfaces ;
- résoudre l'équation de Poisson pour la pression ;
- corriger le vecteur vitesse et les flux à partir de la nouvelle pression ;
- résoudre les autres équations de transport (si présentes) et
- si la convergence est atteinte, arrêter, sinon procéder à l'itération subséquente afin d'obtenir un nouvel estimé pour la vitesse.

Plusieurs extensions à cet algorithme ont été proposées telles que SIMPLE révisé (SIMPLER) [243], SIMPLE consistant (SIMPLEC) [313] et PISO (*Pressure Implicit with Splitting of Operators*) [136]. Dans la méthode SIMPLER, une équation de la continuité discrétisée est utilisée pour obtenir une équation discrétisée pour la pression plutôt qu'une correction de pression. Dans l'algorithme SIMPLEC, une forme approximée des termes de vitesses issues des cellules voisines est maintenue lors du calcul de la correction de vitesse. Finalement, le schéma PISO intègre, quant à lui, une seconde étape de correction de pression. Ce dernier schéma a l'avantage d'être plus robuste pour des écoulements instationnaires [316].

Schéma de discrétisation pour les flux

Le calcul des flux pour les termes convectifs aux faces joignant les volumes de contrôle constitue le coeur de la méthode des volumes finis. Un schéma de discrétisation de flux devrait avoir les propriétés ci-dessous [316] :

- Précision : un schéma devrait être suffisamment précis et peu diffusif. Un schéma de second ordre est donc nécessaire pour maintenir une précision suffisante.
- Conservativité : un schéma doit permettre une construction consistante des flux afin d'assurer une formulation conservative.
- Limitabilité : cette propriété peut se résumer brièvement par le fait qu'en absence de source, la valeur d'une quantité physique doit rester bornée par ses conditions

limites et initiales. Quand cette propriété n'est pas préservée, des oscillations peuvent se manifester dans la solution. Ceci est un enjeu récurrent dans les problèmes où le transport domine et en présence de discontinuités telles que des ondes de choc [307].

— Transport : un schéma de flux doit respecter la direction physique de la propagation de l'information. Ceci est critique pour une résolution stable des équations hyperboliques. Un tel schéma est qualifié transporteur.

Cependant, peu de schémas possèdent toutes ces propriétés. Le schéma *upwind*, de loin le plus connu, est conservatif, limité et transporteur, mais souffre d'une piètre précision (premier ordre) et est hautement diffusif lorsque l'écoulement n'est pas aligné avec le maillage. Le schéma centré, bien que de second ordre, n'est pas limité ni transporteur. Il peut donc être inadapté lorsque les équations ont un fort caractère hyperbolique. Dans ce cas, ses défauts peuvent être allégés par l'usage de schémas hybrides qui combinent les schémas *upwind* et centrés afin de tirer avantage des forces combinées des deux schémas. Une autre famille de schéma qui possède l'ensemble des propriétés désirées est les schémas à variation totale décroissante (*Total Variation Diminishing - TVD*) tels que les schémas MUSCL ou TVD-QUICK. En effet, ces schémas sont à la fois précis au second ordre et sont conservatifs, limités et transporteurs si un limiteur cohérent est utilisé.

2.4.3 La méthode de Boltzmann sur réseau

La méthode de Boltzmann sur réseau (LBM, de *Lattice Boltzmann Method*) est une méthode numérique relativement récente qui bénéficie de beaucoup d'attention depuis deux décennies. Cet intérêt peut en partie être attribué au caractère local de ce schéma numérique, ce qui en fait un candidat idéal pour le calcul haute performance [317]. Bien que la méthode fut originalement obtenue à partir des automates cellulaires, la LBM est maintenant perçue comme un schéma numérique à part qui a peu en commun avec ses racines d'automate. Le livre de Succi [290] retrace cette histoire avec grâce.

La MBR consiste en une famille de schéma qui utilise des étapes de propagation et de collisions sur une grille cartésienne structurée afin de résoudre une équation aux dérivées partielles (EDP). Bien qu'elle puisse être utilisée pour résoudre plusieurs EDP) [62], la MBR est principalement conçue pour résoudre les équations de la mécanique des fluides.

Dans ce dernier contexte, la MBR peut être vue comme la projection du sous-espace des vitesses microscopiques de l'équation de Boltzmann sur une base de polynômes d'Hermite isotropes et orthonormaux dont seuls les premiers moments sont résolus [207]. La MBR ne résout pas les équations de Navier-Stokes incompressibles à proprement dit, mais la forme faiblement compressible et athermique de l'équation de Navier-Stokes. Celle-ci, dans la li-

mite d'un faible nombre de Mach, tend vers les équations de Navier-Stokes incompressibles isothermiques [290].

Dans ce contexte, l'équation de Boltzmann avec son espace des vitesses discrétisé, que nous nommerons dorénavant équation de ξ-Boltzmann, prend la forme :

$$\frac{\partial f_i\left(\boldsymbol{x}, \boldsymbol{\xi}_i, t\right)}{\partial t} + \boldsymbol{\xi}_i \cdot \nabla_x \left(f\right) = \Omega_i \tag{2.37}$$

avec f_i l'ensemble des populations discrètes associées aux $\boldsymbol{\xi}_i$ vitesses discrètes et Ω_i l'opérateur de collision qui y est associé. Cet ensemble de vitesses discrètes définit le type de noeuds utilisé dans le réseau. Ces noeuds sont généralement nommés DxQy, où x est la dimension physique du problème (le nombre de dimensions spatiales) et y le nombre de vitesses discrètes.

L'opérateur de collision peut prendre plusieurs formes, mais nous nous limiterons ici au contexte plus simple d'un opérateur de collision de type BGK. Pour cet opérateur, l'équation ξ-Boltzmann prend la forme :

$$\frac{\partial f_i\left(\boldsymbol{x}, \boldsymbol{\xi}_i, t\right)}{\partial t} + \boldsymbol{\xi}_i \cdot \nabla_x \left(f_i\right) = \frac{\left(f_i^{eq} - f_i\right)}{\tau} \tag{2.38}$$

où f^{eq} est la distribution à l'équilibre des populations. Cette équation peut être écrite sous une forme discrète en prenant l'approximation en différences finies de la dérivée temporelle et en intégrant par la méthode des trapèzes sur le long des courbes caractéristiques (c.-à-d. les directions du réseau), menant à :

$$f_i\left(\boldsymbol{x} + \boldsymbol{\xi}_i \Delta t, \boldsymbol{\xi}_i, t + \Delta t\right) - f_i\left(\boldsymbol{x}, \boldsymbol{\xi}_i, t\right) = \frac{1}{\bar{\tau}}\left(f_i^{eq}\left(\boldsymbol{x}, \boldsymbol{\xi}_i, t\right) - f_i\left(\boldsymbol{x}, \boldsymbol{\xi}_i, t\right)\right) \tag{2.39}$$

avec $\bar{\tau}$ le temps de relaxation adimensionnel, qui sera relié à la viscosité dynamique du fluide ultérieurement.

À l'aide d'un dévelopement de Chapman-Enskogg, on peut montrer que l'Équation (2.39), accompagnée de la distribution à l'équilibre appropriée, permet de récupérer les équations de Navier-Stokes athermique sous leur forme faiblement compressible. Deux chemins distincts employant de ce dévelopement peuvent mener à cette conclusion. Par souci de concisions, ces deux approches seront brièvement résumées ici. La première consiste à calculer les moments en vitesse de l'équation de ξ-Boltzmann discrétisée (2.39) après le dévelopement de Chapman-Enskogg. Ceci permet d'obtenir une équation de conservation discrète pour les deux premiers moments (la masse volumique et la quantité de mouvement) et de fermer les tenseurs d'ordre supérieurs qui apparaissent dans l'équation de conservation de la quantité de mouvement. Cette approche, plus classique, est présentée en détails dans la thèse de Matilla [200].

Une seconde avenue consiste à projeter les composantes de vitesse de l'équation de Boltzmann continue avec un opérateur de collision (par exemple BGK), ainsi que la distribution à l'équilibre (2.32) (la m,axwellienne), sur une base de polynômes d'Hermite orthonormaux avant d'effectuer l'expansion de Chapman-Enskogg. En obtenant les moments dans l'espace des vitesses de cette équation, une tâche facilitée par la projection sur la base de polynômes d'Hermite, on obtient une équation continue pour les moments dont la conservation est désirée (masse volumique, quantité de mouvement, énergie). Cependant, afin de fermer les équations, le développement polynomiale d'Hermite de la distribution à l'équilibre (2.32) doit être tronquée. Une troncature au second ordre permet de retrouver la forme athermique des équations de Navier-Stokes faiblement compressible, ce qui est la forme couramment utilisée dans la littérature. Une troncature à l'ordre supérieur permet quand à elle de retrouver les équations de Navier-Stokes sous les formes athermiques compressible et compressible, respectivement.

De cette seconde approche, on constate que l'ordre de troncature de la maxwellienne impose non seulement le degré du polynôme employé pour la distribution à l'équilibre, mais aussi le nombre de vitesses discrètes employées, car ce dernier est dicté par le degré du polynôme devant être intégré exactement. Conséquemment, les vitesses discrètes, ainsi que leurs poids respectifs, ne sont rien de moins que des points dans une quadrature de Gauss-Hermite permettant l'intégration exacte d'une fonction polynomiale dans l'espace des vitesses. De tels concepts sont abordés dans les démonstrations de Malaspinas [190] et de Shan *et al.* [275]

Pour une troncature de second ordre, la distribution à l'équilibre f^{eq} prend la forme :

$$f_i^{eq} = w_i \rho \left(1 + \frac{(\boldsymbol{\xi}_i \cdot \boldsymbol{u})}{c_s^2} + \frac{(\boldsymbol{\xi}_i \cdot \boldsymbol{u})^2}{2c_s^4} - \frac{\boldsymbol{u} \cdot \boldsymbol{u}}{2c_s^2} \right) \tag{2.40}$$

avec $c_s = \frac{1}{\sqrt{3}} \frac{\Delta x}{\Delta t}$ la célérité du réseau et ω_i le poid associé à la population i. Le temps de relaxation adimensionnel est choisi afin de retrouver la viscosité dynamique :

$$\bar{\tau} = \frac{\mu}{\rho c_s^2 \Delta t} + \frac{1}{2} \tag{2.41}$$

Les moments d'intérêt, c'est à dire la masse volumique et la quantité de mouvement, sont obtenus en sommant les populations sur l'ensemble des vitesses discrètes :

$$\rho = \sum_i f_i \tag{2.42}$$

$$\rho \boldsymbol{u} = \sum_i f_i \boldsymbol{\xi}_i \tag{2.43}$$

L'algorithme sous-jacent à la LBM se divise en deux étapes distinctes. Premièrement, l'opérateur de collision est appliqué à chaque noeud du réseau. Puis, les particules sont advectées à la vitesse caractéristique qui leur est associée, ce qui permet de calculer à nouveau les variables macroscopiques à chaque noeud. Bien que ceci ne soit pas démontré ici, le schéma numérique résultant est du second ordre en temps et en espace sous réserve que des conditions limites appropriées soient utilisées.

2.4.4 La modélisation de la turbulence

Il existe de nombreuses manières de réduire le nombre de degrés de liberté causés par le large éventail d'échelles associées à la turbulence [270]. Cependant, la quasi-totalité de ces approches requière l'utilisation de la mécanique des fluides numérique (CFD) afin de résoudre les équations de Navier-Stokes et, parfois, celles d'un modèle de turbulence. Maintenant que nous avons présentés les deux approches de CFD considéré dans cette thèse, nous pouvons retourner à la problématique de la modélisation de la turbulence.

La première classe de modèle est basée sur le moyennage temporel des équations de Navier-Stokes pour toutes les échelles (*Reynolds averaged Navier-Stokes - RANS*) dans laquelle la solution exacte est divisée en la somme de sa moyenne statistique (temporelle ou d'ensemble) $\bar{\boldsymbol{u}}$ et une fluctuation $\boldsymbol{u}'$. Cette décomposition, généralement nommée décomposition de Reynolds permet d'obtenir les équations RANS [57] :

$$\nabla \left(\bar{\boldsymbol{u}} \otimes \bar{\boldsymbol{u}} \right) = -\frac{1}{\rho} \nabla p + \nu \nabla^2 \bar{\boldsymbol{u}} - \nabla \left(\boldsymbol{u}' \otimes \boldsymbol{u}' \right) \tag{2.44}$$

Il est cependant nécessaire de modéliser le tenseur de Reynolds $(\boldsymbol{u}' \otimes \boldsymbol{u}')$ et c'est à ce niveau que réside une grande partie des défis associés aux méthodes RANS. La majeure partie des modèles de fermeture utilisés ajoutent une viscosité turbulente à la viscosité physique du fluide afin de modéliser le processus dissipatif associé à la cascade de Kolmogorov, tel que discuté à la Section 2.1.3. Des exemples de tels modèles sont les modèles $k-\epsilon$, $k-\omega$, Spallart-Allmaras, etc. Chacun de ces modèles a ses forces et ses faiblesses et leur usage doit être corrélé avec la configuration de l'écoulement (ouvert, fermé, etc.). Le modèle de $k-\epsilon$ demeure le plus utilisé dans plusieurs configurations d'écoulements telles que les mélangeurs [115, 299].

L'approche RANS peut aussi être utilisée pour obtenir une solution instationnaire. De telles méthodes sont baptisées URANS et, globalement, permettent de capturer les structures à basse fréquence d'un écoulement. De manière générale, les simulations RANS et URANS peuvent être employées avec des maillages relativement grossiers, car la totalité de la cascade turbulente est modélisée par le modèle de fermeture employé pour le tenseur de Reynolds.

Une approche complètement différente est la simulation des grandes larges échelles (LES, de l'anglais *Large Eddy Simulation*) dans laquelle un filtre passe-bas est appliqué pour modéliser les petites échelles turbulentes tandis que les grandes échelles sont complètement résolues par le maillage [270]. Ceci permet d'obtenir des équations filtrées dans lesquelles la dissipation due aux contraintes de sous-maille est modélisée par une viscosité turbulente. Les simulations LES requièrent des maillages nettement plus fins que les simulations RANS afin de résoudre les grandes échelles, mais ne requièrent pas d'équations de transport supplémentaires comme le font les modèles RANS. De surcroît, la LES est intrinsèquement instationnaire et ne permet pas d'obtenir une solution en régime permanent. Il est donc nécessaire de moyenner des résultats instationnaires afin d'obtenir un résultat moyen représentatif de l'écoulement. Finalement, ces modèles ont tendance à surestimer la dissipation en proche paroi et requièrent l'usage de fonction d'amortissement (*wall damping functions*) afin d'obtenir des résultats valables à cet endroit. Le modèle de sous-maille le plus commun demeure le modèle de Smagorinsky, qui a été utilisé avec un franc succès dans la modélisation de l'écoulement turbulent dans des mélangeurs par Derksen *et al.* [78,79] et Guha *et al.* [115]. On note cependant que le modèle de Smagorinsky demeure limité et que des alternatives plus performantes, telles que celles basées sur l'usage de filtre dynamique [104], démontrent une meilleure performance et une plus grande généralité.

2.4.5 Conditions limites pour des corps en mouvements

Comme nous l'avons mentionné précédemment, la simulation des procédés de mélange nécessite une stratégie permettant de modéliser des géométries complexes en mouvement. Ceci, bien que d'apparence triviale, représente un défi important en simulation numérique.

Pour des configurations simples, la rotation de l'agitateur peut être simplifiée par un changement de référentiel [50]. Cependant, l'ajout d'obstacles tels que des chicanes ou le décentrement de l'agitateur rend cette approche invalide. De nombreuses stratégies ont été développées afin de s'affranchir de ce problème [50].

Historiquement, la condition limite d'agitateur, une méthode semi-empirique, fut la première méthode proposée. Dans cette approche, l'agitateur est exclu du domaine de simulation et est remplacé par des conditions limites de Dirichlet imposées à l'aide de données expérimentales. Cette approche est fortement limitée et imprécise, car elle requiert des données expérimentales et néglige l'interaction entre l'agitateur et le reste de la géométrie [98].

Une seconde approche est la méthode des référentiels multiples (*multiple reference frame - MRF*) introduite par Luo *et al.* [187]. Dans cette approche, le domaine physique est décomposé en sous-domaines cylindriques non superposés qui évoluent dans des référentiels

différents. Dans le cas d'un mélangeur, l'agitateur est considéré dans un référentiel en rotation alors que le reste de la cuve est dans un domaine statique. De l'information est échangée entre les deux référentiels à leur interface, et celle-ci doit préférablement être située suffisamment loin de tout élément de géométrie. Cette méthode est uniquement valide pour des études stationnaires [187].

La méthode de maillage glissant (*Sliding mesh - SG*) est la première approche à maillage conforme qui est valide pour des écoulements instationnaires. Cette méthode s'appuie sur une décomposition identique à la méthode de référentiels multiples. Cependant, au lieu de modifier le référentiel selon le domaine, c'est plutôt le maillage qui est mis en mouvement. Ceci entraîne un défi additionnel, car il est nécessaire de déplacer le maillage et d'interpoler les flux de masse à l'interface entre les sous-domaines de manière conservative lorsque la conformité des maillages n'est plus parfaite. Cependant, cette méthode a l'avantage d'être valide en régime instationnaire. Elle est applicable à toutes les géométries où les volumes balayés par les agitateurs ne se superposent pas.

Une stratégie complètement différente réside dans les méthodes de conditions limites immergées (*immersed boundary method*) [110] et de domaine fictif [32]. Dans ces méthodes, la géométrie en mouvement n'est pas discrétisée à l'aide d'un maillage conforme. Elle apparaît plutôt comme un ensemble de points de contrôle (ou de volumes de contrôle) à l'intérieur du fluide qui sont utilisés pour imposer les conditions limites. Le fluide est quant à lui généralement maillé à l'aide d'un maillage cartésien structuré, avec ou sans raffinement local. Plusieurs types de méthode de cette nature existent et ils se différencient principalement par la stratégie et la formulation mathématique utilisées pour imposer la vitesse du solide aux points de contrôle. Deux familles de stratégie principales existent [217,249]. Dans la première, dite de forçage continu, un terme supplémentaire continu est ajouté au sein des équations de Navier-Stokes directement [7, 107]. Dans la seconde, les équations de Navier-Stokes sont résolues de manière régulière et le champ de vitesse obtenu est modifié a posteriori pour prendre en considération le corps solide [95, 189, 311].

2.5 Modélisation numérique des écoulements multiphasiques de type solide-fluide

Dans la section précédente, nous avons discuté des méthodes pouvant être utilisées pour résoudre les équations de Navier-Stokes incompressibles. La modélisation d'écoulements diphasiques de type solide-liquide est cependant nettement plus complexe et l'extension des méthodes précédemment abordées à ce type d'écoulement requiert l'usage de stratégies spécifiques aux écoulements solide-fluide.

L'objectif principal de cette section est de couvrir un large éventail de modèles numériques pouvant être utilisés pour modéliser les écoulements solide-fluide. Plusieurs modèles existent et ceux-ci ne sont pas valides dans tous les contextes. Dans cette présentation, nous nous limitons à présenter les méthodes qui sont valables pour tout nombre de Reynolds particulaire ($Re_p = \frac{\rho_f d_p |\boldsymbol{u}-\boldsymbol{v}|}{\mu}$). Ainsi, les méthodes de méthode de couplage de force (*Force coupling method*) [202,332], de dynamique stokésienne (*Stokesian dynamics*) [46,90] et de dynamique stokésienne accélérée (*accelerated Stokesian dynamics*) [20,280], qui sont limitées à des nombres de Reynolds tels que $Re_p << 1$, ne sont pas considérées. De plus, les méthodes basées sur des modèles purement phénoménologiques [101, 212] ou sur des automates granulaires [197, 198] ne sont pas considérées compte tenu de leur manque de généralité.

2.5.1 Les équations de Navier-Stokes moyennées volumiquement

Les équations de Navier-Stokes moyennées volumiquement (VANS) sont la pierre angulaire de nombreux modèles numériques qui seront abordés ultérieurement dans cette revue de littérature. Ici, nous nous limitons à une présentation de ces équations dans un contexte solide-fluide où le solide est la phase dispersée (statique ou en mouvement) et le fluide la phase continue.

Les équations VANS sont obtenues à l'aide d'une fonction indicatrice de phase $\chi_i(\boldsymbol{x}, t)$ pour chaque phase i. Cette fonction vaut 1 si la phase est présente à la position $\boldsymbol{x}$ au temps t et 0 autrement. Ceci permet de décrire la moyenne d'ensemble d'une variable ϕ comme $\langle\phi\rangle = \frac{\langle\phi\chi_i\rangle}{\langle\chi_i\rangle}$. Sous une hypothèse d'ergodicité, cette moyenne peut aussi être perçue comme une moyenne volumique ou temporelle, selon le contexte. Pour le cas d'une moyenne volumique, l'hypothèse d'ergodicité implique que le volume utilisé pour constituer la moyenne doit être statistiquement représentatif de l'écoulement multiphasique. Une discussion étendue sur ce qui constitue une moyenne volumique appropriée est effectuée en grand détail dans le Chapitre 6 du livre de Crowe *et al.* [70].

On note que ces équations ont été obtenues sous différentes formes par différents auteurs, parmi ceux-ci [4, 44, 70, 89, 105, 194, 195, 254]. Les différences entre les formulations obtenues dépendent de la procédure utilisée pour la moyenne, des hypothèses de fermeture utilisées. Qui plus est, la formulation du terme couplant les phases solide et liquide dépend du type de description (Eulérienne ou Lagrangienne) utilisée pour la phase solide. Ainsi, plusieurs formes des équations VANS seront introduites lorsque nécessaire. Nous nous contentons ici

de poser une forme très générique pour chaque phase i :

$$\frac{\partial \epsilon_i \rho_i}{\partial t} + \nabla \cdot (\epsilon_i \rho_i \boldsymbol{u}_i) = 0 \tag{2.45}$$

$$\frac{\partial \epsilon_i \rho_i \boldsymbol{u}_i}{\partial t} + \nabla \cdot (\epsilon_i (\rho_i \boldsymbol{u}_i) \otimes \boldsymbol{u}_i) = \epsilon_i (\boldsymbol{F}_g - \nabla p) + \nabla \cdot \boldsymbol{\tau} \tag{2.46}$$

avec $\boldsymbol{F}_g$ une force volumique, $\boldsymbol{\tau}$ le tenseur des contraintes visqueuses, et ϵ_i, ρ_i, $\boldsymbol{u}_i$ la fraction volumique, la densité et la vitesse de la phase i.

Résolution des équations VANS par la LBM

La LBM serait un outil numérique pertinent pour résoudre les équations VANS. Cependant, comme ces dernières ne sont pas conservatives pour chaque phase, leur écriture dans une description mésoscopique est un défi théorique important compte tenu de l'équation d'état non idéale qui en résulte. Deux familles de schéma ont été proposées pour résoudre les équations VANS dans la LBM. La première approche est basée sur un opérateur de collision modifié pour prendre en compte la fraction volumique de fluide ainsi que l'ajout d'un terme source de force afin de corriger le gradient de pression [272,321,330,334]. Cependant, cette approche n'a jamais été testée pour des cas où la fraction volumique de fluide variait considérablement dans l'espace et sa convergence vers les équations VANS n'a jamais été confirmée numériquement.

La seconde approche consiste à formuler les équations VANS sous forme non-conservative à l'aide de termes sources de masse et de quantité de mouvement [286].Cependant, cette approche brise le caractère explicite de la LBM compte tenu de l'ajout d'un terme source de masse. À nouveau, la convergence de cette approche n'a pas été démontrée.

Ainsi, bien que la LBM apparaisse comme un outil intéressant pour la résolution des équations VANS, rien dans la littérature actuelle indique qu'on puisse l'utiliser pour résoudre les équations VANS.

2.5.2 Les modèles deux fluides

Les modèles à deux fluides (TFM) sont une famille d'approche Euler-Euler qui considère que les phases (gaz-solide, solide-liquide, gaz-liquide) sont deux milieux continus interpénétrants pouvant être représentés par les équations VANS. Plusieurs variantes de ces formulations existent et leur formulation dépend principalement de la nature (solide, liquide, gaz) et de la concentration (dense, concentrée, diluée) des deux phases [70,135]. Nous nous limiterons ici à présenter ces équations dans un contexte URANS pour la modélisation d'écoulement solide-liquide, ce qui est la formulation utilisée dans la littérature de mélange solide-liquide (voir

par exemple [129, 148, 149, 183, 211, 212, 218, 219, 228, 294, 296–299]). Celle-ci est généralement résolue par des codes commerciaux tels que Fluent [8].

Dans le modèle deux fluides, la conservation de la masse et de la quantité de mouvement (QDM) pour une phase i peut s'écrire :

$$\frac{\partial \epsilon_i \rho_i}{\partial t} + \nabla \cdot (\epsilon_i \rho_i \boldsymbol{u}_i) = 0 \tag{2.47}$$

$$\frac{\partial \epsilon_i \rho_i \bar{\boldsymbol{u}}_i}{\partial t} + \nabla \cdot (\epsilon_i (\rho_i \bar{\boldsymbol{u}}_i) \otimes \bar{\boldsymbol{u}}_i) = \epsilon_i (\boldsymbol{F}_g - \nabla p) + \boldsymbol{\mathcal{M}}_{ij} + (\mu_i + \mu_t) \nabla \cdot \left(\nabla \bar{\boldsymbol{u}}_i + (\nabla \bar{\boldsymbol{u}}_i)^T \right) \tag{2.48}$$

avec $\boldsymbol{F}_g$ les forces volumiques, μ_t la viscosité turbulente et $\boldsymbol{\mathcal{M}}_{ij}$ le terme de transfert de quantité de mouvement (momentum) entre une phase i et une phase j. Le terme de transfert de quantité de mouvement est généralement constitué uniquement de la traînée et prend la forme :

$$\boldsymbol{M}_{12} = C_D (\bar{\boldsymbol{u}}_2 - \bar{\boldsymbol{u}}_1) \tag{2.49}$$

avec C_D le coefficient de traînée qui doit être adapté dans une formulation Euler-Euler et doit prendre une forme telle que celles proposées par Ishii-Zuber [135], Schiller-Nauman [183], Ihme [183], Clift [299] Beetstra [26] et Wen-Yu-Ergun [94, 323].

2.5.3 La méthode des éléments discrets

La méthode des éléments discrets (DEM, de l'anglais *Discrete Element Method*) est une méthode basée sur la solution de la seconde loi de Newton dans un référentiel Lagrangien. Ainsi, la position et la vitesse de chacune des particules sont connues et ces dernières sont libres d'entrer en collision avec leurs voisins ou des éléments de géométrie [31, 337]. Deux formes de la DEM, souple (DEMs) et rigide (DEMh), existent et se distinguent par l'approche employée pour résoudre les collisions entre les particules. Dans la DEMs, un léger chevauchement des particules est permis et est utilisé pour calculer les forces de collision à partir de modèles de forces [337] tandis que dans la DEMh, les collisions entre les particules sont instantanées, binaires et le calcul des vitesses post-collisionnelles s'effectue directement à partir des propriétés des particules et non à travers des modèles de force [128]. Ces deux stratégies distinctes ont chacune leur forces et leur faiblesses propres. Compte tenu de la rigidité des solides, un très faible pas de temps, relié à la vitesse de propagation des ondes de Rayleigh et au diamètre des particules, doit être utilisé en DEMs. En DEMh, le caractère instantané des collisions limite la méthode à des collisions binaires, rendant la méthode inapplicable pour des écoulements où la concentration volumique locale de particules surpasse 5%.

Les types de forces prise en considération dans la DEM sont choisis individuellement par l'utilisateur [337] et requièrent chacun un modèle distinct. Comme chaque particule est un corps discret, elle peut avoir sa propre taille et sa propre masse volumique.

La présentation dans le présent chapitre sera limitée à la DEMs, de par son applicabilité aux écoulements concentrés ainsi qu'au cas des particules parfaitement sphériques, bien que des extensions à la DEMs permettent la simulation de particules non-sphériques [31, 186, 240]. Ce dernier point demeure un sujet de recherche actif.

2.5.4 Méthode des éléments discrets souple - DEMs

Dans la DEMs, la seconde loi de Newton pour une particule i s'écrit [337] :

$$m_i \frac{d\boldsymbol{v}_i}{dt} = \sum_j \boldsymbol{F}_{c,ij} + \sum_k \boldsymbol{F}_{nc,ik} + \boldsymbol{F}_{pf,i} + \boldsymbol{F}_{g,i} \tag{2.50}$$

$$I_i \frac{d\boldsymbol{\omega}_i}{dt} = \sum_j \boldsymbol{M}_{ij} \tag{2.51}$$

où m_i est la masse de la particule, $\boldsymbol{v}_i$ sa vitesse, $\boldsymbol{F}_{c,ij}$ les forces de contacts dues à la collision avec la particule j, $\sum_k \boldsymbol{F}_{nc,ik}$ les forces à longue portée - telles que les forces de van der Waals ou de lubrification - entre les particules i et k, $\boldsymbol{F}_{pf,i}$ les forces dues au fluide environnant, $\boldsymbol{F}_{g,i}$ la gravité, I_i le moment d'inertie de la particule, $\boldsymbol{\omega}_i$ sa vitesse angulaire et $\boldsymbol{M}_{ij}$ les moments appliqués à la particule i en contact avec une particule j. Le schéma à la figure 2.3 illustre l'action de ces forces. Numériquement, ces équations sont intégrées dans le temps pour calculer la vitesse et la position de chaque particule i en utilisant un schéma d'intégration explicite tel qu'un schéma d'Euler [86], de Gear [19] ou de Verlet [102]. Grâce à sa simplicité, à sa précision (allant jusqu'à l'ordre 4) et à son faible usage de mémoire, le schéma de Verlet est optimal [102].

Au coeur de la DEMs réside le modèle de collision basé sur le chevauchement (*overlap*) des particules. Ce chevauchement modélise la déformation des particules entrant en contact. Les forces résultantes de ce contact sont décomposées en deux composantes : tangentielles ($\boldsymbol{F}_{ct,ij}$) et normales ($\boldsymbol{F}_{cn,ij}$), qui sont modélisées séparement [31, 161, 337]. Les forces de contact s'expriment sous la forme :

$$\boldsymbol{F}_{c,ij} = \boldsymbol{F}_{cn,ij} + \boldsymbol{F}_{ct,ij} \tag{2.52}$$

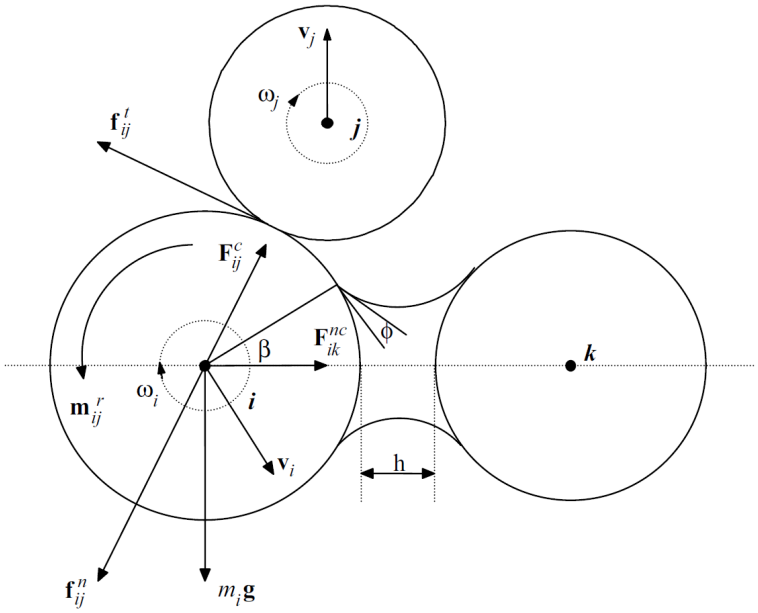

Figure 2.3 Représentation des forces pouvant être prises en considération dans la DEM entre des particules qui sont en contact (i,j) ou qui sont distantes (i,k) - reproduit de [337]

Forces de contact normales

Kruggel-Emden *et al.* [161] ont effectué une revue de littérature et une comparaison exhaustive des modèles de force de contact normale et a recensé quatre catégories :

- modèles à potentiel continu ;
- modèles viscoélastiques linéaires ;
- modèles viscoélastiques non-linéaires et ;
- modèles à hystérésis

Les modèles à potentiel continus sont obtenus à partir de potentiels répulsifs qui ne dépendent que de la distance interparticulaire tel que le potentiel de Lennard-Jones [9]. Ces potentiels donnent des résultats peu physiques pour les écoulements granulaires, car ils introduisent des forces de contact normales entre les particules qui sont non-nulles lorsque les particules ne sont pas en contact [161].

Les modèles linéaires viscoélastiques regroupent principalement des variantes du modèle à ressort et amortisseur linéaire introduit par Cundall et Strack [71] :

$$\boldsymbol{F}_{cn,ij} = -k_n \boldsymbol{\delta}_{n,ij} - \gamma_n \dot{\boldsymbol{\delta}}_{\boldsymbol{n}} \tag{2.53}$$

avec k_n la rigidité du ressort, γ_n le coefficient d'amortissement, $\boldsymbol{\delta}_{n,ij}$ le chevauchement normal

entre les particules i et j et $\dot{\boldsymbol{\delta}}_{\boldsymbol{n}}$ sa dérivée temporelle. Généralement, les paramètres k_n et γ_n peuvent être calculé en se basant sur des corrélations en terme du module de Young, du coefficient de Poisson, du diamètre, de la masse volumique ainsi que le coefficient de restitution des particules.

Les modèles viscoélastiques non-linéaires dérivent de la théorie de Hertz [125] pour la collision purement élastique entre deux sphères rigides. Ces modèles combinent généralement la force élastique de Hertz avec un amortisseur linéaire [178] ou non-linéaire (dépendant du chevauchement normal) [166, 309] afin de représenter le caractère dissipatif des collisions. On note qu'un amortisseur linéaire donne une dissipation maximale au début de l'impact, ce qui n'est pas cohérent avec les observations expérimentales. Un modèle non-linéaire performant est celui proposé par Tsuji [309] :

$$\boldsymbol{F}_{cn,ij} = -k_n \boldsymbol{\delta}_{n,ij}^{\frac{3}{2}} - \gamma_n \left| \boldsymbol{\delta}_{n,ij}^{\frac{1}{4}} \right| \dot{\boldsymbol{\delta}}_{\boldsymbol{n}} \tag{2.54}$$

Les modèles à hystérésis reproduisent le caractère dissipatif des collisions dû à la déformation en utilisant une rigidité du ressort variable. Conséquemment, la rigidité du ressort est plus élevée durant la phase d'amorçage de la collision ($|\dot{\boldsymbol{\delta}}_{n,ij}| \geq 0$) que dans le désamorçage de celle-ci ($|\dot{\boldsymbol{\delta}}_{n,ij}| \leq 0$) [305, 318].

Kruggel-Emden *et al.* [161] ont montré que les modèles de ressort et amortisseur linéaires ainsi que le modèle de Tsuji reproduisaient le plus fidèlement les résultats expérimentaux pour des rebonds simples.

Forces de contact tangentielles

Les forces tangentielles revêtent aussi de l'importance pour reproduire de manière précise les écoulements granulaires [31], mais les modèles de forces tangentielles sont moins développés compte tenu du défi important que représentent les expériences de rebonds avec un angle [162]. Deux types de modèle existent : linéaires ou non-linéaires.

Les modèles non-linéaires sont généralement basés sur la théorie de Mindlin-Deresiewicz [162, 215, 304] pour la composante élastique et supplémentés d'un amortisseur tangentiel non-linéaire. Sans perte de généralité, ces deux types de modèle peuvent s'écrire sous la forme générale :

$$\boldsymbol{F}_{ct,ij} = -k_t \boldsymbol{\delta}_{t,ij} + \gamma_t \dot{\boldsymbol{\delta}}_{t,ij} \tag{2.55}$$

avec k_t la rigidité du ressort, γ_t le coefficient d'amortissement tangentiel, $\boldsymbol{\delta}_{t,ij}$ le chevauche-

ment tangentiel et $\dot{\boldsymbol{\delta}}_{t,ij}$ sa dérivée temporelle. Dans les modèles non-linéaires, k_t est généralement une fonction de $\boldsymbol{\delta}_{n,ij}$.

Il est important de noter que les forces tangentielles sont bornées par la force de friction de Coulomb, force limite à partir de laquelle se produit du glissement entre les particules en contact. L'expression résultante est :

$$\boldsymbol{F}_{t,ij} = -\min\left(\left|k_t\boldsymbol{\delta}_{t,ij}\right|, \left|\mu_f\boldsymbol{F}_{n,ij}\right|\right)\operatorname{sign}\left(\boldsymbol{\delta}_{t,ij}\right) \tag{2.56}$$

2.5.5 CFD-DEM

La CFD-DEM n'est pas un modèle proprement dit, mais plutôt le résultat du couplage entre la mécanique des fluides numérique (CFD) et la DEM. Deux grandes familles de CFD-DEM peuvent être identifiées : la CFD-DEM résolue et non résolue.

Dans la CFD-DEM résolue, le maillage fluide est discrétisé plus finement que les particules et celles-ci se manifestent comme des conditions limites pour le fluide. Le couplage entre les deux phases découle directement de l'application de la condition limite de non-glissement à la paroi des particules [81, 82, 107, 108, 167–169]. La nécessité de résoudre l'écoulement à l'échelle des particules limite fortement le nombre de particules pouvant être simulé. Par exemple, lorsque la LBM est utilisée comme schéma numérique, un minimum de 8 noeuds par diamètre de particules doit être utilisé afin de garantir une précision suffisante [302]. De surcroît, l'application des conditions limites de non-glissement à la surface des particules en mouvement requiert un schéma spécifique, généralement basé sur des conditions limites immergées, ce qui augmente fortement les temps de calcul.

La seconde classe de CFD-DEM, la CFD-DEM non-résolue, consiste à résoudre les équations VANS pour la phase fluide à une échelle plus grande que celle des particules, tout en décrivant le comportement de la phase solide à l'aide de la DEM. Ainsi, plusieurs particules peuvent occuper une même maille fluide. Le couplage entre les deux phases s'effectue en employant des expressions explicites pour chaque force d'interaction solide-liquide : traînée, portance de Saffman, etc. [336]. La forme des équations de VANS utilisée requiert aussi une attention particulière. Les trois formulations partagent la même équation de conservation de la masse :

$$\frac{\partial}{\partial t}\left(\epsilon_f\right) + \nabla\cdot\left(\epsilon_f\boldsymbol{u}\right) = 0 \tag{2.57}$$

mais la formulation de l'équation de conservation de la quantité de mouvement diffère entre les trois modèles :

Forme A (ou II) :

$$\rho_f \left(\frac{\partial}{\partial t} (\epsilon_f \boldsymbol{u}) + \nabla \cdot (\epsilon_f \boldsymbol{u} \otimes \boldsymbol{u}) \right) = -\epsilon_f \nabla p + \epsilon_f \nabla \cdot (\boldsymbol{\tau}_f) - \boldsymbol{F}_{pf}^{II} + \rho_f \epsilon_f \boldsymbol{g} \tag{2.58}$$

$$\boldsymbol{F}_{pf}^{II} = \frac{1}{\Delta V} \sum_i^{n_p} (\boldsymbol{f}_{pf,i} - \boldsymbol{f}_{\nabla p,i} - \boldsymbol{f}_{\nabla \cdot \boldsymbol{\tau},i}) \tag{2.59}$$

Forme B (ou I) :

$$\rho_f \left(\frac{\partial}{\partial t} (\epsilon_f \boldsymbol{u}) + \nabla \cdot (\epsilon_f \boldsymbol{u} \otimes \boldsymbol{u}) \right) = -\nabla p + \nabla \cdot (\boldsymbol{\tau}_f) - \boldsymbol{F}_{pf}^{I} + \rho_f \epsilon_f \boldsymbol{g} \tag{2.60}$$

$$\boldsymbol{F}_{pf}^{I} = \frac{1}{\Delta V} \sum_i^{n_p} \boldsymbol{f}_{pf,i} \tag{2.61}$$

Forme B simplifiée (ou III) :

$$\rho_f \left(\frac{\partial}{\partial t} (\epsilon_f \boldsymbol{u}) + \nabla \cdot (\epsilon_f \boldsymbol{u} \otimes \boldsymbol{u}) \right) = -\nabla p + \nabla \cdot \boldsymbol{\tau} - \boldsymbol{F}_{pf}^{III} + \rho_f \epsilon_f \boldsymbol{g} \tag{2.62}$$

$$\boldsymbol{F}_{pf}^{III} = \frac{1}{\epsilon_f \Delta V} \sum_i^{n_p} (\boldsymbol{f}_{pf,i} - \boldsymbol{f}_{\nabla p,i} - \boldsymbol{f}_{\nabla \cdot \boldsymbol{\tau},i}) - \frac{1}{\Delta V} \sum_i^{n_p} \rho_f V_{p,i} \boldsymbol{g} \tag{2.63}$$

avec

$$\boldsymbol{f}_{pf,i} = \boldsymbol{f}_{d,i} + \boldsymbol{f}_{\nabla p,i} + \boldsymbol{f}_{\nabla \cdot \boldsymbol{\tau},i} + \boldsymbol{f}_{\mathrm{vm},i} + \boldsymbol{f}_{B,i} + \boldsymbol{f}_{\mathrm{Saff},i} + \boldsymbol{f}_{\mathrm{Mag},i} \tag{2.64}$$

où $\boldsymbol{F}_{pf}$ est le terme de transfert de momentum entre le fluide et la phase solide, $V_{p,i}$ le volume des particules, n_p le nombre de particules et $\boldsymbol{f}_{pf,i}$ est la force individuelle agissant sur la particule due à la présence du fluide environnant. La forme B simplifiée n'est pas générique, car elle est valide uniquement si :

$$\rho_f (1 - \epsilon_f) \left(\frac{\partial \boldsymbol{u}}{\partial t} + \nabla \cdot (\boldsymbol{u} \otimes \boldsymbol{u}) \right) \to 0 \tag{2.65}$$

Concrètement, ceci implique que l'écoulement du fluide circulant entre les particules est en régime stationnaire. Les formes A et B sont quant à elles complètement génériques et il est facile de montrer que, suite à quelques manipulations algébriques, elles sont mathématiquement équivalentes. Cependant, elles se distinguent de par la manière dont l'incompressibilité est mise en oeuvre. Dans la forme A, ϵ_f multiplie directement le gradient de pression, ce qui mène à une toute autre équation pour la pression, lorsque comparée aux équations de

Navier-Stokes standard. Il fut montré par Bouillard *et al.* [43] et Gidaspow [105] que cette forme peut souffrir d'une perte du caractère hyperbolique. La définition d'une telle perte et les conséquences s'y rattachant sont définies dans l'annexe A.

Dans la forme B, la pression est résolue de manière traditionnelle, et la pression au temps antérieur est alors soustraite de celle-ci pour faire apparaître le facteur ϵ_f devant le gradient de pression. Comme nous en avons discuté dans la section 2.1, la pression dans les équations de Navier-Stokes incompressibles, et aussi les équations VANS incompressibles, est définie instantanément en fonction du champ de vitesse compte tenu de la vitesse infinie de la propagation des ondes de pression. Conséquemment, l'utilisation d'une pression antérieure pour calculer la pression subséquente peut parfois mener à des instabilités numériques.

Kafui *et al.* [144] ont comparé les résultats obtenus par ces deux formulations pour la fluidisation de particules et ont montré que les résultats obtenus par la forme A se comparaient favorablement avec des expériences. Cependant, les commentaires soumis à cet article par Feng et Yu [96], ainsi que les réponses de Kafui *et al.* [145] mènent à la conclusion que les deux formes donnent des résultats qui sont théoriquement équivalents. L'analyse de Zhou *et al.* confirme cette hypothèse [336].

Il est intéressant de constater, à partir des formulations A et B, que le couplage solide-liquide requiert un nombre minimal d'hypothèses et permet d'intégrer toutes les forces hydrodynamiques désirées à partir de leurs expressions individuelles. Théoriquement, les formes A et B sont génériques et applicables à toute concentration, à toute valeur de Re_p et à tout régime d'écoulement.

Une étape importante du couplage entre les phases, qui est rarement détaillée, est le schéma de projection utilisé pour projeter les particules sur le maillage eulérien afin de définir la fraction volumique de fluide ϵ_f et de calculer le terme de forçage $\boldsymbol{F}_{pf}$. Le schéma employé pour cette projection doit conserver la masse et doit produire un champ ϵ_f menant à des simulations stables tout en ayant un coût de calcul acceptable.

La méthode standard proposée dans la littérature consiste à attribuer le volume d'une particule à une cellule fluide si le centroïde de cette particule réside dans la cellule [199]. Cette méthode donne de bons résultats pour les cas où $\frac{d_p}{\Delta x} \leq 3$, avec Δx la grandeur caractéristique des cellules. Cependant, lorsque le maillage est raffiné, cette méthode mène à des fractions volumiques fortement discontinues. Les méthodes suivantes ont été proposées pour améliorer l'étape de projection :

- le comptage de particules [199] ;
- la nuée conservative et non conservative de particules [199] ;
- la projection Gausienne préservant les moments [199] ;

— la formulation à deux grilles [75] ;
— l'approche divisée [61, 113, 156] et
— le reprisage de chaussettes (*darning socks*) [251].

Les travaux de Marshall *et al.* [199] et de Pirker *et al.* [251] ont analysé les capacités de certaines de ces méthodes. Les auteurs ont conclu que l'approche standard, le reprisage de chaussettes et la nuée conservative étaient les méthodes les plus appropriées, car elles étaient conservatives et menaient à un champ de fraction volumique bien posé. L'approche divisée, qui sous-divise une particule en poids de Gauss qui sont ensuite projetés par la méthode standard, ne fait que raffiner la méthode standard et possède les mêmes avantages tout en étant dotée d'un meilleur comportement lorsque Δx diminue. La méthode à deux grilles, qui emploie deux maillages différents pour la CFD et pour la définition de la fraction volumique, donne de fort bons résultats, mais est nettement plus complexes au niveau de l'implémentation et difficilement généralisable au cas de maillages non structurés. Il est important de noter que ceci demeure un sujet de recherche actif et qu'aucune méthode de projection ne réussit à être à la fois conservative, bien posée dans la limite où $\Delta x \to 0$ (et de mener à un champ $\epsilon_f \in C^0$, ou préférablement $\epsilon_f \in C^1$) et à un coût de calcul acceptable.

Applications

La CFD-DEM a été utilisée de manière étendue pour étudier principalement les écoulements gaz-solide dans des lits fluidisés [68, 87, 144, 247] et dans le convoyage pneumatique [163–165]. Cependant, son utilisation dans des géométries complexes reste limitée. Pour le cas où la phase continue est un liquide, à la connaissance de l'auteur, la méthode a été utilisée uniquement pour des cas où la phase liquide est de l'eau dans des applications de sédimentation [85, 87], d'hydrocyclones [336]. Elle a aussi été utilisé dans le contexte du mélange solide-liquide sous la forme CFD-DEMh par Derksen [80] Ayranci *et al.* [15], Gua *et al.* [115]. Les limites de ces études et les conclusions qui s'y rattachent seront abordées dans la section 2.6.

2.5.6 Méthode de particules en cellules multiphase (MP-PIC)

La méthode de particules en cellules multiphase (MP-PIC, de l'anglais *Multiphase Particles-In-Cells*) est une extension lagrangienne des méthodes de particules en cellules (voir la revue de Harlow *et al.* [120]) qui combinent une description eulérienne du fluide avec une approche par densité de population pour la phase solide, résultant en une description mixte lagrangienne et eulérienne [6]. Cette méthode a connu un regain de popularité récent en raison du développement du code commercial Barruda VR® [285]. Elle fut introduite pour la première

fois dans la fin des années 90 en 1D par Andrews *et al.* [5,6], puis ensuite généralisée en 2D par Snider [284] avant d'être finalement généralisée en 3D par Snider *et al.* [282]. Cette méthode est en constante évolution depuis lors, mais nous tenterons de la présenter sous sa forme la plus épurée par souci de concision.

Dans la méthode MP-PIC, le fluide est résolu en utilisant les équations VANS par une approche volume fini [6, 282] et les particules sont suivies en utilisant une description mixte lagrangienne-eulérienne. Dans leur description lagrangienne, les particules sont regroupées en plusieurs *parcelles*, qui sont définies comme des groupes de particules possédant la même position, la même vitesse et les mêmes propriétés physiques. Leur dynamique est décrite par une population (ou distribution) f régie par une équation de Langevin :

$$\frac{\partial f}{\partial t} + \nabla_x \cdot (f\boldsymbol{v}) + \nabla_v \cdot (f\boldsymbol{A}) = \Omega \tag{2.66}$$

avec $\boldsymbol{v}$ la vitesse de la phase solide, ∇_x et ∇_v les opérateurs ∇ dans l'espace des phases (ou des vitesses) et dans l'espace physique et Ω l'opérateur de collision qui permet aux particules de relaxer à l'équilibre. En premier lieu, nous ne considérerons pas cet opérateur dans notre présentation. Le terme $\boldsymbol{A}$ est constitué des forces agissant sur les particules et est égal à :

$$\boldsymbol{A} = C_D\left(\boldsymbol{u} - \boldsymbol{v}\right) - \frac{1}{\rho_p}\nabla_x P + \boldsymbol{g} - \frac{1}{\epsilon_s \rho_s}\nabla_x \cdot \boldsymbol{\tau_s} \tag{2.67}$$

Ces termes représentent les forces dues à la traînée, au gradient de pression dans le fluide, à la gravité ainsi qu'au gradient de contraintes granulaires respectivement.

Comme la résolution de ces populations s'effectue dans l'espace des phases ($\mathbb{R}^6$), les collisions ne sont pas prises en considération durant la résolution et les parcelles peuvent littéralement se traverser. Ceci n'a pas d'impact pour les écoulements solide-fluide très dilués, mais est évidemment non réaliste pour les cas plus concentrés où les collisions entre les particules ont un impact important sur l'écoulement et la répartition des solides. Pour permettre la simulation d'écoulements non dilués, les collisions entre les particules sont considérées par la projection du volume des parcelles sur le maillage eulérien afin de calculer la fraction volumique de particules ($\epsilon_p = 1 - \epsilon_f$). Cette dernière est ensuite utilisée pour calculer le tenseur de contrainte granulaire ($\boldsymbol{\tau_s}$), un tenseur diagonal et isotrope qui permet de calculer le gradient de pression granulaire [109] et ainsi empêcher que la fraction de solide ne surpasse la fraction maximale de solide. L'expression de ce tenseur est :

$$\boldsymbol{\tau_s} = \frac{P_s \epsilon_p^{\beta}}{\epsilon_{p,m} - \epsilon_p}\boldsymbol{\mathcal{I}} \tag{2.68}$$

avec P_s une constante qui a les unités de la pression, $\epsilon_{p,m}$ la fraction maximale de solide et $\beta \in [2, 5]$ un exposant empirique. Plusieurs formulations alternatives existent pour cette contrainte [6, 29, 282], mais les différences entre elles sont mineures et visent principalement à stabiliser la pression dans la limite $\epsilon_p \to \epsilon_{p,max}$. Numériquement, le calcul du gradient de pression granulaire sur les trajectoires des particules est non trivial compte tenu de la raideur du gradient de pression granulaire et requiert des schémas semi-implicites particuliers qui sont détaillés par Snider *et al.* [282].

Pour résumer, dans la forme la plus simple de la MP-PIC, les particules échangent de la quantité de mouvement entre-elles uniquement par l'intermédiaire du gradient de pression granulaire, qui lui est un terme calculé dans un référentiel eulérien sur le maillage volume fini. Malgré la modélisation en apparence simple et naïve des collisions, la MP-PIC produit d'excellents résultats [282].

La modélisation des collisions entre les particules au sein de la MP-PIC fut progressivement améliorée afin de permettre un échange de quantité de mouvement entre les particules au sein des mêmes cellules via l'utilisation d'un opérateur de collision de type BGK [234–236]. Ceci requiert des stratégies de répartition de la quantité de mouvement afin d'éviter de devoir scinder les parcelles à cause de la non-uniformité de leur état post-collisionnel [235]. L'usage de l'opérateur de collision de type BGK nécessite la définition de temps de relaxation, qui peut cependant être calculé à partir du coefficient de restitution ainsi que du rayon de Sauter [236]. Cette approche permet cependant aux particules d'échanger de la quantité de mouvement entre elles et de relaxer vers un équilibre maxwellien local à travers les processus de collision modélisés. Le modèle devient alors nettement plus précis dans les zones de concentration intermédiaire où la pression granulaire est insuffisante pour modéliser l'échange de quantité de mouvement entre les particules [234].

À la connaissance de l'auteur, la méthode MP-PIC a été utilisée uniquement dans le contexte de systèmes gaz-solide (tels que [176, 283, 329, 335]), mais sa formulation mathématique est générique et permet de l'appliquer au cas de systèmes solide-liquide sans obstacle évident. Bien que le traitement de la phase solide soit plus grossier que celui des méthodes CFD-DEM, la description lagrangienne permet une modélisation de l'interaction solide-fluide nettement plus fine que dans les méthodes à deux fluides.

2.5.7 Méthode de quadrature de moments et de bilan de population

La méthode de quadrature de moments (QMOM, de *quadrature method of moment*) est une approche Euler-Euler où la phase solide est modélisée à partir des premiers moments (dans l'espace des vitesses) de l'équation de Boltzmann [99, 241].

L'idée principale derrière la méthode QMOM vient du fait qu'une résolution complète de l'équation de Boltzmann en $\mathbb{R}^6$ ($\mathbb{R}^3$ pour l'espace et $\mathbb{R}^3$ pour la vitesse) est numériquement irréaliste pour traiter un grand nombre de particules, mais aussi qu'une telle résolution fournirait de l'information superflue sur l'état des particules. Ainsi, la méthode QMOM résout les premiers moments (deux ou trois) dans l'espace des vitesses de l'équation de Boltzmann afin de modéliser la phase solide de manière précise sans avoir à résoudre l'entièreté de l'équation de Boltzmann. En notation de Einstein, les équations résultantes sont :

$$\frac{\partial M^0}{\partial t} + \frac{\partial M_i^1}{\partial x_i} = 0 \tag{2.69}$$

$$\frac{\partial M_i^1}{\partial t} + \frac{\partial M_{ij}^2}{\partial x_j} = F_i^1 \tag{2.70}$$

$$\frac{\partial M_{ij}^2}{\partial t} + \frac{\partial M_{ijk}^3}{\partial x_k} = F_{ij}^2 + \Omega(v_i, v_j) \tag{2.71}$$

$$\frac{\partial M_{ijk}^3}{\partial t} + \frac{\partial M_{ijkl}^4}{\partial x_l} = F_{ijk}^3 + \Omega(v_i, v_j, v_k) \tag{2.72}$$

où M^q est le $q^{ième}$ moment, F la force volumique et Ω l'opérateur de collision. Le lecteur attentif notera que pour résoudre chaque équation, il est nécessaire de connaître le moment d'ordre supérieur. L'idée principale derrière la méthode QMOM est de fermer les moments d'ordres supérieurs inconnus (et les termes de collision s'y rattachant) en intégrant les moments d'ordre inférieur à l'aide d'une quadrature dont les abscisses et les poids sont définis dynamiquement par leur capacité à reproduire les moments d'ordres inférieurs [204]. Ceci mène à un système d'équations qui doit être résolu pour les poids w_i et les abscisses (qui sont ici les vitesses discrètes dans l'espace des vitesses, U_i) :

$$M^0 = \sum_{\alpha=1}^{\beta} w_\alpha \tag{2.73}$$

$$M_i^1 = \sum_{\alpha=1}^{\beta} w_\alpha U_{\alpha,i} \tag{2.74}$$

$$M_{ij}^2 = \sum_{\alpha=1}^{\beta} w_\alpha U_{\alpha,i} U_{\alpha,j} \tag{2.75}$$

$$M_{ijk}^2 = \sum_{\alpha=1}^{\beta} w_\alpha U_{\alpha,i} U_{\alpha,j} U_{\alpha,k} \tag{2.76}$$

Cette méthode a de nombreux avantages lorsque comparée aux méthodes TFM. Puisqu'un plus grand nombre de moments de la phase particulaire sont résolus, la méthode est à la fois capable de reproduire les écoulements dilués avec une plus grande précision tout en

maintenant sa précision dans les régimes concentrés. Elle est aussi particulièrement efficace dans les situations où des jets dilués en particules se croisent, car ce sont des situations où l'équilibre maxwellien n'est pas atteint à cause du court temps de contact. Ceci explique pourquoi l'usage de cette méthode a été principalement réservé à l'étude de jets de particules et d'aérosols [100, 146, 175].

2.6 Le mélange solide-liquide

Après nous être penchés sur la physique des écoulements de type solide-liquide ainsi que les méthodes numériques pour les modéliser, nous portons maintenant notre attention sur l'étude du mélange solide-liquide. Comme nous l'avons mentionné en Section 2.2, on distingue généralement deux types de suspensions : les suspensions homogènes, qui se comportent comme un seul fluide de rhéologie complexe, et les suspensions non homogènes, dont l'écoulement est réellement polyphasique. Dans cette section, nous nous limiterons au cas de suspensions non homogènes réellement polyphasiques, car elles sont les plus problématiques à mélanger.

Nous aborderons d'abord les différents états des suspensions dans les opérations de mélange solide-liquide ainsi que la littérature se rattachant à la détermination de la vitesse minimale de mise en suspension (N_{js}, *just-suspended speed*). Dans l'état de l'art actuel, la détermination de cette vitesse demeure de loin une des problématiques les plus importantes [297]. Une revue exhaustive des différentes méthodes théoriques et expérimentales sera établie. Il est important de noter que la littérature aborde très peu le mélange en régimes laminaire et transitoire et que les études portant sur le mélange solide-liquide dans ces régimes sont quasiment inexistantes. Conséquemment, nous aborderons cette thématique dans une perspective plus large en nous souciant de tous les régimes d'opération.

2.6.1 L'état d'une suspension

Selon le *Handbook of Industrial Mixing* [245], l'objectif principal du mélange solide-liquide est de créer et de maintenir une suspension ainsi que de promouvoir le transfert de masse entre la phase solide et la (ou les) phases liquides.

Concrètement, ces objectifs se réalisent lorsque le niveau désiré de suspension solide-liquide est atteint. On peut identifier trois niveaux pour la suspension : suspension partielle, complète et uniforme. Ces états sont illustrés à la Figure 2.4.

Lorsque la suspension est partielle, une fraction (petite ou grande) des particules demeure en contact avec le fond de la cuve alors que les autres particules sont suspendues (c.-à-d. complètement immergées) dans le liquide. Dans la suspension complète, la totalité des

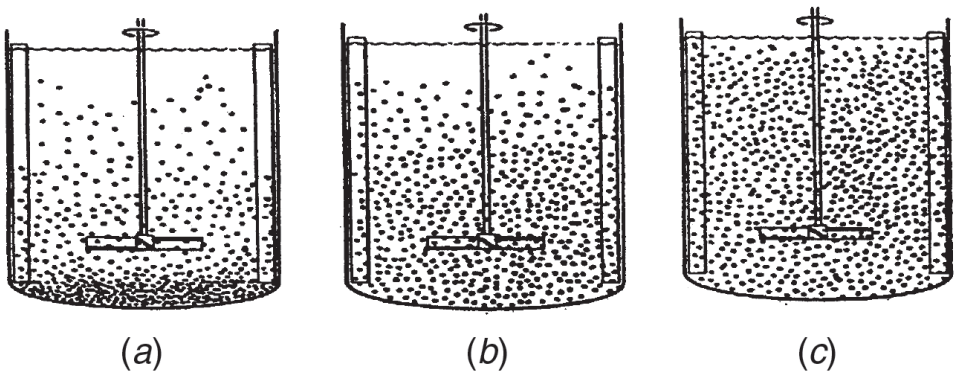

Figure 2.4 Les trois niveaux de suspension (a) suspension partielle (b) suspension complète et (c) suspension uniforme - extrait de [245]

particules est suspendue et aucune particule demeure en contact avec le fond de la cuve pour plus de deux secondes. Finalement, le niveau de suspension uniforme se réfère à l'état d'une suspension où la fraction volumique de solide est homogène partout dans la cuve.

2.6.2 Vitesse minimale de suspension complète

Selon Zwietering, Kneule [157] est le premier auteur à avoir identifié l'état de suspension complète comme étant le point optimal d'opération des unités de mélange solide-liquide. Une fois ce niveau atteint, le transfert de masse n'est uniquement amélioré que par l'augmentation de la vitesse relative entre le fluide et le solide et non par une augmentation de la surface de contact entre le solide et le liquide. L'approche de Kneule basée sur la caractérisation de la consommation de puissance par unité de volume a rapidement été suivie par les travaux de Zwietering [339] qui a établi la première corrélation pour calculer la vitesse minimale de suspension complète (N_{js}). Selon Zwietering, la vitesse minimale de suspension complète est définie comme la vitesse à laquelle il n'y a plus de particule qui reste plus qu'une ou deux seconde immobile au fond de la cuve. En observant la variation de N_{js} en fonction des paramètres du système et en employant plusieurs agitateurs (turbine Rushton, hélice marine, etc.) Zwietering a établi la corrélation empirique suivante [306] :

$$N_{js} = S\nu_l^{0.1}\left(\frac{(\rho_p - \rho_l)\, g}{\rho_l}\right)^{0.45} d_p^{0.2} X^{0.1} D^{0.15} \tag{2.77}$$

avec ν la viscosité cinématique du fluide, D le diamètre de l'agitateur, S une constante empirique qui dépend de la configuration géométrique de la cuve (dégagement de l'agitateur,

diamètre de l'agitateur, présence ou non de chicanes, etc.) et X le rapport entre la masse de solide et de liquide ($\frac{m_{solide}}{m_{fluide}}$). D'autres auteurs ont introduit des corrélations pour calculer N_{js} tels que Nienow *et al.* [225], Narayanan *et al.* [223], Baldi *et al.* [18], Mersmann *et al.* [208], Grenville *et al.* [114] et Tamburini *et al.* [292]. Une revue de littérature étendue de la majeure partie de ces corrélations est établie par Kasat et Prandit [149] et par Jafari *et al.* [139]

La corrélation introduite par Zwietering est de loin la plus utilisée, mais présente d'importantes limitations pour certaines applications. Premièrement, la corrélation modélise l'impact de la géométrie (diamètre de l'agitateur, de la cuve, dégagement au fond, etc.) à l'aide de la seule constante S. Conséquemment, cette constante doit être ajustée pour chaque type de configuration, limitant la généralité de l'approche. De plus, bien que la corrélation inclut l'influence de la viscosité, il a été montré par Ibrahim *et al.* [130, 132] qu'elle pouvait commettre une erreur de l'ordre de 90% en régime transitoire pour une viscosité de 1 Pa.s. Dans le cadre de fluides non newtoniens, Wu *et al.* [327] ont trouvé que la corrélation surestimait fortement N_{js}. De surcroît, Ayranci *et al.* [14] et Grenville *et al.* [114] ont montré que la corrélation était peu précise pour la prédiction de N_{js} lorsque la suspension n'était pas diluée. Finalement, Ayranci *et al.* ont montré que la corrélation ne permettait pas de prédire N_{js} pour le cas d'un mélange de particules de deux tailles différentes.

Il est important de noter que les autres corrélations partagent aussi les faiblesses de la corrélation de Zwietering. De manière générale, on peut dire que les approches heuristiques telles que celle de Zwietering sont condamnées à un manque de généralité compte tenu de la complexité de l'interaction solide-liquide et du caractère réellement tridimensionnel de l'écoulement dans la cuve, une conclusion partagée par Ayranci dans la conclusion de sa thèse [12].

2.6.3 Détermination de N_{js} par des méthodes expérimentales

Depuis les travaux originaux de Zwietering et les balbutiements de méthodes d'observation visuelle, plusieurs techniques ont été développées pour déterminer N_{js}. Selon Tamburini *et al.* [297], on peut distinguer deux catégories de méthode : les méthodes directes et les méthodes indirectes. Nous présenterons brièvement un éventail de ces méthodes, mais nous référons le lecteur à Tamburini *et al.* [297] et Kasat et Prandit [149] pour une revue complète.

La méthode directe la plus utilisée demeure l'observation du fond de la cuve à l'aide d'un miroir. N_{js} est alors défini comme la vitesse à partir de laquelle aucune particule ne demeure au fond pour plus que 1 ou 2 secondes. Cette méthode requiert une cuve transparente et son usage est particulièrement problématique pour des suspensions non diluées. Selon Oldshue, elle ne devrait pas être utilisée pour des fractions massiques supérieures à 8%. Cependant, certains auteurs, tels que Grenville *et al.* [114], l'ont utilisée pour des fractions massiques de

plus de 20%. Cette méthode souffre de sa grande subjectivité. Une méthode alternative se base sur la mesure de la hauteur du lit de particules [126], mais cette méthode ne s'applique pas si les dernières particules suspendues proviennent du centre de la cuve. Une autre approche consiste aussi à mesurer la taille du cône de particule sédimenté à l'aide d'une caméra à haut temps d'exposition [51], mais cette dernière technique se limite à des cas sans chicanes où les dernières particules suspendues sont issues du centre de la cuve. Ainsi, ces deux dernières méthodes, bien que relativement efficaces, sont limitées en terme de géométrie. De surcroît, toutes les méthodes directes énoncées ne permettent pas de mesurer la fraction de particules suspendues.

Les méthodes indirectes sont quant à elles plus nombreuses. Une méthode relativement récente dotée d'un grand potentiel est la technique de pression de jauge (PGT) introduite par Brucato *et al.* [53] et améliorée par Micale *et al.* [210] [3]. Cette méthode se base sur le fait qu'une fois les particules suspendues, la densité apparente du liquide augmente et qu'il est ainsi possible de mesurer une augmentation de la pression hydrostatique et d'ainsi obtenir la fraction de solide suspendue. Comme il est impossible de mesurer uniquement la pression statique, Micale *et al.* [210] propose d'employer une régression quadratique ($P = aN^2 + b$) afin d'extraire la pression statique de la pression totale mesurée. Cette méthode a l'avantage d'être objective et de mesurer la fraction de solide suspendue et non seulement la vitesse minimale pour la suspension complète.

De nombreuses autres méthodes basées sur des quantités dérivées, telles que celles fondées sur la mesure de la hauteur du nuage de particules [158], du nombre de puissance (N_p), [297], sur le temps adimensionnel de mélange [55], sur le coefficient de variation [297], sur les vibrations acoustiques [257], sur la conductivité électrique [141, 142]. Les résultats obtenus grâce à ces méthodes varient fortement en qualité et ne sont généralement pas applicables à tous les systèmes. On peut constater que le simple fait qu'un si large éventail de méthodes existe est une preuve de la complexité de l'étude de la vitesse minimale de mise en suspension.

2.6.4 Mesures de la concentration de particules

La connaissance de la vitesse minimale de mise en suspension complète ne donne que de l'information partielle sur l'état de la suspension. La connaissance des profils de concentration au sein de la cuve est essentielle pour de nombreux procédés, tels que les cristallisoirs. Elle est aussi nécessaire afin d'acquérir une meilleure compréhension des mécanismes de mise en

3. Cette méthode est parfois classifiée de directe, notamment par Tamburini *et al.* [297], mais comme elle emploie la pression comme variable intermédiaire afin de calculer la fraction de particules suspendues, il semble contre-indiqué de la qualifier de directe

suspension [295].

On compte deux familles d'approches pour mesurer la concentration de particules : les méthodes intrusives et les méthodes non-intrusives [295]. Les techniques intrusives affectent localement l'écoulement en sondant la cuve, ce qui en retour peut affecter la qualité des résultats ainsi obtenus. Ces méthodes sont basées sur des mesures de concentration locale via, par exemple, de l'échantillonnage isocinétique ou des sondes à impédance, optiques ou acoustiques.

Les méthodes non-intrusives ont l'avantage de ne pas perturber l'écoulement. Un exemple de telles méthodes est la résonance magnétique nucléaire (NMR) dans laquelle un fort champ magnétique est utilisé pour obtenir un profil de fraction volumique de fluide. Cette méthode requiert toutefois de l'instrumentation complexe et est limitée à des géométries simples. D'autres alternatives existent qui se basent notamment sur l'usage de traceurs radioactifs dont la position est suivie à l'aide de détecteurs de rayonnement. Finalement, un large éventail de méthodes basées sur la tomographie électrique ou l'atténuation de lumière et d'ondes sonores [314, 315] existent. Cependant, les résultats issus de ces méthodes demeurent davantage qualitatifs que quantitatifs [295].

2.7 Modélisation numérique du mélange solide-liquide

Compte tenu de sa complexité, il n'est pas étonnant que le mélange solide-liquide ait fait l'objet de nombreuses études de dynamique des fluides numérique. Dans la majeure partie de ces travaux, une approche euler-euler employant un modèle à deux fluides est employé conjointement avec une approche de type MRF ou SM. Comme nous le constaterons, peu de travaux ont été réalisés avec des méthodes de type euler-lagrange.

À la connaissance de l'auteur, la littérature sur l'étude du mélange solide-liquide en régimes laminaire et transitoire est quasi non-existante. Le seul article portant sur le régime transitoire fut écrit par Montante *et al.* [218] et porte sur l'application du concept de Metzner-Otto dans le contexte de suspension solide-liquide. De manière générale, la quasi-totalité des travaux se concentre sur l'étude du mélange solide-liquide pour des suspensions diluées et en régime complètement turbulent. Afin de tout de même présenter l'état de l'art, nous résumerons ces résultats.

2.7.1 Modèle à deux fluides (TFM)

Les études clefs employant cette approche ont été réalisées de manière conjointe par Micale *et al.* [212], Brucato *et al.* [50], Montante *et al.* [219, 220] et, plus récemment, par Tamburini

et al. [293, 294, 296–299]. Ces travaux concernent l'étude du mélange solide-liquide en régime turbulent par une approche RANS avec des agitateurs à décharge radiale ou mixte dans des configurations avec chicanes. Dans ces travaux, les forces de Basset, de masse virtuelle, de Saffman et de Magnus sont négligées et la viscosité de la phase solide est présumée égale à celle du fluide.

Micale *et al.* [211] ont étudié la hauteur du nuage de particules (*cloud height*) pour de nombreuses vitesses d'agitation. Les auteurs ont montré que le modèle à deux fluides pouvait reproduire qualitativement la position de l'interface entre le nuage et le fluide pur, mais que les mesures expérimentales étaient particulièrement difficiles à réaliser compte tenu de l'instabilité de l'interface et de son caractère fortement transitoire.

Dans [299], Tamburini *et al.* ont développé une méthodologie pour analyser la suspension complète et partielle de particules. En premier lieu, ils ont introduit un algorithme (*Excess Volume Correction - EVC*) afin de distribuer la fraction solide entre les cellules volumes finis et ainsi prévenir une sur-sédimentation des particules. Sans ce type de procédure (ou l'ajout d'une équation d'état rigide pour la pression granulaire de la phase solide), la fraction volumique de solide pourrait surpasser la fraction maximale d'empilement. Les travaux subséquents de Tamburini *et al.* [293, 294, 296–298] s'appuyant sur cette méthodologie représentent le corpus le plus complet et le plus moderne de travaux portant sur la simulation du mélange solide-liquide par une approche à deux fluides. Dans [294], les auteurs ont étudié le comportement des suspensions dans des états partiellement suspendus et ont montré que, d'un point de vue opérationel, cet état pourrait être fortement désirable. Dans [296], ils ont montré que leur modèle pouvait prédire de manière précise la fraction de solide suspendue de suspensions monodisperses en la comparant avec la fraction de particules qui n'étaient pas dans des cellules volume finis où ($\epsilon_p = \epsilon_s max$). Cette méthode est baptisée critère de volume non suspendu (*unsuspended volume criterion - UVC*). Cependant, les auteurs ont montré que les résultats issus de leurs simulations n'étaient valides que si une correction pour l'influence de la turbulence non résolue sur le coefficient de traînée était ajoutée au coefficient de traînée standard. De plus, leurs résultats étaient fortement liés à la forme employée pour cette correction (soit celle de Pinelli [250] ou Brucato [52]). La forme de Pinelli donnait une meilleure prédiction de la courbe de suspension tandis que celle de Brucato prédisait mieux la distribution spatiale des solides. Ainsi, bien que ce modèle soit précis pour certaines configurations, il n'est pas générique.

Il est évident que la prédiction de N_{js} est une application désirée de la CFD, car ce paramètre demeure le plus important à prédire. Cependant, tel qu'expliqué par Tamburini *et al.* [297], le critère de Zwietering se transpose mal dans un contexte Euler-Euler pour une raison

évidente : les particules ne sont pas discrètes. Dans [297], Tamburini *et al.* comparent plusieurs méthodes pour calculer N_{js} dans le contexte à deux fluides au niveau de leur précision et de leur subjectivité. Les méthodes comparées sont énumérées ci-dessous et brièvement décrites :

- Fraction volumique locale : N_{js} est la vitesse à laquelle $\epsilon_p < \frac{\epsilon_{p,max}}{2}$ partout dans la cuve en régime permanent (moyenne de phase) [150].
- Vitesse axiale des particules : N_{js} est la vitesse à laquelle la moyenne de la vitesse axiale des particules au fond de la cuve est positive (dans la direction opposée à la gravité) [319].
- Intersection de tangente : Une courbe où la fraction de fluide moyennée à 1 mm au-dessus du fond de la cuve est tracée en fonction de la vitesse de l'agitateur. Deux tangentes sont tracées aux points de pentes maximale et minimale et N_{js} est défini comme le point d'intersection de ces deux pentes [129].
- Nombre de puissance : L'augmentation de la densité apparente de la suspension lorsque les particules sont suspendues devrait se traduire par une augmentation de la puissance consommée par l'agitateur. Cette méthode définie donc N_{js} comme la vitesse à laquelle le nombre de puissance atteint un plateau [255, 259].
- Fraction de cellules saturées : Selon cette approche, la fraction de solide suspendue peut directement être corrélée avec la fraction de particules qui ne sont pas dans des cellules où $\epsilon_p = \epsilon_{p,m}$ [294, 296].

Tamburini *et al.* ont montré que seules les méthodes UVC et de nombre de puissance pouvaient donner des résultats consistants avec les prédictions expérimentales de N_{js} prédites par la PGT. Les autres méthodes sous-estiment ou surestiment considérablement la valeur de N_{js}. Ils notent aussi que la technique UVC demeure la moins subjective et la plus consistante.

La Figure 2.5 récapitule les résultats obtenus par Tamburini *et al.* pour N_{js} avec les différentes approches pour différentes tailles de particules et différentes fractions massiques dans une configuration où l'agitateur est une turbine Rushton et où la cuve est équipée de chicane.

Les profils de concentration obtenus dans les modèles à deux fluides ont été étudiés principalement pour des agitateurs axiaux [129, 183] et radiaux [295]. Bien qu'il soit établi que la concentration de solide puisse varier fortement axialement, [129, 183, 295, 298] ont aussi montré que de forts profils radiaux pouvaient être présents, trahissant un manque d'homogénéité dans la suspension.

2.7.2 Approche Euler-Lagrange : CFD-DEM résolue et non résolue

Les approches Euler-Lagrange offrent une description plus intuitive des écoulements solide-liquide, car les particules sont considérées comme des éléments discrets et non comme un

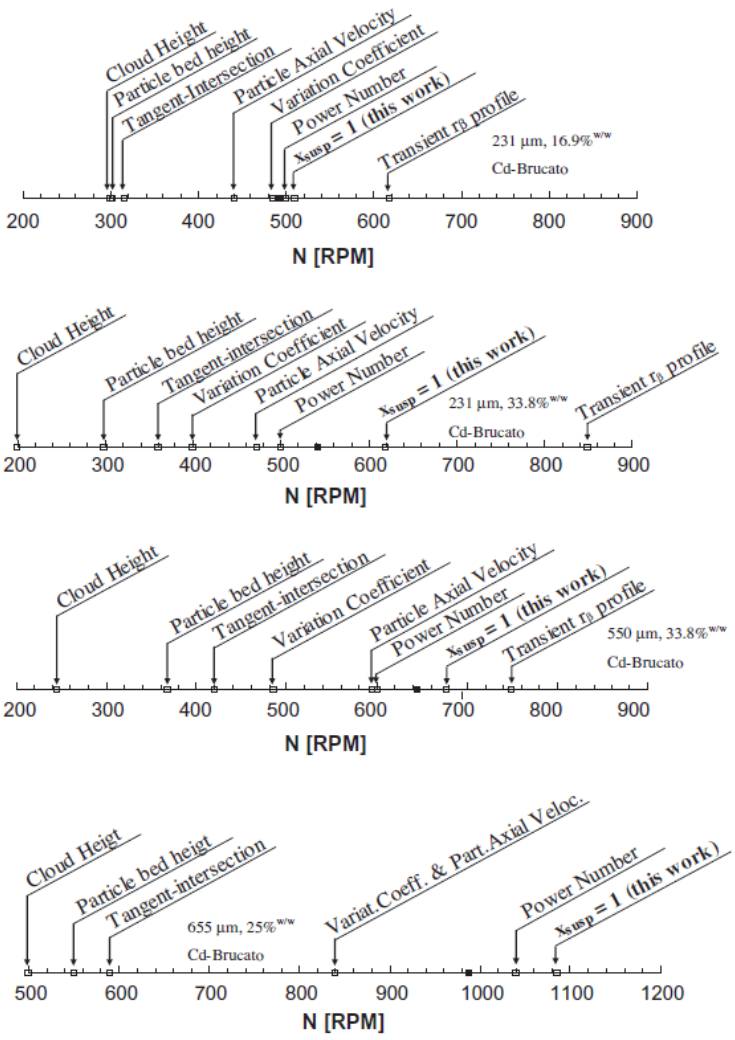

Figure 2.5 Valeur de N_{js} pour toutes les méthodes comparées par [297] (Le carré plein est le résultat obtenu par la corrélation de Zwietering)

milieu continu.

La majeure partie des travaux effectués à l'aide de ce type de modèles ont été effectués en régime turbulent pour des suspensions peu concentrées (<4% vol) en employant des modèles CFD-DEMh. Derksen [80] a utilisé la CFD-DEMh non résolue pour étudier l'écoulement pleinement turbulent de particules de 300 μm et 470 μm dans de l'eau dans une cuve agitée dotée d'une turbine Rushton ainsi que de chicanes.

Dans [80], Derksen a évalué l'impact de chaque force solide-liquide (à l'exception de la force de Basset) sur la dynamique de mélange. En comparant ses simulations avec et sans ces forces, Derksen a montré que seule la traînée avait un impact important sur la dynamique du mélange et que les forces de portance ainsi que celles dues aux gradients macroscopiques de pression et de contrainte visqueuse étaient négligeables. La Figure 2.6 illustre le type de profil de concentration ainsi obtenu.

Ces résultats ont été comparés avec des résultats numériques obtenus à l'aide du modèle à deux fluides ainsi que des résultats expérimentaux par Guha *et al.* et les auteurs ont montré que le modèle CFD-DEMh permettait une meilleure prédiction de la vitesse de la phase solide, de la hauteur du nuage ainsi que du profil de fraction volumique dans la région de l'agitateur.

Bien qu'intéressante, l'approche de Derksen est limitée, car le modèle DEMh ne permet pas de modéliser des concentrations locales de plus de 5% volumique ainsi que des collisions impliquant plus que deux éléments, qui sont fréquentes dans la zone près de l'agitateur. Ainsi, il est impossible de simuler le démarrage d'un procédé et les particules doivent être distribuée de manière homogène au sein de la cuve au moment initial. Finalement, Derksen utilise directement les équations de Navier-Stokes plutôt que les équations de Navier-Stokes moyennées volumiquement dans son schéma numérique, ce qui mène à un écoulement erroné dans les zones où la concentration de solide n'est pas négligeable, c.-à-d. où la fraction de solide $\epsilon_p > 5\%$ [70].

Derksen a aussi utilisé une approche CFD-DEMh résolue pour étudier le mélange solide-liquide en utilisant la simulation numérique directe (DNS) pour résoudre l'écoulement faiblement turbulent ($Re = 1920$) [83]. Cependant, ses simulations sont limitées à un faible nombre de particules (3600) et à un faible ratio entre la taille de l'agitateur et les particules ($\frac{D}{d_p}$). De plus, le faible de rapport de tailles entre les particules et l'agitateur (24 à 60) limite fortement l'applicabilité des profils turbulents obtenus.

À ce jour, aucun travail n'a été réalisé en régime laminaire ou transitoire et, surtout, pour des concentrations non diluées. De plus, la quasi-totalité des travaux employant la CFD-DEM

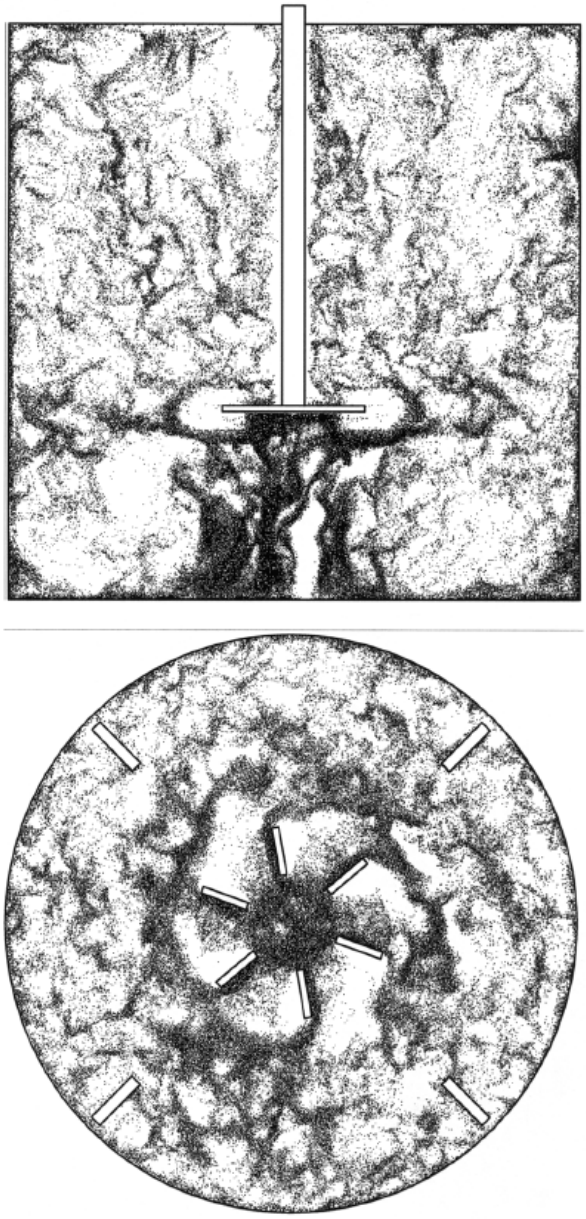

Figure 2.6 Distribution instantannée des particules dans une cuve agitée par une turbine Rushton - extrait de [80]

pour étudier le mélange solide-liquide se sont limités à l'utilisation de modèle de DEM rigides (DEMh) et n'ont pas étudié le démarrage de la cuve ou des concentrations non-diluées. Seul les modèles employant la DEMs plutôt que la DEMh permettraient de simuler ces dernières situations.

CHAPITRE 3 SYNTHÈSE ET ORGANISATION DE LA THÈSE

Compte tenu de l'étendue de la revue de littérature, nous effectuerons dans ce chapitre une brève synthèse de celle-ci afin de mettre en relief les lacunes et les avenues inexploitées dans l'état de l'art sur le mélange solide-liquide. Ensuite, les objectifs de recherche découlant de cette synthèse seront énoncés. Finalement, l'organisation de la thèse, s'articulant autour des objectifs, sera établie.

3.1 Synthèse de la revue de littérature

À la lumière de la revue de littérature, il apparaît évident que des défis importants concernant la compréhension, la caractérisation et la conception d'opérations de mélange solide-liquide demeurent. En premier lieu, la littérature n'aborde que très peu le cas du mélange solide-liquide en régime laminaire ou le début du régime transitoire. Pourtant, comme nous l'avons vu, les seuls travaux où la fin du régime transitoire fut étudiée ont clairement démontré les piètres performances de la corrélation de Zwietering dans ce contexte et l'incapacité des corrélations à prédire ce régime. Ainsi, tout est inconnu en ce qui concerne le mélange solide-liquide dans les régimes laminaires ou transitoire.

De surcroît, l'approche actuelle consistant à étudier des systèmes de mélange et à concevoir des corrélations pour la vitesse minimale de mise en suspension (N_{js}) ne répond pas à certains besoins industriels. Cette approche souffre fortement de la subjectivité de la définition de cette vitesse. Les concepts de fraction de solide suspendue et de vitesse de suspension suffisante, N_{ss}, sont en meilleure adéquation avec les besoins industriels, car chaque type d'opération requiert des niveaux de suspension différents. Qui plus est, une conception uniquement basée sur N_{js} peut mener à des surdimensionnements (ou sousdimensionnements, pour un cristallisoir par exemple) qui causent une consommation fortement exagérée de puissance (ou un procédé inefficace). Compte tenu de la variation en N^3 de la puissance consommée [245] (avec N la vitesse de l'agitateur), le surdimensionnement d'opérations industrielles n'est pas une pratique viable et entraîne une consommation énergétique et un coût d'équipement prohibitifs.

Finalement, pour certains procédés, il est nécessaire de prédire davantage d'informations sur les caractéristiques de l'écoulement, telles que :

— le degré d'homogénéité et le profil de fraction volumique ;
— le patron d'écoulement ;

— le couple sur l'agitateur ;
— le temps de mélange et
— les coefficients de transfert de masse à l'échelle des particules.

Compte tenu du caractère tridimensionnel et instationnaire des écoulements en cuve agitée, ces informations peuvent difficilement être obtenues de manière robuste (ex. du point de vue de la mise à l'échelle) à l'aide de corrélations.

La modélisation des écoulements au sein de cuves agitées à l'aide de la mécanique des fluides polyphasique apparaît comme un outil très prometteur pour pallier aux difficultés reliées à l'étude expérimentale de ces systèmes. Cette approche a l'avantage de permettre l'étude d'un vaste éventail de systèmes, à faible coût, tout en fournissant de l'information locale difficilement accessible par des mesures en laboratoire. La modélisation d'écoulements solide-liquide représente un défi particulier à cause des deux phases interagissant à une multitude d'échelles de temps et d'espace ainsi que la présence d'un agitateur en mouvement. Nous avons présenté l'éventail des modèles existant pour traiter de manière générale les écoulements solide-liquide. Cependant, aucun de ceux-ci ne fut utilisé pour étudier le mélange solide-liquide en régime laminaire ou transitoire, malgré le fait que tous ces modèles présentant un fort potentiel.

La quasi-totalité des travaux portant sur le mélange solide-liquide en régime turbulent, tels que les excellents articles de Tamburini *et al.*, emploient des modèles à deux fluides. Cependant, ces modèles souffrent de multiples faiblesses. Compte tenu du fait qu'ils modélisent les particules comme un milieu continu, ces modèles offrent une description plus grossière de l'interaction solide-liquide et solide-solide. Ceci cause des problèmes, notamment pour prédire la fraction de solide dans les régions où celle-ci atteint la fraction maximale d'empilement. Cette dernière situation est inévitable lors de la mise en suspension de particules et lors de l'étude du régime transitoire ou de la suspension partielle.

Les modèles de type CFD-DEMs non résolu, couplant la CFD et les équations VANS avec la DEM souple, peuvent à la fois simuler précisément la phase solide tout en adoptant une description plus grossière du fluide, permettant de simuler des écoulements de plus grande taille contenant davantage de particules. Dans la dernière décennie, ces modèles ont permis d'obtenir des résultats impressionnants pour les problèmes gaz-solide, mais n'ont jamais été appliqués de manière robuste et rigoureuse à l'étude des écoulements solide-liquide et encore moins à celle du mélange solide-liquide et à la mise en suspension des particules. De par leur formulation, ils pourraient être utilisés pour étudier le mélange solide-liquide en régime laminaire, transitoire et turbulent avec un nombre très limité d'hypothèses et de simplifications. Cependant, des avancées mathématiques et numériques importantes sont

nécessaires avant de pouvoir simuler le mélange solide-liquide par un modèle CFD-DEM non résolu.

Les modèles de type MP-PIC seraient eux aussi intéressants à cause de leur description précise de la trajectoire des particules et leur capacité à simuler la séparation d'échelles. Cependant, les problèmes qu'ils rencontrent pour imposer la fraction volumique maximale de particules de manière robuste et stable limitent leur applicabilité à des situations de démarrage de cuve. Ainsi, les modèles de type CFD-DEM non résolu sont plus appropriés.

3.2 Objectifs de recherche

L'objectif principal de cette thèse est donc de concevoir un modèle CFD-DEMs non résolu robuste qui permet de modéliser la dynamique des écoulements solide-liquide dans géométries complexes telles que des mélangeurs [1].

Cet objectif est divisible en sous-objectifs qui, lorsqu'articulés ensemble, permettront l'atteinte de l'objectif principal. Ces sous-objectifs sont définis ci-dessous.

- Concevoir un schéma numérique pour résoudre les équations VANS.
- Établir une procédure pour vérifier la justesse de la résolution des équations VANS.
- Proposer une méthode de conditions limites immergées adaptées à la CFD-DEM.
- Développer un modèle CFD-DEM applicable à l'étude du mélange solide-liquide en régimes laminaire et transitoire et le valider.
- Identifier les éléments favorisant un mélange solide-liquide efficace en régimes laminaire et transitoire.
- Étendre le modèle CFD-DEM à l'étude du mélange en régime turbulent et le valider.
- Établir une méthodologie permettant de mesurer la fraction de particules suspendue, la vitesse de mise en suspension complète et la qualité du mélange pour les modèles de type CFD-DEM.

Un objectif supplémentaire qui est aussi réalisé dans ce travail est de concevoir un schéma numérique nouveau basé sur la LBM permettant de résoudre les équations VANS.

1. À partir de maintenant, le modèle CFD-DEMs non résolu sera référé simplement sous l'appellation modèle CFD-DEM afin de simplifier la nomenclature.

3.3 Organisation de la thèse

Les chapitres subséquents de cette thèse visent l'atteinte des objectifs énoncés à la section 3.2. Le Chapitre 4 traite de la méthodologie générale employée dans la thèse. La plateforme logicielle CFDEM, un cadriciel (*framework*) intégrant Open∇FOAM et LIGGGHTS et servant de fondation à cette thèse, sera présenté. Les notions de vérification et de validation de modèles numériques seront abordées, car elles sont à la base de la stratégie employée dans cette thèse.

Le Chapitre 5 (Article 1) traite du schéma numérique volumes finis développé pour résoudre les équations VANS ainsi que l'approche basée sur la méthode des solutions manufacturées employée pour vérifier le modèle. Cette approche de vérification numérique est ensuite utilisée au Chapitre 6 (Article 2) pour concevoir un nouvel opérateur de collision pour la méthode LBM pour résoudre les équations VANS.

Au Chapitre 7 (Article 3), une nouvelle méthode de conditions immergées semi-implicite, adaptée à la CFD-DEM et applicable à des maillages non structurés dans le contexte de la méthode des volumes finis est présentée. Le schéma mathématique sous-jacent est vérifié sur des cas tests académiques avant d'être validé dans le contexte du mélange monophasique.

Le Chapitre 8 (Article 4) résulte de la combinaison directe des approches développées aux chapitres 5 et 7 pour former un modèle CFD-DEM applicable au mélange solide-liquide. Ce chapitre représente le cœur de cette thèse. Le modèle CFD-DEM solide-liquide y est présenté avec tous les détails nécessaires et différents aspects du schéma reliés au couplage entre les phases sont abordés. Finalement, le modèle est validé à l'aide de données expérimentales pour le mélange solide-liquide.

L'Annexe B (Article M.L. 1) présente un article dont l'auteur de la présente thèse est second auteur. Cet article fut principalement rédigé par Manon Lassaigne durant sa maitrise. Cependant, les résultats de cet article ainsi que la méthodologie qui y est employée sont fortement complémentaires aux travaux du Chapitre 8. L'article a donc été inclus en annexe pour cette raison.

Le Chapitre 9 (Article 5) présente l'extension du modèle aux écoulements en régime turbulent, sa validation par comparaison avec l'expérience et le développement de deux nouvelles stratégies pour déterminer la fraction de particules suspendues. L'efficacité de ces stratégies est établie par comparaison avec le large éventail de méthodes disponibles dans la littérature.

Dans le Chapitre 10 (Article 6), le mélange solide-liquide en régime laminaire et transitoire est revisité. La sensibilité du modèle à ses paramètres est étudiée. Les étapes du mécanisme d'érosion des particules sont détaillées. Finalement, différentes configurations géométriques

sont étudiées en introduisant des chicanes dans la cuve agitée et en variant le dégagement au fond de l'agitateur afin d'identifier quelle configuration est optimale non seulement pour la mise en suspension des particules, mais aussi pour leur homogénéisation.

La Figure 3.1 présente l'organisation des chapitres (ou les articles) et les relations entre ceux-ci. On peut constater que la progression de la thèse n'est pas linéaire et que l'interdépendance entre les chapitres est très forte.

Il est recommandé au lecteur souhaitant se pencher davantage sur le mélange solide-liquide de consulter les chapitres selon l'ordre 5-7-B-8-9-10. Le chapitre 6 ne dépend que du chapitre 5 et son contenu, qui est davantage mathématique, n'est pas utilisé à nouveau dans les autres chapitres.

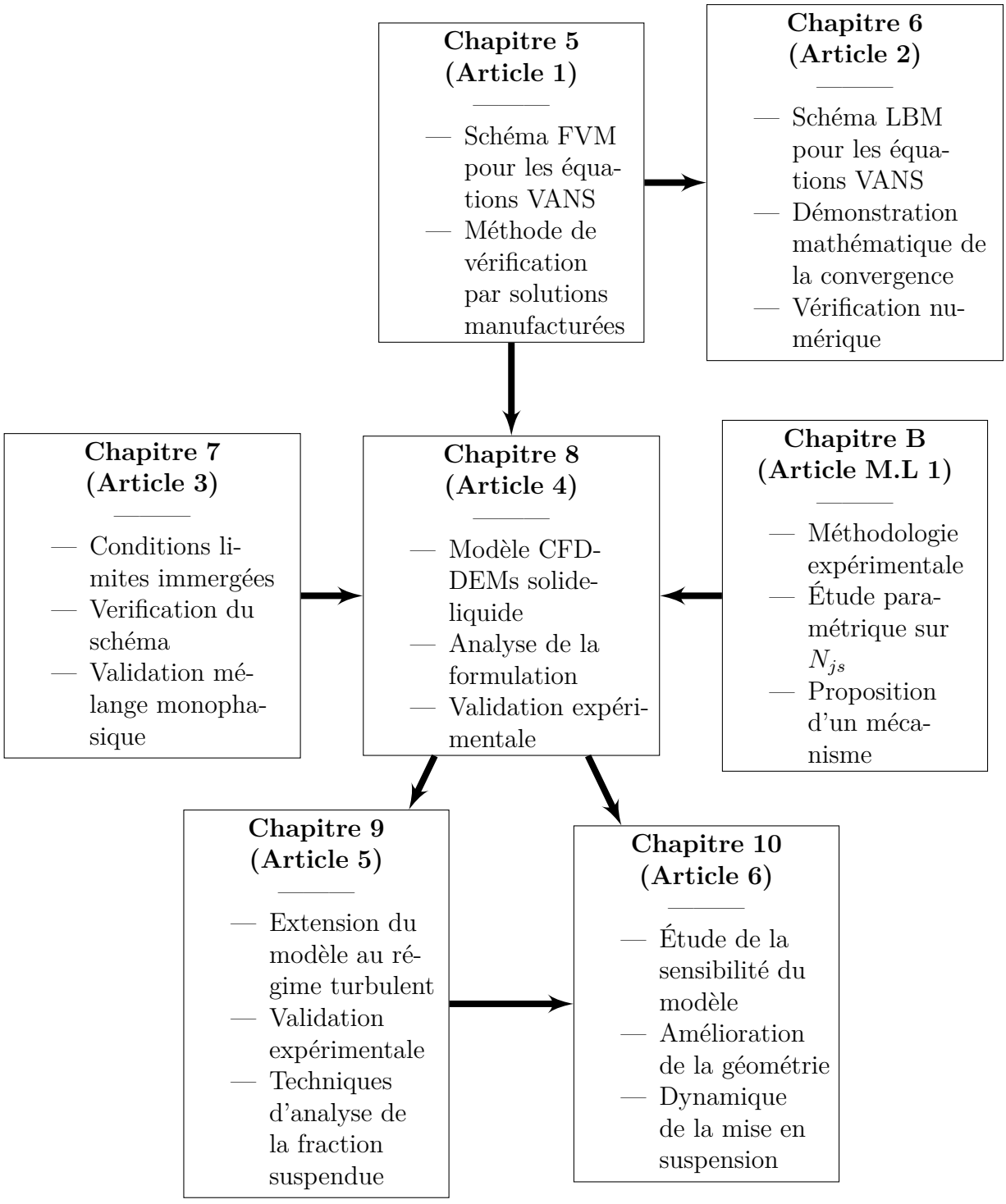

Figure 3.1 Le coeur de cette thèse (Article 4) a été possible grâce aux connaissances développées dans les Articles 1, 3 et M.L 1. Il a permis des analysises plus poussées du mélange solide-liquide (Articles 5 et 6).

CHAPITRE 4 MÉTHODOLOGIE

Dans ce chapitre, nous présentons brièvement la méthodologie employée dans la présente thèse. En premier lieu, la plateforme (ou cadriciel) CFDEM et ses composantes sont décrites. Ensuite, l'approche de vérification et de validation employée dans ce travail est détaillée. Le but de cette section est d'introduire la plateforme CFDEM et les éléments la constituant dans un cadre unifié. La méthodologie plus spécifique à chaque chapitre (article) est présentée dans le chapitre même et n'est donc pas abordée ici afin d'éviter toute redondance.

4.1 La plateforme CFDEM

La plateforme (ou *framework* en anglais) CFDEM est une extension du logiciel de CFD en volume finis Open∇FOAM [1]. Cette plateforme combine Open∇FOAM au logiciel de DEM LIGGGHTS [2]. Tous ces logiciels sont du domaine libre, sont gratuits et leurs codes sources C++ sont ouverts. Nous présenterons d'abord Open∇FOAM et LIGGGHTS avant de décrire la plateforme CFDEM permettant de les articuler ensemble.

Open∇FOAM

Open∇FOAM est un logiciel libre écrit en C++ orienté objet employant la méthode des volumes finis pour résoudre des problèmes génériques de mécanique des milieux continus. Il est cependant orienté vers la mécanique des fluides. Le logiciel fonctionne avec des maillages non structurés (sans restriction, les maillages peuvent être des polyèdres quelconques) et emploie une formulation au centroïde des cellules (*cell-centered*) sauf pour le calcul des flux, qui eux sont calculés aux faces. Le logiciel permet l'utilisation d'une multitude de schémas semi-implicites de correction de pression (SIMPLE, PIMPLE, PISO), intègre un large éventail de modèles de turbulence RANS et LES et permet aussi un parallélisme à mémoire distribuée à l'aide de la librairie MPI et de plusieurs stratégies de décomposition de domaine (SCOTCH et METIS). Concrètement, un solveur Open∇FOAM est un exécutable indépendant incluant les librairies nécessaires afin de résoudre la physique souhaitée. Par exemple, le solveur employant une méthode SIMPLE se nomme *SimpleFOAM* et sa variante employant un référentiel en rotation (SRF) se nomme *SRFSimpleFOAM*. Les modèles de turbulence, les conditions limites, etc. sont des librairies chargées au lancement du logiciel, rendant le code source d'un solveur relativement simple et malléable. Le logiciel est cependant fortement

1. Qui signifie Open Field Operation And Manipulation.
2. LAMMPS improved for general geometry and granular heat transfer simulations.

enraciné dans une logique orientée objet, ce qui peut rendre son utilisation intimidante pour les utilisateurs peu familiers avec cette logique.

LIGGGHTS

LIGGGHTS, pour *LAMMPS Improved for General Geometry and Granular Heat Transfer Simulations* est une extension du logiciel LAMMPS (*Large-scale Atomic/Molecular Massively Parallel Simulator*) de dynamique moléculaire (MD). La DEM a beaucoup en commun avec la dynamique moléculaire d'un point de vue algorithmique. Les deux emploient une description lagrangienne des éléments, un intégrateur temporel de type Verlet, une liste de Verlet à boîtes pour la détection des contacts ainsi que des particules fantômes permettant le parallélisme à mémoire distribuée. Ainsi, l'extension d'un logiciel de MD en un logiciel de DEM est une chose naturelle. Concrètement, LIGGGHTS ajoute à LAMMPS la capacité de traiter des maillages surfaciques (STL ou VTK) pour simuler des géométries industrielles dessinées par ordinateur ainsi que de mettre en mouvement des maillages. De plus, des fonctions de post-traitement ainsi que des fonctionnalités permettant le transfert et la réception d'informations avec Open∇FOAM via des librairies MPI sont disponibles.

CFDEM : Couplage Open∇FOAM et LIGGGHTS

Concrètement, la plateforme CFDEM est constituée d'une librairie (*cfdemCloud*) et d'une multitude de solveurs. La librairie *cfdemCloud* s'occupe de toutes les étapes nécessaires à la réalisation du couplage entre les phases, c'est-à-dire :

- la réception de l'information sur les particules provenant LIGGGHTS ;
- le calcul du champs de fraction massique de fluide (ϵ_f) à partir de la position et du rayon des particules ;
- le calcul de toutes les forces de couplages solide-fluide et
- l'envoi des forces de couplage solide-fluide vers LIGGGHTS.

Comme nous en avons discuté dans la revue de littérature, la CFD et la DEM n'ont pas les mêmes critères de stabilité pour le pas de temps. Il n'est donc pas nécessaire que les deux schéma effectuent le même nombre d'itérations. Dans la pratique, le pas de temps DEM est généralement plus contraignant que le pas de temps CFD et plusieurs itérations DEM sont effectuées pour chaque itération CFD. La figure 4.1 illustre le déroulement d'une itération CFD-DEM.

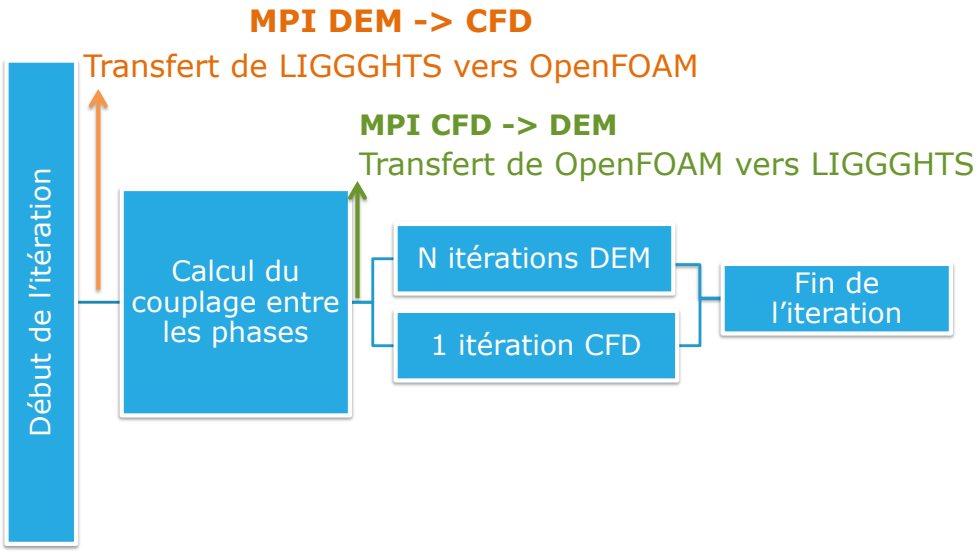

Figure 4.1 Une itération CFD-DEM comprend généralement N itérations DEM pour une itération CFD-DEM

4.2 Stratégie de vérification et de validation employée dans cette thèse

Le développement d'un modèle CFD complexe tel que le modèle CFD-DEM conçu dans cette thèse requiert une méthodologie rigoureuse de vérification et de validation. Nous rappelons la définition de ces deux concepts. La vérification consiste à s'assurer que l'implémentation numérique d'un modèle permet bien d'obtenir la solution de ce modèle à l'ordre de précision prescrit par le schéma numérique. La validation consiste à déterminer à quel point un modèle est une représentation précise d'un procédé physique. Ceci peut être accompli, par exemple, en comparant les résultats issus du modèles avec des données obtenues expérimentalement. Nous référons le lecteur au livre d'Oberkampf [227] pour une description plus détaillée de ces deux concepts.

Compte tenu de la complexité et du nombre d'équations résolues, il est nécessaire de s'assurer que la totalité des aspects du modèle numérique soient cohérents avec le modèle théorique. Il est important de noter qu'il n'existe pas de solutions analytiques pour des problèmes CFD-DEM réellement couplés et que, de manière générale, il n'y a pas de solution analytique connue et non-triviale pour des écoulements $2D$ dans le contexte des équations VANS.

Dans cette thèse, nous procéderons de manière progressive afin de vérifier les aspects importants du modèle CFD-DEM avant de le valider. En premier lieu, nous vérifierons la résolution des équations VANS. Ensuite, nous vérifierons le modèle de conditions immergées. Ce modèle sera validé expérimentalement pour le cas plus simple du mélange monophasique. C'est seulement une fois tous ces éléments établis que nous vérifierons le modèle CFD-DEM couplé dans les limites du possible compte tenu de la complexité du schéma. Finalement, le modèle sera validé expérimentalement. Cette approche de vérification et de validation requiert évidemment davantage de temps, mais elle a l'avantage de nous permettre d'être confiants de la précision et de la robustesse de chaque sous-aspects du modèle avant qu'il soit utilisé pour l'étude du mélange solide-liquide. Étant donné l'étendu du modèle, ce type d'approche est essentielle.

Les travaux de validation expérimentale ont été réalisés en collaboration avec Manon Lassaigne, étudiante à la maitrise (Article 3, Article 4 ainsi que l'Article M.L. 1) puis avec Olivier Bertrand, étudiant à la maitrise (Article 5) [3]. Cette coopération et collaboration entre des travaux expérimentaux et numériques a permis une progression nettement plus rapide des travaux de recherche présentés dans le cadre de cette thèse.

3. L'auteur de cette thèse aimerait à nouveau remercier M. Lassaigne et O. Bertrand pour leur précieuse aide.

CHAPITRE 5 Article 1 : On the use of the Method of Manufactured Solutions for the Verification of CFD Codes for the Volume-Averaged Navier-Stokes Equations

Bruno Blais and François Bertrand
Published in Computers & Fluid volume 114, pages 121-129 March 12 2015

Abstract : The volume-averaged Navier-Stokes (VANS) equations are a key constituent of numerous models used to study complex problems such as flows in porous medias or containing multiple phases (e.g solid-liquid flows). These equations solve the mesoscopic scale of the flow without taking into account explicitly each individual solid particles, therefore greatly reducing computational cost. However, due to a lack of analytical solutions, the models using the VANS equations are generally validated directly against experimental data or empirical correlations. In this work, a framework to design analytical solutions and verify codes that solve the VANS equations via the method of manufactured solutions is presented for the first time. Three test cases of increasing complexity are designed with this method and used to assess the second-order convergence of a finite volume solver developed in Open∇FOAM. The proposed approach is suitable for the verification of any code that solves the VANS equations with any CFD technique such as the finite element method or the lattice Boltzmann method.

5.1 Introduction

It is well established that the Navier-Stokes equations govern the evolution of the velocity and pressure of the incompressible flow of an isothermal Newtonian fluid. However, this is not true for two phase flows for which a generic set of governing equations has yet to be established despite the extensive literature on the subject [4, 44, 70, 89, 105, 254]. The intrinsic multiscale nature of multiphase flows is another issue that renders their modeling very challenging. For instance, in the case of particle-laden flow, particle-particle collisions and solid-fluid interactions taking place at the microscopic scale can affect the flow at the mesoscopic and macroscopic scales [308]. This multiscale phenomenon complexifies the coupling between the phases and, when relevant, turbulence modeling. The resulting multiphase problem is hard to tackle with a single generic approach. For example, in solid-liquid mixing, it becomes computationally intractable to resolve fluid flow around more than a few thousand particles in a stirred tank. Therefore, different families of models have been designed, which can resolve the scales of interest with varying precision. These modeling scales can be referred to

as macro, meso and micro [308].

The use of averaged equations for the description of the fluid phase consists in a meso approach that allows the investigation of multiphase flows at industrial and lab scales, such as the concentrated particle-laden flows in fluidized bed [85, 338] and mixing systems [276].

Various formulations of the governing averaged equations have been developed, as in [4, 105, 134]. In this paper, we focus on the case of a solid phase dispersed in another continuous phase, within the context of our work on solid-liquid mixing in both laminar and turbulent regimes.

For dispersed multiphase flows, the volume averaged Navier-Stokes equations (VANS) are a key constituent in more than one model. They are at the foundation of the well-known two-fluid model in which both the fluid and the dispersed phases are considered to be governed by continuum fluid mechanics. This two-fluid model has been used to study a large number of solid-fluid processes, for instance in fluidized beds [320] and solid-liquid mixing [293]. The VANS equations have also been used to simulate porous media flows [121]. Furthermore, these equations are inherent to Euler-Lagrange models such as the Unresolved CFD-DEM, which combines the discrete element method (DEM) [31,337] for the solid particles and the volume averaged Navier-Stokes equation for the fluid phase [336]. This approach combining CFD and DEM is particularly promising for the study of solid-liquid mixing due to its capacity to predict maximum packing fraction [337] and its suitability over the entire range of granular regimes (quasi-static to fast) [65].

However, work is still needed to understand the limitations of current CFD-DEM models. For instance, it remains unclear how DEM parameters such as the rolling friction and coefficient of restitution, or the different solid-fluid interaction forces (Saffman, Magnus, etc.) affect the flow at the macroscopic scale of the process. While this has been partly addressed by [80] for the solid-liquid interactions in stirred-tanks and [112] for the impact of rolling friction in fluidized beds, these reports are limited in scope as they pertain to specific flow situations.

More particularly, the past decade has seen an increase in the number of techniques used to solve the VANS equations for the continuous phase in CFD-DEM based models. While a large body of work has solved the fluid phase by classical finite volume [85, 103, 144, 336] or finite difference methods [247], alternative approaches have been proposed, based on smoothed particle hydrodynamics (SPH) [264] or the lattice Boltzmann method (LBM) [286].

CFDEM, an open source CFD-DEM framework [61], combines the finite volume method for the continuous fluid phase with the DEM for the particles. More precisely, this framework introduced by Kloss *et al.* [156] comprises the finite volume library Open∇FOAM [233] with

the DEM code LIGGGHTS [155, 182] based on the molecular dynamic software LAMMPS [252]. It is highly interesting due to its open source nature and the large user community surrounding Open∇FOAM, LAMMPS and LIGGGHTS. Furthermore, the platform is fully parallel, allowing it to handle relatively large problems.

The development of any simulation model, including those based on the CFD-DEM paradigm, should comprise a verification and validation step in order to assess its accuracy and performance. The definitions given by the American Institute of Aeronautics and Astronautics (AIAA) [1] and the American Society of Mechanical Engineers (ASME) [3] for these two concepts are :

— *Verification* : The process of determining that a model implementation accurately represents the developer's conceptual description of the model and the solution to the model.

— *Validation* : The process of determining the degree to which a model is an accurate representation of the real world from the perspective of the intended uses of the model.

Consequently, a verification procedure should establish that a numerical model for a set of partial differential equations with its associated boundary conditions converges towards the desired analytical solution at the asymptotic convergence rate prescribed by the mathematical analysis of the space and time discretizations used in the numerical scheme. On the other hand, validation refers to the comparison between experimental results and the solution obtained by the model. Therefore, one should first verify that a numerical implementation of a model is coherent before comparing it with experimental results. Failure to do so can lead to confusion as one is then unable to distinguish if the disagreement between experimental results and a model arise from fundamental inadequacies in the model or if it is solely due to coding errors, an incorrect discretization or the improper convergence of the underlying numerical scheme. We refer the reader to the seminal books by Roache [262] and Oberkampft and Roy [227] for a thorough discussion on verification procedures in computational science and scientific computing in general.

Numerous validation studies have been reported for CFD-DEM models on a large variety of topics such as liquid fluidized beds [85], gas fluidized beds [247], rotor granulators [224], pneumatic conveying [163]. However, numerical verification work has been limited. Garg *et al.* [103] have carried out an extensive verification of the DEM resolution and solid-fluid coupling of the MFIX CFD-DEM software. Other analyses have been carried out on mass conservation [326] and on the algorithm used to project DEM particles onto a CFD mesh [199]. However, to our knowledge, a systematic numerical verification procedure for the VANS equations has not been proposed yet. This is mainly due to the lack of analytical solutions for the VANS equations. Although solutions are available for two-fluid models through the use

of analytical Riemann solvers and wave ordering, as for example in [124], these solutions are limited to the context of inviscid compressible flows. One can refer to the book of Toro [307] for more details on the Riemann solution of Euler systems of equations.

An alternative method for the verification of CFD models is the so-called method of manufactured solutions (MMS), which can design analytical solutions for a set of partial differential equations [227,262]. This method has been used with great success for the verification of wall-bounded turbulent flow [91], eddy-viscosity models [92] and Reynolds Averaged Navier-Stokes equations in turbulence modeling [93].

In this work, the lack of analytical solutions to the VANS equations is remedied by extending the method of manufactured solutions and using it to develop a step-by-step verification procedure for CFD codes solving these equations. Although this verification is carried out in the context of a pressure implicit with splitting of operators (PISO) finite volume solver implemented in Open∇FOAM, the proposed framework can serve to verify any code that solves the VANS equations with any CFD technique such as the finite element method or the lattice Boltzmann method.

The VANS equations are first recalled in the context of solid-liquid flow problems. The method of manufactured solutions applied to such multiphase flows is next introduced to design three test cases of increasing complexity, all of which are then used to verify the accuracy of the PISO scheme. Finally, some comments are given on the capability of the proposed approach to identify formulation errors within a CFD code and mass conservation properties of the PISO scheme in the context of the VANS equations.

5.2 Volume Averaged Navier-Stokes Equations

There exist a number of forms for the VANS equations that have been proposed in the literature for solid-liquid flows. The main differences between these forms lie principally in the treatment of the stress tensor of the fluid and the solid-fluid coupling, as thoroughly discussed by Zhou *et al.* [336] for the two-fluid and the CFD-DEM models.

Following the notation of these authors, set I (original model B) of the VANS equations, which is based on local averaging [4], is used in the current work. We refer the reader to the article of Zhou *et al.* [336] for an in-depth description of the origin of the model and its comparison to set II (model A) and set III (simplified model B).

This formulation, which has shown its suitability for solid-liquid flows [336], will be simply referred to as the VANS equations in the remainder of this paper.

The incompressible VANS equations are :

$$\frac{\partial \epsilon_f}{\partial t} + \nabla \cdot (\epsilon_f \boldsymbol{u}) = 0 \tag{5.1}$$

$$\frac{\partial (\rho_f \epsilon_f \boldsymbol{u})}{\partial t} + \nabla \cdot (\rho_f \epsilon_f \boldsymbol{u} \otimes \boldsymbol{u}) = -\nabla p + \nabla \cdot \boldsymbol{\tau} + \rho \epsilon_f \boldsymbol{g} - \boldsymbol{F}_{pf} \tag{5.2}$$

where ϵ_f is the void fraction, ρ_f the density of the fluid, p the pressure, $\boldsymbol{u}$ the velocity and $\boldsymbol{g}$ the gravity. The viscous stress tensor $\boldsymbol{\tau}$ is defined as :

$$\boldsymbol{\tau} = \mu \left((\nabla \boldsymbol{u}) + (\nabla \boldsymbol{u})^T - \frac{2}{3} (\nabla \cdot \boldsymbol{u}) \boldsymbol{\delta}_k \right) \tag{5.3}$$

where μ is the dynamic viscosity and $\boldsymbol{\delta}_k$ the identity tensor. The volumetric particle-fluid interaction term $\boldsymbol{F}_{pf}$ can be broken down into a sum of forces :

$$\boldsymbol{F}_{pf} = \frac{1}{\Delta V} \sum_i^{n_p} f_{pf,i} \tag{5.4}$$

$$\boldsymbol{f}_{pf,i} = \boldsymbol{f}_{d,i} + \boldsymbol{f}_{\nabla p,i} + \boldsymbol{f}_{\nabla \cdot \boldsymbol{\tau},i} + \boldsymbol{f}_{\mathrm{vm},i} + \boldsymbol{f}_{B,i} + \boldsymbol{f}_{\mathrm{Saff},i} + \boldsymbol{f}_{\mathrm{Mag},i} \tag{5.5}$$

where n_p is the number of particles and $\boldsymbol{f}_{pf,i}$ is the sum of all fluid-solid interaction forces involving particle i : drag ($\boldsymbol{f}_{d,i}$), pressure gradient ($\boldsymbol{f}_{\nabla p,i}$), viscous stress gradient ($\boldsymbol{f}_{\nabla \cdot \boldsymbol{\tau},i}$), virtual mass ($\boldsymbol{f}_{\mathrm{vm},i}$), Basset force ($\boldsymbol{f}_{B,i}$), Saffman lift ($\boldsymbol{f}_{\mathrm{Saff},i}$) and Magnus lift ($\boldsymbol{f}_{\mathrm{Mag},i}$). In practice, this term then requires information from the DEM part. For this reason, it is omitted in this work as we are interested in the verification of the codes that solve the VANS equations and not in the coupling between solid and fluid.

It is important to note that the velocity and void fraction resulting from these equations are not separately divergence free, which means that all terms of the stress tensor are *a priori* non-zero. In particular, this may lead to the appearance of normal stresses even if the fluid is Newtonian and the flow is incompressible.

5.3 Numerical solution of the VANS equations

As previously noted in the introduction, numerous methods can be used to solve the VANS equations. In the present work, a finite volume method based on a PISO pressure predictor-corrector scheme [136] was implemented using the Open∇FOAM library. The key idea is to solve the momentum and pressure equations separately, and to use the pressure in order to ensure mass conservation by correcting iteratively the predicted velocity. Although alternative predictor-corrector schemes such as SIMPLE [244] would also be adequate, the choice of the

PISO scheme is motivated by its good performance for the simulation of transient flows. One can refer to the book by Versteeg and Malasekera [316] for a comprehensive overview of some of the pressure-corrector schemes available in the literature. For a more generic presentation of the cell-centered finite volume formulations available in Open∇FOAM, the reader is referred to the work of Weller *et al.* [322] and Jasak *et al.* [140].

In this section, a modified PISO algorithm that allows for a resolution of the VANS equations in conservative form is presented. This scheme was originally used in the work of Kloss *et al.* [156], although it was not described. It is detailed and extended upon in the present work.

A notation close to the one used in the book by Ferziger and Perić [97] is followed as it is similar to the Open∇FOAM formalism.

The VANS equations alongside generic mass and momentum source terms $H(\boldsymbol{x}, t)$ and $\boldsymbol{G}(\boldsymbol{x}, t)$ are given by :

$$\frac{\partial \epsilon_f}{\partial t} + \nabla \cdot (\epsilon_f \boldsymbol{u}) = H \tag{5.6}$$

$$\frac{\partial (\rho_f \epsilon_f \boldsymbol{u})}{\partial t} + \nabla \cdot (\rho_f \epsilon_f \boldsymbol{u} \otimes \boldsymbol{u}) = -\nabla p + \nabla \cdot \boldsymbol{\tau} + \boldsymbol{G} \tag{5.7}$$

where the void fraction ϵ_f is calculated via a projection of the particle positions and radii onto the mesh. Therefore, ϵ_f is constant through the whole time step m.

The pressure predictor-corrector scheme begins with the solution of a predictor step for velocity $\boldsymbol{u}^{\mathrm{m}^*}$ using the pressure and velocity at time step $m-1$ (or the initial condition when $m = 1$) :

$$A_{\mathrm{i}} \boldsymbol{u}_{\mathrm{i}}^{\mathrm{m}^*} + \sum_{\mathrm{j}} A_{\mathrm{j}} \boldsymbol{u}_{\mathrm{j}}^{\mathrm{m}^*} = Q_{\boldsymbol{u},\epsilon_f}^{\mathrm{m}-1} - \left(\frac{\delta p^{\mathrm{m}-1}}{\delta x} \right) + \boldsymbol{G} \tag{5.8}$$

The content of A and $Q_{\boldsymbol{u},\epsilon_f}^{\mathrm{m}-1}$ can be deduced from (5.7). The indices i and j refer to the cell centroids and to the neighboring cells, respectively. The pressure term is given explicitely and the symbolic derivative represents the centered spatial discretization scheme used in the present work. For an exhaustive presentation of this classical discretization scheme and a truncation error analysis, we refer the reader to the book by Ferziger and Perić [97]. The resulting velocity $\boldsymbol{u}_{\mathrm{i}}^{\mathrm{m}^*}$ does not respect (5.6), hence the need for a pressure corrector step.

First, a correction is applied to prevent velocity-pressure decoupling and checkboard pheno-

menon following the work of Rhie and Chow [147] :

$$\boldsymbol{u}_{\mathrm{i}}^{\mathrm{m}^{**}} = \frac{Q_{\boldsymbol{u},\epsilon_f}^{\mathrm{m}^{*}-1} - \sum_{\mathrm{j}} A_{\mathrm{j}} \boldsymbol{u}_{\mathrm{j}}^{\mathrm{m}^{*}}}{A_{\mathrm{i}}} \tag{5.9}$$

This velocity and the cell-centered void fraction ϵ_f are used to calculate new mass fluxes at the cell faces via linear interpolation :

$$\phi_{\mathrm{F}}^{\mathrm{m}^{**}} = \langle \boldsymbol{u}_{\mathrm{i}}^{\mathrm{m}^{**}} \epsilon_{f,\mathrm{i}} \rangle_{\mathrm{F}} \cdot \boldsymbol{S}_{\mathrm{F}} \tag{5.10}$$

where the $\langle . \rangle_{\mathrm{F}}$ operator denotes the face interpolation of a variable, the value of which is known at the cell centroids, and where $\boldsymbol{S}_{\mathrm{F}}$ is the surface normal vector term.

A similar interpolation is performed for the interpolation of the velocity coefficient A and the void fraction, which are known only at the cell centroids.

The following pressure correction correction equation is then applied :

$$\begin{aligned} \sum_{\mathrm{F}} \langle \frac{\epsilon_{f,\mathrm{i}}}{A_{\mathrm{i}}} \rangle_{\mathrm{F}} \boldsymbol{S}_{\mathrm{F}} \cdot \nabla p^{\mathrm{m}^{**}} = & \sum_{\mathrm{F}} \phi_{\mathrm{F}}^{\mathrm{m}^{**}} + \sum_{\mathrm{F}} \langle \frac{\epsilon_{f,\mathrm{i}}}{A_{\mathrm{i}}} \rangle_{\mathrm{F}} \langle \boldsymbol{G} \rangle_{\mathrm{F}} \cdot \boldsymbol{S}_{\mathrm{F}} \\ & + \frac{\delta \epsilon_{f,\mathrm{i}}}{\delta t} - H \end{aligned} \tag{5.11}$$

where again the symbolic time derivative is used to represent the discretization scheme used for the time derivative of the void fraction. In the present work, a second-order Crank-Nicholson scheme is used.

Finally, the velocity is corrected :

$$\boldsymbol{u}_{\mathrm{i}}^{\mathrm{m}^{***}} = \boldsymbol{u}^{\mathrm{m}^{**}} + \frac{1}{A_{\mathrm{i}}} \left(-\frac{\delta p^{\mathrm{m}^{**}}}{\delta x} + \boldsymbol{G} \right) \tag{5.12}$$

If Neumann or Robin boundary conditions are imposed in the domain, they are updated using the current value of the velocity and pressure.

This corrector step is generally carried out twice as in the original PISO method. This VANS PISO scheme has very good mass conservation properties because the equations are solved in their conservative formulation. We will come back to this in the results section.

In this work, the second-order centered scheme was used for cell face interpolations and gradients calculations. A second-order Crank-Nicholson scheme was used for time integration.

The block diagram in Figure 5.1 summarizes the VANS PISO scheme used in this work.

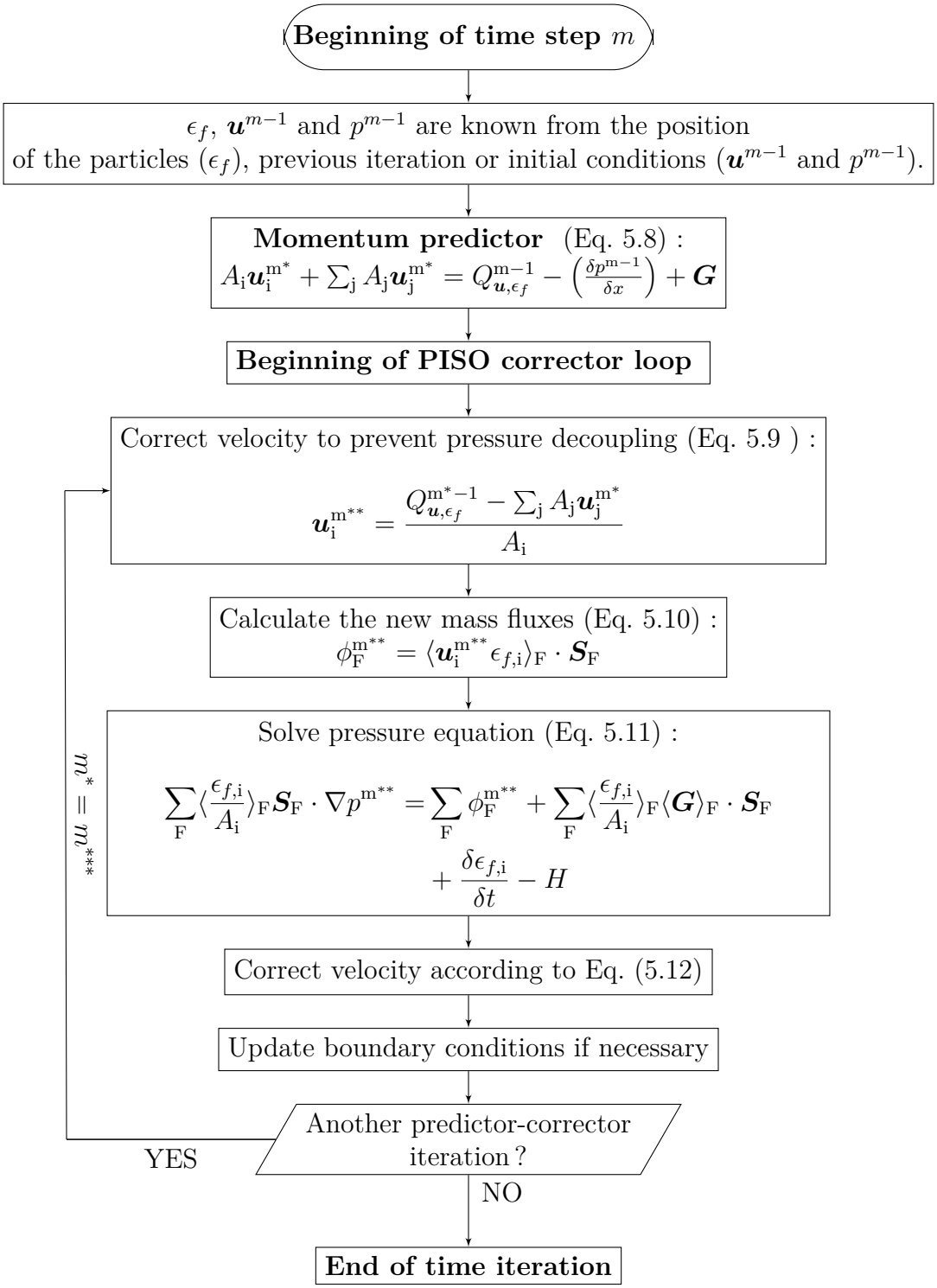

Figure 5.1 Flow chart for the VANS PISO scheme

5.4 Verification of the Volume Averaged Navier-Stokes equations using the Method of Manufactured Solutions

The method of manufactured solutions (MMS) is a generic approach that allows one to build analytical solutions to given partial differential equations (PDE) [227, 262]. The complexity of the analytical solution can be chosen arbitrarily, allowing one to design a test case for which all the terms in the PDE are of the same order of magnitude. In this section, we show how this approach can be applied to develop analytical solutions to the VANS equations in order to create a rigorous verification procedure for a code that solves these equations. For a detailed presentation of the MMS in a general scientific computing context, we refer the reader to the review paper by Roache [263] as well as to the books by Roache [262] and Oberkampft and Roy [227].

The MMS procedure is straightforward. First, we consider the VANS equations (Eqs. (5.6) and (5.7)) in the absence of solid-fluid interactions ($\boldsymbol{F}_{pf} = 0$). We choose a velocity field $\boldsymbol{u}$, a void fraction ϵ_f and a pressure p, and build a vector of manufactured variables $\boldsymbol{s}_{\mathrm{M}} = [\boldsymbol{u}^T, \epsilon_f, p]^T$ that satisfy the continuity equation (5.6).

For cases where the void fraction is time independent, it is preferable to chose a velocity and a void fraction that are intrinsically mass conservative, which means $H = 0$, as experience has shown us that this leads to a system that is more stable and closer to the real context of application of the VANS equations. In all cases, $\boldsymbol{s}_{\mathrm{M}}$ is not a solution of the complete VANS equations since it does not satisfy the momentum conservation (5.7). To do so, the following momentum source term $\boldsymbol{G}$ is added to the latter equation :

$$\boldsymbol{G}(\boldsymbol{s}) = \frac{\partial\left(\rho_f \epsilon_f \boldsymbol{u}\right)}{\partial t} + \nabla \cdot \left(\rho_f \epsilon_f \boldsymbol{u} \otimes \boldsymbol{u}\right) + \nabla p - \nabla \cdot \boldsymbol{\tau} \tag{5.13}$$

where

$$\boldsymbol{\tau} = \mu \left(\left(\nabla \boldsymbol{u}\right) + \left(\nabla \boldsymbol{u}\right)^T - \frac{2}{3} \left(\nabla \cdot \boldsymbol{u}\right) \boldsymbol{\delta}_k \right) \tag{5.14}$$

With this definition of $\boldsymbol{G}$, the manufactured solution is an analytical solution of the VANS equations.

This solution can be used to assess the accuracy of the scheme described in Figure 5.1 by monitoring the decrease of the Euclidean norm of the error ($\|e\|_2$) with respect to the mesh size (Δx). On a Cartesian, homogenous and regular structured meshes, this error is defined

for a variable $\boldsymbol{\xi}$ as [227] :

$$\|e_{\boldsymbol{\xi}}\|_2 = \sqrt{\frac{1}{N}\sum_{i}^{N} \|\boldsymbol{\xi}_{\mathrm{M},i} - \boldsymbol{\xi}_i\|^2} \tag{5.15}$$

where N is the number of mesh cells, $\boldsymbol{\xi}_{\mathrm{M}}$ the manufactured solution and $\boldsymbol{\xi}$ the numerical solution. The order of convergence obtained via simulations can be compared with the theoretical order of convergence of the scheme used for the solution of the VANS equations.

In the case of transient problems and if the simulations are carried out with a constant Courant-Friedrichs-Lewy number ($\mathrm{CFL} = \frac{\Delta t|\boldsymbol{u}|}{\Delta x}$), it follows that :

$$\|e_{\boldsymbol{\xi}}\|_2 \propto \alpha\,(\Delta x)^n + \beta \frac{\mathrm{CFL}^k}{|\boldsymbol{u}|^k}\,(\Delta x)^k \tag{5.16}$$

where α and β are unknown numerical constants, and where n and k are the theoretical orders of convergence of the space and time discretization used. If the orders of convergence for both the space and time discretizations are equal ($n = k$) as is the case in the present work where a linear space discretization is combined with a Crank-Nicolson time integration scheme, the error reduces to :

$$\|e_{\boldsymbol{\xi}}\|_2 \propto \gamma\,(\Delta x)^n \tag{5.17}$$

with γ an unknown numerical constant.

If the numerical model is consistent, the order of convergence measured via simulations should be the one predicted by theoretical analysis. Disagreement between the measured and the prescribed orders of convergence would imply that there is a formulation error, a coding mistake or a discretization inconsistency. This approach is particularly powerful in the context of pressure-corrector schemes as inconsistencies in iterative approaches are hard to identify.

The source terms H and $\boldsymbol{G}$ can be calculated using a symbolic manipulator and directly inserted in the code. In the present work, Mathematica 8 [258] was used and the output was adapted to the OpenFOAM C++ syntax using regular expressions and Python 2.7.

The manufactured solution should be sufficiently differentiable, at least twice, to ensure that all members of the underlying discretized equations are non-zero. Therefore, the velocity, pressure and void fraction should preferably be polynomial, trigonometric or exponential functions. Furthermore, this method is most efficient when the manufactured solution gene-

rates terms in the PDE that are of the same order of magnitude. This prevents errors in one term of the equations from being damped by the stronger magnitude of others terms and ensure that all terms are significant in the calculation of the error. In the case of the VANS equations, this can be achieved by using Re = 1. The values of the variables should also remain consistent with the physics of the equations. For instance, we should have $\epsilon_f \in]0, 1]$.

In the case of unresolved CFD-DEM, the void fraction ϵ_f is accounted for by projecting the particle positions and radii onto the CFD mesh. In this case, ϵ_f must be manufactured like $\boldsymbol{u}$ and p, although it is not a variable that is solved for. However, even if the void fraction is known analytically on the entire domain, its value should only be specified at the cell centroids and the boundary surfaces in the same manner as the other state variables. Failure to do so may lead to inconsistencies in the surface interpolation. Finally, the source term $\boldsymbol{G}$ and its divergence $\nabla \cdot \boldsymbol{G}$ are present in the momentum predictor and pressure correction equations, respectively. Although $\nabla \cdot \boldsymbol{G}$ is known by construction, it is calculated explicitly within the CFD scheme in order to maintain consistency. These are subtle details that can have an impact on the conclusions drawn from the order of convergence analysis.

5.5 Simulation and test case set-up

All the test cases designed involve either Dirichlet or periodic boundary conditions. Three different tests of increasing complexity are proposed, the last of which fully investigates all aspects of the VANS equations. The test cases are designed in 2D for simplicity and speed, and permutation of coordinates allows for a verification of all coordinates. The extension to 3D is straightforward.

All the simulations were carried out in transient regime using the VANS PISO predictor-corrector scheme described in Section 5.3, with a CFL of 0.2 (see Eq. (5.17)). Convergence to the steady-state solution was reached when the velocity and pressure residuals were inferior to 10^{-8}. The simulations were carried out on a large number of meshes (over 15), which involved from 400 to 250000 cells. The order of convergence was calculated via a least-squares linear regression of the Euclidean norm of the error with respect to the mesh size.

The domain of all three simulations is $\Omega = [-1, 1] \times [-1, 1]$. Since the manufactured solutions are periodic in nature, this corresponds to a full period of the velocity and pressure fields.

The three test cases are presented next along with the corresponding graphs of the Euclidean error between the analytical solution and the numerical solution obtained with the VANS PISO scheme for different mesh sizes. The results are analyzed in Section 5.6.

5.5.1 Case 1 : steady-state divergence-free flow problem

The first manufactured case is defined as :

$$\boldsymbol{u} = 2\begin{bmatrix} -\left(\sin\left(\pi x\right)\right)^2 \sin\left(\pi y\right)\cos\left(\pi y\right) \\ \sin\left(\pi x\right)\cos\left(\pi x\right)\left(\sin\left(\pi y\right)\right)^2 \\ 0 \end{bmatrix} \tag{5.18}$$

$$p = \sin\left(\pi x\right)\sin\left(\pi y\right) \tag{5.19}$$

$$\epsilon_f = \frac{1}{2} + \frac{1}{4}\sin\left(\pi x\right)\sin\left(\pi y\right) \tag{5.20}$$

This case requires only a momentum source term ($\boldsymbol{G}$) in (5.7). This source term is calculated using (5.13) and is given by the following expression :

$$\begin{aligned} G_x =& \pi\sin(\pi y)\left(\cos(\pi x)\left(\sin^3(\pi x)\sin(\pi y)(\sin(\pi x)\sin(\pi y)+2)+1\right)\right) \\ &+ \pi\sin(\pi y)\left(4\pi\mu\cos^2(\pi x)\cos(\pi y)\right) \\ &- 12\pi^2\sin(\pi y)\mu\sin^2(\pi x)\cos(\pi y)) \end{aligned} \tag{5.21}$$

$$\begin{aligned} G_y =& \pi\sin(\pi x)\cos(\pi y)(\sin^3(\pi x)\sin^3(\pi y)(\sin(\pi x)\sin(\pi y)+2)+1) \\ &+ \frac{1}{8}\pi\sin(2\pi x)(\sin(2\pi x)\sin(2\pi y)\sin^2(\pi y)(\sin(\pi x)\sin(\pi y)+2) \\ &+ 16\pi\mu(1-2\cos(2\pi y))) \end{aligned} \tag{5.22}$$

In this case, the velocity, pressure and void fraction are all steady and sufficiently differentiable fields. Furthermore, the velocity field is divergence free. Therefore, the normal stresses in the viscous stress tensor are all zero.

The u and v components of $\boldsymbol{u}$, the pressure and the void fraction are shown in Figure 5.2.

The graph of the Euclidean norm of the error as a function of the mesh size is given in Figure 5.3.

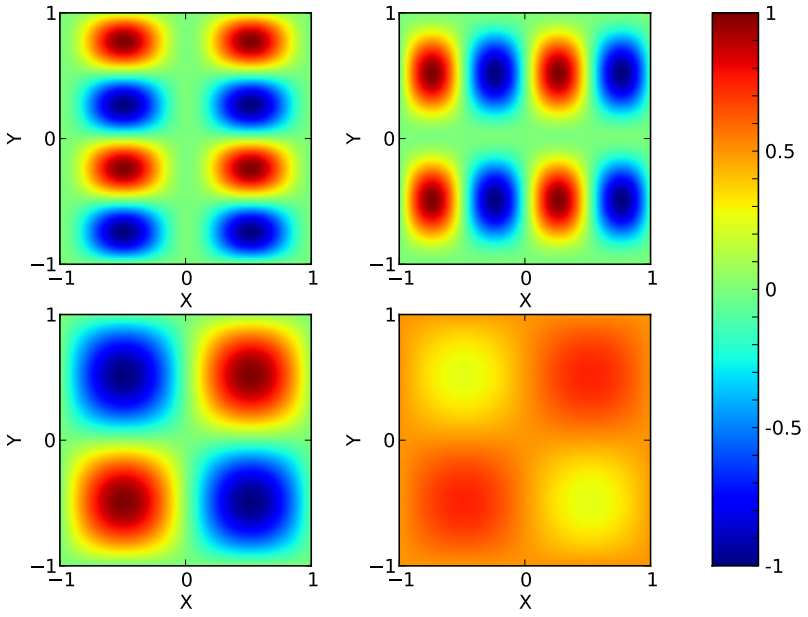

Figure 5.2 Analytical solution for Case 1. Top left panel : u component of velocity — Top right panel : v component of velocity — Bottom left panel : pressure — Bottom right panel : void fraction

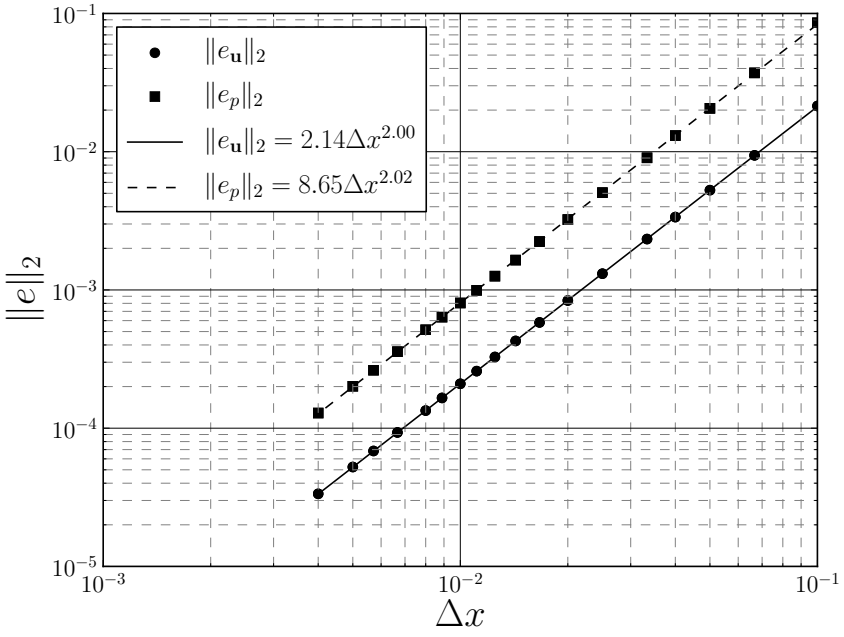

Figure 5.3 Graph of the Euclidean norm of the error for $\boldsymbol{u}$ and p with respect to mesh size for case 1.

5.5.2 Case 2 : steady-state non divergence-free flow problem

The second manufactured solution is defined as :

$$\boldsymbol{u} = \frac{1}{e}\begin{bmatrix} e^{\sin(\pi x)\sin(\pi y)} \\ e^{\sin(\pi x)\sin(\pi y)} \\ 0 \end{bmatrix} \tag{5.23}$$

$$p = \frac{1}{2} + \frac{1}{2}\sin(\pi x)\sin(\pi y) \tag{5.24}$$

$$\epsilon = \frac{1}{e}e^{-\sin(\pi x)\sin(\pi y)} \tag{5.25}$$

Figure 5.4 presents contour plots of the elements of this manufactured solution. Contrary to Case 1, the divergence of the velocity field is now non-zero, although mass conservation (5.6) is still satisfied. Therefore, all the component of the full viscous stress tensor for a compressible flow are present in the VANS equations. For this case, only a momentum source ($\boldsymbol{G}$) calculated using (5.13) is necessary. Due to its length, this term is not given here.

Figure 5.5 displays the graph of the Euclidean norm of the error as function of the mesh size.

5.5.3 Case 3 : unsteady non divergence-free flow problem

This test case is the unsteady extension of case 2, for which the solution is defined as :

$$\boldsymbol{u} = \frac{\cos(Tt)}{e}\begin{bmatrix} e^{\sin(\pi x)\sin(\pi y)} \\ e^{\sin(\pi x)\sin(\pi y)} \\ 0 \end{bmatrix} \tag{5.26}$$

$$p = \frac{1}{2} + \frac{1}{2}\cos(Tt)\sin(\pi x)\sin(\pi y) \tag{5.27}$$

$$\epsilon_f = \frac{1 - 0.1\cos(Tt)}{e}e^{-\sin(\pi x)\sin(\pi y)} \tag{5.28}$$

where T is the frequency of the velocity field, which is chosen here to be equal to 2π.

Figure 5.6 presents contour plots at time $t = 2$s. This test case is the most complete of the three since it is unsteady and the velocity field non-divergence free. Note that, since the void fraction is also unsteady, mass (H) and momentum ($\boldsymbol{G}$) source terms are required in (5.6) and (5.7), respectively.

Figure 5.7 displays the graph of the Euclidean norm of the error as a function of the mesh

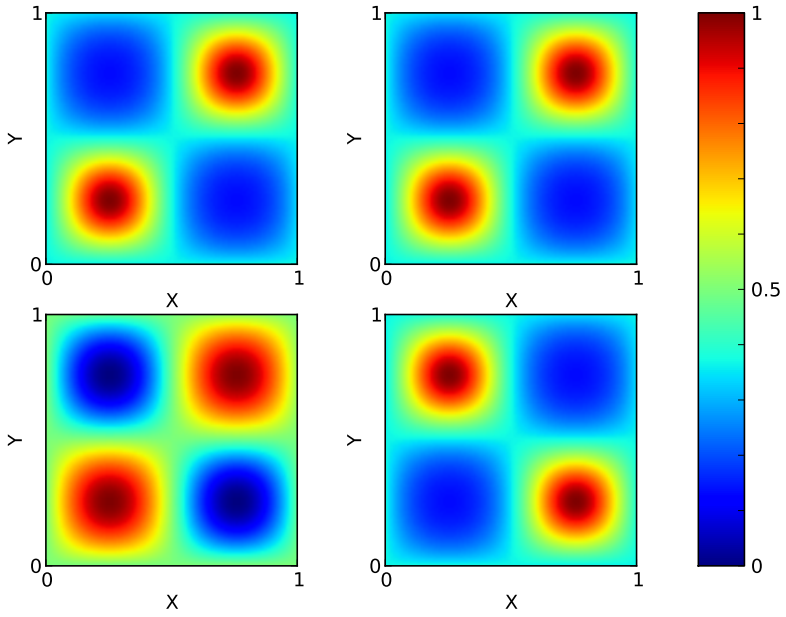

Figure 5.4 Analytical solution for Case 2. Top left panel : u component of velocity — Top right panel : v component of velocity — Bottom left panel : pressure — Bottom right panel : void fraction

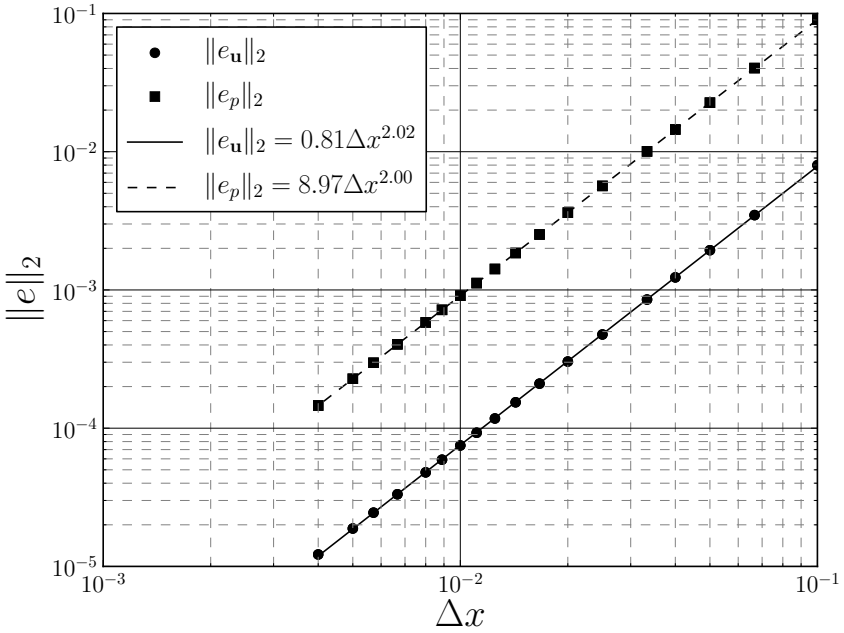

Figure 5.5 Graph of the Euclidean norm of the error for $\boldsymbol{u}$ and p with respect to mesh size for case 2.

size at time $t = 2$s.

5.6 Discussion

The graphs displayed in Figures 5.3, 5.5 and 5.7 show that the velocity and the pressure solved by the VANS PISO scheme exhibit second-order convergence in both time and space. Since the time integration and the space discretization schemes for the calculation of the face fluxes and gradients are second-order accurate, these results highlight the fact that the VANS PISO approach within the CFDEM framework preserves this second-order accuracy. These results are in agreement with the theoretical development of the PISO approach [136]

Furthermore, the scheme has very good properties in terms of mass conservation. Indeed, for all simulations, the maximal local mass losses within one time iteration were observed to be of the order of 10^{-8}, whereas total mass conservation was ensured up to 10^{-10}. Even better mass conservation could be reached by the reducing the residual tolerance in the iterative solver or increasing the number of PISO loops.

One may notice in Figures 5.3, 5.5 and 5.7 that the second-order convergence rate for both pressure and velocity is reached even for relatively coarse meshes, with R^2 coefficients always larger than 0.9999. However, it is important to recall that a convergence rate is asymptotic by definition, which means that it is not always reached for coarse meshes. One should therefore remain careful and analyze the asymptotic rate of convergence, as the order of convergence for very coarse meshes can be different than the one predicted by the theoretical analysis, hinting a priori at an inconsistent scheme. This is clearly not the case for the meshes used in Figures 5.3, 5.5 and 5.7, but it has been observed for larger mesh sizes ($\Delta x > 0.1$) and for other types of boundary conditions.

One of the advantages of the combination of the MMS with the order of convergence analysis lies in its quantitative aspect. Indeed, one only needs to compare the order of convergence obtained with the theoretical order of convergence related to the space and time discretization schemes used, to ensure that the code implementation and the overall iterative scheme are consistent with the model equations. This is less error-prone than simple visual observation for which local errors can be difficult to pinpoint. The method is sensitive as a single error in a mesh cell, a term in the equations or the boundary conditions, may be sufficient to reduce the order of convergence. During the course of the verification carried out in this work, formulation errors in the VANS PISO scheme implemented in the CFDEM framework were identified and corrected. We would also like to stress the need for more than one single test case. Indeed, test cases can be designed to investigate a specific portion of the code or of

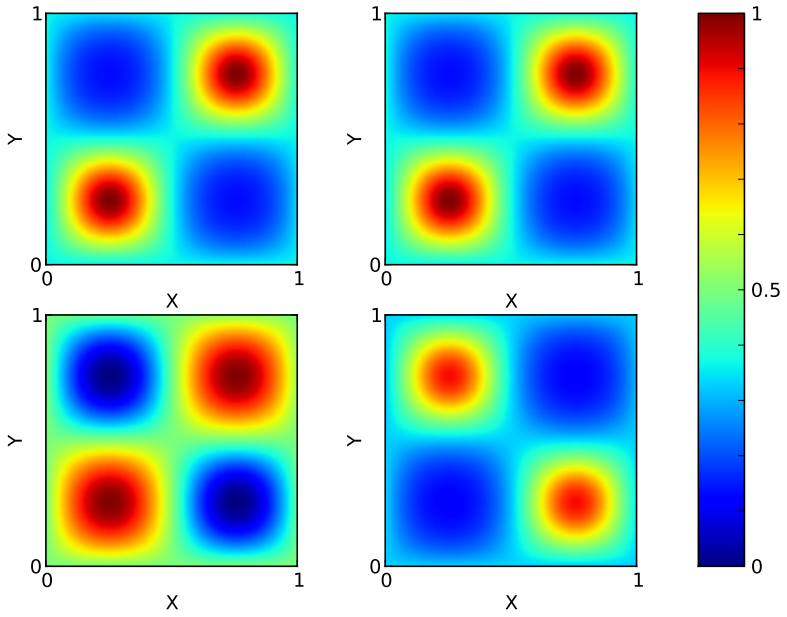

Figure 5.6 Analytical solution for Case 3 at time $t = 2$s. Top left panel : u component of velocity — Top right panel : v component of velocity — Bottom left panel : pressure — Bottom right panel : void fraction

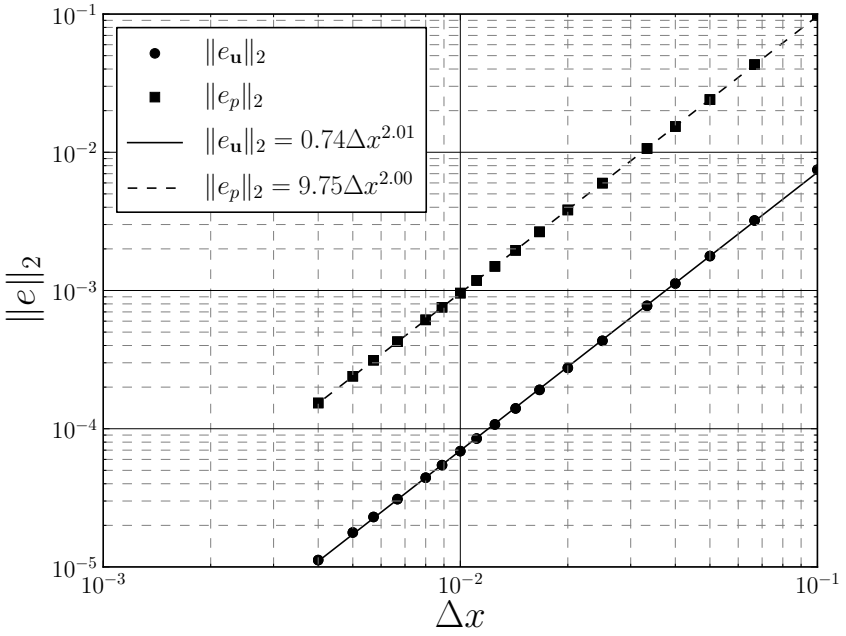

Figure 5.7 Graph of the Euclidean norm of the error for $\boldsymbol{u}$ and p with respect to mesh size for case 3.

the PDE. For example, Case 2 is different from Case 1 as it brings into play the full viscous stress tensor in the VANS equations. In particular, it allowed us to identify errors in the implementation of components of this tensor related to the occurent of a non-divergence free velocity.

5.7 Conclusion

The volume averaged Navier-Stokes equations can serve to model multiphase or porous medias flows in various applications. Indeed, they are part of numerous models in which they can describe all phases, such as in two-fluid models, or only the suspending fluid, as is the case in unresolved CFD-DEM.

The open source CFDEM platform combining LIGGGHTS and Open∇FOAM is highly interesting because of its open source character and the large community surrounding these two software tools. However, this platform is relatively new and requires thorough verification. In this article, it was shown that a PISO VANS scheme used within this coupling strategy is second-order accurate in both time and space, by applying the method of manufactured solutions to the VANS equations. This allowed the verification of the implementation of these model equations.

It is important to mention that the approach proposed in this work is general and can be applied to any volume averaged formulation, be it for a two-fluid model, flow in porous media or a Euler-Lagrange model that relies on the finite volume, finite element or lattice Boltzmann method, as well as any other method based on a Eulerian description of the volume averaged phases. Furthermore, the step-by-step methodology based on the three test cases developed with the method of manufactured solutions allows one to easily identify errors that are linked to the incorrect discretization of a specific term of the VANS equations.

Finally, the methodology introduced here could also be extended to problems where the VANS equations must include a turbulence model, by manufacturing a solution that accounts for this turbulence model. In all situations, designing verification test cases via the MMS allows for a clear and quantitative verification of a code before the corresponding model is validated by comparison with experimental data.

5.8 Acknowledgements

The financial support from the Natural Sciences and Engineering Research Council of Canada (NSERC) is gratefully acknowledged. In particular, Bruno Blais is thankful for the

NSERC Vanier Scholarship. The authors also acknowledge technical support and computing time provided by Compute Canada, as well as Prof. Dominique Pelletier from Polytechnique Montreal for fruitful discussions on the method of manufactured solutions and its application to predictor-corrector schemes in the context of the finite volume method. Finally, we are grateful to DI Dr. Christoph Goniva from DCS computing for discussions on the formulation of the VANS equations within the CFDEM framework.

CHAPITRE 6 Article 2 : A Conservative Lattice Boltzmann Model for the Volume-Averaged Navier-Stokes Equations Based on a Novel Collision Operator

Bruno Blais, Jean-Michel Tucny, David Vidal, François Bertrand
Published in the Journal of Computational Physics volume 294, pages 258-273 August 1 2015

Abstract : The volume-averaged Navier-Stokes (VANS) equations are at the basis of numerous models used to investigate flows in porous media or systems containing multiple phases, one of which is made of solid particles. Although they are traditionally solved using the finite volume, finite difference or finite element method, the lattice Boltzmann method is an interesting alternative solver for these equations since it is explicit and highly parallelizable. In this work, we first show that the most common implementation of the VANS equations in the LBM, based on a redefined collision operator, is not valid in the case of spatially varying void fractions. This is illustrated through five test cases designed using the so-called method of manufactured solutions. We then present a LBM scheme for these equations based on a novel collision operator. Using the Chapman-Enskog expansion and the same five test cases, we show that this scheme is second-order accurate, explicit and stable for large void fraction gradients.

6.1 Introduction

Multiphase flows play a critical role in numerous key unit operations in the process industry such as mixing [245], transport [70] and fluidization [338]. Due to their complexity, they are often the bottleneck in the design and the operation of these units. Although the experimental study of these systems has led to a better understanding of their behavior, numerical simulation has proved an efficient and complementary tool to gain a deeper knowledge of the underlying flows.

Due to the steady increase of computational power, the last decades have witnessed the development of numerous numerical models that are capable of resolving multiphase flows with various length and time scales [308]. Among these, the two-fluid model [4, 105], the combination of classical CFD approaches and the discrete element method (DEM) dubbed CFD-DEM [337], and the multiphase particle-in-cell (MP-PIC) method [282] have been used extensively to study, in particular, solid-fluid flows such as those in solid-liquid mixing [293], fluidized beds and pneumatic transport [338]. In such cases, these methods all have in common that they are based on the solution of a volume-averaged form of the Navier-Stokes (VANS)

equations for either the two phases (two-fluid model) or for the fluid only (CFD-DEM and MP-PIC). The VANS equations have also been used extensively in the study of porous media, in which the porosity is a function of space [121].

Traditionally, the VANS equations have been solved using classical numerical methods such as the finite volume method [85, 103, 144, 336], the finite difference method [247] or the finite element method [121]. However, alternative numerical approaches have been proposed in recent years in the hope of increasing the versatility and the computational speed of the standard methods. These models are based on the use of smoothed particle dynamics (SPH) [265] or the lattice Boltzmann method (LBM) [286, 321, 330, 334].

Between the last two numerical paradigms, the lattice Boltzmann method is an appealing candidate for the solution of the VANS equations. Indeed, this method is explicit and highly parallelizable, making it the ideal fluid solver in models such as CFD-DEM, which is generally computationally intensive because it requires small CFD time steps to ensure the stability of the coupling between the two phases. However, the solution of the VANS equations using the LBM requires a modified scheme to take into account the void fraction. The schemes that have been proposed in the literature can be grouped into two main categories. The first kind is based on a reformulation of the collision operator and an additional term to recover a pressure gradient that is independent of the void fraction [321, 330, 334]. In the present work, this type of model is referred to as pressure-correction LBM-VANS scheme. The second kind is based on a non-conservative formulation of the VANS equations, and uses the classical LBM scheme along with mass and momentum source terms to recover the VANS equations [286].

As will be demonstrated in this paper, the pressure correction schemes are generally inadequate, even in the case of small void fraction gradients, due to their lack of robustness and accuracy. On the other hand, the non-conservative schemes require the use of mass source terms for which the implementation in the LBM is much more complex, requiring the solution of matrix systems and local sub-iterations. Furthermore, the expected second-order convergence of these two types of schemes has not been verified for non-trivial test cases in which the velocity and the volume fraction vary in space. This can be explained, at least in part, by the lack of non-trivial analytical solutions for the VANS equations.

Recently, Blais and Bertrand [37] have shown that the method of manufactured solutions (MMS) can be used to design complex test cases for the VANS equations, for which the convergence analysis of a solver can be carried out. They applied it successfully for the verification of the VANS equations within the CFDEM framework [61], which is based on the finite volume library Open∇FOAM [233] and DEM code LIGGGHTS [155, 182].

In this work, we briefly present the VANS equations and recall the pressure-correction LBM-

VANS scheme that has been proposed in the literature. Then, we explain how the method of manufactured solutions can be used to design analytical solutions for these equations. We show by means of five test cases that this pressure-correction LBM-VANS scheme suffers from instabilities, notably in situations where the fluid is static (no-flow tests). We then introduce a new LBM-VANS scheme that relies on a new collision operator originating from the so-called immiscible multiphase lattice Boltzmann method [177]. This model is analyzed theoretically using a Chapman-Enskog expansion before it is verified using the same five test cases. We show that this new LBM-based model is second-order accurate and discuss its robustness.

6.2 Volume-Averaged Navier-Stokes Equations

A number of forms of the VANS equations have been proposed in the literature for multiphase flows. The main differences between these forms relate to the treatment of the interphase coupling and the expression for the stress tensor, as thoroughly discussed by Zhou *et al.* [336] for the two-fluid and the CFD-DEM models.

In this work, we consider without loss of generality the so-called form A of the VANS equations, which is based on local averaging. We refer to the book by Gidaspow [105] for an in-depth description of the origin of the model. The form A of the VANS equations will be simply referred to as the VANS equations in the remainder of this work.

The incompressible VANS equations are :

$$\frac{\partial \epsilon_f}{\partial t} + \nabla \cdot (\epsilon_f \boldsymbol{u}) = 0 \tag{6.1}$$

$$\frac{\partial \left(\rho_f \epsilon_f \boldsymbol{u}\right)}{\partial t} + \nabla \cdot (\rho_f \epsilon_f \boldsymbol{u} \otimes \boldsymbol{u}) = -\epsilon_f \nabla p + \nabla \cdot \boldsymbol{\tau} + \boldsymbol{F} \tag{6.2}$$

where ϵ_f is the void fraction, ρ_f the density of the fluid, p the pressure, $\boldsymbol{u}$ the velocity and $\boldsymbol{F}$ a momentum source term. The viscous stress tensor, $\boldsymbol{\tau}$, is defined as [337] :

$$\boldsymbol{\tau} = \mu \epsilon_f \left((\nabla \boldsymbol{u}) + (\nabla \boldsymbol{u})^T - \frac{2}{3} (\nabla \cdot \boldsymbol{u}) \boldsymbol{\delta}_k \right) \tag{6.3}$$

where μ is the dynamic viscosity and $\boldsymbol{\delta}_k$ the identity tensor.

It is important to note that the velocity and void fraction resulting from these equations are not individually divergence free, which means that all terms of the stress tensor are *a priori* non-zero.

6.3 Lattice Boltzmann Method

The Lattice Boltzmann Method (LBM) is based on the kinetic theory of gas and comes from the discretization in space, velocity and time of the Boltzmann equation. In fact, the LBM may be interpreted as the projection of the velocity space of the Boltzmann equation onto an isotropic orthonormal Hermite polynomial basis [207]. Consequently, the lattice Boltzmann method does not solve the incompressible Navier-Stokes equations *per se*, but a weakly compressible and athermal form of these equations which tend towards their incompressible form in the limit of low Mach number [290]. In the present work, only a brief presentation of the LBM is given. We refer the reader to the books by Succi [290] and Guo [117] for more details.

In the LBM, the primitive variable $f_i(\boldsymbol{x}, t)$ is mesoscopic and describes the ith population (probability density function) of particles at position $\boldsymbol{x}$ and time t, with discrete velocity $\boldsymbol{\xi}_i$. Using the Bhatnagar-Gross-Krook (BGK) approximation [34], the particle population collision process is governed by the following lattice Boltzmann equation (LBE) :

$$f_i\left(\boldsymbol{x} + \boldsymbol{\xi}_i \Delta t, t + \Delta t\right) - f_i\left(\boldsymbol{x}, t\right) = \frac{1}{\bar{\tau}}\left(f_i^{eq}\left(\boldsymbol{x}, t\right) - f_i\left(\boldsymbol{x}, t\right)\right) + \Delta t \boldsymbol{G}_i \tag{6.4}$$

with Δx the lattice spacing, $\bar{\tau}$ the dimensionless relaxation time, $\boldsymbol{G}_i$ a forcing term, Δt the time step, the term f_i^{eq} is the equilibrium distribution function :

$$f_i^{eq} = w_i \rho_f \left(1 + \frac{\left(\boldsymbol{\xi}_i \cdot \boldsymbol{u}\right)}{c_s^2} + \frac{\left(\boldsymbol{\xi}_i \cdot \boldsymbol{u}\right)^2}{2c_s^4} - \frac{\boldsymbol{u} \cdot \boldsymbol{u}}{2c_s^2}\right) \tag{6.5}$$

where c_s is the lattice speed of sound (celerity) defined as :

$$c_s = \frac{1}{\sqrt{3}} \frac{\Delta x}{\Delta t} \tag{6.6}$$

Furthermore, the forcing term $\boldsymbol{G}_i$ in the lattice Boltzmann equation is in the form proposed by Guo [117] :

$$\boldsymbol{G}_i = \left(1 - \frac{1}{2\bar{\tau}}\right) w_i \left(\frac{\left(\boldsymbol{\xi}_i - \boldsymbol{u}\right)}{c_s^2} + \frac{\left(\boldsymbol{\xi}_i \cdot \boldsymbol{u}\right)}{c_s^4} \boldsymbol{\xi}_i\right) \cdot \boldsymbol{F} \tag{6.7}$$

where w_i is the discrete weight associated with discrete velocity $\boldsymbol{\xi}_i$.

Finally, the dimensionless relaxation time $\bar{\tau}$ can be related to the dynamic viscosity of the fluid μ via the lattice spacing Δx, the time step Δt and the density of the fluid ρ_f, using the

following relation :

$$\bar{\tau} = \frac{\mu}{\rho_f c_s^2 \Delta t} + \frac{1}{2} \tag{6.8}$$

In the present work, we solve the LBE in 2D using the well-established D2Q9 lattice stencil, which uses 9 discrete velocities [170]. More explicitly, the discrete velocities and weights are given by :

$$\boldsymbol{\xi}_i = \begin{cases} (0,0) & \text{for } i = 0 \\ \left(cos[\pi\frac{(i-1)}{2}], sin[\pi\frac{(i-1)}{2}]\right)\frac{\Delta x}{\Delta t} & \text{for } i \in [1,4] \\ \left(cos[\pi\frac{(i-\frac{9}{2})}{2}], sin[\pi\frac{(i-\frac{9}{2})}{2}]\right)\sqrt{2}\frac{\Delta x}{\Delta t} & \text{for } i \in [5,8] \end{cases} \tag{6.9}$$

$$w_i = \begin{cases} \frac{4}{9} & \text{for } i = 0 \\ \frac{1}{9} & \text{for } i \in [1,4] \\ \frac{1}{36} & \text{for } i \in [5,8] \end{cases} \tag{6.10}$$

From a computational point of view, the LBE is solved using a two-step process. First, a collision step is done, followed by a propagation step. These two steps can be written respectively as :

$$f_i\left(\boldsymbol{x}, t^+\right) = f_i\left(\boldsymbol{x}, t\right) - \frac{1}{\bar{\tau}}\left(f_i\left(\boldsymbol{x}, t\right) - f_i^{eq}\left(\boldsymbol{x}, t\right)\right) + \Delta t \boldsymbol{G}_i \tag{6.11}$$

$$f_i\left(\boldsymbol{x} + \boldsymbol{\xi}_i \Delta t, t + \Delta t\right) = f_i\left(\boldsymbol{x}, t^+\right) \tag{6.12}$$

This LBM scheme has been implemented in the *vansBurst* LBM code, which is a 2D serial C++ code designed by our group for an easy integration of alternative collision operators.

6.4 Pressure-correction LBM-VANS scheme

The lattice Boltzmann method is intrinsically linked to the Navier-Stokes equations. Consequently, it requires modifications before it can be used to solve the volume-averaged Navier-Stokes equations. One method to obtain the VANS equations in the context of the LBM, as has been proposed by [321, 330, 334], is based on a rescaling of the density in the equilibrium distribution function by the void fraction. Using this approach, one obtains the following

expression for the populations at equilibrium :

$$f_i^{eq} = w_i \rho_f \epsilon_f \left(1 + \frac{(\boldsymbol{\xi}_i \cdot \boldsymbol{u})}{c_s^2} + \frac{(\boldsymbol{\xi}_i \cdot \boldsymbol{u})^2}{2c_s^4} - \frac{\boldsymbol{u} \cdot \boldsymbol{u}}{2c_s^2}\right) \tag{6.13}$$

Using this expression, the following equations are recovered in the low Mach number limit [334] :

$$\frac{\partial \rho_f \epsilon_f}{\partial t} + \nabla \cdot (\rho_f \epsilon_f \boldsymbol{u}) = 0 \tag{6.14}$$

$$\frac{\partial (\rho_f \epsilon_f \boldsymbol{u})}{\partial t} + \nabla \cdot (\rho_f \epsilon_f \boldsymbol{u} \otimes \boldsymbol{u}) = -\nabla (p \epsilon_f) + \nabla \cdot \boldsymbol{\tau} + \boldsymbol{F} \tag{6.15}$$

As can be seen, the pressure term resulting from this rescaling does not correspond to the one in Eq. (5.2) of the VANS equations. Therefore, the pressure must be corrected by adding $\boldsymbol{F}^P(\boldsymbol{x}, t) = p \nabla \epsilon_f$ to $\boldsymbol{F}(\boldsymbol{x}, t)$ in (6.7), which gives :

$$\boldsymbol{G}_i = \left(1 - \frac{1}{2\bar{\tau}}\right) w_i \left(\frac{(\boldsymbol{\xi}_i - \boldsymbol{u})}{c_s^2} + \frac{(\boldsymbol{\xi}_i \cdot \boldsymbol{u})}{c_s^4} \boldsymbol{\xi}_i\right) \cdot \left(\boldsymbol{F} + \boldsymbol{F}^P\right) \tag{6.16}$$

This additional source term must be enforced separately using for instance the method proposed by Guo [117]. In our implementation of this scheme, this gradient is calculated using a second-order centered finite difference scheme. This approach is referred to as the pressure correction LBM-VANS scheme. In theory, it allows to recover the VANS equations. However, the pressure in the LBM is defined using an equation of state that depends on ρ_f :

$$p = \rho_f c_s^2 \tag{6.17}$$

Assuming that ϵ_f is sufficiently smooth, refining the grid should lead to a converged expression for both ρ_f and $\nabla \epsilon_f$. However, Eqs. (6.6) and (6.8) show that, for a constant relaxation time $\bar{\tau}$, c_s^2 increases to infinity asymptotically as the mesh is refined. This scheme is thus expected to be ill-behaved in the limit $\Delta x \to 0$, which prevents it from converging consistently to the VANS equations. To our knowledge, the present work is the first time that a thorough convergence study is done for this scheme using test cases that involve non constant void fractions.

6.5 Method of Manufactured Solutions

The method of manufactured solutions (MMS) is a generic approach that allows one to build analytical solutions to partial differential equations (PDE) [227]. Its particular strength is

that it allows to choose *a priori* a solution to a PDE with given properties (e.g., infinite differentiability or local integrability). Such a solution can then be used to verify rigorously and in a flexible manner the implementation of any given solver.

The MMS procedure is straightforward. In the case of the VANS equations for a single fluid, we choose a velocity field $\boldsymbol{u}$ and a void fraction ϵ_f, and build a vector of manufactured variables $\boldsymbol{s}_{\mathrm{M}} = [\boldsymbol{u}^T, \epsilon_f]^T$ that satisfies the continuity equation (6.1).

In general, $\boldsymbol{s}_{\mathrm{M}}$ is not a solution of the complete VANS equations because it does not satisfy the momentum conservation equation (6.2). To do so, the following momentum source term $\boldsymbol{H}$ is added to this momentum conservation equation :

$$\begin{aligned}\boldsymbol{H}(\boldsymbol{s}_M) =& \frac{\partial\left(\rho_f \epsilon_f \boldsymbol{u}\right)}{\partial t} + \nabla\cdot\left(\rho_f\epsilon_f \boldsymbol{u}\otimes\boldsymbol{u}\right) + \epsilon_f \nabla p \\ &- \nabla\cdot\left(\mu\epsilon_f\left(\left(\nabla\boldsymbol{u}\right) + \left(\nabla\boldsymbol{u}\right)^T - \frac{2}{3}\left(\nabla\cdot\boldsymbol{u}\right)\boldsymbol{\delta}_k\right)\right)\end{aligned} \tag{6.18}$$

With this definition of $\boldsymbol{H}$, the manufactured solution is an analytical solution of the VANS Equations (6.1) and (5.2).

This solution can be used to assess the accuracy of the pressure-correction LBM-VANS scheme (or any other scheme) by monitoring the decrease of the Euclidean norm of the error ($\|e\|_2$) with respect to the lattice spacing (Δx). As the LBM uses a Cartesian, homogenous and regular structured grid, this error is defined as :

$$\|e_{\boldsymbol{\chi}}\|_2 = \sqrt{\frac{1}{N}\sum_j^N \|\boldsymbol{\chi}_{M,j} - \boldsymbol{\chi}_j\|^2} \tag{6.19}$$

where N is the number of lattices, $\boldsymbol{\chi}_{M,j}$ the manufactured (or analytical) solution at cell j, and $\boldsymbol{\chi}_j$ the numerical solution at the same position. The order of convergence obtained via simulations can be compared with the theoretical second order of convergence of the LBM scheme. Another type of error that will be monitored in some of the test cases described in the next section is the infinity norm, which is defined as :

$$\|e_{\boldsymbol{\chi}}\|_\infty = \max_j \|\boldsymbol{\chi}_{\mathrm{M},j} - \boldsymbol{\chi}_j\| \tag{6.20}$$

In the present work, analytical expressions for the source terms $\boldsymbol{H}(x, y)$ were obtained symbolically through Eq. (6.18) calculated using Mathematica 8 [258]. These expressions were translated to C++ syntax and directly integrated in our *art2 : :eq : :vansBurst* LBM code using the CForm command of Mathematica.

6.6 Methodology

In this section, we present five test cases of increasing complexity that we used to assess the validity of the LBM-VANS schemes. For all these test cases, the simulations were carried out for numerous lattice grids on the two-dimensional domain $\Omega = [-1, 1] \times [-1, 1]$. Periodic boundary conditions were used in order to preclude the possible effect on accuracy of the method of, for instance, the technique considered for the imposition of non-zero Dirichlet boundary conditions. For the convergence analysis, grids comprised from 400 to 160000 lattice cells. The relaxation time $\bar{\tau}$ was set to 1 for each simulation, resulting in a diffusive scaling for the time step and an asymptotically vanishing Mach number.

6.6.1 Case 1 : constant void fraction

The first manufactured case is defined as :

$$\boldsymbol{u} = 2 \begin{bmatrix} -\left(\sin\left(\pi x\right)\right)^2 \sin\left(\pi y\right) \cos\left(\pi y\right) \\ \sin\left(\pi x\right) \cos\left(\pi x\right) \left(\sin\left(\pi y\right)\right)^2 \end{bmatrix} \tag{6.21}$$

$$\epsilon_f = \frac{3}{4} \tag{6.22}$$

where x and y are the coordinates in the Cartesian frame of reference.

This test case is rather simplistic as the void fraction ϵ_f is constant and the pressure correction term in Eq. (6.16) is zero. While it does not represent a comprehensive test for the VANS equations, it serves to verify the implementation of the LBM schemes in our code.

6.6.2 Case 2 : no-flow with continuous void fraction

The second test case consists of what is referred to as a no-flow test, which means that the velocity is static : $\boldsymbol{u} = [0,\ 0]^T$. However, the void fraction is a continuous field :

$$\epsilon_f = \frac{3}{4} + \frac{1}{4} \sin\left(\pi x\right) \sin\left(\pi y\right) \tag{6.23}$$

The interest of this test, for which the momentum source term $\boldsymbol{H} = 0$ in Eq. (6.18), comes from the fact that it can serve to assess the stability of a scheme in the presence of void fraction gradients in the domain. In this case, the velocity should remain zero as there is no driving force for the flow.

6.6.3 Case 3 : no-flow with discontinuous void fraction

The third test case is also a no-flow test. It involves the following discontinuous void fraction :

$$\epsilon_f = \begin{cases} 0.75, \ \ \forall \ \ (x,y) \in \Omega_s = [-0.04, 0.04] \times [-0.04, 0.04] \\ 1, \ \ \forall \ \ (x,y) \in \Omega \backslash \Omega_s \end{cases} \tag{6.24}$$

It is similar to a two-dimensional step function. Such discontinuous functions are often encountered as an initial condition in real applications. For example, a bed of particles at the bottom of a vessel can be associated with a one-dimensional step function.

6.6.4 Case 4 : steady-state divergence-free flow

The fourth case is defined as :

$$\boldsymbol{u} = 2 \begin{bmatrix} -\left(\sin\left(\pi x\right)\right)^2 \sin\left(\pi y\right) \cos\left(\pi y\right) \\ \sin\left(\pi x\right) \cos\left(\pi x\right) \left(\sin\left(\pi y\right)\right)^2 \end{bmatrix} \tag{6.25}$$

$$\epsilon_f = \frac{3}{4} + \frac{1}{4} \sin\left(\pi x\right) \sin\left(\pi y\right) \tag{6.26}$$

This case is different from Case 1 since the void fraction is now a function of space.

6.6.5 Case 5 : steady-state non divergence-free flow

The fifth case is defined as :

$$\boldsymbol{u} = A e^{K \sin(\pi x) \sin(\pi y)} \left[1, \ 1\right]^T \tag{6.27}$$

$$\epsilon = B e^{-K \sin(\pi x) \sin(\pi y)} \tag{6.28}$$

where A, B, K are constants whose values are respectively 0.5, 0.7 and 0.3. This test case is the most complete of the five cases as the velocity field is non-divergence free and the void fraction varies in space. Therefore, all the terms of the viscous stress tensor (Eq. (6.3)) are non-zero.

6.7 Results and discussion on the pressure-correction LBM-VANS scheme

The graph in Figure 6.1 shows that, for Case 1, the velocity exhibits second-order convergence. However, as previously mentioned, this test is incomplete as the use of a constant void fraction implies that the pressure correction term in (6.16) is zero.

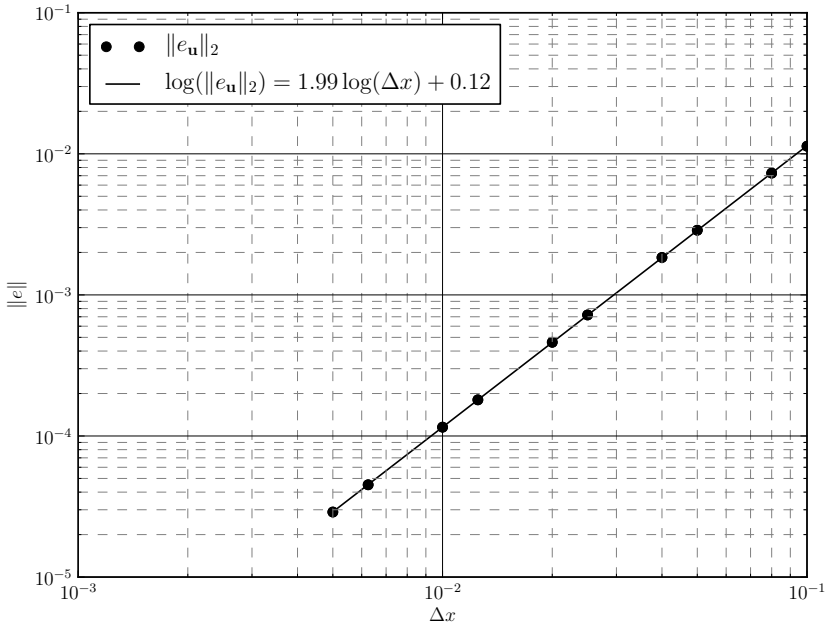

Figure 6.1 Euclidean norm of the error on $\boldsymbol{u}$ as a function of lattice spacing, and order of convergence for Case 1.

The results reported in Figures 6.2 and 6.3 show that, for Case 2, the fluid does not converge towards a static solution even though there is no driving force. It can also be drawn from Figures 6.3 and 6.4 that the magnitude of this spurious velocity is more important in regions of higher void fraction gradients.

Case 3 highlights this last fact. In this test case, the analytical void fraction is a two-dimensional step function, which means that its gradient cannot converge towards a constant value, but rather increases as the grid is refined. Consequently, the velocity is expected to diverge as the grid is refined, which is what is observed in Figure 6.5. More precisely, it shows that the infinity norm of the error in velocity exhibits a first-order divergence with respect to grid spacing, which can be related to the increase of the void fraction gradient.

Finally, results for Cases 4 and 5 (not presented here) have further ascertained that the pressure-correction LBM-VANS scheme always yields a wrong velocity field when the void fraction is not constant. In fact, this scheme was highly unstable for these two cases and most of the simulations could not converge due to numerical instabilities. This lack of robustness was amplified as the grid was refined, which prevented us from carrying any convergence study with these two cases.

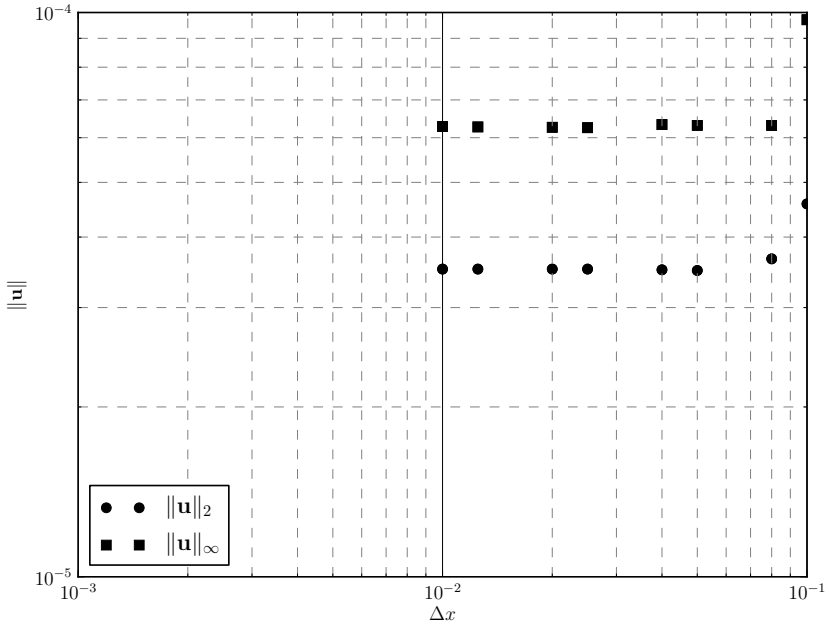

Figure 6.2 Euclidean and infinity norms of the velocity as a function of lattice spacing (Δx) for Case 2.

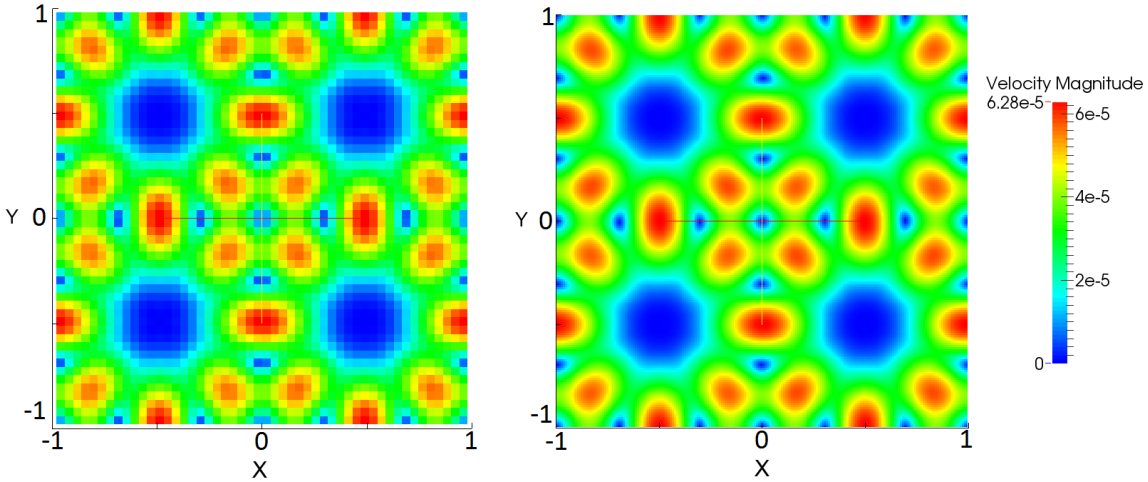

Figure 6.3 Magnitude of the velocity. Left panel : coarse grid (50×50) — Right panel : fine grid (200×200)

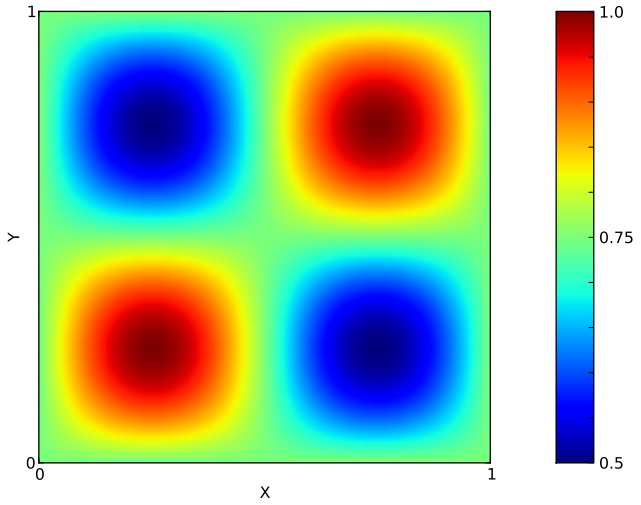

Figure 6.4 Void fraction ϵ_f for Case 2.

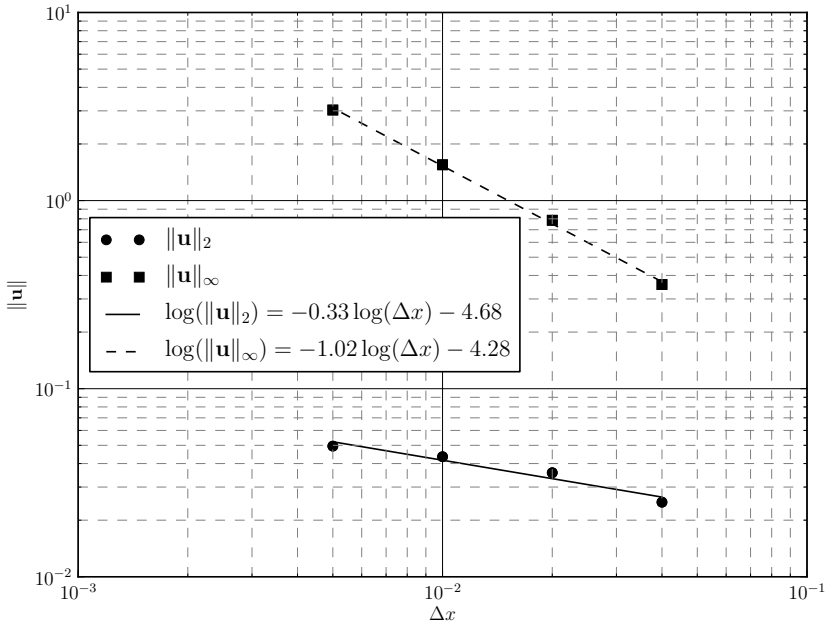

Figure 6.5 Euclidean and infinity norms of the velocity as a function of lattice spacing (Δx) for Case 3.

All these results indicate that the pressure-correction LBM-VANS scheme is not adequate. The error arises from the pressure correction and the related additional forcing term in Eq. (6.16). More precisely, the pressure resulting solely from the collision operator is false in the presence of a void fraction gradient and the addition of a forcing term was shown in this section to lead to an inconsistent and unstable scheme. This also indicates that an adequate LBM scheme for the VANS equations, which should yield the correct pressure gradient through a proper collision operator, is needed. Such a scheme will be developed and verified in the following sections.

6.8 LBM formulation for the VANS equations using a novel collision operator

As previously shown, the instability of the pressure-correction LBM-VANS scheme stems from an incorrect discretization of the pressure. This can be corrected by introducing a new collision operator in which the population at rest and the other populations are defined differently, thereby modifying the equation of state for the pressure. Such strategy has been used in multiphase LBM schemes such as the Shan-Chen model [274] or Rothman-Keller type schemes [174, 177].

We carry out our demonstration using Einstein's notation in 2D for the D2Q9 lattice, although it can straightforwardly be extended to 3D and other lattices. The main idea behind the scheme is to change the collision operator to obtain a pressure gradient term that does not include the void fraction (ϵ_f). The zeroth-, first- and second-order moments that we need to recover are :

$$\sum_i f_i^{eq} =: \rho_f^{(0)} = \rho_f \epsilon_f \tag{6.29}$$

$$\sum_i f_i^{eq} \xi_{i,\alpha} =: j_\alpha^{(0)} = \rho_f \epsilon_f u_\alpha \tag{6.30}$$

$$\sum_i f_i^{eq} \xi_{i,\alpha} \xi_{i,\beta} =: \Pi_{\alpha\beta}^{(0)} = (\rho_f - \rho_\infty)\, c_s^2 \delta_{\alpha\beta} + \rho_f \epsilon_f u_\alpha u_\beta \tag{6.31}$$

where ρ_∞ is an arbitrary constant, independent of time and space, which we will use to ensure the positivity of the population at rest f_0^{eq}. We define the equilibrium population f_i^{eq} as a second-order polynomial [64] :

$$f_0^{eq} = A_0 + D\boldsymbol{u} \cdot \boldsymbol{u} \tag{6.32}$$

$$f_i^{eq} = A_1 + B\boldsymbol{\xi}_i \cdot \boldsymbol{u} + C\left(\boldsymbol{\xi} \cdot \boldsymbol{u}\right)^2 + D\boldsymbol{u} \cdot \boldsymbol{u}, \quad \forall \ i \in \ [1, 8] \tag{6.33}$$

Using these expression, Eqs. (6.29), (6.30) and (6.31) can be solved analytically, leading to

the following expressions for the equilibrium populations :

$$f_0^{eq} = w_0 \left(\frac{9\rho_f \epsilon_f - 5\rho_f + 5\rho_\infty}{4} - \rho_f \epsilon_f \left(\frac{\boldsymbol{u} \cdot \boldsymbol{u}}{2c_s^2} \right) \right) \tag{6.34}$$

$$f_i^{eq} = w_i \left(\rho_f - \rho_\infty + \rho_f \epsilon_f \left(\frac{(\boldsymbol{\xi}_i \cdot \boldsymbol{u})}{c_s^2} + \frac{(\boldsymbol{\xi}_i \cdot \boldsymbol{u})^2}{2c_s^4} - \frac{\boldsymbol{u} \cdot \boldsymbol{u}}{2c_s^2} \right) \right), \quad \forall \ i \in [1, 8] \tag{6.35}$$

If $\rho_\infty = 0$, the positivity of f_0^{eq} is not guaranteed for $\epsilon_f < \frac{5}{9}$. By choosing the constant ρ_∞ correctly, one can however ensure the positivity of this population for a wider range of void fractions. Since ρ_∞ is constant in both time and space, this corresponds to defining the pressure up to a different constant, but does not modify the pressure gradient, thus ensuring that the correct VANS equations are obtained.

The third-order moment of this scheme resulting from Eqs. (6.34) and (6.35), which will be used in the Chapman-Enskog analysis for the reconstruction of the viscous tensor arising from the non-equilibrium part of the populations, is :

$$\sum_i f_i \xi_{i,\alpha} \xi_{i,\beta} \xi_{i,\gamma} =: S^{(0)}_{\alpha\beta\gamma} = \rho_f \epsilon_f c_s^2 \left(u_\alpha \delta_{\beta\gamma} + u_\beta \delta_{\alpha\gamma} + u_\gamma \delta_{\alpha\beta} \right) \tag{6.36}$$

6.8.1 Chapman-Enskog analysis of the new LBM-VANS scheme

In this section, we carry out a Chapman-Enskog analysis for the new collision operator. As the first part of the Taylor expansion of the LBM equation and the corresponding analysis are identical to those for the regular LBM scheme, they will be briefly presented. For a more detailed development, the reader is referred to [64, 117, 200]. However, as the derivation of the deviatoric stress tensor resulting from the second-order moment of the non-equilibrium populations is more subtle than in the classical analysis, it will be thoroughly derived.

We first recall the lattice Boltzmann equation (Eq. (6.4)), without the forcing term $\boldsymbol{G}_i$:

$$f_i \left(\boldsymbol{x} + \boldsymbol{\xi}_i \Delta t, t + \Delta t \right) - f_i \left(\boldsymbol{x}, t \right) = \frac{1}{\bar{\tau}} \left(f_i^{eq} \left(\boldsymbol{x}, t \right) - f_i \left(\boldsymbol{x}, t \right) \right) \tag{6.37}$$

We begin by giving a Taylor expansion in time (Δt) and space (Δx) of the left-hand side of

this equation, up to the second order :

$$\begin{aligned} f_i\left(\boldsymbol{x}+\boldsymbol{\xi}_i\Delta t, t+\Delta t\right) = f_i\left(\boldsymbol{x},t\right) &+ \Delta t\partial_t\left(f_i\left(\boldsymbol{x},t\right)\right) \\ &+ \Delta t\xi_{i,\alpha}\partial_\alpha\left(f_i\left(\boldsymbol{x},t\right)\right) + \frac{\Delta t^2}{2}\partial_t\partial_t\left(f_i\left(\boldsymbol{x},t\right)\right) \\ &+ \Delta t^2\xi_{i,\alpha}\partial_\alpha\partial_t\left(f_i\left(\boldsymbol{x},t\right)\right) + \frac{\Delta t^2}{2}\xi_{i,\alpha}\xi_{i,\beta}\partial_\alpha\partial_\beta\left(f_i\left(\boldsymbol{x},t\right)\right) \end{aligned} \tag{6.38}$$

We then carry out a classical Chapman-Enskog multiple time-scale analysis using an expansion parameter λ that is related to the Knudsen number. Introducing the following populations and differential operators :

$$f_i =: f_i^{(0)} + \lambda f_i^{(1)} + \lambda^2 f_i^{(2)} =: f_i^{(0)} + \lambda f_i^{neq} \tag{6.39}$$

$$f_i^{neq} =: f_i^{(1)} + \lambda f_i^{(2)} \tag{6.40}$$

$$\partial_t =: \lambda\frac{\partial}{\partial t_1} + \lambda^2\frac{\partial}{\partial t_2} =: \lambda\partial_t^{(1)} + \lambda^2\partial_t^{(2)} \tag{6.41}$$

$$\partial_\alpha =: \lambda\partial_\alpha^{(1)} \tag{6.42}$$

and regrouping the terms in Eq. (6.38) by the order of λ, we find by substitution into Eq. (6.37) :

$$\mathcal{O}\left(\lambda^0\right) : 0 = -\omega\left(f_i^{(0)} - f_i^{eq}\right) \tag{6.43}$$

$$\mathcal{O}\left(\lambda^1\right) : \partial_t^{(1)} f_i^{(0)} + \xi_{i,\alpha}\partial_\alpha^{(1)} f_i^{(0)} = -\frac{\omega}{\Delta t} f_i^{(1)} \tag{6.44}$$

$$\mathcal{O}\left(\lambda^2\right) : \partial_t^{(2)} f_i^{(0)} + \left(1-\frac{\omega}{2}\right)\left(\partial_t^{(1)} f_i^{(1)} + \xi_{i,\alpha}\partial_\alpha^{(1)} f_i^{(1)}\right) = -\frac{\omega}{\Delta t} f_i^{(2)} \tag{6.45}$$

where $\omega = \frac{1}{\tilde{\tau}}$. Using Eq. (6.43), we can identify $f_i^{(0)}$ with f_i^{eq}. Next, we impose the following constraints on the non-equilibrium populations [64, 117, 268] :

$$\sum_i f_i^{(k)} = 0, \quad \forall \ \ k > 0 \tag{6.46}$$

$$\sum_i f_i^{(k)}\xi_i = 0, \quad \forall \ \ k > 0 \tag{6.47}$$

We can next calculate the zeroth-, first- and second-order moments of Eq. (6.44) in order to

recover the equations for the conserved moments. To do so, we define :

$$\sum_i f_i^{(k)} =: \rho_f^{(k)} \tag{6.48}$$

$$\sum_i f_i^{(k)} \xi_{i,\alpha} =: j_\alpha^{(k)} \tag{6.49}$$

$$\sum_i f_i^{(k)} \xi_{i,\alpha} \xi_{i,\beta} =: \Pi_{\alpha\beta}^{(k)} \tag{6.50}$$

$$\sum_i f_i^{(k)} \xi_{i,\alpha} \xi_{i,\beta} \xi_{i,\gamma} =: S_{\alpha\beta\gamma}^{(k)} \tag{6.51}$$

It follows from, Eqs. (6.46) and (6.48), and Eqs.(6.47) and (6.49), respectively, that :

$$\rho_f^{(k)} = 0 \ \ \forall \ \ k > 0 \tag{6.52}$$

$$j_\alpha^{(k)} = 0 \ \ \forall \ \ k > 0 \tag{6.53}$$

From the moments of Eq. (6.44), we then get :

$$\sum_i \rightarrow \ \partial_t^{(1)} \left(\rho_f \epsilon_f\right) + \partial_\alpha^{(1)} \left(\rho_f \epsilon_f u_\alpha\right) = 0 \tag{6.54}$$

$$\sum_i \xi_{i,\alpha} \rightarrow \ \partial_t^{(1)} \left(\rho_f \epsilon_f u_\alpha\right) + \partial_\beta^{(1)} \left(\rho_f \epsilon_f u_\alpha u_\beta\right) + \partial_\alpha^{(1)} (\rho_f - \rho_\infty) c_s^2 = 0 \tag{6.55}$$

$$\sum_i \xi_{i,\alpha} \xi_{i,\beta} \rightarrow \ \partial_t^{(1)} \left(\Pi_{\alpha\beta}^{(0)}\right) + \partial_\gamma^{(1)} \left(S_{\alpha\beta\gamma}^{(0)}\right) = -\frac{\omega}{\Delta t} \Pi_{\alpha\beta}^{(1)} \tag{6.56}$$

Applying the same procedure to Eq. (6.45), we obtain :

$$\sum_i \rightarrow \ \partial_t^{(2)} \left(\rho_f \epsilon_f\right) = 0 \tag{6.57}$$

$$\sum_i \xi_{i,\alpha} \rightarrow \ \partial_t^{(2)} \left(\rho_f \epsilon_f u_\alpha\right) + \left(1 - \frac{\omega}{2}\right) \partial_\beta^{(1)} \left(\Pi_{\alpha\beta}^{(1)}\right) = 0 \tag{6.58}$$

Next, following along the lines of Guo and Shu [117] for the standard LBM scheme, the zeroth- (Eqs. (6.54) and (6.57)) and first-order (Eqs. (6.55) and (6.58)) moment equations on the λ and λ^2 scales can be combined to yield :

$$\partial_t \left(\rho_f \epsilon_f\right) + \partial_\alpha \left(\rho_f \epsilon_f u_\alpha\right) = 0 \tag{6.59}$$

$$\partial_t \left(\rho_f \epsilon_f u_\alpha\right) + \partial_\beta \left(\rho_f \epsilon_f u_\alpha u_\beta\right) + \partial_\beta \left((\rho_f - \rho_\infty) c_s^2 \delta_{\alpha\beta}\right) = -\lambda \left(1 - \frac{\omega}{2}\right) \partial_\beta \left(\Pi_{\alpha\beta}^{(1)}\right) \tag{6.60}$$

where ∂_t and ∂_β are defined in Eqs. (6.41) and (6.42). It is then necessary to close the Chapman-Enskog expansion and calculate the second-order moment of the non-equilibrium

populations, which will be linked to the deviatoric stress tensor. As is the case in the classical analysis [117], the second-order moment of the non-equilibrium populations, Eq. (6.56), is given by :

$$-\frac{\omega}{\Delta t}\Pi^{(1)}_{\alpha\beta} = \partial^{(1)}_t\left(\Pi^{(0)}_{\alpha\beta}\right) + \partial^{(1)}_\gamma\left(S^{(0)}_{\alpha\beta\gamma}\right) \tag{6.61}$$

We recall that the second-order and third-order moments of the equilibrium populations, Eqs. (6.31) and (6.36), are :

$$\Pi^{(0)}_{\alpha\beta} = \left(\rho_f - \rho_\infty\right) c_s^2\delta_{\alpha\beta} + \rho_f\epsilon_f u_\alpha u_\beta \tag{6.62}$$

$$S^{(0)}_{\alpha\beta\gamma} = \rho_f\epsilon_f c_s^2\left(u_\alpha\delta_{\beta\gamma} + u_\beta\delta_{\alpha\gamma} + u_\gamma\delta_{\alpha\beta}\right) \tag{6.63}$$

Combining Eqs. (6.61), (6.62) and (6.63) leads to :

$$\begin{aligned}-\frac{\omega}{\Delta t}\Pi^{(1)}_{\alpha\beta} =& \partial^{(1)}_t\left(\left(\rho_f - \rho_\infty\right) c_s^2\delta_{\alpha\beta}\right) + \partial^{(1)}_t\left(\rho_f\epsilon_f u_\alpha u_\beta\right)\\ &+ \partial^{(1)}_\gamma\left(\rho_f\epsilon_f c_s^2\left(u_\alpha\delta_{\beta\gamma} + u_\beta\delta_{\alpha\gamma} + u_\gamma\delta_{\alpha\beta}\right)\right)\end{aligned} \tag{6.64}$$

One problem in this expression is that ρ_f is not a conserved moment and that no state equation for $\partial^{(1)}_t\rho_f$ exists. In order to use the classical LBM scheme demonstration, we can rewrite Eq. (6.64) in the following form, by first adding and subtracting $\partial^{(1)}_t\left(\rho_f\epsilon_f c_s^2\delta_{\alpha\beta}\right)$ to its right-hand side, and then eliminating the term involving constant ρ_∞ as its derivative is zero :

$$\begin{aligned}-\frac{\omega}{\Delta t}\Pi^{(1)}_{\alpha\beta} =& \underbrace{\partial^{(1)}_t\left(\rho_f\epsilon_f c_s^2\delta_{\alpha\beta}\right)}_{I} + \underbrace{\partial^{(1)}_t\left(\rho_f\epsilon_f u_\alpha u_\beta\right)}_{II}\\ &+ \underbrace{\partial^{(1)}_\gamma\left(\rho_f\epsilon_f c_s^2\left(u_\alpha\delta_{\beta\gamma} + u_\beta\delta_{\alpha\gamma} + u_\gamma\delta_{\alpha\beta}\right)\right)}_{III}\\ &+ \underbrace{\partial^{(1)}_t\left(\rho_f c_s^2\delta_{\alpha\beta}\right) - \partial^{(1)}_t\left(\rho_f\epsilon_f c_s^2\delta_{\alpha\beta}\right)}_{IV}\end{aligned} \tag{6.65}$$

Using the conservation equations for the zeroth- and first-order moments of the equilibrium populations, Eqs. (6.54) and (6.55), the time derivatives of the conserved moments ($\rho^{(0)}_f = \rho_f\epsilon_f$) and ($j^{(0)}_\alpha = \rho_f\epsilon_f u_\alpha$) can be expressed as :

$$\partial^{(1)}_t\left(\rho_f\epsilon_f\right) = -\partial^{(1)}_\gamma\left(\rho_f\epsilon_f u_\gamma\right) \tag{6.66}$$

$$\partial^{(1)}_t\left(\rho_f\epsilon_f u_\alpha\right) = -\partial^{(1)}_\alpha\left(\rho_f c_s^2\right) - \partial^{(1)}_\gamma\left(\rho_f\epsilon_f u_\alpha u_\gamma\right) \tag{6.67}$$

which enables us to rewrite the right-hand side of Eq. (6.65). We initially focus on terms (I, II, III) of this equation as their treatment is similar to the case of the classical LBM scheme. By distributing the derivatives, we get :

$$\begin{aligned}-\frac{\omega}{\Delta t}\Pi^{(1)}_{\alpha\beta} =&\partial_t^{(1)}\left(\rho_f\epsilon_f\right)\delta_{\alpha\beta}c_s^2 \\ &+\frac{j_\beta}{\rho_f\epsilon_f}\partial_t^{(1)}\left(j_\alpha\right)+\frac{j_\alpha}{\rho_f\epsilon_f}\partial_t^{(1)}\left(j_\beta\right)-\frac{j_\alpha j_\beta}{\left(\rho_f\epsilon_f\right)^2}\partial_t^{(1)}\left(\rho_f\epsilon_f\right) \\ &+\partial_\gamma^{(1)}\left(\rho_f\epsilon_f c_s^2\left(u_\alpha\delta_{\beta\gamma}+u_\beta\delta_{\alpha\gamma}+u_\gamma\delta_{\alpha\beta}\right)\right)+IV\end{aligned} \tag{6.68}$$

Simplifying the mass and momentum terms using Eqs. (6.66) and (6.67), it follows that :

$$\begin{aligned}-\frac{\omega}{\Delta t}\Pi^{(1)}_{\alpha\beta} =&-\partial_\gamma^{(1)}\left(\rho_f\epsilon_f u_\gamma\right)\delta_{\alpha\beta}c_s^2 \\ &-u_\beta\left(\partial_\alpha^{(1)}\left(\rho_f c_s^2\right)+\partial_\gamma^{(1)}\left(\rho_f\epsilon_f u_\alpha u_\gamma\right)\right) \\ &-u_\alpha\left(\partial_\beta^{(1)}\left(\rho_f c_s^2\right)+\partial_\gamma^{(1)}\left(\rho_f\epsilon_f u_\beta u_\gamma\right)\right) \\ &+u_\alpha u_\beta\partial_\gamma^{(1)}\left(\rho_f\epsilon_f u_\gamma\right) \\ &+\partial_\gamma^{(1)}\left(\rho_f\epsilon_f c_s^2\left(u_\alpha\delta_{\beta\gamma}+u_\beta\delta_{\alpha\gamma}+u_\gamma\delta_{\alpha\beta}\right)\right)+IV\end{aligned} \tag{6.69}$$

Tedious but simple calculus then leads to :

$$\begin{aligned}-\frac{\omega}{\Delta t}\Pi^{(1)}_{\alpha\beta} =&\rho_f\epsilon_f\partial_\alpha^{(1)}\left(u_\beta\right)c_s^2+\rho_f\epsilon_f\partial_\beta^{(1)}\left(u_\alpha\right)c_s^2-\partial_\gamma^{(1)}\left(\rho_f\epsilon_f u_\alpha u_\beta u_\gamma\right) \\ &+u_\alpha\left(\partial_\beta^{(1)}\left(\rho_f\epsilon_f c_s^2\right)-\partial_\beta^{(1)}\left(\rho_f c_s^2\right)\right)+u_\beta\left(\partial_\alpha^{(1)}\left(\rho_f\epsilon_f c_s^2\right)-\partial_\alpha^{(1)}\left(\rho_f c_s^2\right)\right) \\ &+IV\end{aligned} \tag{6.70}$$

Next, we can rearrange term IV in Eq. (6.70) using Eq. (6.54), to obtain the final form of the viscous stress tensor. The resulting equation, which is consistent with the classical LBM scheme, is :

$$\begin{aligned}-\frac{\omega}{\Delta t}\Pi^{(1)}_{\alpha\beta} =&\rho_f\epsilon_f\partial_\alpha^{(1)}\left(u_\beta\right)c_s^2+\rho_f\epsilon_f\partial_\beta^{(1)}\left(u_\alpha\right)c_s^2-\partial_\gamma^{(1)}\left(\rho_f\epsilon_f u_\alpha u_\beta u_\gamma\right) \\ &+u_\alpha\left(\partial_\beta^{(1)}\left(\rho_f\epsilon_f c_s^2\right)-\partial_\beta^{(1)}\left(\rho_f c_s^2\right)\right)+u_\beta\left(\partial_\alpha^{(1)}\left(\rho_f\epsilon_f c_s^2\right)-\partial_\alpha^{(1)}\left(\rho_f c_s^2\right)\right) \\ &+\partial_\gamma^{(1)}\left(\rho_f\epsilon_f u_\gamma\right)c_s^2\delta_{\alpha\beta}-c_s^2\left(\frac{\partial_\gamma^{(1)}\left(\rho_f\epsilon_f u_\gamma\right)+\rho_f\partial_t^{(1)}\left(\epsilon_f\right)}{\epsilon_f}\right)\end{aligned} \tag{6.71}$$

This simplification of term IV leads to an expression with no time derivatives for ρ_f, thereby eliminating the need to store this variable at two consecutive iterations in order to maintain the second-order accuracy of the scheme.

Combining Eqs. (6.8), (6.60) and (6.71), and simplifying the resulting expression leads to :

$$\partial_t \left(\rho_f \epsilon_f u_\alpha\right) + \partial_\beta \left(\rho_f \epsilon_f u_\alpha u_\beta\right) + \partial_\beta \left((\rho_f - \rho_{\infty)} c_s^2 \delta_{\alpha\beta}\right) = \partial_\beta \left(\Theta_{\alpha\beta}\right) \tag{6.72}$$

where $\Theta_{\alpha\beta}$ is defined as :

$$\begin{aligned}\Theta_{\alpha\beta} = & \underbrace{\mu\epsilon_f \partial_\alpha \left(u_\beta\right) + \mu\epsilon_f \partial_\beta \left(u_\alpha\right)}_{i} - \underbrace{\frac{\mu}{\rho_f c_s^2} \partial_\gamma \left(\rho_f \epsilon_f u_\alpha u_\beta u_\gamma\right)}_{ii} \\ & + \underbrace{\frac{\mu}{\rho_f} \left(u_\alpha \left(\partial_\beta \left(\rho_f \epsilon_f\right) - \partial_\beta \left(\rho_f\right)\right) + u_\beta \left(\partial_\alpha \left(\rho_f \epsilon_f\right) - \partial_\alpha \left(\rho_f\right)\right)\right)}_{iii} \\ & + \underbrace{\frac{\mu}{\rho_f} \partial_\gamma \left(\rho_f \epsilon_f u_\gamma\right) \delta_{\alpha\beta} - \frac{\mu}{\rho_f} \left(\frac{\partial_\gamma \left(\rho_f \epsilon_f u_\gamma\right) + \rho_f \partial_t \left(\epsilon_f\right)}{\epsilon_f}\right)}_{iv}\end{aligned} \tag{6.73}$$

We recall that the deviatoric stress tensor of the VANS equations is [337] :

$$D_{\alpha\beta} = \epsilon_f \mu \left(\partial_\alpha \left(u_\beta\right) + \partial_\beta \left(u_\alpha\right) - \underbrace{\frac{2}{3} \partial_\gamma \left(u_\gamma\right) \delta_{\alpha\beta}}_{v}\right) \tag{6.74}$$

It can be seen by comparing Eqs. (6.73) and (6.74) that the viscous stress tensor that arises from the new collision operator and its underlying equilibrium populations, Eqs. (6.34) and (6.35), is not consistent with the one from the VANS equations. More precisely, term (i) is the classical deviatoric stress tensor that is present in the regular LBM scheme (with $\epsilon_f = 1$). Term (ii) is also present in the regular LBM scheme and is considered to be asymptotically vanishing with the Mach number. Terms (iii) and (iv) do not exist in the regular LBM scheme. Finally, term (v) of the deviatoric stress tensor is missing in Eq. (6.73). Note that this term is also absent in the regular LBM scheme. In the latter, the velocity field is asymptotically divergence free in the incompressible limit so that this term vanishes. This is not the case for the VANS equations.

We can conclude from the above discussion that the viscous stress tensor arising from the new LBM-VANS scheme is not valid without modifications ; terms (iii) and (iv) must be removed and term (v) must be added. This can be accomplished by the addition of an appropriate forcing term to the formulation.

Following Eqs. (6.59) and (6.72), the resulting equations for the new scheme are :

$$\partial_t \left(\rho_f \epsilon_f\right) + \partial_\gamma \left(\rho_f \epsilon_f u_\gamma\right) = 0 \tag{6.75}$$

$$\partial_t \left(\rho_f \epsilon_f u_\alpha\right) + \partial_\gamma \left(\rho_f \epsilon_f u_\gamma u_\alpha\right) = -\nabla \left(\rho_f c_s^2\right) + \partial_\beta \left(\Theta_{\alpha\beta}\right) - \partial_\beta \left(\Theta_{\alpha\beta}^C\right) + F_\alpha^P \tag{6.76}$$

where $\Theta_{\alpha\beta}^C$ is a correction tensor defined as :

$$\begin{aligned}\Theta_{\alpha\beta}^C =& \frac{\mu u_\alpha}{\rho_f}\left(\partial_\beta \left(\rho_f \epsilon_f\right) - \partial_\beta \left(\rho_f\right)\right) + \frac{\mu u_\beta}{\rho_f}\left(\partial_\alpha \left(\rho_f \epsilon_f\right) - \partial_\alpha \left(\rho_f\right)\right) \\ &+ \frac{\mu}{\rho_f}\partial_\gamma \left(\rho_f \epsilon_f u_\gamma\right)\delta_{\alpha\beta} - \frac{\mu}{\rho_f \epsilon_f}\left(\partial_\gamma \left(\rho_f \epsilon_f u_\gamma\right) + \rho_f \partial_t \left(\epsilon_f\right)\right) \\ &+ \frac{2}{3}\mu \epsilon_f \partial_\gamma \left(u_\gamma\right)\delta_{\alpha\beta}\end{aligned} \tag{6.77}$$

F_α^P is a pressure correction force term needed to recoved $\epsilon_f \nabla p$:

$$F_\alpha^P = (1-\epsilon_f)\partial_\alpha \left(\rho_f c_s^2\right) \tag{6.78}$$

Eqs. (6.75) and (6.76) are asymptotically equivalent to the following VANS equations :

$$\frac{\partial \epsilon_f}{\partial t} + \nabla \cdot \left(\epsilon_f \boldsymbol{u}\right) = 0 \tag{6.79}$$

$$\frac{\partial \left(\rho_f \epsilon_f \boldsymbol{u}\right)}{\partial t} + \nabla \cdot \left(\rho_f \epsilon_f \boldsymbol{u} \otimes \boldsymbol{u}\right) = -\epsilon_f \nabla p + \nabla \cdot \boldsymbol{\tau} \tag{6.80}$$

We note that the correction tensor, $\Theta_{\alpha\beta}^C$, is well-posed as it is only dependent on μ, ρ_f, ϵ_f, $\boldsymbol{u}$ and their derivatives. Therefore, it converges towards a constant value when the grid is refined. This is why this scheme is different from the pressure-correction LBM-VANS scheme of Section 6.4, and why it should solve adequately the no-flow tests of Sections 6.6.2 and 6.6.3. Furthermore, the regular lattice Boltzmann method is recovered when $\epsilon_f = 1$. Consequently, the scheme is consistent with the classical implementation of the LBM.

In practice, the additional source terms in Eq. (6.76) are calculated outside the collision step (Eq. (6.11)). They involve first- and second-order derivatives, which are approximated by means of a standard second-order finite difference formula. Moreover, the divergence of the correction tensor (Eq. (6.77)), which is required in Eq. (6.76), involves the calculation of $\partial_\alpha \partial_\beta \epsilon_f$ with $\alpha \neq \beta$. This is done on the LBM structured grid (with $\Delta x = \Delta y$) using the

following diagonal stencil :

$$\frac{\partial^2 \epsilon_f(x,y,t)}{\partial\alpha\partial\beta} = \frac{\epsilon_f(\alpha+\Delta x,\beta+\Delta x,t)+\epsilon_f(\alpha-\Delta x,\beta-\Delta x,t)}{4\Delta x^2} - \left(\frac{\epsilon_f(\alpha-\Delta x,\beta+\Delta x,t)+\epsilon_f(\alpha+\Delta x,\beta-\Delta x,t)}{4\Delta x^2}\right) \tag{6.81}$$

6.9 Results with the LBM-VANS scheme and the new collision operator

We present the results obtained with the LBM-VANS scheme introduced in the previous section for the five different test cases. Figures 6.6, 6.7 and 6.8 display the evolution of the Euclidean norm of the error on $\boldsymbol{u}$ as a function of the lattice spacing for Cases 1, 4 and 5. These three graphs show that the velocity exhibits second-order convergence even for the most complex manufactured solution (Case 5), which involves a complete non-zero viscous stress tensor. It should be recalled that the pressure-correction LBM-VANS scheme of Section 6.4 was not stable for Cases 4 and 5, causing a blow-up of the simulations. As predicted by the theoretical analysis done in Section 6.8.1, the new LBM-VANS scheme and its underlying corrective source terms converges towards the desired form of the VANS equations up to the second-order. Furthermore, the scheme exhibits very good mass conservation properties as the average density was preserved up to 10^{-14} kg.m^{-3} upon convergence in all simulations. We note that the results obtained for Cases 1 in Figure 6.6 are identical to those obtained with the pressure-correction scheme in Figure 6.1. For a constant void fraction, as is the case in Case 1, all the source terms are zero and, consequently, both schemes give identical results.

Next, Figures 6.9 and 6.10 show that the velocity for the two no-flow tests (Cases 2 and 3) is negligible for all grids ($|\boldsymbol{u}| < 10^{-11}$ m.s^{-1}). We consider that this is an essential property that any scheme should possess as it indicates that it does not create kinetic energy in the absence of fluid flow. However, we note that, although the spurious velocities in these two figures are negligible, their magnitude increases when the grid is refined. This is due to the fact that our code uses SI units instead of lattice units. Therefore the lattice speed of sound, c_s, increases when Δx decreases under diffusive scaling. Indeed, the only remaining source term in this case comes from Eq. (6.78), and its magnitude is related to the numerical error (floating point operations) in the centered finite difference formula for the evaluation of $\partial_\alpha \rho_f$. This term, which is multiplied by the lattice speed of sound squared (c_s^2), is responsible for these spurious but very small velocities.

Some comments are in order concerning the stability of the new scheme. We have found that, for low void fractions ($\epsilon_f < 0.45$), the model suffers from a pressure checkerboard effect, leading to instabilities and loss of convergence. This lower bound for stability increases to

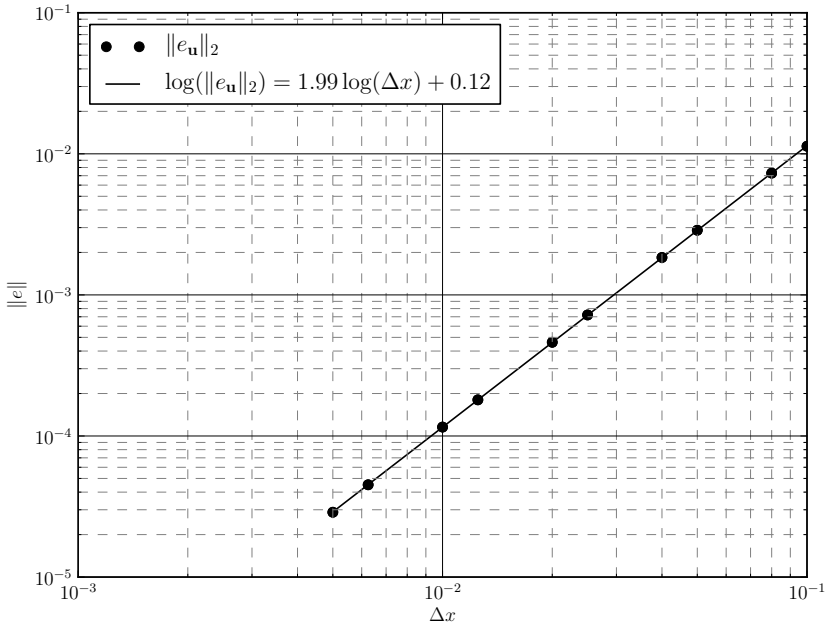

Figure 6.6 Euclidean norm of the error on the velocity as a function of lattice spacing, and order of convergence for Case 1 with the new LBM-VANS scheme.

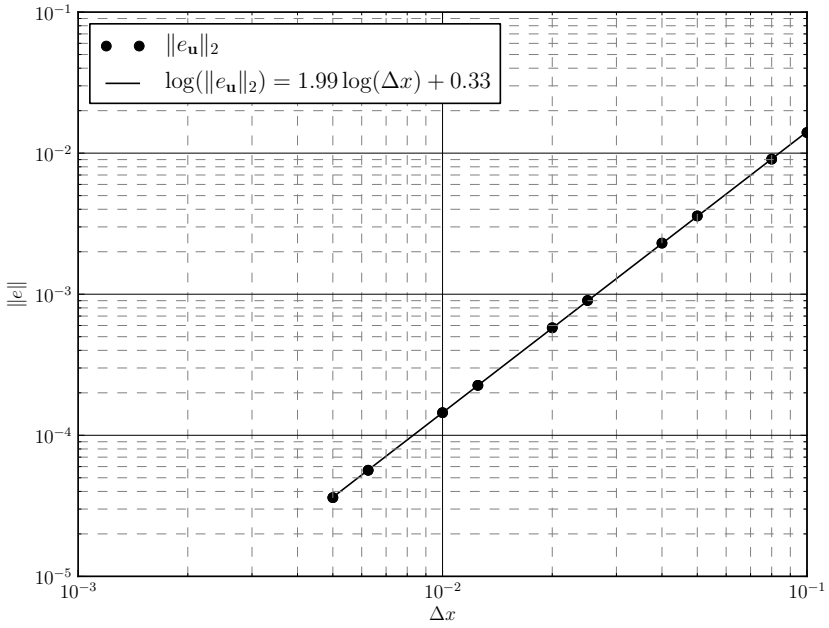

Figure 6.7 Euclidean norm of the error on the velocity as a function of lattice spacing, and order of convergence for Case 4 with the new LBM-VANS scheme.

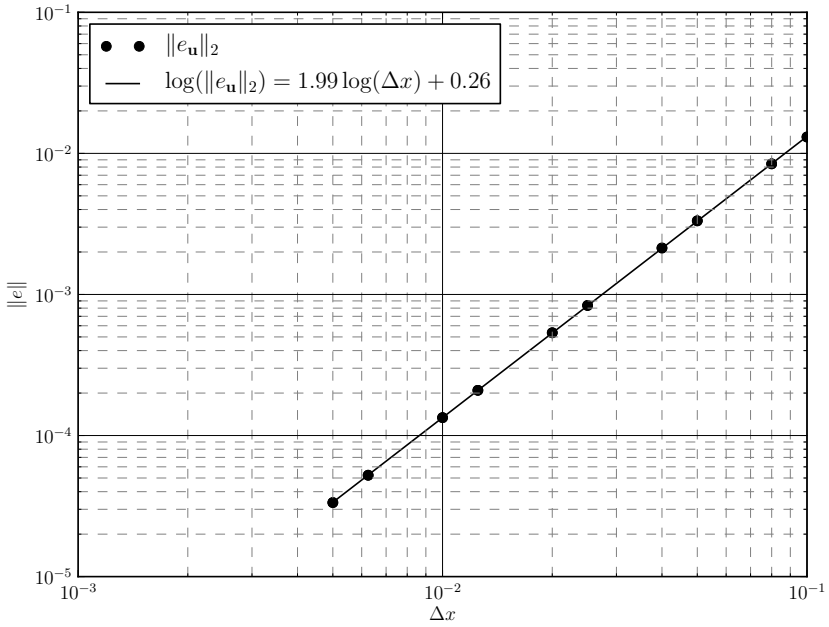

Figure 6.8 Euclidean norm of the error on the velocity as a function of lattice spacing, and order of convergence for Case 5 with the new LBM-VANS scheme.

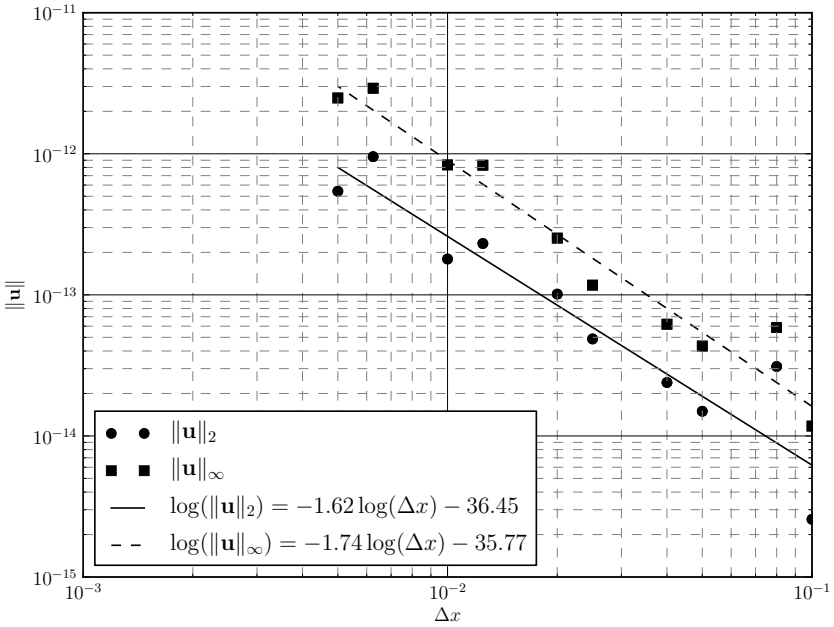

Figure 6.9 Euclidean and infinity norms of the velocity as a function of lattice spacing (Δx) for Case 2 with the new LBM-VANS scheme.

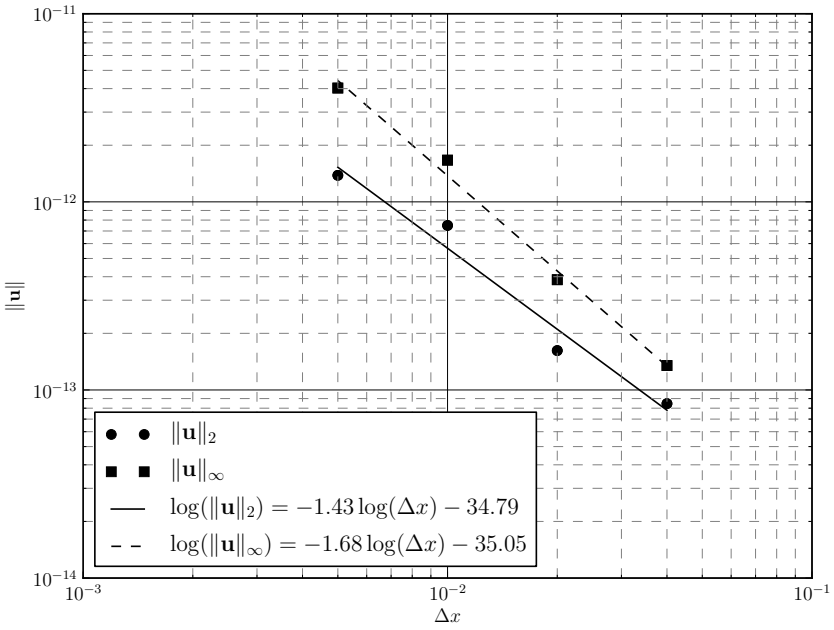

Figure 6.10 Euclidean and infinity norms of the velocity as a function of lattice spacing (Δx) for Case 3 with the new LBM-VANS scheme.

$\epsilon_f = 0.55$ for small relaxation times ($\bar{\tau} \in]0.5, 0.51]$). Note that this behavior is unaffected by the variation of parameter ρ_∞. Although results were observed for 10^4 lattice grids ($\Delta x = 0.02$), this behavior was not affected significantly by the lattice spacing and could not be eliminated by refining or coarsening the grid.

A straightforward solution to this problem consists of rescaling the density and void fraction so that they lie in the stability range of the scheme, while maintaining a constant mass per lattice cell. To do so, we introduce a density $\rho_{f,1}$ and void fraction $\epsilon_{f,1}$ such that :

$$\rho_{f,1}\epsilon_{f,1} = \rho\epsilon_f = \bar{\rho} \tag{6.82}$$

with $\epsilon_{f,1} > \epsilon_f$ and $\rho_{f,1} < \rho_f$. For instance, one could take $\rho_{f,1} = \frac{\rho_f}{\theta}$ and $\epsilon_{f,1} = \theta\epsilon_f$, so that $\epsilon_{f,1} > 0.45$, thus ensuring the stability of the scheme. We have found that, even for large values of ϵ_f such as $\epsilon_f = 3$ and for large variations of ϵ_f such as $max(\epsilon_f) - min(\epsilon_f) = 2.5$, the scheme remains stable, mass conservative and second-order accurate for all grid sizes.

6.10 Conclusion

The volume-averaged Navier-Stokes equations are commonly used for the modeling of multiphase flows in industrial applications. Indeed, they are part of numerous approaches in which they describe either all phases, as in two-fluid models, or the suspending fluid only, as in the case of unresolved CFD-DEM models.

The VANS equations are traditionally solved by means of the finite volume method or the finite element method. However, the lattice Boltzmann method is an interesting alternative to solve these equations because it is fully explicit, easily parallelizable owing to its local operations, and second-order accurate.

In the literature, the use of the LBM to solve the VANS equations has been done by means of two approaches. The first one is based on a modified collision operator and a pressure correction forcing term [321, 330, 334]. As we have shown in the present work, this method does not solve adequately the no-flow test (Cases 2 and 3), and is unstable in the case of problems involving void fraction gradients (Cases 4 and 5). The other type of implementation of the VANS equations within the LBM has been done using additional mass and momentum source terms [286]. However, this approach had not been shown to be second-order accurate, is more computationally intensive, requires sub-iterations and does not solve the VANS equation in a conservative formulation.

In this work, a VANS model for the lattice Boltzmann method based on a new collision operator involving two correction terms has been proposed. It is fully explicit and requires the same stencil as the classical lattice Boltzmann scheme. A Chapman-Enskog analysis has proven that the VANS equations are recovered with the correct deviatoric stress tensor. By designing analytical test cases using the method of manufactured solutions, this model has been shown to be second-order accurate for complex 2D cases, something that, to our knowledge, had never been done with other LBM-VANS models. Furthermore, the results obtained with the no-flow tests have revealed that this model predicts the pressure adequately.

Although our model suffers *a priori* from a stability problems at low void fractions, a slight modification entailing a rescaling of the density and void fraction has been observed to be an efficient workaround. Furthermore, this model is stable for very large void fraction gradients, which represents a significant improvement over current models.

Future work includes the extension of the model to 3D using D3Q19 lattices, which is a natural extension of the D2Q9 scheme within the scope of flows in porous media or solid-fluid flows using a CFD-DEM combination.

6.11 Acknowledgements

The financial support from the Natural Sciences and Engineering Research Council of Canada (NSERC) is gratefully acknowledged. In particular, Bruno Blais is thankful for the NSERC Vanier Scholarship. The authors would also like to acknowledge the technical support and computing time provided by Compute Canada. Finally, the authors would like to thank Pr. Dominique Pelletier from Polytechnique Montréal for fruitful and enlightening discussions on the method of manufactured solutions.

CHAPITRE 7 Article 3 : A Semi-Implicit Immersed Boundary Method and its Application to Viscous Mixing

Bruno Blais, Manon Lassaigne, Christoph Goniva, Louis Fradette, François Bertrand
Published in Computers & Chemical Engineering volume 85, pages 136-146, 2016

Abstract : Computational fluid dynamics (CFD) simulations in the context of single-phase mixing remain challenging notably due the presence of a complex rotating geometry within the domain. In this work, we develop a parallel semi-implicit immersed boundary method based on Open∇FOAM, which is applicable to unstructured meshes. This method is first verified on academic test cases before it is applied to single phase mixing. It is then applied to baffled and unbaffled stirred tanks equipped with a pitched blade impeller. The results obtained are compared to experimental data and those predicted with the single rotating frame and sliding mesh techniques. The proposed method is found to be of comparable accuracy in predicting the flow patterns and the torque values while being straightforwardly applicable to complex systems with multiples impellers for which the swept volumes overlap.

7.1 Introduction

In the process industry, mixing is often a critical unit operation that has a large impact on the yield, physical attributes and manufacturing cost of a product [245]. Single phase mixing, although relatively well understood, remains a challenging topic notably due to turbulence [79, 312] or rheology [116, 289] in the tank and to the arduous scale-up (or scale-down) of units, as is discussed in Machado *et al.* [188].

On the other hand, multiphase mixing, such as solid-liquid or gas-liquid mixing, is more complex due to the two-way coupling between the phases, which takes place at both the microscopic and mesoscopic flow scales [312]. This coupling usually has an impact on the global characteristic of the flow, the complexity of which can be exacerbated by rheology or turbulence. Furthermore, it renders highly challenging the prediction of macroscopic mixing quantities such as the torque on the impeller, the just-suspended speed or the gas hold-up.

In both single-phase and multiphase mixing, computational fluid dynamics (CFD) has proven to be an inexpensive, fast and efficient tool to gain insight into the flow behavior in various set-ups [245]. For example, for solid-liquid mixing, two-fluid models have been solved via

the finite volume method using FLUENT and to obtain, rather successfully in the turbulent regime, suspension curves [296], minimum speed for complete suspension [297] and solid particle distributions [298]. However, many challenges remain in solid-liquid mixing, such as the possibility of simulating suspensions of particles of different sizes and densities [13, 15], and suspensions in the laminar and transitional regimes [130, 132]. These are only tractable with complex models such as the CFD-DEM approach that combines a CFD technique for the fluid phase and the discrete element method (DEM) for the solid particles [336]. Similar problematic exist for the cases of gas-liquid and liquid-liquid (emulsion) mixing, for which non-trivial models such as population balance models [196] have the potential to shed light on the dynamics prevailing in this type of operations.

One of the recurring obstacle to the use of CFD in mixing, especially in complex multiphase models such as those based on CFD-DEM, is related to the presence of a single or multiple rotating impellers within the tank, with or without baffles, combined with the unsteady character of the flow and the need for distributed memory parallelism owing to large computational times.

The three usual approaches to tackle this problem are : the sliding mesh (SM), multiple reference frame (MRF) and the single rotating frame (SRF) methods. However, they are known to suffer from limitations in terms of the type of geometry they can handle [312] and their capability to solve the unsteady- or steady-state Navier-Stokes equations [187,312]. These issues, which provided the impetus for the present work, are discussed thoroughly in the next section.

The immersed boundary (IB) and fictious domain (FD) methods are interesting alternatives as they can handle complex geometries in a parallel and computationally efficient manner, without requiring an explicit mesh of the geometry. Moreover, they can be generalized to complex configurations, such as those involving multiple impellers for which the swept volumes overlap, and to full six degrees of freedom kinematics.

Although their use in mixing is not widespread, the IB and FD methods are efficient for many applications. For instance, a fictious domain based on the finite element method, developed by Bertrand *et al.* [32], was used to study numerous types of mixing configurations such as coaxial [303], rotor-stator [21] and planetary mixers [300]. However, for the study of single phase and multiphase flows, the finite volume method has highly interesting local mass conversation properties that make it an adequate scheme, especially for hybrid methods such as CFD-DEM or for extensive turbulence modeling using large eddy simulation (LES). Consequently, there is a need for accurate finite volume based IB and FD methods applicable to the study of complex multiphase flow in mixing systems.

Most finite volume based IB and FD methods developed so far rely on fractional-step methods [154,273] on structured Cartesian hexahedral meshes, which renders their implementation in the context of a generic cell-centered unstructured CFD solvers problematic. In the present work, we remedy this issue by means of the Open∇FOAM [233] library by developing a new semi-implicit immersed boundary method that brings into play a pressure implicit with splitting of operators (PISO) formulation. This immersed boundary method, which is directly integrated within the CFDEM framework [61,112], has the following properties : it is efficient on unstructured meshes, compatible with static or dynamic mesh refinement, and requires only the use of a surface mesh to describe a moving object within the computational domain.

First, the main categories of approaches for conformal meshes or immersed boundaries are reviewed and their respective limitations are discussed. This review paves the way to the design of a new semi-implicit immersed boundary method based on a PISO scheme, which is first verified using three academic test cases. Next, this method is applied to the study of the single phase mixing of a viscous fluid in a stirred tank provided with a pitched blade turbine, with and without baffles. The validity of the proposed IB approach is further assessed by comparing numerical results obtained with it to experimental data and other results coming from single rotating frame (SRF) and sliding mesh (SM) techniques. Finally, the accuracy of the proposed method and its potential for the study of complex mixing systems for both single and multiphase flows are discussed.

7.2 Strategies for moving boundaries

In this section, a brief review of the various approaches for the simulation of rotating objects is carried out with an emphasis on formulations and their theoretical limitations in the context of the finite volume method. The focus is geared towards the simulation of mixing flows using rigid impellers, and all issues related to fluid-structure interactions in the context of a flexible geometry are not addressed.

This review is split into two parts. The first one refers to conformal mesh techniques and the second to immersed boundary and fictitious domain methods.

7.2.1 Conformal mesh techniques

In conformal mesh methods, the impeller geometry is explicitly meshed and its motion is accounted for using surface boundary conditions. Semi-empirical methods such as those involving impeller boundary conditions (IBC) [50] are not discussed here, as their accuracy is highly dependent on the quality of local flow measurements and they cannot be extended

to unsteady simulations. Consequently, they are not generic methods for moving boundaries and offer poor accuracy when compared to the methods presented in this section. For an extensive review of the results obtained via conformal mesh approaches in the context of mixing, the reader is referred to Brucato *et al.* [50].

Single rotating frame technique

The single rotating frame of reference (SRF) approach solves for the motion of the impeller by changing the formulation of the problem from the laboratory frame of reference to the Lagrangian frame of this impeller rotating at velocity $\boldsymbol{\omega}$. Consequently, zero-velocity no-slip boundary conditions are applied to the impeller whereas a the angular velocity imposed along the tank walls. The Navier-Stokes equations can be written for $\boldsymbol{u}$ in this rotating frame of reference, which requires the addition of Coriolis and centrifugal forces :

$$\nabla \cdot \boldsymbol{u} = 0 \tag{7.1}$$

$$\partial_t \rho \boldsymbol{u} + \nabla \cdot \rho \boldsymbol{u} \otimes \boldsymbol{u} + 2\rho \boldsymbol{\omega} \times \boldsymbol{u} + \rho \boldsymbol{\omega} \times (\omega \times \boldsymbol{r}) = -\nabla p + \nabla \cdot \boldsymbol{\tau} \tag{7.2}$$

where $\boldsymbol{r}$ is the distance to the axis of rotation, $\boldsymbol{\omega}$ the angular velocity and p the pressure. The viscous stress tensor $\boldsymbol{\tau}$ for an incompressible flow is [35] :

$$\boldsymbol{\tau}_R = \mu \left(\nabla \boldsymbol{u} + (\nabla \boldsymbol{u})^T \right) \tag{7.3}$$

where μ is the dynamic viscosity and ρ the density of the fluid.

Note that this method is valid for both transient and steady-state simulations. It is limited to geometries in which the static part of the tank is invariant by rotation. In the case of mixing, it is limited to set-ups comprising a single shaft (with one or many impellers) rotating in an unbaffled tank.

Sliding mesh technique

In the sliding mesh technique, the mesh is decomposed into $k+1$ non-overlapping regions : a static region, the tank and k rotating regions, each of which rotates along with the impeller it encompasses. Consequently, the flow equations are solved for each rotating region and contain the acceleration terms corresponding to a the rotating grid, whereas flow in the static region is solved in the laboratory frame of reference. The static region and each of the rotating subdomains regions are implicitly coupled at their interface by using face interpolation, to ensure a conservative distribution of the fluxes going from one subdomain to an adjacent one,

as the mesh faces on each side do not usually coincide. Slightly different implementations of this technique exist and we refer the reader to the respective user's guides (such as [8] for FLUENT) for more details.

Multiple reference frame technique

In the multiple reference frame technique, the domain is decomposed into two subdomains, one using the Lagrangian frame of reference of the impeller it contains, and the other one in the (Eulerian) laboratory frame of reference. The Navier-Stokes equations are solved in each subdomain and the velocities at their interface are matched at each iteration of the underlying scheme. This method is limited to steady-state simulations as the coupling between the two subdomains assumes a steady flow condition at their interface [187].

7.2.2 Immersed boundary and fictious domain methods

Immersed boundary and fictious domain methods refer to a very large class of methods used to discretize a static or moving, and flexible or rigid geometry onto a grid without using a body-fitted mesh. The mathematical formulation of immersed boundary problems is the subject of many papers in the literature, and we refer the reader to Peskin [249] and Mitall and Iccarino [217] for extensive reviews on this topic. In the following description of the various approaches, we use the terminology from Mittal and Iccarino [217].

Two main categories of immersed boundary formulations exist, depending on whether the immersed boundary conditions are enforced into the Navier-Stokes equations in a discrete or continuous manner.

In the continuous forcing approach, as introduced by the work of Peskin [248], no-slip boundary conditions are enforced by introducing a forcing term directly into the continuous Navier-Stokes equations. This forcing term acts on so-called control points that discretize the fictitious part of the geometry. In the case of an impeller or another moving part, these points, which are located on its surface, move according to the corresponding kinematics. They can be viewed as Dirac distributions that are spread over the surface of the fictitious part using a smoothing kernel function [217]. As this method was originally developed for elastic bodies, its extension to rigid boundaries, as in the case of an impeller, requires the use of either a very stiff elastic modulus [217] or of an iterative forcing scheme such as the one proposed by Goldstein *et al.* [110].

An alternative consists of using direct penalization methods coupled with Navier-Stokes/Brinkman type models and a variable permeability to enforce the motion of a solid part [7, 152]. Two

types of direct penalization can be distinguished : the velocity can be directly penalized in the Navier-Stokes equation by either adding a Brinkman permeability term or increasing the viscosity within the solid part. The reader is referred to Angot *et al.* [7] for a mathematical analysis and a comparison of these two approaches. A different alternative considers that the solid part is a fluid subjected to a rigidity constraint [72, 107, 242, 278]. In this technique, a continuous forcing term, the magnitude of which depends on the relative velocity between the fluid and the solid part, is applied to the fluid within or at the surface of this solid part to take into account its motion. These two alternate approaches are iterative in nature and require the integration of continuous terms within the Navier-Stokes equations, which makes them well-suited for a PISO scheme.

In the discrete approach, the regular Navier-Stokes equations are solved and the flow is modified *a posteriori* by taking into account the no-slip boundary conditions related to the moving part either directly [95] or indirectly through ghost cells [189] or a cut-cell approach [311].

7.3 PISO immersed boundary scheme

The PISO immersed boundary (PISO-IB) scheme developed in the present work can be seen as a semi-implicit PISO extension of the work of Glowinski [107], Patankar *et al.* [242] and, more recently, Shirgaonkar *et al.* [278] and Curet *et al.* [72]. The aim of the PISO-IB scheme is to add an immersed boundary method to the standard PISO scheme by using the current PISO loops to impose the velocity of the immersed rigid body while maintaining mass conservation. This means that no additional loops are required. Furthermore, it leads to a less stiff system than with a direct penalization approach, especially if the part is in motion. This scheme is tailored to have good parallel efficiency and can be used with unstructured polyhedral meshes. It is also suitable for hybrid meshes where the static geometry is discretized using a conformal mesh and the moving part (e.g an impeller) is taken into account through the immersed boundary method.

The PISO-IB scheme is presented in two steps. The discretization of the immersed body using cell center and vertex flagging is first introduced before the scheme itself is presented in detail. This stair-casing approach was chosen in the present work due to its speed, but the PISO-IB scheme is also compatible with surface-based forcing using control points. The reader is referred to the paper by Peskin for a thorough description of the latter technique [249].

7.3.1 Discretization of the geometry using cell and vertices flagging

The PISO-IB method requires a surface mesh of the immersed body. The projection of this body onto the finite volume mesh is then carried out by generating a boolean list indicating which cell centers and vertices of this finite volume mesh intersect with it. This operation, which adds to the computational cost of the scheme as compared to the traditional PISO approach, is highly parallelizable as the corresponding operations, which are proportional to the number of cell centers and vertices in the mesh, can be done independently by many processors (or cores). Figure 7.1 illustrates schematically this cell center and vertex detection technique, which creates two lists of so-called fluid and solid nodes, respectively.

Using these two lists, a solid fraction is generated for each cell i by attributing an equal weight to the sum of the vertices in this cell and its center :

$$\beta_i = \frac{N_{vc,i} + N_{cc,i} N_{v,i}}{2 N_{v,i}} \tag{7.4}$$

where $N_{v,i}$ is the number of vertices in cell i (eg. 8 for a hexahedron), and $N_{vc,i}$ and $N_{cc,i}$ are the number of vertices and centers intersecting the immersed body, respectively.

The vertices and the centers are also used to define the velocity of cell i that intersects the immersed body :

$$\boldsymbol{u}_{ib,i} = \boldsymbol{v}_{ib} + \frac{1}{N_{vc,\mathrm{i}} + N_{v,\mathrm{i}}} \left[\left(\sum_{j}^{N_{vc,i}} \boldsymbol{\omega} \times (\boldsymbol{x}_{v,j} - \boldsymbol{x}_{ib}) \right) + N_{v,i} \boldsymbol{\omega} \times (\boldsymbol{x}_{c,\mathrm{i}} - \boldsymbol{x}_{ib}) \right] \tag{7.5}$$

where $\boldsymbol{u}_{ib,\mathrm{i}}$ is the velocity of the cell i, $\boldsymbol{v}_{ib}$ is its translational velocity, $\boldsymbol{x}_{ib}$ its center of rotation, and $\boldsymbol{x}_{c,i}$ and $\boldsymbol{x}_{v,j}$ the coordinates of its center and vertices. Note that the expression within the brackets corresponds to the angular component of the velocity of the immersed body at the position of the cell i, which is not know analytically due to the stair-casing. For a fully covered cell, this becomes equal to the angular velocity of the cell center.

Using this approach, the volume of the projected immersed body is not exactly the same as the volume the region delimited by its surface mesh. Consequently, the so-called halo layer, which corresponds to the cells i in which the body fraction $\beta_i \in]0, 1[$, is shrunk or expanded to correct the volume of the discretized immersed body. In particular, this ensures that this volume is not affected by cell alignment. This entire procedure is summarized in the block diagram of Figure 7.2.

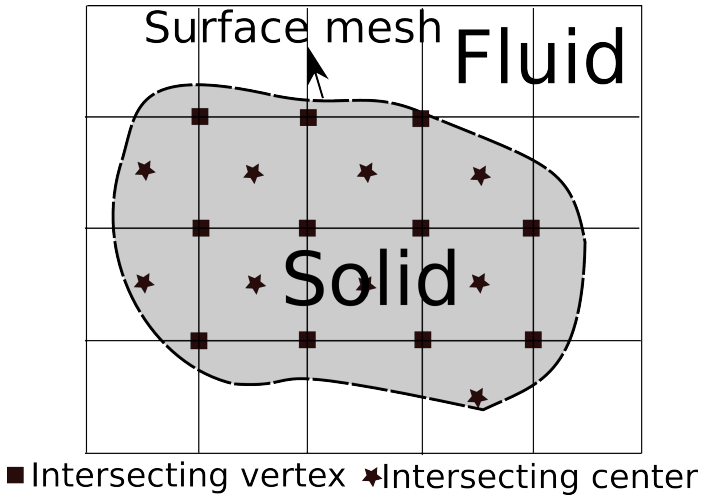

Figure 7.1 Illustration of the cell center and vertices flagging method.

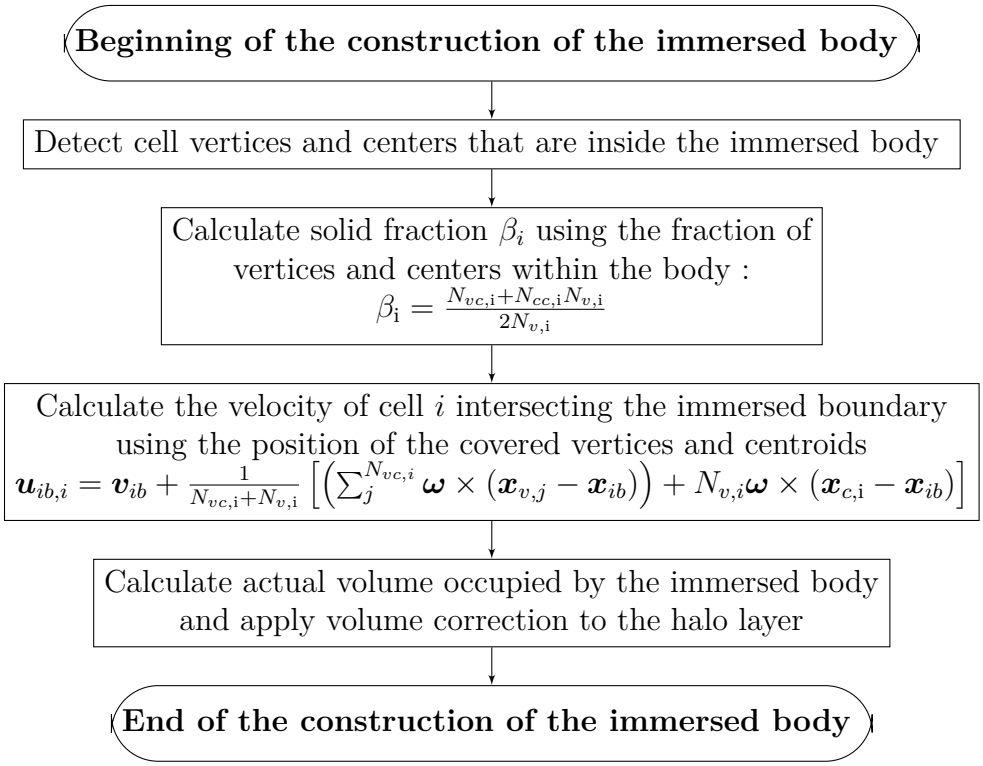

Figure 7.2 Block diagram for the construction of the immersed body and its velocity

7.3.2 The PISO-IB scheme

The PISO-IB scheme makes use of the intrinsic cycling within the PISO loop to iterate on the continuous forcing term added to the momentum equation to take into account the immersed body and its motion. We refer to the work of Issa [136] for a full presentation of the standard PISO scheme. In the present development, a notation close to that in the book by Ferziger and Perić [97] is used. For a more generic presentation of the cell-centered finite volume formulations available in Open∇FOAM, which is used in the current work, the reader is referred to Weller *et al.* [322] and Jasak *et al.* [140].

The Navier-Stokes equations with the immersed boundary forcing term $\boldsymbol{H}$ are given by :

$$\nabla \cdot \boldsymbol{u} = 0 \tag{7.6}$$

$$\partial_t \boldsymbol{u} + \nabla \cdot \boldsymbol{u} \otimes \boldsymbol{u} = -\frac{1}{\rho}\nabla p + \frac{1}{\rho}\nabla \cdot \boldsymbol{\tau} + \boldsymbol{H} \tag{7.7}$$

Time iteration begins with the update of the immersed body. The forcing term is then updated ($\boldsymbol{H}^{\mathrm{m}^*} = \boldsymbol{H}^{\mathrm{m}-1}$) so that it is zero outside of the immersed body. Next, the pressure-correction scheme starts with the solution of a predictor step for velocity $\boldsymbol{u}^{\mathrm{m}^*}$ using the pressure and velocity at time step $m-1$ (or the initial condition when $m = 1$) and the forcing term $\boldsymbol{H}^{\mathrm{m}^*}$:

$$A_{\mathrm{i}}\boldsymbol{u}_{\mathrm{i}}^{\mathrm{m}^*} + \sum_{\mathrm{j}} A_{\mathrm{j}}\boldsymbol{u}_{\mathrm{j}}^{\mathrm{m}^*} = Q_{\boldsymbol{u},\mathrm{i}}^{\mathrm{m}-1} - \left(\frac{\delta p^{\mathrm{m}-1}}{\delta x}\right)_{\mathrm{i}} + \boldsymbol{H}_{\mathrm{i}}^{\mathrm{m}^*} \tag{7.8}$$

The content of A is linked to the discretization of the fluxes and velocity gradient whereas $Q_{\boldsymbol{u},\mathrm{i}}^{\mathrm{m}-1}$ can be deduced from the discretization of the time derivative in (7.7). The indices i and j refer to cell i and to the neighboring cells, respectively. The pressure term is given explicitly and the symbolic derivative is approximated by the centered scheme. The resulting velocity $\boldsymbol{u}_{\mathrm{i}}^{\mathrm{m}^*}$ is not divergence free, hence the requirement of a pressure correction step.

First, a correction in the spirit of the Rhie and Chow interpolation procedure is applied to prevent the decoupling of the velocity from the pressure and the forcing term is applied [147, 260] :

$$\boldsymbol{u}_{\mathrm{i}}^{\mathrm{m}^{**}} = \frac{Q_{\boldsymbol{u},\mathrm{i}}^{\mathrm{m}^*} - \sum_{\mathrm{j}} A_{\mathrm{j}}\boldsymbol{u}_{\mathrm{j}}^{\mathrm{m}^*}}{A_{\mathrm{i}}} \tag{7.9}$$

By means of a linear interpolation of the cell-centered velocity, the mass fluxes can be updated

at the cell faces :

$$\phi_{\mathrm{F}}^{\mathrm{m}^{**}} = \langle \boldsymbol{u}_{\mathrm{i}}^{\mathrm{m}^{**}} \rangle_{\mathrm{F}} \cdot \boldsymbol{S}_{\mathrm{F}} \tag{7.10}$$

where $\langle . \rangle_{\mathrm{F}}$ denotes the face interpolation of a variable from its value at the surrounding cell centers, and where $\boldsymbol{S}_{\mathrm{F}}$ is the surface normal vector.

A pressure correction equation that includes the forcing term $\boldsymbol{H}_{\mathrm{i}}^{\mathrm{m}^{*}}$ is then solved :

$$\sum_{\mathrm{F}} \langle \frac{1}{A_{\mathrm{i}}} \rangle_{\mathrm{F}} \boldsymbol{S}_{\mathrm{F}} \cdot \nabla p_{\mathrm{i}}^{\mathrm{m}^{**}} = \sum_{\mathrm{F}} \phi_{\mathrm{F}}^{\mathrm{m}^{**}} + \sum_{\mathrm{F}} \langle \frac{1}{A_{\mathrm{i}}} \rangle_{\mathrm{F}} \langle \boldsymbol{H}_{\mathrm{i}}^{\mathrm{m}^{*}} \rangle_{\mathrm{F}} \cdot \boldsymbol{S}_{\mathrm{F}} \tag{7.11}$$

which allows for the correction of the velocity using this new pressure as well as the forcing term :

$$\boldsymbol{u}_{\mathrm{i}}^{\mathrm{m}^{***}} = \boldsymbol{u}_{\mathrm{i}}^{\mathrm{m}^{**}} + \frac{1}{A_{\mathrm{i}}} \left(- \left(\frac{\delta p^{\mathrm{m}^{**}}}{\delta x} \right)_{\mathrm{i}} + \boldsymbol{H}_{\mathrm{i}}^{\mathrm{m}^{*}} \right) \tag{7.12}$$

Finally, this forcing term is corrected using the difference between the current velocity and the prescribed one within the immersed body :

$$\boldsymbol{H}_{\mathrm{i}}^{\mathrm{m}^{***}} = \boldsymbol{H}_{\mathrm{i}}^{\mathrm{m}^{*}} + \frac{\alpha \beta_{\mathrm{i}}}{\Delta t} \left(\boldsymbol{u}_{ib,\mathrm{i}} - \boldsymbol{u}_{\mathrm{i}}^{\mathrm{m}^{***}} \right) \tag{7.13}$$

where $\alpha \in]0, 0.9]$ is a relaxation coefficient. The algorithm then proceeds to another corrector step until the desired number of iterations or the convergence of the forcing term is reached. The required number of iterations for convergence of either $\boldsymbol{H}$ or p is dependent on a number of factors such as the value of α and the Reynolds number of the flow.

The overall scheme is given as a block diagram in Figure 7.3.

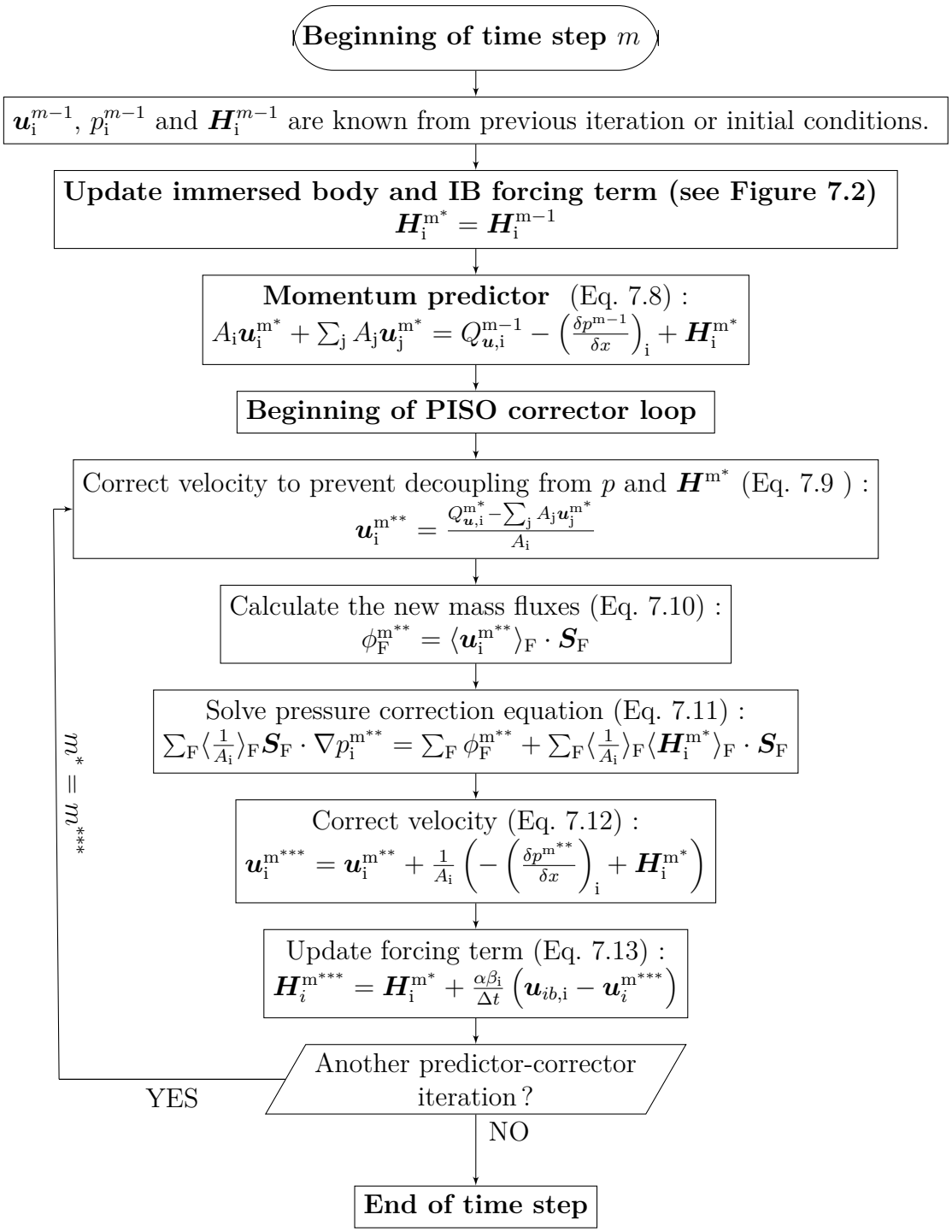

Figure 7.3 Block diagram for the PISO-IB scheme

7.4 Verification of the PISO-IB scheme

The PISO-IB scheme is first verified on three test cases : a Taylor-Couette flow, and the prediction of von Karman vortex streets past static and moving cylinders.

7.4.1 Taylor-Couette Flow

The Taylor-Couette flow, or flow between two-concentric cylinders, is a well-established test case for immersed boundary conditions due to the fact that the geometry is not aligned with the mesh and that such flow possesses an analytical solution. In the present case, we consider two co-axial cylinders of radii $R_i = 0.25$m and $R_o = 0.1$m, with the inner cylinder rotating. The cylinders are both discretized using the immersed boundary method on a square domain $\Omega = [-0.11, 0.11] \times [-0.11, 0.11]$. Assuming that the flow is laminar, the azimuthal velocity profile between the two cylinders is given by [35] :

$$u_\theta(r) = \Omega_i \kappa R_o \frac{\left(\frac{R_o}{r} - \frac{r}{R_o}\right)}{\left(\frac{1}{\kappa} - \kappa\right)} \tag{7.14}$$

where Ω_i is the angular velocity of the inner cylinder and κ the ratio of the radius of the inner cylinder to the outer cylinder ($\kappa = \frac{R_i}{R_o}$). This test case can be used to carry out an order of convergence analysis by monitoring the decrease of the Euclidean norm of the error with the mesh size. The Euclidean norm of the error on the velocity is defined as :

$$\|e_{\boldsymbol{u}}\|_2 = \sqrt{\frac{1}{a_T} \sum_j^N a_j \|\boldsymbol{u}_{\Delta x,j} - \boldsymbol{u}_j\|^2} \tag{7.15}$$

where a_j is the area of fluid cell j, a_T is the total area of the geometry, and $\boldsymbol{u}_{\Delta x,j}$ the numerical velocity. This definition is general enough to be used with both conformal (body-fitted) and Cartesian homogeneous meshes. In the case of a conformal mesh, the characteristic mesh size Δx is calculated as follows :

$$\Delta x = \sqrt{\frac{a_T}{N}} \tag{7.16}$$

The graph in Figure 7.4 shows the variation of the Euclidean norm of the error on $\boldsymbol{u}$ with respect to the mesh size, and the order of convergence for both the PISO-IB method and the standard PISO scheme with a body-fitted mesh. For the PISO-IB method, the simulations were carried out using meshes containing from 20x20 to 200x200 cells. For both approaches,

the order of convergence was calculated using a linear least-square regression.

It can be noted that the PISO-IB scheme degrades the order of convergence of the method from 2 to 1.33. Secondly, the convergence is noisy and a refinement of the mesh does not always lead to a reduction of the error. This is due to the stair-casing approach that is used to discretize the immersed body. However, the envelope of the error decreases as the mesh size decreases. Finally, although the PISO-IB method degrades the order of convergence, the error obtained with it compares well with the error inherent to the standard PISO scheme and the body-fitted mesh.

7.4.2 Von Karman vortex street past static and moving cylinders

The unsteady flow behind a cylinder has been the topic of many experimental and numerical investigations due to the complexity of the hydrodynamics in its unsteady oscillating wake [47]. This flow is an interesting test case because of the intrinsically periodic and complex phenomenological behavior within its vortex street. This is why it has been used by numerous authors such as [30, 33, 67, 122, 123, 152, 269, 325] for the verification of their implementation of an immersed boundary.

This test case can be studied in two different ways. The classical way is to simulate the flow past a static cylinder with a constant upstream fluid velocity, and to measure the perpendicular (lift) and parallel (drag) forces acting on it. This setup is illustrated in Figure 7.5. The second approach is to consider that the cylinder is moving at a constant velocity in a stagnant fluid. While this is nothing but the static problem with a simple change of reference frame, it entails a moving geometry. The setup for the latter case is identical to the static one, except that the length of the domain is increased to $L = 256$m, in order to allow sufficient time for the von Karman instability to develop. Consequently, this moving cylinder problem is more computationally demanding if the same mesh size is used, as the length of the domain is increased significantly. However, it is a pertinent test case because the moving geometry causes, at each time step, the generation of new solid and fluid nodes.

To assess the precision of the proposed immersed boundary method, both the static and moving cylinder cases were considered at $Re = 200$, which is sufficiently high to allow for vortex shedding at a constant frequency h. This frequency can be related to the upstream velocity u_∞ (or the velocity of the cylinder in the moving case) and the diameter of the cylinder (D), via the Strouhal number :

$$St = \frac{hD}{u_\infty} \tag{7.17}$$

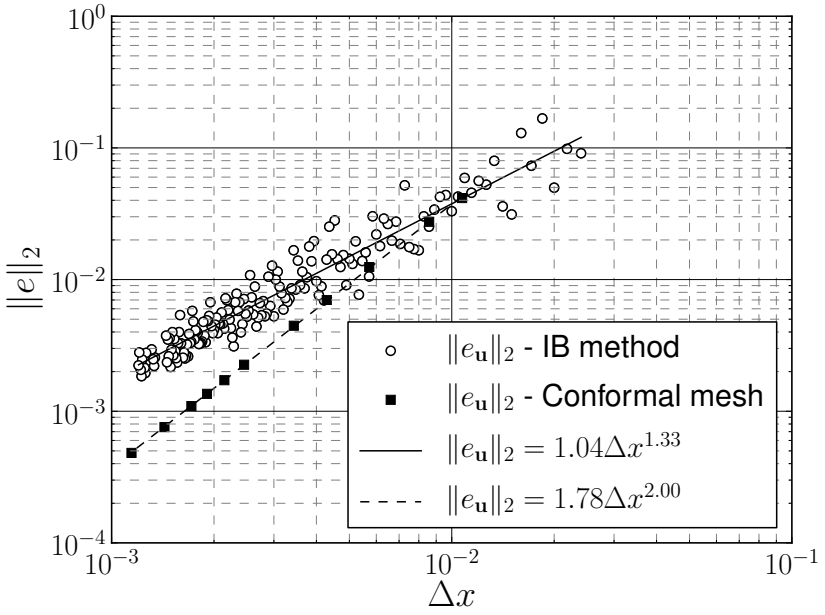

Figure 7.4 Euclidean norm of the error on $\boldsymbol{u}$ as a function of the mesh size, and order of convergence for the Taylor-Couette case.

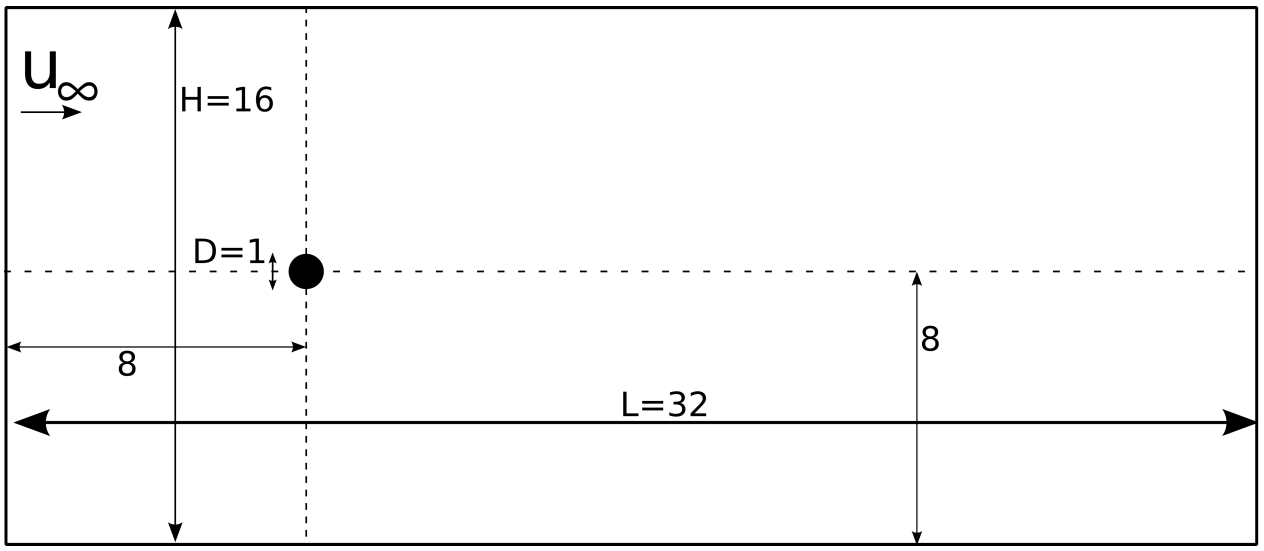

Figure 7.5 Von Karman vortex past a static cylinder : geometrical characteristics (dimensions in meters)

The evaluation of the force $\boldsymbol{F}_C$ acting on the cylinder using our PISO-IB formulation is simple ; it is the volume integral of the constraint acting on the immersed cylinder :

$$\boldsymbol{F}_c = \int_{\Omega_c} \rho \boldsymbol{H} dV \tag{7.18}$$

where Ω_c is the domain occupied by this cylinder and $\boldsymbol{H}$ is the forcing term in (7.7).

Drag (C_D) and lift (C_L) coefficients can be defined using the x and y components of $\boldsymbol{F}_c$:

$$C_D = \frac{2F_{c,x}}{\rho u_\infty^2 D} \tag{7.19}$$

$$C_L = \frac{2F_{c,y}}{\rho u_\infty^2 D} \tag{7.20}$$

The simulations for both the moving and the static cases were carried out on Cartesian structured meshes. The corresponding number of cells and mesh size for both cases are presented in Table 7.1. For the static case, a convergence analysis (not shown here) revealed that the forces on the cylinder did not change significantly ($< 1\%$) if the mesh was further refined. The same mesh size was used in the dynamic case. Simulations were run for 200s to allow for a full development of the von Karman instability. The Strouhal number was calculated by obtaining the frequency of the shedding via a fast Fourier transform (FFT) of the lift coefficient. The time interval chosen for the FFT analysis was a subset of the simulation, within which the shedding frequency was constant, let alone after around 100s (see Figure 7.7).

Case	Δx	N_x	N_y
Static cylinder	0.0228	1400	700
Moving cylinder	0.0228	11225	700

Table 7.1 Mesh size and number of cells used for the static and moving cylinder cases

Figures 7.6, 7.7 and 7.8 present the evolution of the drag and lift coefficients, and the amplitude of the FFT spectrum of the lift coefficient for the static and moving cylinder cases. In both cases, the drag coefficient C_D exhibits a similar behavior, decreasing steadily before the von Karman instability starts developing, and then increasing and leveling off to a slightly oscillating value. Once C_D has stabilized, it can be observed that the lift coefficient C_L oscillates between two values of opposite sign, as expected for this type of flow.

Table 7.2 compares to literature data the C_D, C_L and St values obtained with the PISO-IB method for the moving and the static cases. First, it can be noticed that there are some

discrepancies in the literature values for this problem. Although the reasons for this are hard to identify, it can be partially attributed to differences in the mesh size, and the channel width and length used for those simulations. Indeed, these parameters are not always given explicitely. In the present work, the configuration of Bhalla *et al.* [33] was used so that similar results were expected.

It can be noticed that for C_D and St, both the moving and the static cases are in good agreement with themselves and the literature data. However, the immersed boundary method underpredicts the lift coefficient C_L in the case of the moving cylinder. This is *a priori* surprising, as the adequacy of the C_D and St results indicates that the flow features of the flows are well predicted. This underprediction of the lift coefficient is a direct consequence of the position update of the immersed cylinder at each time step, which results in the occurence of new fluid cells on which to apply the forcing term $\boldsymbol{H}$. It is interesting to note that these cells are also responsible for high-frequency peaks in the FFT spectrum of the lift coefficient in Figure 7.8.

From these results, it can be concluded that the proposed PISO-IB method reproduces with good accuracy the von Karman vortex street and is therefore a valid approach for periodic unsteady flows. This verification step highlights that it was important to solve this problem for both the moving and static frames of reference, as the motion of the immersed cylinder had an impact on the quality of the results.

Study	C_D	C_L	St
PISO-IB - Static cylinder	1.37 ± 0.05	± 0.69	0.200
PISO-IB - Moving cylinder	1.35 ± 0.1	± 0.51	0.200
Braza *et al.* [47]	1.40 ± 0.05	± 0.75	-
Choi *et al.* [67]	1.36 ± 0.048	± 0.64	0.191
Wright *et al.* [325]	1.33 ± 0.04	± 0.68	0.196
Bergmann *et al.* [30]	1.35	-	0.198
Russel and Wang *et al.* [269]	1.29 ± 0.022	± 0.50	0.195
Henderson *et al.* [123]	1.341	-	0.197
He *et al.* [122]	1.3560	-	0.198
Bhalla *et al.* [33]	1.39	-	0.200

Table 7.2 Comparison of the PISO-IB results to literature data, for C_D, C_L and St

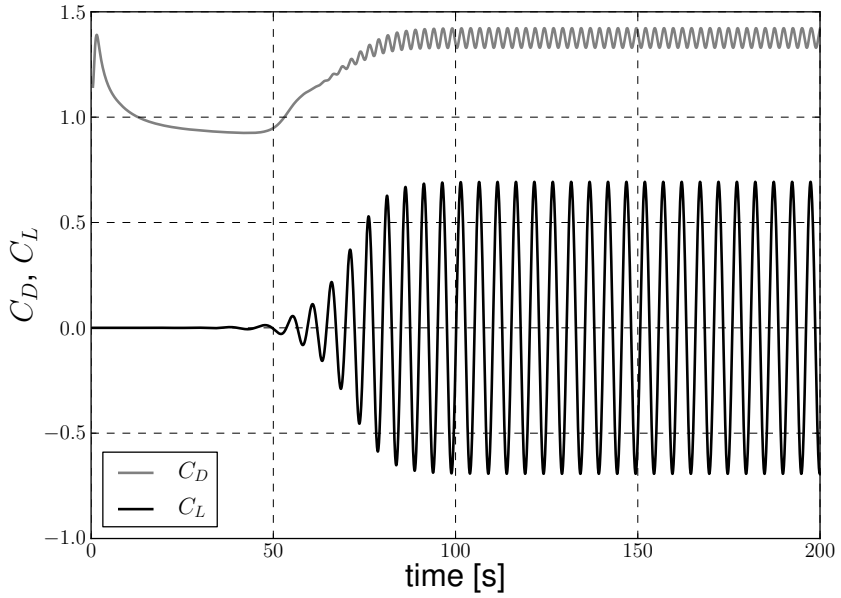

Figure 7.6 Drag and lift coefficients for the flow past a static cylinder.

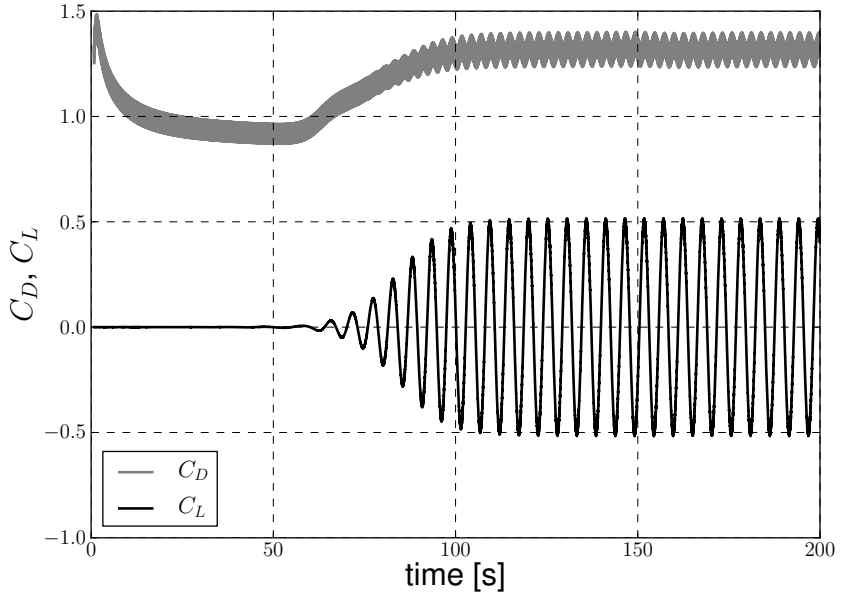

Figure 7.7 Drag and lift coefficients for the flow past a moving cylinder.

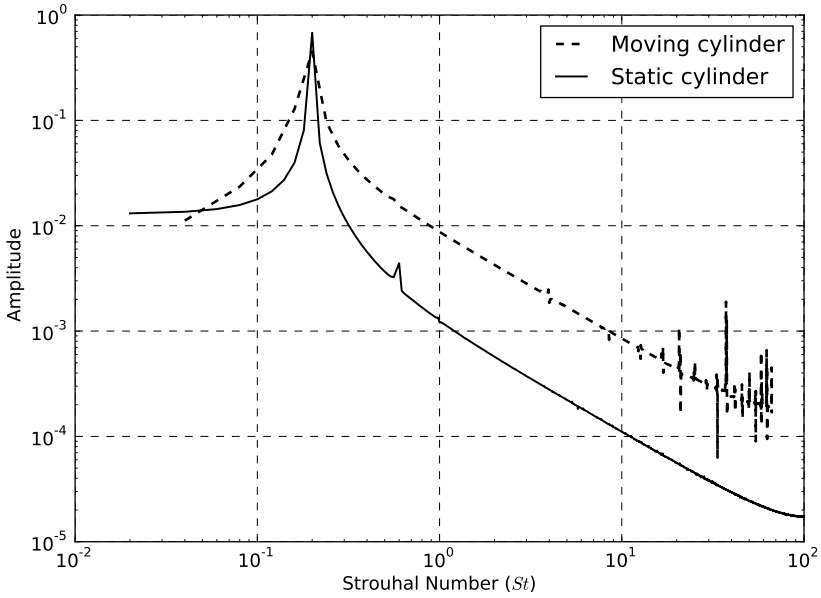

Figure 7.8 Amplitude of the FFT spectrum of the lift coefficient for the static and moving cylinder cases once the instabilities were fully developed.

7.5 Methodology for mixing experiments and simulations

A thorough verification of the proposed PISO-IB scheme was carried out in the previous section. The method is now validated in the context of mixing. This is accomplished by comparing its accuracy to that obtained with classical conformal mesh methods, namely the SRF and the SM techniques, by means of experimental data obtained in our lab.

The experimental set-up consisted of a 0.365 m diameter (T) flat-bottomed, cylindrical and transparent vessel equipped with a T/3 diameter pitched blade turbine (PBT). The tank was equipped with four removable baffles (W=T/10), and the clearance was set at a standard value of C=T/4. The height of the liquid was fixed to that of the tank diameter (H=T). The dimensions of this mixing rig are shown in Figure 7.9 and their values are summarized in Table 7.3. The choice of a PBT is due to its widespread use in the chemical process industry. Furthermore, as the complexity of this impeller is such that it cannot be discretized with a structured mesh, it represents an excellent test case for the PISO-IB method.

The torque on the shaft was first measured for several single-phase experiments using a 0-5 N.m torque-meter provided by Ono Sukki, with a minimum resolution of 0.001 N.m and 0.2 % F.S. accuracy. These torque values were used to establish the dependency of the power number N_P on the Reynolds number Re, a relationship that can also be obtained with simulations.

In the context of mixing, these two dimensionless number are defined as follows [245] :

$$N_p = \frac{P}{\rho N^3 D^5} = \frac{2\pi\Gamma}{\rho N^2 D^5} \tag{7.21}$$

$$Re = \frac{\rho D^2 N}{\mu} \tag{7.22}$$

with N the speed of the impeller, P the power consumption and Γ the torque on the impeller.

The liquid used consisted of Newtonian glucose solutions. Its viscosity was modified by varying the proportion of glucose and water within the tank. Four viscosities were considered : 32, 8.5, 4 and 0.84 Pa.s, at a temperature of 25°C. They were measured using an Anton Paar MCR 502 rheometer with a cone and plate geometry. Silicone oil was used to prevent evaporation in the rheometer. For all samples, the viscosity was found to be independent of the shear rate from 1 to 10 s^{-1}. Note that the viscosity of the solutions in the tank was found to be sensitive to temperature. An Arrhenius function was therefore used to obtain an expression for $\mu(T)$ and a thermocouple was installed in the tank to monitor the temperature of the solutions during the experiments. Using the fit for $\mu(T)$, the right process viscosity could be recovered from the temperature measurements. The underlying hypothesis is that the temperature was assumed to be homogenous throughout the tank during the experiments.

For each experiment, the speed of the impeller was gradually increased with 30 RPM steps from 30 RPM to 800 RPM, which was the maximum velocity that could be reached without air entrapment or surface instabilities. The torque measurements for the impeller without load was removed from the raw values, and the power number resulting from these torque measurements was plotted agaisnt the Reynolds number to produce a power curve. The curves obtained were superimposed to sweep a large range of Re values and confirm the consistency of the torque values. Both baffled and unbaffled configurations of the tank were investigated. It must be noted that some bubbles were observed, mainly in the case of the 32 Pa.s solution, which were entrapped during the filling of the tank. Although larger bubbles

Symbol	**Name**	**Dimension**
T	Tank diameter	0.365m
D	Impeller diameter	T/3
H	Liquid level	T
C	Off-bottom clearance	T/4
W_i	Blade width	D/5
W_b	Baffle width	T/10

Table 7.3 Dimensions of the mixing rig

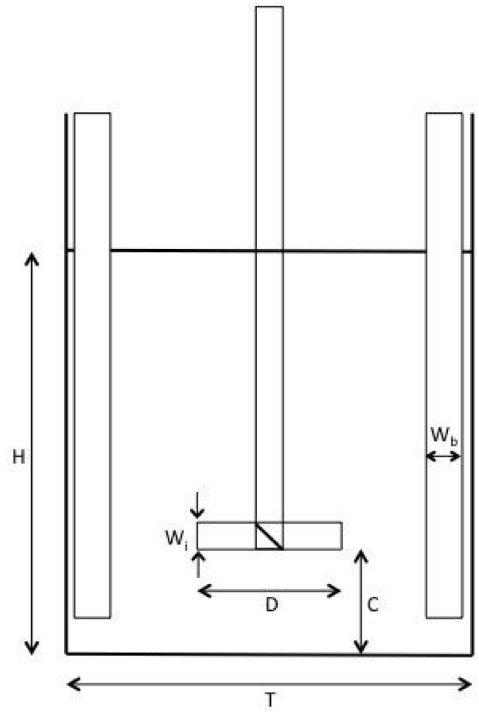

Figure 7.9 Scheme of the mixing rig used for the experiments and the simulations.

were given sufficient time to exit the tank, a small amount of small bubbles could not be removed due to the relatively large viscosity of the solutions.

Other possible sources of uncertainty in the experiments are related to the torque and impeller speed measurements and the vibration of the shaft. Only the error on the torque measurements was taken into account and the other sources of uncertainty were considered negligible.

7.5.1 Simulation set-up

Simulations for the unbaffled tank baffles were carried out using the SM, SRF and PISO-IB methods. For the baffled configuration, only the SM and PISO-IB methods were investigated because the SRF model would not work in such a case. The simulations were carried out at a constant viscosity ($\mu = 0.5$ Pa.s) and at a large range of impeller speeds N = 1 ($Re = 0.75$), 2 (1.5), 5 (3.8), 10 (7.5), 25 (19), 50 (38), 100 (75), 150 (113), 200 (150), 250 (188) and 300 (225) RPM to capture both the laminar and the transitional regimes. More points were taken in the transitional region to achieve greater accuracy in capturing the non-linear character of N_p. For each method, the mesh was refined progressively until no significant differences ($< 1\%$) could be observed in the measured torque.

For the SRF and SM methods, a hexahedral background mesh of the tank was first generated with 33x88x60 (r,θ,z) cells. The impeller was then integrated to it using the snappyHexMesh utility of OpenFOAM which led to a combination of around 95% of hexahedra and 5% of polyhedra. In the case of the SM method, the same resulting mesh was further split into two regions, one encompassing the impeller and the other one complementing the computational domain. In all cases, the meshes were locally refined in the regions of the impeller and the baffles, yielding more than 210k cells.

In the case of the PISO-IB method, only the tank was meshed. The impellers and the baffles, when present, were taken into account using the IB forcing scheme described in Section 7.3. A mesh refinement procedure was applied using the dynamic mesh objects of OpenFOAM in order to refine the mesh in the volume swept by the impeller (Figure 7.10) and in the region of the baffles. Although this procedure increased the number of cells compared to the use of a dynamic mesh refinement technique, it was found to be much more efficient because it allowed for static memory allocation and efficient load balancing between the processors. The background hexahedral mesh consisted of 33x88x60 (r,θ,z) cells and, following the mesh refinement in the swept volume of the impeller and near the baffles, the final mesh contained more than 368k cells.

All simulations were unsteady. A centered scheme and a second-order Crank-Nicholson method were used for the space and time discretizations, respectively. For the SRF and the SM methods, a standard two-loop PISO scheme was used. For each simulation, a Courant-Friedrichs-Lewy stability condition $CFL = 0.5$ was considered. The simulation time was 40s, which was sufficient in all cases to reach convergence for the torque as well as for the flow patterns.

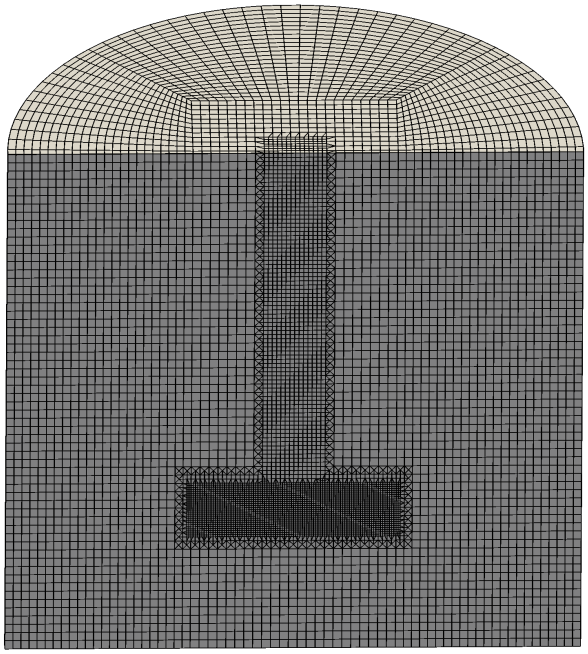

Figure 7.10 Slice of the hexahedral mesh with refinement in the volume swept by the impeller for the PISO-IB method

7.6 Results and discussion

Figure 7.11 present a slice of the axial velocity contours obtained with the SRF, SM and PISO-IB methods at $Re = 250$ for the case without baffles. Apart from minor differences among these contours, there is a good agreement between all three approaches. Comparisons (not shown here) for other planes and other components of the velocity field, for any of the values of Re considered (see Secton 7.5) led to the same conclusion.

The variation of the power number with respect to the Reynolds number is given in Figures 7.12 and 7.13 for unbaffled and baffled tanks, respectively. The simulations results are in good agreement with the experimental data and lie within the experimental error bars. In particular, one can note that the numerical models capture the early transitional regime ($Re \in [10, 100]$) with adequate accuracy. In fact, all three SRF, SM and IB methods give indistinguishable results, except for a slight deviation in the case of the SRF method at the highest Reynolds number investigated ($Re = 225$). This slight gap is most likely due to differences in the resolution of the large-scale unsteady structures that develop in the flow. Furthermore, we recall that in the laminar regime, $Np \propto Re^{-1}$ [245]. Using a linear regression on the data for which $Re \leq 5$, a slope of -1.0 was obtained with a R^2 coefficient equal to 0.9999 for all three methods.

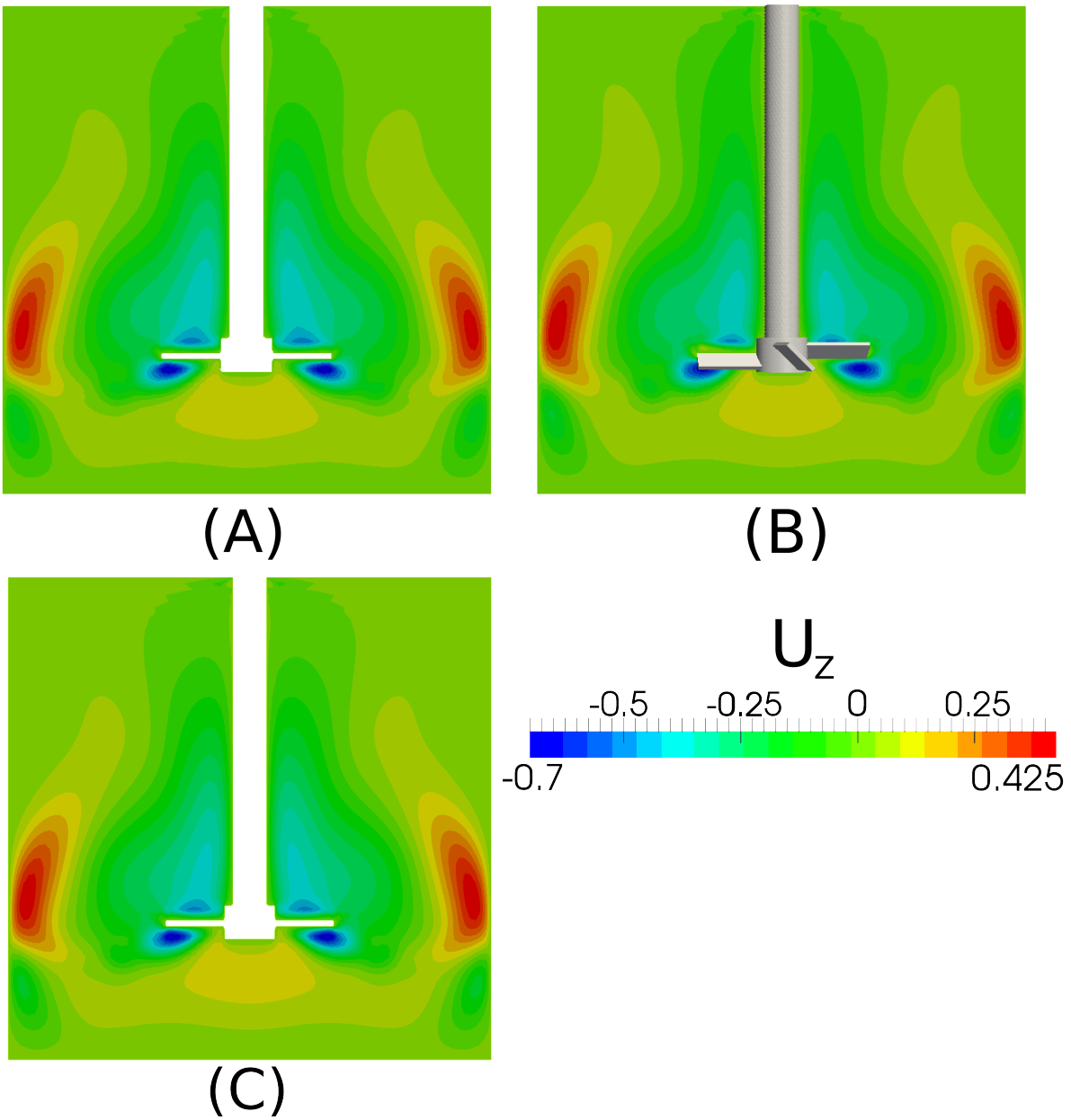

Figure 7.11 Axial velocity contours on a cross-section plane after $30s$ for $Re = 250$: (A) SRF technique, (B) PISO-IB technique and (C) SM technique

The results obtained show that all three methods give qualitative (velocity profiles) and quantitative (power curves) results of comparable quality. The use of local mesh refinement to guarantee accurate results with the PISO-IB scheme add to its computational cost. Taking the SRF technique as a reference and considering meshes that yield the same level of accuracy for the torque, we found that the SM and the IB methods increased their computational cost by a factor of 1.2 and 2, respectively, when 6 Intel Westmere 2.67 Ghz processor cores were used. When 12 cores were used, this factor increased to 1.4 for the SM method, but remained 2 for the PISO-IB method. This indicates that, although the PISO-IB method is *a priori* more expensive, it has better parallel scaling properties than the SM technique.

The PISO-IB method also benefits from other advantages. First, the method does not require a body-fitted mesh, the generation of which can be time-consuming. Next, it can be used for geometries within which the volume swept by multiple impellers overlap. Secondly, contrary to the SM method, it entails the use of a static mesh. For solid-liquid simulations, this enables the fast detection of the mesh cells in which particles reside, a feature essential for an efficient CFD-DEM model such as the one developed by our group [40].

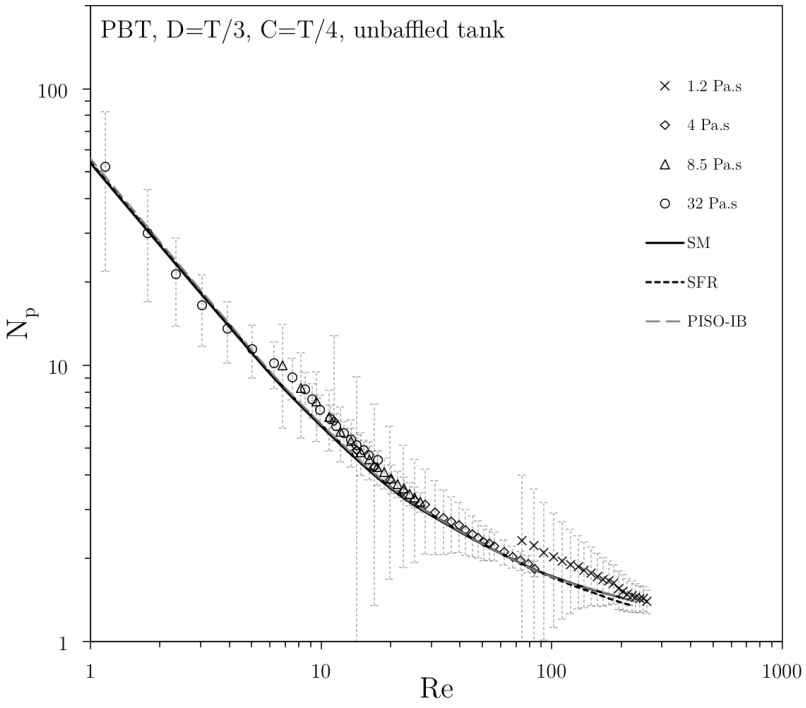

Figure 7.12 Power curve for the PBT in an unbaffled tank.

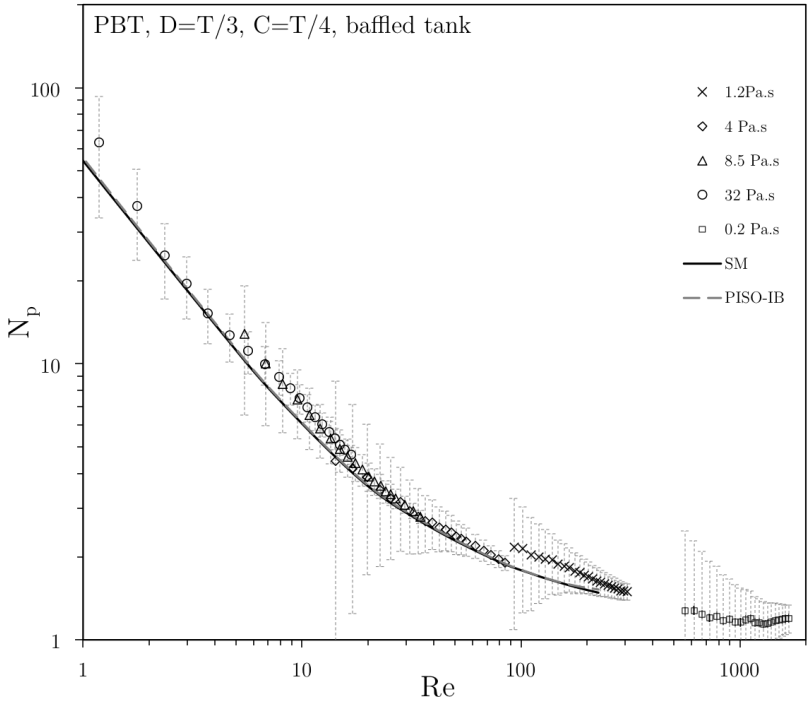

Figure 7.13 Power curve for the PBT in a baffled tank. Note the superposition of the PISO-IB and SM results.

7.7 Conclusion

The modeling of fluid flow in stirred tanks may still be challenging due to the impeller geometry and kinematics, the presence of baffles and configurations in which the volume swept by the mutiple impellers overlap. In the latter case, the use of an immersed boundary method is essential.

In this work, we introduced a novel semi-implicit immersed boundary (PISO-IB) method based on the addition of a forcing term to a PISO finite volume solver that is applicable to unstructured meshes. With this method, both static and dynamic mesh refinement strategies are tractable. Furthermore, this method works with a static mesh, which in the context of solid-liquid mixing enables the fast detection of particles in the cells of this mesh, an essential characteristic of CFD-DEM and the likes.

This method was implemented in the open-source CFDEM framework, which is based on Open∇FOAM for the liquid phase and LIGGGHTS for modeling the flow of particles when they are present. Our implementation was first verified by performing an order of convergence analysis using the Taylor-Couette test case and by comparing to literature data numerical results obtained for the flow around static and moving cylinders. Although a degradation of the order of convergence of the method was observed, it was found that the method yields very good velocity profiles and can be used to accurately measure the forces acting on a moving body. The method was then validated in the context of single-phase mixing, more precisely in the case of a pitched blade turbine in baffled and unbaffled tanks. The torque measurements obtained via the PISO-IB method are in good agreement with those predicted by the SRF and the SM techniques as well as with experimental data, despite the challenge posed by the non-alignment of the moving pitched blade turbine with the mesh cells.

In future work, our immersed boundary method will be used in combination with the CFD-DEM model of the CFDEM framework to study solid-liquid mixing in baffled stirred tanks, including tanks provided with more complex configurations such as planetary mixers.

7.8 Acknowledgements

The financial support from the Natural Sciences and Engineering Research Council of Canada (NSERC) is gratefully acknowledged. In particular, Bruno Blais is thankful for the NSERC Vanier Scholarship. The authors would like to thank Gilles Lenfant for measuring the viscosity of the glucose solutions.

Computations were made on supercomputer Briaree from University of Montreal, managed

by Calcul Québec and Compute Canada. The operation of this supercomputer is funded by the Canada Foundation for Innovation (CFI), the Ministère de l'Économie, de l'Innovation et des Exportations du Québec (MEIE), RMGA and the Fonds de recherche du Québec - Nature et technologies (FRQ-NT).

CHAPITRE 8 Article 4 : Development of an unresolved CFD-DEM model for the flow of viscous suspensions and its application to solid-liquid mixing

Bruno Blais, Manon Lassaigne, Christoph Goniva, Louis Fradette, François Bertrand
Published in Journal of Computational Physics volume 318, pages 201-221, 2016

Abstract : Although viscous solid-liquid mixing plays a key role in industry, the vast majority of the literature on the mixing of suspensions is centered around the turbulent regime of operation. However, the laminar and transitional regimes pose considerable challenges. In particular, it is important to know the minimum impeller speed (N_{js}) that guarantees the suspension of all particles. In addition, local information on the flow patterns is necessary to evaluate the quality of mixing and identify the presence of dead zones. Multiphase computational fluid dynamics (CFD) is a powerful tool that can be used to gain insight into local and macroscopic properties of mixing processes. Among the variety of numerical models available in the literature, which are reviewed in this work, unresolved CFD-DEM, which combines CFD for the fluid phase with the discrete element method (DEM) for the solid particles, is an interesting approach due to its accurate prediction of the granular dynamics and its capability to simulate large amounts of particles. In this work, the unresolved CFD-DEM method is extended to viscous solid-liquid flows. Different solid-liquid momentum coupling strategies, along with their stability criteria, are investigated and their accuracies are compared. Furthermore, it is shown that an additional sub-grid viscosity model is necessary to ensure the correct rheology of the suspensions. The proposed model is used to study solid-liquid mixing in a stirred tank equipped with a pitched blade turbine. It is validated qualitatively by comparing the particle distribution against experimental observations, and quantitatively by compairing the fraction of suspended solids with results obtained via the pressure gauge technique.

8.1 Introduction and literature review

Solid-liquid mixing plays a key role in the production, transport and homogenization operations inherent to the pharmaceutical, mining, chemical, food processing and cosmetics industries. For these industries, poor mixing can be responsible for large operating costs due to poor yield, over-consumption of energy and product fouling [245]. Solid-liquid mixing has been the subject of considerable work, both experimental (*e.g.* [18, 208, 223, 225, 339]) and numerical (*e.g.* [80, 129, 150, 219, 297, 299, 319]), but the quasi-totality of it has been centered

on the turbulent regime of operation and dilute particle concentrations.

Although this is partially justified by the more common occurrence of turbulent flows in the mixing of suspensions, viscous solid-liquid mixing operations in the transitional and laminar regimes occur frequently in the previously cited industries. These regimes of operation face numerous challenges. For instance, it remains unclear how the rheology of a suspension, the particle-particle interactions and the kinematics of the rotating impeller affect the distribution and dispersion of the solid particles and the flow patterns within the tank.

According to the Handbook of Industrial Mixing [245] :

> *The main objectives of solid-liquid mixing are to create and maintain slurry and/or to promote and enhance the rate of mass transfer between the solid and liquid phases.*

The accomplishment of these objectives is well described by the state (or level) of solid-liquid suspensions : on-bottom, off-bottom, and uniform suspension [245], all of which are illustrated in Figure 8.1.

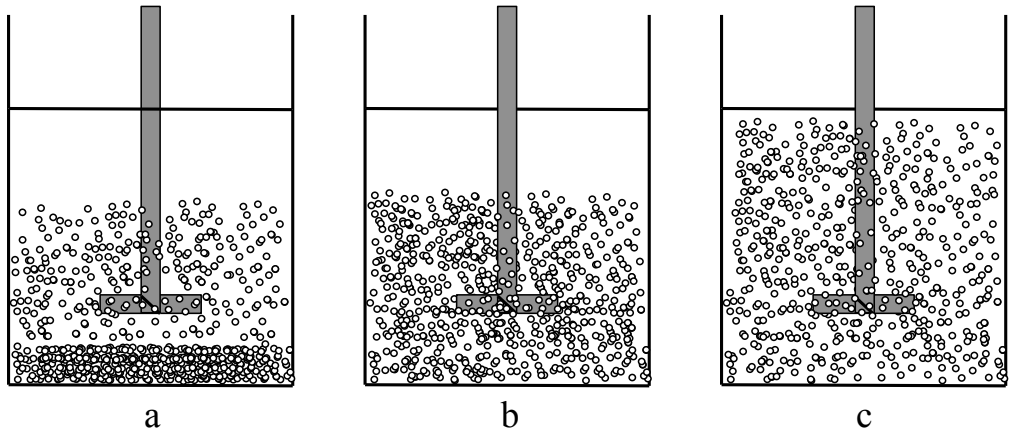

Figure 8.1 Three levels of suspension : (left) on-bottom suspension, (middle) off-bottom suspension, and (right) uniform suspension. Adapted from [173].

In his 1956 study [157], Kneule identified the state of off-bottom suspension as the optimal operating point. Beyond this level, mass transfer is mainly enhanced by the increased velocity of the fluid and not by an increase of the contact area between the solid and liquid phases. His work was followed by the work of Zwietering [339] who obtained a correlation for the just-suspended speed (N_{js}), which is defined as the minimum impeller speed at which no solid particles rest motionless on the vessel bottom for more than 1 or 2 seconds. The Zwietering correlation is highly limited in the laminar and transitional regimes of operation associated

with viscous fluids [130, 132, 173], and for high solid loadings [14]. Other authors have introduced correlations to calculate N_{js}, notably Nienow *et al.* [225], Narayanan *et al.* [223], Baldi *et al.* [18], Mersmann *et al.* [208], but they all share the same limitations to some extent. We refer the reader to Kasat and Pandit [149], and Jafari *et al.* [139] for a review of these correlations.

It must be noted that the experimental results at the basis of the Zwietering correlation, and the majority of the other aforementioned correlations, have been obtained via visual observation. Many alternatives for either direct or indirect measurement of N_{js} exist, as reviewed by Kasat and Pandit [149] and by Tamburini *et al.* [297]. Among these, a robust way to measure the suspension of particles is the so-called pressure gauge technique introduced by Brucato *et al.* [53] and by Micale *et al.* [210]. This technique was used recently by Lassaigne *et al.* [173] to investigate viscous solid-liquid mixing. Their results indicate that more fundamental work is required to better understand the mechanisms behind the suspension of particles in the laminar and transitional regime, as well as the role of the particle and fluid physical properties.

In light of this review, it is obvious that more work, whether numerical or experimental, is needed to shed light on viscous solid-liquid mixing in order to predict not only the just-suspended speed, but also the local flow characteristics prevailing in the tank. Simulation of such systems may then be used to follow the evolution of both local and global quantities throughout the entire tank. Thus, the development of a robust and efficient computational model would help to a gain deeper insight into the many open issues related to solid-liquid mixing. Numerous models have been designed for solid-liquid flows and each possesses its range of applicability, its strengths and weaknesses. Those applicable to the study of solid-liquid mixing are now reviewed.

8.1.1 Computational models for solid-liquid flows

Three categories of models are of interest for the study of solid-liquid mixing. They can be distinguished by the scales considered for the representation of each phase (fluid-solid) using the nomenclature proposed by Tsuji [308] : meso-meso, meso-micro, micro-micro.

For micro-micro models, the fluid flow is resolved at a scale smaller than the particle size, and the motion of each particle is tracked. The particle-particle collisions are handled via a method such as the Discrete Element Method (DEM) using either a soft- (DEMs) or hard-collision (DEMh) model. We refer the reader to the papers by Zhu *et al.* [337] or Bertrand *et al.* [31] for a review of the DEM. Such models are referred to as resolved CFD-DEM. In this type of model, the coupling between the two phases results from the application of no-slip

boundary conditions on the surface of the particles. A good example of its application to solid-liquid mixing is given by Derksen [83] where it was used for the study of a small-scale mixing tank containing 3000 particles in the turbulent regime.

Since it resolves the detail of the flow at the particle level, this type of approach is accurate and requires a relatively small number of parameters. However, it suffers from severe limitations in terms of the number of particles it can handle (generally less than 10000) and the scale of the geometries. This is due to the fact that the particle diameter over mesh spacing ratio ($\frac{d_p}{\Delta x}$) must be kept larger than a certain value (such as $\frac{d_p}{\Delta x} > 6$ for the LBM, as noted by ten Cate *et al.* [302], or $\frac{d_p}{\Delta x} > 8$ as found by Hager *et al.* [119]), resulting in untractable numbers of grid cells for the simulation of large industrially relevant geometries. Furthermore, lubrication forces should be added to micro-micro models when particles undergo collisions since the mesh is then unable to resolve the full squeezing flow that results from such collisions. The stability and accuracy of such models remain uncertain for dense solid-liquid flows where particles undergo multiple enduring contacts such as at the start-up of stirred tank mixing operation.

At the other end of the spectrum lies the meso-meso approaches such as the two-fluid model in which both the solid and the fluid phases are considered as interpenetrating continua. This type of model is described in detail in the reference books by Gidaspow [105], Crowe *et al.* [70], Prosperetti and Tryggvason [254] and Ishii and Hibiki [135]. In the context of mixing, it has been used to study solid-liquid systems in the turbulent regime at various concentrations in a wide variety of situations [129, 148, 149, 183, 211, 212, 218, 219, 228, 293, 294, 296–299]. A complete overview of the results obtained in these papers would require a review article on its own. Since these results pertain to the turbulent regime and are therefore unrelated to the regime of the present study, we prefer to focus on the limitations and strengths of the meso-meso models.

Because the two-fluid model describes granular matter as a continuum, the computational cost is greatly reduced compared to approaches where each particle is tracked individually. However, the underlying formulation has inherent limitations. First, reproducing the maximal packing fraction of solids requires the addition of either a granular pressure term or an ad-hoc method, to distribute adequately the particles, such as the excess solid volume correction (ESVC) algorithm proposed by Lettieri *et al.* [180]. Secondly, two-fluid models do not allow for scale separation (so-called Burnett or super-Burnett behavior [109]) and predict an instant relaxation of the granular phase, which is invalid in regions of low particle concentrations (dilute or fast granular flows). This has been shown to be highly problematic in situations such as impinging gas-solid flows [65]. This issue can be remedied by using more complex

quadrature methods of moment approaches (QMOM) or population balance methods [196], which preserve higher moments of the particle momentum and allow for scale separation, albeit at a higher computational cost.

In between these two classes of approaches lies the meso-micro family of models such as the unresolved CFD-DEM model [336, 337]. In unresolved CFD-DEM, the fluid is solved at a coarser scale than that of the particle using the volume-averaged Navier-Stokes equations (VANS), and the motion of the particles and their collisions are described using DEM (soft or hard). The coupling between the solid and fluid phases is carried out by using explicit expressions for hydrodynamic forces such as drag, lift, etc., the relevance of which depends on the local characteristics of the flow [337].

This method gives a coarser description of the flow field due to the use of volume-averaged equations, yet it can model the granular dynamics with a high degree of fidelity. Consequently, it is valid for all granular regimes and can reproduce characteristics of granular media such as the maximal packing fraction naturally. Since it can handle much larger amounts of particles due to the use of coarser CFD meshes (up to 10^7 [247], or even 10^8 [58]), this model appears as a highly promising candidate for the investigation of mixing in stirred tanks. However, to the best of our knowledge, this method has only been used in the context of gas-solid or solid-liquid flows where the suspending liquid is non-viscous (usually water). Derksen previously proposed and used an unresolved CFD-DEMh for the study of turbulent mixing of dilute suspensions of particles ($< 4vol\%$) where he analyzed the contribution of the lift and drag hydrodynamic forces to the mixing dynamics and found that the contribution of drag was the dominant one [80]. An improved version of his CFD-DEMh method was recently used to investigate the mixing of dilute bidisperse suspensions by Ayranci *et al.* [15]. However, since this model is based on a hard-sphere DEM, it cannot handle high solids contents or simulate the start-up of a stirred tank. This is not the case for soft-sphere DEM models.

We note that other approaches lie in between the meso-meso and micro-micro descriptions. That is the case for instance of the multiphase particle-in-cell (MP-PIC) [282]. However, they do not reproduce the dynamics of the particles with the same degree of accuracy as unresolved CFD-DEM models.

8.1.2 Present work

In this work, we present an extension of the unresolved soft-sphere CFD-DEM model for simulating the flow of viscous suspensions. This model is integrated within the CFDEM [61, 112] framework, which combines Open∇FOAM for the CFD part [233] and LIGGGHTS [155, 182] for the DEM part. Firstly, the model is presented in detail along with implicit

and explicit momentum coupling strategies. The stability criteria inherent to the model are discussed in the context of a viscous suspending fluid. The advantages and drawbacks of both momentum coupling strategies are also studied via the fluidization of a bed of particles in a viscous fluid. Then, the rheology of the unresolved CFD-DEM model is investigated. Next, the proposed CFD-DEM model is applied to the study of viscous solid-liquid mixing in a stirred tank equipped with a pitched blade turbine (PBT). It is validated against the experimental results of Lassaigne *et al.* [173] by comparing the particle flow patterns and the fraction of suspended particles. Finally, conclusions are drawn on the potential of the model for further investigations.

8.2 Model Formulation

The CFD-DEM approach consists in using a continuous description for the fluid coarser than the particle scale via the volume-averaged Navier-Stokes equations while using the discrete element method to model the granular phase accurately. The two models operate independently, but they are coupled at regular intervals, usually with multiple DEM time steps for a single CFD time step. In this section, the equations for each component of the CFD-DEM model used in the present work are described.

8.2.1 Governing equations for the solid-phase (DEM)

The discrete element method (DEM) bears a high degree of resemblance to molecular dynamics (MD). Both methods are based on the integration of Newton's second law to obtain the evolution in time of the (translational and rotational) velocity and position of the particles.We only give here a brief presentation of the governing equations for the DEM solved using LIGGGHTS, adopting the notation of Zhou *et al.* [336]. For a thorough description, we refer the reader to Bertrand *et al.* [31], Zhu *et al.* [337, 338] and to the LIGGGHTS user manual [182].r

Using Newton's second law of motion, the governing equations for the translational ($\boldsymbol{v}_i$) and rotational ($\boldsymbol{\omega}_i$) motion of a particle i can be written as :

$$m_i \frac{d\boldsymbol{v}_i}{dt} = \sum_j (\boldsymbol{f}_{c,ij}) + \sum_k \boldsymbol{f}_{lr,ik} + \boldsymbol{f}_{pf,i} + \boldsymbol{f}_{g,i} \tag{8.1}$$

$$I_i \frac{d\boldsymbol{\omega}_i}{dt} = \sum_j (\boldsymbol{M}_{t,ij} + \boldsymbol{M}_{r,ij}) \tag{8.2}$$

where m_i is the mass of particle i, I_i its moment of inertia, $\boldsymbol{f}_{c,ij}$ the contact force between particles i and j, $\boldsymbol{f}_{lr,ik}$ the non-contact (long-range) forces between particles i and k, $\boldsymbol{f}_{pf,i}$

the particle-fluid interaction forces, $\boldsymbol{f}_{g,i}$ a body force ($e.g$ gravity), and $\boldsymbol{M}_{t,ij}$ and $\boldsymbol{M}_{r,ij}$ the tangential and rolling friction moments acting on particles i and j. In the present work, non-contact forces, such as the electrostatic or van Der Waals forces, are not taken into account since they are orders of magnitude smaller than the hydrodynamic or contact forces for the particles considered. The expression for the particle-fluid interaction force depends on which interactions are taken into account (drag, lift, etc.). This is discussed in Section 8.2.3.

At the core of the DEM lies the contact model for particle-particle interactions. The contact force $\boldsymbol{f}_{c,ij}$ between two particles, which contains both elastic and dissipative forces, is split into two components : normal ($\boldsymbol{f}_{cn,ij}$) and tangential ($\boldsymbol{f}_{ct,ij}$) [337]. This results in the following expressions :

$$\boldsymbol{f}_{c,ij} = \boldsymbol{f}_{cn,ij} + \boldsymbol{f}_{ct,ij} \tag{8.3}$$

$$\boldsymbol{f}_{c,ij} = -k_{n,ij}\boldsymbol{\delta}_{n,ij} - \gamma_{n,ij}\dot{\boldsymbol{\delta}}_{n,ij} - k_{t,ij}\boldsymbol{\delta}_{t,ij} - \gamma_{t,ij}\dot{\boldsymbol{\delta}}_{t,ij} \tag{8.4}$$

where $k_{n,ij}$ and $k_{t,ij}$ are the normal and tangential stiffness coefficients, $\gamma_{n,ij}$ and $\gamma_{t,ij}$ the normal and tangential damping coefficients, $\boldsymbol{\delta}_{n,ij}$ and $\boldsymbol{\delta}_{t,ij}$ the normal and tangential particle overlaps, and $\dot{\boldsymbol{\delta}}_{n,ij}$ and $\dot{\boldsymbol{\delta}}_{t,ij}$ their corresponding derivatives with respect to time.

In the present work, the Tsuji model [309] based on the Hertz theory for the normal forces [125, 143] is combined with the Mindlin model for the tangential forces [214, 215]. These models link the stiffness and the damping coefficients to the Young's modulus of the material (Y), its Poisson ratio (ν) and coefficient of restitution (e_r), using the equations in Table 8.1. Furthermore, the tangential overlap $\boldsymbol{\delta}_{t,ij}$ is limited by Coulomb's law to ensure that $\boldsymbol{f}_{ct,ij} \leq -\mu_{s,ij} \left|\boldsymbol{f}_{cn,ij}\right| \frac{\boldsymbol{\delta}_{t,ij}}{|\boldsymbol{\delta}_{t,ij}|}$.

Determination of the model coefficient

It is readily seen that the DEM model contains numerous parameters, the values of which are not always thoroughly given in the literature. Although their impact is well-established in the context of pure DEM wherein the suspending fluid is neglected, this is not the case for strongly coupled gas-solid and, even more so, solid-liquid flows. For example, it has not yet been established if the coefficient of restitution that is used in solid-liquid flow simulations should be measured using dry particles or if the apparent coefficient of restitution, which decreases significantly as the Stokes number ($St = \frac{\rho_p d_p^2 u_0}{18\mu l_0}$, with u_0 and l_0 characteristic velocity and length respectively) decreases [111], should be used. This is critical, since the latter is flow dependent. In the present work, the parameters taken for each simulation come from Di Renzo and Di Maio [87], Di Renzo *et al.* [85] and Shao *et al.* [276], which are good examples of work where glass particles were suspended in a liquid. We emphasize that more

Parameter	Equation
Normal stiffness	$k_{n,ij} = \frac{4}{3} Y^*_{ij} \sqrt{R^*_{ij} \delta_{n,ij}}$
Tangential stiffness	$k_{t,ij} = 8 G^*_{ij} \sqrt{R^*_{ij} \delta_{n,ij}}$
Normal damping	$\gamma_{n,ij} = -2\sqrt{\frac{5}{6}} \frac{\ln(e_r)}{\sqrt{\ln^2(e_r)+\pi^2}} \sqrt{\frac{2}{3} k_{n,ij} m^*_{ij}}$
Tangential damping	$\gamma_{t,ij} = -2\sqrt{\frac{5}{6}} \frac{\ln(e_r)}{\sqrt{\ln^2(e_r)+\pi^2}} \sqrt{k_{t,ij} m^*_{ij}}$
Coulomb limit for tangential force	$\boldsymbol{f}_{ct,ij} \leq -\mu_{s,ij} \lvert \boldsymbol{f}_{cn,ij} \rvert \frac{\boldsymbol{\delta}_{t,ij}}{\lvert \boldsymbol{\delta}_{t,ij} \rvert}$
Torque by tangential forces	$\boldsymbol{M}_{t,ij} = \boldsymbol{r}_i \times (\boldsymbol{f}_{ct,ij})$
Rolling friction torque	$\boldsymbol{M}_{r,ij} = -\mu_{r,ij} \lvert \boldsymbol{f}_{cn,ij} \rvert \frac{\boldsymbol{\omega}_{ij}}{\lvert \boldsymbol{\omega}_{ij} \rvert} R^*_{ij}$
Equivalent mass	$\frac{1}{m^*_{ij}} = \frac{1}{m_i} + \frac{1}{m_j}$
Equivalent radius	$\frac{1}{R^*_{ij}} = \frac{1}{R_i} + \frac{1}{R_j}$
Equivalent Young's modulus	$\frac{1}{Y^*_{ij}} = \frac{\left(1-\nu_i^2\right)}{Y_i} + \frac{\left(1-\nu_j^2\right)}{Y_j}$
Equivalent shear modulus	$\frac{1}{G^*_{ij}} = \frac{2(2+\nu_i)(1-\nu_i)}{Y_i} + \frac{2(2+\nu_j)(1-\nu_j)}{Y_j}$
Sliding friction coefficient	$\mu_{s,ij}$
Rolling friction coefficient	$\mu_{r,ij}$
Distance to contact point for particle i	$\boldsymbol{r}_i$
Radius of particle i	R_i

Table 8.1 Equations for the DEM model

work would be necessary to shed light on the influence of these parameters on solid-liquid flow behavior.

8.2.2 Governing equations for the liquid-phase flow (CFD)

In this work, form A (or set II in [336]) of the incompressible volume-averaged Navier-Stokes (VANS) equations is considered for the liquid phase [105]. For a thorough description of the origin of this formulation and its comparison with model B (set I in [336]) and simplified model B (set III in [336]), we refer the reader to Zhou *et al.* [336]. Form A of the VANS equations, which we will simply refer to as the VANS equations in the remainder of this work, is given by :

$$\frac{\partial \epsilon_f}{\partial t} + \nabla \cdot (\epsilon_f \boldsymbol{u}) = 0 \tag{8.5}$$

$$\frac{\partial \left(\rho_f \epsilon_f \boldsymbol{u}\right)}{\partial t} + \nabla \cdot (\rho_f \epsilon_f \boldsymbol{u} \otimes \boldsymbol{u}) = -\epsilon_f \nabla p + \nabla \cdot \boldsymbol{\tau} - \boldsymbol{F}_{pf} \tag{8.6}$$

where ϵ_f is the void fraction, ρ_f the density of the fluid, p the pressure, $\boldsymbol{u}$ the velocity and $\boldsymbol{g}$ the gravity. The viscous stress tensor $\boldsymbol{\tau}$ is defined as :

$$\boldsymbol{\tau} = \epsilon_f \mu \left((\nabla \boldsymbol{u}) + (\nabla \boldsymbol{u})^T - \frac{2}{3} (\nabla \cdot \boldsymbol{u}) \boldsymbol{\delta}_k \right) \tag{8.7}$$

where μ is the dynamic viscosity and $\boldsymbol{\delta}_k$ is the identity tensor.

The momentum exchange term from the particles to the fluid, $\boldsymbol{F}_{pf}$, is defined as :

$$\boldsymbol{F}_{pf} = \frac{1}{\Delta V} \sum_{i}^{n_p} \boldsymbol{f}_{pf,i} - \boldsymbol{f}_{\nabla p,i} - \boldsymbol{f}_{\nabla \cdot \boldsymbol{\tau},i} - \boldsymbol{f}_{Ar,i} \tag{8.8}$$

where

$$\boldsymbol{f}_{pf,i} = \boldsymbol{f}_{d,i} + \boldsymbol{f}_{\nabla p,i} + \boldsymbol{f}_{\nabla \cdot \boldsymbol{\tau},i} + \boldsymbol{f}_{Ar,i} \boldsymbol{f}_{\mathrm{vm},i} + \boldsymbol{f}_{B,i} + \boldsymbol{f}_{\mathrm{Saff},i} + \boldsymbol{f}_{\mathrm{Mag},i} \tag{8.9}$$

and where n_p is the number of particles, ΔV the volume of the cell in which particle i lies and $\boldsymbol{f}_{pf,i}$ is the sum of all fluid-solid interaction forces involving particle i : drag ($\boldsymbol{f}_{d,i}$), pressure gradient ($\boldsymbol{f}_{\nabla p,i}$), viscous stress (or shear stress) ($\boldsymbol{f}_{\nabla \cdot \boldsymbol{\tau},i}$), Archimedes force ($\boldsymbol{f}_{Ar,i}$), virtual mass ($\boldsymbol{f}_{\mathrm{vm},i}$), Basset force ($\boldsymbol{f}_{B,i}$), Saffman lift ($\boldsymbol{f}_{\mathrm{Saff},i}$) and Magnus lift ($\boldsymbol{f}_{\mathrm{Mag},i}$). We note that the pressure gradient and viscous forces are applied to each particle on an individual basis, but that they manifest themselves directly in the VANS equations, contrary to the other forces which are regrouped within the source term $\boldsymbol{F}_{pf}$. This is the key distinction between models A and B [336] because it changes the pressure equation within the predictor-corrector scheme. This has consequences on the possible loss of hyperbolicity of model A, a phenomenon discussed in the books by Gidaspow [105] and Prosperetti and Tryggvason [254].

In the present work, Equations (8.5) and (9.6) are solved using a pressure implicit with splitting of operators (PISO) scheme [136] that was recently extended to the VANS equations. This scheme is described in detail and verified using the method of manufactured solutions by Blais and Bertrand [37]. Using an order of convergence analysis, we showed that the scheme was second-order accurate in space and time for both pressure and velocity. A second-order implicit backward time integration scheme and centered gradient and interpolation schemes are also used here, thus preserving the second-order accuracy for pressure and velocity.

8.2.3 Governing equations for the solid-liquid coupling strategy

In CFD-DEM, an expression for each force entering into the solid-liquid coupling strategy must be given. Only the drag, pressure and viscous (shear) forces are taken into account in this work. The expressions for these forces are given in Table 8.2.

The pressure and viscous (shear) forces are needed because, with the unresolved approach, the particles are not discretized explicitely in the CFD part. More precisely, as demonstrated by Crowe *et al.* [70], expressions for these forces can be obtained by integrating the pressure gradient (and the divergence of the shear stress) over the volume occupied by each of these particles. These forces should not be confused with the viscous and pressure components of

the drag force, both of which are taken into account by the drag model.

In this work, the Rong drag model [266] is used because of its accuracy over a large range of Reynolds numbers and void fractions. This drag term was derived via DNS simulations carried out with the Lattice Boltzmann method over a large range of solid packings obtained using the DEM. The minimum void fraction investigated by the authors was $\epsilon_f = 0.37$, which means that the Rong drag model is accurate from this situation to very dilute cases ($\epsilon_f \to 1$).

Lift forces, virtual mass and Basset forces are not considered due to the very small relative velocity between the viscous fluid and the particles, and the very low particle relaxation time ($\tau_p = \frac{d_p^2 \rho_p}{18\mu}$).

Force	Equation
Pressure gradient [337]	$-\frac{\pi}{6} d_{p,i}^3 \nabla p$
Viscous force [337]	$-\frac{\pi}{6} d_{p,i}^3 \nabla \cdot \boldsymbol{\tau}$
Drag - Rong model [266]	$\frac{1}{8} C_D d_{p,i}^2 \rho_f \left\|\boldsymbol{u} - \boldsymbol{v_i}\right\| (\boldsymbol{u} - \boldsymbol{v}_i) \epsilon_f^{2-\beta\left(\epsilon_f, Re_p\right)}$
	with $C_D = \left(0.63 + \frac{4.8}{\sqrt{Re_p}}\right)^2$
	$\beta\left(\epsilon_f, Re_p\right) = 2.65\left(\epsilon_f + 1\right) - \left(5.3 - 3.5\epsilon_f\right) \epsilon_f^2 e^{-\frac{\left(1.5 - \log {Re_p}^2\right)}{2}}$
	and $Re_p = \frac{\rho_f d_{p,i} \left\|\boldsymbol{u} - \boldsymbol{v_i}\right\|}{\mu}$

Table 8.2 Expressions for the forces taken into account in the CFD-DEM model, for particle i moving at velocity $\boldsymbol{v}_i$ in the solid-liquid coupling strategy on a particle i

Calculation of the void fraction and momentum exchange term for the liquid phase flow (CFD)

In this work, two-way coupling is carried out by projecting the volume of the particles and the solid-fluid forces onto the CFD mesh in order to calculate the void fraction ϵ_f and the momentum exchange term $\boldsymbol{F}_{pf}$. Although details on this step are often overlooked in the literature, it must be carried out with care to ensure mass conservation and minimize the occurence of discontinuities for ϵ_f and $\boldsymbol{F}_{pf}$. The naive approach consisting in locating the particles using the position of their centroid has been reported to lead to significant discontinuities and potential instabilities when grid size $\Delta x < 3d_p$ [199, 251].

In the present work, we use the so-called divided approach of the CFDEM framework. It subdivides the projected particle into 27 regions of equal volumes, each of which is represented by a point that is located on the mesh in order to calculate the void fraction and the momentum exchange term. This approach has the significant advantage of being mass conservative while

smoothing the void fraction and the momentum exchange term. This is illustrated in Figure 8.2 on a simplified 2D representation with 5 points (or regions) per particle.

Momentum exchange strategies

Two strategies may be distinguished to apply the momentum exchange force ($\boldsymbol{F}_{pf}$). The simplest one is to add this force directly to the momentum equation as an explicit source term, as in (9.6). As we will show later, this strategy comes with its own stability criterion. A secondary strategy is to apply this force while taking into account the relative velocity between the solid and fluid phases, leading to :

$$\frac{\partial \left(\rho_f \epsilon_f \boldsymbol{u}\right)}{\partial t} + \nabla \cdot \left(\rho_f \epsilon_f \boldsymbol{u} \otimes \boldsymbol{u}\right) = -\epsilon_f \nabla p + \nabla \cdot \boldsymbol{\tau} + \rho \epsilon_f \boldsymbol{g} + K_{pf} \left(\boldsymbol{u_p} - \boldsymbol{u}\right) \tag{8.10}$$

where $\boldsymbol{u}_p$ is the particle average velocity within the corresponding grid cell and K_{pf} is a scalar used to scale the magnitude of the momentum exchange force :

$$K_{pf} = \frac{|\boldsymbol{F}_{pf}|}{|\boldsymbol{u}_p - \boldsymbol{u}|} \tag{8.11}$$

The underlying assumption of this approach is that this force is co-linear with the relative velocity ($\boldsymbol{u_p} - \boldsymbol{u}$), which makes it suitable for implicit coupling strategies.

Smoothing of the momentum exchange force and of the void fraction

Even if the divided approach that projects the particles onto the CFD mesh implicitly smooths the void fraction and the momentum exchange force to a relatively large extent, additional smoothing may be necessary to stabilize the particle-fluid coupling. Various strategies have been reported by Pirker *et al.* [251], such as isotropic diffusive smoothing or the particle cloud and the "darning socks" models. It was shown by this group that both isotropic diffusive smoothing and the "darning socks" model could be efficient for discrete element simulations. In the present work, isotropic diffusive smoothing is applied on the void fraction (ϵ_f) and the momentum exchange force using a parabolic filter. For a given variable $\boldsymbol{\xi}$, this entails solving :

$$\frac{\partial \boldsymbol{\xi}}{\partial t} = \nabla^2 \left(\frac{\lambda^2}{\Delta t_{CFD}} \boldsymbol{\xi} \right) \tag{8.12}$$

where λ is a characteristic smoothing length and Δt_{CFD} the time step used to solve CFD equations (8.5) and (9.6). This smoothing method is chosen because it is conservative, easy to implement and can be easily controlled via the smoothing length λ. In this work, a smoothing length of $\lambda = 2d_p$ was found to be sufficient to improve the stability of all simulations.

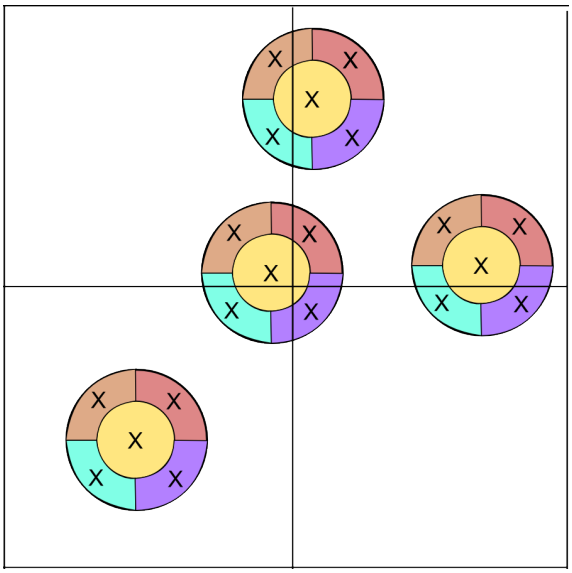

Figure 8.2 2D simplified illustration of the divided approach for the projection of particles onto a CFD grid.

8.2.4 Rotating geometries

Rotating geometries inherent to the stirred tanks investigated in this work are handled using the semi-implicit immersed boundary method (PISO-IB) previously introduced by Blais *et al.* [41]. We refer the reader to this latter paper for a description of the underlying scheme, its verification and validation in the context of single-phase mixing. This scheme was seamlessly integrated within the CFDEM framework.

8.3 Stability Analysis of the Model

Four numerical stability criteria are inherent to the two-way coupling unresolved CFD-DEM model proposed in this work.

For the CFD part, if an implicit scheme is used for the viscous component of the VANS equations, the Courant-Friedrich-Lewy (CFL) condition leads to [97] :

$$CFL = \Delta t_{CFD} \max\left(\frac{|\boldsymbol{u}|}{\Delta x}\right) < 1 \tag{8.13}$$

The definition of a stability criterion for the DEM is more arduous due to the possibility of multiple collisions and the non-linearity of the inherent Hertz collision model. In the present

work, the time step for a stable DEM scheme is taken as a fraction of the Rayleigh time step :

$$\Delta t_{DEM} = \alpha \Delta t_{Ra} = \alpha \frac{\Pi}{2} d_p \sqrt{\frac{\rho_p}{G}} \left(\frac{1}{0.1631\nu + 0.8766} \right) \tag{8.14}$$

where α is a constant lower than unity and $G = \frac{Y}{2(2+\nu)(1-\nu)}$ is the shear modulus (with Y the Young's modulus and ν the Poisson ratio). Different choices have been made for α, such as 0.5 [66], 0.4 [127, 276], 0.1 [256, 331]. Here, a conservative value of $\alpha \leq 0.15$ is taken to ensure stability. We note that alternative stability criteria have been proposed based on the characteristic frequency of the spring [216] or a unit cell approach using the eigenvalues of the stiffness and mass matrices related to multiple collisions [301].

The stability of the fluid-solid coupling step, that is of the impact of the fluid on the DEM equations describing the motion of each individual particle, is linked to the particle relaxation time. By neglecting all solid-fluid forces in Eq. (8.9) except for drag ($\boldsymbol{f}_{d,i}$) and by assuming an explicit scheme such as the Euler scheme, one can then derive the following stability criterion by analyzing the amplification factor of the discrete equations :

$$\Delta t_{fp} \leq \frac{4}{3} \frac{d_p \rho_p}{C_d \rho_f} \frac{1}{|\boldsymbol{u} - \boldsymbol{v}_i|} \tag{8.15}$$

For a single isolated particle in the limit of Stokes flow ($C_D = \frac{24}{Re_p}$), the stability criterion reduces to the particle relaxation time : $\Delta t_c < \frac{d_p^2 \rho_p}{18\mu}$. Taking into account the hindering effect of the surrounding particles via the term $\epsilon_f^{2-\beta(\epsilon_f, Re_p)}$ in the drag model (Table 8.2) can greatly decrease the value of Δt_{fp} by a factor up to 50.

In the case of an explicit solid-fluid coupling, the action of the drag force on the fluid is also subject to a stability constraint that can be calculated using the relative inertia of the two phases within a finite volume cell, which leads to :

$$\Delta t_{pf} \leq \frac{4}{3} \frac{\epsilon_f}{(1-\epsilon_f)} \frac{d_p}{C_d} \frac{1}{|\boldsymbol{u} - \boldsymbol{v}_i|} \tag{8.16}$$

This criterion becomes limiting in cases where $\frac{\epsilon_f}{1-\epsilon_f} << 1$ such as in a dense particle bed. However, this issue can be resolved by resorting to an implicit momentum coupling. In practice, the coupling time step (Δt_c) for the two-way coupling must satisfy :

$$\Delta t_c \leq \min\left(\Delta t_{pf}, \Delta t_{fp}\right) \tag{8.17}$$

In this work, Δt_{CFD} is taken equal to Δt_c and satisfies both (8.13) and (8.17).

8.4 Comparison of the Coupling Strategies

In this section, we compare the stability and precision of the implicit and explicit coupling strategies for the case of a viscous liquid. This is achieved via a simple test-case, which consists in the fluidization of a bed of particles.

8.4.1 Presentation of the fluidization test case

This case consists of a cylinder, at the bottom of which a bed of particles is initially at rest. At the bottom of this cylinder, a constant velocity inlet U is applied to the fluid whereas a constant pressure boundary condition is imposed at the top. Slip boundary conditions are applied on the walls of the cylinder, ensuring that the pressure drop is only due to the apparent weight of the particles. For these particles, the bottom of the cylinder is closed by a solid wall.

The pressure drop in the cylinder can be calculated directly by substracting the average pressure at the top from the average pressure at the bottom. Figure 8.3 shows the geometry and its initial configuration with the particles at rest. The parameters used for the simulation are presented in Table 8.3. They were extracted from the work Di Renzo and Di Maio [87], Di Renzo *et al.* [85] and Shao *et al.* [276] for glass beads suspended in a liquid, although the Young's modulus of the particles was decreased in order to relax the Rayleigh time step (Eq. (8.14)).

Particle diameter (d_p)	1 mm
Particle density (ρ_p)	2000 kg.m^{-3}
Young's modulus (Y)	5 MPa
Coefficient of restitution (e_r)	0.9
Poisson ratio (ν)	0.25
Coefficient of friction (μ_f)	0.3
Rolling friction (μ_r)	0.1
DEM time step (Δt_{DEM})	1×10^{-6}s
Liquid density (ρ_f)	1000 kg.m^{-3}
Liquid viscosity (μ)	0.1 Pa.s
CFD time step(Δt_{CFD})	5×10^{-6}s
Coupling time-step (Δt_c)	5×10^{-6}s
Diameter of the cylinder (D)	0.028 m
Length of the cylinder (L)	0.055 m
Mesh ($n_r \times n_\theta \times n_z$)	$8 \times 32 \times 24$

Table 8.3 Parameters and geometry for the fluidization test case

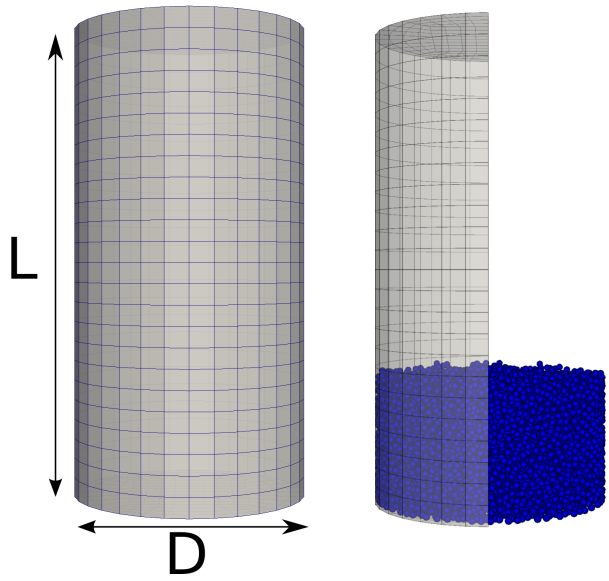

Figure 8.3 Geometry, mesh and initial configuration of the particles for the fluidization test case

By changing the inlet velocity, the stability of the scheme and its accuracy in reproducing both the minimum fluidization velocity and the pressure drop across the bed can be assessed. The pressure drop Δp through a bed can be evaluated by the Ergun equation [133] :

$$\frac{\Delta p}{L_b} = 150\frac{(1-\epsilon_f)^2}{\epsilon_f^3}\frac{\mu U}{d_p^2} + 1.75\frac{1-\epsilon_f}{\epsilon_f^3}\frac{\rho u^2}{d_p} \tag{8.18}$$

where L_b is the length of the bed of particles. From this equation and under the assumption that $Re_p < 1$, which is true in the present case, the minimal fluidization velocity is given by :

$$U_{mf} = \frac{d_p^2\,(\rho_p - \rho_f)\,g\epsilon_f^3}{150\mu\,(1-\epsilon_f)} \tag{8.19}$$

8.4.2 Influence of the coupling strategy

The graph in Figure 8.4 presents the evolution of the pressure drop within the bed as a function of time for a constant inlet velocity of $200\mu\text{m.s}^{-1}$, for both the implicit and explicit momentum exchange coupling schemes. One can readily see that the pressure drop for the implicit scheme suffers from very large oscillations whereas these oscillations are significantly dampened when using an explicit coupling formulation. Note that no oscillations have been observed by Kloss *et al.* [156] and Goniva and Pirker [113] in the case where the fluid is a gas. For the present configuration, the minimal fluidization velocity is very small ($100\mu\text{m.s}^{-1}$), so that the error inherent to the averaging of the particle velocities, which vary slightly due

to particle-particle contacts and interpolation, affect the average particle velocity $\boldsymbol{u}_p$. The magnitude of this error in the particle velocity field is comparable to that of the minimal fluidization velocity. Therefore, owing to the very short relaxation time of these particles, of the order of $10^{-4}s$, the stiff solid-liquid coupling leads to sharp pressure oscillations in the case of the implicit coupling. The velocity fluctuations also result in the violation of the assumption that the drag force is co-linear with the relative velocity, giving rise to a snowball effect on the fluctuations. For the explicit coupling, these issues are non-existent since the particle-fluid force is applied directly without any averaging. However, we do note the presence of slight oscillations, which occur when small clusters of particles undergo significant collisions. The graph of Figure 8.5 shows that with the explicit momentum coupling, the right pressure drop and minimal fluidization velocity are recovered accurately.

8.5 Rheology of the CFD-DEM model

It is well known that at low Reynolds number, the viscosity of a rigid-sphere suspension depends on the volume fraction of the particles [246]. Einstein demonstrated that the relative viscosity(η_r) of a dilute suspension ($\epsilon_p < 5\%$, [209]) in Stokes flow is given by [209] :

$$\eta_r = \frac{\eta_s}{\mu} = 1 + 2.5\epsilon_p \tag{8.20}$$

where η_s is the apparent viscosity of the suspension, $\epsilon_p = 1 - \epsilon_f$ is the volume fraction of particles.

Einstein reached this result by superimposing the alteration of the velocity field ($\boldsymbol{u}_1$) due to the presence of a single sphere in an infinite medium on top of a constant shear-flow and by integrating the stress due to $\boldsymbol{u}_1$. The seminal paper by Batchelor and Green [24] considered the case of binary interactions to analyze more concentrated suspensions ($\epsilon_p < 10\%$ or $< 15\%$, [209]) and obtained a second-order expression ϵ_s.

For more concentrated suspensions, models have been designed to express the effect of the volume fraction of particles on the viscosity, such as the Kreiger-Dougherty model [160] :

$$\eta_r = \left(1 - \frac{\epsilon_p}{\epsilon_{p,m}}\right)^{-[\eta]\epsilon_{p,m}} \tag{8.21}$$

where $\epsilon_{p,m}$ is the maximal packing fraction (0.64 for mono-disperse spheres) and $[\eta]$ the intrinsic viscosity (2.5 for spheres).

Although Einstein's results and, to a lesser extent those by Batchelor [24], are not applicable as such for non-dilute concentrations in solid-liquid mixing operations, they indicate that the increase of the viscosity of a suspension is not due to solid-fluid forces such as drag *per se*,

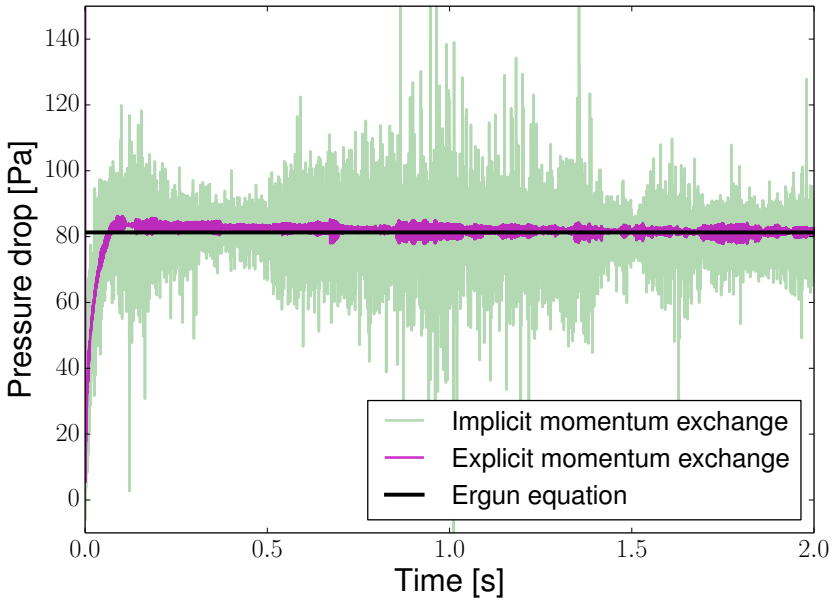

Figure 8.4 Pressure drop through the cylinder as a function of time for both momentum exchange coupling schemes at a constant inlet velocity of 200μm.s^{-1}.

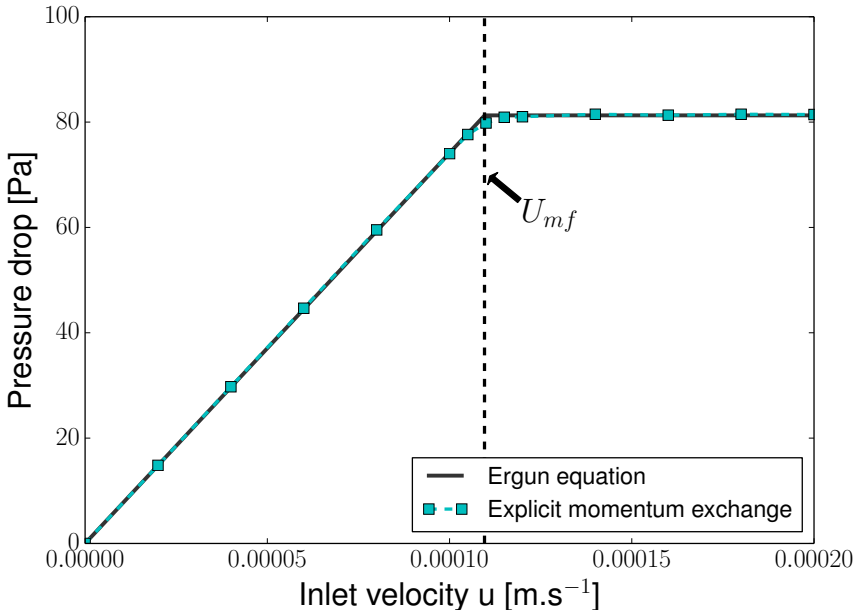

Figure 8.5 Pressure drop through the cylinder as a function of the inlet velocity.

but is caused by an increased viscous dissipation in the fluid due to flow disturbances caused by the presence of the particles. This phenomenon happens at the particle and sub-particle scales, and cannot, in theory, be reproduced accurately by an unresolved simulation model. To confirm this, simulations of the shear flow between two parallel plates were carried out with our model at various solids fractions ranging from 0 vol% to 35 vol% using the parameters in Table 8.4. These parameters were mainly taken from the work of Di Renzo and Di Maio [87], Di Renzo *et al.* [85] and Shao *et al.* [276] for glass beads suspended in a liquid. However, the Young's modulus of the particles was decreased in order to allow for a larger Rayleigh time step (Δt_{DEM}, Eq. (8.14)). Also note that the density of the particles was matched to that of the liquid. By measuring the viscous dissipation between the plates and the force acting on the moving plate, the relative viscosity of the fluid could be evaluated. To our knowledge, such a test has not been carried out previously in the literature.

Particle diameter (d_p)	400 μm
Particle density (ρ_p)	1000 kg.m^{-3}
Young's modulus (Y)	10 MPa
Coefficient of restitution (e_r)	0.9
Poisson ratio (ν)	0.25
Coefficient of friction (μ_f)	0.3
Rolling friction (μ_r)	0.1
DEM time step (Δt_{DEM})	1×10^{-6}s
Liquid density (ρ_f)	1000 kg.m^{-3}
Liquid viscosity (μ)	0.05 Pa.s
CFD time step (Δt_{CFD})	1×10^{-5}s
Coupling time-step (Δt_c)	1×10^{-5}s
Plate width and depth (L_x,L_y)	0.025 m
Plate gap (L_z)	0.01 m
Plate velocity (V_x)	0.01 m.s^{-1}
Mesh ($n_x \times n_y \times n_z$)	$20 \times 20 \times 10$

Table 8.4 Simulation parameters for the flow between two parallel plates

The graph in Figure 8.6 compares the evolution of the relative viscosity η_r predicted by the unresolved CFD-DEM model to that from the Krieger-Dougherty model. It can readily be seen that the CFD-DEM model does not reproduce the rheology of the suspension in such a case. This is coherent with our previous analysis as the increase in viscosity due to hydrodynamics at the particle and sub-particle scales is not resolved by our unresolved model. The literature does not propose a solution to this problem. In the present work, this is corrected by the introduction of a viscosity model in which the viscosity depends on the local solids fraction ($\epsilon_p = 1 - \epsilon_f$). This can be seen as a viscous analog to the sub-grid closure used

in large eddy simulations, as in the Smagorinsky model [281], to resolve sub-grid stresses. This was implemented by modeling the viscosity in the VANS equations as a space- and time-dependent function of the volume fraction of particles in the same fashion as a classical turbulent viscosity model or a rheological model (where μ would be a function of the shear rate). In the present work, the Krieger-Dougherty model (8.21) is used to obtain the apparent viscosity as a function of the solids concentration. Unsurprisingly, the graph in Figure 8.6 shows that with the introduction of this viscosity model, the right rheology is recovered. This demonstrates that there is no interaction between the solid-liquid coupling forces and the viscosity model, since the apparent viscosity measured in the simulations matches that of the analytical model.

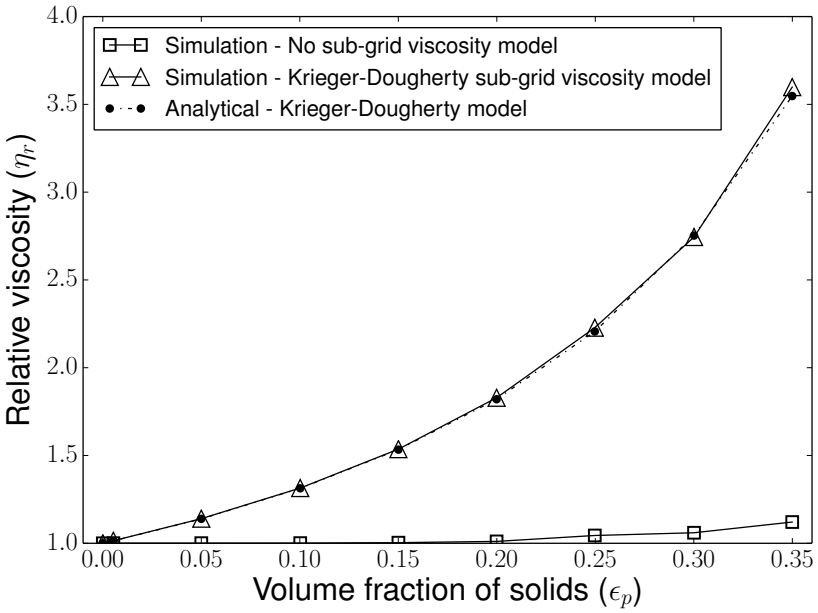

Figure 8.6 Evolution of the relative viscosity as a function of the volume fraction of solid particles for the unresolved CFD-DEM model, with and without the sub-grid viscosity model, and comparison to the results obtained with the Krieger-Dougherty model.

8.6 Study of solid-liquid mixing

8.6.1 Methodology

In this section, the unresolved CFD-DEM model is validated for the case of solid-liquid mixing in the laminar and transitional regimes of operation. We first present the methodology for the experiments and the simulations. Then, we compare the simulation results to experimental

data in terms of the flow patterns and fractions of suspended solids. Finally, the simulation results are used to expand our analysis of the solid-liquid mixing in the agitated vessel of this work.

Experimental set-up

The solid-liquid mixing experiments were carried out using glass beads of 3mm diameter at 10 wt% loading in a glucose solution of 1Pa.s viscosity. The properties of both the fluid and the particles are given in Table 8.5. The set-up, illustrated in Figure 8.7, consisted in a 0.365m (T) diameter, cylindrical, flat bottomed and unbaffled tank, stirred by a D=T/3 pitched blade turbine that was set at a C=T/4 off-bottom clearance. The dimensions of the experimental rig are summarized in Table 8.6.

It has been reported that the use of a flat-bottomed tank creates recirculation loops that restrict particle suspension at the wall-to-bottom junction [277]. However, a flat bottom is more suitable for the pressure gauge technique measurement, which is described below. The system was studied without baffles as it has been reported that baffles are not recommended for solid suspensions in viscous fluids because they can cause dead zones and lead to the accumulation of particles [51, 299].

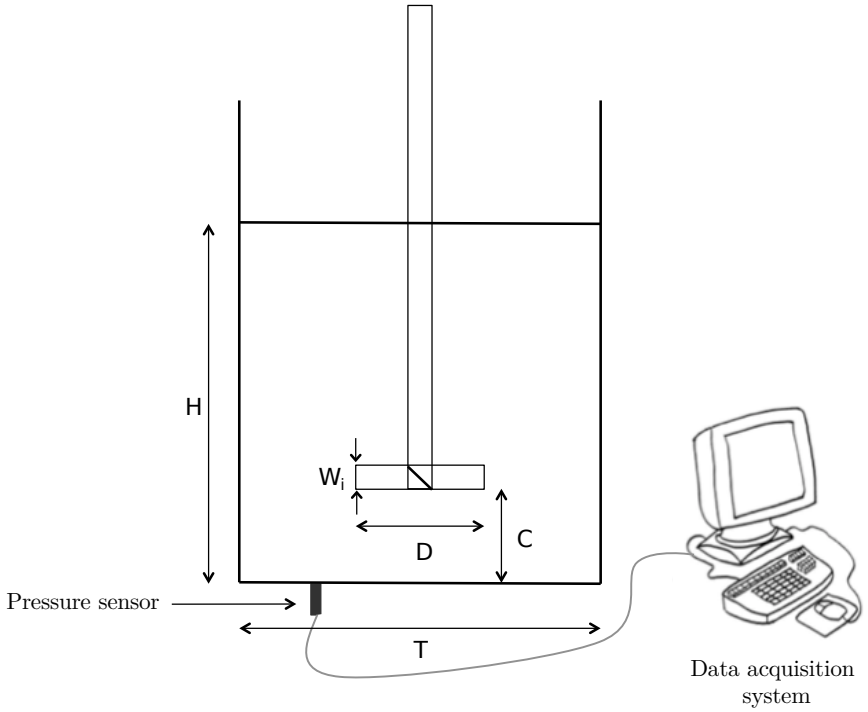

Figure 8.7 Experimental set-up

Symbol	Name	Value
ρ_f	Density of the fluid	1390 kg.m^{-3}
μ	Dynamic viscosity of the fluid	1 Pa.s
ρ_p	Density of the solid particles	2500 kg.m^{-3}
d_p	Range of diameters for the solid particles	2.66-3.5 mm
$d_{p,32}$	Sauter diameter	3.02 mm
x_s	Mass fraction of solid particles	10 %
ϵ_p	Volume fraction of solid particles	5.8 %

Table 8.5 Physical properties of the fluid and the particles

Symbol	Name	Dimension
T	Tank diameter	0.365m
D	Impeller diameter	$\frac{T}{3}$
H	Liquid level	T
C	Off-bottom clearance	$\frac{T}{4}$
W_i	Blade width	$\frac{D}{5}$

Table 8.6 Dimensions of the mixing rig

The fraction of suspended solids was obtained experimentally using the pressure gauge technique [53, 173, 210, 296]. The pressure at the bottom of the tank was measured by a pressure sensor supplied by Freescale (MPX5010DP), with a precision of 5%, connected to a small 4 mm hole at the bottom of the tank and protected from particle clogging by a fine mesh, as depicted in Figure 8.8.

During the experiments, the weight of the particles, which are initially held by the tank bottom and lateral walls, is transferred to the fluid as these particles get suspended. This increases the apparent density of the fluid, resulting in an increase of the hydrostatic pressure that is measured by the pressure sensor. This pressure increase is in fact proportional to the fraction of suspended solids. However the dynamic pressure that results from the fluid motion is also felt by the pressure sensor, and thus needs to be removed. Micale *et al.* [210] estimated that beyond N_{js}, only the dynamic component of the total pressure influences the pressure data measurements. Consequently, by fitting a quadratic polynomial to the pressure for large value of N, one can obtain a fit for the dynamic pressure and remove it from the raw pressure results. This produces a corrected curve with a plateau, the onset of which reveals the values of N_{js} and corresponding pressure increase ΔP_{js}. This procedure, with the raw pressure and corrected measurements, is illustrated in Figure 8.9. The suspended fraction of solids, $X_{suspended}$, can be obtained by plotting the ratio of pressure increase $\frac{\Delta P}{\Delta P_{js}}$ as a function of impeller speed (as in Figure 8.9). Generally, it can be described by a Weibull function, as

noted by Micale *et al.* [210]. In the present work, the experiments were repeated three times to evaluate the uncertainty on the suspended fractions of solids measured by the pressure gauge technique.

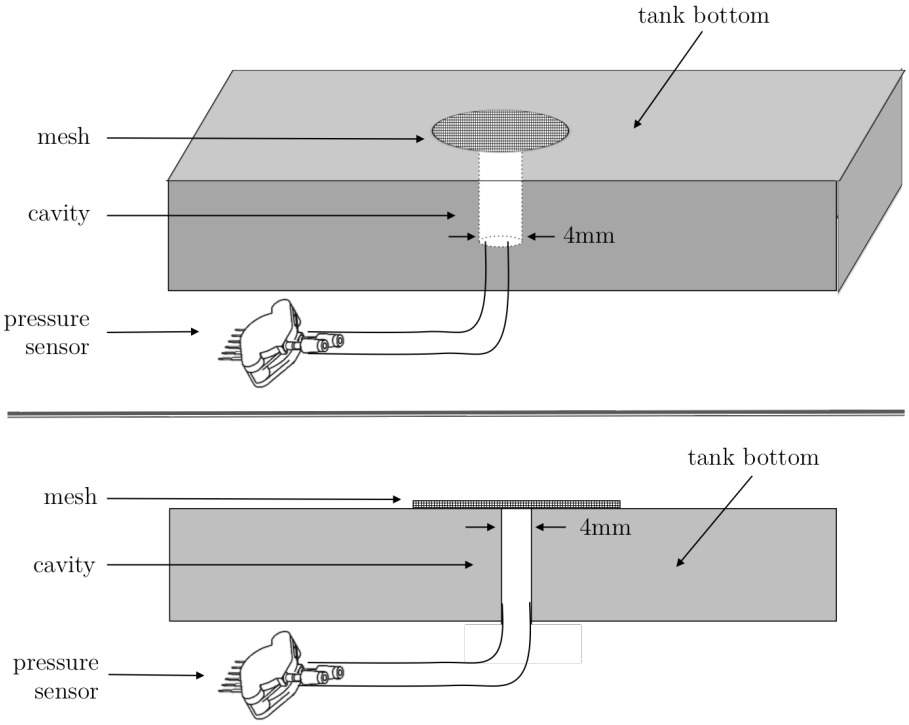

Figure 8.8 Lateral and oblique views of the pressure sensor at the bottom of the tank

Simulation set-up

Simulations were carried out using the unresolved CFD-DEM model presented in Section 8.2 on the mixing system of dimensions and properties given in Tables 8.6 and 8.5, respectively. Additional model parameters used in the simulations are presented in Table 8.7. These values were chosen based on the work Di Renzo and Di Maio [87], Di Renzo *et al.* [85] and Shao *et al.* [276] for glass beads suspended in a liquid. The same mechanical properties were given to the tank, the impeller and the particles. To reproduce the size distribution of the particles measured experimentally, 10 different diameters were used. A total of 148 700 particles were required to obtain the desired mass fraction of 10 %.

Starting with a fully settled bed of particles, obtained via a pure DEM simulation using LIGGGHTS, CFD-DEM simulations were carried out with explicit momentum coupling. The background hexahedral mesh consisted of 33x88x60 (r,θ,z) cells, which was refined in

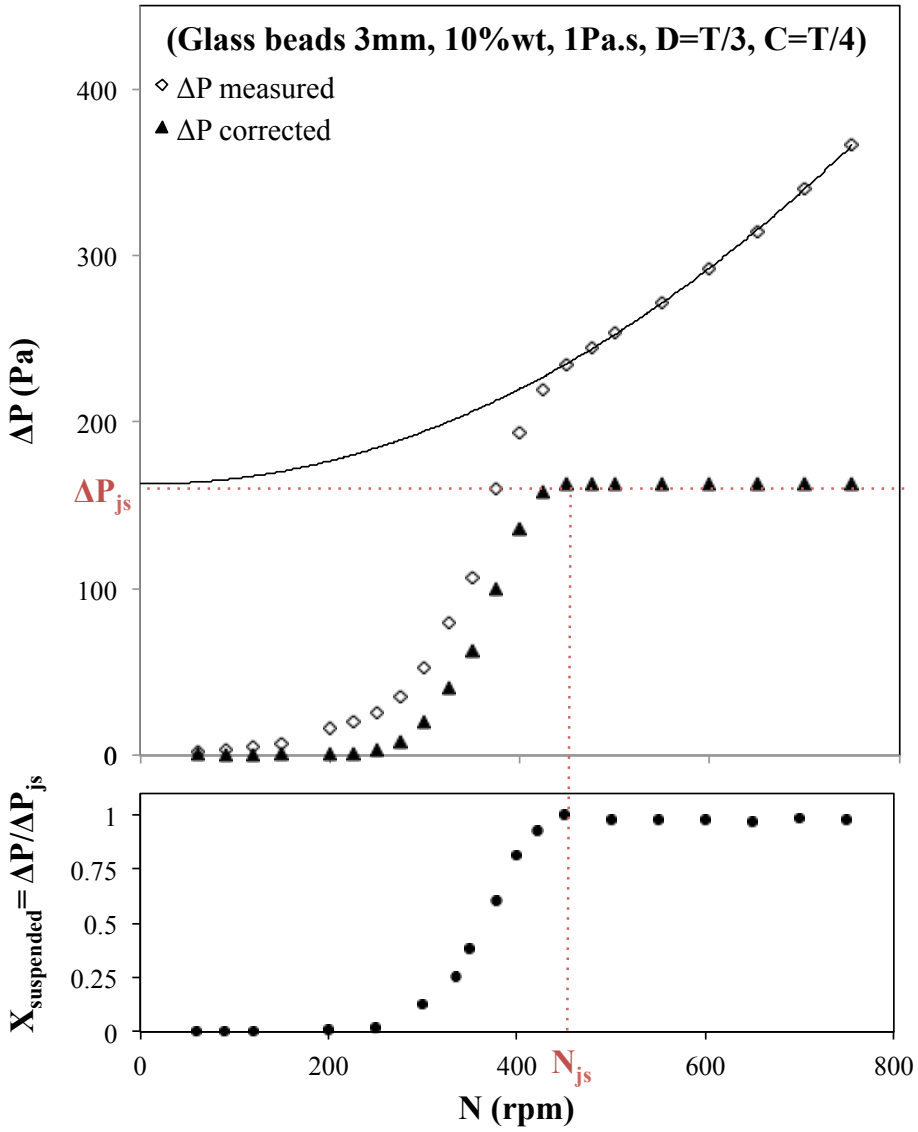

Figure 8.9 Illustration of the procedure used to obtain the suspension curve from the raw pressure data

Young's modulus (Y)	100 MPa
Coefficient of restitution (e_r)	0.9
Poissons ratio (ν)	0.25
Coefficient of friction (μ_s)	0.3
Rolling friction (μ_r)	0.1
DEM time step (Δt_{DEM})	5×10^{-6}s
CFD time step (Δt_{CFD})	1×10^{-4}s
Coupling time-step (Δt_c)	1×10^{-4}s

Table 8.7 Simulation parameters for the solid-liquid mixing simulation

the swept volume of the impeller, thus yielding a total of slightly more than 350k cells. Blais *et al.* [37] found that for this same geometry, more refined meshes did not lead to measurable changes in the torque ($< 1\%$) and the velocity field. A cutoff view of this mesh is presented in Figure 8.10. The impeller velocity ranged from 100 RPM to 700 RPM (Re=40 to 275), which encompasses the N_{js} value of 425 RPM that was measured experimentally via the pressure gauge technique. The same time step was used for all simulations and the Courant-Friedrichs-Lewy condition (CFL in Eq. (8.13)) for the simulations at 700 RPM was 0.7. In fact, the solid-fluid coupling criterion (Δt_{pf} in (8.16)) is the factor that prevented simulations with higher time steps for lower impeller velocities.

For the comparison with the pressure gauge measurements, the simulated pressure was evaluated at the bottom of the stirred tank by averaging its values therein for all cell faces that were comprised within a radius of $0.45R$ to $0.55R$, to comply with the position of the actual pressure sensor. This is illustrated in Figure 8.11.

It must be noted that the experiments were carefully designed so that they could be reproduced in the simulations, in particular with regards to the number of particles and the stability criteria (more precisely Δt_{fp} and Δt_{pf} in Equations (8.15) and (8.16), respectively). However, the relatively high viscosity (1Pa.s) of the fluid entails a fluid-solid stability criterion of $\Delta t_{fp} \leq 1 \times 10^{-3}$s. In the Rong drag model in Table 8.2, reducing the void fraction ϵ_f increases the value of the drag force, as discussed in Section 8.3. In the stirred tank, the minimal value that the void fraction ϵ_f can reach is $1 - \epsilon_{p,m} = 0.36$ in regions of maximal packing (the static bed of particles). This leads to a fluid-particle stability criterion of the order of $\Delta t_{fp} \leq 2 \times 10^{-5}$ and, consequently, a solid-fluid stability criterion of $\Delta t_{pf} \leq 7 \times 10^{-6}$ within the bed due to the effect of ϵ_f. This would lead to prohibitively time-consuming simulations.

To resolve this issue, the value of the the void fraction used in the Rong drag equation was limited to $\epsilon_{f,l} = \max(\epsilon_f, 0.8)$, which yields $\Delta t_{pf} \leq 1.0 \times 10^{-4}$. This allowed us to perform 200s of simulation time within a 40-day time frame, instead of the 300 days that would be

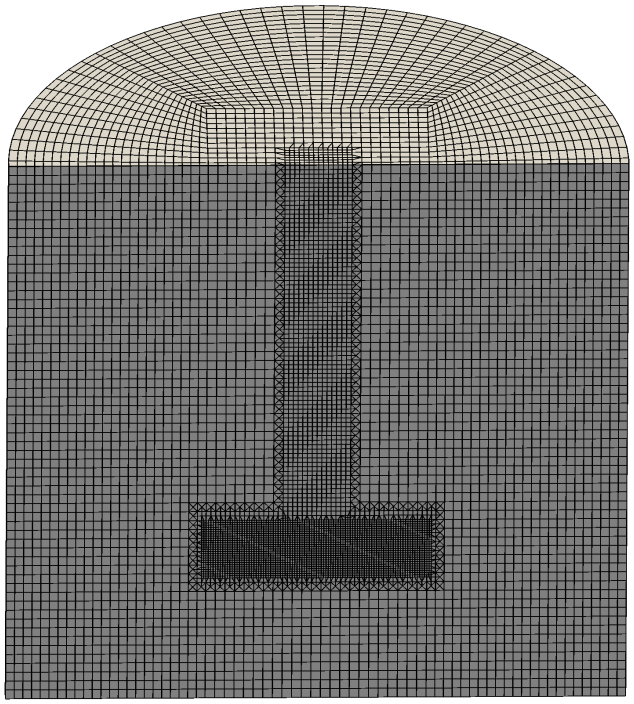

Figure 8.10 Cutoff view of the CFD mesh

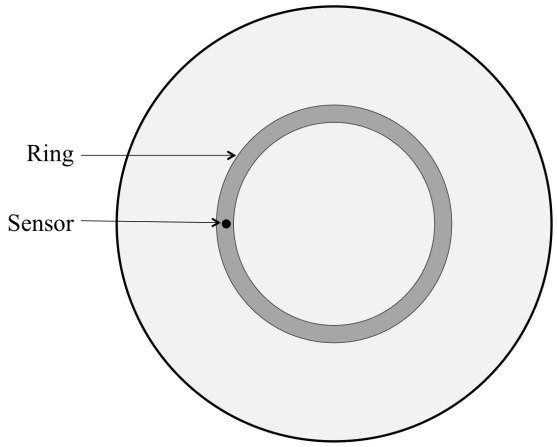

Figure 8.11 Position of the pressure sensor and ring used to average the simulated pressure results

required without this simplification. The consequence of this is that, in very dense regions ($\epsilon_f < 0.8$) of the tank, the Stokes number was made slightly artificially larger. We recall the definition of the Stokes number :

$$St = \frac{\tau_p}{\tau_f} \tag{8.22}$$

where $\tau_p = \frac{d_p^2 \rho_p}{18\mu}$ is the particle relaxation time for a single isolated particle and τ_f the fluid relaxation time. In a mixing tank, the shortest relaxation time of the fluid, near the impeller, is proportional to the inverse impeller velocity $\frac{1}{N}$, with N in RPS.

The Stokes number at the largest impeller speed (700 RPM) and for a single particle of the smallest diameter considered ($d_p = 2.66mm$) is $St_m \approx 0.015$. It must be noted that for such a low value of the Stokes number, the particles are expected to behave like passive scalars and thus follow the streamlines, as shown in the simulations of Garg *et al.* [103]. When the Rong drag model dependence on the void fraction is limited, as is proposed here, the particle relaxation time is increased artificially (since the drag force is increased) and so is the Stokes number. However, such limitation of the Rong drag model dependence on ϵ_f does not occur in regions where there is actual flow, but only within quasi-static regions such as in the dense particle bed, at the bottom of the tank, where the local value of the Stokes number is orders of magnitudes lower than St_m. Therefore, this limitation is expected to have no significant impact on the dynamics of the solid-liquid flow within the tank. This was confirmed by carrying out a full simulation at 700 RPM without any limitation on ϵ_f, for which a steady-state could be reached after $20s$ (approximatively 30 days of simulation). This simulation revealed that the simplification had no effect on the particle distribution, and the pressure and velocity fields.

All the simulations were carried out on the Briaree cluster of Calcul Québec. Each simulation used 2 Intel Westmere processors, each of which consisted of 6 physical cores with a frequency of 2.67 GHz and 12 Go of memory (24 Go total). Each simulation was carried out for 40 days of wall time, resulting in a total consumption of 30 core-years for the 20 impeller velocities investigated.

8.6.2 Results and discussion

Visual observation of the particle distribution allows for an effective qualitative comparison between experiments and simulations. For $N < 150$ RPM, only a weak displacement of the particles at the top of the bed could be noticed, like a gentle simmer, the energy imparted by the pitched blade turbine being not strong enough to suspend any of them. By increasing the velocity, peculiar flow patterns were triggered for $N \in [150, 250]$. At these velocities,

the occurence of a pinching flow was such that particles were initially sucked towards the bottom of the impeller (Figure 8.12 (I)), which then led to the formation of a cone-shaped (or umbrella-shaped) region below the impeller, isolated from the bulk of the liquid flow (Figure 8.12 (II)). No significant particle motion across this conical region could be observed. Further increasing the velocity over a critical value of around 300 RPM led to the erosion of the outer part of the bed where particles were lifted close to the wall in a region above the impeller. Once this suspension began, visual observation became difficult due to the opacity of the system. However, it could be noticed both experimentally and from the simulation results that some particles were dragged upward in the near-wall region and downward in the near-shaft region. This comparison, albeit qualitative, showed that the numerical model was able to reproduce the main hydrodynamic transitions and flow patterns that were observed experimentally.

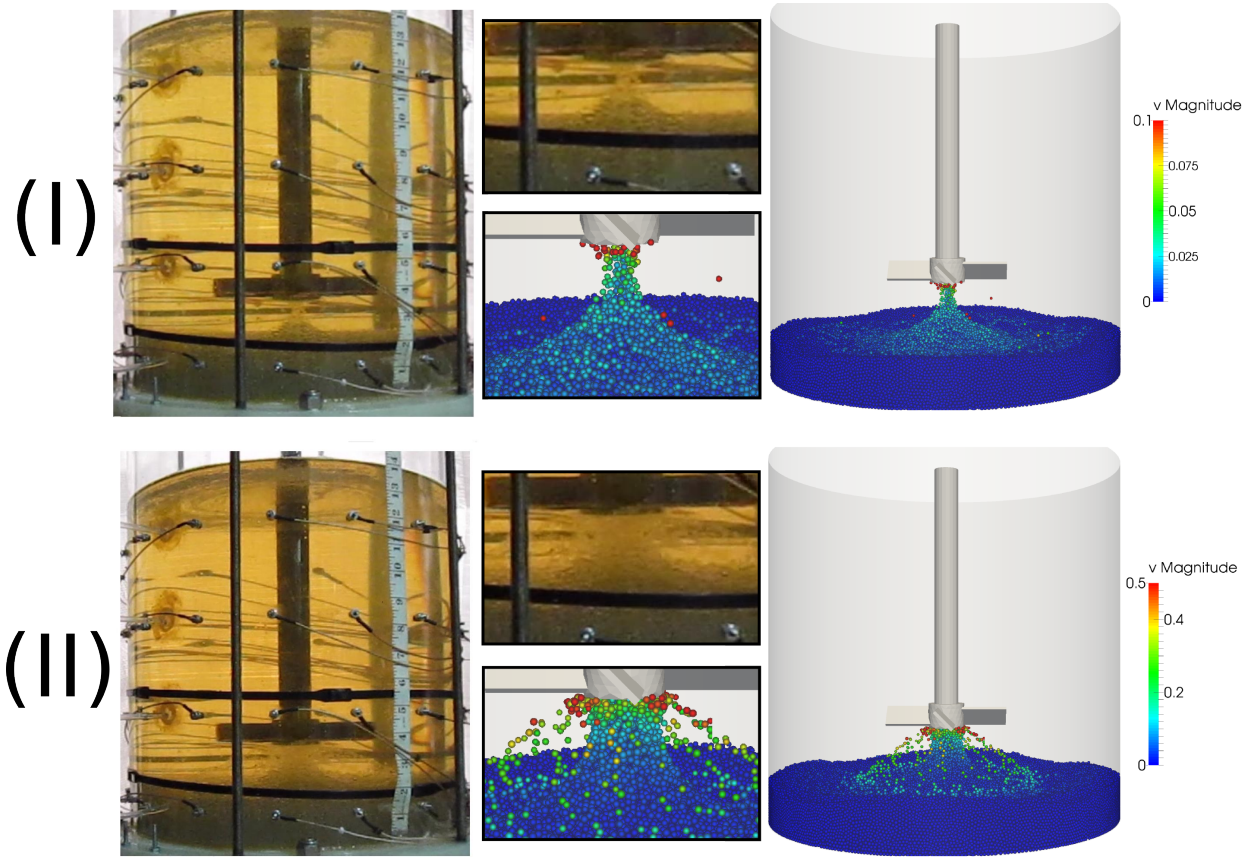

Figure 8.12 Visual comparison of the behavior of the solid particles in the transitional flow regime for $N = 200$ RPM. (I) : Onset of the bed erosion - (II) : Formation of a stable cone of particles

As mentioned in Section 8.6.1, the pressure gauge technique allows for a quantitative de-

termination of the fraction of suspended particles. The graph in Figure 8.13 shows that a constant pressure at the bottom is reached after 200s for all impeller speeds, although the time required to reach this pressure, which corresponds to the steady-state regime, varies greatly with the impeller speed. This steady-state pressure is the sum of the static pressure due to the increased apparent density and the dynamic pressure. The graph in Figure 8.14 compares the pressure at the bottom of the tank obtained experimentally to that predicted by our simulation model and averaged using the described in Section 8.6.1. Although the departure from a zero pressure variation occurs similarly around 300 RPM, the pressure obtained via numerical simulation is larger than the pressure measured experimentally. This is significant for $N \geq N_{js} = 425$ RPM, which corresponds to the speed above which the increase in pressure is solely due to the increase of the dynamic pressure [210]. Note that the time-average value of the pressure was not affected significantly by changes to the size of the ring used in the averaging procedure. This discrepancy can be largely attributed to the set-up used to measure the pressure experimentally (Figure 8.8). It is measured within a 4 mm hole, which is protected from the particles by a fine mesh. Consequently, the dynamic pressure measured by the probe is significantly underestimated since the flow is damped by the mesh as well as by the presence of a cavity between this probe and the tank. From a practical point of view, both the mesh and the cavity act together as a damper and a low-pass filter for the dynamic pressure. This has the inherent advantage of giving smooth and stable pressure measurements.

Consequently, it is more appropriate to apply the PGT procedure on the two signals and remove the dynamic pressure seperately before comparing the fractions of suspended solids. This is presented in the graph of Figure 8.15. We note the excellent agreement between the experimental data and simulation results. The transition from a non-suspended to a fully suspended state happens sharply in a small velocity range from 300 to 425 RPM. This transition is subject to larger uncertainties as can be seen by the size of the error bars, compared to those for both the fully unsuspended and suspended states. However, it can be noticed that the simulations estimate accurately, within a 95% confidence interval, the speed at which the suspension of particles is triggered and the just suspended speed, as well as the portion of the curve between these two end points.

The model was also used to investigate the distribution of the solid particles and the flow patterns in the tank. Figure 8.16 shows the azimuthal average of the void fraction and its standard deviation at 700 RPM, at steady state, which is far above $N_{js} = 425$ RPM. It appears that, although the PGT indicates that all the particles are suspended, there is a small cone-shaped region below the impeller, within which a small fraction of particles ($< 5\%$ of the total mass) remains unsuspended. Such a zone of accumulation of particles in a conical

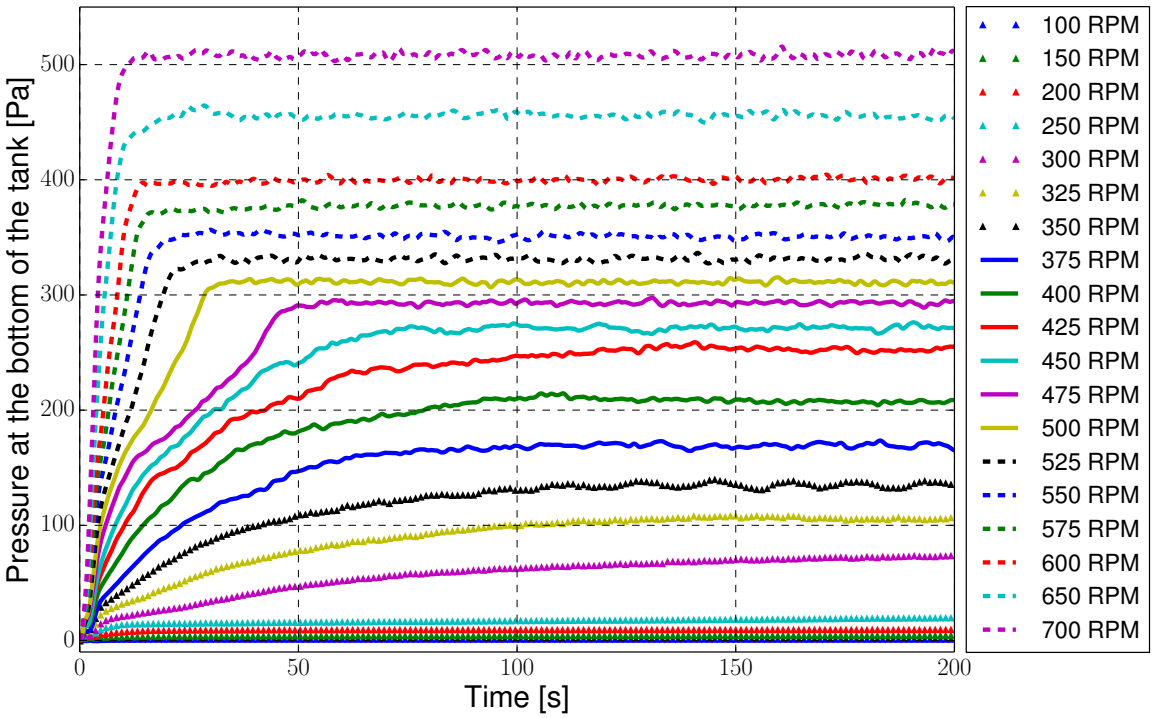

Figure 8.13 Time evolution of the pressure at the bottom of the tank for various impeller speeds.

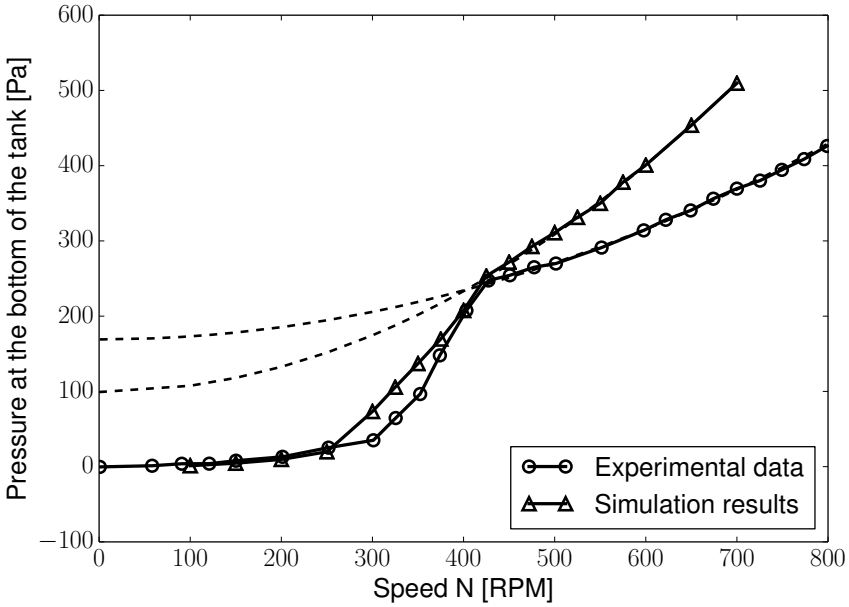

Figure 8.14 Comparison between the pressure measured experimentally at the bottom of the tank and the simulation results.

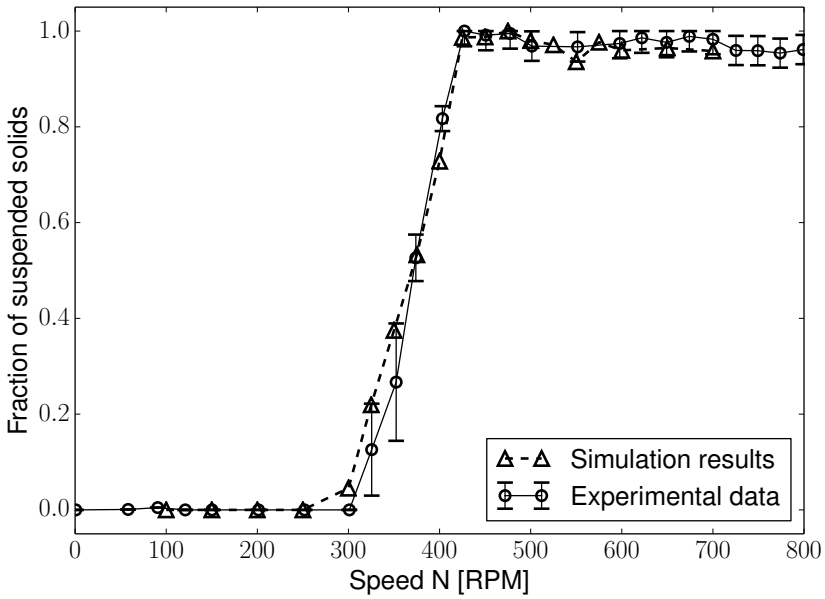

Figure 8.15 Comparison of the experimental and numerical suspension curves after application of the PGT procedure and the removal of the dynamic pressure component. The error bars represent a 95% confidence interval.

region has already been observed in unbaffled tanks, albeit in the turbulent regime [51]. Such a segregated cone is larger at lower velocity (*e.g.* at 500 RPM), as evidenced in Figure 8.17. Due to the small total mass of particles contained within this cone and its relatively small erosion with the increase of the impeller speed (as can be seen qualitatively by compairing Figure 8.17 for 500 RPM and Figure 8.16 for 700 RPM), its presence is not captured by the PGT.

It is also interesting to note that a low concentration segregated zone of particles, of toroidal shape, is present above the impeller blades at these speeds. Such peculiar patterns have been previously identified by Lamberto *et al.* [172] and Cabaret *et al.* [56], in the laminar and transitional regimes for PBTs in unbaffled tanks.

Finally, Figure 8.18 highlights the azimuthal average of the radial, azimuthal and axial components of the liquid velocity within the tank. It can be observed that although the PBT is a mixed discharge impeller, it behaves as a radial discharge impeller for the range of Reynolds numbers considered in this work ($Re \leq 275$, $N \leq 700$RPM). In particular, the poor axial discharge below the impeller is responsible for the formation of the cone of particles therein.

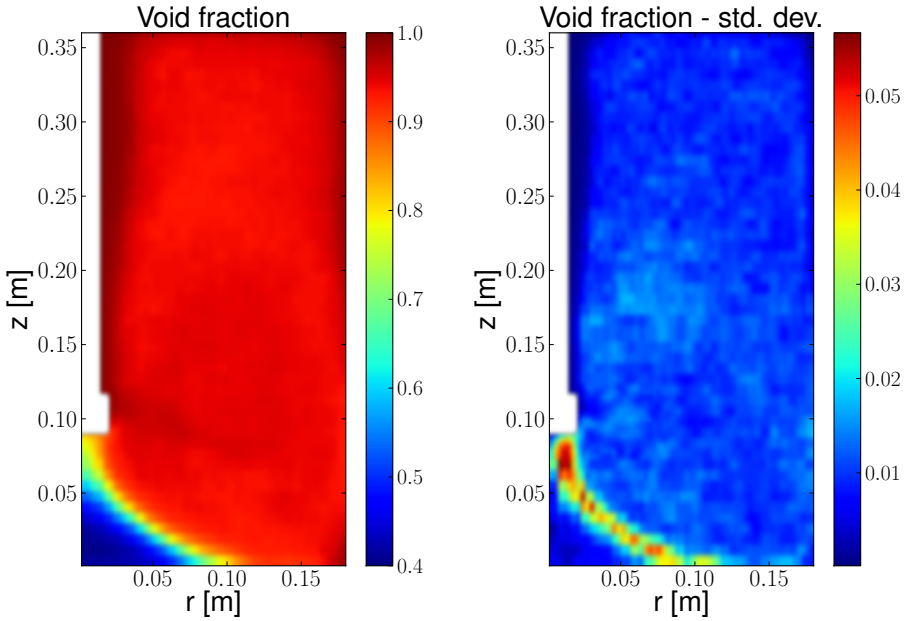

Figure 8.16 Azimuthal average and standard deviation of the void fraction for $N = 700$ RPM at steady state

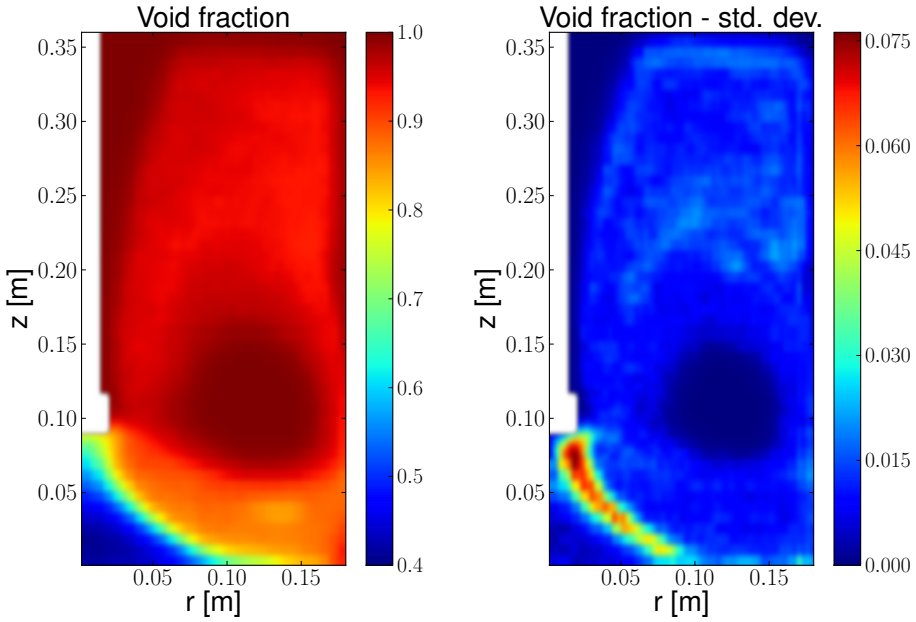

Figure 8.17 Azimuthal average and standard deviation of the void fraction for $N = 500$ RPM at steady state

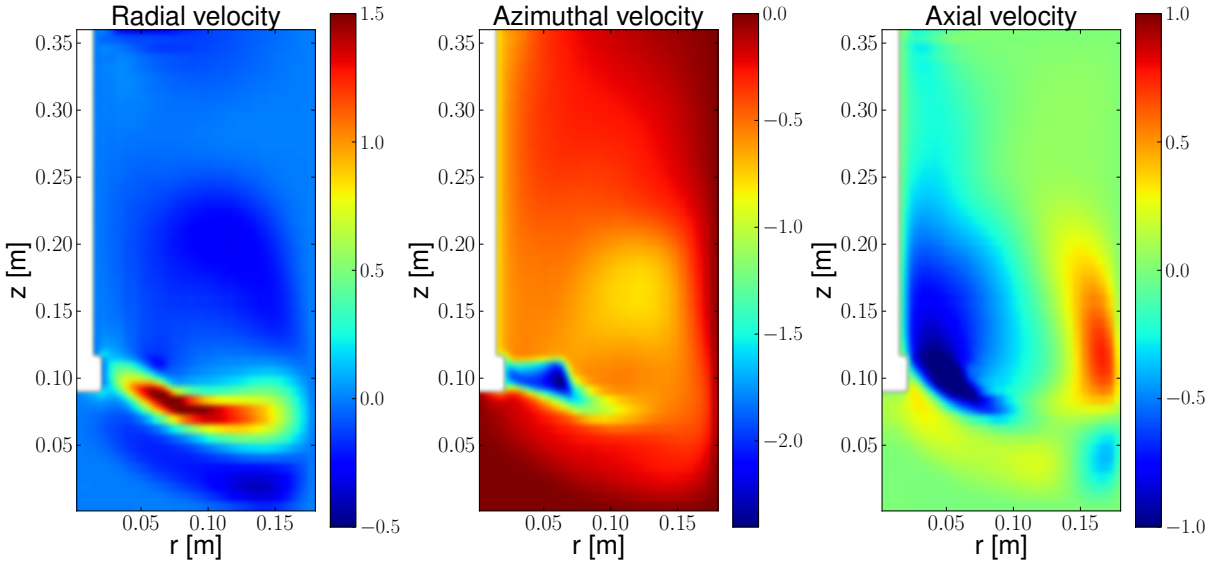

Figure 8.18 Azimuthal average of the radial, azimuthal and axial components of the liquid velocity for 700 RPM at steady state.

8.7 Conclusion

The mixing of solid suspensions in the viscous regime is a challenging topic that remains unsolved due to the complex particle-particle and particle-fluid interactions, and the presence of a rotating impeller that generates unsteady 3D flow patterns. Due to its accurate description of the solid phase and computationally tractable description of the fluid, the unresolved CFD-DEM model is a good candidate to the investigation of solid-liquid mixing. However, the validity of this type of approach for viscous suspensions had, to our knowledge, never been assessed.

In the present work, we introduced a CFD-DEM model for viscous suspensions and established stability criteria related to the fluid-fluid, solid-solid, solid-fluid and fluid-solid interactions. Next, we compared implicit and explicit momentum coupling strategies, and showed that in the case of a viscous suspending fluid, the explicit strategy was more accurate in estimating the pressure drop across a bed of particles, mainly due to the significant error introduced by the averaging of the particle velocity within the grid cells. Then, we showed that the apparent rheology of suspensions inherent to the unresolved CFD-DEM model did not reproduce that of a real suspension of particles, which can be attributed to the absence of viscous dissipation at the particle and sub-particle scales. This was remedied by the introduction of a sub-grid viscosity model that brings into play the local void fraction, an approach that is reminescent of the subgrid Smagorinsky-type model used in large eddy simulation.

The unresolved CFD-DEM model for viscous solid-liquid flows developed in this work was used to investigate solid-liquid mixing behavior in a stirred tank equipped with a PBT. Visual observation in the lab showed that the model was able to reproduce the peculiar flow patterns observed when the particles get suspended in the tank. By comparing the fraction of the suspended particles as measured experimentally by the PGT to the pressure averaged at the bottom of the tank in the simulations, we showed that the unresolved CFD-DEM model can predict with excellent accuracy the fraction of suspended particles from the onset of their suspension to the fully suspended state, thus validating the model in a quantitative manner.

The model was finally used to shed light on the solids distribution and the flow patterns prevailing in the tank. It was found that the PBT behaved like a radial discharge impeller in the laminar and early transitional flow regimes. Even for impeller speeds above the value of N_{js} determined by the PGT, an accumulation of particles within a cone-shaped region below the impeller could be identified, indicating that the suspension could not reach a fully homogenized state. This will be investigated in detail in future work.

This work also opens possibilities for topics related to solid-liquid mixing. In parallel, we are

interested in clarifying thoroughly the role of the DEM parameters such as the coefficient of restitution, the coefficients of translational and rolling friction and the Young's modulus on the dynamics of solid-liquid flows.

8.8 Acknowledgements

The financial support from the Natural Sciences and Engineering Research Council of Canada (NSERC) is gratefully acknowledged. In particular, Bruno Blais is thankful for the NSERC Vanier Scholarship. Computations were made on supercomputer Briaree from the University of Montreal, managed by Calcul Québec and Compute Canada. The operation of this supercomputer is funded by the Canada Foundation for Innovation (CFI), Ministère de l'Économie, de l'Innovation et des Exportations du Québec (MEIE), RMGA and the Fonds de recherche du Québec - Nature et technologies (FRQ-NT). The authors would also like to acknowledge the efficient support from Calcul Québec systems analysts.

CHAPITRE 9 Article 5 : Unresolved CFD-DEM simulations of turbulent solid-liquid mixing : Prediction of suspension curve and just-suspended speed

Bruno Blais, Olivier Bertrand, Louis Fradette, François Bertrand
Submitted to AIChE Journal, 2016

Abstract : Solid-liquid mixing faces considerable challenges, notably regarding the prediction of the impeller speed required to suspend the particles (N_{js}). In this work, we extend to the turbulent regime a CFD-DEM model developed recently in our group for solid-liquid mixing. The model is used to study the mixing of glass particles in a baffled stirred tank equipped with a down-pumping pitched blade turbine. The liquid dynamics as well as the distribution and motion of the particles are investigated. The fraction of suspended particles predicted by the model is validated against experimental data obtained via the pressure gauge technique (PGT). Two new methods to calculate the fraction of suspended particles, the so-called Lagrangian suspended fraction analysis and the decorrelated fraction analysis techniques are introduced. The results obtained with these two methods, and others taken from the literature, are compared to the Zwietering correlation and to the results obtained by the PGT.

9.1 Introduction

Solid-liquid mixing operations are present in a wide range of processes. For example, stirred tanks are used as reactors for crystallization and catalytic reactions, and play a key role in the homogenization of products and the dissolution of solids in the pharmaceutical, cosmetic and food industries [245]. For many of these operations, it is sufficient to operate the impeller at the just-suspended speed (N_{js}), thus ensuring that the particles are maintained off-bottom. In such a case, the contact surface between the solid and liquid phases is near optimal and little enhancement to mass transfer can be obtained by increasing the impeller speed [157, 226]. A large body of the work in the solid-liquid mixing literature has been geared towards the prediction of the just-suspended speed, which was defined by Zwietering [339] as the speed at which no solid particles remain motionless at the bottom of the vessel for longer than 1 or 2 s. Using experimental data obtained by visual observation of the vessel bottom, Zwietering proposed the following correlation for N_{js} :

$$N_{js} = S\nu_f^{0.1}\left(\frac{(\rho_p - \rho_f)\, g}{\rho_f}\right)^{0.45} d_p^{0.2} X^{0.1} D^{0.15} \tag{9.1}$$

with S an empirical constant that depends on the tank configuration, ρ_f the fluid density, ρ_p the solid density, d_p the particle diameter, D the impeller diameter, ν_f the fluid kinematic viscosity, g the gravity and X the solid mass concentration. The assessment of the just-suspended speed is important for process design and has been the the focus of considerable work, as reviewed by Kasat and Pandit [149] and Jafari *et al.* [139]. The Zwietering correlation suffers from severe limitations. The correlation has been found to be innacurate in the laminar and transitional regimes of operation [130, 132, 173], for high solids loadings [14] and for bidisperse particles [13]. Furthermore, the empiric character of the parameter S, which is very sensitive to the geometry (type of agitator, off-bottom clearance, baffle width, baffle off-bottom clearance, etc.) [14], severely limits its applicability. These limitations are shared, to varying degrees, by other correlations in the literature, such as those introduced by Nienow *et al.* [225], Narayanan *et al.* [223], Baldi *et al.* [18], Mersmann *et al.* [208], Grenville [114] and Tamburini [292].

In fact, the definition of N_{js} itself, and more importantly, the methods which have been used for measuring it, are insufficiently general. Visual observation is subjective and should not be applied for particle concentrations above $X = 8wt\%$ [231]. Although it has been used at higher solids contents, notably by Ayranci *et al.* [14] and Grenville *et al.* [114], its precision and subjectivity remain uncertain in this context. Furthermore, as noted by Tamburini *et al.* [296] and by Kasat and Prandit [149], situations occur where small amounts ($<$1 or 2% vol) of particles remain unsuspended and form fillet in relatively stagnant regions (e.g. below the impeller, below the baffles or near the wall-bottom junction of the tank). Kasat and Prandit [149] suggest that these small unsuspended fillets should be ignored in the determination of N_{js} by means of visual observation. However, this increases the already high subjectivity of visual observation.

Although these unsuspended particles are often insignificant from a process point of view - it is not the case for crystallization operations - they require a substantial increase of the impeller speed to get suspended. For example, Brucato and Brucato [49] showed that for an impeller speed of 80% of that predicted by Zwietering correlation, all but a few particles were suspended. Similarly, Kasat and Pradit [149] observed in one of their systems that all the particles in the bulk of the flow could be suspended for impeller speed 66% to 83% of N_{js}. In the case of Brucato and Brucato [49], lowering the speed to 80% of the value of N_{js} comes with a reduction of the power consumption of $\approx 51\%$, whereas for the most extreme example discussed by Kasat and Prandit [149], this represents a reduction of $\approx 30\%$ of the original power consumption. Clearly, this can lead to considerable energy savings with little to no effect on the process efficiency.

As noted by Tamburini *et al.* [296], a large number of industrial processes are operated at speeds below N_{js} (examples can be found in the book by Oldshue [232]). Yet, all the correlations for N_{js}, such as the one proposed by Zwietering [339], are unable to predict adequately suspended conditions or the fraction of suspended solids. Surprisingly, despite the interest in operating in a partially suspended state due to the aforementioned reasons, little work has been dedicated to this issue. In fact, the core of the work on this topic has been done by Brucato *et al.* [53], Micale *et al.* [210] and Tamburini *et al.* [293, 296]. Brucato *et al.* [53] and Micale *et al.* [210] introduced the pressure gauge technique (PGT), whereby the fraction of suspended solids can be measured by means of a pressure probe at the bottom of the tank. Using this method, Micale *et al.* [210] defined the sufficiently suspended speed N_{ss} as the impeller speed required to suspend 98.2% of the particles. The pressure gauge technique was used recently by Lassaigne *et al.* [173] to investigate solid-liquid mixing for non-dilute concentrations in viscous fluids, and it was found to be a very accurate mean of measuring the speed required to suspend the particles.

The use of CFD-based models has shown to be an adequate complement to experimental investigations. As reviewed by Blais *et al.* [40], mainly two types of models have been used extensively to study solid-liquid mixing : two-fluid (Euler-Euler) models and unresolved (Euler-Lagrange) CFD-DEM models. A large proportion of CFD solid-liquid mixing studies (*e.g.* [129, 148, 149, 183, 211, 212, 218, 219, 228, 293, 294, 296–299]) have been carried out using two-fluid models, which despite inherent limitations, such as the difficulty of reproducing the maximal packing fraction and the particle dynamics in dilute regions, can simulate any number of particles. However, as reviewed by Tamburini *et al.* [297], the traditional definition of N_{js} is not applicable in a continuum context (Euler-Euler) since the notion of a single particle does not make sense. Numerous procedures to obtain N_{js} have been devised for these models, among which the tangent intersection [129], the variation coefficient [319], the unsuspended solid criterion [297], and the power number [255, 259] methods. These methods were reviewed and compared by Tamburini *et al.* [297] who observed large deviations (sometimes up to 100%) among them. Note that these discrepancies are not systematic, but depend on the system studied. However, the unsuspended solid criterion and the power number methods have revealed to compare adequately to experimental data. Additionally, in another article by the same group [296], an excellent agreement was obtained between the unsuspended solid criterion method for the fraction of suspended solids and experimental data obtained via the pressure gauge technique. However, for larger particles (> 0.5 mm), the quality of the simulation results was dependent on the presence or not of correlations that take into account the effect of free stream turbulence on the drag force, such as those suggested by Brucato *et al.* [52] and Pinelli *et al.* [250].

In Euler-Lagrange models, such as unresolved CFD-DEM, the position and the velocity of each particle are tracked so that the dynamics of the solid phase is described with more accuracy than with Euler-Euler approaches. However, these models are computationally intensive and their use has been limited. Derksen [80] introduced an unresolved CFD-DEM model for solid-liquid mixing based on a hard-sphere collision model. With this model, he investigated the role of the various solid-liquid forces and concluded that drag was the dominating interaction force whereas the Saffman and Magnus lift forces played but a negligible role in the mixing dynamics. This type of model is limited to low particle concentrations since it is based on a hard-sphere collision approach and the use of regular Navier-Stokes equations. Because of this limitation to low concentrations, it cannot be used to simulate the start-up of a stirred tank. On the other hand, unresolved CFD-DEM models based on the use of the volume-averaged Navier-Stokes equations and soft-sphere DEM do not suffer from these limitations. Shao *et al.* [276] used an unresolved CFD-DEM model, combining commercial software Fluent and EDEM, to study solid-liquid mixing in a baffled tank equipped with a Rushton turbine. They investigated the evolution of the solid concentration at two impeller speeds and identified a clustering phenomenon at the tank bottom. Furthermore, contrary to Derksen [80], they concluded that the Magnus force plays an important role in the lift of the particles. The reason for this rather unexpected result will be clarified in the present work.

Despite their inherent capability to reproduce the maximal packing fraction of particles and its accurate description of the granular dynamics, unresolved CFD-DEM models have not been used to assess partially suspended conditions, the sufficiently suspended speed (N_{ss}) or the just-suspended speed (N_{js}). Recently, Blais *et al.* [40] introduced a robust unresolved CFD-DEM model for solid-liquid flows based on the CFDEM framework [61, 112], which combines Open∇FOAM for the CFD part [233] and LIGGGHTS [155, 182] for the DEM part. This model was validated in the context of solid-liquid mixing in laminar and transitional regimes using a set-up consisting of a pitched blade impeller and involving non-dilute (10 wt%) concentrations of particles. Albeit more computationally intensive than two-fluid models, this framework allowed for the determination of the fraction of suspended particles at various impeller speeds with a high degree of accuracy and with few modeling parameters or hypotheses.

In this work, the unresolved CFD-DEM model for solid-liquid mixing introduced by our group [40] is extended to the turbulent regime of operation by means of large eddy simulation (LES). First, the flow system investigated, which consists of glass beads and a glucose solution in a baffled stirred tank equipped with a pitched blade turbine, is described and the CFD-DEM model is introduced. Then, various techniques to calculate N_{js}, N_{ss} and the fraction of suspended solids (X_{susp}) are presented. Two novel techniques to measure the fraction

of suspended solids, the Lagrangian suspended fraction analysis (in two variants, LSFA-$\Delta\boldsymbol{x}$ and LSFA-Δz) and the decorrelated fraction analysis (DFA) methods are introduced. The potential of the model to predict the fraction of suspended solids is validated against experimental data obtained via the pressure gauge technique. Alternative metrics for the determination of N_{js} and N_{ss} are compared to results obtained from both existing correlations and experimental measurements. The model is also used to investigate the phase-average flow patterns, the solids distributions and, more generally, the dynamics of mixing in the stirred tank.

9.2 Flow system

The mixing rig consisted of a 0.365 m diameter (T) flat-bottomed, cylindrical and transparent vessel equipped with a T/3 diameter (D) down-pumping pitched blade turbine (PBT). The choice of the latter is justified by its large use in the industry for solid-liquid mixing [245]. The tank was equipped with four baffles (W=T/10), and the clearance was set at a standard value of C=T/4. The height of the liquid was equal to the tank diameter (H=T). The particles were glass beads with a Sauter diameter ($d_{p,32}$) of 3.02 mm at a 10% w/w loading in a Newtonian glucose solution of viscosity μ of 0.0516 Pa.s. The maximum impeller speed was 900 RPM, corresponding to a Reynolds number of $Re = \frac{\rho_f N D^2}{\mu} \approx 5200$ (with N in RPS). This set-up is illustrated in Figure 9.1. The dimensions of this mixing rig and the properties of the fluid and solid particles are summarized in Table 9.1.

9.3 Model Formulation

The unresolved CFD-DEM approach consists in solving the fluid flow equations at a scale larger than that of the individual particles, while accounting for their effect on the fluid. This is achieved by using a pointwise description for the particles and by projecting both their volumes and the forces resulting from the solid-fluid interactions onto the CFD mesh, in order to calculate the void fraction and the solid-fluid momentum exchange, respectively. This projection, which can be seen as a local volume filtering techique [58], leads to a volume averaged form of the Navier-Stokes (VANS) equations [4,336]. In order to handle the particle-particle and particle-geometry collisions, the soft-sphere discrete element method (DEM) is used [31, 337]. These two models, which operate independently, are coupled at a regular interval - for instance at each CFD iteration - and the positions and velocities of the particles are used to update the solid-fluid coupling. The model presented in this work can be seen as an extension of our recent work [40, 41] to turbulent flows using large eddy simulation

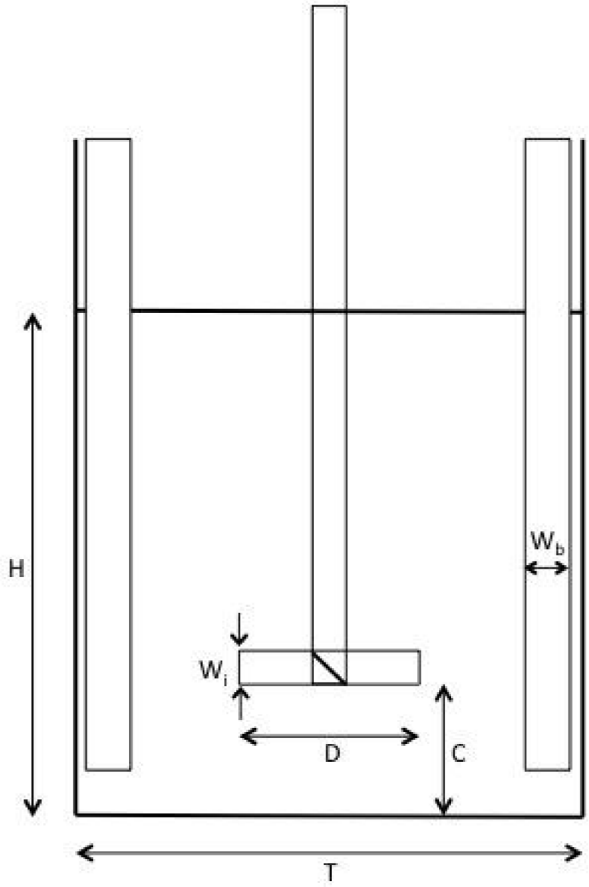

Figure 9.1 Experimental set-up, adapted from [41]

Symbol	**Name**	**Value**
T	Tank diameter	0.365m
D	Impeller diameter	$\frac{T}{3}$
H	Liquid level	T
C	Off-bottom clearance	$\frac{T}{4}$
W_i	Blade width	$\frac{D}{5}$
W_b	Baffle width	$\frac{T}{10}$
ρ_f	Density of the fluid	1207 kg.m^{-3}
μ	Dynamic viscosity of the fluid	0.0516 Pa.s
ρ_s	Density of the particles	2500 kg.m^{-3}
d_p	Diameter of the particles	2.66-3.5 mm
$d_{p,32}$	Sauter diameter	3.02 mm
x_s	Mass fraction of the particles	10 %
ϵ_s	Volume fraction of the particles	5.1 %

Table 9.1 Dimensions of the mixing rig and physical properties of the fluid and solid particles

(LES). First, we present the equations for the DEM, then the equations for the CFD part and, finally, the two-way coupling between the particles and the fluid.

9.3.1 Governing equations for the solid-phase (DEM)

In the discrete element method (DEM), the position and velocity of each particle are tracked, and collisions are handled by allowing minute overlaps between spheres. This overlap is decomposed into normal and tangential directions, and used within contact models that contain elastic and dissipative components, thus allowing for the treatment of inelastic particle-particle collisions [31, 337].

As a result of Newton's second law of motion, the governing equations for the translational ($\boldsymbol{v}_i$) and rotational ($\boldsymbol{\omega}_{p,i}$) motion of particle i can be written as [182] :

$$m_i \frac{d\boldsymbol{u}_i}{dt} = \sum_j \boldsymbol{f}_{c,ij} + \sum_k \boldsymbol{f}_{lr,ik} + \boldsymbol{f}_{pf,i} + \boldsymbol{f}_{g,i} \tag{9.2}$$

$$I_i \frac{d\boldsymbol{\omega}_{p,i}}{dt} = \sum_j (\boldsymbol{M}_{t,ij} + \boldsymbol{M}_{r,ij}) \tag{9.3}$$

where m_i is the mass of particle i, I_i the moment of inertia of particle i, $\boldsymbol{f}_{c,ij}$ the contact forces between particles i and j, $\boldsymbol{f}_{lr,ik}$ the non-contact (long-range) forces between particles i and k, $\boldsymbol{f}_{pf,i}$ the particle-fluid interaction forces, $\boldsymbol{f}_{g,i}$ a body force, and $\boldsymbol{M}_{t,ij}$ and $\boldsymbol{M}_{r,ij}$ the tangential and rolling friction torques acting on particles i and j. In the present work, non-contact forces, such as the electrostatic or van Der Waals forces are neglected due to the size and nature of the particles (3 mm glass beads). The expression for the particle-fluid interaction forces depends on which interactions are taken into account (drag, virtual mass, lift, etc.). This is discussed in Section 9.3.3.

The contact forces between two particles are split into normal ($\boldsymbol{f}_{cn,ij}$) and tangential ($\boldsymbol{f}_{ct,ij}$) [337] components :

$$\boldsymbol{f}_{c,ij} = \boldsymbol{f}_{cn,ij} + \boldsymbol{f}_{ct,ij} = -k_{n,ij}\boldsymbol{\delta}_{n,ij} - \gamma_{n,ij}\dot{\boldsymbol{\delta}}_{n,ij} - k_{t,ij}\boldsymbol{\delta}_{t,ij} - \gamma_{t,ij}\dot{\boldsymbol{\delta}}_{t,ij} \tag{9.4}$$

where $k_{n,ij}$ and $k_{t,ij}$ are the normal and tangential stiffness coefficients, $\gamma_{n,ij}$ and $\gamma_{t,ij}$ the normal and tangential damping coefficients, $\boldsymbol{\delta}_{n,ij}$ and $\boldsymbol{\delta}_{t,ij}$ the normal and tangential overlaps, and $\dot{\boldsymbol{\delta}}_{n,ij}$ and $\dot{\boldsymbol{\delta}}_{t,ij}$ their derivatives with respect to time.

In the present work, a model proposed by Tsuji *et al.* [309] based on the Hertz theory [125,143] is used for the normal forces. For the tangential force, the Mindlin model [214, 215] is used. These models are combined to link the stiffness and the damping coefficients to the Young's modulus of the material (Y), the Poisson ratio (ν) and the coefficient of restitution (e_r), using the equations described in Table 9.2. The tangential overlap $\boldsymbol{\delta}_{t,ij}$ is truncated by means

of Coulomb's law to ensure that $\boldsymbol{f}_{ct,ij} \leq -\mu_{s,ij} \left|\boldsymbol{f}_{cn,ij}\right| \frac{\boldsymbol{\delta}_{t,ij}}{|\boldsymbol{\delta}_{t,ij}|}$.

Parameter	Equation
Normal stiffness	$k_{n,ij} = \frac{4}{3} Y^*_{ij} \sqrt{R^*_{ij} \delta_{n,ij}}$
Tangential stiffness	$k_{t,ij} = 8 G^*_{ij} \sqrt{R^*_{ij} \delta_{n,ij}}$
Normal damping	$\gamma_{n,ij} = -2\sqrt{\frac{5}{6}} \frac{\ln(e_r)}{\sqrt{\ln^2(e_r)+\pi^2}} \sqrt{\frac{2}{3} k_n m^*_{ij}}$
Tangential damping	$\gamma_{t,ij} = -2\sqrt{\frac{5}{6}} \frac{\ln(e_r)}{\sqrt{\ln^2(e_r)+\pi^2}} \sqrt{k_t m^*_{ij}}$
Coulomb friction force	$\boldsymbol{f}_{ct,ij} \leq -\mu_{s,ij} \left\|\boldsymbol{f}_{cn,ij}\right\| \frac{\boldsymbol{\delta}_{t,ij}}{\|\boldsymbol{\delta}_{t,ij}\|}$
Torque by tangential forces	$\boldsymbol{M}_{t,ij} = \boldsymbol{r}_i \times (\boldsymbol{f}_{ct,ij})$
Rolling friction torque	$\boldsymbol{M}_{r,ij} = -\mu_{r,ij} \left\|\boldsymbol{f}_{cn,ij}\right\| \frac{\boldsymbol{\omega}_{p,ij}}{\|\boldsymbol{\omega}_{p,ij}\|} R^*_{ij}$
Equivalent mass	$\frac{1}{m^*_{ij}} = \frac{1}{m_i} + \frac{1}{m_j}$
Equivalent radius	$\frac{1}{R^*_{ij}} = \frac{1}{R_i} + \frac{1}{R_j}$
Equivalent Young's modulus	$\frac{1}{Y^*_{ij}} = \frac{\left(1-\nu_i^2\right)}{Y_i} + \frac{\left(1-\nu_j^2\right)}{Y_j}$
Equivalent shear modulus	$\frac{1}{G^*_{ij}} = \frac{2(2+\nu_i)(1-\nu_i)}{Y_i} + \frac{2(2+\nu_j)(1-\nu_j)}{Y_j}$
Sliding friction coefficient	$\mu_{s,ij}$
Rolling friction coefficient	$\mu_{r,ij}$
Distance to contact point for particle i	$\boldsymbol{r}_i$
Radius of particle i	R_i

Table 9.2 Equations for the DEM model

9.3.2 Governing equations for the liquid flow (CFD)

Form A (or set II using the notation of Zhou *et al.* [336]) of the incompressible volume-averaged Navier-Stokes (VANS) equations are solved for the liquid phase [105]. A filtering kernel [270] is applied to these equations, leading to the following filtered VANS equations :

$$\frac{\partial \epsilon_f}{\partial t} + \nabla \cdot (\epsilon_f \bar{\boldsymbol{u}}) = 0 \tag{9.5}$$

$$\frac{\partial \left(\rho_f \epsilon_f \bar{\boldsymbol{u}}\right)}{\partial t} + \nabla \cdot (\rho_f \epsilon_f \bar{\boldsymbol{u}} \otimes \bar{\boldsymbol{u}}) = -\epsilon_f \nabla \bar{p} + \nabla \cdot \boldsymbol{\tau} + \nabla \cdot \boldsymbol{\tau_{sgs}} - \boldsymbol{F}_{pf} \tag{9.6}$$

where ϵ_f is the void fraction, ρ_f the density of the fluid, $\bar{p}$ the filtered pressure, $\bar{\boldsymbol{u}}$ the filtered velocity and $\boldsymbol{g}$ the gravity. The viscous stress tensor $\boldsymbol{\tau}$ is defined as :

$$\boldsymbol{\tau} = \epsilon_f \mu \left(2\bar{\boldsymbol{S}} - \frac{2}{3} (\nabla \cdot \bar{\boldsymbol{u}}) \boldsymbol{\delta}_k\right) \tag{9.7}$$

$$\bar{\boldsymbol{S}} = \frac{1}{2} (\nabla \bar{\boldsymbol{u}}) + (\nabla \bar{\boldsymbol{u}})^T \tag{9.8}$$

where μ is the dynamic viscosity of the fluid, $\boldsymbol{\delta}_k$ the identity tensor and $\bar{\boldsymbol{S}}$ the strain-rate tensor of the resolved velocity. In the present work, the sub-grid scale Reynolds stress tensor

$\boldsymbol{\tau_{sgs}}$, which is brought into play due to the filtering of the advection term in the VANS equations, is based on the Smagorinsky model [97] :

$$\boldsymbol{\tau}_{sgs} = \epsilon_f \mu_t \left(2\bar{\boldsymbol{S}} - \frac{2}{3} \nabla \cdot \bar{\boldsymbol{u}} \boldsymbol{\delta}_k \right) \tag{9.9}$$

In this equation, μ_t is the subgrid-scale eddy viscosity given by :

$$\mu_t = C_s \rho_f \Delta^2 \left| \bar{S} \right| \tag{9.10}$$

where $C_s = 0.17$ is the Smagorinsky constant [253], Δ is the grid size and $\left|\bar{S}\right| = \sqrt{\bar{\boldsymbol{S}} : \bar{\boldsymbol{S}}}$.

The momentum exchange (or coupling) term from the particles to the fluid $\boldsymbol{F}_{pf}$ can be broken down into the following components :

$$\boldsymbol{F}_{pf} = \frac{1}{\Delta V} \sum_{i}^{n_p} \boldsymbol{f}_{pf,i} - \boldsymbol{f}_{\nabla p,i} - \boldsymbol{f}_{\nabla \cdot \boldsymbol{\tau},i} - \boldsymbol{f}_{\mathrm{Ar},i} \tag{9.11}$$

$$\boldsymbol{f}_{pf,i} = \boldsymbol{f}_{d,i} + \boldsymbol{f}_{\nabla p,i} + \boldsymbol{f}_{\nabla \cdot \boldsymbol{\tau},i} + \boldsymbol{f}_{\mathrm{Ar},i} + \boldsymbol{f}_{\mathrm{vm},i} + \boldsymbol{f}_{B,i} + \boldsymbol{f}_{\mathrm{Saff},i} + \boldsymbol{f}_{\mathrm{Mag},i} \tag{9.12}$$

where n_p is the number of particles and $\boldsymbol{f}_{pf,i}$ is the sum of all solid-liquid interaction forces involving particle i : drag ($\boldsymbol{f}_{d,i}$), pressure gradient ($\boldsymbol{f}_{\nabla p,i}$), viscous force ($\boldsymbol{f}_{\nabla \cdot \boldsymbol{\tau},i}$), Archimedes force ($\boldsymbol{f}_{\mathrm{Ar},i}$), virtual mass ($\boldsymbol{f}_{\mathrm{vm},i}$), Basset force ($\boldsymbol{f}_{B,i}$), Saffman lift ($\boldsymbol{f}_{\mathrm{Saff},i}$) and Magnus lift ($\boldsymbol{f}_{\mathrm{Mag},i}$). We recall that the effect of the pressure, viscous and Archimedes forces are included directly into the continuous VANS equations, which explains why they are removed from the $\boldsymbol{F}_{pf}$ term.

These equations are solved here using a pressure implicit with splitting of operators (PISO) scheme [136] that was extended to the VANS equations and verified using the method of manufactured solutions, by Blais and Bertrand [37]. A second-order centered scheme is combined with a second-order implicit backward time integration scheme, thus preserving the second-order accuracy of the overall scheme for pressure and velocity in both space and time.

The PISO-IB method, a semi-implicit immersed boundary method developed by Blais *et al.* [41] is used to take into account the rotating impeller. This immersed boundary method is inserted directly within the PISO scheme for the VANS equations and allows the use of unstructured meshes with local refinement. This way, the rotating impeller can be modelled without using sliding mesh techniques, which has the advantage of preserving the mesh topology, thus leading to a faster detection of the particle location within the mesh as well as to a more stable void fraction field.

9.3.3 Solid-liquid coupling

In CFD-DEM, the solid-liquid interaction forces (or coupling), as presented in the previous subsection, are modeled by the expressions given in Table 9.3.

Force	Equation
Pressure gradient - $\boldsymbol{f}_{\nabla p,i}$ Viscous force - $\boldsymbol{f}_{\nabla\cdot\boldsymbol{\tau},i}$ [337]	$-V_p\nabla\bar{p}$ $-V_p\nabla\cdot\boldsymbol{\tau}$
Drag -$\boldsymbol{f}_{d,i}$ Rong model [266]	$\frac{1}{8}C_D d_p^2\rho_f\left\|\bar{\boldsymbol{u}}-\boldsymbol{v}_i\right\|\left(\bar{\boldsymbol{u}}-\boldsymbol{v}_i\right)\epsilon_f^{2-\beta\left(\epsilon_f,Re_p\right)}$ with $\boldsymbol{v}_i$ the velocity of particle i $C_D=\left(0.63+\frac{4.8}{\sqrt{Re_p}}\right)^2$, $\beta\left(\epsilon_f,Re_p\right)=2.65\left(\epsilon_f+1\right)-\left(5.3-3.5\epsilon_f\right)\epsilon_f^2 e^{-\frac{\left(1.5-\log {Re_p}^2\right)}{2}}$, and $Re_p=\frac{\rho_f d_p\left\|\bar{\boldsymbol{u}}-\boldsymbol{v}_i\right\|}{\mu}$
Saffman Lift - $\boldsymbol{f}_{\text{Saff},i}$ Mei model [185, 205, 206]	$J^*1.614\rho_f^{\frac{1}{2}}\mu_f^{\frac{1}{2}}\left(\bar{\boldsymbol{u}}-\boldsymbol{v}_i\right)\times\frac{\boldsymbol{w}}{\left\|\boldsymbol{w}\right\|^{\frac{1}{2}}}$ with $J^*=0.3\left(1+\tanh\left(\frac{5}{2}\left(\log_{10}\sqrt{\frac{w^*}{Re_p}}+0.191\right)\right)\right)$ $\left(\frac{2}{3}+\tanh\left(\sqrt{\frac{w^*}{Re_p}}-1.92\right)\right)$, $\boldsymbol{w}=\nabla\times\bar{\boldsymbol{u}}$, $w^*=\frac{\left\|\boldsymbol{w}\right\|d_p}{\left\|\bar{\boldsymbol{u}}-\boldsymbol{v}_i\right\|}$,

Table 9.3 Expressions for the solid-liquid interaction forces

In particular, the expressions for the Saffman lift force proposed by McLaughin [205] and subsequently by Mei [206] were derived for small values of the particle Reynolds number (Re_p). However, it was shown to be reasonable for $Re_p < 50$ and $w^* < 0.8$ by Loth [184], values which should not be exceeded in the bulk of the flow for the system studied in the present work due to the maximal impeller speed considered (900 RPM). Note that the impact of the void fraction (ϵ_f) on this lift force has not been investigated and it is assumed in the present work that the expression proposed by Mei [206] remains valid with increasing particle concentrations.

It must be noted that the Basset ($\boldsymbol{f}_B$), Magnus lift ($\boldsymbol{f}_{Mag}$) and virtual mass ($\boldsymbol{f}_{vm}$) forces are neglected in the present study.

The Basset force, sometimes referred to as the history force due to its time integral form, is due to the formation of a viscous boundary layer around a particle. For a single particle, it is written as [70] :

$$\boldsymbol{f}_{B,i}=\frac{3}{2}\pi\mu d_p^2\int_0^t\frac{\frac{d\left(\boldsymbol{u}-\boldsymbol{v}_i\right)}{d\theta}}{\pi\nu\left(t-\theta\right)^{\frac{1}{2}}}d\theta \tag{9.13}$$

Since it results from the integration in time along the particle trajectory, the calculation of the Basset force is computationally challenging. This force could have a significant impact only close to the impeller region due to the strong velocity fluctuations that occur in this region [80]. For the geometry considered in the present work, a pitched blade turbine (PBT) with 4 blades, the frequency ξ of the time-varying flow field close to the impeller can be estimated as $\xi = 4N$ with N in revolutions per second. Thus, the ratio between the Basset force and the Stokes drag (for $Re_p < 1$) can be estimated ,using the expressions of Table 9.3, as $\frac{|\boldsymbol{f}_B|}{|\boldsymbol{f}_d|} = 0.1\sqrt{\frac{d_p^2 \mu \xi}{\rho_f}}$, which is 0.5 for the maximum impeller speed (900RPM) considered in this work. However, for this velocity, the particle Reynolds number $Re_p = \frac{\rho_f d_p |\boldsymbol{u}-\boldsymbol{v}|}{\mu}$ in the region of the impeller for the fluid and particle properties given in Table 9.1 is of the order of 50. Therefore, the Stokes law does not apply and the drag coefficient is significantly higher than what is predicted by the Stokes formula. This indicates that the real ratio $\frac{|\boldsymbol{f}_B|}{|\boldsymbol{f}_d|} << 1$ and that the Basset force can be neglected. Finally, we note that the above expression for the Basset force is valid only for a single particle, and the effect on this force of non-dilute concentrations of particles or the Reynolds number has, to our knowledge, not been studied. In other words, it is unknown whether the presence of other particles increases or decreases the value of the Basset force felt by a particle.

The Magnus lift forc is generated by the angular velocity of a particle, as illustrated in Figure 9.2. For a single particle, it is given by the following expression [230] :

$$\boldsymbol{f}_{M,i} = \frac{\pi}{8} d_p^2 \rho_f C_M \left|\boldsymbol{u} - \boldsymbol{v}_i\right| \frac{(\boldsymbol{w} - 2\boldsymbol{\omega}_p) \times (\boldsymbol{u} - \boldsymbol{v}_i)}{|\boldsymbol{w} - 2\boldsymbol{\omega}_p|} \tag{9.14}$$

where $\boldsymbol{w}$ is the vorticity of the fluid and C_M the Magnus coefficient, which depends on Re_p and on the rotational Reynolds number $Re_R = \frac{\mu |\boldsymbol{w} - \boldsymbol{\omega}_{p,i}|}{2 d_p^2 \rho_f}$.

The integration of the Magnus lift force within unresolved CFD-DEM simulations is a complex issue. Although the angular momentum is solved for each particle, the angular motion of the particles (and that of the fluid around it) is not felt by the fluid since the latter is solved at a scale coarser than that of the particles. Moreover, no conservation equation is solved for the vorticity. Consequently, in standard CFD-DEM simulations, the angular velocity of a particle will change only when it comes into contact with an element of the geometry or with another particle. If the Magnus lift force is kept in Eq. (10.8), the angular momentum of the particle will be one-way coupled with the translational momentum of the particle and that of the fluid. Therefore, a freely rotating particle will affect its translational momentum and that of the fluid while maintaining a constant angular momentum, a behavior that is not physical. One way around this would be to add a solid-liquid term on the right-hand side of Eq. (9.3) to account for the viscous (or turbulent) dissipation of the angular momentum

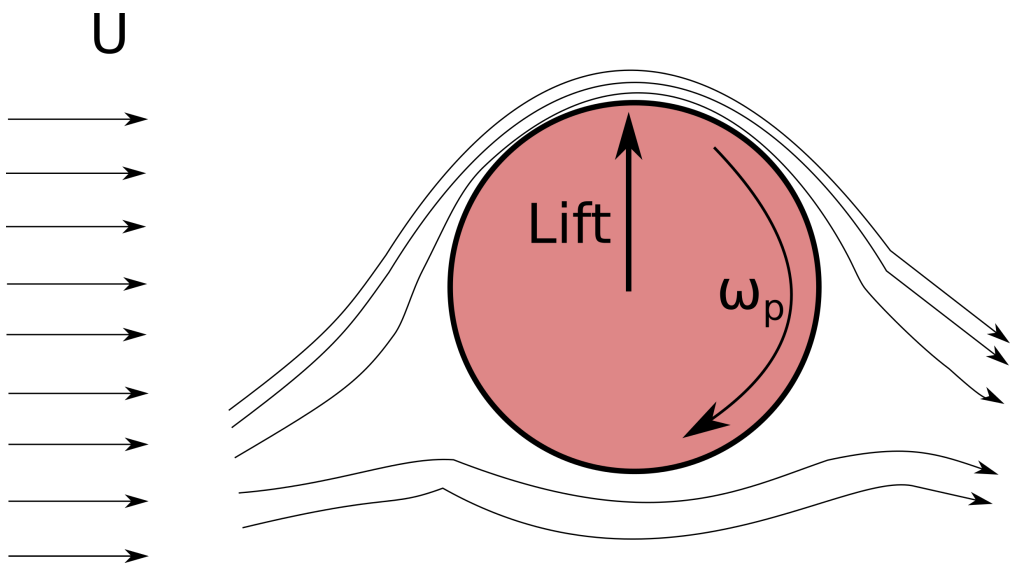

Figure 9.2 Scheme of the Magnus lift force due to the perturbation of the mean flow U caused by the angular motion ω_p of a particle

of the particle due to the presence of the liquid. This may explain why some investigations from the literature, which did not include such a force (*e.g.* Shao *et al.* [276]), have reported surprisingly large contributions of the Magnus force to the solid-liquid mixing dynamics.

Derksen [80] remedied this shortcoming by introducing a so-called solid-liquid torque based on the analytical solution of the flow of a particle rotating in a viscous fluid, as calculated by Dennis *et al.* [77]. The resulting solid-fluid torque is given by :

$$\boldsymbol{M}_{i,pf} = \pi \mu d_p^3 \left(\frac{1}{2} \boldsymbol{\omega} - \boldsymbol{\omega}_p \right) \tag{9.15}$$

This torque can be added on the right hand side of Eq (9.3). However, since we do not solve explicitely for the angular momentum of the fluid, this term cannot be applied on the VANS equations, thus breaking the two-way coupling. Furthermore, we note that the effect of the void fraction on the Magnus lift force and that of the Reynolds numbers (Re_p and Re_R) on this solid-liquid torque have not been established. In fact, the presence of neighbouring particles is expected to affect the magnitude of the solid-liquid torque significantly, as it does for drag (as can be seen in the Rong drag model in Table (9.3)). In this case, the angular velocity of the particles is likely to relax in a very short time, decreasing considerably the effect of the Magnus lift force. Clearly, the issue of the angular momentum coupling in unresolved Euler-Lagrangian models requires further investigation, which is out of the scope of the present work. Consequently, following along the lines of Arolla and Desjardins [11], we did not consider in our CFD-DEM model the Magnus lift force.

The virtual mass force manifests itself as additional inertia due to the displacement of the fluid caused by the motion of a particle, as illlustrated in Figure 9.3. It can be expressed as :

$$\boldsymbol{f}_{\mathrm{vm},i} = \frac{\rho_f V_p}{2} \frac{\partial}{\partial t} \left(\boldsymbol{u} - \boldsymbol{v}_i \right) \tag{9.16}$$

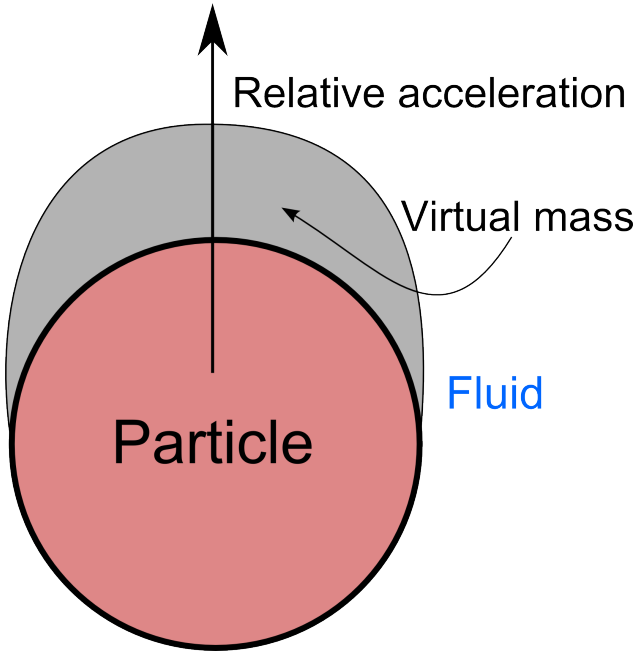

Figure 9.3 Scheme of the virtual mass force, adapted from Crowe *et al.* [70]

Although negligible if the suspending fluid is air, this force is of greater importnace in the case of a liquid. However, as noted by Arolla and Desjardins [11], no expression has been developed for this force in the case of non-vanishing Re_p or non-dilute particle concentrations. Consequently, the contribution of this force to the solid-liquid dynamics was not taken into account in our model.

We note that authors such as Derksen [80] have implemented the virtual mass by adding $\pi \rho_f \frac{d_p^3}{12}$ to the inertia of the particles on the left side of Eq. (9.2). We believe this is not an adequate implementation of this force as it does not take into account the time derivative of the fluid velocity and is not two-way coupled.

Work is definitely required to design a virtual mass expression that is valid for a wide range of solids concentrations and particle Reynolds numbers.

9.4 Determination of the just-suspended speed and the fraction of suspended particles

In this section, the methods used in the current work to evaluate the just-suspended speed and the fraction of suspended particles by means of a Euler-Lagrange model are presented. Two novel methods are introduced. The first one, the so-called Lagrangian suspended fraction analysis technique (in two variants : LSFA-$\Delta\boldsymbol{x}$ and LSFA-Δz), is based on the analysis of the motion of each individual particle. The second one, dubbed the decorrelated fraction analysis (DFA) technique, makes use of the mixing index introduced by Doucet *et al.* [88] to quantify the degree of decorrelation between the particles with respect to time. The pressure gauge technique, as proposed by Micale *et al.* [210], is first presented in detail since it is used extensively in this work. Other methods from the literature are also briefly introduced. A thorough review of the methods available to measure N_{js} can be found in Tamburini *et al.* [297] and Kasat and Prandit [149].

9.4.1 Pressure gauge technique

The pressure gauge technique measures the fraction of suspended particles by correlating it with the increase of the static pressure at the bottom of the vessel [53, 210].

More precisely, as the particle bed is eroded and the suspension process begins, the apparent density of the liquid increases as particles are dragged by the liquid, which results in an increase of the hydrostatic pressure at the bottom of the tank. Once all the particles have been suspended, the apparent density and the hydrostatic pressure level off to a constant value. Consequently, the fraction of suspended particles can be obtained from the increase of the hydrostatic pressure (ΔP_{susp}). Given that the probe measures the total pressure at the bottom of the tank, and the increase of the impeller velocity increases the dynamic component of this pressure, it is necessary to extract the static pressure from this total pressure. By fitting a second order polynomial curve ($\Delta P = aN^2 + b$) on the pressure measurement past the inflexion point on the total pressure curve, it is possible to subtract the dynamic component of the pressure from the total pressure and thus deduce the variation of the hydrostatic pressure (ΔP_{susp}). The fraction of suspended solids (X_{susp}) can also be obtained straightforwardly from the variation of the hydrostatic pressure. The reader is referred to the work of Micale *et al.* [210] or to our recent work [40, 173] for more details.

This measurement method can be easily applied to CFD-DEM simulation results. Indeed, we showed that, in the laminar and transitional regimes, the total pressure at the bottom of the tank can be obtained from unresolved CFD-DEM simulations by averaging the pressure

within a ring at the bottom of the vessel [40]. Our results revealed that the fraction of suspended solids predicted with the same CFD-DEM model used in the current work compared well to our experimental data [173].

9.4.2 Lagrangian suspended fraction analysis (LSFA) technique

It is often mentioned in the literature (*e.g.* [297]) that Euler-Lagrange simulations of solid-liquid mixing should allow for a natural interpretation of Zwietering criterion. We recall that, according to Zwietering [339], N_{js} corresponds to the impeller speed at which no particle remains motionless at the bottom for more than 1 or2 s.

However, translating this relatively heuristic definition to an objective criterion based on a Lagrangian description of the particles is not straightforward. This criterion consists of observing each particle at the bottom of the tank - that is a particle in contact with either the tank bottom or the particle bed - within a time window (Δt_{js}), and considering that a particle is suspended if it has moved a certain distance either in any direction ($\Delta \boldsymbol{x}_{js}$) or along the axial direction (Δz_{js}) of the tank. The use of either $\Delta \boldsymbol{x}_{js}$ (LSFA-$\Delta \boldsymbol{x}$) or Δz_{js} (LSFA-Δz), the latter being a harsher criterion, is debatable. However, $\Delta \boldsymbol{x}_{js}$ appears to be closer to industrial needs. For instance, a particle can remain very close to the vessel bottom, but circulate and be in contact with constantly renewed fluid, thus allowing efficient mass transfer. Both approaches will be considered in the present work and their efficiencies will be compared. Figure 9.4 illustrates the different cases that may occur over a time duration Δt_{js} with the LSFA-Δz approach. The LSFA-$\Delta \boldsymbol{x}$ approach is identical with the exception that the displacement is in all directions ($\mathbb{R}^3$) instead of solely along the $\boldsymbol{z}$ axis.

Defining values for Δt_{js} and Δz_{js} or $\Delta \boldsymbol{x}_{js}$ is not trivial since multiple time scales and length scales co-exist within the stirred tank. On the basis of Zwietering's original definition, it seems appropriate to define $\Delta t_{js} \in [0.5, 3]$. Furthermore, since the suspension process is intuitively linked to the diameter of the particles, Δz_{js} (or $\Delta \boldsymbol{x}_{js}$) should be defined accordingly ; a possible choice is then $\Delta z_{js} = \kappa d_p$, with $\kappa \in [0.5, 5]$. This will be investigated in the present work.

9.4.3 Decorrelated fraction analysis (DFA) technique

The decorrelated fraction analysis technique uses the weak mixing index introduced by Doucet *et al.* [88] to measure the degree of suspension of the particles.

This index quantifies the efficiency of mixing operations using the Lagrangian trajectories of particles (or massless tracers). It is based on a principal component analysis (PCA) [279],

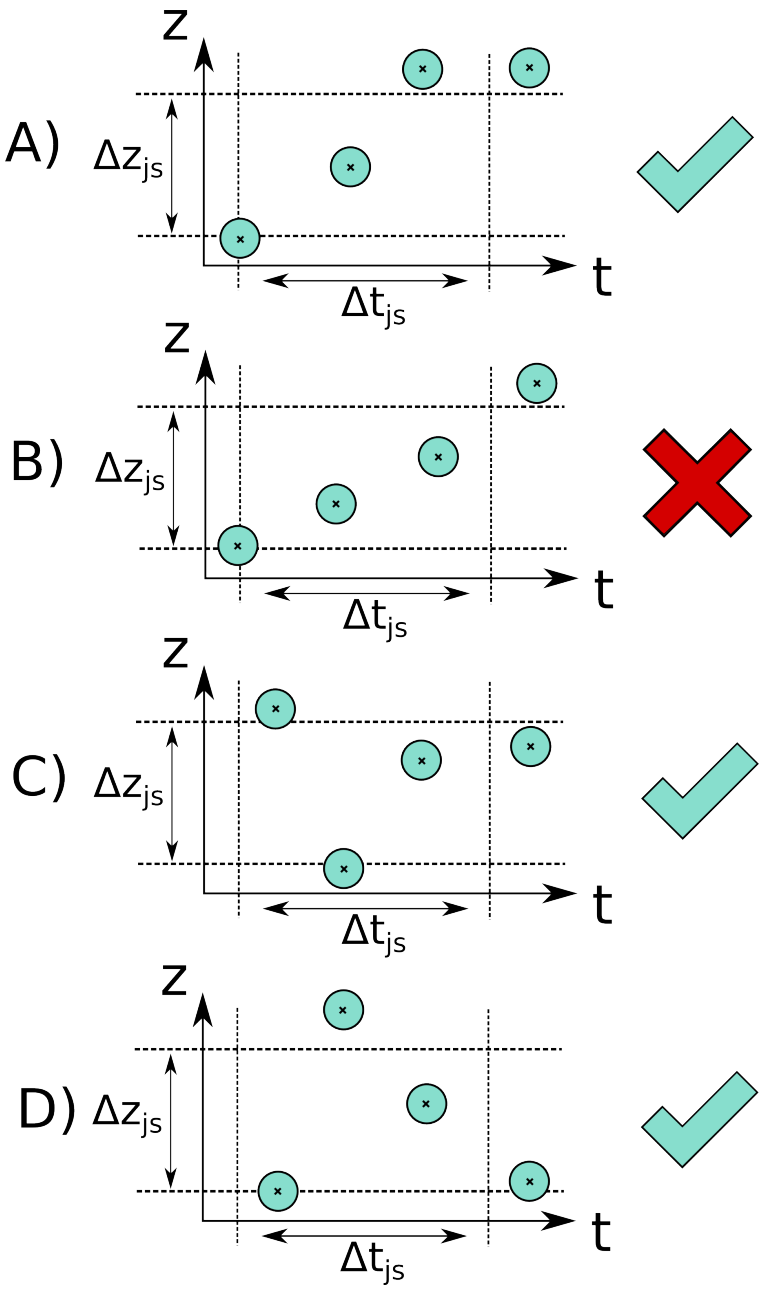

Figure 9.4 Scenarios that may occur over a time duration Δt_{js} with the Lagrangian suspended fraction analysis technique : (A) the particle is sufficiently lifted up from the bottom, (B) the particle is unsufficiently lifted up from the bottom, (C) the particle settles during the time window and is displaced unsufficiently, and (D) the particle is first lifted up and then settles to the tank bottom

which measures the correlation between the position of all particles at time t ($\boldsymbol{x}_t$) and their position at time t_0 ($\boldsymbol{x}_{t_0}$) (weak index). The position can be supplemented by particles properties (*e.g.* size, shape, density), leading to the strong mixing index [88].

The PCA results in the solution of an eigenvalue problem for a $d \times d$ system of equations, where d is the number of dimensions considered. The mixing index is calculated by normalizing the largest eigenvalue ($\lambda_k = \max(\lambda_j)$, with $j \in [1, d]$) with respect to its initial value. If this eigenvalue decreases to a constant that is not asymptotically zero, the system is considered to be poorly mixed along the direction corresponding to the eigenvector associated with λ_k. However, this condition is a necessary but not sufficient condition for a system to be well-mixed. In other words, an asymptotically decreasing mixing index ($\lambda_k \to 0$) does not necessary imply a well-mixed system, whereas a non-zero value ($\lambda_k \to C > 0$) reveals that the system does not mix well, depending on how C is close to zero. The reader is referred to [38] for more details.

The mixing index can be used to measure the degree of suspension in stirred tanks. At time $t_0 + \Delta t_{js}$, only a particle that was already in a suspended state or that was suspended during this time interval can have its position decorrelated from that at time t_0. Otherwise, if a particle remains unsuspended, then its actual position still correlates to its initial one. The value of the normalized eigenvalue (λ_k) is thus linked to the fraction of unsuspended particles, assuming that once a particle gets suspended, it is also considered distributed or mixed. This is a plausible hypothesis in the turbulent regime due to the presence of unsteady turbulent structures. The mixing index analysis in this work is carried out in cylindrical coordinates ($[\boldsymbol{e}_r, \boldsymbol{e}_\theta, \boldsymbol{e}_z]$) since this is the most appropriate coordinate system to represent the motion of particles in a stirred tank.

9.4.4 Tangent-intersection analysis (TIA) technique

The tangent-intersection analysis (TIA) technique [129] is based on the evaluation of the average solids concentration on a plane at a height 1 mm above the tank bottom. The mean solids concentration is plotted as a function of the impeller speed and two tangents lines to the curve are drawn where the slope is minimum and maximum. N_{js} is then defined as the speed at which these two lines intercept.

9.4.5 Local particle concentration technique

In this method introduced by Bourne and Sharma [45], the particle concentration is measured as a function of the impeller speed in a zone below the impeller but above the top of the bed

of particles. This fraction, initially small, increases with the impeller speed as the number of suspended particle increases. Above a certain impeller speed, the particles at the vessel bottom get all suspended. Past this point, further increasing the impeller speed only increases the homogeneity of the suspension, which results in a decrease of the particle concentration in the measurement zone. Bourne and Sharma [45] define the just-suspended speed N_{js} as the impeller speed at which this change occurs.

9.4.6 Transient solids concentration technique

Kee and Tan [150] monitored the solids volume fraction in the cells in contact with the vessel bottom and proposed to identify N_{js} as the impeller speed at which the solids concentration at all points above the vessel bottom reaches a steady-state value smaller than 50% of the initial packed volume fraction ($\epsilon_{p,m}$). According to these authors, if all cells above the impeller bottom reach such a constant steady-state value, it is reasonable to consider that the quantity of solids circulating in the tank does not fluctuate with time. Furthermore, if particles accumulate at the bottom of the tank, those regions will have a volume fraction larger than $0.5\epsilon_{p,m}$, thus violating the criterion.

9.4.7 Power number technique

This method is based on the analysis of the variation of the power number ($N_p = \frac{P}{\rho_f D^5 N^3}$, with P the power consumption) with the increase of the impeller speed. Different authors have observed varying trends for N_p as N increases, as reviewed by Tamburini *et al.* [293]. In particular, Rewatkar *et al.* [259] noted a decrease of N_p when N is below N_{js}, which they related to the reorganization of the particles in the bed. Then, they observed a sudden increase of N_p due to the increase of the apparent density caused by the suspended particles, until a constant N_p was reached. Other authors, such as Rghava Rao *et al.* [255] and Michelleti [213] obtained a monotonically increasing value of N_p with N until a plateau is reached. Rhagava Rao *et al.* [255] and Rewatkar [259] proposed to define N_{js} as the speed at which this plateau was attained, since, above this point, the apparent density of the suspension remains constant.

9.5 Methodology

In this section, the methodology used for both experiments and simulations are described in detail.

9.5.1 Experimental set-up for the PGT measurements

The experimental rig used is presented in Figure 9.1 of Section 9.2. In this rig, the pressure is measured by means of a Freescale sensor (MPX5010DP), with a precision of 5%, connected to a tube which is in turn connected to a hole at the bottom of the tank. This allows for the recording of the evolution of the pressure with time. The end of the tube at the bottom of the tank is fitted out with a thin screen, which prevents clogging and dims the effects of the variation of the dynamic pressure due to turbulent fluctuations, thereby reducing the noise level in the total pressure measurements. The experiments were carried out four times in order to assess the repeatability and estimate the errors on the measurements by means of confidence intervals. One seperate experiment where the impeller speed was ramped up and down revealed no hysteresis in the measurements.

9.5.2 Simulation set-up

Simulations were carried out using the unresolved CFD-DEM model presented in Section 9.3. The model parameters used are given in Table 9.4. The same mechanical properties are given to both the walls and the particles. These mechanical properties were taken from the work of Di Renzo and Di Maio [87], Di Renzo *et al.* [85] and Shao *et al.* [276] for glass beads suspended in a liquid. To reproduce the size distribution of the particles that were used experimentally, 10 different diameters d_p were considered ranging from 2.66 to 3.5 mm. A total of 130 000 particles were required to reach the mass fraction of 10%.

The background hexahedral mesh generated for the CFD part consisted of 33x136x90 (r,θ,z) cells with local mesh refinement in the swept volume of the impeller and close to the free surface, the tank walls and the baffles, for a total of 1.2M fluid cells. It was found that mesh refinement past this level did not lead to measurable changes in the torque ($< 1\%$) for single phase flows. The maximal Courant-Friedrichs-Lewy condition for all simulations was below 0.70, which means stable solutions were obtained. The time step for the DEM particles was below 15% of the characteristic time of Rayleigh waves ensuring the stability of DEM results. We recall the expression for the characteristic time of the Rayleigh waves (Δt_{Ra}) [182] :

$$\Delta t_{Ra} = \frac{\Pi}{2} d_p \sqrt{\frac{\rho_p}{G}} \left(\frac{1}{0.1631\nu + 0.8766} \right) \tag{9.17}$$

The simulations were carried out on the Colosse cluster of Calcul Québec. Each simulation used 4 Intel Xeon X5560 quad-core 2.8 GHz processors distributed on two nodes (total of 16 cores) with 12 GB of memory available for each processor (48 GB total). The memory required for the simulations was less than 10GB. The simulations required from 2 to 3 weeks

of computational time depending on the time steps used.

9.6 Results and discussion

In this section, the flow patterns and the distribution of particles obtained with the LES-based unresolved CFD-DEM model described in Section 9.3 are discussed. Then, the model is validated by comparing the fraction of suspended particles measured in our lab using the pressure gauge technique (PGT) to the results obtained with the unresolved CFD-DEM model. More precisely, the results from the Lagrangian suspended fraction analysis (LSFA-$\Delta\boldsymbol{x}$ and LSFA-Δz) and the decorrelated fraction analysis (DFA) techniques are compared to the PGT data. Finally, the potential of all methods described in Section 9.4 to predict N_{js} (and N_{ss}) with respect to Zwietering correlation is assessed.

9.6.1 Flow patterns and solids distribution

The flow profiles were phase averaged over a period of 6 s for a relatively large number of impeller revolutions (10 at the lowest impeller speed investigated (100 RPM) and 90 at 900 RPM) on two planes :

- $\boldsymbol{P}_y$: normal vector $[0\ 1\ 0]^T$ and centered at (0 0.005 0). This plane is adjacent to the baffles ;
- $\boldsymbol{P}_{xy}$: normal vector $[1\ 1\ 0]^T$ and centered at (0 0 0)

These planes are illustrated in Figure 9.5.

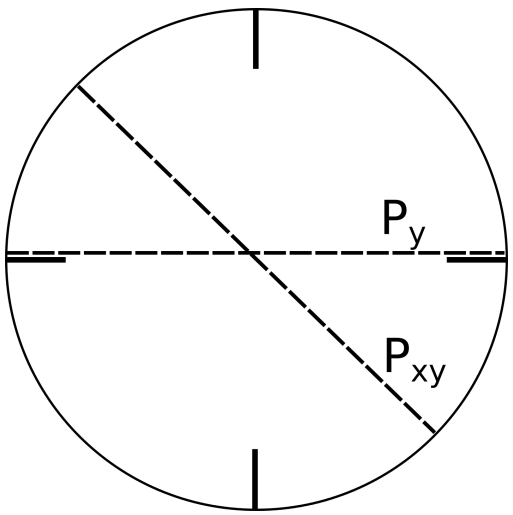

Figure 9.5 Illustration of the planes on which the phase averaging was carried out.

Symbol	Name	Value
Y	Young's modulus	100 MPa
e_r	Coefficient of restitution	0.9
ν	Poisson ratio	0.25
μ_f	Coefficient of friction	0.3
μ_r	Rolling friction	0.1
Δt_{DEM}	DEM time step	5×10^{-6}
$\Delta t_{CFD,N\leq 225}$	CFD time step	2×10^{-4}
$\Delta t_{CFD,N\in[250,450]}$	CFD time step	1×10^{-4}
$\Delta t_{CFD,N>450}$	CFD time step	5×10^{-5}
$\Delta t_{c,N\leq 225}$	Coupling time step	2×10^{-4}
$\Delta t_{c,N\in[250,450]}$	Coupling time step	1×10^{-4}
$\Delta t_{c,N>450}$	Coupling time step	5×10^{-5}

Table 9.4 Parameters for the solid-liquid mixing simulations

Figure 9.6 shows the phase averaged void fraction ϵ_f at 500 RPM, a speed at which the experiments and the PGT results (shown in Figure 9.11 and discussed later) indicate a fully suspended state.

Zones of higher concentration can be identified at the wall-bottom junction. Their locations coincide with the zones where the last particles were observed to get suspended in the experiments.

Figure 9.7 presents the void fraction ϵ_f at $N = 900$ RPM, the maximum impeller speed investigated in the present work. It can be seen that even at such a high impeller speed, the particle concentration is not homogeneous in the tank. More precisely, it is higher in the near-baffle region where the particles are dragged upward along the tank wall. A toroid can also be observed below the impeller, within which the particle concentration approaches zero. Albeit slightly visible at $N = 500RPM$ (Figure 9.6), this structure is enhanced significantly at $N = 900$ RPM (Figure 9.7). We believe that this phenomenon is due to the presence of a high-vorticity toroid-like turbulent structure, which expels the particles.

The contours in Figure 9.8 show the phase averaged void fraction in the $\boldsymbol{P}_y$ plane at impeller speeds of 100 RPM, 200 RPM, 300 RPM, while the velocity magnitude profiles at the same impeller speeds are presented in Figure 9.9. At low speed ($N = 100$ RPM), the kinetic energy is insufficient to erode the particle bed. For the impeller, the particles at the bottom of the tank are like a rigid volume, which leads to more radial flow patterns where the magnitude of the velocity is only significant above the bed. Increasing the impeller speed eventually leads to the deformation of the particle bed, in reaction to the fluid jet induced by the PBT. The motion of the particles in turn alters the fluid flow patterns, the magnitude of which become

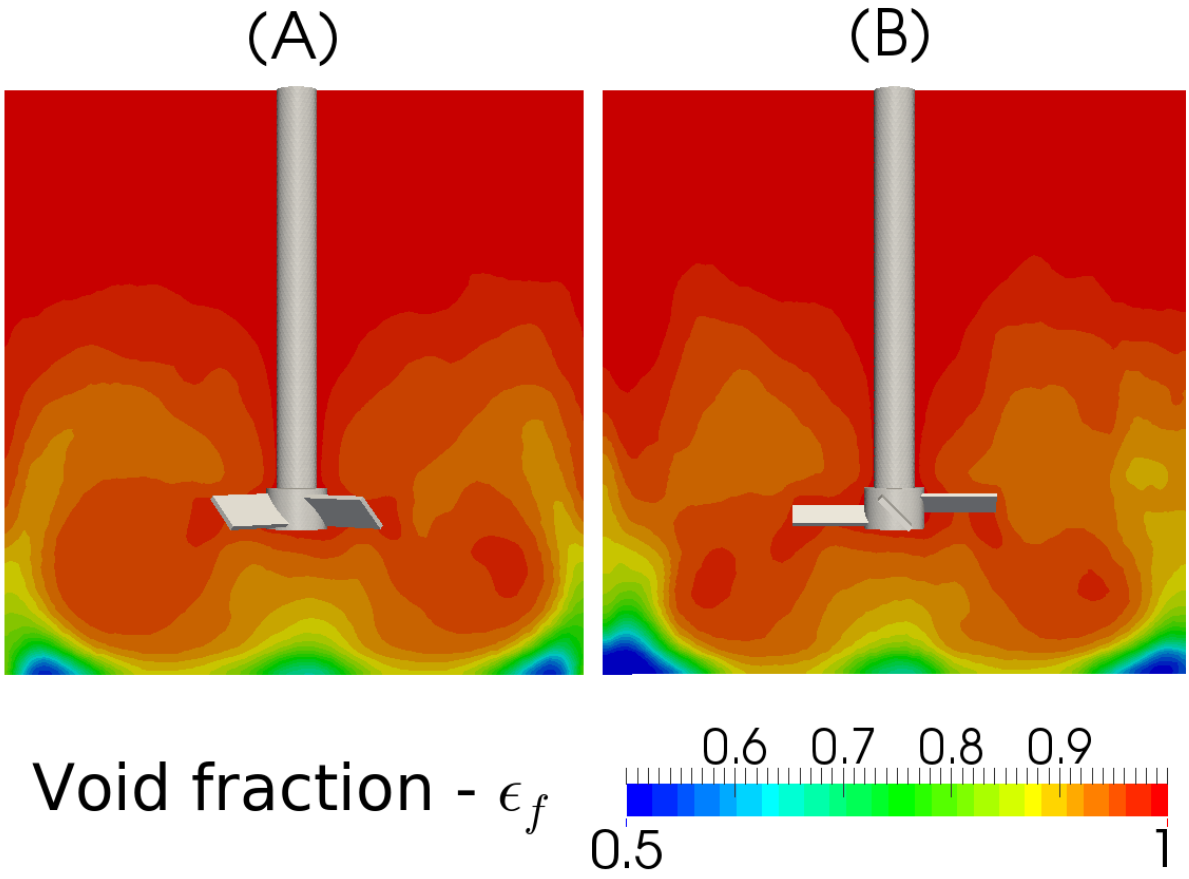

Figure 9.6 Phase averaged void fraction (ϵ_f) for $N = 500$RPM on the (A) $\boldsymbol{P}_{xy}$ and (B) $\boldsymbol{P}_y$ planes.

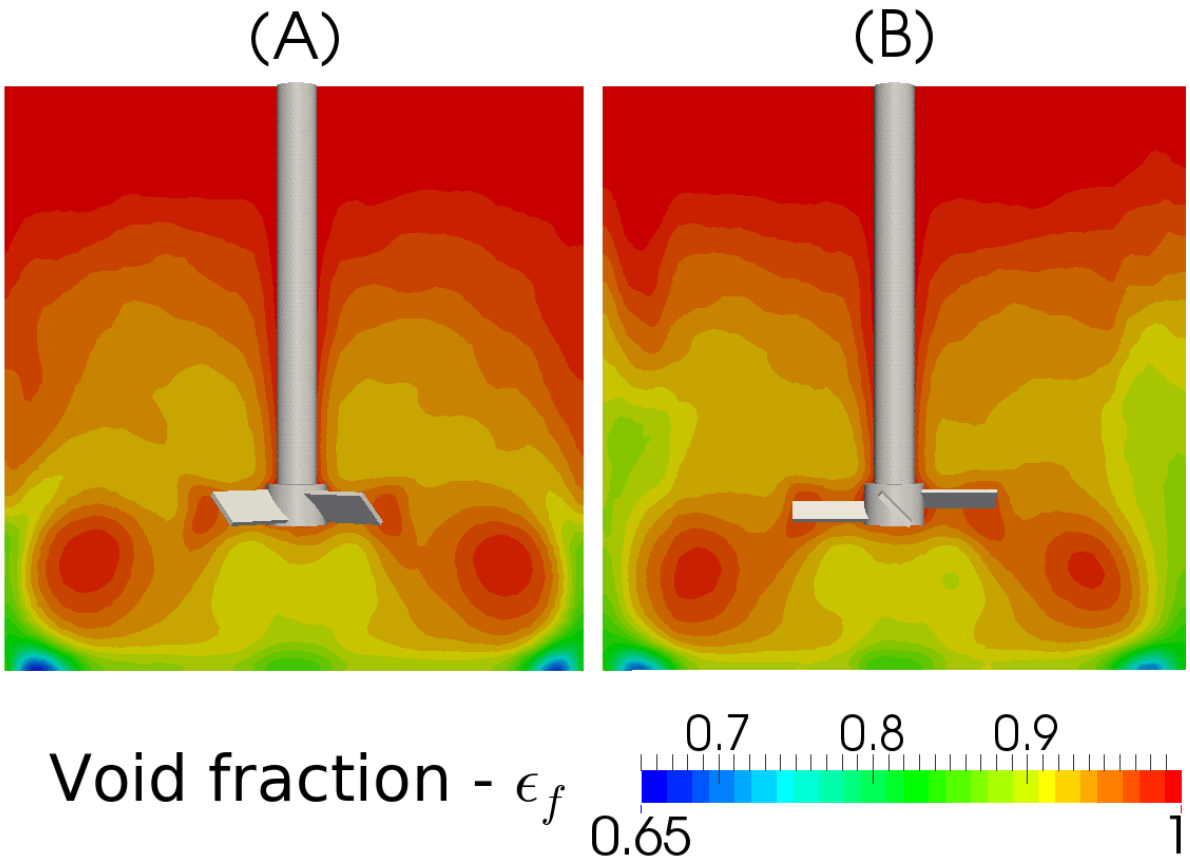

Figure 9.7 Phase averaged void fraction (ϵ_f) for $N = 900$RPM on the (A) $\boldsymbol{P}_{xy}$ and (B) $\boldsymbol{P}_y$ planes.

more and more significant at the bottom of the impeller. Consequently, the discharge of the impeller becomes more and more axial as the impeller speed is increased and the particle bed is eroded. At $N = 300$ RPM, the particles at the center of the vessel are all in motion, since the volume fraction of fluid (ϵ_f) is way above the fluid fraction at the maximal solids packing ($\epsilon_f = 1 - \epsilon_{p,m} = 0.36$), and the flow patterns are fully axial. The unsuspended particles are mainly located at the wall-bottom junction. At higher impeller speed, the velocity profile is not altered significantly and remains principally axial.

It is interesting to observe where the relative velocity between the particles and the fluid (characterized by the particle Reynolds number $Re_p = \frac{\rho_f d_p |\bar{\boldsymbol{u}} - \boldsymbol{v}|}{\mu}$) is significant. Figure 9.10 shows the value of Re_p for $N = 900$ RPM in the $\boldsymbol{P}_{xy}$ and $\boldsymbol{P}_y$ planes, which is the velocity at which the maximal values of Re_p were observed. Re_p appears to be relatively large in small regions close to the impeller, the baffles and the tank bottom. Elsewhere, the positive values of Re_p are only due to the action of gravity that pulls the particles down. It can be concluded that, on average, slip between the liquid and solid phases only occurs due to the components of the geometry, with the impeller and the baffles playing the most important role.

9.6.2 Suspension curves and just-suspended speed

In this section, the CFD-DEM model is validated for the fraction of suspended solids. Then, various ways to obtain suspension curves and the just-suspended speed are investigated. An extensive comparison between all these techniques is carried out.

Pressure gauge technique : experimental and numerical investigation

The graph in Figure 9.11 shows the fraction of suspended particles as a function of the impeller speed for both the experiments and the simulations. The error bars represent a 95% confidence interval established with a two-sided Student distribution. Due to the limited number of repetitions of each experiment (4 times), these errors are 2.78 times the standard deviation, which explains the relatively large error bars in Figure 9.11.

It can be seen that the CFD-DEM model is able to predict the speed at which full suspension is achieved with remarkable accuracy. However, at low speed ($N \leq 200$ RPM), the model appears to underestimate the fraction of suspended particles by the order of 10%. However, all the data with the exception of $N = 175$ RPM are within the error bars. Overall, we note that the transition from a fully sedimented state to a fully suspended state is sharper for the numerical model than what is measured experimentally. This difference could be due to unresolved hydrodynamic effects related to the use of the VANS equations and the LES

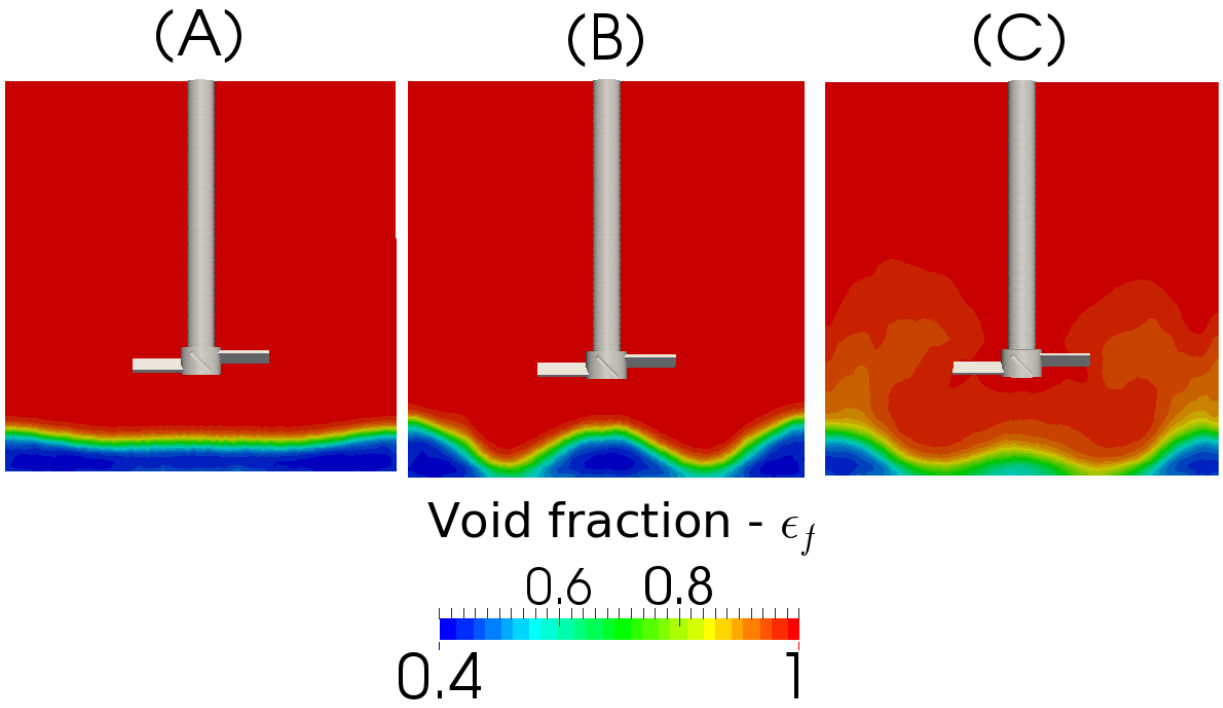

Figure 9.8 Phase averaged void fraction (ϵ_f) on the $\boldsymbol{P}_y$ plane for (A) $N = 100$ RPM, (B) $N = 200$ RPM and (C) $N = 300$ RPM.

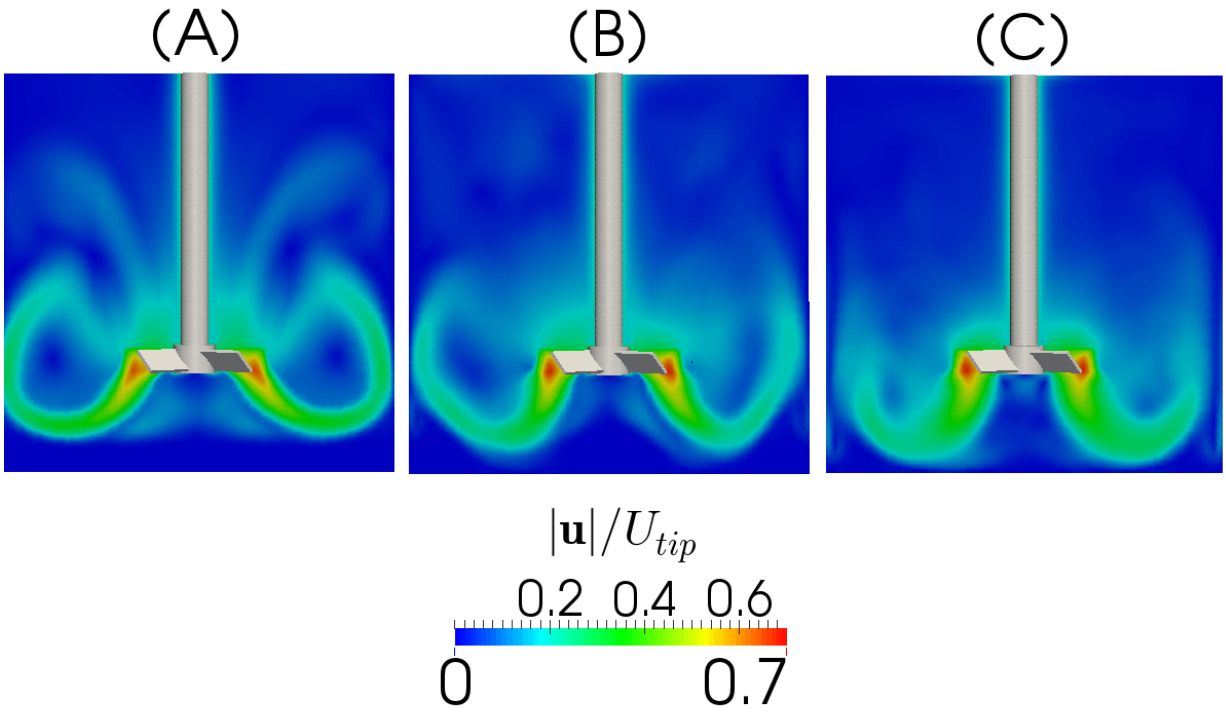

Figure 9.9 Phase averaged velocity magnitude ($|\bar{\boldsymbol{u}}|$) on the $\boldsymbol{P}_y$ plane for (A) $N = 100$ RPM, (B) $N = 200$ RPM and (C) $N = 300$ RPM.

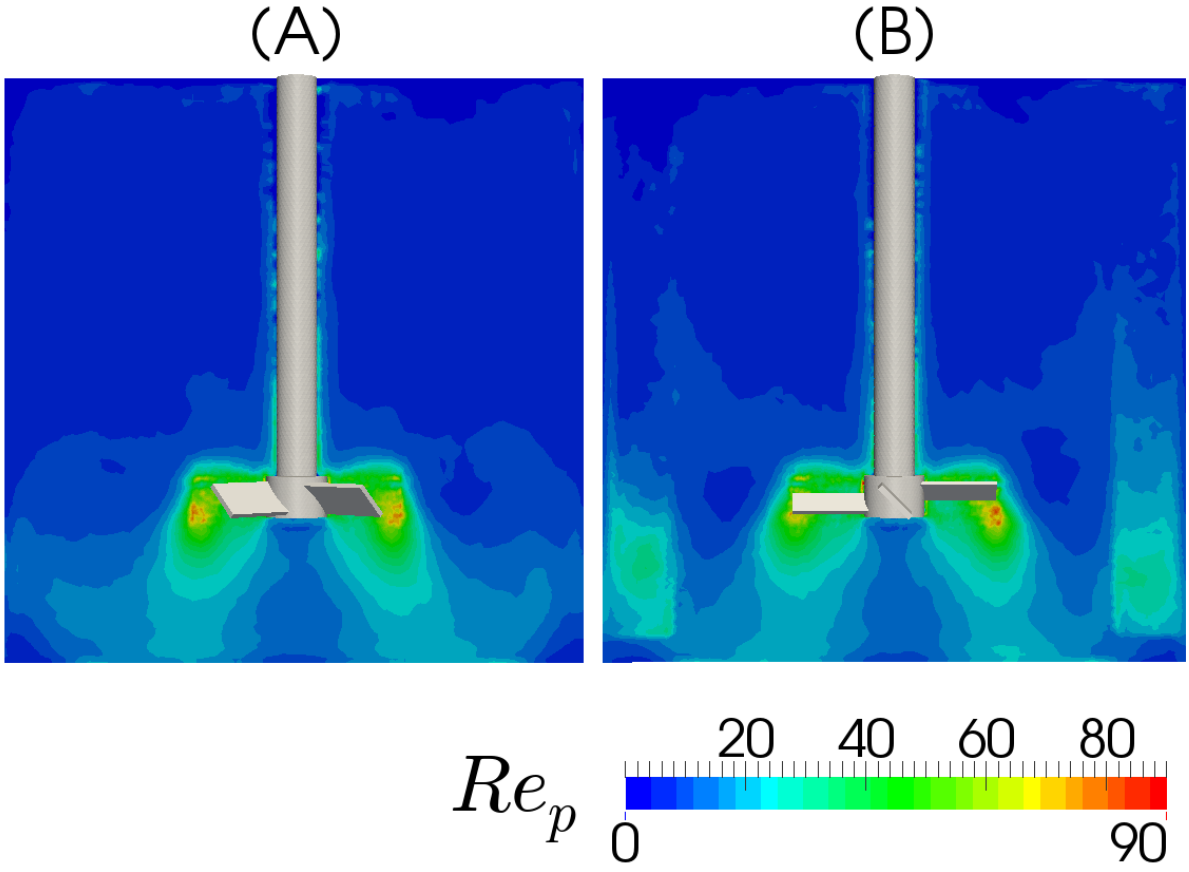

Figure 9.10 Phase averaged Re_p values for $N = 900$ RPM on the (A) $\boldsymbol{P}_{xy}$ and (B) $\boldsymbol{P}_y$ planes.

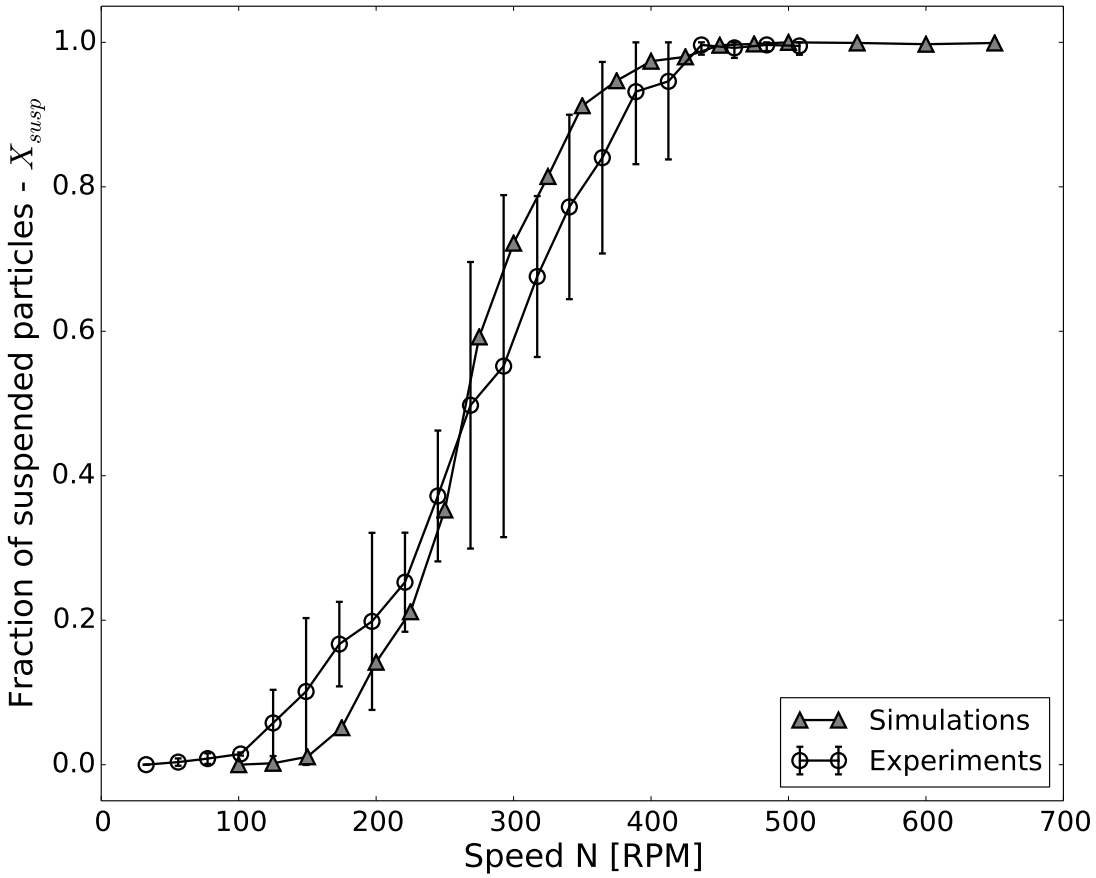

Figure 9.11 Comparison of the experimental and numerical suspension curves after application of the PGT procedure and the removal of the dynamic pressure component. The error bars represent a 95% confidence interval.

sub-grid closure model (see section 9.3.2).

Lagrangian suspended fraction analysis technique

As described in Section 9.4, translating Zwietering criterion to an objective metric that can be reproduced numerically is not straightforward, mainly due to the need of defining a time observation window (Δt_{js}) as well as a minimal displacement ($\Delta \boldsymbol{x}_{js}$) or ($\Delta z_{js}$) for a particle to be considered suspended. The graph in Figure 9.12 contains typical suspension curves obtained via $LSFA - \Delta \boldsymbol{x}$ at steady-state using observation windows (Δt_{js}) up to 3 s, for various impeller speeds and a minimal displacement of $\Delta \boldsymbol{x}_{js} = d_p$.

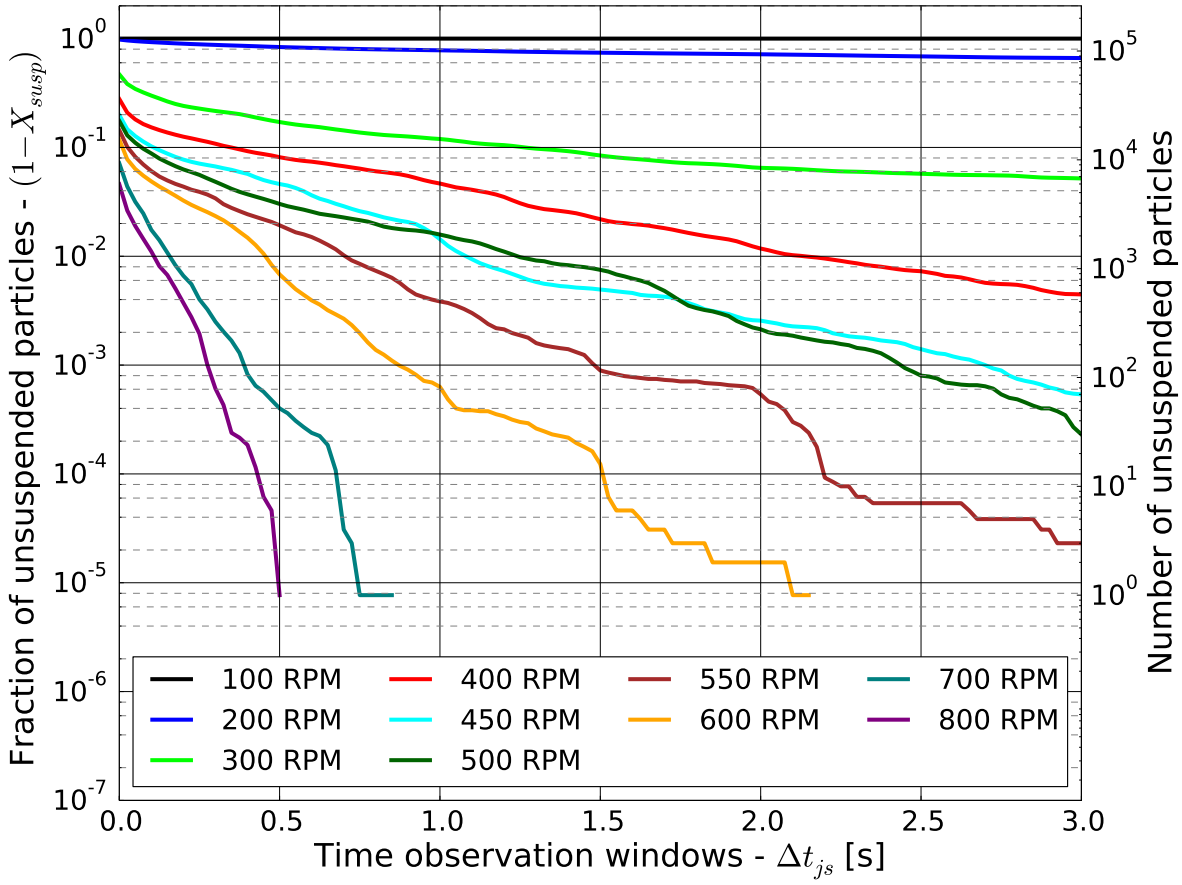

Figure 9.12 Evolution of the fraction of unsuspended particles calculated via LSFA-$\Delta \boldsymbol{x}$, as function of time, for various impeller speeds (N) and $\Delta \boldsymbol{x}_{js} = d_p$.

For all values of N, the fraction of unsuspended particles initially tends to change abruptly,

then decreases monotonically with time. These results also show that the fraction of suspended solids defined through this approach is sensitive to the choice of Δt_{js}. In order to remain within the scope of Zwietering's original definition, the time window should be taken as $\Delta t_{js} \in [0.5, 3]$.

We notice that for large impeller speeds ($N \geq 600RPM$), all particles get suspended very quickly. For $N \geq 450$, more than 99.7% of the particles get suspended within 2 s. In other words, increasing N above 450 RPM has no real benifits. An analysis with LSFA-Δz (not shown here) leads to similar results, although with larger fractions of unsuspended solids for each impeller speed.

The graphs in Figure 9.13 and 9.14 show the evolution of the fraction of suspended particles as a function of impeller speed N for various values of Δt_{js} and Δz_{js}, as evaluated with LSFA-$\Delta \boldsymbol{x}$ and LSFA-Δz, respectively.

We observe that all trends are similar and take the form of a Weibull (or S-shaped) function akin to what can be observed with the PGT results. Furthermore, for both LSFA-$\Delta \boldsymbol{x}$ and LSFA-Δz, increasing Δt_{js} increases X_{susp} whereas increasing $\Delta \boldsymbol{x}_{js}$ (or Δz_{js}) decreases X_{susp} without affecting the shape of the curve, except the sharpness of the transition and the speed at which the fully suspended plateau is reached. In particular, the effect of Δt_{js} is more pronounced than that of $\Delta \boldsymbol{x}_{js}$, indicating that once particles get suspended, they move significantly. All the curves converge to 1 for large enough values of N. Although the onset of the suspension is similar for LSFA-$\Delta \boldsymbol{x}$ and LSFA-Δz, the LSFA-Δz results seem to consistently underpredict the fraction of suspended particles for $N > 450$ RPM, when compared to the PGT results. In such a case the PGT and LSFA-$\Delta \boldsymbol{x}$ result indicate full suspension, at least for many values of Δt_{js} and Δx_{js} whereas the LSFA-Δz results tend to predict non-negligible amount of unsuspended particles. This is due to the presence of moving particles close to the vessel bottom, which are considered suspended by LSFA-$\Delta \boldsymbol{x}$ and the PGT, but which suffer from poor axial velocity and are not considered as suspended with LSFA-Δz. These particles are located close to the tank walls in the zones of higher concentration identified in Section 9.6.1.

The LSFA-$\Delta \boldsymbol{x}$ results agree more nicely with the PGT. The method can predict adequately the fraction of suspended particles over a large range of impeller speeds and, although it seems to slightly overpredict X_{susp} for $N \in [200, 400]$, the results obtained with this technique remain within the confidence intervals.

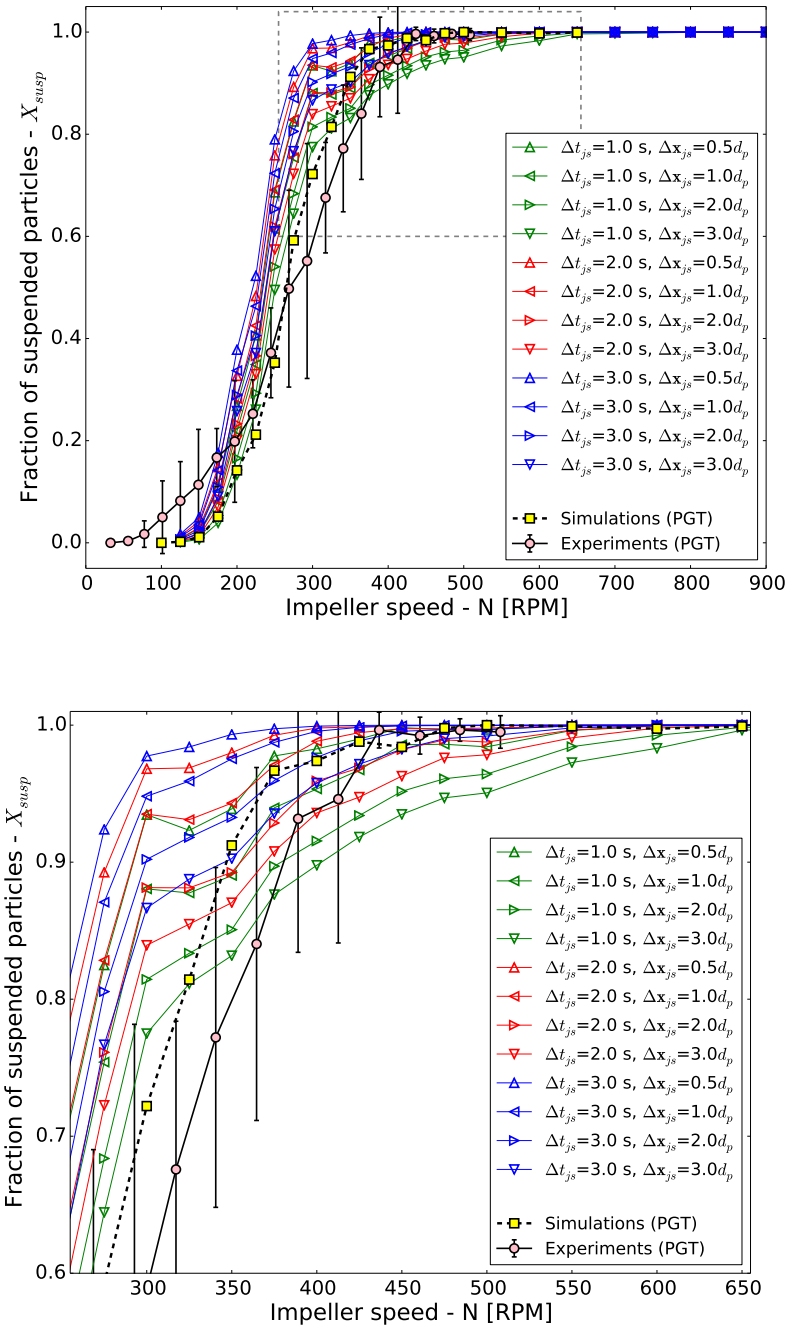

Figure 9.13 (Top) Fraction of suspended particles measured by LSFA-$\Delta \boldsymbol{x}_{js}$ as a function of the impeller velocity (N), and comparison with the PGT results, and (Bottom) zoom-in onto the area delimited by the grey rectangle in (Top).

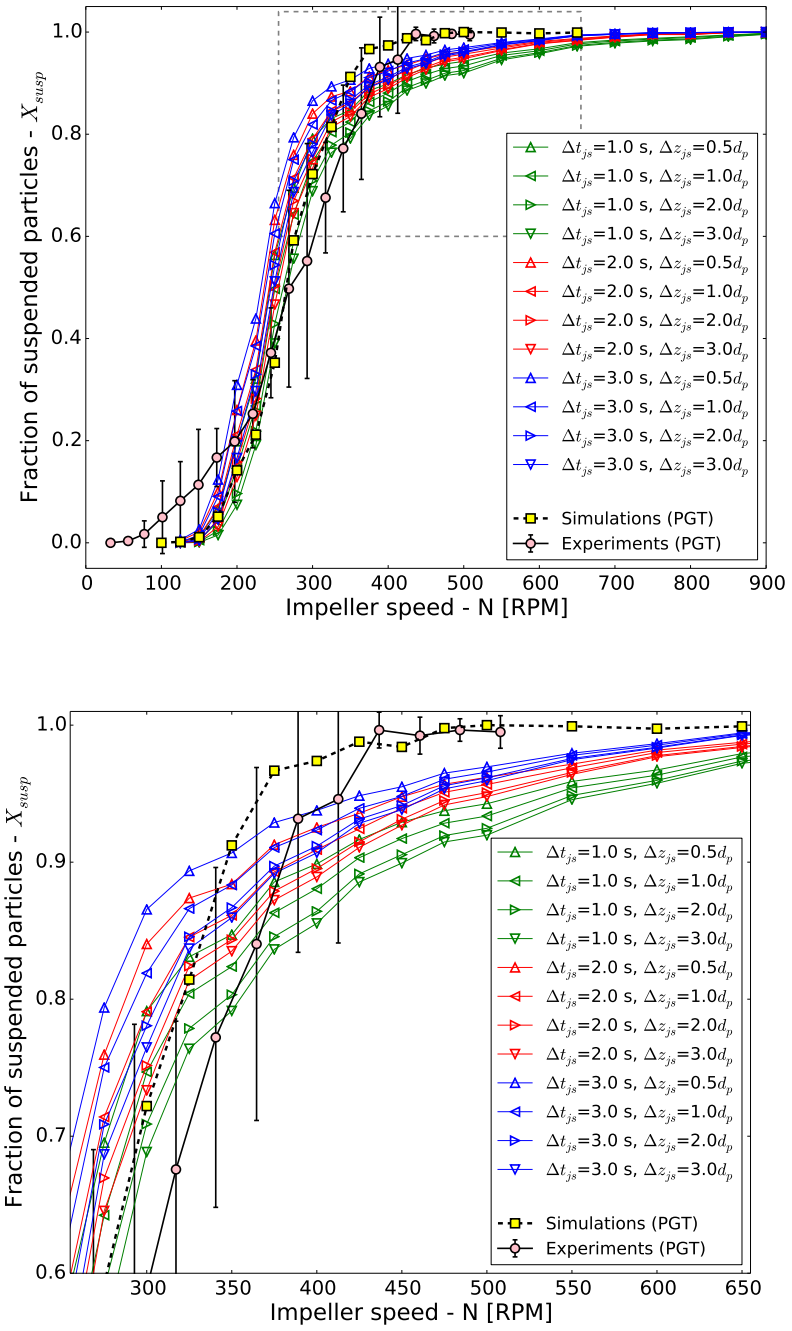

Figure 9.14 (Top) Fraction of suspended particles measured by LSFA-$\Delta \boldsymbol{z}_{js}$ as a function of the impeller speed (N), and comparison with the PGT results, and (Bottom) zoom-in onto the area delimited by the grey rectangle in (Top).

Decorrelated fraction analysis

By comparison with the LSFA technique, the decorrelated fraction analysis (DFA) approach only requires the selection of an observation time Δt_{js}. The graph in Figure 9.15 compares the results obtained with the DFA to the PGT experimental and simulations.

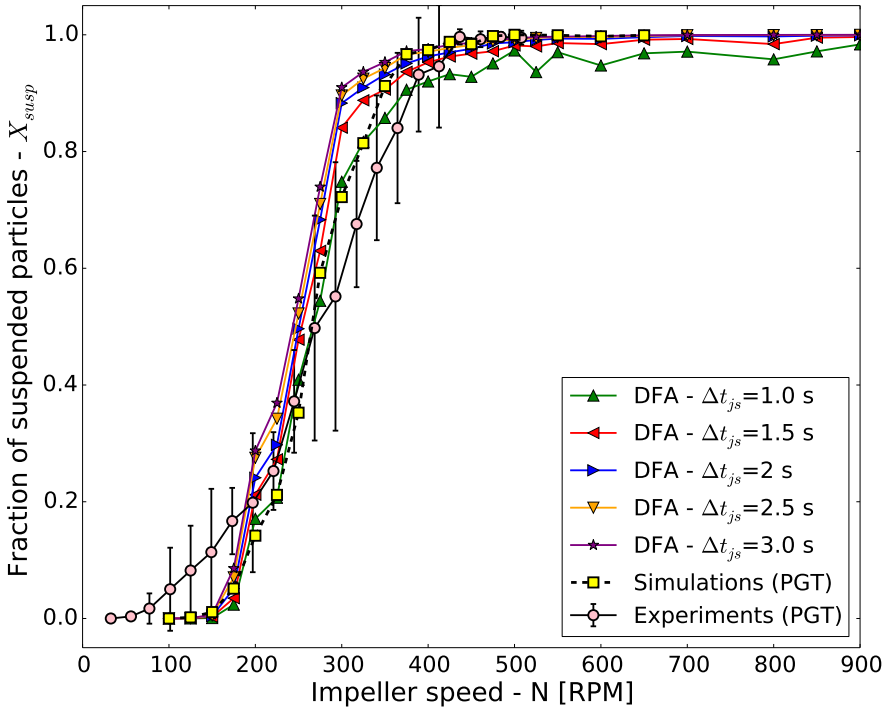

Figure 9.15 Fraction of suspended particles measured by DFA for various observation times (Δt_{js}), and comparison to PGT experimental and numerical results.

For $\Delta t_{js} = 1$ s, the values of X_{susp} are below the PGT results for almost all impeller speeds. This is especially noticeable for $N > 425$, where X_{susp} reaches a plateau slightly below 1 even though a fully suspended state is observed at these speeds according to the PGT and LSFA-$\Delta \boldsymbol{x}$ methods (Figure 9.11 and 9.13). This means that the observation window is insufficiently long to allow for a full decorrelation of the positions of the particles even at speeds where adequate mixing occurs. The quality of the results improves for $\Delta t_{js} = 1.5$ s, but a plateau is again reached a little short of $X_{susp} = 1$. However, for $\Delta t_{js} \geq 2$ s, an excellent agreement is observed between the DFA and the PGT techniques, with the exception of a slight overprediction by the former for $N \in [300, 400]$ RPM. It is interesting to note that, for $\Delta t_{js} \geq 2$, the results become far less sensitive to the value of Δt_{js} as evidenced by the overlap

in the $\Delta t_{js} \geq 2$ curves. Therefore, not only does this method not require the definition of a length, but there exists a time window above which the results converge to a constant value. Furthermore, it is interesting to note that this mixing index quantifies both the fraction of suspended solids and the efficiency with which these particles are mixed in the tank.

Tangent-intersection analysis technique

The graph in Figure 9.16 presents the results obtained by the tangent-intersection analysis (TIA) approach. A sharp transition in the void fraction ϵ_f with respect to the impeller speed can be observed starting from 175 RPM to 325 RPM. After 325 RPM, the void fraction slowly increases, but never reaches a constant plateau. Value of the average void fraction $\epsilon_f = 83\%$ at $N = 900$ RPM indicates the system never reaches a fully homogeneous state. Moreover, the N_{js} value obtained with this method, $N_{js,TIA} = 375$ is significantly below the values measured with the PGT, LSFA-$\Delta \boldsymbol{x}$ and DFA. This will be discussed in Section 9.6.2.

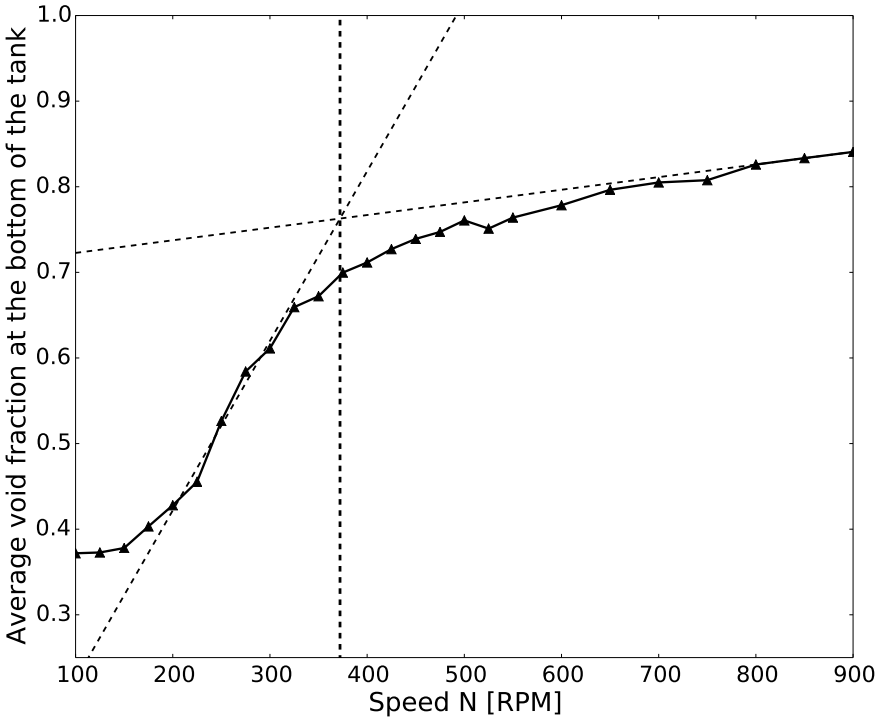

Figure 9.16 Evolution of the average void fraction 1 mm above the bottom of the tank and application of the tangent-intersection analysis approach.

Power consumption technique

The graph in Figure 9.17 gives the power comsumption as a function of the impeller speed. Each value has been averaged over a period of 3 s. The power consumption can be observed to grow with N^3, indicating that the power number (N_p) is constant. The value of N_{js} cannot, in all likelihood, be determined from this curve.

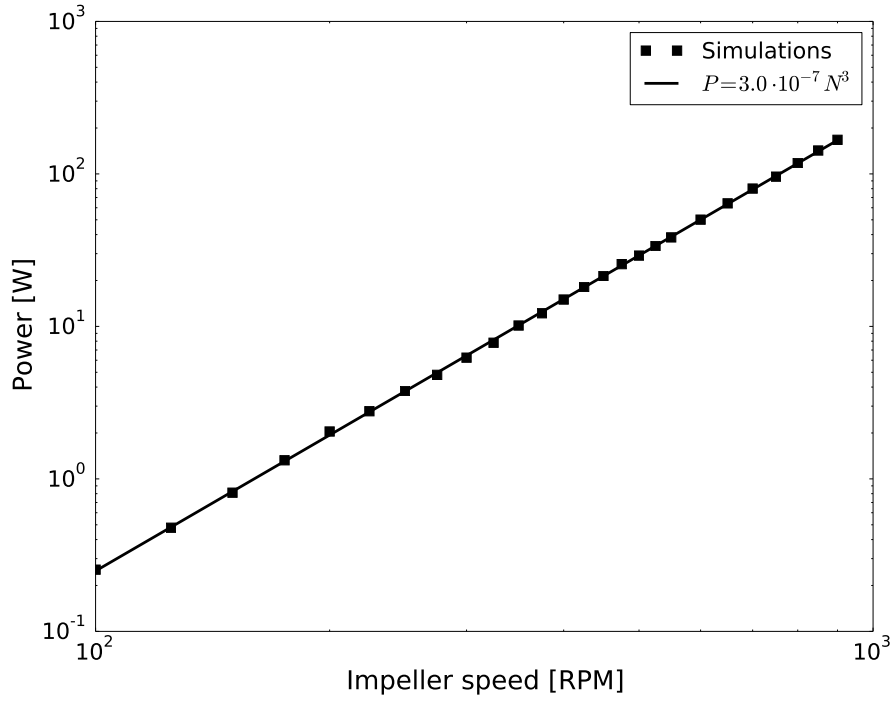

Figure 9.17 Power number as a function of impeller speed

Local particle concentration technique

Phase averaged values of local particle concentrations were measured at three different positions on the phase averaged $\boldsymbol{P}_{xy}$ plane located below the impeller and 7 cm above the bottom of the vessel. These positions are illustrated at Figure 9.18

The graph in Figure 9.19 presents the values of the local void fraction at the three measurement locations with respect to the impeller speed. No clear trend from which N_{js} could be calculated can be observed. The failure of this approach to measure N_{js} for this system may be due to the fact that complete homogeneity is never reached. Indeed, the value of the void

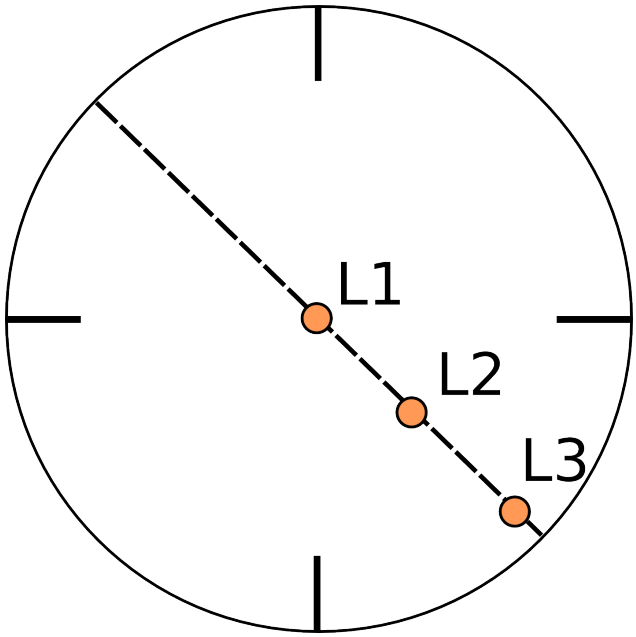

Figure 9.18 Positions of the measurement points for the local particle concentration technique

fraction for the L1 and L3 measurements is far below that at complete homogeneity which is $\epsilon_f = 0.949$, since the volume fraction of particles is 5.1% (see Table 9.1).

Transient solid concentration technique

The graphs in Figure 9.20 display the phase averaged values of the void fraction on the $\boldsymbol{P}_{xy}$ plane for $N = 900$ RPM, 1 mm above the bottom of the tank. It can be seen that even at such a high impeller speed, where all particles are known to be suspended, there are still zones where the solid concentration is more than half of the maximal packing fraction, that is $\epsilon_p = (1-\epsilon_f) > \frac{\epsilon_{p,m}}{2}$ (as highlighted in blue in Figure 9.20 (B)). Consequently, no estimation of N_{js} can be made with this approach.

Comparison of the strategies for the determination of N_{js}

As discussed in the previous sections, no clear estimation of N_{js} could be obtained by analyzing the power consumption (Section 9.6.2), local particle concentrations (Section 9.6.2) and transient solids concentrations (Section 9.6.2). This inability to predict N_{js} with these approaches could be due to their lack of generality, which make them inadequate for systems involving relatively large particles in an early turbulent regime as in the current work ($d_p = 3$ mm, $Re < 6000$). In fact, there appears to be little physical foundation to sup-

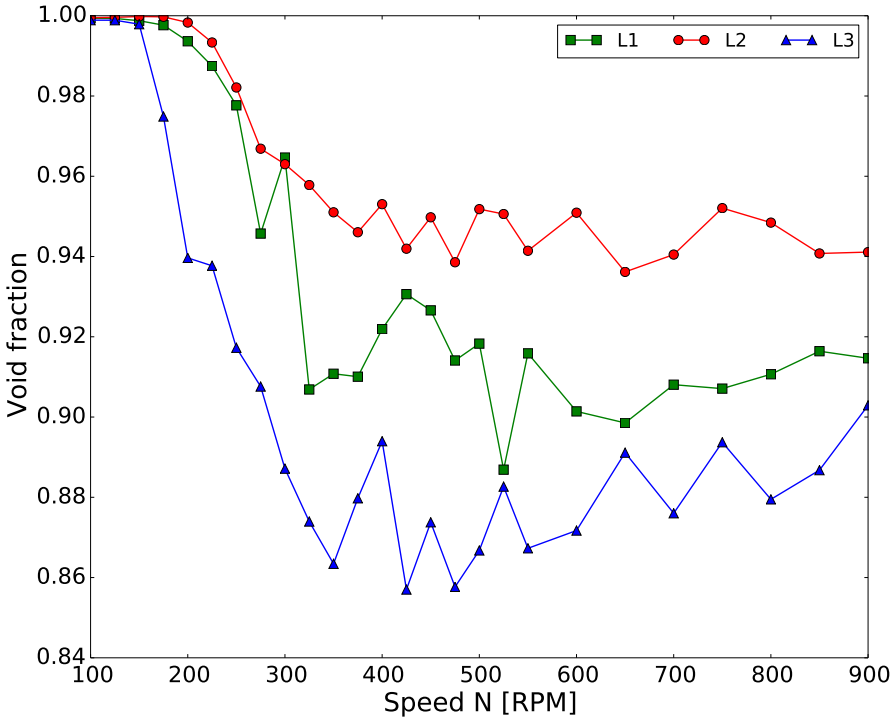

Figure 9.19 Values of the void fraction at the three measurement points with respect to the impeller speed.

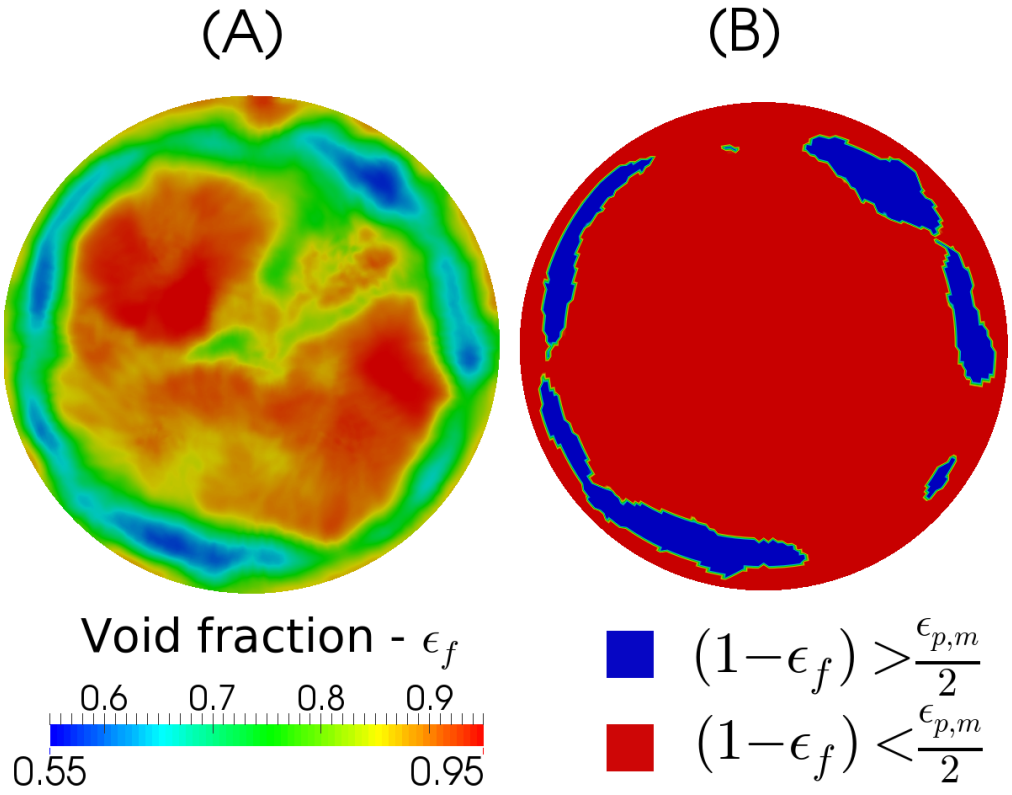

Figure 9.20 (A) void fraction on the $\boldsymbol{P}_z$ plane 1 mm above the bottom of the tank, and (B) zones where $(1-\epsilon_f) > \frac{\epsilon_{p,m}}{2}$ at the bottom of the tank, for $N = 900$ RPM

port the tangent intersection (Section 9.6.2), transient solids concentration and local particle concentration approaches. Although more physically sound, the power consumption approach seems not sensitive enough to account for the suspension of the particles in the mixing system, which is most likely due to the fact that the impeller sees a fraction of particles that is too small to affect in an observable manner the power draw. The PGT, which is also based on the increase of the apparent density, does not suffer from such a drawback as it is a more global approach.

The PGT (Section 9.6.2), LSFA (Section 9.6.2) and DFA (Section 9.6.2) approaches were observed to be suitable for the evaluation of the fraction of suspended particles. In particular, this they can serve to obtain the sufficiently suspended speed (N_{ss}), the latter being the speed at which $X_{susp} = 0.982$ [210] (see Section 9.1). The sufficiently suspended speed is expected to be slightly lower than N_{js}, but is used in this work with the PGT, LSFA and DFA techniques to approximate N_{js}. Results obtained with the TIA approach are also presented for completeness.

Table 9.5 compares the values of N_{ss} obtained via the PGT, LSFA, DFA techniques to the values of N_{js} from the TIA technique and those predicted by the Zwietering correlation. The four rightmost columns of this table display the fraction of suspended particles X_{susp} at the impeller speed given in the corresponding rows. These values of X_{susp} were obtained by interpolating the experimental and numerical PGT (Figure 9.11), LSFA-$\Delta \boldsymbol{x}_{js}$ (Figure 9.13) and DFA (Figure 9.15) results to the values of N_{js} or N_{ss} obtained with the techniques in the first column. These results can in fact serve to compare the variability of the X_{susp} values obtained with the PGT, LSFA and DFA techniques. The N_{js} and N_{ss} results are also displayed as a histogram in Figure 9.21.

We can see in Table 9.5 that the TIA technique underestimates the values of N_{js} with respect to that predicted by the Zwietering correlation, $N_{js} = 402$, which is itself slightly below the values of N_{ss} obtained with the other techniques. As N_{js} is expected to be higher than N_{ss}, these result indicate that the Zwietering correlation does not give an accurate prediction of N_{js}.

We note in Figure 9.21 the good agreement between the PGT (experiments and simulations) and the LSFA-$\Delta \boldsymbol{x}$ and DFA approaches, considering the difficulty in defining adequate time windows for the latter two approaches. More precisely, a very good agreement can be obtained between the PGT and LSFA-$\Delta \boldsymbol{x}$ results for $\Delta t_{js} \in [1, 1.5]$ s, whereas a good agreement between the PGT and DFA results is obtained for $\Delta t_{js} \in [2, 3]$ s. Moreover, we note that these two techniques yield accurate fractions of suspended particles for all impeller speeds, as was shown in Figures 9.13 and 9.15, respectively. Fromn a practical point of view, our

findings indicate that the PGT, LSFA-$\Delta\boldsymbol{x}$ and DFA techniques are all three suitable when analysing the fraction of suspended solids from Euler-Lagrange simulations. Although it is accurate and compares very well to experimental data, the PGT technique requires numerous simulation results at various impeller speeds to correct the dynamic pressure. Indeed, this correction can only be calculated when in a fully suspended state. As the impeller speed at which this state is reached is not known a priori, a relatively large number of simulations at various impeller speeds may indeed be needed. On the other hand, the LSFA-$\Delta\boldsymbol{x}$ and DFA approaches can be easily applied to any impeller speed, which is an advantage over the PGT technique as fewer simulations are likely to be required. Finally, these two methods are applicable to any vessel geometry, which is not the case of the PGT technique, which requires a flat or conical vessel bottom.

			X_{susp}			
Technique or correlation	N_{js}	N_{ss}	Exp. PGT (Figure 9.11)	Sim. PGT (Figure 9.11)	LSFA-$\Delta\boldsymbol{x}$ (Figure 9.13)	DFA (Figure 9.15)
Zwietering correlation	402	-	94.7%	97.4%	97.9%	96.3%
TIA	375	-	87.9%	94.6%	95.7%	95.1%
PGT - Experiments	-	428	98.2%	97.9%	98.6%	97.8%
PGT - Simulations	-	430	98.3%	98.2%	98.6%	97.8%
LSFA-$\Delta\boldsymbol{x}$ ($\Delta\boldsymbol{x}_{js} = d_p$, $\Delta t_{js} = 1.5$ s)	-	416	95.3%	97.8%	98.2%	97.5%
LSFA-Δz ($\Delta\boldsymbol{z}_{js} = d_p$, $\Delta t_{js} = 2$ s)	-	616	100%	100%	100%	99.4%
DFA ($\Delta t_{js} = 2$ s)	-	466	99.3%	99.7%	99.4%	98.2%

Table 9.5 The first three columns of this table compare the different values of N_{js} and N_{ss} obtained via techniques investigated in this work. The other columns give the fraction of suspended particles X_{susp} as calculated by the PGT (experiments and simulations), LSFA-$\Delta\boldsymbol{x}$ ($\Delta\boldsymbol{x}_{js} = d_p$, $\Delta t_{js} = 1.5$ s) and DFA ($\Delta t_{js} = 2$ s) techniques for the corresponding values of N_{js} or N_{ss} obtained in the second or third column.

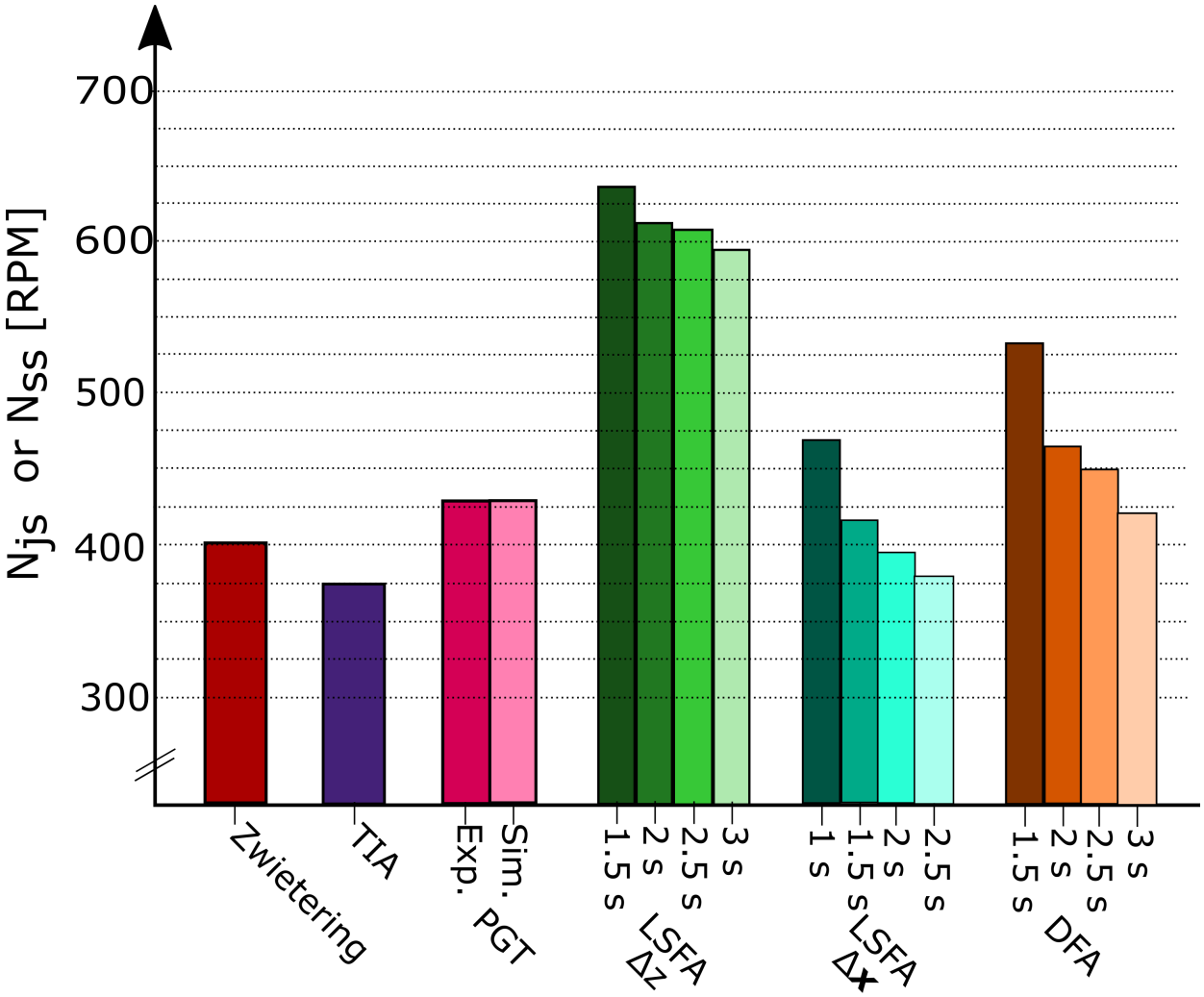

Figure 9.21 N_{js} or N_{ss} values for the various techniques investigated. The LSFA results are for $\Delta z_{js} = d_p$.

9.7 Conclusion

Predicting the required agitation speed to suspend the desired amount of particles in solid-liquid mixing systems remains a challenging topic of industrial interest. This is not only because of the complex hydrodynamics and the solid-liquid interactions that take place within the agitated vessel, but also because different types of operations (chemical reactors, crystallizer, etc.) require specific levels of suspension. In particular, the just-suspended speed (N_{js}) is not the adequate operating condition for all processes and may lead to large power over-consumption. The development of novel numerical models, such as those combining

CFD for the fluid and DEM for the solid particles, is a promising way to investigate such multiphase systems.

In the present work, we have extended the laminar and transitional solid-liquid mixing model introduced by our group [40], based on the CFDEM framework (combining LIGGGHTS and Open∇FOAM), to turbulent flows by means of LES. Numerous techniques to measure the just-suspended speed (or the sufficiently suspended speed N_{ss} as an approximation) as well as the fraction of suspended particles were discussed. Two new approaches, the Lagrangian suspended fraction analysis (in two variants, LSFA-$\Delta\boldsymbol{x}$ and LSFA-Δz) and decorrelated fraction analysis (DFA) techniques, were introduced. Both methods are global metrics based on the analysis of the time-dependent position of each particle. While the LSFA technique is based directly on the displacement of the particles, the DFA technique relies on a mixing index developed in our group [88] to analyze the loss of correlation of the positions of the particles with respect to their initial positions. Thus, it also assesses the mixing efficiency.

A standard set-up consisting of a baffled stirred tank equipped with a PBT and filled with a non-dilute concentration ($10wt\%$) of glass beads was studied. The PBT was found to behave much like an axial discharge impeller with single loop patterns. It was also observed that the particle Reynolds number was significant only close to specific elements of the geometry (vessel bottom, baffles, impeller) and that in other location in the tank, the particle velocity was close to that of the fluid. Analysis of solid concentration profiles highlighted zones of particle accumulation at the bottom-wall junction, which was corroborated by our experimental observations.

The fraction of suspended particles was investigated theoretically via the Zwietering correlation, experimentally using the pressure gauge technique (PGT) and via CFD-DEM using a variety of numerical techniques : pressure gauge, LSFA-Δz, LSFA-$\Delta\boldsymbol{x}$, DFA, TIA, power consumption, local particle concentration and transient solids concentration. No usable results could be obtained with the latter three approaches. In fact, this revealed the lack of generality of these methods. An excellent agreement was obtained between the experimental and numerical PGT N_{ss} results, which validated the accuracy of the unresolved CFD-DEM model proposed in this work.

The TIA technique and Zwietering correlation predicted a value of N_{js} below the values for N_{ss} predicted by the PGT. The LSFA-Δz was found to overpredict the value of N_{ss} when compared to the PGT. However, a good agreement was obtained with the LSFA-$\Delta\boldsymbol{x}$. A good agreement was also observed with the DFA technique, although this required a larger observation time $\Delta t_{js} \geq 2$ s. These two techniques, as well as the pressure gauge technique, are highly promising, because they provide a global assessment of the suspension of the

particles and are based on physical grounds very close to Zwietering's original definition. Furthermore, both the LSFA-$\Delta \boldsymbol{x}$ and DFA techniques can assess the fraction of suspended particles at a given velocity with only one simulation contrary to the PGT technique that requires many simulations to remove the dynamic component from the total pressure curve. This renders their use far less time-consuming and less error-prone due to the absence of the dynamic pressure correction. Furthermore, they are suitable for all kinds of vessels, contrary to the PGT technique which works only with flat-bottomed or conical vessels.

Due to its accurate resolution of the particle dynamics and tractable overall computational times, the unresolved CFD-DEM model proposed in this work paves the way to a new generation of models for solid-liquid mixing.

9.8 Acknowledgements

The financial support from the Natural Sciences and Engineering Research Council of Canada (NSERC) is gratefully acknowledged. In particular, Bruno Blais is thankful for the NSERC Vanier Scholarship. The authors would like to thank Gilles Lenfant for the rheological measurements of the glucose solution and Manon Lassaigne for fruitful discussion on the design of experiments. Computations were made on supercomputer Colosse from the University Laval, managed by Calcul Québec. In particular, the authors would like to acknowledge the efficient support received from Calcul Québec systems analysts.

CHAPITRE 10 Article 6 : CFD-DEM investigation of viscous solid-liquid mixing : impact of particle properties and mixer characteristic

Bruno Blais, François Bertrand
In preparation for AIChE Journal, 2016

Abstract : In chemical engineering, numerous processes require the suspension of particles in a laminar or transitional regime. For such operations, predicting the fraction of suspended particles as well as their distribution and homogeneity is a major concern. In this work, the unresolved CFD-DEM model introduced by our group for solid-liquid mixing is used to investigate the mixing dynamics of viscous suspensions. The techniques chosen to characterize the degree of suspension, the homogeneity and the distribution of the particles are presented. They are used to assess the efficiency of a pitched blade turbine with a clearance of $C = T/4$. The impact of solid properties on mixing dynamics is investigated by varying the Young's modulus, the coefficient of restitution and the sliding friction coefficient in the DEM model. Lastly, five alternative configurations of the mixing rig are investigated by varying the clearance of the impeller and introducing baffles.

10.1 Introduction

Solid-liquid mixing in mechanically agitated vessels is a widely used process in a multitude of industries, including ore processing, pharmaceuticals and cosmetics. Although it has been the subject of numerous investigations since the pioneering work of Kneule [157] and Zwietering [339], it remains an active field of research in which many questions remain unanswered. This is, at least in part, due to the complex multi-scale solid-liquid physics of particle-particle and particle-fluid interactions and the variety of flow regimes and unsteady flow structures in agitated vessels. Most studies on solid-liquid mixing have focused on the assessment of the minimum agitation speed (or just-suspended speed N_{js}) required to suspend the particles in the turbulent regime. The resulting correlations, such as the one proposed by Zwietering [**?**], perform poorly in the laminar and transitional operation regimes [130, 132, 173]. We recently showed that the underlying hydrodynamics involved in the suspension of non-dilute suspensions are different in the transitional regime than in the turbulent regime [173]. We took measurements using the pressure gauge technique (PGT) in an unbaffled stirred tank equipped with a pitched blade turbine and found that the dependence on the just-suspended speed of fluid viscosity μ and particle diameter d_p were the opposite of what was predicted

by the Zwietering correlation [**?**] and other correlations, including those proposed by Nienow [225], Baldi [18], Rao *et al.* [255], Takashi *et al.* [291], Armenante *et al.* [10], and Grenville *et al.* [114]. This is not surprising given that these correlations were derived for the turbulent regime. However, our results with respect to the influence of viscosity on N_{js} showed that increasing μ decreases N_{js}, which is in agreement with recent work by Tamburini *et al.* [292], who investigated the impact of viscosity on N_{js} for a wide range of viscosities using an unbaffled stirred tank with a covered top.

Predicting N_{js} is insufficient for some operations such as chemical reactors with a solid catalyst, for food processing, and for crystallization processes. In these cases, it is important that the concentration of particles be homogeneous throughout the tank, which generally requires that the operating speed exceeds N_{js}. However, little is known about the distribution and dispersion of particles in the laminar and transitional regimes. This lack of information on local concentrations of particles is mostly due to the difficulties in measuring this quantity. While optical, sampling, radioactive, and conductivity based methods exist to measure local concentrations of particles (see reviews by Kasat and Pandit [149] and Tamburini *et al.* [295]), their accuracy is limited and, more importantly, they cannot measure the velocity field and the particle concentration throughout the entire vessel. The cloud height, for which Bittorf and Kresta introduced a predictive model based on wall jets in the turbulent regime [36], is an interesting concept, but is not a measure of the distribution of the particles and gives no insights into the possible presence of dead zones.

Multiphase computational fluid dynamics (CFD) is a powerful and versatile tool that overcomes the experimental issues mentioned above. We introduced an unresolved CFD-DEM model [40] within the CFDEM framework [61, 112] that combines Open∇FOAM for the CFD [233] and LIGGGHTS [155, 182] for the DEM. The underlying finite volume scheme was first verified using the method of manufactured solutions [37, 91–93, 227] and combined with a new semi-implicit immersed boundary method that we devised and validated in the context of mixing [41]. The immersed boundary technique, which was integrated into our CFD-DEM scheme, was used to study the fraction of suspended particles in an unbaffled stirred tank equipped with a PBT with clearance of $C = \frac{T}{4}$. A very good agreement was obtained for both the particle flow patterns and the fraction of suspended particles as measured by the PGT. During this investigation, we noted that for $N > N_{js}$, the concentration of particles in a conical zone below the impeller remains considerably higher than in the rest of the tank. However, since our aim was to validate the unresolved CFD-DEM model, we did not extend our analysis to studying the dynamics of the mixing, distribution and dispersion of the particles in the tank or the role of solid properties or solid-fluid forces. Our analysis was also limited to a single clearance. The goal of the present work is to shed light on these

issues.

First, we describe in detail the unresolved CFD-DEM model. We present various techniques used to investigate the degree of suspension and the global mixing of particles, and discuss their capacities. Notably, we revisit the mixing index first introduced by Doucet *et al.* [88] and discuss some of its limitations. We then perform a thorough analysis using various mixing metrics, and we investigate the role of the Saffman lift force and the physical properties of the particles to gain insight into the suspension mechanism in the tank. Lastly, we discuss the impact of the impeller clearance and the presence of baffles. The information obtained from these simulations is used to propose guidelines for the design of mixing processes operating in the laminar and transitional regimes.

10.2 Model Formulation

The CFD-DEM approach combines the resolution of the fluid at a coarser scale than that of the particles by using the volume averaged Navier-Stokes (VANS) equations and the discrete element method (DEM) for the solid particles. The two schemes are coupled at regular intervals. The constitutive equations of the models are presented briefly, and we refer to our earlier work [40, 41] for a full description of the unresolved CFD-DEM scheme and the immersed boundary method used to model the rotating impeller.

10.2.1 Governing equations for the solid-phase (DEM)

In soft-sphere DEM, the governing equations for the translation ($\boldsymbol{v}_i$) and rotational ($\boldsymbol{\omega}_i$) motion of particle i are [31, 182, 337] :

$$m_i \frac{d\boldsymbol{u}_i}{dt} = \sum_j (\boldsymbol{f}_{c,ij}) + \sum_k \boldsymbol{f}_{lr,ik} + \boldsymbol{f}_{pf,i} + \boldsymbol{f}_{g,i} \tag{10.1}$$

$$I_i \frac{d\boldsymbol{\omega}_{p,i}}{dt} = \sum_j (\boldsymbol{M}_{t,ij} + \boldsymbol{M}_{r,ij}) \tag{10.2}$$

where m_i is the mass of particle i, I_i is the moment of inertia of particle i, $\boldsymbol{f}_{c,ij}$ is the contact force between particles i and j, $\boldsymbol{f}_{lr,ik}$ is the sum of the non-contact (long-range) forces between particles i and k, $\boldsymbol{f}_{pf,i}$ is the sum of the particle-fluid interaction forces, $\boldsymbol{f}_{g,i}$ is a body force (*i.e.* gravity), and $\boldsymbol{M}_{t,ij}$ and $\boldsymbol{M}_{r,ij}$ are the tangential and rolling friction torques acting on the particles. Since large particles are considered in the present work, non-contact forces are ignored. The expression for the particle-fluid interaction forces (drag, lift, etc.) are discussed in Section 10.2.3.

The contact forces between two particles are split into normal ($\boldsymbol{f}_{cn,ij}$) and tangential ($\boldsymbol{f}_{ct,ij}$)

[337] components :

$$\boldsymbol{f}_{c,ij} = \boldsymbol{f}_{cn,ij} + \boldsymbol{f}_{ct,ij} = -k_{n,ij}\boldsymbol{\delta}_{n,ij} - \gamma_{n,ij}\dot{\boldsymbol{\delta}}_{n,ij} - k_{t,ij}\boldsymbol{\delta}_{t,ij} - \gamma_{t,ij}\dot{\boldsymbol{\delta}}_{t,ij} \tag{10.3}$$

where $k_{n,ij}$ and $k_{t,ij}$ are the normal and tangential stiffnesses, $\gamma_{n,ij}$ and $\gamma_{t,ij}$ are the normal and tangential damping coefficients, $\boldsymbol{\delta}_{n,ij}$ and $\boldsymbol{\delta}_{t,ij}$ are the normal and tangential overlaps, and $\dot{\boldsymbol{\delta}}_{n,ij}$ and $\dot{\boldsymbol{\delta}}_{t,ij}$ their derivatives with respect to time.

In the present work, the model proposed by Tsuji [309] for the normal force is combined with the Mindlin model for the tangential force [214,215]. This is done in order to relate the stiffness and the damping coefficients to the Young's modulus of the material (Y), the Poisson ratio (ν) and the coefficient of restitution (e_r) using the equations in Table 10.1. The tangential overlap $\boldsymbol{\delta}_{t,ij}$ is truncated by Coulomb's law to ensure that $\boldsymbol{f}_{ct,ij} \leq -\mu_{s,ij} \left|\boldsymbol{f}_{cn,ij}\right| \frac{\boldsymbol{\delta}_{t,ij}}{|\boldsymbol{\delta}_{t,ij}|}$.

Parameter	Equation
Normal stiffness	$k_{n,ij} = \frac{4}{3} Y^*_{ij} \sqrt{R^*_{ij}\delta_{n,ij}}$
Tangential stiffness	$k_{t,ij} = 8 G^*_{ij} \sqrt{R^*_{ij}\delta_{n,ij}}$
Normal damping	$\gamma_{n,ij} = -2\sqrt{\frac{5}{6}} \frac{\ln(e_r)}{\sqrt{\ln^2(e_r)+\pi^2}} \sqrt{\frac{2}{3} k_n m^*_{ij}}$
Tangential damping	$\gamma_{t,ij} = -2\sqrt{\frac{5}{6}} \frac{\ln(e_r)}{\sqrt{\ln^2(e_r)+\pi^2}} \sqrt{k_t m^*_{ij}}$
Coulomb limit for the tangential force	$\boldsymbol{f}_{ct,ij} \leq -\mu_{s,ij} \left\|\boldsymbol{f}_{cn,ij}\right\| \frac{\boldsymbol{\delta}_{t,ij}}{\|\boldsymbol{\delta}_{t,ij}\|}$
Tangential torque	$\boldsymbol{M}_{t,ij} = \boldsymbol{r}_i \times (\boldsymbol{f}_{ct,ij})$
Rolling friction torque	$\boldsymbol{M}_{r,ij} = -\mu_{r,ij} \left\|\boldsymbol{f}_{cn,ij}\right\| \frac{\boldsymbol{\omega}_{p,ij}}{\|\boldsymbol{\omega}_{p,ij}\|} R^*_{ij}$
Equivalent mass	$\frac{1}{m^*_{ij}} = \frac{1}{m_i} + \frac{1}{m_j}$
Equivalent radius	$\frac{1}{R^*_{ij}} = \frac{1}{R_i} + \frac{1}{R_j}$
Equivalent Young's modulus	$\frac{1}{Y^*_{ij}} = \frac{\left(1-\nu_i^2\right)}{Y_i} + \frac{\left(1-\nu_j^2\right)}{Y_j}$
Equivalent shear modulus	$\frac{1}{G^*_{ij}} = \frac{2(2+\nu_i)(1-\nu_i)}{Y_i} + \frac{2(2+\nu_j)(1-\nu_j)}{Y_j}$
Sliding friction coefficient	$\mu_{s,ij}$
Rolling friction coefficient	$\mu_{r,ij}$
Distance to the contact point for particle i	$\boldsymbol{r}_i$
Radius of particle i	R_i

Table 10.1 Equations for the DEM model

10.2.2 Governing equations for the liquid-phase flow (CFD)

Form A of the incompressible volume-averaged Navier-Stokes (VANS) equations is solved for the liquid phase [105] and is given by :

$$\frac{\partial \epsilon_f}{\partial t} + \nabla \cdot (\epsilon_f \boldsymbol{u}) = 0 \tag{10.4}$$

$$\frac{\partial (\rho_f \epsilon_f \boldsymbol{u})}{\partial t} + \nabla \cdot (\rho_f \epsilon_f \boldsymbol{u} \otimes \boldsymbol{u}) = -\epsilon_f \nabla p + \nabla \cdot \boldsymbol{\tau} - \boldsymbol{F}_{pf} \tag{10.5}$$

where ϵ_f is the void fraction, ρ_f is the density of the fluid, p is the pressure, and $\boldsymbol{u}$ is the velocity of the fluid. The viscous stress tensor $\boldsymbol{\tau}$ is defined as :

$$\boldsymbol{\tau} = \epsilon_f \mu \left((\nabla \boldsymbol{u}) + (\nabla \boldsymbol{u})^T - \frac{2}{3} (\nabla \cdot \boldsymbol{u}) \boldsymbol{\delta}_k \right) \tag{10.6}$$

where μ is the dynamic viscosity and $\boldsymbol{\delta}_k$ is the identity tensor.

The momentum exchange term from the particles to the fluid $\boldsymbol{F}_{pf}$ is defined as :

$$\boldsymbol{F}_{pf} = \frac{1}{\Delta V} \sum_{i}^{n_p} \boldsymbol{f}_{pf,i} - \boldsymbol{f}_{\nabla p,i} - \boldsymbol{f}_{\nabla \cdot \boldsymbol{\tau},i} - \boldsymbol{f}_{\mathrm{Ar},i} \tag{10.7}$$

$$\boldsymbol{f}_{pf,i} = \boldsymbol{f}_{d,i} + \boldsymbol{f}_{\nabla p,i} + \boldsymbol{f}_{\nabla \cdot \boldsymbol{\tau},i} + \boldsymbol{f}_{\mathrm{Ar},i} + \boldsymbol{f}_{\mathrm{vm},i} + \boldsymbol{f}_{B,i} + \boldsymbol{f}_{\mathrm{Saff},i} + \boldsymbol{f}_{\mathrm{Mag},i} \tag{10.8}$$

where n_p is the number of particles and $\boldsymbol{f}_{pf,i}$ is the sum of all the fluid-solid interaction forces involving particle i : drag ($\boldsymbol{f}_{d,i}$), pressure gradient force ($\boldsymbol{f}_{\nabla p,i}$), viscous force ($\boldsymbol{f}_{\nabla \cdot \boldsymbol{\tau},i}$), Archimedes force ($\boldsymbol{f}_{\mathrm{Ar},i}$), virtual mass force ($\boldsymbol{f}_{\mathrm{vm},i}$), Basset force ($\boldsymbol{f}_{B,i}$), Saffman lift force ($\boldsymbol{f}_{\mathrm{Saff},i}$) and Magnus lift force ($\boldsymbol{f}_{\mathrm{Mag},i}$). The pressure, viscous and Archimedes forces are removed from $\boldsymbol{F}_{pf}$ since they are included directly in the continuous expression of form A of the VANS equations.

These equations are solved using a pressure implicit with splitting of operators (PISO) scheme [136] that we extended for the VANS equation and that we verified using the method of manufactured solutions [37]. The PISO-IB method, a semi-implicit immersed boundary method developed earlier by our group [41], is used to take the rotating impeller into account. This method integrates a forcing term directly into the momentum equation of VANS equations within the semi-implicit PISO scheme that imposes the velocity of the rigid body.

10.2.3 Governing equations for the solid-liquid coupling

The expressions for drag, pressure, viscous stress, and the Saffman lift forces are given in Table 10.2.

The virtual mass, Basset, and Magnus lift forces are not taken into account due to the low particle relaxation time caused by the high viscosity of the fluid considered.

Force	Equation
Pressure gradient - $\boldsymbol{f}_{\nabla p,i}$ [337]	$-V_p \nabla p$
Viscous force - $\boldsymbol{f}_{\nabla \cdot \boldsymbol{\tau},i}$ [337]	$-V_p \nabla \cdot \boldsymbol{\tau}$
Rong drag model -$\boldsymbol{f}_{d,i}$ [266]	$\frac{1}{8} C_D d_p^2 \rho_f \left\|\boldsymbol{u}-\boldsymbol{v}_i\right\| \left(\boldsymbol{u}-\boldsymbol{v}_i\right) \epsilon_f^{2-\beta\left(\epsilon_f, Re_p\right)}$ with $C_D = \left(0.63 + \frac{4.8}{\sqrt{Re_p}}\right)^2$ $\beta\left(\epsilon_f, Re_p\right) = 2.65\left(\epsilon_f + 1\right) - \left(5.3 - 3.5\epsilon_f\right)\epsilon_f^2 e^{-\frac{\left(1.5-\log {Re_p}^2\right)}{2}}$ and $Re_p = \frac{\rho_f d_p \left\|\boldsymbol{u}-\boldsymbol{v}\right\|}{\mu}$
Saffman lift - $\boldsymbol{f}_{\text{Saff},i}$ McLaughlin model [205]	$J^* 1.614 \rho_f^{\frac{1}{2}} \mu_f^{\frac{1}{2}} \left(\boldsymbol{u}-\boldsymbol{v}_i\right) \times \frac{\boldsymbol{w}}{\left\|\boldsymbol{w}\right\|^{\frac{1}{2}}}$ with $J^* = 1 - \frac{0.287\left(\left\|\boldsymbol{u}-\boldsymbol{v}_i\right\|^2\right)}{\left\|\boldsymbol{w}\right\|}$ and $\boldsymbol{w} = \nabla \times \boldsymbol{u}$

Table 10.2 Expressions for the solid-liquid forces

10.3 Evaluation of the quality of the mixing and the fraction of suspended solids

Mixing is an intuitive concept related to the reduction of the inhomogeneities of a quantity (in the case of solid-liquid mixing, the concentration or volume fraction of particles) both globally and locally. However, no unique mathematical definition of it has been proposed, despite the large body of work discussing this issue, such as the book by Ottino for laminar mixing [237].

Euler-Lagrange models, such as the unresolved CFD-DEM, suffer from the generation of a considerable amount of data (*i.e.* the position and the velocity of all particles at all desired times) that is hard to post-process efficiently. While visually appealing, animating the motion of the particles does not give quantitative information on the state of the mixing. A quantitative assessment of the quality of the mixing simulated by Euler-Lagrange simulations requires strategies to extract the essential information from the particle positions.

In this section, we present various approaches for measuring both the degree of homogeneity (or mixing) of the particles as well as the fraction of suspended particles (X_{susp}). We discuss their limitations and strengths, but we do not distinguish between the dispersion and distribution of the particles. This is not an exhaustive presentation and not all the methods are reviewed.

10.3.1 Measuring the homogeneity and the overall mixing efficiency

Void fraction analysis

An intuitive way to evaluate the distribution of the particles is to project their volume onto the Eulerian CFD mesh. This is already inherent to the unresolved CFD-DEM model since the void fraction (ϵ_f) is part of the VANS equations. The same projection can be also used on the velocity (translation or rotational) of the particles to extract a cell-averaged particle velocity.

The Eulerian cell-averaged representation of the Lagrangian data can be used to obtain statistical information on the distribution of the particles, including histograms of the void fraction. This information can also be used to establish the steady-state concentration profiles using phase averaging.

Mixing index

Doucet *et al.* (2008) introduced a metric (the so-called weak sense mixing index) to measure the efficiency of mixing in granular and fluid flow systems from Lagrangian trajectories [88]. Their method consists of using principal component analysis (PCA) to measure the correlation between the positions of the particles ($\boldsymbol{x} \in \mathbb{R}^d$, where d is dimensionality of the domain) at time t ($\boldsymbol{x}_t$) and their initial position ($\boldsymbol{x}_0$). If the PCA analysis results in asymptotically vanishing eigenvalues, the system is deemed mixed in the weak sense. Concretely, this means that no component (direction in $\mathbb{R}^d$) can be identified, which explains most of the motion of the particles. In the case of non-vanishing eigenvalues, the vector corresponding to the highest eigenvalue can be used to extract the direction of poorer mixing, thus allowing the investigator to isolate bottlenecks more efficiently. Doucet *et al.* (2008) showed that this approach can be used to provide an accurate measure of the degree of mixing for granular systems in a cylindrical drum and in a V-blender as well as that of viscous mixing in a Kenics static mixer.

Furthermore, this metric can be augmented by including additional information ($\boldsymbol{\zeta}$), such as the size of the particles, to constitute an augmented initial state vector ($\boldsymbol{\chi}_0^T = [\boldsymbol{x}_0^T, \boldsymbol{\zeta}_0^T]$) on which the PCA can be carried out. Doucet *et al.* (2008) used this so-called strong sense mixing index to measure the mixing efficiency of a cylindrical drum in the case of bidispersed particles and showed that the segregation phenomena, which plague these types of mixers, can be identified using this metric, whereas they are not detected using the weak sense mixing index. The same method was used by Bouffard *et al.* [42] to study the mixing of bidispersed solid particles in a spheronizer. In this case, the strong mixing index was used to determine

the impact of the angular velocity of the bottom plate of the spheronizer on the segregation of the two sizes of particles.

To remain concise, we refer the reader to the tutorial of Shlens for the theoretical background on PCA [279]. PCA has limitations [279], which are not discussed in [88] or [42], but which must be taken into account when using such mixing indices. While the discussion that follows is centered on the weak sense mixing index, the conclusions derived apply in a straightforward way to the strong sense mixing index.

Let f be a function related to a process (*i.e.* mixing) that maps the particles from their initial position $\boldsymbol{x}_0$ to their position $\boldsymbol{x}_t$ at time t. Given a PCA using the state $\boldsymbol{x}_t$ and the initial state $\boldsymbol{x}_0$, let $\boldsymbol{\Lambda} \in \mathbb{R}^{d \times d}$ be the resulting diagonal matrix of the eigenvalues, λ_j the eigenvalues and $\boldsymbol{R}$ the corresponding matrix of eigenvectors with $\boldsymbol{r_j}$ the column eigenvector associated with λ_j. A major assumption in PCA is that linearity frames the problem [279]. Consequently, if the largest eigenvalue $\lambda_k = \max(\lambda_j)$ tends toward a constant value, a direction $\boldsymbol{r}_k$ exists that explains a larger portion of the variance than any other direction. If this value is large, the system is considered ill-mixed because an axis obtained after a linear change of basis represents f. However, if f is a non-linear function, then λ_k can decrease asymptotically to zero even if this transformation does not lead to efficient mixing. In fact, an uncountable amount of functions exist that lead to a vanishing mixing index, but that do not actually lead to efficient mixing. Therefore, an asymptotically vanishing mixing index is a necessary, but not a sufficient condition for a well-mixed system. That is, if the mixing index decreases toward a non-vanishing large constant then the system is poorly mixed. However, if the mixing index decreases toward zero, the system may or may not be mixed. This critical issue was not discussed in [88] and will now be illustrated using a simple, yet realistic, example.

Consider a circle filled with particles in the configuration depicted in Figure 10.1 in a 2D ($x - y$ or $r - \theta$) plane. Initially, the particles are segregated by their color in the θ and r directions. A time-independent Lamb-like vortex is then applied [171] for which the velocity field $\boldsymbol{u}$ on domain $\Gamma = [-1, 1] \times [-1, 1]$ is given by :

$$\boldsymbol{u} = [u_r, \;\; u_\theta]^T \tag{10.9}$$

$$\boldsymbol{u} = [0, \;\; \frac{1}{5r}\left(1 - e^{-r^2}\right)]^T \tag{10.10}$$

where u_r and u_θ are the radial and azimuthal velocities. Figures 10.1 present the configuration of the particles after 200 s and 1000 s of flow. We can see that the cyan-blue and the red-yellow particles are well mixed, but that, since there is no radial flow, the system remains segregated in the r direction. Clearly this system is poorly mixed. This is no surprise, since any $2D$ stationary flow is incapable of achieving a mixed state [237].

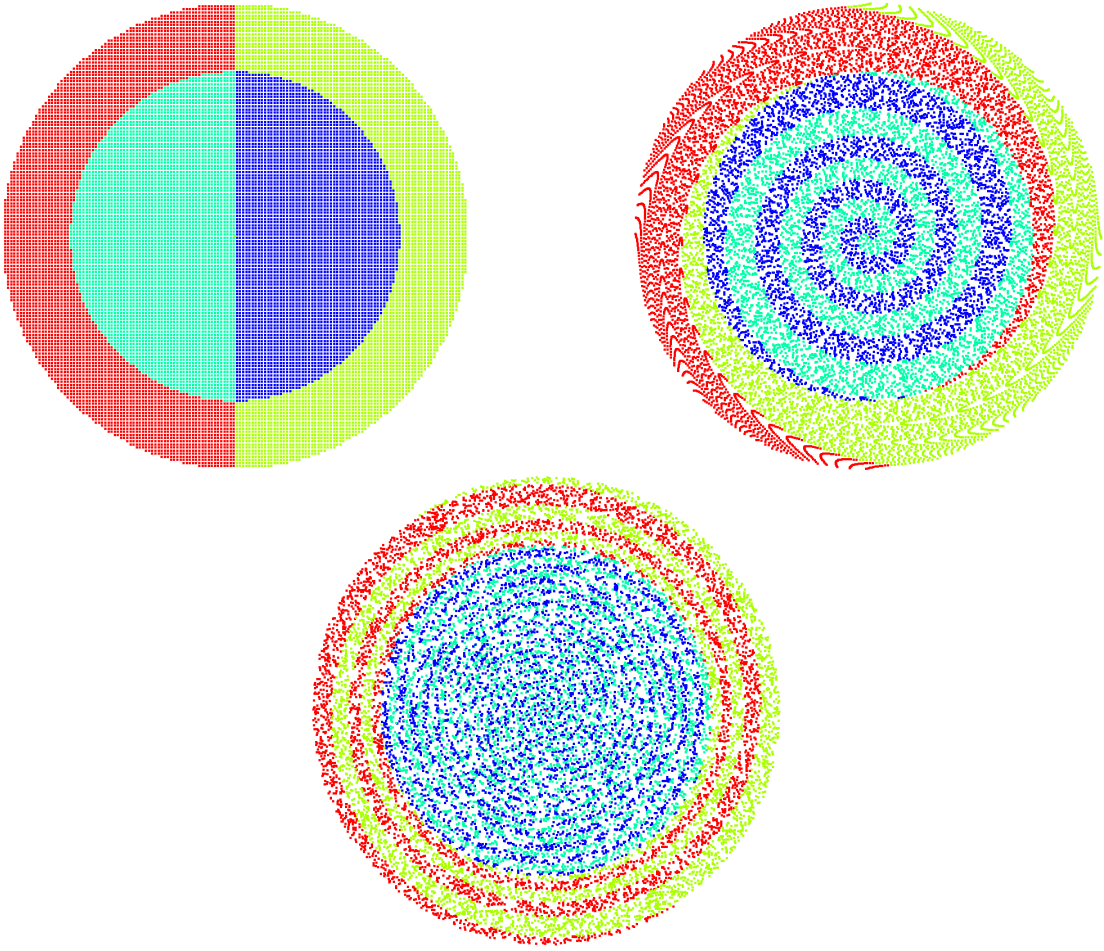

Figure 10.1 Mixing using a Lamb-like vortex at 0s, 200s and 1000s respectively.

We then study this system using the mixing index in the weak sense for long periods of time using Cartesian coordinates $\boldsymbol{x} = [x, y]^T$. The graphs in Figure 10.2 present the evolution of the mixing index and the associated eigenvector as annotations. We can see that, while this flow is incapable of mixing the particles in the radial direction, the mixing index decreases to a value close to zero (0.029). This is because the Lamb-like vortex is a non-linear process that mixes only in the θ direction, which violates one of the prerequisites for such analysis, *i.e.*, linearity.

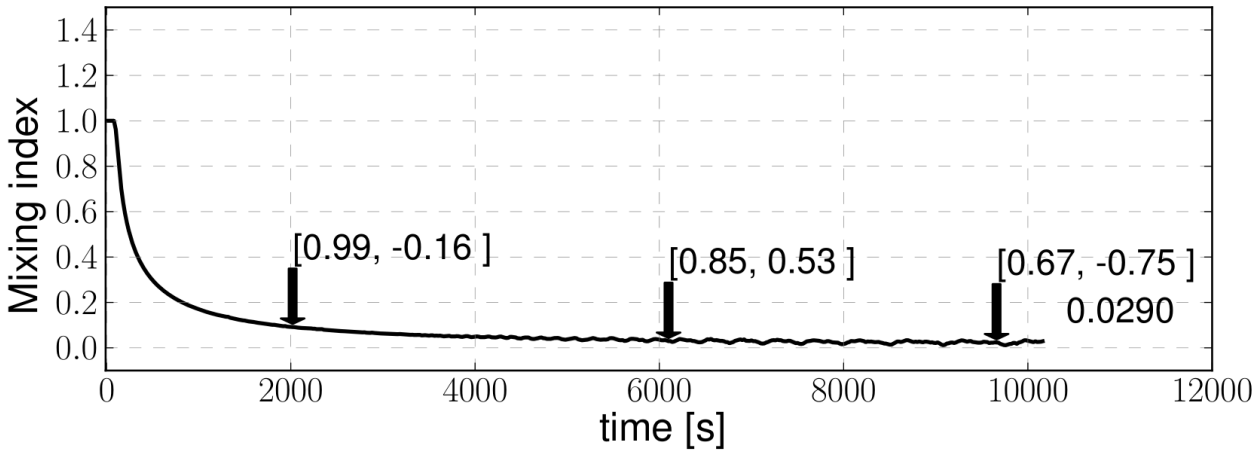

Figure 10.2 Evolution of the mixing index for a PCA analysis carried out in a $x-y$ coordinate system. The values in brackets represent the eigenvectors associated with the current value of the mixing index. The last value is the final value.

One way to make the mixing index more robust is to study the system in a set of coordinates that naturally describes the corresponding process. For instance, the motion in stirred tanks is well described using cylindrical coordinates (r, θ, z). If we perform the mixing index analysis using cylindrical coordinates, we obtain the results in Figure 10.3 showing that the mixing index remains 1, with the associated eigenvector being $\boldsymbol{r}$. Thus, with the appropriate set of coordinates, the mixing index can identify such an ill-mixed system. From this analysis, we can conclude that while a decreasing mixing index is a necessary but not sufficient condition for a well-mixed system, its performance can be augmented using an appropriate set of coordinates that more adequately describes the position of the particles. Furthermore, when the mixing index converges to a constant, non-zero value, it is an indicator of an ill-mixed system. As such, we performed all the mixing index calculations discussed in the subsequent sections using cylindrical coordinates.

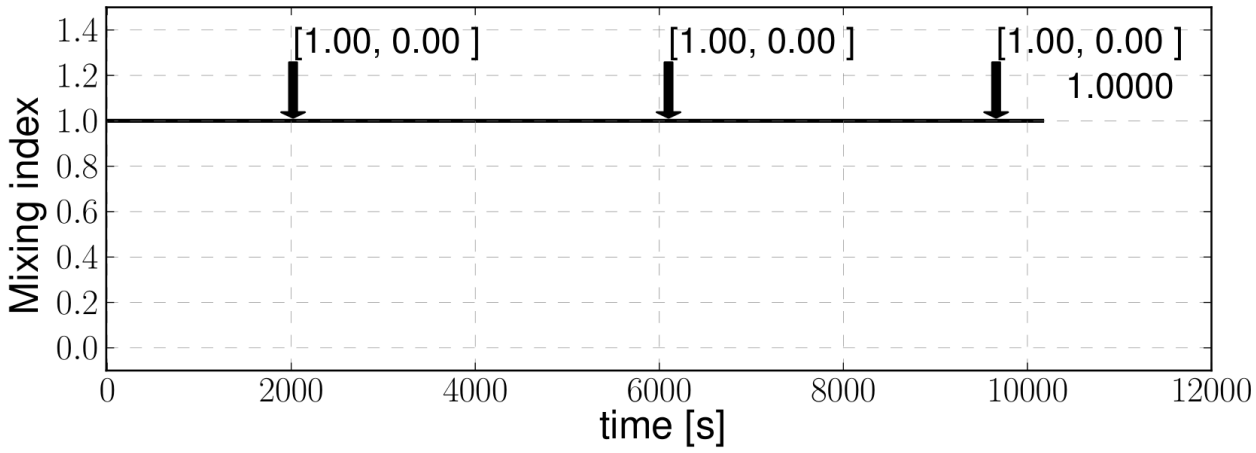

Figure 10.3 Evolution of the mixing index for a PCA analysis carried out in a $r-\theta$ coordinate system. The values in the brackets represent the eigenvectors associated with the current value of the mixing index. The last value is the final value.

10.3.2 Measuring the fraction of suspended solids

Pressure gauge technique

The PGT measures the fraction of suspended particles by the increase in the apparent density of a suspension due to the presence of the particles.

At the start of a mixing operation, before the impeller is put in motion, the particles are at rest at the bottom of the tank and their weight is thus held by the lateral and bottom walls of the vessel. As the speed of the impeller is increased and the particles are progressively suspended, their weight gets held more and more by the fluid flow (*e.g.*, by the drag force) and, consequently, the apparent density of the fluid increases. This increase in density translates into an increase in hydrostatic pressure, which can be measured at the bottom of the tank. Once all the particles are suspended, the apparent density of the suspension reaches a constant value, as does the increase in static pressure (ΔP_{susp}). However, changes in the impeller velocity also induce a change in the hydrodynamic pressure, which needs to be taken into account. By fitting a parabola to the pressures obtained once all the particles are suspended, the dynamic pressure effect can be subtracted from the total pressure to isolate the changes in static pressure and, to deduce the fraction of suspended particles. This is illustrated in Figure 10.4. This method, which is called the pressure gauge technique (PGT) [53,210], can be used experimentally to obtain the fraction of suspended particles. We recently showed [39,40] that this technique can be used in a CFD-DEM model by averaging the pressure at the bottom of

the tank and by applying the same procedure to correct for the dynamic pressure. The results obtained with this method for the fraction of suspended particles compared very well with the experimental data for the laminar, transitional and turbulent regimes. However, this method can only be applied to flat-bottomed and conical vessels, and requires simulations over a large range of impeller speeds to capture the region where the dynamic pressure correction can be established. This makes it computationally intensive.

Lagrangian suspended fraction analysis

The Lagrangian suspended fraction analysis (LSFA) recently introduced by our group [39] can be used to calculate the fraction of suspended particles from the positions of the particles. This method is intuitively linked to the original definition of N_{js} introduced by Zwietering that states that N_{js} is the impeller speed at which no particle remains motionless at the bottom of the tank for more than 1 or 2 s. In the LSFA technique, the displacement of each particle located in a region close to the bottom of the tank is monitored during a time interval Δt_{js}. If a particle displaces by an amount larger than Δx_{js} during this interval, it is considered suspended. We investigated two different criteria based on the displacement in the axial direction (LSFA-Δz) or the overall displacement (LSFA-$\Delta \boldsymbol{x}$) and found that much better agreement was obtained between the LSFA-$\Delta \boldsymbol{x}$ and the PGT (both numerical and experimental) results for the fraction of suspended particles. Defining the threshold values of the displacement (Δx_{js}) and the observation time (Δt_{js}) remained slightly subjective. We reported [39] that there is good agreement between Zwietering's original definition and that the PGT results can be obtained by setting $\Delta t_{js} = 2$ s and $\Delta \boldsymbol{x}_{js} = d_p$. This choice was justified by the fact that d_p is the characteristic length pertaining to the motion and dynamics of the particles. The LSFA technique is valid for any geometry and can be applied directly to a single simulation without requiring the investigation of numerous impeller speeds, unlike the PGT technique. While there is a degree of subjectivity in the choice of Δt_{js} and $\Delta \boldsymbol{x}_{js}$, this method can be used in a straightforward way to compare the efficiencies of various geometries as long as the same set of parameters are used.

Decorrelated fraction analysis

The decorrelated fraction analysis (DFA) technique, which was also recently introduced by our group [39], uses the mixing index of Section 10.3.1 to calculate the fraction of suspended particles by measuring the degree of decorrelation occurring in a system during a time interval Δt_{js}.

At time $t_0 + \Delta t_{js}$, only a particle that is already suspended or that got suspended during

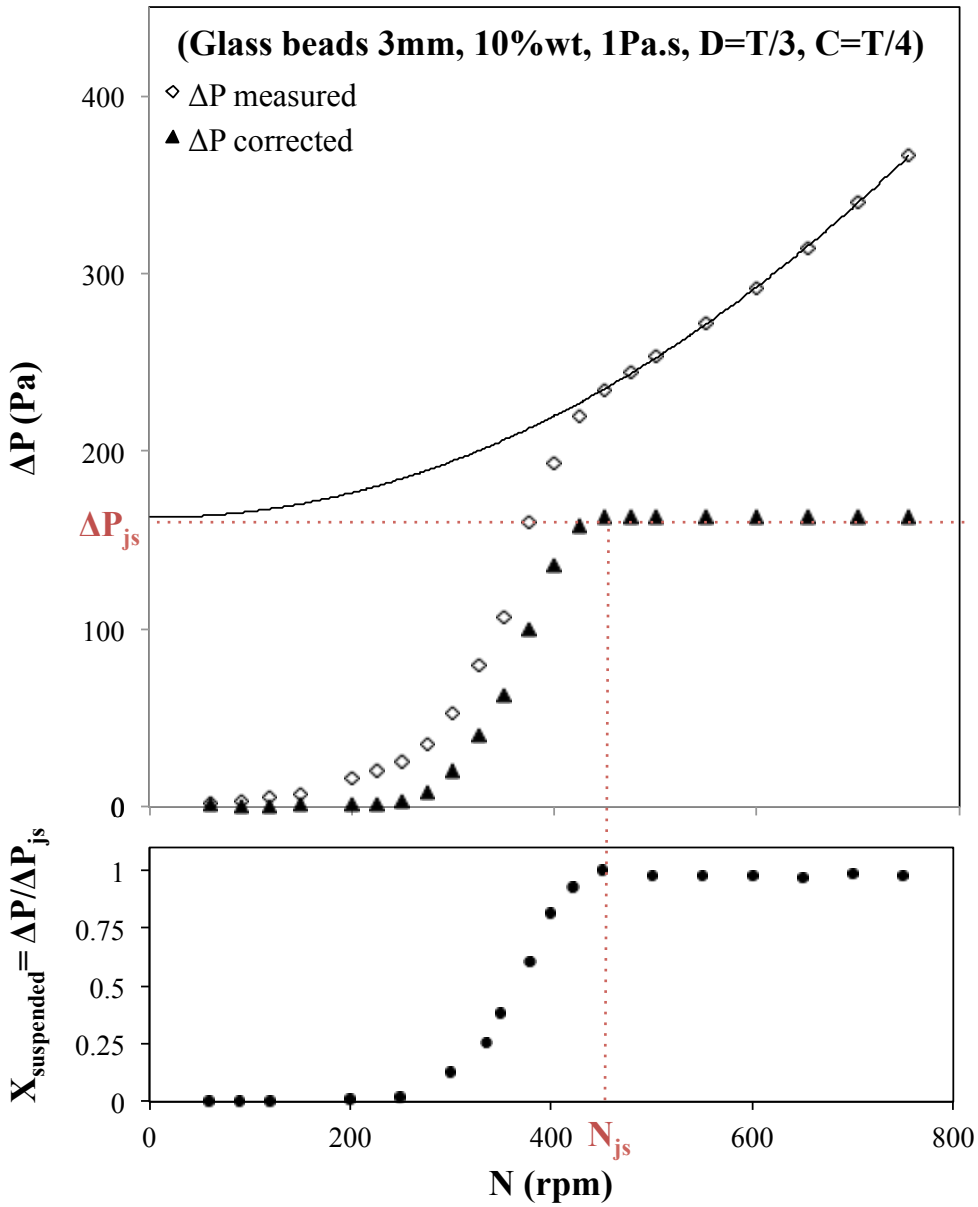

Figure 10.4 Evolution of the total pressure and static pressure using the pressure gauge technique. The parabola is the correction for the hydrodynamic pressure. Adapted from Blais *et al.* [40]

this time interval can have its position decorrelated from its position at time t_0. Otherwise, if a particle remains unsuspended, then its position is practically unchanged and is perfectly correlated with its initial position. Therefore, the value of the mixing index (λ_k, the largest eigenvalue) should be linked to the fraction of unsuspended particles. The only assumption behind this approach is that once particles are suspended, they are also dispersed. Indeed, if particles move as large clusters, a large correlation would be retained among them. It remains to be determined whether this method can be applied in the laminar and transitional regimes where the dispersion of the particles usually occurs over a relatively long time scale.

We showed in earlier work [39] that the DFA technique can be used to measure the fraction of suspended particles in a stirred tank in the turbulent regime. We reported that the observation window should be sufficiently large to allow for the full decorrelation of the system at high impeller speed. In the case of the turbulent regime, we reported that, for $\Delta t_{js} \geq 2$ s, the results for the fraction of suspended particles were less sensitive to Δt_{js}.

The mixing index analysis in the present study is based on cylindrical coordinates ($[\boldsymbol{e}_r, \boldsymbol{e}_\theta, \boldsymbol{e}_z]$), as discussed in Section 10.3.1.

10.4 Methodology

10.4.1 Mixing system

The mixing rig studied consists of a 0.365 m diameter (T) flat-bottomed, cylindrical transparent vessel equipped with a T/3 diameter (D) pitched blade turbine (PBT). The height of the liquid is set to that of the tank diameter (H=T). The particles are glass beads (10% w/w) with a Sauter ($d_{p,32}$) diameter of 3.02 mm in a glucose solution with a viscosity of 1 Pa.s. The set-up is shown in Figure 10.5.

The present study is separated into two parts. The aim of the first part is to characterize the mechanisms and dynamics of the suspension of the particles as well as the influence of the DEM parameters used for the simulations. We use the set-up described by Lassaigne *et al.* [173], with a clearance of $C = T/4$. The dimensions of the mixing rig for this part of the study are summarized in Table 10.3.

The aim of the second part of this work is to study the impact of the geometrical configuration (impeller clearance and presence of baffles) on the ability of the stirred tank to suspend and distribute the particles. In the present work, the clearance is set to three different standard C values ($T/5$, $T/4$, and $T/3$). The set-ups are studied with and without four baffles of width $W = T/10$.

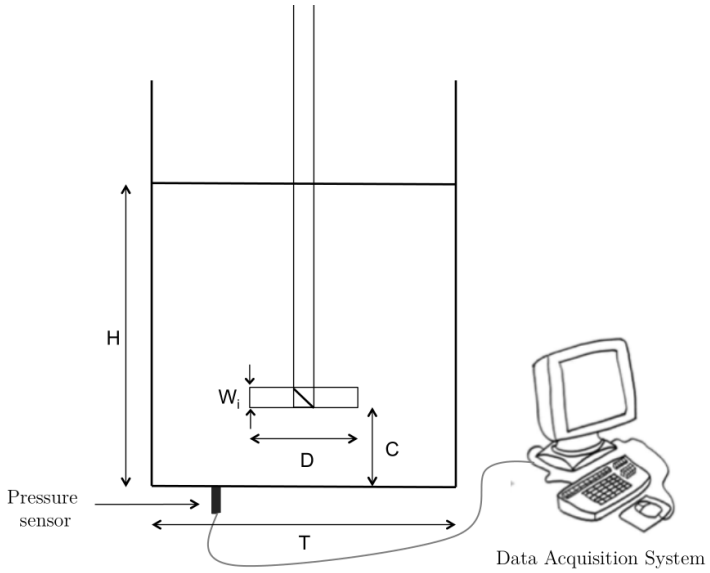

Figure 10.5 Experimental set-up

Symbol	Name	Dimension
T	Tank diameter	0.365m
D	Impeller diameter	$\frac{T}{3}$
H	Liquid level	T
C	Off-bottom clearance	$\frac{T}{4}$
W_i	Blade width	$\frac{D}{5}$

Table 10.3 Dimensions of the mixing set-up

Symbol	Name	Value
ρ_f	Density of the fluid	1390 kg.m^{-3}
μ	Dynamic viscosity of the fluid	1 Pa.s
ρ_p	Density of the solid particles	2500 kg.m^{-3}
d_p	Range of diameters of the solid	2.66-3.5 mm
$d_{p,32}$	Sauter diameter	3.02 mm
x_s	Mass fraction of solid	10 %
ϵ_s	Volume fraction of solid	5.8 %

Table 10.4 Physical properties of the fluid and the particles

10.4.2 Simulation set-up

The simulations were performed using the CFD-DEM model presented in Section 10.2. The model parameters used in the simulation are presented in Table 10.5. The parameters are based on the work of Di Renzo and Di Maio [87], Di Renzo *et al.* [85], and Shao *et al.* [276] for glass beads suspended in a liquid. The same mechanical properties were given to both the walls and the particles. The sensitivity of the model to variations of the DEM parameters (E, e_r, μ_f) is discussed in Section 10.5.5. To reproduce the size distribution of the particles that was measured experimentally, 10 different diameters were used. A total of 148 700 particles were required to reproduce the mass fraction of 10%. The model used for the simulations includes all the hydrodynamic forces presented in Section 10.2.3. The Saffman lift force is included in this model, but was not in a previous investigation [40]. The impact of this force will be assessed in Section 10.5.1 by comparing the results obtained in the present study with those from the earlier investigation [40].

In the simulations, the pressure was monitored at the bottom of the tank and was averaged using the procedure described in [40].

The background hexahedral mesh used for the CFD consisted of 33x88x60 (r,θ,z) cells with additional mesh refinement in the swept volume of the impeller (and close to the baffles, when present), for a total of 350k (400k with the baffles) cells. We found that, for this geometry, mesh refinement past this level did not lead to any measurable change in the torque ($< 1\%$) or the velocity field [40]. The same time step was used for all the simulations. The Courant-Friedrichs-Lewy condition was satisfied for all the simulations and was below 0.75. The coupling time step Δt_c was chosen to ensure stable solid-fluid coupling as per our previous stability analysis [40]. The time step for the DEM particles was below 15% of the characteristic time of Rayleigh waves (Δt_{Ra}) ensuring the stability of the DEM part. The

Symbol	Name	Value
Y	Young's modulus	100 MPa
e_r	Coefficient of restitution	0.9
ν	Poisson ratio	0.25
$\mu_{s,ij}$	Coefficient of sliding friction	0.3
$\mu_{r,ij}$	Rolling friction	0.1
Δt_{DEM}	DEM time step	5×10^{-6}
Δt_{CFD}	CFD time step	1×10^{-4}
Δt_c	Coupling time-step	1×10^{-4}

Table 10.5 Parameters for the simulations of solid-liquid mixing

expression for Δt_{Ra} is :

$$\Delta t_{Ra} = \frac{\Pi}{2} d_p \sqrt{\frac{\rho_p}{G}} \left(\frac{1}{0.1631\nu + 0.8766} \right) \tag{10.11}$$

The dependency of the Rong drag model on the void fraction was relaxed to ensure the stability of the explicit solid-fluid and fluid-solid coupling. We refer the reader to the stability analysis performed in [40] for a thorough explanation of this procedure.

10.5 Investigation of the mixing dynamics and suspension mechanisms

In this section, we first evaluate the role of the lift force. We then investigate the dynamics of the solid-liquid mixing operation and evaluate the fraction of suspended particles and the efficiency of the mixing using the approaches presented in Section 10.3, namely the LSFA-$\Delta \boldsymbol{x}$, DFA, and mixing index techniques. We then investigate the role of the particle properties in order to establish the sensitivity of the model to the DEM parameters and to isolate the dominant particle-particle forces.

10.5.1 Validation of the model with lift forces

We recently studied the mixing system considered in this work without including the Saffman lift force for the solid-fluid interactions [40]. However, given the high viscosity of the suspension and the high shear forces at the surface of the bed of particles, these forces could potentially influence the fraction of suspended particles when in a partially suspended state.

The graph in Figure 10.6 presents the evolution of the fraction of suspended particles as a function of the impeller speed, as measured by the PGT, with and without the Saffman lift force, and compares it to the experimental data of Lassaigne *et al.* [173].

It can be seen that adding the Saffman lift force increases the fraction of suspended particles slightly for all impeller speeds, but does not affect the results significantly. In both cases (with and without the lift forces), the model appears to slightly overestimate the fraction of suspended particles for $N < 400$ RPM . The impeller speed $N = 425$ RPM corresponds to N_{js} since, according to the experimental and numerical PGT results, all the particles are suspended.

We conclude from these results that the Saffman lift force plays a negligible role in the suspension of the particles.

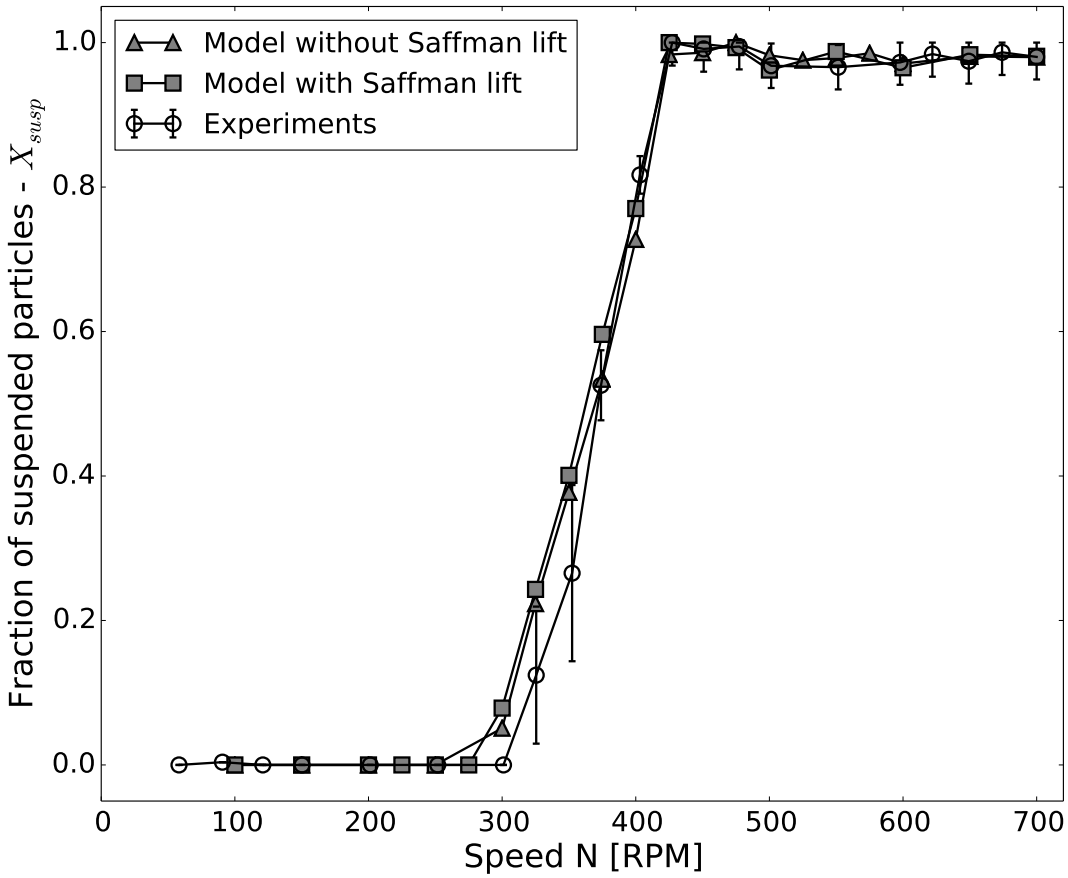

Figure 10.6 Evolution of the fraction of suspended particles as function of the impeller speed, as measured in the numerical simulations with and without lift forces, and in the experiments

10.5.2 Flow patterns and solids distribution

The velocity profiles, the particle concentration profiles and the particle dynamics are next considered. All the slices of the stirred vessel presented in this section were obtained by averaging the quantity of interest over multiple impeller rotations (at least more than 10) in the plane of the normal vector $\boldsymbol{e}_y$ ($P_{\boldsymbol{y}}$ plane).

The slices in Figure 10.7 present the phase-averaged solid volume fraction (or concentration) for three impeller speeds (150, 250, and 350 RPM), while Figure 10.8 shows the corresponding velocity profiles. As can be seen, the particles are only suspended in a region below the impeller at low speed, leading to the formation of an umbrella structure below the impeller. Increasing the velocity leads to the onset of erosion where the particles ascended along the lateral walls of the tank. As soon as they are eroded along these walls, the particles are able to reach a considerable height due to the high viscosity of the fluid. The particles become increasingly distributed and dispersed as the impeller speed is increased.

Figures 10.9 and 10.10 show the phase-averaged void fraction and velocity profiles for higher impeller speeds of 450, 550 and 650 RPM, respectively. As can be seen, at all these speeds, the PBT behaves much like a radial discharge impeller since the fluid jets coming out of the impeller blades are directed toward the lateral walls. For values of N larger than $N_{js} =$ 425 RPM predicted by the PGT technique, a significant amount of particles accumulate in a dense conical region directly below the impeller, as can be seen in Figure 10.9. An examination of the pressure profiles (not shown here) revealed that the accumulation of particles appears in part to be due to the negative dynamic pressure below the impeller caused by the high speed of the impeller rotation and the large rigid body-like, angular motion of the fluid therein. It should be noted that the size of this dense cone of particles tends to decrease slightly as the impeller speed increases from $N = 450$ to $N = 650$ RPM.

It is quite clear, however, that while the PGT technique indicates full suspension, the system does not reach a fully suspended state even at an impeller speed of $N = 650$ RPM. In fact, the cone of particles at the bottom of the vessel is at least stable for $N \in [425, 700]$ RPM and might remain stable at higher impeller speed. Consequently, increasing the speed past $N = 425$ RPM does not significantly increase the number of suspended particles and, as a result, the hydrostatic pressure remains constant for $N > 425$ RPM. Thus, when the dynamic pressure correction is applied to the PGT, the system appears to be fully suspended at $N = 425$ RPM since the maximal value of the hydrostatic pressure is reached at this velocity. However, it must be kept in mind that approximately 5 to 10 % of the particle volume remains unsuspended or at least isolated from the bulk of the flow for $N \geq 425$ RPM.

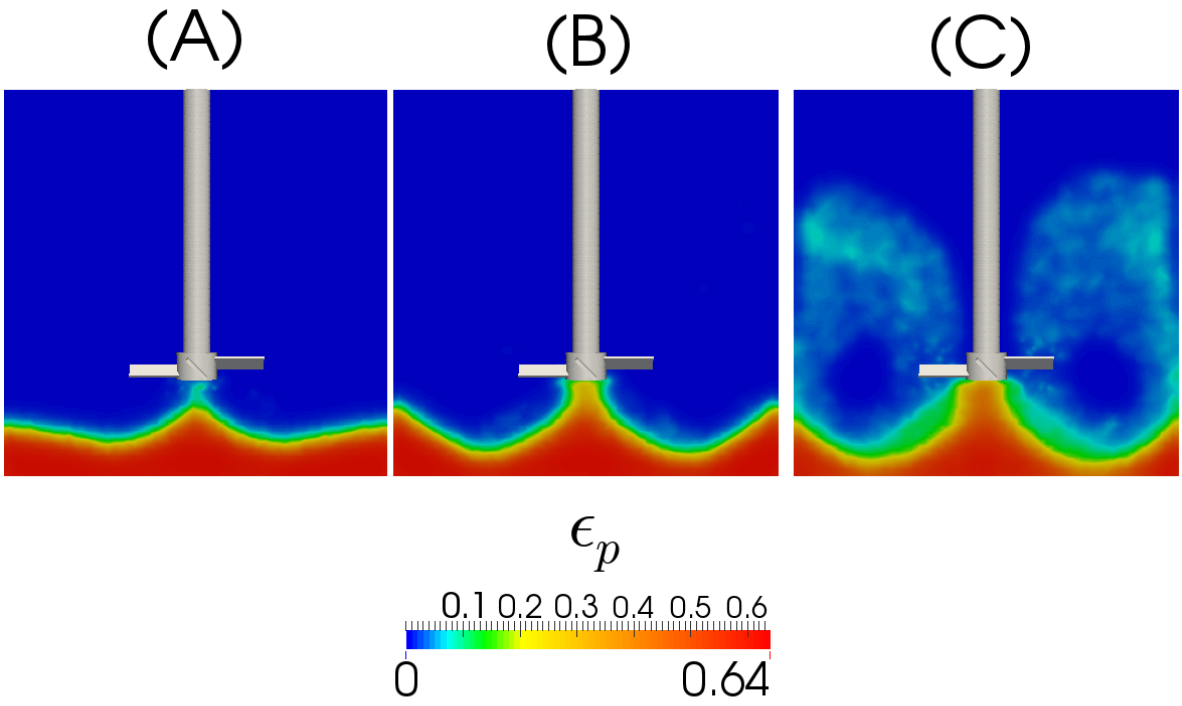

Figure 10.7 Phase-averaged solid volume fraction in the P_y plane for impeller speed of (A) 150 RPM, (B) 250 RPM and (C) 350 RPM

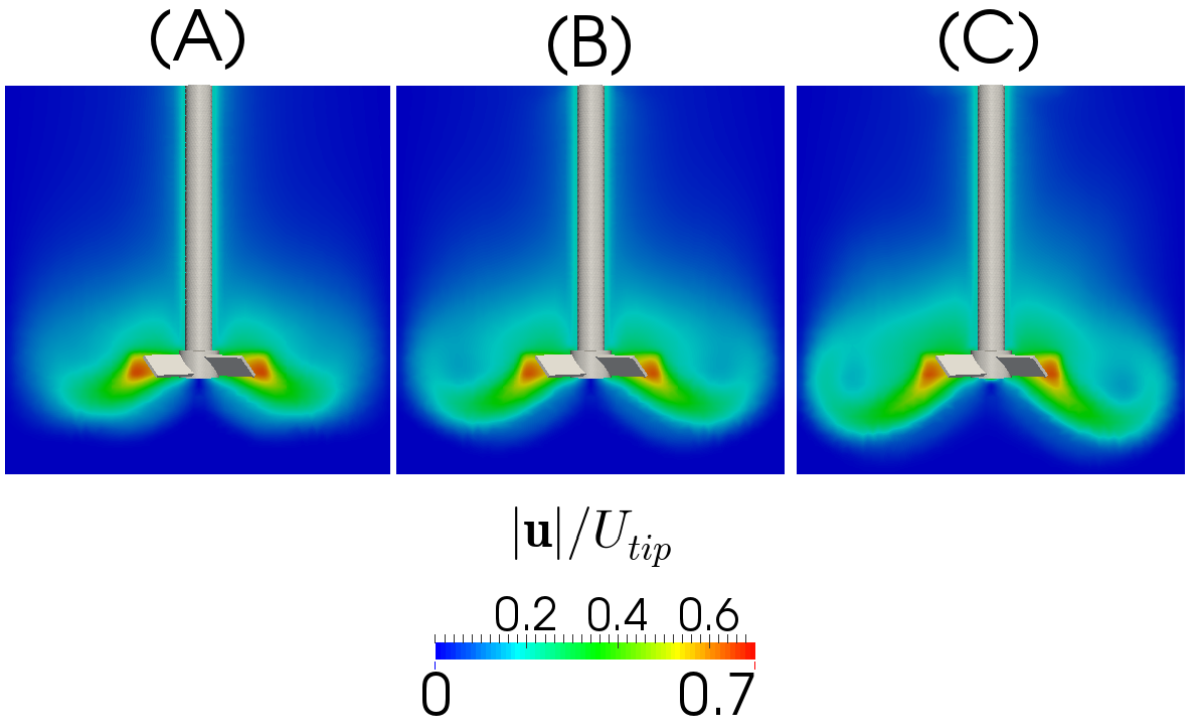

Figure 10.8 Phase-averaged velocity magnitude in the P_y plane for impeller speed of (A) 150 RPM, (B) 250 RPM and (C) 350 RPM

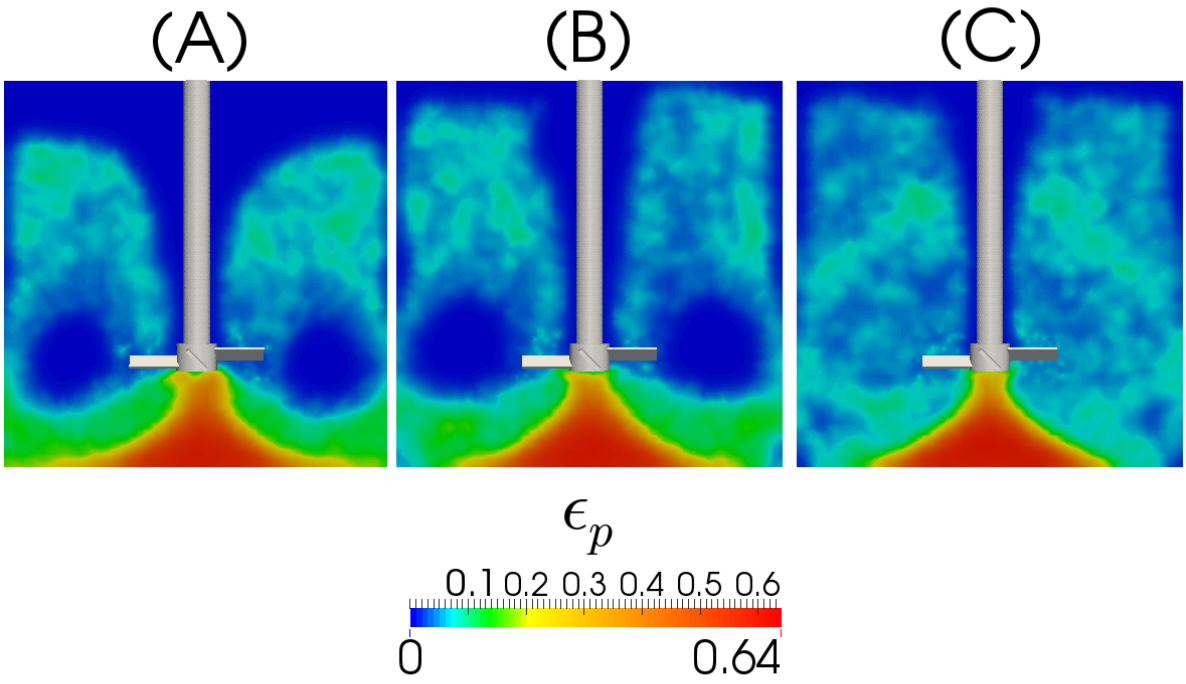

Figure 10.9 Phase-averaged solid volume fraction in the P_y plane for impeller speed of (A) 450 RPM, (B) 550 RPM and (C) 650 RPM.

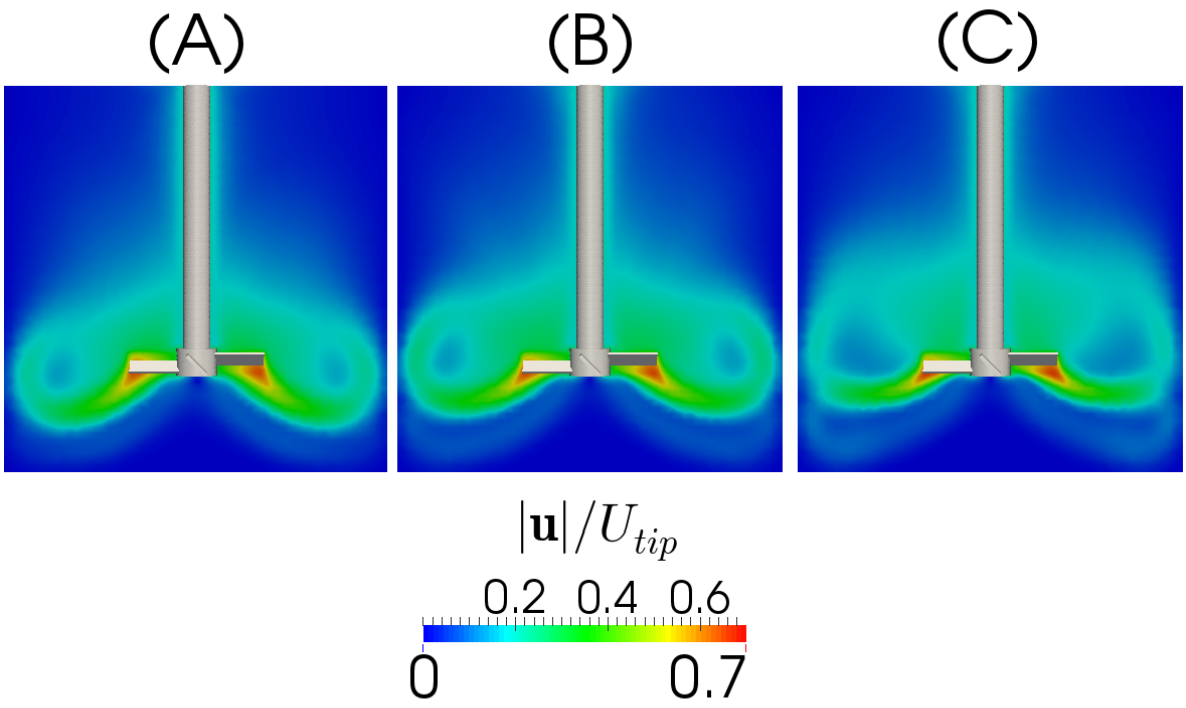

Figure 10.10 Phase-averaged velocity magnitude in the P_y plane for impeller speed of (A) 450 RPM, (B) 550 RPM and (C) 650 RPM

Based on these results, it appears that the PGT technique should be used with care. It only provides a valid assessment of the fraction of suspended particles if the system is able to reach full suspension. This is not the case for the present mixing system.

Furthermore, at lower impeller speeds (N = 450 and 550 RPM), Figures 10.9 (A) and (B) reveal that toroidal zones devoid of particles appear at the top of the impeller blade. Similar zones were identified previously by Lamberto *et al.* [172] and Cabaret *et al.* [56] using colorimetric experiments with single phase flow systems and various types of impellers. We recently showed [39] that this structure can also appear in a turbulent regime when baffles are present. At a higher impeller speed ($N \geq 650$ RPM, Figure 10.9 (C)), the toroid becomes unstable and disappears.

The cross-section in Figure 10.11 shows the logarithmic values of the particle Reynolds number ($Re_p = \frac{\rho_f d_p |\boldsymbol{u}-\boldsymbol{v}|}{\mu}$) for an impeller speed of 650 RPM. It can clearly be seen that, with the exception of the regions near the impeller and close to the lateral walls, the particle Reynolds number is very low, indicating that, in the bulk of the flow, the particles behave like a passive scalar. Since the particles follow the streamlines in the bulk of the flow, they are able to rise sufficiently high in the liquid. This explains why the particles are well distributed in the phase-averaged void fraction profiles of Figures 10.9 (B) and (C).

10.5.3 Lagrangian analysis of the fraction of suspended solids

While the PGT predicts a fully suspended state (numerically and experimentally) based on observations of the phase-averaged volume fraction, a portion of the particles accumulate and remains unsuspended at the bottom of the vessel below the impeller, even at high impeller speeds.

We used the DFA and LSFA-$\Delta\boldsymbol{x}$ techniques to analyze the fraction of suspended particles based on their position.

The graph in Figure 10.12 shows the fraction of suspended particles obtained with the LSFA-$\Delta\boldsymbol{x}$ technique. At low impeller speeds, LSFA-$\Delta\boldsymbol{x}$ appears to overestimate the fraction of suspended particles compared to the PGT results. This is due to the motion of the particles at the top of the particle bed, which are considered suspended by the LSFA-$\Delta\boldsymbol{x}$ technique since they are in motion, but which does not appear in the PGT measurements since their weight is still partially held by the walls of the vessel or the particles underneath them. Better agreement with the experimental measurements is obtained at higher impeller speeds. However, even at higher speeds, the fraction of suspended particles X_{susp} measured by the LSFA-$\Delta\boldsymbol{x}$ technique reaches a maximum of $X_{susp} = 96\%$ for $\Delta x_{js} = d_p$ and $\Delta t_{js} = 2$ s when

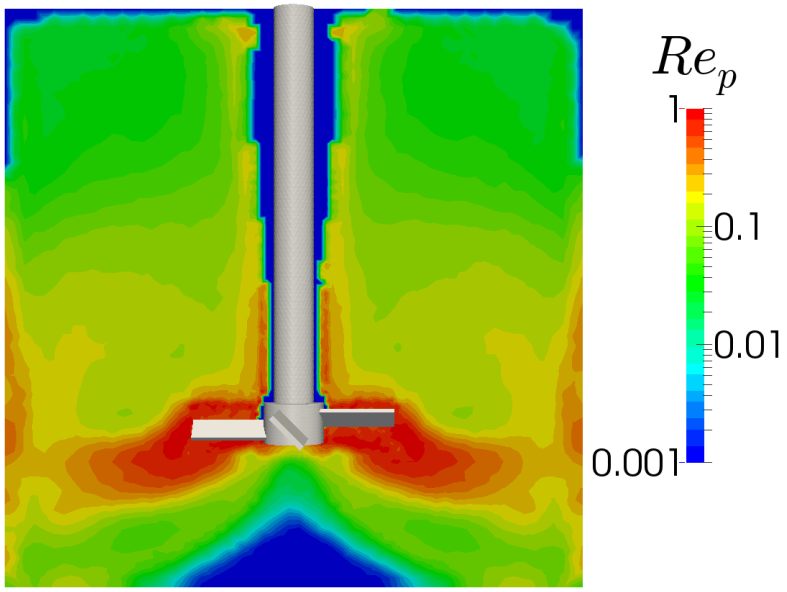

Figure 10.11 Phase-averaged particle Reynolds number (Re_p) in the P_y plane for $N = 650$ RPM. Note that the scale is logarithmic.

N reaches 450 RPM, before leveling off to a plateau at $X_{susp} = 91\%$ for $\Delta x_{js} = d_p$ and $\Delta t_{js} = 2$ s, indicating incomplete suspension. This result is consistent with the void fraction profiles obtained in Section 10.5.2 and indicates that the system is incapable of reaching a fully suspended state. However, the presence of a maximum at $N = 450$ RPM with the LSFA-$\Delta \boldsymbol{x}$ technique is surprising. This is possibly an artifact of the method where some particles are considered suspended because they are in motion, despite the fact that they are still in contact with the particles at the bottom of the vessel. This LSFA-$\Delta \boldsymbol{x}$ result is not in agreement with the phase averaged solid concentration of Figure 10.10 where the size of the cone appears to decrease with an increase in the impeller speed.

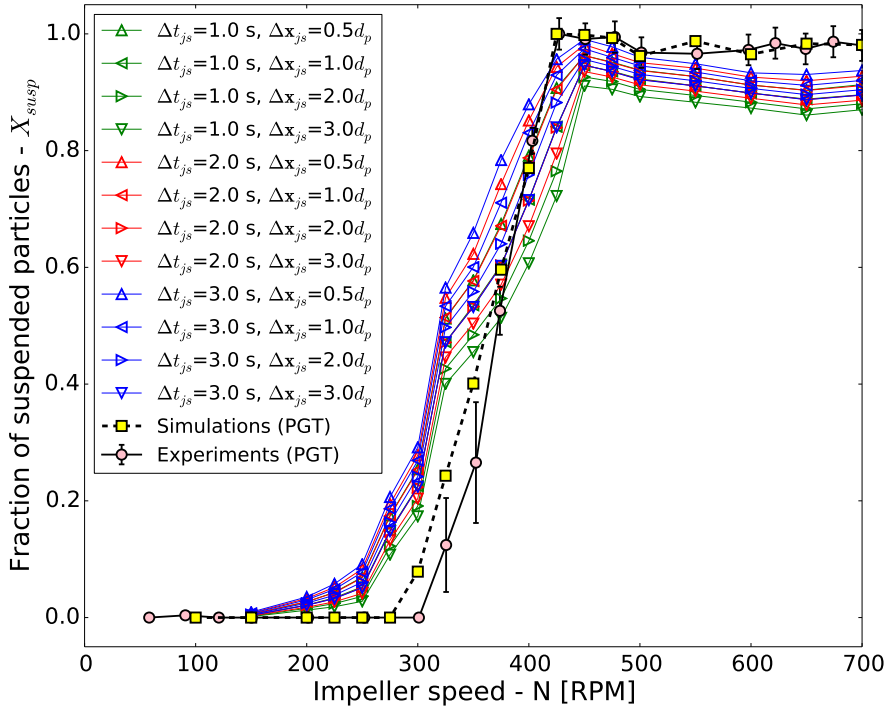

Figure 10.12 Evolution of the fraction of suspended particles as measured by the LSFA-$\Delta \boldsymbol{x}$ technique and comparison with the PGT results

The graph in Figure 10.13 shows the decorrelated fraction as a function of the impeller speed for the DFA technique and three values of the time interval Δt_{js}. It can clearly be seen that the DFA results do not coincide with the fraction of suspended particles measured by the PGT or the LSFA-$\Delta \boldsymbol{x}$ technique in Figure 10.12. In a previous study [39], the DFA technique was used in the turbulent regime. Thus, as soon as the particles were suspended, they were distributed and dispersed, and were thus decorrelated. This method could thus be used to

directly assess the fraction of suspended particles in the turbulent regime. In the present case, the flow is laminar or transitional and the dispersion of the particles thus occurs over a much longer time scale ($>> \Delta t_{js}$) since there is no turbulent eddies to contribute to their motion. It thus appears that the DFA technique cannot be used with the laminar and transitional regimes to measure the fraction of suspended particles.

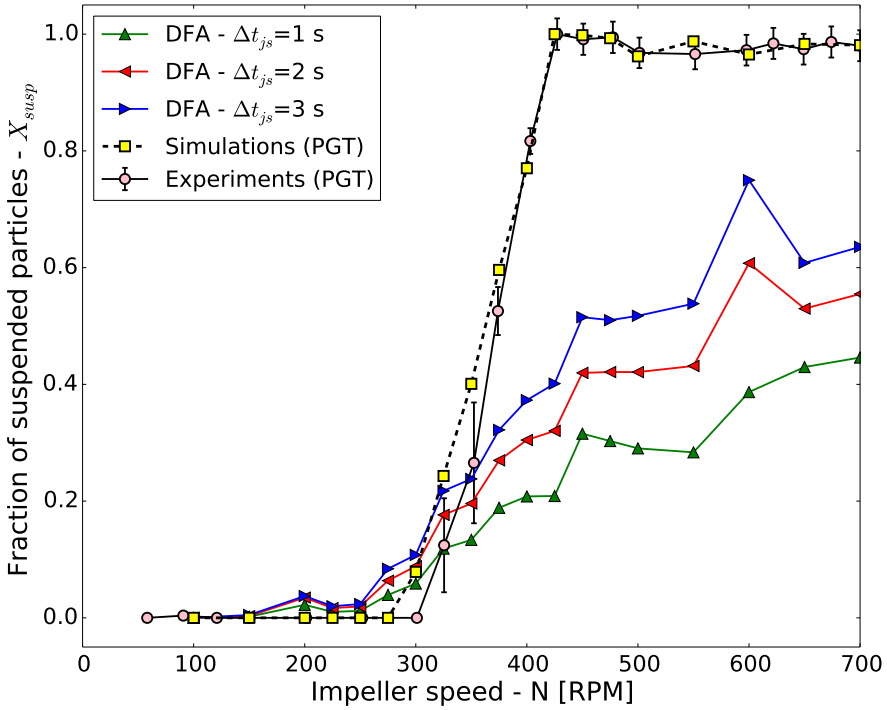

Figure 10.13 Evolution of the fraction of suspended particles as measured by the DFA and comparison with the PGT results

10.5.4 Mixing index

The results obtained with the solid concentration profiles and the LSFA-$\Delta \boldsymbol{x}$ technique in Sections 10.5.2 and 10.5.3, respectively, show that the system does not reach a fully mixed state since not all the particles are fully suspended. However, it remains to be determined whether the particles within the cone below the impeller circulate between the cone and the bulk of the flow or whether they remain isolated.

The mixing index is able to measure the degree of mixing and thus can be used to identify the presence of dead zones. The graph in Figure 10.14 displays the value of the mixing index after

100 s of mixing as a function of the impeller speed. As can be seen, the mixing index decreases before reaching a minimum value at $N = 450$ RPM and then increases asymptotically to a positive value. This is in agreement with the observed results of the LSFA-$\Delta\boldsymbol{x}$ analysis and indicates that particles not only accumulate within the cone below the impeller, but that they remain in this position indefinitely.

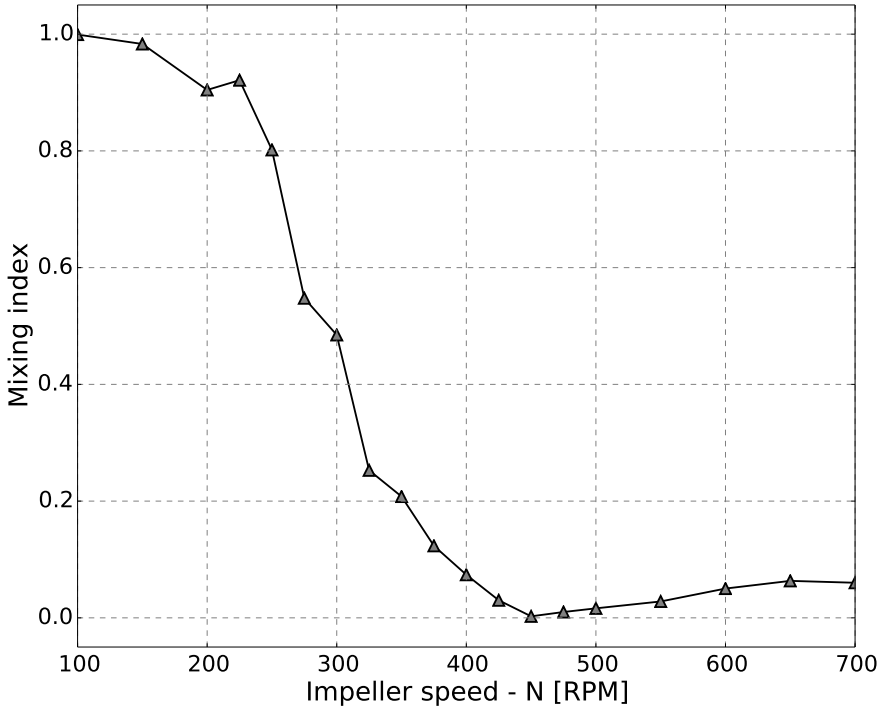

Figure 10.14 Evolution of the mixing index for a period of 100 s as a function of the impeller speed.

It is interesting to note that for all $N \geq 450$ RPM, the eigenvector corresponding to the mixing index (λ_k) is $\boldsymbol{r_k} = 0.8\boldsymbol{e}_r + 0.5\boldsymbol{e}_z$. This vector corresponds approximately to the vector normal to the cone of accumulated particles at the bottom of the tank, as can be seen in Figure 10.9. This once again indicates incomplete mixing since this direction is the one along which there is the highest degree of correlation between the particles.

10.5.5 Role of the mechanical properties of the particles

In a recent investigation [40], we used a set of DEM parameters taken from [85,87,276] for the properties of glass beads. However, in [40], we noted that the roles of the solid properties, let

alone the friction coefficient (μ_s), the coefficient of restitution (e_r) and the Young's modulus (Y), and their impact on the dynamics of solid-liquid flows were unclear. In particular, we questioned the use of a coefficient of restitution based solely on rebound experiments in air since the results reported by Gondret *et al.* [111] showed that the apparent coefficient of restitution of a particle quickly decreases towards zero when the Stokes number ($St = \frac{U\tau_p}{L}$, where τ_p is the particle relaxation time, U the fluid velocity and L a length scale) is low ($St < 1$). It is thus important to determine the sensitivity of the results obtained previously to variations of the values of these three major solid properties. The standard set-up presented in Section 10.4 and the solid properties considered are given in Table 10.6. The effect of these parameters is evaluated at four impeller speeds : N = 250, 375, 450 and 600 RPM. These impeller speeds correspond to four distinct regimes (see Section 10.5.6) : the formation of an umbrella of particles (N = 250 RPM), erosion above the impeller (N = 375 RPM), close to N_{js} measured via the PBT (N = 450 RPM), and at high impeller speeds where the particles are well distributed (N = 600 RPM).

The graphs in Figures 10.15 and 10.16 present the evolution of the pressure at the bottom of the tank at impeller speeds of 250, 375, 450 and 600 RPM for the cases described in Table 10.6. As can be seen, reducing the coefficient of restitution (*std* or *inelastic*) or changing the stiffness (*std*, *soft* or *hard*) of the particles at all velocities have no effect on the dynamics of the suspension since all pressure curves are superimposed on the *std* curve. Given the large changes applied to the stiffness and coefficient of restitution in these cases, we can conclude that the model is not sensitive to variations of these parameters.

The effect of the coefficient of sliding friction μ_s is more pronounced. At a low impeller speed (N = 250 RPM), where the eroded particles are in the umbrella region below the impeller, changing the friction coefficient does not alter the formation of this structure (not shown here), indicating that this coherent and stable pattern is not due to friction forces or

Case	μ_s	e_r	Y
std	0.3	0.9	100 MPa
soft	0.3	0.9	**10 MPa**
hard	0.3	0.9	**1000 MPa**
inelastic	0.3	**0.01**	100 MPa
low μ_s	**0.1**	0.9	100 MPa
high μ_s	**0.9**	0.9	100 MPa
no-tf (no tangential forces)	-	0.9	100 MPa

Table 10.6 Sets of particle mechanical properties considered to assess their impact on flow dynamics

particle/particle contacts.

At $N = 375$ RPM, as can be seen in Figure 10.15, the friction coefficient plays a significant role. Increasing the friction coefficient increases the fraction of suspended particles as well as the speed at which the particles are eroded. In fact, at such a speed, the PGT predicts 50% of the particles are suspended in the *std* case (Figure 10.6), allowing perfect slip between the particles ($\mu_s = 0$) prevents the particles from being suspended. At an impeller speed of 450 RPM, as can be seen in Figure 10.16, the friction coefficient only affects the speed at which the particles are eroded, but does not affect the status of the suspension at steady state. At an impeller speed of $N = 600$ RPM, changing the value of the friction coefficient does not alter the dynamics of the mixing in any fashion.

Based on the PGT measurements (Figure 10.6), it appears that the coefficient of friction only alters the fraction of suspended particles at intermediate impeller speeds and the speed at which steady state is reached. Lastly, we can be conclude from these simulation results that μ_s is the only DEM parameter that requires calibration for this type of viscous solid-liquid flows.

10.5.6 Discussion on the suspension mechanisms

Some partial conclusions can be drawn from our analyses. First, four distinct regimes can be established for the solid-liquid dynamics that occurs in the mixing rig investigated :

- At a low impeller speed ($N < 150$ RPM), only a gentle "simmering" occurs at the top of the particle bed, but no particles are suspended.
- For $N \in [150, 275]$ RPM, the particles are drawn below the impeller and remain therein, forming an umbrella, and as such, do not circulate in the bulk of the tank.
- For $N > 275$ RPM, the umbrella of particles is still present, but the particles begin to erode and are lifted in the bulk of the flow toward the lateral walls.
- For $N > 450$ RPM, some particles remain unsuspended underneath the impeller. Increasing the impeller speed increases the maximal height reached by the particles.

We showned using flow visualization, the LSFA-$\Delta\boldsymbol{x}$ technique, and the mixing index that at all impeller speeds, a dead zone is present in the center of the vessel below the impeller where the particles accumulate and are not allowed to circulate in the bulk of the flow. Thus, the system in this configuration cannot be fully mixed except possibly by greatly increasing the impeller speed ($N > 700$ RPM).

Our investigation of the role of the DEM parameters also highlighted the fact that the coefficient of sliding friction is the particle-particle collision property that plays the key role in the dynamics of erosion of the particles. This is in agreement with the experimental findings

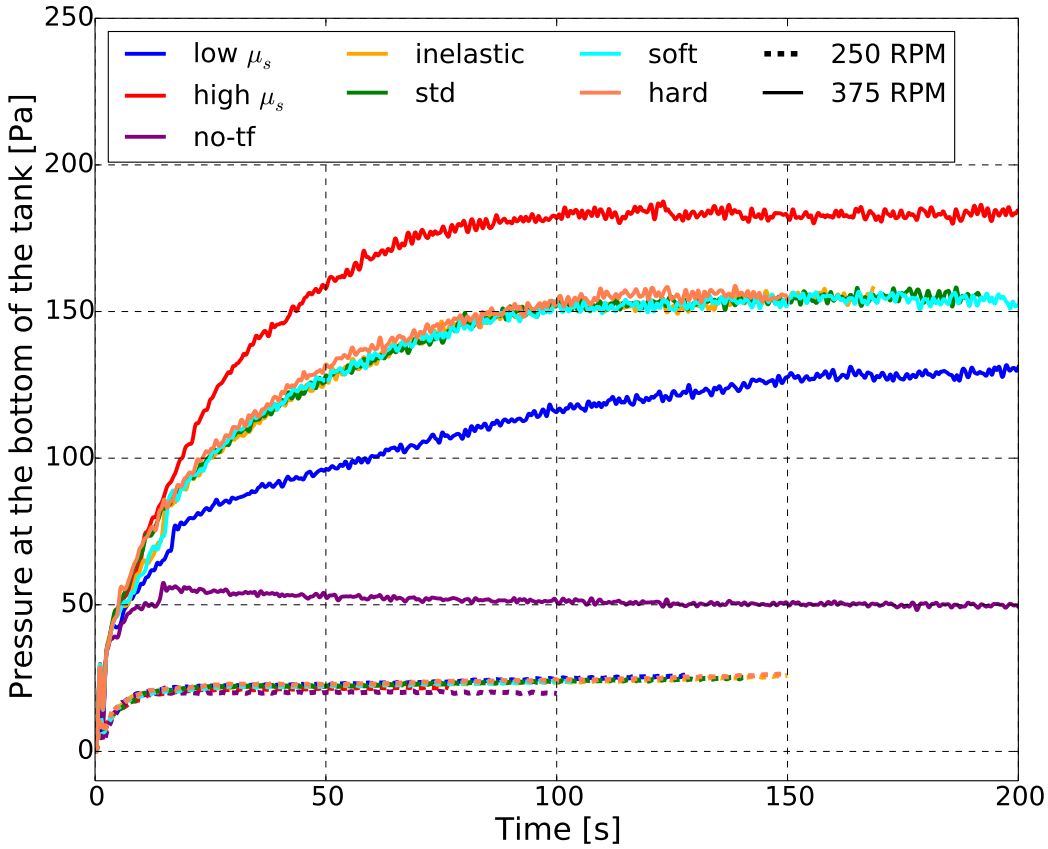

Figure 10.15 Influence of particle properties on the pressure measured at the bottom of the tank for $N = 250$ RPM and $N = 375$ RPM. Note the superposition of the *std*, *inelastic*, *soft* and *hard* curves for all impeller speeds.

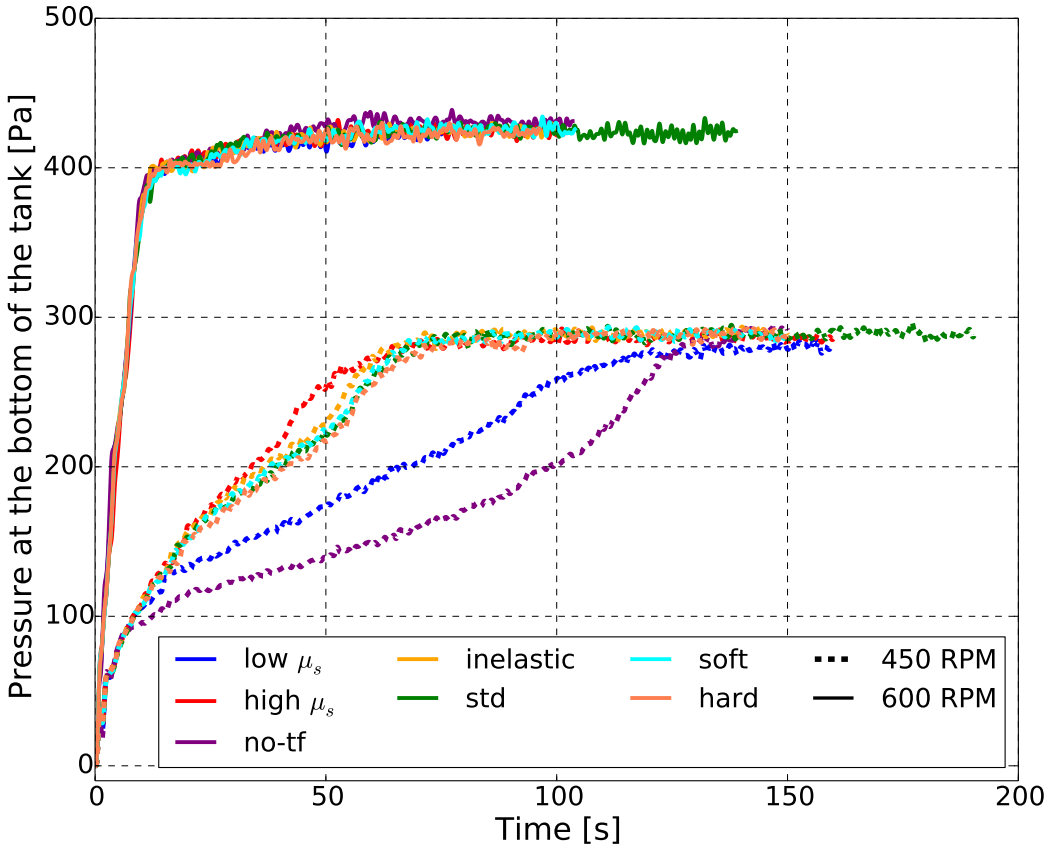

Figure 10.16 Influence of particle properties on the pressure measured at the bottom of the tank for $N = 450$ RPM and $N = 600$ RPM. Note the superposition of the *std*, *inelastic*, *soft* and *hard* curves for all impeller speeds.

of Lassaigne *et al.* [173], who reported that the suspension of particles seemed to behave like the erosion of a particle bed, where the Shields number ($\theta = \frac{\tau}{(\rho_p - \rho_f) g d_p}$ where τ is the shear stress) is the key parameter. Our results indicate that particles are indeed put in motion by the shear stress linked to particle-particle collisions in the upper layer of the particle bed.

10.6 Influence of mixer characteristics

Lastly, we investigated in this section the influence of the bottom clearance (C) and the presence of baffles, on the solid-liquid dynamics, the fraction of suspended particles and their distribution in the tank.

We consider three clearances ($C = \frac{T}{5}$, $\frac{T}{4}$ and $\frac{T}{3}$), with and without baffles. The case where $C = \frac{T}{4}$ and without baffles corresponds to the set-up studied in Section 10.5.

The graph in Figure 10.17 shows the evolution of the fraction of suspended particles measured using the LSFA-$\Delta \boldsymbol{x}$ technique with $\Delta x_{js} = d_p$ and $\Delta t_{js} = 2$s, for all six cases investigated.

It can be seen that the baffled configurations are unable to suspend the particles at the impeller speeds investigated. They perform very poorly compared to the unbaffled configurations. The velocity profiles (not shown here) show that the baffles greatly inhibit the axial flow produced by the PBT. This prevents the erosion of the particle bed and greatly reduces the height reached by the suspended particles. In fact, of baffles amplify the radial discharge when the PBT is operated in the laminar or transitional regime.

As can be seen in Figure 10.17, increasing the clearance from $T/4$ to $T/3$ is detrimental to the suspension of the particles. As revealed by the solid fraction profiles in Figure 10.18, a cone of particles similar to the cone formed at $C = T/4$ forms below the impeller. However, since the impeller is positioned significantly higher, there is a larger zone below the impeller where there is no flow and a negative pressure. This leads to the accumulation of a much larger amount of particles.

Decreasing the clearance from $C = T/4$ to $C = T/5$ increases the fraction of suspended particles at all impeller speeds, with perhaps an exception at $N = 450$ RPM, for which X_{susp} is slightly higher for $C = T/4$. Figure 10.19 shows the void fraction for the two clearances at $N = 450$ RPM. The accumulated particles are close to the bottom-vessel junction whereas most of the unsuspended particles for the $C = T/4$ case are below the impeller.

At an impeller speed of $N = 650$ RPM, the $C = T/5$ configuration is able to fully suspend almost all the particles, as can be seen in Figures 10.17 and 10.20, whereas the fraction of suspended particle in the $C = T/4$ configuration does not approach unity as the particles

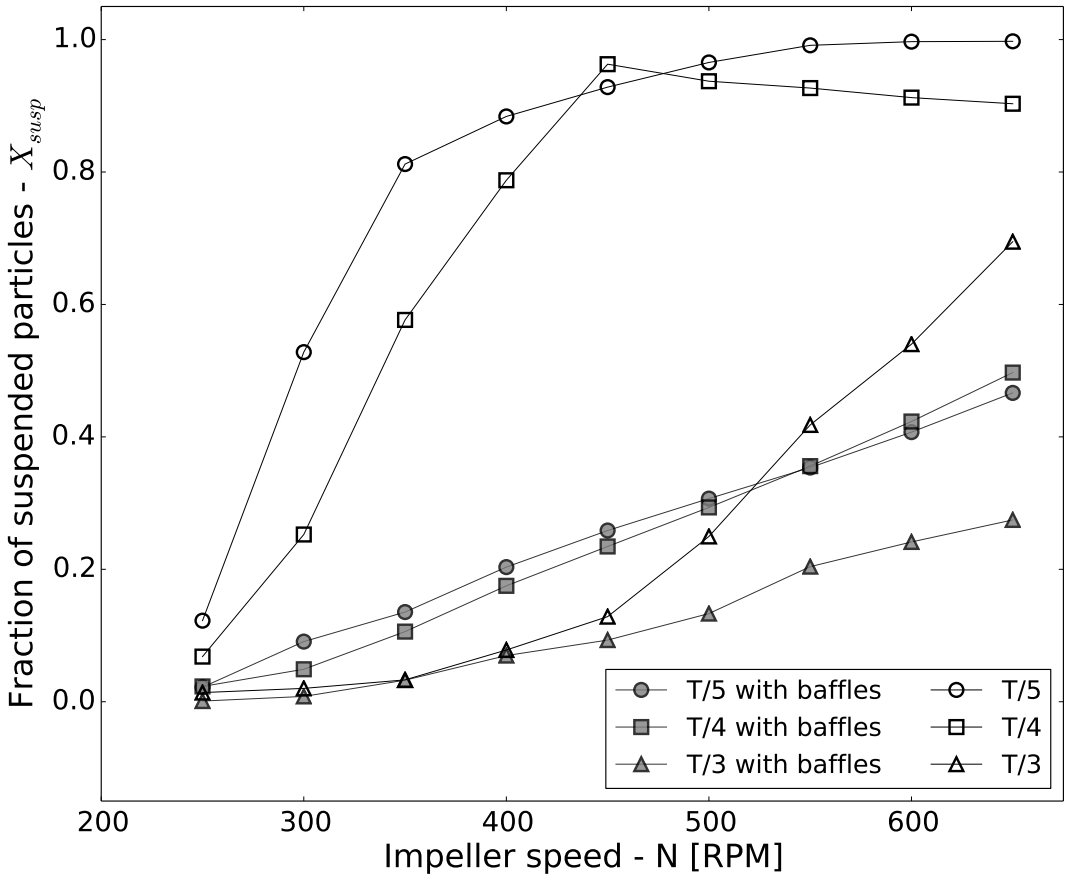

Figure 10.17 Fraction of suspended solid as a function of impeller speed for the six configurations investigated

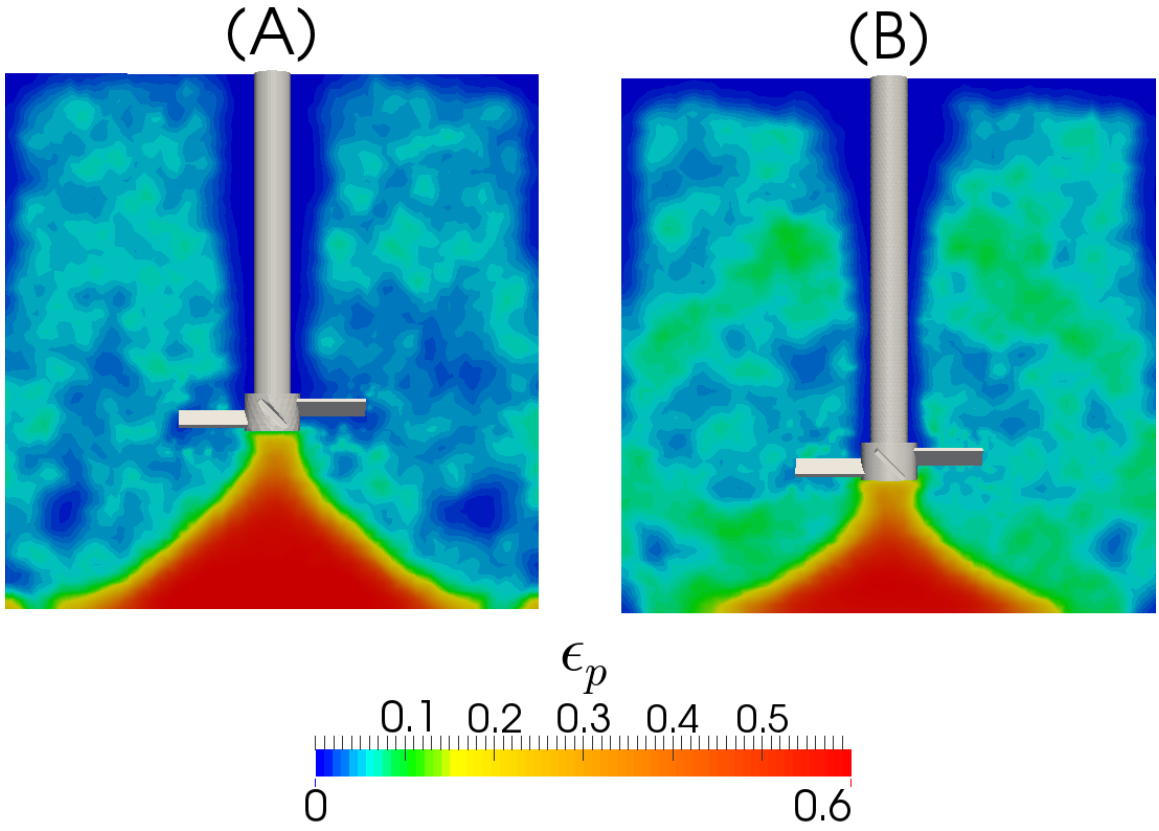

Figure 10.18 Solid volume fraction ($\epsilon_p = 1 - \epsilon_f$) on the P_y cross-section at $N = 650$ RPM for (A) $C = T/3$ and (B) $C = T/4$

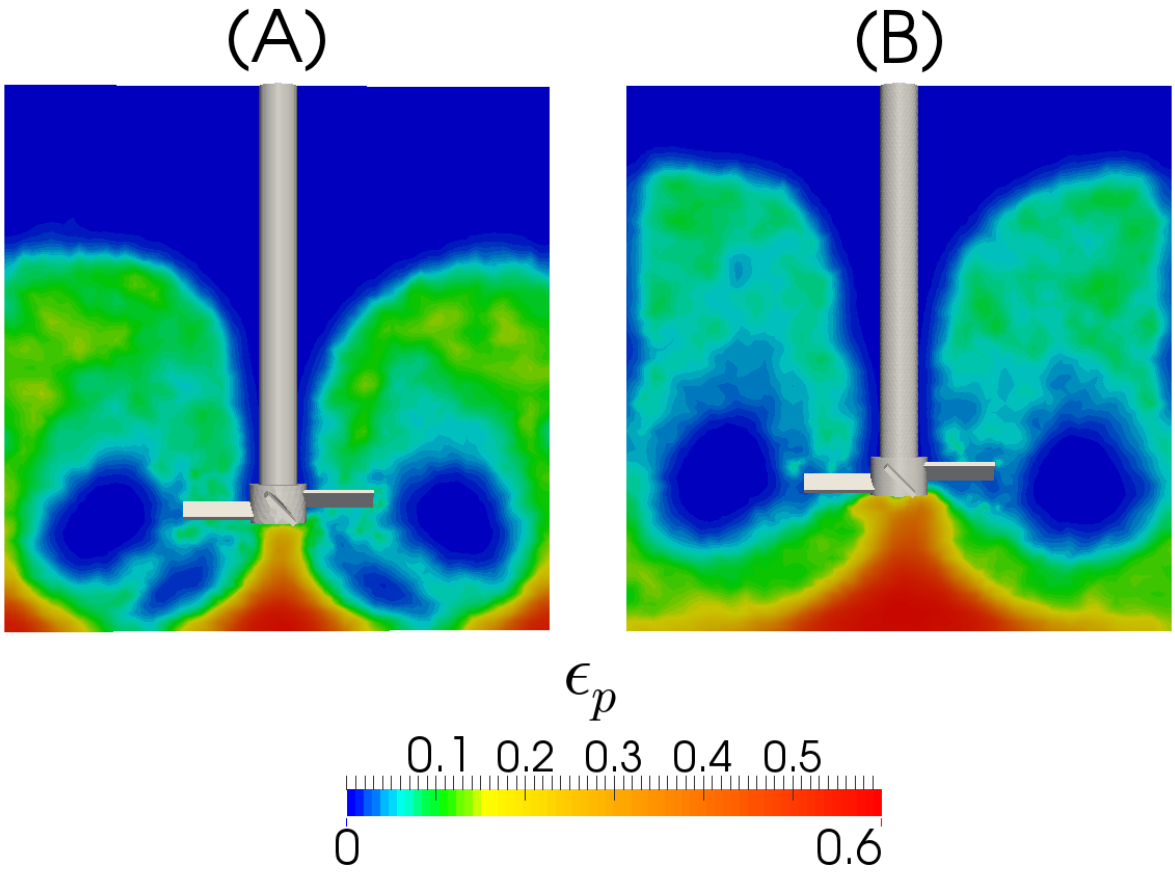

Figure 10.19 Solid volume fraction ($\epsilon_p = 1 - \epsilon_f$) on the P_y cross-section at $N = 450$ RPM for (A) $C = T/5$ and (B) $C = T/4$

accumulate in the cone below the impeller. This is because the cone barely existed for $C = T/5$. At such a low clearance, the structure is not stable since the hydrodynamic interactions between the impeller and the bottom of the tank are much more significant.

The cross-sections in Figure 10.19 show that the eroded particles reach a greater height for $C = T/4$ than for $C = T/5$, indicating that using a lower clearance slightly inhibits the distribution of the particles throughout the tank. However, even for the lowest clearance, the particles are able to reach the top of the vessel at higher impeller speeds, as can be seen in Figure 10.20.

Figures 10.19 and 10.20 show that toroidal zones that are depleted of particles are present for both impeller clerances. For $C = T/4$, this zone is slightly above the impeller blades whereas there are two zones for $C = T/5$: a large one at the same level as the blades and a smaller one below the blades. While this structure broke down at an impeller speed of $N \geq 600$ for $C = T/4$, it remains stable at an impeller speed of $N = 650$ RPM for $C = T/5$.

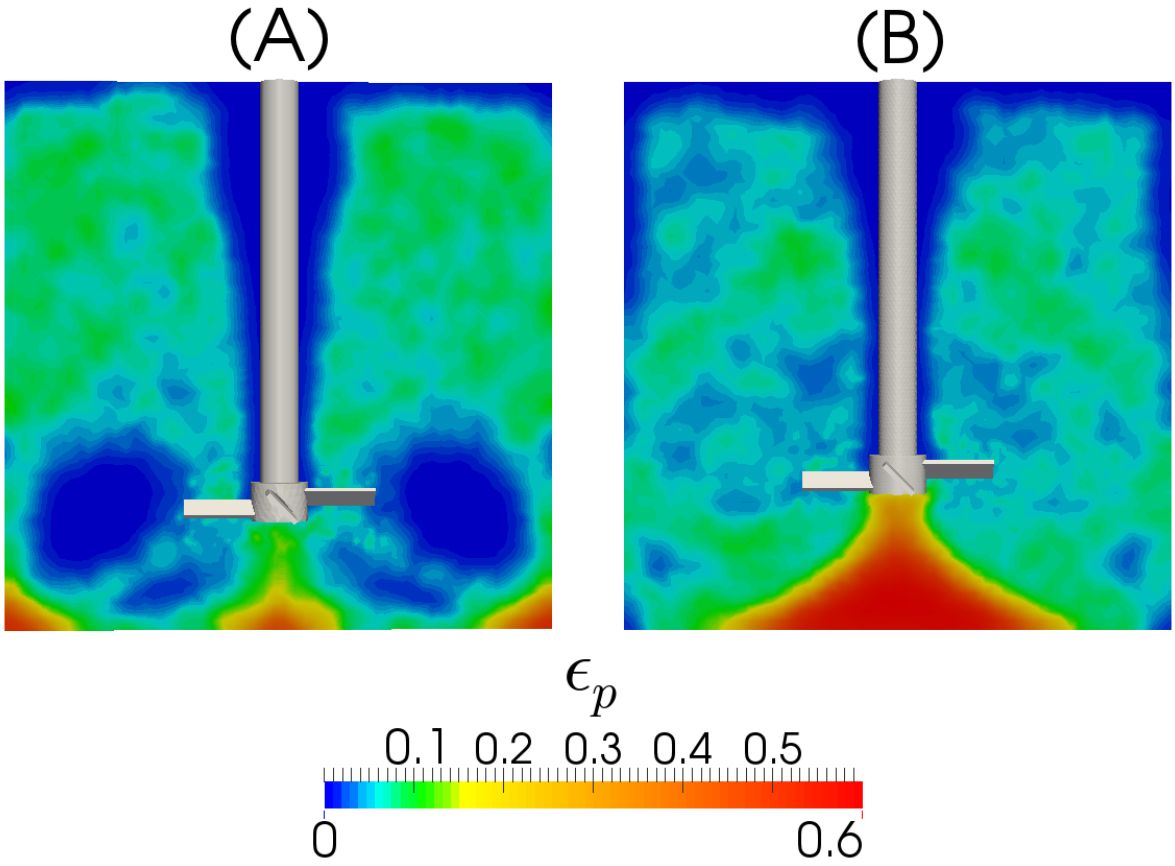

Figure 10.20 Solid volume fraction ($\epsilon_p = 1 - \epsilon_f$) on the P_y cross-section at $N = 650$ RPM for (A) $C = T/5$ and (B) $C = T/4$

10.7 Conclusion

The solid-liquid mixing of viscous suspensions is a challenging topic since little is known about the laminar and transitional regimes in which it occurs. We previously showed [40, 173] that a general understanding for the turbulent regime cannot be applied in a straightforward way to the laminar and transitional regimes.

In the present study, we used the unresolved CFD-DEM model previously developed by our group [39, 40], which is based on the CFDEM framework, to study solid-liquid mixing in a stirred tank (with and without baffles) equipped with a PBT at varying impeller clearances.

We first showed that the Saffman lift force does not play a significant role in the suspension dynamics. We then investigated the phase averaged solid fraction and velocity profiles, and showed that the extent of erosion of the bed of particles depends on the impeller speed. The flow patterns indicated that the PBT mainly behaves like a radial discharge impeller in the laminar and transitional regimes. It was only at higher impeller speeds that the particles become suspended along the lateral walls and reach the bulk of the flow.

However, full suspension was never achieved as some particles accumulated in a static conical region below the impeller. We used the LSFA-$\Delta\boldsymbol{x}$ technique and the mixing index to show that these particles never get suspended and are not put significantly into motion, indicating that this cone is, in reality, a dead zone.

We investigated alternative geometrical configurations by varying the clearance and by adding baffles, and found that the addition of baffles greatly inhibits the axial component of the flow and prevents the suspension of particles. Increasing the clearance was detrimental to the suspension of particles and led to the formation of an even larger cone below the impeller. However, decreasing the clearance to $C = T/5$ allowed for the full suspension of the particles and, overall, proved to be more efficient at suspending the particles than the $C = T/4$ clearance at all impeller speeds, except perhaps at $N = 450$ RPM where the behavior was slightly better at $C = T/4$. However, the cloud height reached by the particles was lower at $C = T/5$.

Consequently, it appears that better suspension can be achieved by decreasing the clearance when using a PBT in the laminar regime. Increasing the impeller diameter, which was not investigated in the present work, would most likely lead to the formation of an even bigger cone of particles and a larger dead zone.

Our work showed that the unresolved CFD-DEM model developed by our group can be used to help in the design of solid-liquid mixing operations and in the choice of an optimal geometry in order to enhance not only the fraction of suspended particles, but also the flow

patterns and particle distribution. Future investigation should examine other geometries, including close-clearance impellers in the laminar regime as well as more traditional radial, mixed and axial discharge impellers in the turbulent regime using the LES extension of this model, which was introduced by our group in a previous publication [39].

10.8 Acknowledgements

The financial support from the Natural Sciences and Engineering Research Council of Canada (NSERC) is gratefully acknowledged. In particular, Bruno Blais is thankful for the NSERC Vanier Scholarship. Computations were made on the supercomputer Briaree from the University of Montreal, managed by Calcul Québec and Compute Canada. The operation of this supercomputer is funded by the Canada Foundation for Innovation (CFI), Ministère de l'Économie, de l'Innovation et des Exportations du Québec (MEIE), RMGA and the Fonds de recherche du Québec - Nature et technologies (FRQ-NT). The authors would like to highlight the support received from Calcul Québec analysts.

CHAPITRE 11 DISCUSSION GÉNÉRALE

On peut reformuler l'objectif principal de cette thèse comme suit :

> Développer et implémenter numériquement un modèle CFD-DEM non-résolu capable de simuler les écoulements de suspensions dans les opérations de mélange solide-liquide et de fournir des prédictions quantitatives à leur sujet.

Compte tenu de la complexité de cet objectif, il fut abordé progressivement dans la présente thèse. Ceci nous a permis de vérifier l'exactitude de tous les sous-éléments du schéma développé. Ainsi, le modèle a pu être validé de manière rigoureuse.

La vérification de schémas numériques fut une thématique récurrente dans cette thèse. Dans l'Article 1 (Chapitre 5), nous avons utilisé une méthodologie basée sur la méthode des solutions manufacturées afin de vérifier un schéma volumes finis basé sur un algorithme PISO et servant à résoudre les équations VANS. Cette méthodologie s'appuie sur la génération automatique de solutions analytiques infiniment différentiables où tous les termes des équations VANS sont non-nuls. À l'aide de ces solutions, des analyses d'ordre de convergence (en temps et en espace) peuvent être effectuées, vérifiant ainsi la méthode de résolution employée. Il est important de noter que cette approche que nous avons développée est valide pour tout les schémas numériques basés sur une description Eulérienne.

La généralité de cette approche fut mise à profit dans l'Article 2 (Chapitre 6). En effet, des travaux préliminaires réalisés dans le cadre de l'examen de synthèse avaient montré que, dans le contexte de la méthode de Boltzmann sur réseau, les méthodes proposées dans la littérature étaient instables si la fraction volumique ϵ_f variait dans l'espace [1]. Cependant, il était difficile de démontrer cela sans avoir accès à des solutions analytiques complexes où ϵ_f n'était pas un champ trivial (tel qu'une constante). Ainsi, en utilisant l'approche développée dans l'Article 1, nous avons montré, dans l'Article 2, que les schémas proposés dans la littérature étaient inadéquats. Muni de solutions analytiques complexes, nous avons construit un nouvel opérateur de collision rigoureux d'un point de vue théorique et qui était stable, robuste et permettait de retrouver le second ordre inhérent à la LBM classique. Ce modèle numérique ne fut pas utilisé dans la suite des travaux compte tenu de la puissance [2] des méthodes de type volumes finis dans un contexte CFD-DEM. Il demeure cependant prometteur pour d'autres applications.

1. et ce même si $\epsilon_f \in \mathcal{C}^\infty$
2. mais surtout la versatilité...

Des travaux préliminaires qui ne sont pas présenté ici avaient montré que la simulation CFD-DEM non-résolu de géométrie en rotation était particulièrement complexe, car la solution de l'équation de la pression dépendait fortement du champ de fraction volumique de liquide (ϵ_f) qui était défini à l'aide de la position des particules. Ainsi, des méthodes plus classiques de changement de référentiel (SRF) ou de maillage glissant (SM) menaient rapidement à des champs de pression aberrants, car elles induisaient des changements rapides de topologie dans le champ de fraction volumique même lorsque le lit de particules était relativement statique. Le développement d'une méthode de conditions limites immergées compatible avec le schéma semi-implicite PISO, qui constitue le cœur de l'Article 3, fut entrepris. Le même niveau de rigueur fut employé pour développer cette condition limite qui fut d'abord vérifiée sur des cas tests académiques avant d'être validée dans un contexte de mélange monophasique. Il fut montré que la méthode dégradait l'ordre de convergence du schéma (à 1.33), mais qu'elle fournissait une précision largement adéquate lorsque comparée à des méthodes de type SRF et SM. Le cas test de l'allée de von Karman derrière un cylindre statique et mobile fut des plus intéressants. En effet, il permit de relever une résolution moins précise des forces de portance lorsque la géométrie était en mouvement.

C'est dans l'Article 4 (Chapitre 8) que le modèle CFD-DEM non résolu est finalement introduit. Le modèle utilise le schéma volumes finis PISO-VANS dévelopé et vérifié dans l'Article 1 est combiné avec la méthode de conditions limites immergées développées dans l'Article 3 afin de simuler le mélange solide-liquide. Le modèle remplit sa vocation avec une précision surprenante. Cette précision est démontrée par une validation expérimentale employant les résultats expérimentaux obtenus par Manon Lassaigne, dont les travaux sont présentés en Annexe B. Il est montré que le modèle est capable de prédire qualitativement les patrons d'écoulements observés dans la cuve et qu'il est aussi capable de prédire avec une précision remarquable la fraction de particules suspendue en fonction de la vitesse d'agitation. À ce stade, le modèle est considéré vérifié et validé pour le contexte des écoulements solide-liquide pour les régimes laminaire et transitoire.

L'assise forte que nous avons bâtie dans les articles 1, 3 et 4 nous a permis d'étendre le modèle au régime turbulent dans l'Article 5 (Chapitre 9). Dans cette étude, nous avons montré que le modèle permettait la simulation aux grandes échelles du mélange solide-liquide en régime turbulent et qu'il permettait donc de prédire la fraction de solide suspendue pour tous régimes d'écoulement [3]. Nous avons aussi introduit de nouvelles métriques permettant de mesurer la fraction de solide suspendue en utilisant directement la position des particules plutôt que des mesures de pression. Cette approche offre une précision similaire, mais est nettement plus

3. En considérant que nous avions réussi à simuler les régimes laminaires et transitoire dans l'Article 4

versatile et moins couteuse en temps de calcul.

L'Article 6 (Chapitre 10) présente un usage du modèle qui se rapproche davantage de l'application souhaitée : l'optimisation et la conception d'opérations de mélange. Dans cet article, le modèle est utilisé afin d'identifier les facteurs inhibant le mélange solide-liquide en régimes laminaire et transitoire dans des configurations où l'agitateur est une turbine à pâles inclinées. Six configurations géométriques ont été testées afin de faire ressortir les modifications qui étaient les plus prometteuses pour optimiser la qualité du mélange. Il a été montré que l'ajout de chicanes inhibait fortement la suspension des particules tandis que la diminution du dégagement au fond de l'agitateur empêchait l'apparition de zones mortes. Finalement, une courte analyse de sensibilité à été effectuée sur le modèle et a montré que seule la force de friction entre les particules pouvaient jouer un rôle dans la paramétrisation de la DEM au sein du modèle CFD-DEM.

Ces articles ont permis de répondre à l'objectif principal, tout en préservant la rigueur nécessaire afin de s'assurer que la démarche était vérifiée et validée correctement. À la lumière de ceci, l'auteur espère que le fil conducteur entre les articles apparaît évident.

CHAPITRE 12 CONCLUSION

En guise de conclusion, nous effectuerons d'abord une synthèse des réalisations accomplies dans le cadre de cette thèse. L'objectif de cette synthèse est de faire ressortir l'essentiel de la contribution à l'état de l'art émanant de cette thèse. Ensuite, les limitations du modèle CFD-DEM proposé seront énoncées ainsi que les nombreuses améliorations et extensions possibles.

12.1 Synthèse des travaux

Nous avons développé un modèle CFD-DEM non résolu, c'est-à-dire un modèle combinant la CFD pour la phase fluide et la DEM pour la phase solide, afin de prédire les écoulements solide-liquide dans des mélangeurs à cuve agitée. Dans ce modèle, la position et la vitesse de chaque particule sont résolues à l'aide d'un bilan de force dans un repère Lagrangien. Ceci confère au modèle une grande précision dans la résolution de la dynamique de la phase solide et lui permet de reproduire naturellement un large éventail de phénomènes associés à la mécanique granulaire tel que l'empilement maximal. Quant à elle, la phase fluide est résolue à une échelle plus grossière que les particules. C'est ce dernier point qui permet au modèle de résoudre des écoulements solide-liquide contenant plusieurs centaines de milliers de particules au sein de géométries complexes.

Ce modèle a nécessité de multiples développements théoriques et informatiques. Il a d'abord été nécessaire de nous assurer que nous étions capables de résoudre les équations VANS inhérentes à la CFD-DEM non résolue de manière juste et précise. Ensuite, la prise en considération de la géométrie complexe qu'est l'agitateur en rotation a nécessité le développement d'un nouveau type de conditions limites fonctionnelles dans le cadre de la CFD-DEM. Tous ces éléments ont ensuite été regroupés et la capacité du modèle à prédire le mélange solide-liquide en régimes laminaire, transitoire et turbulent a pu être validée.

Le modèle validé a ensuite servi à mieux établir la dynamique du mélange solide-liquide et la mise en suspension des particules. Il a aussi permis de remettre en question la validité de l'approche consistant à concevoir un système d'agitation uniquement autour du concept de la vitesse minimale de mise en suspension. Il a été montré qu'il est davantage approprié d'étudier la fraction de particules suspendues ainsi que leur distribution dans la cuve, car ces deux aspects étaient davantage important pour la conception de mélangeurs solide-liquide. De plus, nous avons pavé la voie à des analyses plus quantitatives suite au développement de

métriques rigoureuses pour déterminer la fraction de particules mise en suspension.

Bien que le modèle issu de cette thèse ait permit d'améliorer notre compréhension du mélange solide-liquide, les avancées principales issues de cette thèse ne résident pas dans cet élément. Il est de l'opinion de l'auteur que la principale contribution de ces travaux réside dans le modèle lui-même. C'est un outil prédictif, quantitatif, et nécessitant peu de calibration qui permet de prédire avec précision la fraction de particules suspendues, peu importe le régime d'écoulement, ainsi que les profils d'écoulement et la répartition des particules solides. Bien que cet outil permette de mieux comprendre les mécanismes de mise en suspension, il est nécessaire de ne pas oublier que l'outil peut également être directement utilisé lors d'une étape de conception, d'optimisation ou de mise à l'échelle de toute opération du génie chimique impliquant une phase solide et une phase liquide.

12.2 Limitations de la solution proposée

Le modèle CFD-DEM proposé a l'avantage d'être valide pour un large éventail de configurations. Il est approprié pour l'étude d'écoulements solide-liquide [1] pour toutes les concentrations de particules possibles, allant du cas le plus dilué ($\epsilon_f \to 1$) au cas où la fraction de solides est maximale ($\epsilon_p \to \epsilon_{p,max}$). De surcroît, il est valable pour tous les régimes d'écoulement du fluide ($\forall Re$) et pour tout les régimes de l'interaction solide-liquide ($\forall Re_p$). Tout ceci est inhérent à la formulation du modèle et ne requiert pas d'artifices afin de maintenir la précision ou la stabilité du modèle.

Évidemment, le modèle conçu dans le cadre de cette thèse a des faiblesses. La principale lacune est le temps de calcul, qui croît avec l'augmentation du nombre de particules. Compte tenu de l'état actuel du modèle, il est prohibitif de faire des simulations contenant davantage que 10^6 particules. Cependant, une amélioration de la parallélisation du logiciel ainsi qu'une stratégie pour l'équilibrage dynamique de la tâche de calcul permettrait d'augmenter suffisamment l'efficacité et de permettre la simulation de cas allant jusqu'à 10^7 particules. Il est clair que la simulation du mélange solide-liquide de très fines particules ($< 100\mu$m) demeure impossible sans stratégie d'agglomération afin de réduire le nombre de particules.

La précision du modèle dépend aussi de la précision des corrélations employées pour calculer les forces d'interaction solide-liquide. Il est nécessaire d'avoir des expressions valides pour un large éventail de Re_p et de ϵ_f. De très bonnes corrélations sont disponibles pour la force de traînée, mais ceci n'est pas le cas pour les forces de portances (Saffman et Magnus), ainsi

1. En fait, le modèle est valide pour les écoulements où le fluide est un liquide ou un gaz, bien que le modèle ne fut pas validé dans le présent travail pour les cas où le fluide est un gaz. À la base, la plateforme CFDEM est conçue pour l'étude des écoulements gaz-solide.

que pour les forces de masses virtuelles ou les termes de Faxxen. Ainsi, à l'heure actuelle, l'introduction de ces forces ne peut être fait qu'en extrapolant les corrélations actuelles à des cas plus concentrés ou à des valeurs supérieures du nombre de Reynolds particulaire, un procédé au mieux hasardeux. Davantage de travaux s'appuyant sur la simulation numérique directe (DNS) sont nécessaires pour établir des corrélations précises pour ces forces.

Comme nous l'avons vu dans l'Article 4 (Chapitre 8), l'usage d'un modèle non résolu permet la simulation d'un nombre nettement plus élevé de particules, mais ne permet pas de résoudre les phénomènes hydrodynamiques qui ont lieu à une échelle plus petite que les particules. Par exemple, nous avons vu à l'Article 4 qu'il était nécessaire d'ajouter un modèle de viscosité ($\mu = \mu(\epsilon_f)$) afin de modéliser la dissipation visqueuse additionnelle due à la perturbation du champ de vitesse causée par la présence des particules. Ceci est une conséquence inévitable de l'usage d'un modèle non résolu et est, par construction, une faiblesse à laquelle on ne peut remédier.

L'approche non résolue limite la taille de maille minimale (et la résolution spatiale maximale) pouvant être atteinte, car il est nécessaire de projeter le volume des particules sur le maillage afin d'établir la fraction volumique. L'usage d'un maillage trop fin rend cette étape instable, car la taille des mailles peut devenir plus petite que celle des particules. Ainsi, il est nécessaire d'employer des maillages relativement grossiers, ce qui entraîne une perte de précision pouvant être dommageable en régime turbulent, surtout en proche paroi. Pour contrer ce phénomène, il serait nécessaire d'employer un schéma d'ordre élevé. À l'heure actuelle, ceci n'est pas possible au sein d'Open∇FOAM et il est peu probable que des schémas à ordre élevé fassent leur apparition au sein de la plateforme avant longtemps.

12.3 Améliorations et travaux futurs

Les améliorations et extensions qu'il est possible d'apporter au modèle développé ainsi qu'à la simulation du mélange solide-liquide sont nombreuses :

- Pour des raisons énoncées dans le cadre de l'Article 5, les forces solide-liquide induites par la rotation des particules n'ont pas été considérées. Il serait pertinent d'introduire de manière rigoureuse la force de portance de Magnus ainsi que le couple d'amortissement visqueux et de mesurer leur action sur la dynamique du mélange solide-liquide. Ceci nécessiterait des travaux préliminaires employant la simulation numérique directe.
- L'influence de la fraction volumique de fluide (ϵ_f) sur les forces de portance ainsi que sur la force de masse virtuelle n'est pas établie. Il serait important d'établir des corrélations à l'aide de la simulation directe pour combler ce besoin.

— En utilisant l'extension ParScale de LIGGGHTS pour la XDEM, il serait possible de simuler des changements au sein de la particule causés par un large éventail de phénomènes tels que la dissolution ou la présence d'une réaction chimique. Ceci permettrait, par exemple, de simuler des réactions chimiques ayant lieu au sein d'un catalyseur solide à l'intérieur d'un réacteur solide-liquide.
— De la même manière, il serait possible de considérer le transfert thermique au sein de la cuve, du fluide et des particules et, si souhaité, de le coupler à une cinétique de réaction chimique.
— Le logiciel étant générique, il serait possible de l'appliquer à des écoulements solide-fluide complexes tels que les écoulements au sein de lits fluidisés, le transport pneumatique de particules ou le transport de suspensions solide-liquide dans les pipelines. L'application du modèle à ce type de cas est une extension évidente de ce qui fut développé dans cette thèse.
— Il serait crucial de développer une stratégie pour agglomérer les particules en agrégats contenant chacun plusieurs particules afin de permettre la simulation d'écoulements solide-liquide contenant un plus grande nombre de particules. Cette stratégie d'agglomération (*coarse graining*) aurait l'avantage de réduire fortement le coût de calcul tout en maintenant un fort degré de précision. De plus, celle-ci pourrait être calibrée à partir de simulations non-agglomérées dans une stratégie multi-échelle.
— Plusieurs stratégie de modélisation multi-échelle peuvent émaner du modèle développée dans la présente thèse. Par exemple, il serait possible de calibrer les forces de traînées et de portances utilisées dans la CFD-DEM non résolue à l'aide d'un modèle CFD-DEM résolu et d'ensuite calibrer un modèle deux fluides à partir du modèle CFD-DEM non résolue. En transférant de l'information des modèles plus fins aux modèles plus grossier, il serait possible d'étudier des géométries de taille industrielle.
— Pour le cas du mélange solide-liquide en régime laminaire, il serait pertinent d'adopter une stratégie de réduction de modèle en employant un modèle Euler-Euler simplifié qui serait calibré à partir du modèle CFD-DEM. Ceci permettrait de faire de l'optimisation de géométrie à une intensité de calcul nettement moindre. Cette stratégie pourrait s'articuler autour de l'usage d'un optimisateur boîte noire tel que le logiciel DAKOTA.
— Compte tenu des limites de résolution spatiale des équations VANS, il serait pertinent de pouvoir employer des schémas compacts d'ordre élevé afin de permettre une résolution plus précise de l'écoulement sans exacerber les problèmes liés à la définition du champ de fraction volumique de fluide ϵ_f.
— Il serait nécessaire d'avoir accès à davantage de données expérimentales afin de faire une validation plus poussée du modèle. Il serait surtout important d'avoir des données

locales, telles que des profils d'écoulements au sein d'opérations de mélange solide-liquide. Ces profils d'écoulements pourraient être obtenus par suivi de particules radioactives (RPT).

12.4 Mot de la fin

Le modèle CFD-DEM non résolu développé dans cette thèse résulte de la combinaison de deux outils performants et libres, Open∇FOAM et LIGGGHTS. C'est en bâtissant à partir des outils déjà disponibles qu'il fut possible d'obtenir les résultats obtenus ici. De la même manière, l'auteur juge qu'il serait possible d'effectuer de grandes avancées en bâtissant sur le contenu de la présente thèse et en étendant ce qui fut développé à d'autres procédés du génie chimique où les écoulements fluide-solide jouent un rôle important.

Il est de l'opinion de l'auteur que l'approche développée dans cette thèse est rigoureuse, physiquement bien construite et qu'elle est appropriée à l'étude du mélange solide-liquide. L'utilisation de logiciels libres (*Open Source*) favorise ce type de rigueur intellectuelle. Les résultats de cette thèse démontrent que l'utilisation de modèles basés sur la CFD est une avenue fortement prometteuse pour la conception et l'optimisation d'opérations unitaires du génie chimique complexes faisant intervenir des écoulements polyphasiques. Cependant, cette utilisation doit être accompagnée d'un niveau de rigueur, mathématique et physique, avancé. Il est de l'opinion de l'auteur que l'approche traditionnelle employée en ingénierie, qui consiste à utiliser des corrélations empiriques ou mécanistiques afin de concevoir des opérations unitaires, est désuette. Le futur de l'ingénierie réside dans une utilisation consciencieuse de la simulation numérique appuyée par de la validation expérimentale. Sans vouloir lui donner raison, peut-être David Hilbert n'avait-il pas complètement tort de statuer que la physique étaient devenue trop complexe pour les physiciens et les ingénieurs...

RÉFÉRENCES

[1] A. I. o. Aeronautics, A. Staf, AIAA Guide for the Verification and Validation of Computational Fluid Dynamics Simulations, American Institute of Aeronautics and Astronautics, 1998.

[2] E. Alizadeh, F. Bertrand, J. Chaouki, Development of a granular normal contact force model based on a non-newtonian liquid filled dashpot, Powder technology 237 (2013) 202–212.

[3] American Society of Mechanical Engineers, Standard for Verification and Validation in Computational Fluid Dynamics and Heat Transfer, American Society of Mechanical Engineers, 2009.

[4] T. Anderson, R. Jackson, A fluid mechanical description of fluidized beds, Ind. Engng Chem. Fundam. 6 (1967) 527–539.

[5] M. J. Andrews, Lagrangian particle method for the simulation of dense particulate flows, American Society of Mechanical Engineers, Fluids Engineering Division (1994) 37–46.

[6] M. J. Andrews, P. J. ORourke, The multiphase particle-in-cell (mp-pic) method for dense particulate flows, International Journal of Multiphase Flow 22 (2) (1996) 379–402.

[7] P. Angot, C.-H. Bruneau, P. Fabrie, A penalization method to take into account obstacles in incompressible viscous flows, Numerische Mathematik 81 (4) (1999) 497–520.

[8] Ansys Fluent, 12.0 theory guide, Ansys Inc (2009).

[9] K. M. Aoki, T. Akiyama, Simulation studies of pressure and density wave propagations in vertically vibrated beds of granules, Physical Review E 52 (3) (1995) 3288–3291.

[10] P. M. Armenante, E. U. Nagamine, Effect of low off-bottom impeller clearance on the minimum agitation speed for complete suspension of solids in stirred tanks, Chemical Engineering Science 53 (9) (1998) 1757–1775.

[11] S. K. Arolla, O. Desjardins, Transport modeling of sedimenting particles in a turbulent pipe flow using euler-lagrange large eddy simulation, International Journal of Multiphase Flow.

[12] I. Ayranci, Suspension of mixtures of solids in stirred tanks : Problem definition and model identification, Ph.D. thesis (2012).

[13] I. Ayranci, S. M. Kresta, Design rules for suspending concentrated mixtures of solids in stirred tanks, Chemical Engineering Research & Design 89 (10A) (2011) 1961–1971.

[14] I. Ayranci, S. M. Kresta, Critical analysis of Zwietering correlation for solids suspension in stirred tanks, Chemical Engineering Research and Design 92 (3) (2014) 413–422.

[15] I. Ayranci, S. M. Kresta, J. J. Derksen, Experiments and simulations on bidisperse solids suspension in a mixing tank, Chemical Engineering & Technology 36 (11) (2013) 1957–1967.

[16] I. Ayranci, M. B. Machado, A. M. Madej, J. J. Derksen, D. S. Nobes, S. M. Kresta, Effect of geometry on the mechanisms for off-bottom solids suspension in a stirred tank, Chemical Engineering Science 79 (2012) 163–176.

[17] I. Ayranci, T. Ng, A. W. Etchells, S. M. Kresta, Prediction of just suspended speed for mixed slurries at high solids loadings, Chemical Engineering Research & Design 91 (2) (2013) 227–233.

[18] G. Baldi, R. Conti, E. Alaria, Complete suspension of particles in mechanically agitated vessels, Chemical Engineering Science 33 (1) (1978) 21–25.

[19] R. Balevicius, A. Dziugys, R. Kacianauskas, A. Maknickas, K. Vislavicius, Investigation of performance of programming approaches and languages used for numerical simulation of granular material by the discrete element method, Computer Physics Communications 175 (6) (2006) 404–415.

[20] A. J. Banchio, J. F. Brady, Accelerated stokesian dynamics : Brownian motion, The Journal of Chemical Physics 118 (22) (2003) 10323.

[21] F. Barailler, M. Heniche, P. A. Tanguy, CFD analysis of a rotor-stator mixer with viscous fluids, Chemical Engineering Science 61 (9) (2006) 2888–2894.

[22] A. Barresi, G. Baldi, Solid dispersion in an agitated vessel, Chemical Engineering Science 42 (12) (1987) 2949–2956.

[23] H. Bashiri, E. Alizadeh, F. Bertrand, J. Chaouki, Investigation of turbulent fluid flows in stirred tanks using a non-intrusive particle tracking technique, Chemical Engineering Science 140 (2016) 233–251.

[24] G. Batchelor, J. Green, The determination of the bulk stress in a suspension of spherical particles to order c2, Journal of Fluid Mechanics 56 (03) (1972) 401–427.

[25] R. Beetstra, M. A. van der Hoef, J. A. M. Kuipers, A lattice-boltzmann simulation study of the drag coefficient of clusters of spheres, Computers & Fluids 35 (8-9) (2006) 966–970.

[26] R. Beetstra, M. A. van der Hoef, J. A. M. Kuipers, Drag force of intermediate reynolds number flow past mono- and bidisperse arrays of spheres, Aiche Journal 53 (2) (2007) 489–501.

[27] R. Beetstra, M. A. van der Hoef, J. A. M. Kuipers, Numerical study of segregation using a new drag force correlation for polydisperse systems derived from lattice-boltzmann simulations, Chemical Engineering Science 62 (1-2) (2007) 246–255.

[28] C. M. Bender, S. A. Orszag, Advanced Mathematical methods for Scientists and Engineers : Asymptotic Methods and Perturbation Theory, Springer, 1999.

[29] S. Benyahia, J. E. Galvin, Estimation of numerical errors related to some basic assumptions in discrete particle methods, Industrial & Engineering Chemistry Research 49 (21) (2010) 10588–10605.

[30] M. Bergmann, A. Iollo, Modeling and simulation of fish-like swimming, Journal of Computational Physics 230 (2) (2011) 329–348.

[31] F. Bertrand, L. A. Leclaire, G. Levecque, DEM-based models for the mixing of granular materials, Chemical Engineering Science 60 (8-9) (2005) 2517–2531.

[32] F. Bertrand, P. A. Tanguy, F. Thibault, A three-dimensional fictitious domain method for incompressible fluid flow problems, International Journal for Numerical Methods in Fluids 25 (6) (1997) 719–736.

[33] A. P. S. Bhalla, R. Bale, B. E. Griffith, N. A. Patankar, A unified mathematical framework and an adaptive numerical method for fluid-structure interaction with rigid, deforming, and elastic bodies, J. Comput. Physics 250 (2013) 446–476.

[34] P. L. Bhatnagar, E. P. Gross, M. Krook, A model for collision processes in gases. i. small amplitude processes in charged and neutral one-component systems, Physical Review 94 (3) (1954) 511–525.

[35] R. B. Bird, W. E. Stewart, E. N. Lightfoot, Transport Phenomena, second edition ed., John Wiley & Sons, 2007.

[36] K. Bittorf, S. Kresta, Prediction of cloud height for solid suspensions in stirred tanks, Chemical Engineering Research and Design 81 (5) (2003) 568–577.

[37] B. Blais, F. Bertrand, On the use of the method of manufactured solutions for the verification of CFD codes for the volume-averaged Navier–Stokes equations, Computers & Fluids 114 (2015) 121–129.

[38] B. Blais, F. Bertrand, Cfd-dem investigation of the viscous solid-liquid mixing in agitated vessels : impact of particle properties and mixer characteristics, In preparation.

[39] B. Blais, O. Bertrand, L. Fradette, F. Bertrand, Unresolved cfd-dem simulations of non-dilute solid-liquid mixing in the turbulent regime : Prediction of suspension curve and just-suspended speed, Submitted to AIChE journal.

[40] B. Blais, M. Lassaigne, C. Goniva, L. Fradette, F. Bertrand, Development of an unresolved CFD–DEM model for the flow of viscous suspensions and its application to solid–liquid mixing, Journal of Computational Physics 318 (2016) 201–221.

[41] B. Blais, M. Lassaigne, C. Goniva, L. Fradette, F. Bertrand, A semi-implicit immersed boundary method and its application to viscous mixing, Computers & Chemical Engineering 85 (2016) 136–146.

[42] J. Bouffard, F. Bertrand, J. Chaouki, H. Dumont, Discrete element investigation of flow patterns and segregation in a spheronizer, Computers & Chemical Engineering 49 (2013) 170–182.

[43] J. X. Bouillard, R. W. Lyczkowski, D. Gidaspow, Porosity distributions in a fluidized-bed with an immersed obstacle, Aiche Journal 35 (6) (1989) 908–922.

[44] J. Boure, J. Delhaye, General equations and two-phase flow modeling, Handbook of Multiphase Systems (1982) 1–36.

[45] J. Bourne, R. Sharma, Suspension characteristics of solid particles in propeller-agitated tanks, in : Proceedings of the First European Conference on Mixing and Centrifugal Separation, Cambridge, vol. 3, BHRA Cranfield, UK, 1974.

[46] J. Brady, Stokesian Dynamics Simulation of Particulate Flows, Butterworth-Heinemen, Stoneham, 1993.

[47] M. Braza, P. Chassaing, H. H. Minh, Numerical study and physical analysis of the pressure and velocity fields in the near wake of a circular cylinder, Journal of fluid mechanics 165 (1986) 79–130.

[48] C. Brennen, Fundamentals of Multiphase Flow, Cambridge University Press, 2005.

[49] A. Brucato, V. Brucato, Unsuspended mass of solid particles in stirred tanks, The Canadian Journal of Chemical Engineering 76 (3) (1998) 420–427.

[50] A. Brucato, M. Ciofalo, F. Grisafi, G. Micale, Numerical prediction of flow fields in baffled stirred vessels : A comparison of alternative modelling approaches, Chemical Engineering Science 53 (21) (1998) 3653–3684.

[51] A. Brucato, A. Cipollina, G. Micale, F. Scargiali, A. Tamburini, Particle suspension in top-covered unbaffled tanks, Chemical Engineering Science 65 (10) (2010) 3001–3008.

[52] A. Brucato, F. Grisafi, G. Montante, Particle drag coefficients in turbulent fluids, Chemical Engineering Science 53 (18) (1998) 3295–3314.

[53] A. Brucato, G. Micale, L. Rizzuti, Determination of the amount of unsuspended solid particles inside stirred tanks by means of pressure measurements, Récent Progrès Génie des Procédés 11 (1997) 3–10.

[54] R. Bubbico, S. D. Cave, B. Mazzarotta, Agitation power for solid-liquid suspensions containing large particles, The Canadian Journal of Chemical Engineering 76 (3) (1998) 428–432.

[55] W. Bujalski, K. Takenaka, S. Paoleni, M. Jahoda, A. Paglianti, K. Takahashi, A. W. Nienow, A. W. Etchells, Suspension and liquid homogenization in high solids concentration stirred chemical reactors, Chemical Engineering Research and Design 77 (3) (1999) 241–247.

[56] F. Cabaret, L. Fradette, P. A. Tanguy, New turbine impellers for viscous mixing, Chemical Engineering & Technology 31 (12) (2008) 1806–1815.

[57] O. Cadot, Introduction à la turbulence, ENSTA Paristech, 2011.

[58] J. Capecelatro, O. Desjardins, An Euler–Lagrange strategy for simulating particle-laden flows, Journal of Computational Physics 238 (2013) 1–31.

[59] P. J. Carreau, D. De Kee, R. P. Chhabra, Rheology of polymeric systems : principles and applications, Hanser, Munich, 1997.

[60] F. Cello, A. Di Renzo, F. P. Di Maio, A semi-empirical model for the drag force and fluid–particle interaction in polydisperse suspensions, Chemical Engineering Science 65 (10) (2010) 3128–3139.

[61] CFDEM, CFDEM- Open Source CFD, DEM and CFD-DEM, URL : http ://www.cfdem.com, 2015.

[62] Z. H. Chai, B. C. Shi, A novel lattice boltzmann model for the poisson equation, Applied Mathematical Modelling 32 (10) (2008) 2050–2058.

[63] S. Chandrasekhar, Hydrodynamic and Hydromagnetic Stability, Dover Publications, 1981.

[64] S. Chen, G. D. Doolen, Lattice boltzmann method for fluid flows, Annual review of fluid mechanics 30 (1998) 329–364.

[65] X. Chen, J. Wang, A comparison of two-fluid model, dense discrete particle model and CFD-DEM method for modeling impinging gas-solid flows, Powder Technology 254 (2014) 94–102.

[66] X. Chen, W. Zhong, X. Zhou, B. Jin, B. Sun, CFD–DEM simulation of particle transport and deposition in pulmonary airway, Powder Technology 228 (2012) 309–318.

[67] J.-I. Choi, R. C. Oberoi, J. R. Edwards, J. A. Rosati, An immersed boundary method for complex incompressible flows, Journal of Computational Physics 224 (2) (2007) 757–784.

[68] K. W. Chu, B. Wang, A. B. Yu, A. Vince, G. D. Barnett, P. J. Barnett, CFD-DEM study of the effect of particle density distribution on the multiphase flow and performance of dense medium cyclone, Minerals Engineering 22 (11) (2009) 893–909.

[69] C. Cossu, Introduction to hydrodynamic instabilities : Lecture notes (2011).

[70] C. Crowe, J. D. Schwartzkopf, M. Sommerfeld, Y. Tsuji, Multiphase Flows with Droplets and Particles Flows, CRC Press, 2012.

[71] P. Cundall, O. Strack, A discrete numerical model for granular assemblies, Geotechnique (29) (1979) 47–65.

[72] O. M. Curet, I. K. AlAli, M. A. MacIver, N. A. Patankar, A versatile implicit iterative approach for fully resolved simulation of self-propulsion, Computer Methods in Applied Mechanics and Engineering 199 (37) (2010) 2417–2424.

[73] J.-S. Darrozes, C. François, Mécanique des fluides incompressibles, Presses de L'ENSTA Paristech, Paris, 1998.

[74] P. Davidson, et al., Turbulence : an introduction for scientists and engineers, Oxford University Press, USA, 2015.

[75] S. Deb, D. K. Tafti, A novel two grid formulation for fluid-particle systems using the discrete element method, Powder Technology.

[76] G. Delaplace, J. Leuliet, V. Relandeau, Circulation and mixing times for helical ribbon impellers. review and experiments, Experiments in fluids 28 (2) (2000) 170–182.

[77] S. Dennis, S. Singh, D. Ingham, The steady flow due to a rotating sphere at low and moderate reynolds numbers, Journal of Fluid Mechanics 101 (02) (1980) 257–279.

[78] J. Derksen, Assessment of large eddy simulations for agitated flows, Chemical Engineering Research & Design 79 (A8) (2001) 824–830.

[79] J. Derksen, H. E. A. Van den Akker, Large eddy simulations on the flow driven by a rushton turbine, AIChE Journal 45 (2) (1999) 209–221.

[80] J. J. Derksen, Numerical simulation of solids suspension in a stirred tank, AIChE Journal 49 (11) (2003) 2700–2714.

[81] J. J. Derksen, Flow-induced forces in sphere doublets, Journal of Fluid Mechanics 608 (2008) 337–356.

[82] J. J. Derksen, Direct meso-scale simulations of fibres in turbulent liquid flow, Canadian Journal of Chemical Engineering 88 (4) (2010) 677–681.

[83] J. J. Derksen, Highly resolved simulations of solids suspension in a small mixing tank, AIChE Journal 58 (10) (2012) 3266–3278.

[84] R. Di Felice, The voidage function for fluid-particle interaction systems, International Journal of Multiphase Flow 20 (1) (1994) 153–159.

[85] A. Di Renzo, F. Cello, F. P. Di Maio, Simulation of the layer inversion phenomenon in binary liquid-fluidized beds by DEM-CFD with a drag law for polydisperse systems, Chemical Engineering Science 66 (13) (2011) 2945–2958.

[86] A. Di Renzo, F. P. Di Maio, Comparison of contact-force models for the simulation of collisions in dem-based granular flow codes, Chemical Engineering Science 59 (3) (2004) 525–541.

[87] A. Di Renzo, F. P. Di Maio, Homogeneous and bubbling fluidization regimes in DEM-CFD simulations : Hydrodynamic stability of gas and liquid fluidized beds, Chemical Engineering Science 62 (1-2) (2007) 116–130.

[88] J. Doucet, F. Bertrand, J. Chaouki, A measure of mixing from lagrangian tracking and its application to granular and fluid flow systems, Chemical Engineering Research and Design 86 (12) (2008) 1313–1321.

[89] D. Drew, Mathematical modeling of two-phase flow, Annual review of fluid mechanics 15 (1) (1983) 261–291.

[90] L. Durlofsky, J. Brady, Dynamic simulation of hydrodynamically interacting particles, Journal of Fluid Mechanics 180 (1987) 21–49.

[91] L. Eça, M. Hoekstra, A. Hay, D. Pelletier, A manufactured solution for a two-dimensional steady wall-bounded incompressible turbulent flow, International Journal of Computational Fluid Dynamics 21 (3-4) (2007) 175–188.

[92] L. Eça, M. Hoekstra, A. Hay, D. Pelletier, On the construction of manufactured solutions for one and two-equation eddy-viscosity models, International Journal for Numerical Methods in Fluids 54 (2) (2007) 119–154.

[93] L. Eça, M. Hoekstra, A. Hay, D. Pelletier, Verification of rans solvers with manufactured solutions, Engineering with Computers 23 (4) (2007) 253–270.

[94] S. Ergun, Fluid flow through packed columns, Chem. Eng. Prog. 48.

[95] E. Fadlun, R. Verzicco, P. Orlandi, J. Mohd-Yusof, Combined immersed-boundary finite-difference methods for three-dimensional complex flow simulations, Journal of Computational Physics 161 (1) (2000) 35–60.

[96] Y. Q. Feng, A. B. Yu, Comments on "discrete particle-continuum fluid modelling of gas-solid fluidised beds" by kafui et al. [chemical engineering science 57 (2002) 2395-2410], Chemical Engineering Science 59 (3) (2004) 719–722.

[97] J. H. Ferziger, M. Perić, Computational methods for fluid dynamics, vol. 3, Springer Berlin, 1996.

[98] M. D. Fokema, S. M. Kresta, P. E. Wood, Importance of using the correct impeller boundary-conditions for cfd simulations of stirred tanks, Canadian Journal of Chemical Engineering 72 (2) (1994) 177–183.

[99] R. O. Fox, A quadrature-based third-order moment method for dilute gas-particle flows, Journal of Computational Physics 227 (12) (2008) 6313–6350.

[100] R. O. Fox, F. Laurent, M. Massot, Numerical simulation of spray coalescence in an eulerian framework : Direct quadrature method of moments and multi-fluid method, Journal of Computational Physics 227 (6) (2008) 3058–3088.

[101] L. Fradette, P. A. Tanguy, F. Bertrand, F. Thibault, J. B. Ritz, E. Giraud, Cfd phenomenological model of solid-liquid mixing in stirred vessels, Computers & Chemical Engineering 31 (4) (2007) 334–345.

[102] F. Y. Fraige, P. A. Langston, Integration schemes and damping algorithms in distinct element models, Advanced Powder Technology 15 (2) (2004) 227–245.

[103] R. Garg, J. Galvin, T. Li, S. Pannala, Open-source MFIX-DEM software for gas–solids flows : Part I - Verification studies, Powder Technology 220 (2012) 122–137.

[104] M. Germano, U. Piomelli, P. Moin, W. H. Cabot, A dynamic subgrid-scale eddy viscosity model, Physics of Fluids A : Fluid Dynamics (1989-1993) 3 (7) (1991) 1760–1765.

[105] D. Gidaspow, Multiphase Flow and Fluidization : Continuum and Kinetic Theory Descriptions, Academic press, 1994.

[106] R. Giguère, L. Fradette, D. Mignon, P. Tanguy, Ert algorithms for quantitative concentration measurement of multiphase flows, Chemical Engineering Journal 141 (1) (2008) 305–317.

[107] R. Glowinski, T.-W. Pan, T. I. Hesla, D. D. Joseph, A distributed lagrange multiplier/fictitious domain method for particulate flows, International Journal of Multiphase Flow 25 (5) (1999) 755–794.

[108] R. Glowinski, T. W. Pan, T. I. Hesla, D. D. Joseph, J. Périaux, A fictitious domain approach to the direct numerical simulation of incompressible viscous flow past moving rigid bodies : Application to particulate flow, Journal of Computational Physics 169 (2) (2001) 363–426.

[109] I. Goldhirsch, Introduction to granular temperature, Powder Technology 182 (2) (2008) 130–136.

[110] D. Goldstein, R. Handler, L. Sirovich, Modeling a no-slip flow boundary with an external force field, Journal of Computational Physics 105 (2) (1993) 354–366.

[111] P. Gondret, E. Hallouin, M. Lance, L. Petit, Experiments on the motion of a solid sphere toward a wall : From viscous dissipation to elastohydrodynamic bouncing, Physics of Fluids 11 (9) (1999) 2803–2805.

[112] C. Goniva, C. Kloss, N. G. Deen, J. A. M. Kuipers, S. Pirker, Influence of rolling friction on single spout fluidized bed simulation, Particuology 10 (5) (2012) 582–591.

[113] C. Goniva, C. Kloss, A. Hager, S. Pirker, An open source CFD-DEM perspective, in : Proceedings of OpenFOAM Workshop, Göteborg, 2010.

[114] R. Grenville, A. Mak, D. Brown, Suspension of solid particles in vessels agitated by axial flow impellers, Chemical Engineering Research and Design (2015) .

[115] D. Guha, P. A. Ramachandran, M. P. Dudukovic, J. J. Derksen, Evaluation of large eddy simulation and euler-euler cfd models for solids flow dynamics in a stirred tank reactor, Aiche Journal 54 (3) (2008) 766–778.

[116] Y. Guntzburger, A. Fontaine, L. Fradette, F. Bertrand, An experimental method to evaluate global pumping in a mixing system : Application to the Maxblend^{TM} for Newtonian and non-Newtonian fluids, Chemical Engineering Journal 214 (2013) 394–406.

[117] Z. Guo, C. Shu, Lattice Boltzmann Method and Its Applications in Engineering, World Scientific Publishing Company Incorporated, 2013.

[118] E. Guyon, J. Hulin, Granites et Fumées : Un peu d'ordre dans le mélange, Sciences (Ed. O. Jacob), Editions Odile Jacob, 1997.
URL `https://books.google.ca/books?id=ut3gUJOwmGoC`

[119] A. Hager, C. Kloss, C. Goniva, Towards an efficient immersed boundary method within an open source framework, in : Proc. of 12th International Conference on Multiphase Flow in Industrial Plants, Ischia (Napoli), Italy, 2011.

[120] F. H. Harlow, Pic and its progeny, Computer Physics Communications 48 (1988) 1–10.

[121] R. E. Hayes, A. Afacan, B. Boulanger, An equation of motion for an incompressible newtonian fluid in a packed bed, Transport in Porous Media 18 (2) (1995) 185–198.

[122] J. W. He, R. Glowinski, R. Metcalfe, A. Nordlander, J. Periaux, Active control and drag optimization for flow past a circular cylinder, Journal of Computational Physics 163 (1) (2000) 83–117.

[123] R. D. Henderson, Nonlinear dynamics and pattern formation in turbulent wake transition, Journal of Fluid Mechanics 352 (1997) 65–112.

[124] J.-M. Hérard, O. Hurisse, A fractional step method to compute a class of compressible gas–liquid flows, Computers & Fluids 55 (0) (2012) 57–69.

[125] H. Hertz, Über die berühung fester elasticher körpe, Journal fur die reine und angewandte Mathematik (1882) 156–171.

[126] M. T. Hicks, K. J. Myers, A. Bakker, Cloud height in solids suspension agitation, Chemical Engineering Communications 160 (1997) 137–155.

[127] A. Hobbs, Simulation of an aggregate dryer using coupled CFD and DEM methods, International Journal of Computational Fluid Dynamics 23 (2) (2009) 199–207.

[128] B. P. B. Hoomans, J. A. M. Kuipers, W. J. Briels, W. P. M. vanSwaaij, Discrete particle simulation of bubble and slug formation in a two-dimensional gas-fluidised bed : A hard-sphere approach, Chemical Engineering Science 51 (1) (1996) 99–118.

[129] S. Hosseini, D. Patel, F. Ein-Mozaffari, M. Mehrvar, Study of solid-liquid mixing in agitated tanks through computational fluid dynamics modeling, Industrial & Engineering Chemistry Research 49 (9) (2010) 4426–4435.

[130] S. Ibrahim, A. W. Nienow, Comparing impeller performance for solid-suspension in the transitional flow regime with Newtonian fluids, Chemical Engineering Research and Design 77 (8) (1999) 721–727.

[131] S. Ibrahim, A. W. Nienow, The effect of viscosity on particle suspension in an aerated stirred vessel with different impellers and bases, Chemical Engineering Communications 197 (4) (2010) 434–454.

[132] S. B. Ibrahim, A. W. Nienow, The effect of viscosity on mixing pattern and solid suspension in stirred vessels, Eighth European Conference on Mixing (136) (1994) 25–32.

[133] K. Iinoya, K. Gotoh, K. Higashitani, Powder Technology Handbook, Marcel Dekker, 1991.

[134] M. Ishii, Themo-Fluid Dynamics Theory of Two-Phase Flow, 1975.

[135] M. Ishii, T. Hibiki, Thermo-Fluid Dynamics of Two-Phase Flow, Springer New York, 2011.

[136] R. I. Issa, Solution of the implicitly discretised fluid flow equations by operator-splitting, Journal of Computational Physics 62 (1) (1986) 40–65.

[137] R. Jafari, P. A. Tanguy, J. Chaouki, Characterization of minimum impeller speed for suspension of solids in liquid at high solid concentration, using gamma-ray densitometry, International Journal of Chemical Engineering 2012.

[138] R. Jafari, P. A. Tanguy, J. Chaouki, Experimental investigation on solid dispersion, power consumption and scale-up in moderate to dense solid–liquid suspensions, Chemical Engineering Research and Design 90 (2) (2012) 201–212.

[139] R. Jafari, P. A. Tanguy, J. Chaouki, Experimental investigation on solid dispersion, power consumption and scale-up in moderate to dense solid-liquid suspensions, Chemical Engineering Research & Design 90 (2) (2012) 201–212.

[140] H. Jasak, A. Jemcov, Z. Tukovic, OpenFOAM : A C++ library for complex physics simulations, in : International workshop on coupled methods in numerical dynamics.

[141] T. Jirout, J. Moravec, F. Rieger, Electrochemical measurement of the impeller speed for off-bottom suspension in a dish-bottomed vessel, Inzynieria Chemiczna I Procesowa 27 (4) (2006) 1507–1516.

[142] T. Jirout, J. Moravec, F. E. Rieger, V. Sinevic, M. Spidla, V. Sobolik, J. Tihon, Electrochemical measurement of impeller speed for off-bottom suspension, Inzynieria Chemiczna I Procesowa 26 (3) (2005) 485–497.

[143] K. Johnson, Normal contact of elastic solids : Hertz theory, Contact Mechanics (1985) 84–106.

[144] K. D. Kafui, C. Thornton, M. J. Adams, Discrete particle-continuum fluid modelling of gas-solid fluidised beds, Chemical Engineering Science 57 (13) (2002) 2395–2410.

[145] K. D. Kafui, C. Thornton, M. J. Adams, Reply to comments by feng and yu on "discrete particle-continuum fluid modelling of gas-solid fluidised beds" by kafui et al, Chemical Engineering Science 59 (3) (2004) 723–725.

[146] D. Kah, F. Laurent, L. Freret, S. de Chaisemartin, R. O. Fox, J. Reveillon, M. Massot, Eulerian quadrature-based moment models for dilute polydisperse evaporating sprays, Flow Turbulence and Combustion 85 (3-4) (2010) 649–676.

[147] F. P. Kärrholm, Rhie-Chow interpolation in OpenFOAM, Appendix from Numerical Modelling of Diesel Spray Injection and Turbulence Interaction at Chalmers University. http ://www. tfd. chalmers. se/hani/kurser/OS CFD.

[148] G. R. Kasat, A. R. Khopkar, V. V. Ranade, A. B. Pandita, CFD simulation of liquid-phase mixing in solid-liquid stirred reactor, Chemical Engineering Science 63 (15) (2008) 3877–3885.

[149] G. R. Kasat, A. B. Pandit, Review on mixing characteristics in solid-liquid and solid-liquid-gas reactor vessels, Canadian Journal of Chemical Engineering 83 (4) (2005) 618–643.

[150] N. C. S. Kee, R. B. H. Tan, CFD simulation of solids suspension in mixing vessels, Canadian Journal of Chemical Engineering 80 (4) (2002) 721–726.

[151] W. Kester, Oversampling interpolating dacs, Data retrieved 14 (2009) 2011.

[152] K. Khadra, P. Angot, S. Parneix, J. Caltagirone, Fictitious domain approach for numerical modelling of Navier-Stokes equations, International Journal for Numerical Methods in Fluids 34 (8) (2000) 651–684.

[153] J. Kim, S. Lee, Modeling drag force acting on the individual particles in low reynolds number flow, Powder Technology 261 (2014) 22–32.

[154] J. Kim, P. Moin, Application of a fractional-step method to incompressible Navier-Stokes equations, Journal of Computational Physics 59 (2) (1985) 308–323.

[155] C. Kloss, C. Goniva, LIGGGHTS – Open Source Discrete Element Simulations of Granular Materials Based on Lammps, John Wiley & Sons, Inc., 2011, pp. 781–788, (TMS).

[156] C. Kloss, C. Goniva, A. Hager, S. Amberger, S. Pirker, Models, algorithms and validation for open source DEM and CFD–DEM, Progress in Computational Fluid Dynamics, an International Journal 12 (2) (2012) 140–152.

[157] F. Kneule, Die prüfung von rührern durch löslichkeitsbestimmung, Chemie Ingenieur Technik 28 (3) (1956) 221–225.

[158] M. Kraume, Mixing times in stirred suspensions, Chemical Engineering & Technology 15 (5) (1992) 313–318.

[159] G. Kremer, An Introduction to the Boltzmann Equation and Transport Processes in Gases, Springer Berlin Heidelberg, 2010.

[160] I. M. Krieger, T. J. Dougherty, A mechanism for non-Newtonian flow in suspensions of rigid spheres, Transactions of The Society of Rheology (1957-1977) 3 (1) (1959) 137–152.

[161] H. Kruggel-Emden, E. Simsek, S. Rickelt, S. Wirtz, V. Scherer, Review and extension of normal force models for the discrete element method, Powder Technology 171 (3) (2007) 157–173.

[162] H. Kruggel-Emden, S. Wirtz, V. Scherer, A study on tangential force laws applicable to the discrete element method (dem) for materials with viscoelastic or plastic behavior, Chemical Engineering Science 63 (6) (2008) 1523–1541.

[163] S. B. Kuang, A. B. Yu, Micromechanic modeling and analysis of the flow regimes in horizontal pneumatic conveying, Aiche Journal 57 (10) (2011) 2708–2725.

[164] S. B. Kuang, A. B. Yu, Z. S. Zou, Computational study of flow regimes in vertical pneumatic conveying, Industrial & Engineering Chemistry Research 48 (14) (2009) 6846–6858.

[165] S. B. Kuang, R. P. Zou, R. H. Pan, A. B. Yu, Application of periodic boundary conditions to CFD-DEM simulation of gas-solid flow in pneumatic conveying, Chemical Engineering Science.

[166] G. Kuwabara, K. Kono, Restitution coefficient in a collision between two spheres, Japanese Journal of Applied Physics 26 (Copyright (C) 1987 Publication Board, Japanese Journal of Applied Physics) (1987) 1230.

[167] A. Ladd, R. Verberg, Lattice-boltzmann simulations of particle-fluid suspensions, Journal of Statistical Physics 104 (5-6) (2001) 1191–1251.

[168] A. J. C. Ladd, Numerical simulations of particulate suspensions via a discretized boltzmann-equation .1. theoretical foundation, Journal of Fluid Mechanics 271 (1994) 285–309.

[169] A. J. C. Ladd, Numerical simulations of particulate suspensions via a discretized boltzmann-equation .2. numerical results, Journal of Fluid Mechanics 271 (1994) 311–339.

[170] P. Lallemand, L. S. Luo, Theory of the lattice boltzmann method : Dispersion, dissipation, isotropy, galilean invariance, and stability, Physical Review E 61 (6) (2000) 6546–6562.

[171] H. Lamb, Hydrodynamics, Cambridge university press, 1932.

[172] D. Lamberto, M. Alvarez, F. Muzzio, Experimental and computational investigation of the laminar flow structure in a stirred tank, Chemical Engineering Science 54 (7) (1999) 919–942.

[173] M. Lassaigne, B. Blais, L. Fradette, F. Bertrand, Experimental investigation of the mixing of viscous liquids and non-dilute concentrations of particles in stirred tanks, Submitted to Chemical Engineering Research & Design (2015) .

[174] M. Latva-Kokko, D. Rothman, Diffusion properties of gradient-based lattice boltzmann models of immiscible fluids, Physical Review E 71 (5).

[175] F. Laurent, M. Massot, P. Villedieu, Eulerian multi-fluid modeling for the numerical simulation of coalescence in polydisperse dense liquid sprays, Journal of Computational Physics 194 (2) (2004) 505–543.

[176] J. Leboreiro, G. G. Joseph, C. M. Hrenya, D. M. Snider, S. S. Banerjee, J. E. Galvin, The influence of binary drag laws on simulations of species segregation in gas-fluidized beds, Powder Technology 184 (3) (2008) 275–290.

[177] S. Leclaire, M. Reggio, J.-Y. Trépanier, Isotropic color gradient for simulating very high-density ratios with a two-phase flow lattice boltzmann model, Computers & Fluids 48 (1) (2011) 98–112.

[178] J. Lee, H. J. Herrmann, Angle of repose and angle of marginal stability - molecular-dynamics of granular particles, Journal of Physics a-Mathematical and General 26 (2) (1993) 373–383.

[179] D. Leighton, A. Acrivos, Viscous resuspension, Chemical engineering science 41 (6) (1986) 1377–1384.

[180] P. Lettieri, L. Cammarata, G. Micale, J. Yates, Computational fluid-dynamics simulations of gas fluidized beds using different Eulerian modelling approaches, International Journal of Chemical Reactor Engineering 1 (2003) 1–21.

[181] P. Löhner, Applied Computational Fluid Dynamics Techniques : An Introduction Based on Finite Element Methods, Wiley, 2008.

[182] LIGGGHTS, LAMMPS Improved for General Granular and Granular Heat Transfer Simulations, URL : hhtp ://www.liggghts.com, 2015.

[183] M. Ljungqvist, A. Rasmuson, Numerical simulation of the two-phase flow in an axially stirred vessel, Chemical Engineering Research & Design 79 (A5) (2001) 533–546.

[184] E. Loth, Lift of a spherical particle subject to vorticity and/or spin, Aiaa Journal 46 (4) (2008) 801–809.

[185] E. Loth, A. Dorgan, An equation of motion for particles of finite reynolds number and size, Environmental fluid mechanics 9 (2) (2009) 187–206.

[186] G. Lu, J. Third, C. Müller, Discrete element models for non-spherical particle systems : From theoretical developments to applications, Chemical Engineering Science 127 (2015) 425–465.

[187] J. Luo, R. Issa, A. Gosman, Prediction of impeller induced flows in mixing vessels using multiple frames of reference, in : Institution of Chemical Engineers Symposium Series, vol. 136, Hemsphere publishing corporation, 1994.

[188] M. B. Machado, K. J. Bittorf, V. T. Roussinova, S. M. Kresta, Transition from turbulent to transitional flow in the top half of a stirred tank, Chemical Engineering Science 98 (2013) 218–230.

[189] S. Majumdar, G. Iaccarino, P. Durbin, RANS solvers with adaptive structured boundary non-conforming grids, Annual Research Briefs, Center for Turbulence Research, Stanford University (2001) 353–466.

[190] O. P. Malaspinas, Lattice boltzmann method for the simulatoin of viscoelastic fluid flows, Ph.D. thesis (2009).

[191] R. Mann, Ert imaging and linkage to cfd for stirred vessels in the chemical process industry, in : Imaging Systems and Techniques, 2009. IST'09, IEEE, 2009.

[192] R. Mann, F. Dickin, M. Wang, T. Dyakowski, R. Williams, R. Edwards, A. Forrest, P. Holden, Application of electrical resistance tomography to interrogate mixing processes at plant scale, Chemical engineering science 52 (13) (1997) 2087–2097.

[193] R. Mann, M. Wang, F. Dickin, T. Dyakowski, P. Holden, A. Forrest, R. Edwards, Resistance tomography imaging of stirred vessel mixing at plant scale, in : Iinstitution of Chemical Engineers Symposium Series, vol. 140, Hemsphere Publishing Corporation, 1996.

[194] M. Marchioro, M. Tanksley, A. Prosperetti, Flow of spatially non-uniform suspensions. : Part i : Phenomenology, International journal of multiphase flow 26 (5) (2000) 783–831.

[195] M. Marchioro, M. Tanksley, W. Wang, A. Prosperetti, Flow of spatially non-uniform suspensions : Part ii : Systematic derivation of closure relations, International journal of multiphase flow 27 (2) (2001) 237–276.

[196] D. L. Marchisio, R. O. Fox, Computational models for polydisperse particulate and multiphase systems, Cambridge University Press, 2013.

[197] M. Marinack, F. Higgs, The inclusion of friction in lattice-based cellular automata modeling of granular flows, Journal of Tribology 133 (3) (2011) 031302.

[198] M. Marinack, J. Mpagazehe, F. Higgs, An eulerian, lattice-based cellular automata approach for modeling multiphase flows, Powder Technology 221 (2012) 47–56.

[199] J. Marshall, K. Sala, Comparison of methods for computing the concentration field of a particulate flow, International Journal of Multiphase Flow 56 (2013) 4–14.

[200] K. Mattila, Implementation techniques for the lattice boltzmann method, Ph.D. thesis (2010).

[201] P. Mavros, Flow visualization in stirred vessels : A review of experimental techniques, Chemical Engineering Research and Design 79 (2) (2001) 113–127.

[202] M. Maxey, B. Patel, Localized force representations for particles sedimenting in stokes flow, International journal of multiphase flow 27 (9) (2001) 1603–1626.

[203] M. R. Maxey, Equation of motion for a small rigid sphere in a nonuniform flow, Physics of Fluids 26 (4) (1983) 883.

[204] R. McGraw, Description of aerosol dynamics by the quadrature method of moments, Aerosol Science and Technology 27 (2) (1997) 255–265.

[205] J. B. McLaughlin, Inertial migration of a small sphere in linear shear flows, Journal of Fluid Mechanics 224 (1991) 261–274.

[206] R. Mei, An approximate expression for the shear lift force on a spherical particle at finite reynolds number, International Journal of Multiphase Flow 18 (1) (1992) 145–147.

[207] M. Meldi, E. Vergnault, P. Sagaut, An arbitrary lagrangian-eulerian approach for the simulation of immersed moving solids with lattice boltzmann method, Journal of Computational Physics 235 (2013) 182–198.

[208] A. Mersmann, F. Werner, S. Maurer, K. Bartosch, Theoretical prediction of the minimum stirrer speed in mechanically agitated suspensions, Chemical Engineering and Processing 37 (6) (1998) 503–510.

[209] J. Mewis, N. J. Wagner, Colloidal suspension rheology, Cambridge University Press, 2012.

[210] G. Micale, F. Grisafi, A. Brucato, Assessment of particle suspension conditions in stirred vessels by means of pressure gauge technique, Chemical Engineering Research and Design 80 (8) (2002) 893–902.

[211] G. Micale, F. Grisafi, L. Rizzuti, A. Brucato, CFD simulation of particle suspension height in stirred vessels, Chemical Engineering Research & Design 82 (A9) (2004) 1204–1213.

[212] G. Micale, G. Montante, F. Grisafi, A. Brucato, J. Godfrey, CFD simulation of particle distribution in stirred vessels, Chemical Engineering Research & Design 78 (A3) (2000) 435–444.

[213] M. Micheletti, L. Nikiforaki, K. C. Lee, M. Yianneskis, Particle concentration and mixing characteristics of moderate-to-dense solid-liquid suspensions, Industrial & engineering chemistry research 42 (24) (2003) 6236–6249.

[214] R. Mindlin, Compliance of elastic bodies in contact, J. of Appl. Mech. 16.

[215] R. D. Mindlin, H. Deresiewica, Elastic spheres in contact under varying oblique forces, Journal of applied mechanics 20.

[216] B. K. Mishra, A review of computer simulation of tumbling mills by the discrete element method : Part i - contact mechanics, International Journal of Mineral Processing 71 (1-4) (2003) 73–93.

[217] R. Mittal, G. Iaccarino, Immersed boundary methods, Annual Review of Fluid Mechanics 37 (1) (2005) 239–261.

[218] G. Montante, F. Magelli, Modelling of solids distribution in stirred tanks : Analysis of simulation strategies and comparison with experimental data, International Journal of Computational Fluid Dynamics 19 (3) (2005) 253–262.

[219] G. Montante, F. Magelli, Mixed solids distribution in stirred vessels : Experiments and computational fluid dynamics simulations, Industrial & Engineering Chemistry Research 46 (9) (2007) 2885–2891.

[220] G. Montante, G. Micale, A. Brucato, F. Magelli, Cfd simulation of particle distribution in a multiple-impeller high-aspect-ratio stirred vessel, 10th European Conference on Mixing (2000) 125–132.

[221] F. A. Morrison, Understanding Rheology, New York, 2001.

[222] Z. Moumni, Mécanique des millieux continus, Presses de L'ENSTA Paristech, Paris, 2011.

[223] S. Narayanan, V. K. Bhatia, D. K. Guha, M. N. Rao, Suspension of solids by mechanical agitation, Chemical Engineering Science 24 (2) (1969) 223–230.

[224] J. Neuwirth, S. Antonyuk, S. Heinrich, M. Jacob, Cfd–dem study and direct measurement of the granular flow in a rotor granulator, Chemical Engineering Science 86 (2013) 151–163.

[225] A. W. Nienow, Suspension of solid particles in turbine agitated baffled vessels, Chemical Engineering Science 23 (12) (1968) 1453–1459.

[226] A. W. Nienow, M. F. Edwards, N. Harnby, Mixing in the process industries, Butterworth-Heinemann, 1997.

[227] W. Oberkampf, C. Roy, Verification and Validation in Scientific Computing, Cambridge University Press, 2010.

[228] A. Ochieng, A. E. Lewis, CFD simulation of solids off-bottom suspension and cloud height, Hydrometallurgy 82 (1-2) (2006) 1–12.

[229] B. Oesterlé, Écoulements multiphasiques : des fondements aux méthodes d'ingénierie, Hermes Science Publications, 2006.

[230] B. Oesterle, T. B. Dinh, Experiments on the lift of a spinning sphere in a range of intermediate reynolds numbers, Experiments in Fluids 25 (1) (1998) 16–22.

[231] J. Oldshue, R. Sharma, The effect of off-bottom distance of an impeller for the "Just Suspended Speed" Njs, in : AIChE Symposium Series, vol. 88, American Institute of Chemical Engineers, 1992.

[232] J. Y. Oldshue, Fluid mixing technology.

[233] OpenCFD, OpenFOAM - The Open Source CFD Toolbox, URL : http ://www.openfoam.com, 2014.

[234] P. J. O'Rourke, D. M. Snider, An improved collision damping time for mp-pic calculations of dense particle flows with applications to polydisperse sedimenting beds and colliding particle jets, Chemical Engineering Science 65 (22) (2010) 6014–6028.

[235] P. J. O'Rourke, D. M. Snider, Inclusion of collisional return-to-isotropy in the mp-pic method, Chemical Engineering Science 80 (2012) 39–54.

[236] P. J. O'Rourke, P. Zhao, D. Snider, A model for collisional exchange in gas/liquid/solid fluidized beds, Chemical Engineering Science 64 (8) (2009) 1784–1797.

[237] J. M. Ottino, The kinematics of mixing : stretching, chaos, and transport, vol. 3, Cambridge university press, 1989.

[238] R. G. Owens, T. N. Phillips, Computational Rheology, Imperial College Press, 2002.

[239] D. Parker, C. Broadbent, P. Fowles, M. Hawkesworth, P. McNeil, Positron emission particle tracking-a technique for studying flow within engineering equipment, Nuclear Instruments and Methods in Physics Research Section A : Accelerators, Spectrometers, Detectors and Associated Equipment 326 (3) (1993) 592–607.

[240] E. J. Parteli, Dem simulation of particles of complex shapes using the multisphere method : application for additive manufacturing, in : AIP Conference Proceedings, vol. 1542.

[241] A. Passalacqua, R. O. Fox, R. Garg, S. Subramaniam, A fully coupled quadrature-based moment method for dilute to moderately dilute fluid-particle flows, Chemical Engineering Science 65 (7) (2010) 2267–2283.

[242] N. A. Patankar, P. Singh, D. D. Joseph, R. Glowinski, T.-W. Pan, A new formulation of the distributed lagrange multiplier/fictitious domain method for particulate flows, International Journal of Multiphase Flow 26 (9) (2000) 1509–1524.

[243] S. V. Patankar, Numerical heat transfer and fluid flow, Taylor & Francis, 1980.

[244] S. V. Patankar, D. B. Spalding, A calculation procedure for heat, mass and momentum transfer in three-dimensional parabolic flows, International Journal of Heat and Mass Transfer 15 (10) (1972) 1787–1806.

[245] E. L. Paul, V. A. Atiemo-Obeng, S. M. Kresta, Handbook of Industrial Mixing - Science and Practice (2004).

[246] S. Peker, S. Helvaci, Solid-Liquid Two Phase Flow, Elsevier Science, 2011.

[247] P. Pepiot, O. Desjardins, Numerical analysis of the dynamics of two- and three-dimensional fluidized bed reactors using an Euler-Lagrange approach, Powder Technology 220 (2012) 104–121.

[248] C. S. Peskin, Flow patterns around heart valves : a numerical method, Journal of Computational Physics 10 (2) (1972) 252–271.

[249] C. S. Peskin, The immersed boundary method, Acta Numerica 11 (2002) 479–517.

[250] D. Pinelli, M. Nocentini, F. Magelli, Solids distribution in stirred slurry reactors : influence of some mixer configurations and limits to the applicability of a simple model for predictions, Chemical Engineering Communications 188 (1) (2001) 91–107.

[251] S. Pirker, D. Kahrimanovic, C. Goniva, Improving the applicability of discrete phase simulations by smoothening their exchange fields, Applied Mathematical Modelling 35 (5) (2011) 2479–2488.

[252] S. Plimpton, P. Crozier, A. Thompson, Lammps-large-scale atomic/molecular massively parallel simulator, Sandia National Laboratories.

[253] S. B. Pope, Turbulent flows, Cambridge university press, 2000.

[254] A. Prosperetti, G. Tryggvason, Computational Methods For Multiphase Flow, Cambridge University Press, 2007.

[255] K. Raghava Rao, V. Rewatkar, J. Joshi, Critical impeller speed for solid suspension in mechanically agitated contactors, AIChE journal 34 (8) (1988) 1332–1340.

[256] B. Ren, W. Zhong, Y. Chen, X. Chen, B. Jin, Z. Yuan, Y. Lu, CFD-DEM simulation of spouting of corn-shaped particles, Particuology 10 (5) (2012) 562–572.

[257] C. J. Ren, X. J. Jiang, J. D. Wang, Y. R. Yang, X. H. Zhang, Determination of critical speed for complete solid suspension using acoustic emission method based on multiscale analysis in stirred tank, Industrial & Engineering Chemistry Research 47 (15) (2008) 5323–5327.

[258] W. Research, Mathematica, version 8.0 ed., Wolfram Research, Champaign, Illinois, 2010.

[259] V. B. Rewatkar, K. S. M. S. R. Rao, J. B. Joshi, Critical impeller speed for solid suspension in mechanically agitated 3-phase reactors .1. experimental part, Industrial & Engineering Chemistry Research 30 (8) (1991) 1770–1784.

[260] C. Rhie, W. Chow, Numerical study of the turbulent flow past an airfoil with trailing edge separation, Aiaa Journal 21 (11) (1983) 1525–1532.

[261] J. F. Richardson, W. N. Zaki, The sedimentation of a suspension of uniform spheres under conditions of viscous flow, Chemical Engineering Science 3 (2) (1954) 65–73.

[262] P. Roache, Verification and Validation in Computational Science and Engineering, Hermosa Publishers, 1998.

[263] P. J. Roache, Code verification by the method of manufactured solutions, Journal of Fluids Engineering 124 (1) (2002) 4–10.

[264] M. Robinson, S. Luding, M. Ramaioli, Grain sedimentation with sph-dem and its validation, in : AIP Conference Proceedings, vol. 1542.

[265] M. Robinson, M. Ramaioli, S. Luding, Fluid-particle flow simulations using two-way-coupled mesoscale sph-dem and validation, International Journal of Multiphase Flow.

[266] L. W. Rong, K. J. Dong, A. B. Yu, Lattice-Boltzmann simulation of fluid flow through packed beds of uniform spheres : Effect of porosity, Chemical Engineering Science 99 (2013) 44–58.

[267] L. W. Rong, K. J. Dong, A. B. Yu, Lattice Boltzmann simulation of fluid flow through packed beds of spheres : Effect of particle size distribution, Chemical Engineering Science.

[268] D. H. Rothman, S. Zaleski, Lattice-gas cellular automata : simple models of complex hydrodynamics, vol. 5, Cambridge University Press, 2004.

[269] D. Russell, Z. Jane Wang, A cartesian grid method for modeling multiple moving objects in 2D incompressible viscous flow, Journal of Computational Physics 191 (1) (2003) 177–205.

[270] P. Sagaut, Large Eddy Simulation for Incompressible Flows, Springer, 2006.

[271] L. Saint-Raymond, Hydrodynamic Limits of the Boltzmann Equation, Springer, 2009.

[272] K. Sankaranarayanan, S. Sundaresan, Lattice boltzmann simulation of two-fluid model equations, Industrial & Engineering Chemistry Research 47 (23) (2008) 9165–9173.

[273] J. H. Seo, R. Mittal, A sharp-interface immersed boundary method with improved mass conservation and reduced spurious pressure oscillations, J Comput Phys 230 (19) (2011) 7347–7363.

[274] X. Shan, H. Chen, Lattice boltzmann model for simulating flows with multiple phases and components, Physical Review E 47 (3) (1993) 1815–1819.

[275] X. Shan, X.-F. Yuan, H. Chen, Kinetic theory representation of hydrodynamics : a way beyond the navier-stokes equation, Journal of Fluid Mechanics 550 (2006) 413–441.

[276] T. Shao, Y. Hu, W. Wang, Y. Jin, Y. Cheng, Simulation of solid suspension in a stirred tank using CFD-DEM coupled approach, Chinese Journal of Chemical Engineering 21 (10) (2013) 1069–1081.

[277] R. N. Sharma, A. A. Shaikh, Solids suspension in stirred tanks with pitched blade turbines, Chemical Engineering Science 58 (10) (2003) 2123–2140.

[278] A. A. Shirgaonkar, M. A. MacIver, N. A. Patankar, A new mathematical formulation and fast algorithm for fully resolved simulation of self-propulsion, Journal of Computational Physics 228 (7) (2009) 2366–2390.

[279] J. Shlens, A tutorial on principal component analysis, arXiv preprint arXiv :1404.1100.

[280] A. Sierou, J. F. Brady, Accelerated stokesian dynamics simulations, Journal of Fluid Mechanics 448.

[281] J. Smagorinsky, General circulation experiments with the primitive equations : I. the basic experiment, Monthly Weather Review 91 (3) (1963) 99–164.

[282] D. M. Snider, An incompressible three-dimensional multiphase particle-in-cell model for dense particle flows, Journal of Computational Physics 170 (2) (2001) 523–549.

[283] D. M. Snider, S. M. Clark, P. J. O'Rourke, Eulerian–lagrangian method for three-dimensional thermal reacting flow with application to coal gasifiers, Chemical Engineering Science 66 (6) (2011) 1285–1295.

[284] D. M. Snider, P. J. O'Rourke, M. J. Andrews, An incompressible two-dimensional multiphase particle-in-cells model for dense particle flows, Ph.D. thesis (1997).

[285] B. Software, Barracuda virtual reactor, http ://cpfd-software.com/barracuda-vr-solutions/barracuda-vr (2013).

[286] F. Song, W. Wang, J. Li, A lattice boltzmann method for particle-fluid two-phase flow, Chemical Engineering Science.

[287] J. Southard, Threshold of movement, special topics : An introduction to fluid motions, sediment transport and current-generated sedimentary structures (2011) 260–284.

[288] M. Špidla, V. Sinevič, M. Jahoda, V. Machoň, Solid particle distribution of moderately concentrated suspensions in a pilot plant stirred vessel, Chemical Engineering Journal 113 (1) (2005) 73–82.

[289] V. Stobiac, L. Fradette, P. A. Tanguy, F. Bertrand, Pumping characterisation of the maxblend impeller for Newtonian and strongly non-Newtonian fluids, The Canadian Journal of Chemical Engineering 92 (4) (2014) 729–741.

[290] S. Succi, The Lattice Boltzmann Equation : For Fluid Dynamics and Beyond, Oxford University Press on Demand, 2001.

[291] K. Takahashi, H. Fujita, T. Yokota, Effect of size of spherical particle on complete suspension speed in agitated vessels of different scale., Journal of chemical engineering of Japan 26 (1) (1993) 98–100.

[292] A. Tamburini, A. Brucato, A. Busciglio, A. Cipollina, F. Grisafi, G. Micale, F. Scargiali, G. Vella, Solid–liquid suspensions in top-covered unbaffled vessels : Influence of particle size, liquid viscosity, impeller size, and clearance, Industrial & Engineering Chemistry Research 53 (23) (2014) 9587–9599.

[293] A. Tamburini, A. Brucato, A. Cipollina, G. Micale, M. Ciofalo, CFD predictions of sufficient suspension conditions in solid-liquid agitated tanks, International Journal of Nonlinear Sciences and Numerical Simulation 13 (6) (2012) 427–443.

[294] A. Tamburini, A. Cipollina, G. Micale, CFD simulation of solid-liquid suspensions in baffled stirred vessels below complete suspension speed, ICHEAP-10 : 10th International Conference on Chemical and Process Engineering 24 (2011) 1435–1440.

[295] A. Tamburini, A. Cipollina, G. Micale, A. Brucato, Particle distribution in dilute solid liquid unbaffled tanks via a novel laser sheet and image analysis based technique, Chemical Engineering Science 87 (2013) 341–358.

[296] A. Tamburini, A. Cipollina, G. Micale, A. Brucato, M. Ciofalo, CFD simulations of dense solid-liquid suspensions in baffled stirred tanks : Prediction of suspension curves, Chemical Engineering Journal 178 (2011) 324–341.

[297] A. Tamburini, A. Cipollina, G. Micale, A. Brucato, M. Ciofalo, CFD simulations of dense solid-liquid suspensions in baffled stirred tanks : Prediction of the minimum impeller speed for complete suspension, Chemical Engineering Journal 193 (2012) 234–255.

[298] A. Tamburini, A. Cipollina, G. Micale, A. Brucato, M. Ciofalo, CFD simulations of dense solid–liquid suspensions in baffled stirred tanks : Prediction of solid particle distribution, Chemical Engineering Journal 223 (2013) 875–890.

[299] A. Tamburini, A. Cipollina, G. Micale, M. Ciofalo, A. Brucato, Dense solid-liquid off-bottom suspension dynamics : Simulation and experiment, Chemical Engineering Research and Design 87 (4) (2009) 587–597.

[300] P. Tanguy, F. Thibault, C. Dubois, A. Ait-Kadi, Mixing hydrodynamics in a double planetary mixer, Chemical Engineering Research and Design 77 (4) (1999) 318–324.

[301] F. A. Tavarez, M. E. Plesha, Discrete element method for modelling solid and particulate materials, International Journal for Numerical Methods in Engineering 70 (4) (2007) 379–404.

[302] A. ten Cate, C. H. Nieuwstad, J. J. Derksen, H. E. A. Van den Akker, Particle imaging velocimetry experiments and lattice Boltzmann simulations on a single sphere settling under gravity, Physics of Fluids 14 (11) (2002) 4012–4025.

[303] F. Thibault, P. Tanguy, Power-draw analysis of a coaxial mixer with Newtonian and non-Newtonian fluids in the laminar regime, Chemical Engineering Science 57 (18) (2002) 3861–3872.

[304] C. Thornton, S. J. Cummins, P. W. Cleary, An investigation of the comparative behaviour of alternative contact force models during elastic collisions, Powder Technology 210 (3) (2011) 189–197.

[305] C. Thornton, Z. M. Ning, A theoretical model for the stick/bounce behaviour of adhesive, elastic-plastic spheres, Powder Technology 99 (2) (1998) 154–162.

[306] R. B. Thorpe, P. Stevenson, Suspension of particles from the bottom of pipes and stirred tanks by gassed and ungassed flows, Canadian Journal of Chemical Engineering 81.

[307] E. F. Toro, Riemann Solvers and Numerical Methods for Fluid Dynamics : A Practical Introduction, Springer-Verlag, Berlin, 2009.

[308] Y. Tsuji, Multi-scale modeling of dense phase gas-particle flow, Chemical Engineering Science 62 (13) (2007) 3410–3418.

[309] Y. Tsuji, T. Tanaka, T. Ishida, Lagrangian numerical-simulation of plug flow of cohesionless particles in a horizontal pipe, Powder Technology 71 (3) (1992) 239–250.

[310] J. Tu, G. Yeoh, C. Liu, Computational Fluid Dynamics : A Practical Approach, Elsevier Science, 2007.

[311] H. Udaykumar, W. Shyy, M. Rao, Elafint : a mixed Eulerian-Lagrangian method for fluid flows with complex and moving boundaries, International journal for numerical methods in fluids 22 (8) (1996) 691–712.

[312] H. E. Van den Akker, The details of turbulent mixing process and their simulation, Advances in Chemical Engineering 31 (2006) 151–229.

[313] J. Van Doormaal, G. Raithby, Enhancements of the simple method for predicting incompressible fluid flows, Numerical heat transfer 7 (2) (1984) 147–163.

[314] M. Vatanakul, Y. Zheng, M. Couturier, Application of ultrasonic technique in multiphase flows, Industrial & Engineering Chemistry Research 43 (18) (2004) 5681–5691.

[315] M. Vatanakul, Y. Zheng, M. Couturier, Ultrasonic technique for measuring phase holdups in multiphase systems, Chemical Engineering Communications 192 (5) (2005) 630–646.

[316] H. Versteeg, W. Malalasekera, An Introduction to Computational Fluid Dynamics : The Finite Volume Method, Pearson Education Limited, 2007.

[317] D. Vidal, R. Roy, F. Bertrand, On improving the performance of large parallel lattice boltzmann flow simulations in heterogeneous porous media, Computers & Fluids 39 (2) (2010) 324–337.

[318] O. Walton, R. Braun, Viscosity, granular-temperature and stress calcualtions for shearing assemblies of inelastic frictional disks, Journal of Rheology 30 (1986) 949–980.

[319] F. Wang, Z. S. Mao, X. Q. Shen, Numerical study of solid-liquid two-phase flow in stirred tanks with Rushton impeller - (II) Prediction of critical impeller speed, Chinese Journal of Chemical Engineering 12 (5) (2004) 610–614.

[320] J. Wang, M. A. van der Hoef, J. A. M. Kuipers, Why the two-fluid model fails to predict the bed expansion characteristics of geldart a particles in gas-fluidized beds : A tentative answer, Chemical Engineering Science 64 (3) (2009) 622–625.

[321] T. F. Wang, J. F. Wang, Two-fluid model based on the lattice boltzmann equation, Physical Review E 71 (4).

[322] H. G. Weller, G. Tabor, H. Jasak, C. Fureby, A tensorial approach to computational continuum mechanics using object-oriented techniques, Computers in Physics 12 (6) (1998) 620–631.

[323] C. Wen, Y. Yu, A generalized method for predicting the minimum fluidization velocity, Aiche Journal 12 (3) (1966) 610–612.

[324] Wikipedia, Saint-georges majeur au crépuscule — Wikipedia, the free encyclopedia, [En ligne ; Mars-2016] (2004).
URL https://fr.wikipedia.org/wiki/Saint-Georges-Majeur_au_cr%C3%A9puscule

[325] J. A. Wright, R. W. Smith, An edge-based method for the incompressible Navier–Stokes equations on polygonal meshes, Journal of Computational Physics 169 (1) (2001) 24–43.

[326] C. L. Wu, K. Nandakumar, A. S. Berrouk, H. Kruggel-Emden, Enforcing mass conservation in dpm-cfd models of dense particulate flows, Chemical Engineering Journal 174 (1) (2011) 475–481.

[327] J. Wu, Y. G. Zhu, L. Pullum, The effect of impeller pumping and fluid rheology on solids suspension in a stirred vessel, Canadian Journal of Chemical Engineering 79 (2) (2001) 177–186.

[328] C. Xie, Image, Process Tomography : Principles, Techniques and Applications (1995) 295–340.

[329] J. Xie, W. Zhong, B. Jin, Y. Shao, Y. Huang, Eulerian–lagrangian method for three-dimensional simulation of fluidized bed coal gasification, Advanced Powder Technology 24 (1) (2013) 382–392.

[330] Q. Xiong, E. Madadi-Kandjani, G. Lorenzini, A lbm–dem solver for fast discrete particle simulation of particle–fluid flows, Continuum Mechanics and Thermodynamics (2014) 1–11.

[331] Y. Xu, K. Kafui, C. Thornton, G. Lian, Effects of material properties on granular flow in a silo using DEM simulation, Particulate Science and Technology 20 (2) (2002) 109–124.

[332] K. Yeo, M. R. Maxey, Simulation of concentrated suspensions using the force-coupling method, Journal of computational physics 229 (6) (2010) 2401–2421.

[333] T. York, Electrical tomography for industrial applications, Electrical Impedance Tomography : Methods, History and Applications (2004) 295–340.

[334] J. Zhang, L. Wang, J. Ouyang, Lattice boltzmann model for the volume-averaged navier-stokes equations, EPL (Europhysics Letters) 107.

[335] P. Zhao, P. J. O'Rourke, D. Snider, Three-dimensional simulation of liquid injection, film formation and transport, in fluidized beds, Particuology 7 (5) (2009) 337–346.

[336] Z. Y. Zhou, S. B. Kuang, K. W. Chu, A. B. Yu, Discrete particle simulation of particle-fluid flow : model formulations and their applicability, Journal of Fluid Mechanics 661 (2010) 482–510.

[337] H. P. Zhu, Z. Y. Zhou, R. Y. Yang, A. B. Yu, Discrete particle simulation of particulate systems : Theoretical developments, Chemical Engineering Science 62 (13) (2007) 3378–3396.

[338] H. P. Zhu, Z. Y. Zhou, R. Y. Yang, A. B. Yu, Discrete particle simulation of particulate systems : A review of major applications and findings, Chemical Engineering Science 63 (23) (2008) 5728–5770.

[339] T. N. Zwietering, Suspending of solid particles in liquid by agitators, Chemical Engineering Science 8 (3) (1958) 244–253.

ANNEXE A Conséquence de la perte du caractère hyperbolique d'une loi de conservation

Cette courte démonstration vise à montrer l'importance de préserver le caractère hyperbolique d'une loi de conservation afin d'en maintenir la stabilité.

Soit un système hyperbolique d'une loi de conservation quelconque :

$$\partial_t \boldsymbol{y} + \mathcal{A}(\boldsymbol{y})\partial_x(\boldsymbol{y}) = 0 \tag{A.1}$$

Avec $\boldsymbol{y} \in \mathbb{R}^n$ et $\mathcal{A} \in \mathbb{R}^{n\times n}$. Tant que le système conserve son caractère hyperbolique, les valeurs propres qu'admet la matrice $\mathcal{A}$ sont réelles. Si le système perd son caractère hyperbolique, la matrice $\mathcal{A}$ admet alors des valeurs propres complexes. La matrice de convection $\mathcal{A}$ étant une matrice réelle, ses valeurs propres complexes seront nécessairement conjuguées deux à deux. Les conséquence de ces valeurs propres conjuguées peuvent s'illustrer facilement à l'aide d'une équation modèle de transport d'un scalaire complexe.

Soit une équation de transport d'un scalaire complexe d'ordre un quelconque tel que :

$$\partial_t \alpha + \lambda\partial_x(\alpha) = 0 \tag{A.2}$$

Avec $\alpha, k \in \mathbb{C}$. La solution à ce problème hyperbolique peut s'écrire comme une solution d'onde de forme $e^{i(\omega t - kx)}$ avec $\omega \in \mathbb{C}$ et $k \in \mathbb{R}$. Ceci revient à résoudre le problème avec une transformée de Fourrier en temps avec ω une pulsation et k un nombre d'onde. Compte tenu de cela, on trouve que ω et k vérifient :

$$i\omega = i\lambda k \tag{A.3}$$

Compte tenu de la nature réelle de k, on constate que :

$$Re(\omega) = Re(\lambda)k \tag{A.4}$$
$$Im(\omega) = Im(\lambda)k \tag{A.5}$$

Ce qui donne une solution sous la forme $e^{i(Re(\lambda)kt - kx) - Im(\omega)t}$. Donc, si la partie imaginaire de

ω est positive, la solution sera stable, sinon, elle sera instable et croîtra exponentiellement. Si nous revenons à notre système hyperbolique avec une matrice de convection $\mathcal{A}$ réelle. Nous avions constaté qu'une perte du caractère hyperbolique du système impliquait la présence de valeur propres complexes conjuguées deux à deux. Ainsi, dans ce contexte, une valeur propre dans chaque paire de valeur propre complexe conjuguée aura une partie imaginaire négative. On en conclut donc, par cet exemple, qu'une perte du caractère hyperbolique d'un système entraîne par le fait même une perte de stabilité.

ANNEXE B Article M. L. 1 : Experimental investigation of the mixing of viscous liquids and non-dilute concentrations of particles in a stirred tank

Manon Lassaigne, Bruno Blais, Louis Fradette, François Bertrand
Published in Chemical Engineering Research & Design volume , pages XXX-XXX, 2016

Abstract : Despite the importance for the process industry of solid-liquid mixing operations involving viscous liquids and high solids concentrations, most of the reported results have been obtained in the turbulent regime with low solids loadings. In this work, the suspension of non-dilute concentrations of spherical particles in viscous liquids is investigated through the determination of the just-suspended speed N_js, the homogenization speed N_H and the homogenization time t_H. The pitched blade turbine, which is a common and suitable agitator for the suspension of solids in the turbulent regime, is chosen. N_js is obtained using the pressure gauge technique, and N_H and t_H via electrical resistance tomography. The impact of the particle diameter d_p, the solids mass concentration X_w, the liquid viscosity μ, and the impeller diameter D and off-bottom clearance C are assessed. In particular, the effect of d_p and μ on N_{js} are observed to be in contradiction with the Zwietering correlation, which was derived in the turbulent regime. This is attributed to the hydrodynamics and mechanisms prevailing in the laminar and early transitional regimes, which are similar to those for the erosion of a particle bed. This also explains the discrepancies between our experimental values and the values of N_{js} predicted by the Zwietering correlation. Also, increasing X_w affects N_{js} in a more complex manner than what is predicted by this correlation. Finally, our results indicate that particle bed erosion is the dominating phenomenon to consider both to suspend the particles and achieve a uniform suspension in the tank.

Introduction

Solid-liquid mixing in agitated vessels is a common unit operation that plays a key role in the chemical process industry. In many of these operations, such as in chemical reactors containing a solid catalyst, the main objective is to reach a certain level of homogeneity, and to maximize the contact area between the two phases. Although most of the literature on solid-liquid mixing relates to the turbulent regime [232, 245], for the cosmetics, food and pharmaceutical industries, for instance, the systems usually involve viscous, possibly non-Newtonian, liquids and large concentrations of solids to suspend. The complexity arising from both the geometry of the vessel and the rheology of the suspensions can lead to the

formation of unfamiliar flow patterns, and the estimation of the key parameters remains unclear. In particular, the Zwietering correlation [339], as further discussed below, has several limitations for high solids loadings and laminar systems, which may lead to poor predictions of the just-suspended speed Njs, causing important quality deterioration and large economic losses [130, 245]. Consequently, it is necessary to improve our understanding of the influence of the geometry, fluid and solid properties, and operating parameters on the flow dynamics of this type of solid-liquid mixing operations. For solid-liquid mixing in stirred tanks, the degree of suspension required depends on the type of operation. On-bottom suspension B.1 (a), in which some of the particles rest on the bottom of the tank can be, for instance, sufficient for highly soluble solids dissolution [245]. To maximize the solid-liquid interfacial surface area and therefore the mass transfer, it is usually necessary to operate at complete off-bottom suspension state, as illustrated in Figure B.1 (b) [17]. This condition corresponds to the just suspended speed N_js, and has been defined by Zwietering as the "impeller speed at which no particle remains stationary at the bottom of the tank for more than 1 or 2 seconds" [339]. He proposed the following correlation :

$$N_{js} = S\nu_f^{0.1}\left(\frac{(\rho_p - \rho_f)\, g}{\rho_f}\right)^{0.45} d_p^{0.2} X^{0.1} D^{0.15} \tag{B.1}$$

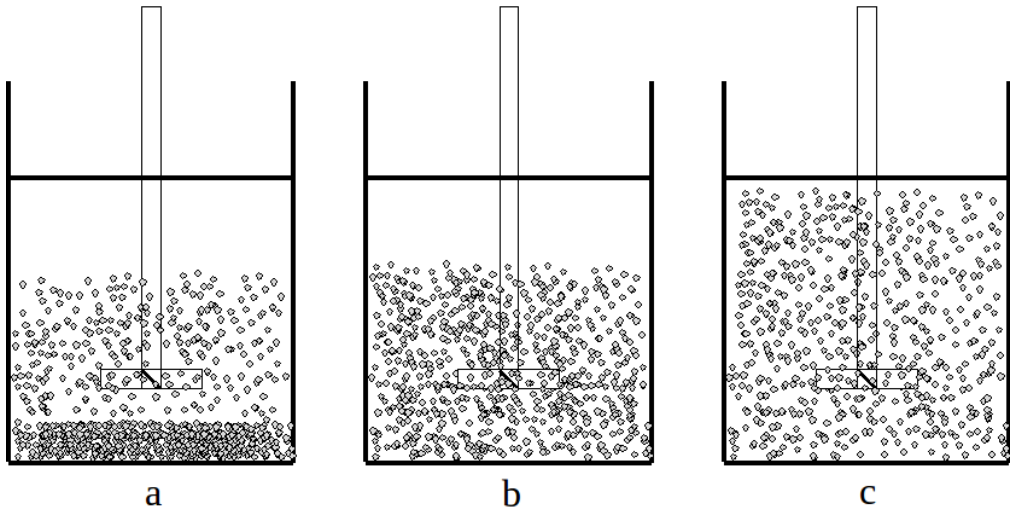

Figure B.1 States of suspension : (a) on-bottom suspension, (b) off-bottom suspension, and (c) homogeneous suspension

where g is the gravity, ρ_s and ρ_l the solid and fluid densities, ν the kinematic viscosity, and X the solids content (solid mass/liquid mass $\times$ 100). Other parameters that affect N_{js} and that are related to the geometry of the mixing system are included in the constant S : the

tank diameter, the impeller type and off-bottom clearance, the tank bottom shape, and the baffle off-bottom clearance [245]. N_{js} is an essential parameter for the design of stirred tanks, which explains the considerable body of research on this topic in the last decades. However, most of the articles referring to the minimum agitation speed for complete suspension relate to the turbulent regime and low concentrations of solids, i.e. inferior to $2wt\%$ according to [17]. Only a few papers have pointed out the unsuitability of the existing correlations for viscous fluids and high solids concentrations [14, 114, 130, 131, 292]. A study performed in the transitional regime using a 1 Pa.s fluid showed that the Zwietering correlation may over-predict N_{js} by more than 90% [130]. These authors reported that, up to 0.01 Pa.s, the Zwietering correlation is applicable, although there are considerable limitations at small values of the Reynolds number (Re). Besides, above solids contents of $2wt\%$, the particle-particle interactions increase and the suspension behavior may deviate from that predicted by the Zwietering correlation [13]. This comes from the fact that the effect of solids loading is complex and that, in particular, the exponent on X depends on the type, number and position of the impeller in the tank [327]. Grenville et al. [114] state that the Zwietering correlation does not account correctly for the effect of μ, $\Delta\rho = \rho_s - \rho_l$ and scale on N_{js}. They propose a new correlation based on experiments and covering a large range of viscosities in the transitional regime. Another source of uncertainty is the constant S in the Zwietering correlation, which is difficult to determine. While it is known to depend on T, D and C [245], it has been reported that the particle diameter and type are also of great importance [13]. Most of the experimental work done so far to determine N_{js} has relied on visual observation of the movement of the particles at the bottom of the tank using a mirror (e.g. [339]. Some work has also used observations from the side of the vessel [158]. Though relatively simple to implement, this method is subjective, and gives no information on the fraction of solids suspended at an impeller velocity below N_{js} [149]. It is also limited to solids concentrations lower than 2%wt and to the use of a transparent vessel, which is uncommon for large-scale systems. Different alternate approaches have been developed to overcome these limitations. One of them is the pressure gauge technique (PGT). This technique is based on the measurement of the pressure at the bottom of the tank and can be applied on double- and three-phase systems over a large range of solids concentrations [53, 210, 212, 296]. For a thorough review on N_{js} and its characterization, the reader is referred to Kasat and Pandit [149], Jafari et al. [139], and Tamburini et al. [297]. A suspension is said to be homogeneous when the distribution and dispersion of the particles are uniform in the tank B.1 (c). When this condition is reached, the impeller speed is called the homogenization speed N_H.

Along this line, the homogenization time t_H corresponds to the time necessary for the agitator to lift the particles, distribute them in the entire tank and obtain the maximum degree of

homogeneity. It depends on the impeller speed and, for this reason, it is measured at $N = N_H$. This time is different from the mixing and the circulation times usually encountered in the literature : the former gives the time for an added volume of fluid to be uniformly mingled in a second fluid [245], and the latter represents the time taken for an element of fluid to achieve a loop in the vessel [76]. A homogenization process can be characterized by measuring the solids concentration throughout the tank. Optical methods are frequently employed for this purpose although they are limited to concentrations under $1-2$ %w/w [288]. Other techniques such as the sample withdrawal method or the conductivity method are also used, but their intrusive effect has been observed to disrupt the flow [22, 288]. To eliminate the drawbacks associated with intrusive methods, Mann et al. [193], for instance, have developed a technique based on electrical resistance tomography (ERT) to measure and characterize mixing in stirred tanks [191–193]. This technique is simple, robust and suitable for opaque systems [201]. Note that radioactive tracer techniques such as positron emission particle tracking PEPT [239], are non intrusive and may also be used in opaque vessels [259], 1991). The radioactive particle tracking (RPT) technique, which has been used in our group to investigate the behavior of granular mixing [2] and gas-liquid mixing [23] systems, could also be considered for the characterization of solid-liquid mixing systems. A review of the state-of-the-art highlighting the importance of the effect of several geometrical factors and mixture properties on solid suspension in the turbulent regime is summarized in Table B.2. For the 5 factors that have been investigated, it can be noticed that different conclusions were drawn depending on the geometry, the experimental technique used or the suspension state sought. The objective of this work is to gain insight into the influence of the operating parameters and governing forces and mechanisms on the suspension in the laminar and early transitional regimes of large concentrations of particles in viscous Newtonian liquids, as provided by a stirred tank equipped with a pitched blade turbine (PBT). First, the methodology, which combines PGT and ERT experimental techniques, as well as torque measurements, is described thoroughly. Results from a design of experiments are then analyzed and discussed.

Table 4.1: Effect of mixer geometry and mixture properties on suspension

	Effect	Impeller type[2]	Experimental method	References
D	- Axial flow impeller are more favorable for solid suspension	PBT, RT, CBT	Gamma-ray densitometry	(Jafari, Tanguy, & Chaouki, 2012a)
	- N_{js} decreases when D increases ($\propto D^{-2}$)	PBT	Visual observation	(Sharma & Shaikh, 2003)
	- D=T/3 impellers are more efficient than D=T/2 in turbulent regime	A310	Visual observation	(Ayranci et al., 2012)
	- D/T=0.35 is the optimal ratio	PBT, HE-3	Visual observation Mathematical modeling	(Bakker et al., 1994)
	- D=T/3 disk turbine shows poor ability to suspend particles in 1Pa.s fluid	Mixed flow, HE3 InterMIGs	Visual observation	(Ibrahim & Nienow, 2009)
d_p	- The plurality of conclusions reflects the complexities of the effect of d_p	LightninA310, PBT	Visual observation	(Ayranci & Kresta, 2013)
	- Two regimes of suspension for particles smaller and bigger than 1mm	HE3, PBT	Visual observation	(Myers, Fasano, & Corpstein, 1994)
	- Smaller particles are easier to suspend in water	RT	Steady cone radius method	(Tamburini, Cipollina, Micale, & Brucato, 2011)
	- Larger d_p implies larger settling velocity and higher N_H	A100, A200, A310, A320	Electrical resistance tomography	(Hosseini et al., 2010)
	- N_{js} is independent of d_p for unbaffled tanks	RT	Steady cone radius method	(Tamburini et al., 2014)
μ	- Poor mixing zones occur in single phase laminar mixing	RT	Visualization techniques	(M. M. Alvarez et al., 2005)
	- Flow patterns change due to the dampening of axial circulation (μ up to 1Pa.s).	RT, PBT, HE3, A310, InterMIGs	Visual observation	(Ibrahim & Nienow, 1999)
	- N_{js} and the specific energy dissipation rate ε_{js} increase when μ increases	RT, PBT, HE3, A310, InterMIGs	Visual observation	(Ibrahim & Nienow, 1999)
	- Axial impellers exhibit a radial profile that leads to a less efficient suspension taking place at the center	RT, PBT, A320	Visualization techniques	(Lamberto et al., 1999)
	- Due to a decrease of the settling velocity, higher μ results in smaller N_{js}	A310, PBT, DT	Laser Doppler velocimetry	(Wu et al., 2001)

[2] *PBT: pitched blade turbine, FBT: flat blade turbine, DT: disk turbine, RT: Rushton turbine, CBT: curved blade turbine, HE3: high efficiency impeller, A100: Lightning propeller, A200: Lightning PBT, A310: Lightning low viscosity impeller, A320: Lightning low Re impeller*

	Effect	Impeller type[2]	Experimental method	References
X_w	- The multiplication of particle interactions leads to an increase in energy dissipation and poorer suspension	A310, PBT	Visual observation	(Ayranci & Kresta, 2011)
	- Mixing times are larger for large solids concentrations (>10wt%)	PBT, DT, propeller	Decolorization method	(Kraume, 1992)
	- Above 10wt% of solid loading, the occurrence of a clear layer at the surface attests to the loss of mixing efficiency	A-310, A-315, InterMIGs	Decolorization method, visual observation	(Bujalski et al., 1999)
	- Increasing solid loading delays the homogenization in a more pronounced way for axial impellers	PBT, RT, CBT	Gamma-ray densitometry	(Jafari, Tanguy, et al., 2012b)
	- Higher settling times facilitates the homogenization once the particles have been lifted	A100, A200, A310, A320	Electrical resistance tomography	(Hosseini et al., 2010)
	- The occurrence of low viscosity cavern around the impeller causes a decrease in the impeller efficiency	PBT, RT	Visualization technique	(Wichterle & Wein, 1981)
C	- The flow patterns change: radial impeller shows axial flow below C=T/5	DT, FBT, PBT, HE3	Visual observation	(Armenante & Nagamine, 1998)
	- For radial impellers, N_{js} increases with an increasing clearance	RT	Visual observation	(Conti et al., 1981)
	- N_{js}=f(C\T) shows 3 zones for PBT: C/T<0.1, constant; 0.1<C/T<0.35, slight increase; C/T>0.35, steep increase	PBT	Visual observation	(Sharma & Shaikh, 2003)
	- Throttling effect: for C/T<0.05, the flow is unable to suspend the particle at the wall/bottom corner	DT, FBT, PBT, HE3	Visual observation	(Armenante & Nagamine, 1998)
	- For 1Pa.s fluid, N_{js} is minimum at C=T/4, as particle accumulation and significant momentum loss are prevented	RT, PBT, HE3, A310, InterMIGs	Visual observation	(Ibrahim & Nienow, 1999)
	- The cloud height and the particle distribution increase with larger clearance	PBT, RT, CBT	Gamma-ray densitometry	(Jafari, Tanguy, et al., 2012b)

[2] *PBT: pitched blade turbine, FBT: flat blade turbine, DT: disk turbine, RT: Rushton turbine, CBT: curved blade turbine, HE3: high efficiency impeller, A100: Lightning propeller, A200: Lightning PBT, A310: Lightning low viscosity impeller, A320: Lightning low Re impeller*

Figure B.2 Effect of mixer geometry and mixture properties on suspension

Material and Methods

Figure B.3 depicts the tank used in this study and Table 2 provides its dimensions. A flat bottom was used because it is more suitable for the implementation of the pressure gauge technique [53], even though it is known that the wall-to-bottom junction makes the particles more difficult to suspend owing to possible recirculation loops therein [277], and dished bottoms are more efficient for solid suspensions [54, 139]. Baffles are not recommended for applications such as crystallization, precipitation and systems involving viscous fluids [51, 299]. In our case, the viscosity is high and a tank without baffles was used to avoid dead zones and the accumulation of particles. Recent results have indicated that the absence of baffles can change the hydrodynamics of the suspension in the tank [292]. Two downward pumping pitched blade turbines (PBT) with T/2 and T/3 diameters, and 3 different bottom clearances of values T/3, T/4, and T/5 were used.

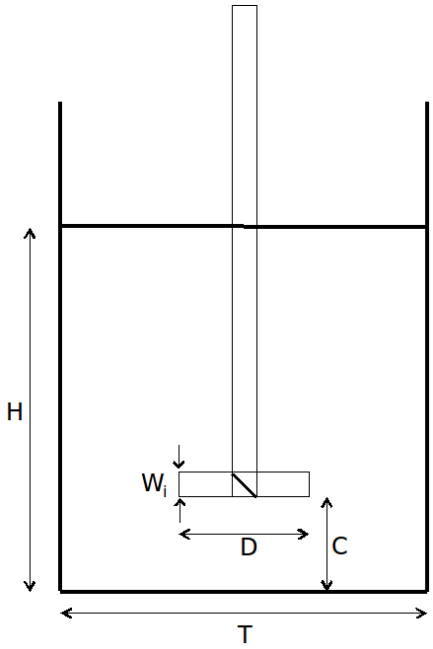

Figure B.3 Cross-section of the tank used for the experimental investigation

The solid particles were glass beads (Potters Industries, $\rho_p = 2500$ kg.m^{-3}; $d_p = 0.5$ and 3 mm) with concentrations ranging from 10% to 35% w/w (6-25 Vol%), leading to bed initial heights representing 11% to 44% of the liquid height. The use of 3 mm beads allowed for a comparison of the experimental data with numerical results obtained with a model developed in our group [40]. The fluid used was a Newtonian glucose solution with a viscosity varying from 1 to 4 Pa.s. This reduced viscosity range was chosen to ensure that the suspension

Symbol	Name	Dimension
T	Tank diameter	0.365 m
D	Impeller diameter	T/3, T/2
H	Liquid Height	T
C	Off-bottom clearance	T/5, T/4, T/3
W_i	Blade width	D/5
e	Blade thickness	D/10

Table B.1 Experimental set-up dimensions

remains in early transitional regime (Re<350), and to avoid extensive settling times. In all cases, the Stokes number ($St = \frac{\rho_p d_p^2 N}{18\mu}$) was between 3.6×10^{-5} and 2.1×10^{-2}, which means that the particles tended to follow the liquid streamlines.

Measurement of Njs using the pressure gauge technique

The pressure gauge technique measures the increase of the apparent density of the fluid as the particles become suspended. The weight of a particle sitting at the tank bottom is transferred to the fluid when this particle is suspended. This lift results in an increase of the hydrostatic head and is captured by a sensor positioned at the bottom of the tank, at a certain distance from the tank wall. This pressure increase ΔP is proportional to the fraction of suspended solids, but also to the dynamic contribution of the kinetic energy. This latter contribution has to be removed from the measurements. Micale et al. [210] consider that above Njs, only the dynamic component affects the pressure so that a parabola (N^2 curve) resulting from the dynamic pressure variations due to an impeller speed increase can be fitted and subtracted from the raw results. This procedure generates a corrected curve that reveals a plateau at ΔP_{js}, from which the value of N_{js} can be deduced (Figure B.4). The fraction of suspended solids $X_{suspended}$ at impeller speed N and corresponding pressure variation ΔP is then equal to $\frac{\Delta P}{\Delta P_{js}}$ as shown in Figure B.5. The resulting curve can be modelled by an "S" shaped Weibull function. Note that the graphs of Figures B.4 and B.5 were obtained using the results of the current work. To our knowledge, it is the first time that the pressure gauge technique is used for viscous liquids. In particular, the plateaus shown in these two figures indicate that the method can be extended to laminar flows. The degree of suspension was monitored by means of a pressure sensor (Freescale : MPX5010DP) with an accuracy of 5% over the full scale, which was located at the bottom of the tank at some distance of from the center and the wall. The acquisition card is a 10-bit microcontroller (ATmega 2560), the resolution of which is improved by an oversampling method [151]. Starting at 30 RPM, the impeller speed was gradually increased by 25 RPM increments up to the maximum value with no air

entrainment. This maximum speed went from 500 RPM for the T/2 PBT, to 1200 RPM for the T/3 PBT, in the case of the 1 Pa.s viscosity solution. The raw pressure measurements were collected via Labview software and were processed using the procedure described above.

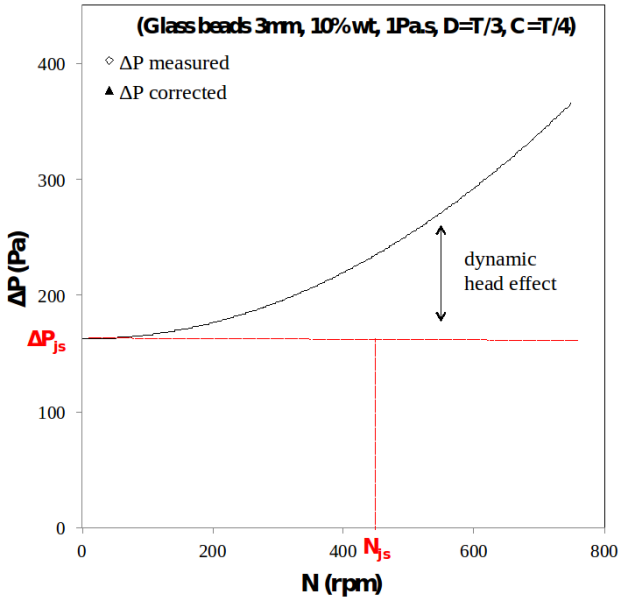

Figure B.4 Bottom pressure increase and modified bottom pressure, as a function of agitation speed

Measurement of the homogenization speed and time using electrical resistance tomography

The homogenization speed and time were measured via electrical resistance tomography (ERT). The ERT apparatus is a commercial system (p2000+ from ITS, United-Kingdom) and consists in 4 planes of 16 electrodes (ne=16) uniformly distributed on the inner wall of the tank and in contact with the fluid. The electrodes are rounded stainless steel bolts positioned every 7.15 cm around the tank wall, and the spacing between each plane is 9 cm. The device is completed by a data acquisition system. The automated calibration procedure built into the equipment was used to set the most appropriate parameters and yielded an electrical current of 1.5 mA at 9,6 kHz. Voltages were collected every 1500 ms on each plane. The complete set-up is depicted in Figure B.6.

The ERT system transmits electrical current through one pair of adjacent electrodes and the resulting voltage is measured at the remaining electrode pairs. This procedure is repeated for the next pair of electrodes until all pairs have been solicited. It creates independent

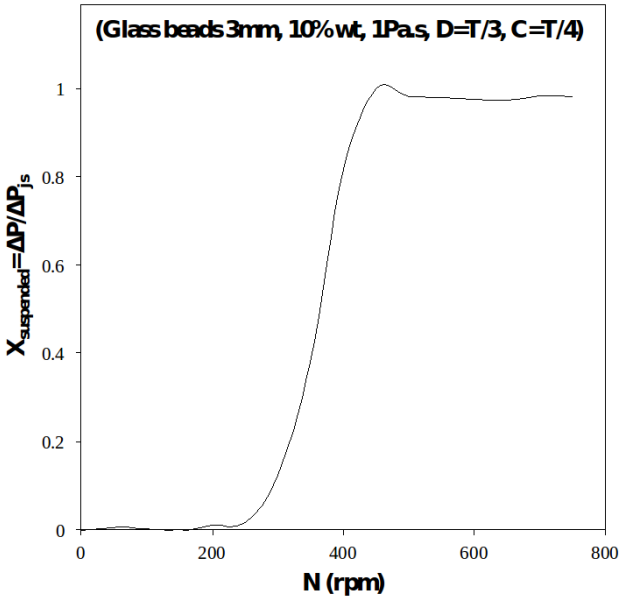

Figure B.5 Fraction of suspended solids, as a function of agitation speed

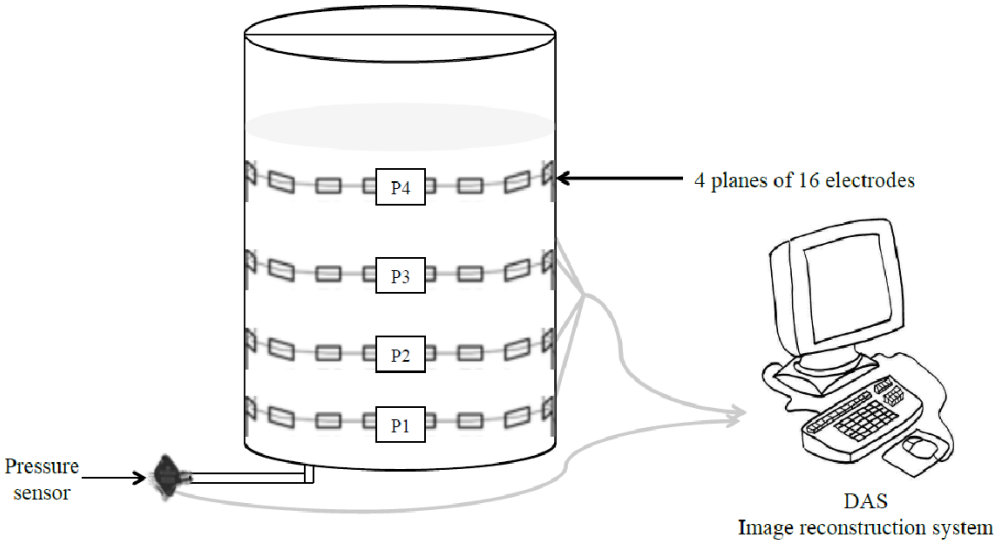

Figure B.6 Complete experimental set-up

measurements for each plane [129]. As mentioned in the ITS documentation, the acquired electrical signal is processed by linear back projection to obtain the conductivity field [328, 333]. The average resistivity map obtained for each plane allows for the determination of N_H and t_H. Homogeneity is reached when the average resistivities measured on each plane level off to constant values. N_H is the impeller speed and t_H the time required to reach this state, as further explained in the next sub-section. This ERT configuration offers a spatial resolution of 10% of the vessel diameter, which means the system cannot provide information for dimensions smaller than 3 cm [106]. However, an adequate estimation of the global particle distribution, and the detection of the time needed to reach homogeneity (uniform solid concentration) on a plane, can be achieved by resorting to average resistivity maps.

Procedure for the determination of NH and tH

To determine N_H, the impeller speed N was increased stepwise as was done for N_{js}. Note that the maximum speed reached in all experiments was high enough for the determination of N_H and t_H. The raw resistivity values r were normalized by the initial resistivity r_0, , and plotted as a function of impeller speed for each plane, as illustrated in Figure B.7. To obtain the homogenization speed, a homogeneity percentage was calculated based on the variation of the slopes of the corresponding curves. More precisely, for each plane j, impeller speed N_i, and corresponding resistivity $R_{i,j}$, the slope s_{ij} was calculated as follows :

$$s_{ij} = \frac{R_{i+1,j} - R_{i,j}}{N_{i+1} - N_i} \tag{B.2}$$

A measure of the level of homogeneity attained at impeller speed N_i was then evaluated and normalized by its maximum value at $N_{i,max}$:

$$\%H_k = \frac{\sum_{i=1}^{k} \sum_{j=1}^{k} s_{ij}}{\sum_{i}^{i,max} \sum_{j}^{4} s_{ij}} \tag{B.3}$$

An example of a $\%H$ vs N curve is given in Figure B.8, where N_H is defined as the experimental impeller speed at which $\%H$95%. Higher values, such as 99%, could be required for a specific process, but this would lead to a higher value of N_H. Note that we observed in this work that values lower than 95% could yield $N_H < N_{js}$, owing to particles remaining at the bottom of the tank at this speed. Obviously, this does not make sense in practice and this is why 95Once N_H was determined, the impeller was stopped and the particles were allowed to settle all the way to the bottom of the tank. After complete settling, the impeller speed was set at N_H and the homogenization time t_H was evaluated using the resistivity measurements,

following the same approach as that used for the determination of N_H. This is illustrated in Figure B.9.

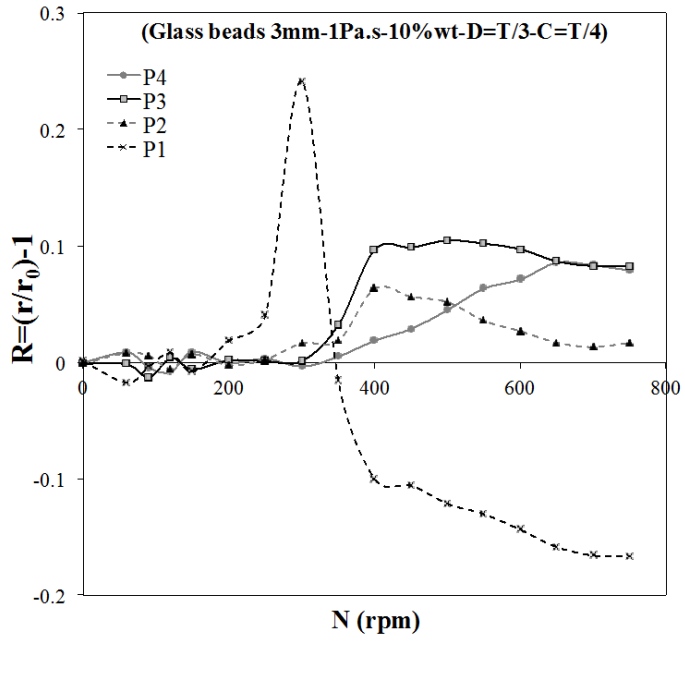

Figure B.7 Determination of NH : normalized resistivity as a function of impeller speed on every plane

Measurement of cloud height and torque

The cloud height was obtained by visual observation and the torque was measured using a high-frequency torque meter (Ono Sokki detector : SS-050, 0 to 5 N.m, $\pm$0.05 N.m). Statistical analysis To assess the effect of every factor (d_p, μ, X_w, C and D) and their interactions, considering 2 modalities for d_p and D, and 3 modalities for μ, X_w, and C, and using a complete design of experiments (DoE), would require 108 experiments. Consequently, an I-optimal DoE involving 32 runs was considered. Statistic software JMP was used to determine the most significant factors and build a model for the prediction of N_{js}, N_H and t_H. Table B.2 presents the modalities investigated for each factor. The values of the 5 factors for each of the 32 experiments are given in Table B.3.

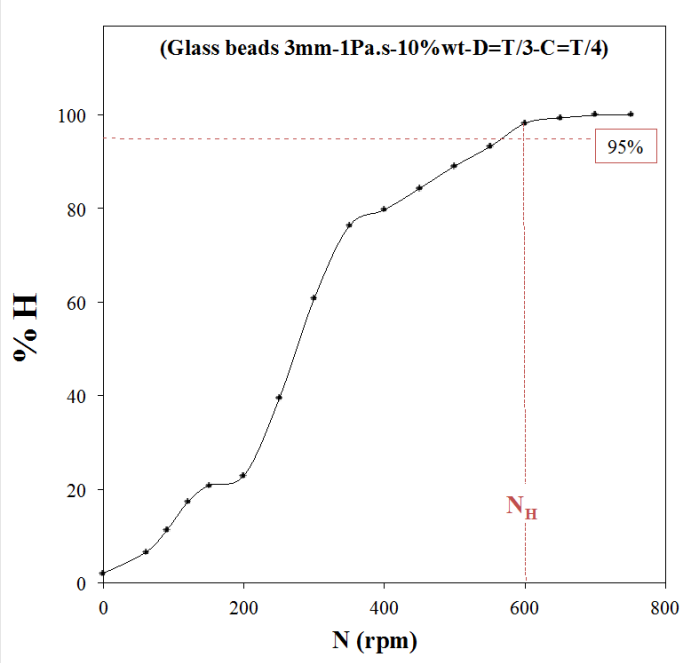

Figure B.8 Determination of NH : level of homogeneity attained as a function of impeller speed

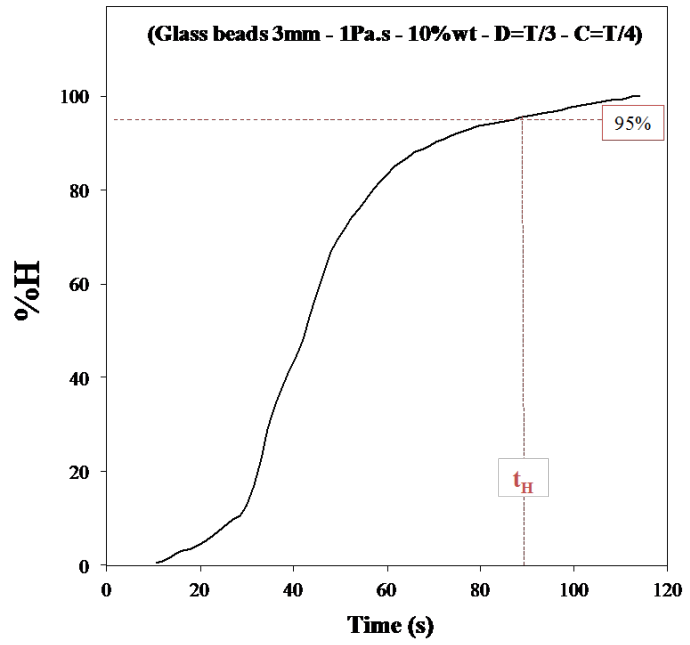

Figure B.9 Determination of tH : level of homogeneity attained as a function of time

Parameter	-	0	+
d_p (mm)	0.5	-	3
μ (Pa.s)	1	2.5	4
X_w (wt%)	10	22.5	35
C	T/5	T/4	T/3
D	T/3	-	T/2

Table B.2 I-optimal DoE modalities

Results and discussion

The reproducibility of the experiments is first assessed for the PGT and ERT. Then, the results of the I-optimal design of experiments are presented, and the effects of the 5 factors investigated on N_{js}, N_H, and t_H, are discussed.

Reproducibility

To evaluate the reproducibility of the PGT and ERT, 3 tests of the same experiment were realized and processed. Figures 9 and 10 present respectively the fraction of suspended particles $X_{suspended}$ and the level of homogeneity %H for the three runs. A good reproducibility can be observed with a standard deviation σ of 3.3% (PGT) and 0.45% (ERT) on average for the higher impeller speeds ($N > 350$ RPM). The error bars represent 95% confidence intervals (average value $\pm$ 1.96$\times\sigma$).

Experimental data set

All the data collected in each experiment, with the exception of the torque measurements, can be superimposed on a single plot : $\Delta P/\Delta P_{js}$ for the normalized pressure, the normalized cloud height CH/H, and %H for the level of homogeneity. This is illustrated in Figure B.12. In this particular case, it can be observed that below $N_0 = 175$ RPM, the particle bed is but slightly altered with the formation of a cone of particles under the impeller and the dispersion of a small amount of isolated particles in the bulk of the tank. This zone appears to be isolated from the rest of the agitated vessel. Above 175 RPM, increasing the velocity of the impeller leads to a sharp increase in the fraction of suspended solids, the cloud height and the level of homogeneity. This indicates a sudden and massive lifting of the particles, which is accompanied by a drastic change in the mixing dynamics observed during the experiment. More precisely, the particles, the motion of which is first confined to a conical region under the impeller, eventually escape the bed and ascend along the tank wall. Figure B.12 shows

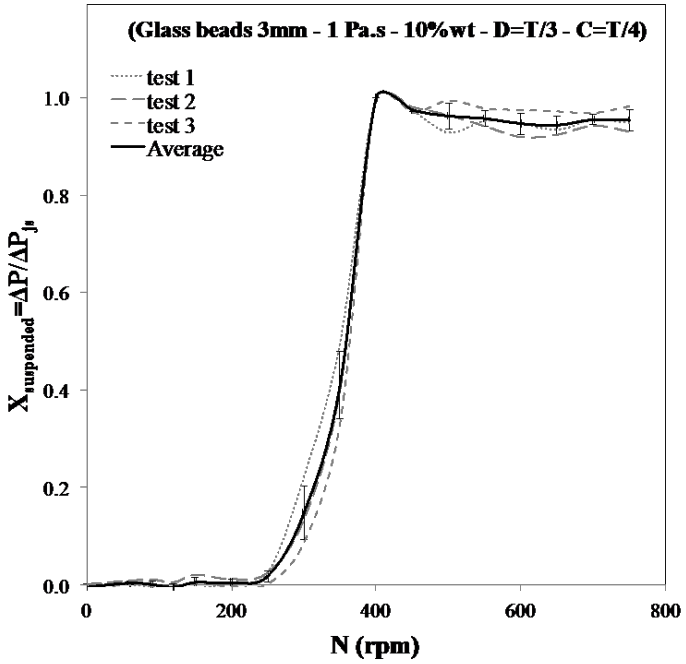

Figure B.10 Reproducibility tests for the pressure measurements with the PGT

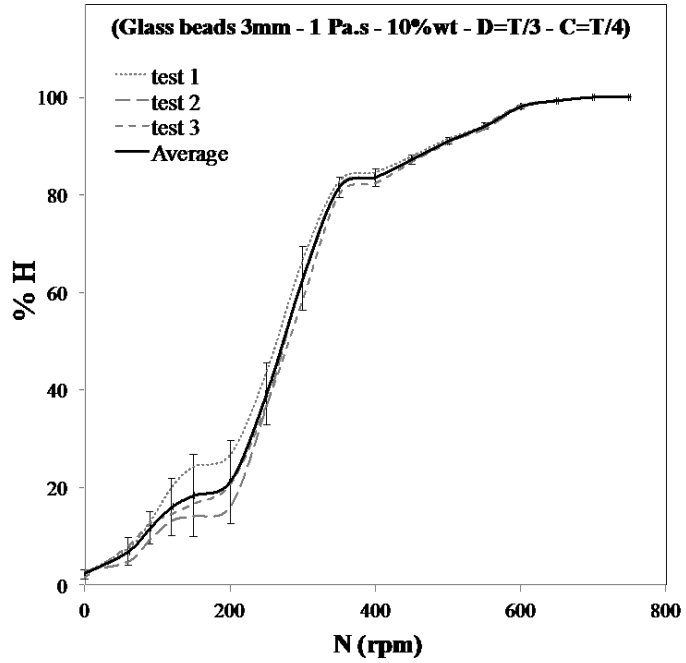

Figure B.11 Reproducibility tests for the level of homogeneity measurements with ERT

that, as the impeller speed is steadily ramped up, the 3 curves level off to constant values. It can be seen that N_{js} is reached at 250 RPM, the particles reach the surface at 275 RPM and the level of homogeneity attains the 95% threshold at $N_H = 325$ RPM. This procedure was repeated for all of the 32 experiments of the I-optimal DoE.

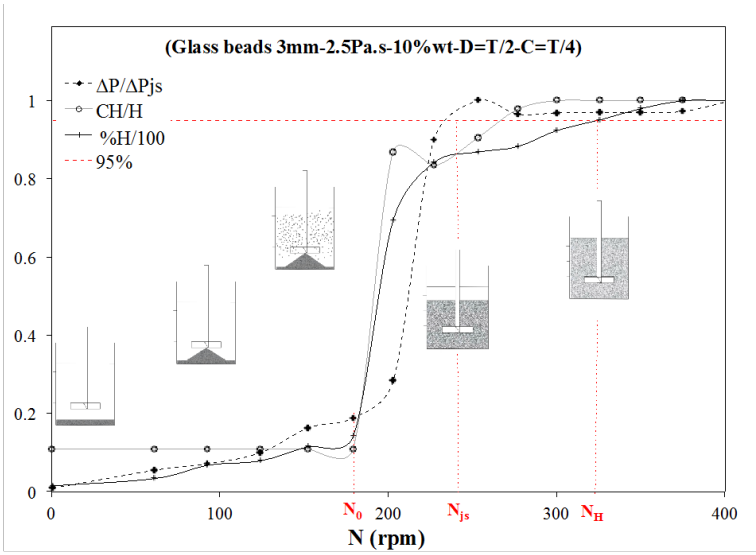

Figure B.12 Global behavior of the mixing system

Statistical analysis and discussion

The 32-run I-optimal DoE and the corresponding responses are presented in Table 4. Based on these results, models were derived (Table 5). The models for N_{js} and N_H show a good agreement with the experiments with 10.3% and 15.2% relative error, respectively ; whereas the model for $N_H \times t_H$ is not as accurate (59.2% relative error). The trends predicted by these models are discussed in detail in the following section.

Just-suspended speed, N_{js}

Figure 12 compares the values of N_{js} measured for the 32 experiments described in Table B.3 to those predicted by the Zwietering correlation and the model of this work (Table B.4). The values of S chosen for the correlation are given in Table 6 as a function of D/T and C/T [16].

It can be readily observed that, while the adequacy of the model derived in this work is good, the Zwietering correlation deviates strongly and in an irregular manner from the experimental

d_p	μ	X_w	C	D	N_{js} [RPM]	N_H [RPM]	t_H [s]	$N_H \times t_H$
-	-	-	-	+	250	275	689	3158
-	-	-	+	-	500	525	1065	9319
-	-	0	0	-	475	725	194	2344
-	-	-	0	+	250	275	518	2374
-	-	+	-	-	800	1000	553	9217
-	-	+	+	+	275	275	557	2553
-	0	-	0	-	575	575	197	1888
-	0	0	-	-	525	850	247	3499
-	0	0	-	+	275	350	303	1768
-	0	0	+	+	300	300	584	2920
-	0	+	+	+	250	400	138	920
-	0	+	+	-	525	725	285	3444
-	+	-	-	-	425	700	466	5437
-	+	-	+	+	250	250	1016	4233
-	+	0	+	-	575	600	635	6350
-	+	+	-	+	350	475	231	1829
-	+	+	0	-	575	900	282	4230
+	-	-	-	-	450	800	62	827
+	-	-	+	+	425	450	144	1080
+	-	0	0	-	425	725	76	918
+	-	+	-	+	225	325	47	255
+	-	+	+	-	450	1000	53	883
+	0	-	0	+	250	325	76	412
+	0	0	-	-	450	1200	79	1053
+	0	0	0	+	225	400	91	607
+	0	0	+	-	425	800	64	853
+	0	+	0	-	450	1200	80	1067
+	+	-	-	+	275	350	101	589
+	+	-	+	-	400	525	164	1435
+	+	0	0	+	250	425	91	645
+	+	+	-	-	350	750	122	1525
+	+	+	+	+	225	275	228	1045

Table B.3 I-optimal DoE results

Parameter	Model	Relative error (%)
N_{js}	$713.9 - 1344D/T - 98.4d_p + 292.7D/Td_p - 2.2X_wd_p$ $-34.3C/TX_w - 20.8D/TX_w - 14.3\mu + 22.3X_W + 760.8C/T$	10.3
N_H	$1142 - 1279D/T + 31.6X_w - 60D/TX_w + 34d_p - 945C/T$	15.2
$N_H \times t_H$	$2.7 \times 10^4 - 1.8 \times 10^4 D/T - 3.4 \times 10^3 d_p + 5.5 \times 10^3 D/Td_p$ $-1.4 \times 10^5 C/T + 211X_W$	59.2

Table B.4 DoE prediction models

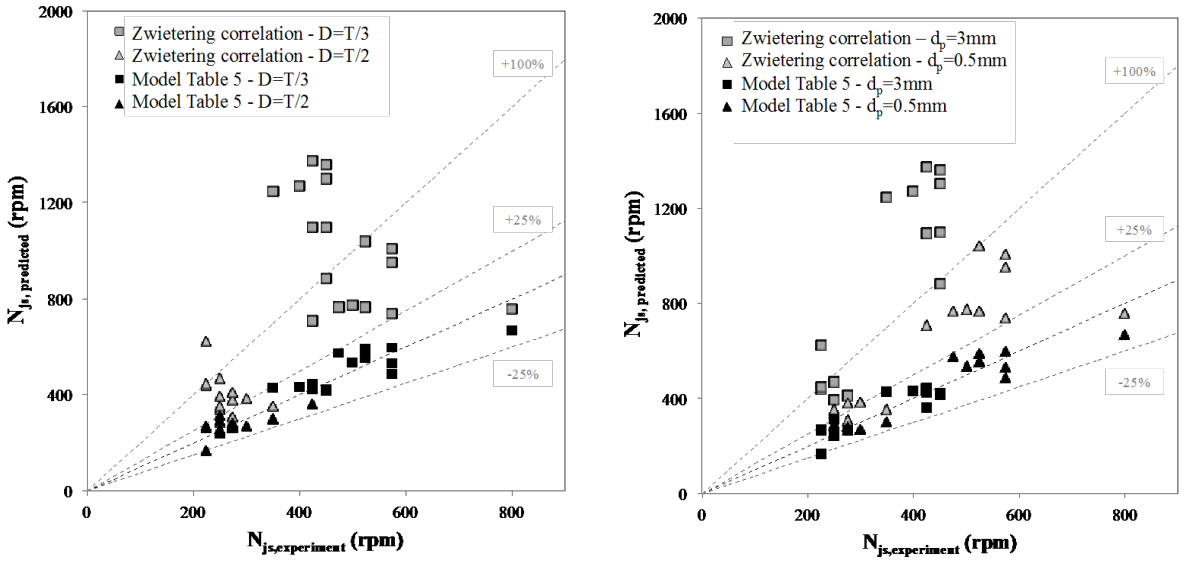

Figure B.13 Comparison of the N_{js} values predicted by the Zwietering correlation and the model of Table B.4 to the experimental data (Left) effect of D/T ; (Right) effect of dp

D	C	S
	T/3	3.40
T/2	T/4	2.77
	T/5	2.72
	T/3	7.15
T/3	T/4	6.18
	T/5	5.75

Table B.5 Values of S chosen for the Zwietering correlation as a function of D/T and C/T

data. More precisely, it over-estimates N_{js} significantly, all the more so when D=T/3 (Figure B.13) or for the 3-mm particles (Figure B.13). In this latter case, such an overestimation has also been reported by Tamburini et al. [292] for top-covered unbaffled tanks in the transitional regime. Our results also indicate that there is no clean trend as regards the impact of X_w, μ and C/T on the accuracy of the Zwietering correlation for non-dilute concentrations of particles in viscous liquids. Figure 12a shows that Njs decreases with an increase of D/T, which is intuitive and has been noticed in previous investigations [**?**,130] It is also of interest to compare the effect of an increase of each of the 3 physical properties (d_p, μ, X_w) on the value of N_{js}, as predicted by the Zwietering correlation and the model of the present work. Table B.6 shows completely opposite trends, with the exception of X_W in the case of small particles. Note that choosing different values of S did not change the results of this table. Such discrepancies, which may come as a surprise, are now analyzed in depth.

Our results indicate that large particles are more easily suspended, which is in opposition to the Zwietering correlation and recent work by Tamburini et al. [292] who concluded that N_{js} does not depend on the particle diameter for unbaffled tanks. To support our results, an analysis of the forces in action is made, as illustrated in Figure B.14. In the turbulent regime, the lift force on resting particles is governed by the gravity ($\boldsymbol{g}$), the buoyancy ($\boldsymbol{b}$), the particle-particle friction ($\boldsymbol{c}$), the force ($\boldsymbol{f}$) due to the liquid flow around the particles, the components of which are the drag and lift forces, and by the burst of turbulent eddies behind these particles [16, 287]. By opposition, in the laminar and early transitional regimes, the viscous forces become more and more predominant as the Reynolds number decreases, which alters significantly the suspension mechanism.

In the turbulent regime, eddies are the main thrust for the lifting of the particles at the bottom of the vessel. In a viscous liquid, such lifting is mainly controlled by the shear and the pressure applied at the surface of the particles [287]. This mechanism is comparable to an erosion phenomenon. Drag forces are prominent and the Kolmogorov energy cascade non-existent [253]. Consequently, the larger the contact surface, the easier it is to erode the

	d_p	μ	X_W
Zwietering	+	+	+
Present work	−	−	+ for small d_p − for large d_p

+ Positive contribution implies an increase in Njs with an increase of the factor
- Negative contribution implies a decrease in Njs with an increase of the factor

Table B.6 Comparison of the factor contributions to Njs for the Zwietering correlation and the model of Table B.4

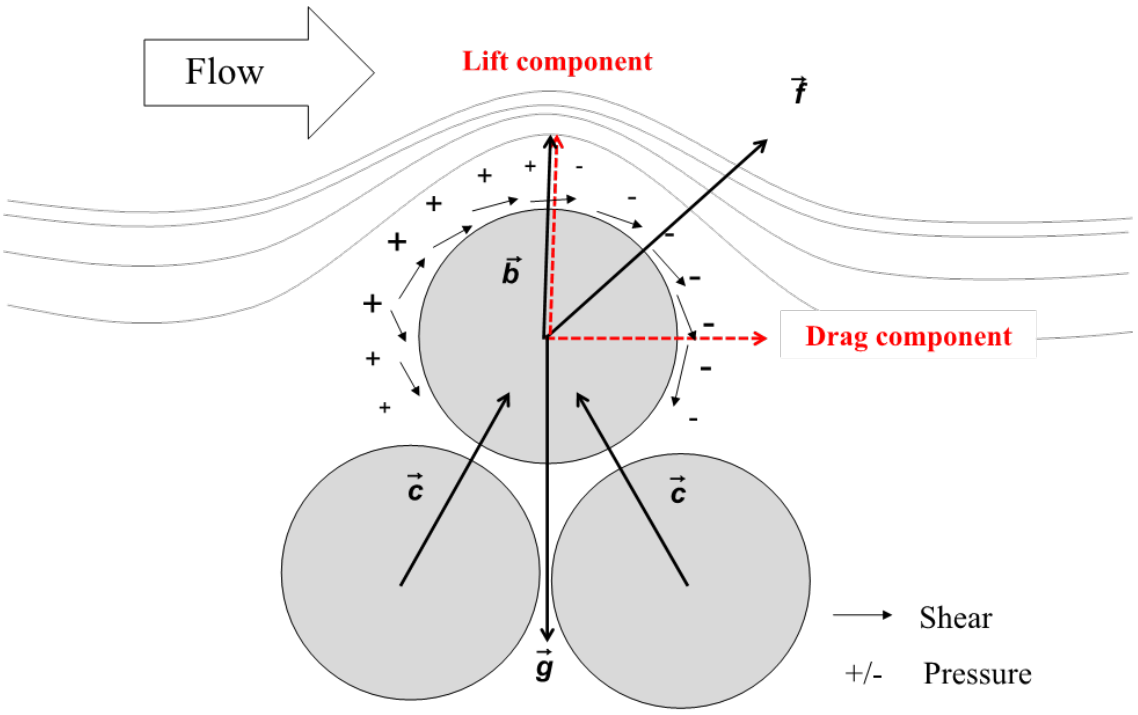

Figure B.14 Forces in action for particles in a viscous fluid

particles resting at the top of the bed. Leighton and Acrivos [179] reported that particle lifting is attributed "to a shear-induced diffusion balancing the downward settling flux". They stated that a critical shear stress τ_{cr} is required to trigger the resuspension mechanism and that this critical value is inversely proportional to the particle diameter. The Shields number, where γ is the shear rate, gives the ratio of the shear stress to the apparent weight of a particle, and can be used here to characterize the erosion of the particle bed. This dimensionless number was used by Derksen [83] to investigate the suspension of particles in a stirred tank in the turbulent regime. Leighton and Acrivos [179] showed that the expansion of a bed, which is directly proportional to the resuspended fraction of solids, increases with θ. Replacing γ by N in the definition of θ, one should then expect that the intensity of the erosion mechanism taking place in a stirred tank is directly proportional to the liquid viscosity μ and the impeller speed N, and inversely proportional to the particle size dp. While this is precisely what is evidenced by our model in Table B.6 for γ and N, the opposite trend can be noticed for dp. As just mentioned, the critical shear stress τ_{cr}, above which the erosion of the bed is triggered, is expected to decrease when d_p increases, by analogy with what was observed by Leighton and Acrivos [179]. This means that a smaller critical Shields number θ_{cr} must be overcome in the case of 3 mm particles, which may explain why lower value of N_{js} are obtained for

this particular size. This suggests that the mechanism of suspension in the laminar and early transitional regimes should be considered more like an erosion phenomenon than a particle pick-up, the latter of which has been suggested for turbulent solid-liquid systems [16, 306]. Table B.6 also highlights that the effect of $X_w$is more complex and depends, in part, on the particle size. The Zwietering correlation predicts an increase of N_{js} when the concentration of particles is increased. On the other hand, our model and the experimental data of this work show the opposite trend when the particles are large. One way to shed light on this behavior is to look more closely at the dynamics of erosion of the bed as was observed during our experiments. At the onset of erosion, the impeller speed and the distance between the top of the bed and the impeller, the so-called apparent clearance, are denoted by N_0 (see Figure B.12) and $C_{app,0}$. The first layers of particles then gets eroded, which leads to an increase of C_{app} from $C_{app,0}$ to $C_{app,1}$ before an equilibrium is reached (Figures B.16 (a)). At this point, the eroded particles are suspended in the viscous liquid and may collide with the bed of particles as they are dragged by this liquid (Figure B.16 (b)). The erosion of the bed of other layers of particles can then be achieved by increasing the impeller speed to N1 before another equilibrium is attained, thereby enlarging the apparent clearance to $C_{app,2}$ (Figure B.16 (c)). This can be repeated all the way down to one single layer of particles remaining at the bottom of the vessel, at which point C_{app} becomes equal to the real clearance C. The suspension of these particles can then take place by increasing impeller speed to what is obviously the just suspended speed N_{js} (Figure B.16 (d)). During the experiments, the surface of the eroding bed did not remain flat but deformed to generate a conical region of particles underneath the impeller, as discussed at the beginning of this section (Figure B.12) and displayed in the schematics of Figure B.16 and the picture of Figure B.17. Note that the size of this cone decreased with the increase of the impeller speed, as more of its particles get suspended in the liquid.

The dynamics of erosion of the bed of particles help understand the effect of X_W on N_{js} as predicted by our model. This effect is believed to be in fact a combination of many factors including the gradual increase of the apparent clearance, the evolution of the apparent viscosity caused by the suspension of an increasing number of particles, and the collision of suspended particles on the bed of remaining particles. The interplay of these 3 phenomena and the underlying impact on the hydrodynamics prevailing in the vessel in all likelihood depend on the concentration and the size of the particles, which would explain, at least in part, the two-fold effect of X_W on N_{js} reported in Table 7. Quite clearly, more work is needed to confirm these explanations. As this entails looking into the detailed flow behavior of both the particles and the liquid phase, such an investigation will be done using our CFD-DEM code and reported in a forthcoming paper [40].

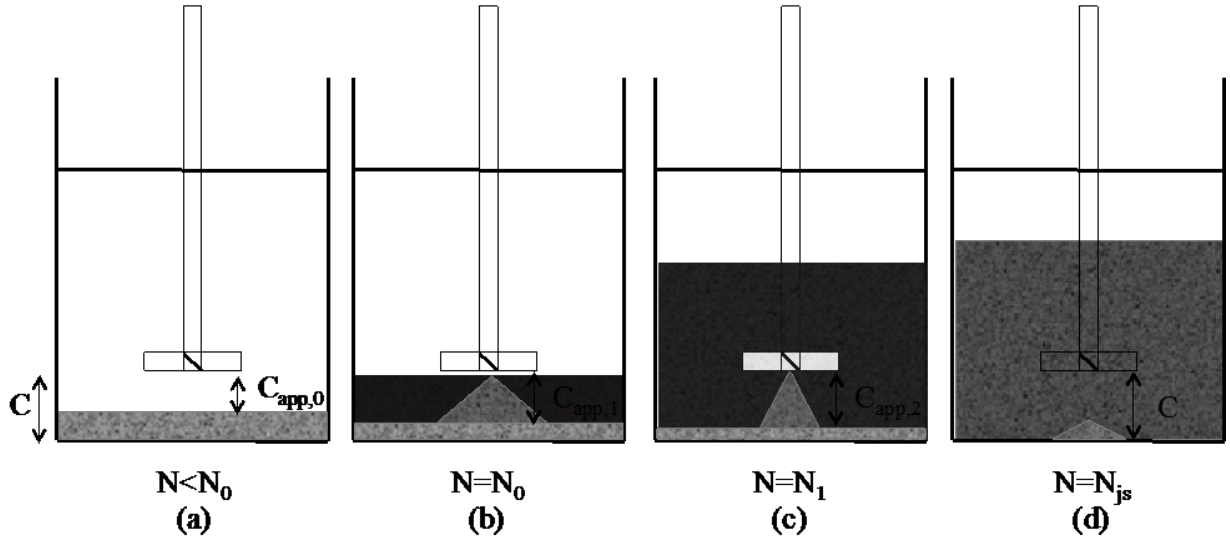

Figure B.15 Schematic representations of the dynamics of erosion of the bed of particles

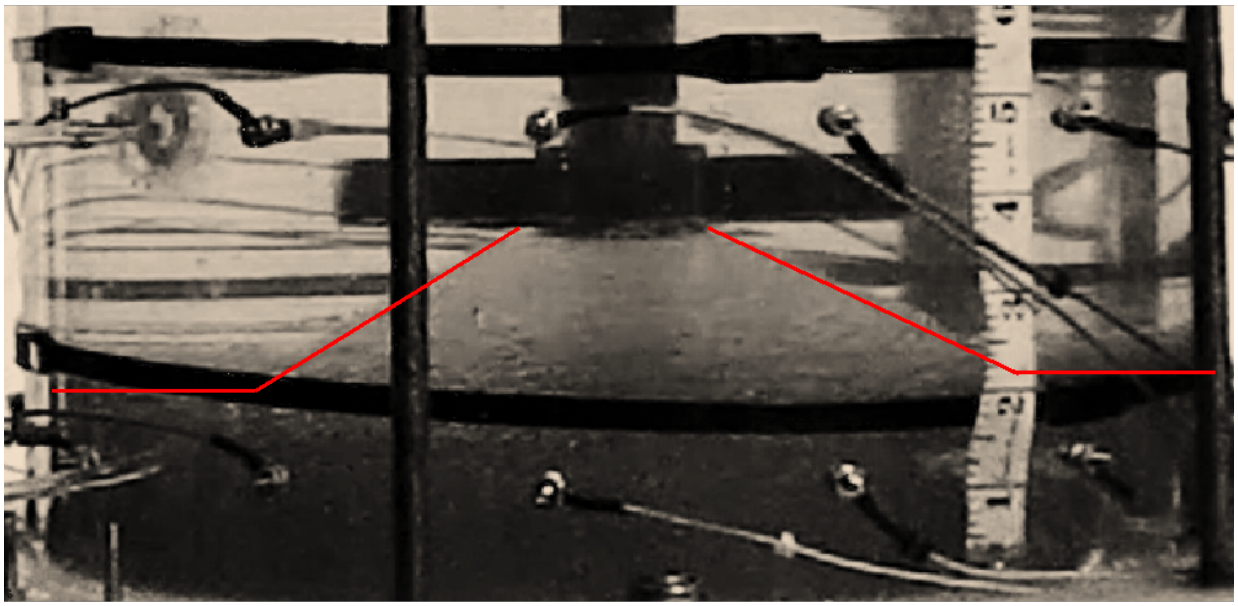

Figure B.16 Picture of the cone of particles observed underneath the impeller

Homogenization speed, NH

Figure **??** shows that the values of N_H measured for the 32 experiments described in Table B.3 can be well predicted by the model given in Table B.4. One can also notice that D/T has a significant impact on N_H. This comes from the fact that the energy delivered per impeller rotation by the large turbine ($D = T/2$) is much higher, thus reducing the impeller speed required to distribute uniformly the particles in the vessel. Figure **??** indicates that the larger X_W, the larger the value of N_H, all the more so when D/T is small. This is of course not surprising as more important particles then need to be homogenized with a smaller capacity turbine [138]. Moreover, as already discussed in the case of N_{js}, the rheological behavior of the suspension may hinder to some extent the uniform distribution of the particles by forming a cavern around the impeller or creating poor mixing zones. The impact of the other factors on N_H is not as clear-cut. For one, each category of points taken as a whole in Figure **??** is regrouped in a way that suggests an increase of N_H with a decrease of C/T, at least with the smaller turbine. This agrees with the work of Jafari [137] in the turbulent regime. Next, it can be observed in Figure **??** that the larger 3-mm particles are more difficult to distribute. As mentioned in Section B, the Stokes numbers related to the suspensions of this work are small (<10-2), so that the particles tend a priori to follow the liquid streamlines. However, the Archimedes number ($Ar = (gd_p^3\rho_l(\rho_p - \rho_l))/\mu^2$) of the 3-mm particle is 216 times larger than that of the 0.5-mm particle, meaning that its tendency to settle out of the suspending liquid and head for the bottom of the vessel is significantly greater. In other words, the larger particles are easier to extract from the bed, owing to a smaller value of N_{js}, but more difficult to drag all the way to the surface of the vessel once they get suspended. Finally, no trend could be established as regards the effect of the liquid viscosity on N_H, which can be attributed to the complex two-way coupling between the particles and the liquid.

Homogenization time, tH

It can be readily seen in Figure B.18 that there are large discrepancies between the values of the dimensionless homogenization time measured by ERT and predicted by the model of Table B.4, the gap exceeding 100% in some cases. This is due to the rather poor accuracy of this model, contrary to those obtained for N_{js} and N_H, which suggests that the homogenization time cannot be expressed as easily as a function of the 5 factors investigated in this work, owing to either complex interactions among these factors or the lack of sensitivity of some of them in this regard. A closer look at the results of Figure B.18 failed to reveal correlations between the magnitude of the error and the values of specific factors. However, Figures **??** and **??** show that $N_H \times t_H$ is larger for the smaller turbine and the larger particles. The effect

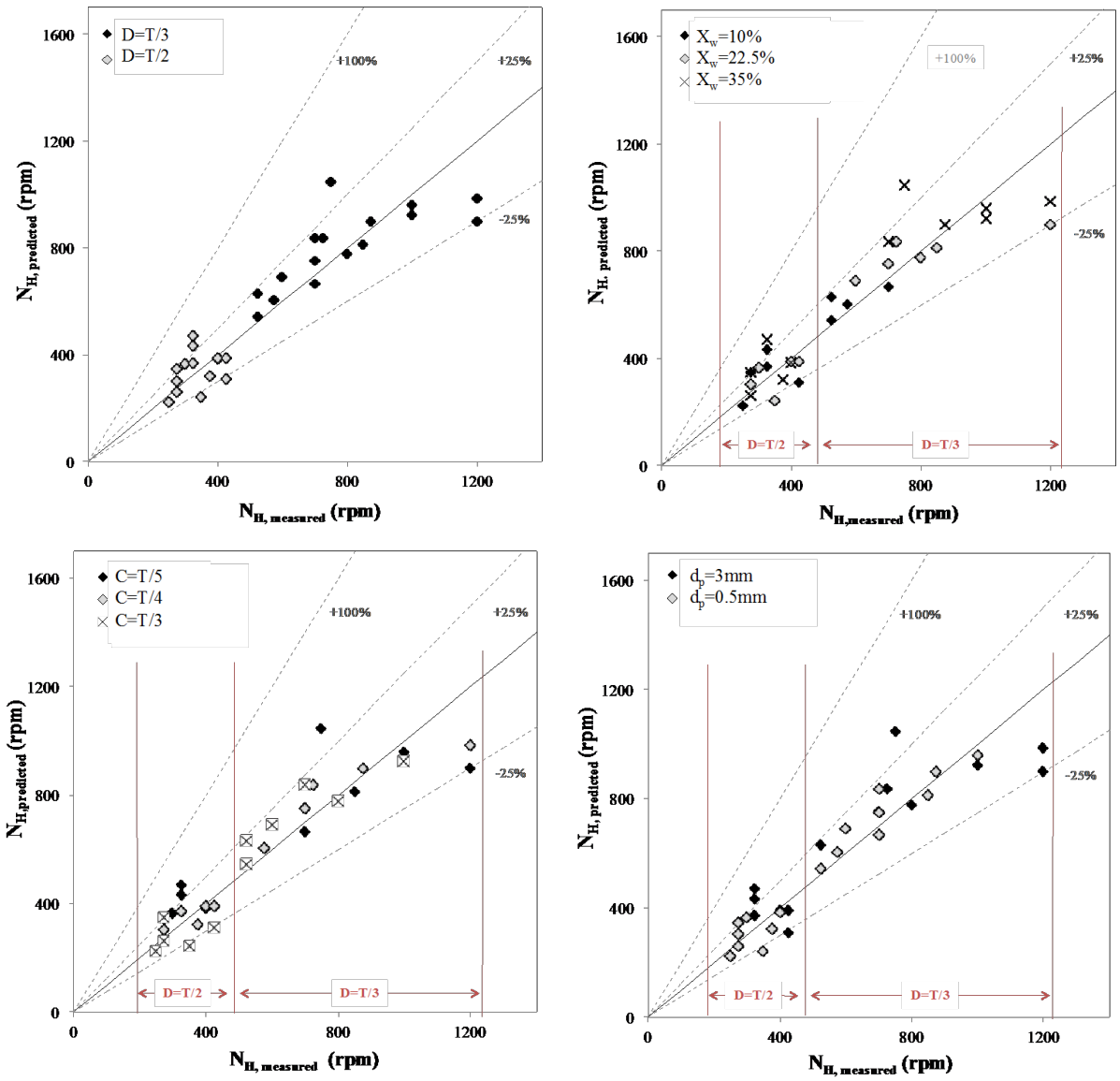

Figure B.17 Comparison of the NH values predicted by the model of Table 5 to the experimental data : (Top left) effect of D/T, (Top right) effect of Xw, (Bottom left) effect of C/T, and (Bottom right) effect of dp

of D/T complies with what was observed for N_H and N_{js}, and can be related to the increased power transferred to the system by the larger impeller at a given impeller speed. The effect of the particle size on the dimensionless homogenization time can be understood by breaking down this time into two components : (1) the erosion time, or the time needed to completely suspend the bed of particles, as discussed in the subsection on N_{js}, and which was measured by the PGT, and (2) the additional time to bring these suspended particles to the liquid surface, which was evaluated by ERT. Figure B.19 compares the PGT-based erosion time to the ERT-based homogenization time. Interestingly, the two values are close, meaning that once the particles are suspended, the time required to distribute them uniformly in the tank is relatively small, as long, of course, as the impeller speed is set to N_H. For instance, the example of Figure B.19 shows that only a few seconds indeed suffice. This also explains why the effects of the particle size on $N_H \times t_H$ (Figure **??**) and on N_{js} (Figure B.13) are similar.

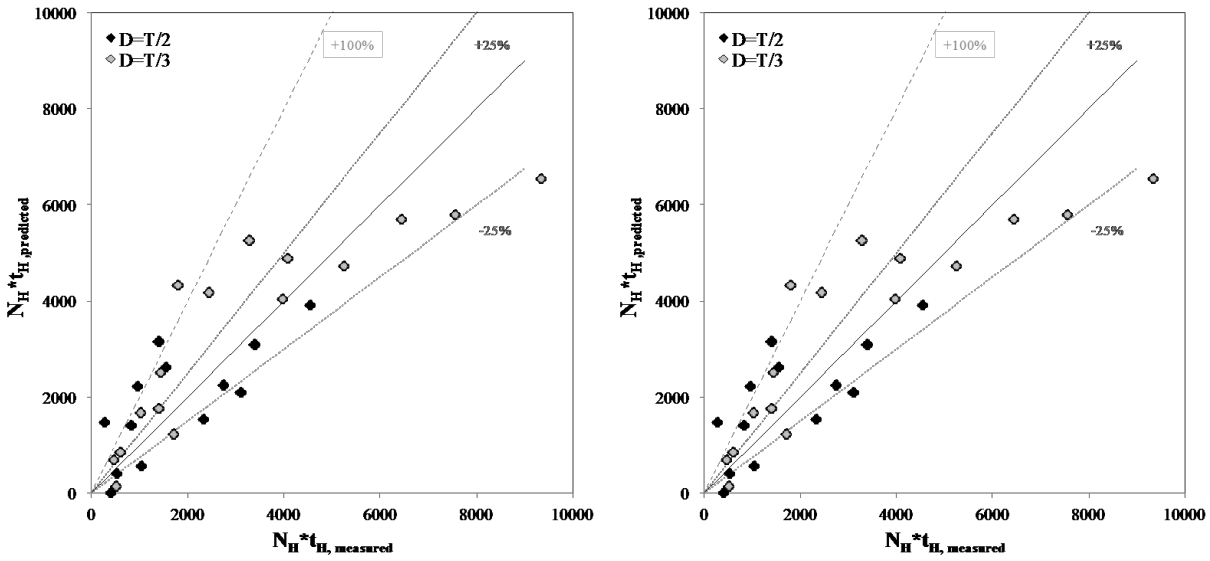

Figure B.18 Comparison of the dimensionless homogenization time predicted by the model of Table 5 to experimental data : (Left) effect of D/T, and (Right) effect of dp

Conclusions

The combination of ERT and the PGT for the characterization of non-dilute suspensions in viscous liquids in the laminar and early transitional regimes provides insight on the behaviour of N_{js}, N_H, and t_H for a stirred tank equipped with a pitched blade turbine. Based on the results obtained, prediction models were developed to investigate the effect on N_{js}, N_H, and t_H of physical properties d_p, X_w and μ, as well as geometrical factors D/T and C/T. The following conclusions were drawn :

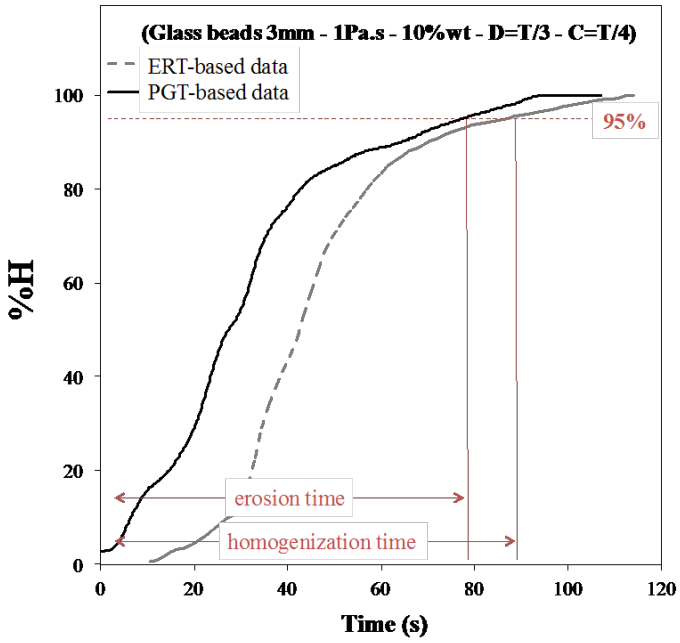

Figure B.19 Comparison between the PGT-based erosion time and the ERT-based homogenization time

— D/T has a strong impact on N_{js}, N_H, and the dimensionless homogenization time $N_H \times t_H$, an increase in D leading to a significant decrease in these quantities ;

— The behavior of N_{js} was shown to be different than that reported for the turbulent regime based on the Zwietering correlation. For instance, we observed that an increase of either d_p or μ leads to a decrease of N_{js}, contrary to what is predicted by this correlation. In addition, the impact of X_w was shown to be more complex than what it predicts, as it depends on the particle size d_p. Consequently, these results suggest that the Zwietering correlation should not be used in transitional and laminar flows ;

— As the main forces acting on the resting particles at the bottom of the tank are the pressure and the shear stress, the suspension mechanism was viewed as that governing the erosion of a bed of particles. It follows that the effects of d_p and μ on N_{js} are similar to those reported in the case of viscous resuspension by Leighton and Acrivos [179], highlighting the importance of the Shields number in this context ;

— While the effects of D/T, X_w, C/T and d_p on N_H were not as obvious, they were found to comply with what has already been reported for the turbulent regime. The homogenization of the particles is easier with large impellers and large clearances, whereas it is hindered when large particles or large concentrations are considered. No conclusion could be drawn about μ ;

— The homogenization process at a constant impeller speed can be divided into two phases : the first one is characterized by an erosion time and captured by the evolution of the pressure at the bottom of the vessel, as monitored by the PGT, and the second one corresponds to the time required to distribute the particles once they have been suspended, as determined by ERT. The erosion time, which was observed to be the time necessary to suspend the particles, is the critical step for the homogenization time t_H.

The results of this work bring insight into the mixing of viscous liquids and non-dilute concentrations of particles in stirred tanks. They also provide the impetus for additional experimental, theoretical and modeling work. In particular, a wider range of viscosities would allow for a better understanding of the effect of this factor. The effect of the particle size distribution and density, as well as that of the fluid rheology would also need to be addressed. Besides, the comparison of different impellers, and the development of alternate correlations based on both experimentation and the use of our CFD-DEM model have already started.

Acknowledgements

The authors would like to thank the Natural Sciences and Engineering Research Council for the financial support, and Dr. Inci Ayranci for insightful discussions.